University of Alberta

TECTONOMETAMORPHIC EVOLUTION OF THE KLUANE METAMORPHIC ASSEMBLAGE, SW YUKON: EVIDENCE FOR LATE CRETACEOUS EASTWARD SUBDUCTION OF OCEANIC CRUST UNDERNEATH NORTH AMERICA

by

JOCHEN ERNST MEZGER

A thesis submitted to the Faculty of Graduate Studies and Research in partial fulfillment of the requirements for the degree of DOCTOR OF PHILOSOPHY

Department of Geology

Edmonton, Alberta

Fall 1997

University of Alberta

Library Release Form

Name of Author: Jochen Ernst Mezger

Title of Thesis: Tectonometamorphic evolution of the Kluane metamorphic assemblage, SW Yukon: evidence for Late Cretaceous eastward subduction of oceanic crust underneath North America

Degree: Doctor of Philosophy

Year this Degree Granted: 1997

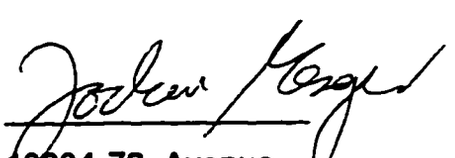

10634-78. Avenue
Edmonton, Alberta
T6E 1P5

June 10, 1997

University of Alberta

Faculty of Graduate Studies and Research

The undersigned certify that they have read, and recommend to the Faculty of Graduate Studies and Research for acceptance, a thesis entitled TECTONOMETAMORPHIC EVOLUTION OF THE KLUANE METAMORPHIC ASSEMBLAGE, SW YUKON: EVIDENCE FOR LATE CRETACEOUS EASTWARD SUBDUCTION OF OCEANIC CRUST UNDERNEATH NORTH AMERICA by JOCHEN ERNST MEZGER in partial fulfillment of the requirements for the degree of DOCTOR OF PHILOSOPHY.

Dr. P. Erdmer

E. L. Jackson for
Dr. T. Chacko

Dr. R. Creaser

Dr. R. Luth

Dr. J. D. Wilson

Dr. T. Forest

E. L. Jackson for
Dr. J. K. Mortensen

03 June 1997

"Ma perchè, se ha percezione di sè non deve aver memoria? La memoria è una potenza dell'anima, e per piccola che sia l'anima che la pietra ha, avrà memoria in proporzione."

"But why, if the stone perceives itself, should it not have memory? Memory is a power of the soul, and however small the soul of a stone, it will have a proportionate memory."

Umberto Eco, "The Island of the Day before"

Abstract

The Kluane metamorphic assemblage (KMA) forms a 160 km NW-SE striking belt of graphitic mica-quartz schist with interlayered ultramafic lenses. It is located east of the Denali fault at the northwestern margin of the Coast Belt of the Western North American Cordillera, between island arc rocks of the Insular Superterrane (INS) to the west and pericratonic assemblages to the east. The lithology of the KMA is distinct from any metamorphic assemblage in the Cordillera.

The dominant structural fabric of the KMA is a pervasive NE-dipping schistosity with a generally east-trending mineral stretching lineation. Mylonitic schists are characterized by a distinct monoclinic fabric that defines westward hangingwall up sense of shear.

The KMA has experienced Late Cretaceous syndeformational high P/low T metamorphism followed by low P/high T thermal overprinting resulting from Early Eocene emplacement of the Ruby Range Batholith (RRB).

Trace element and neodymium isotope signatures of the KMA distinguish its protolith from adjacent flysch of the Dezadeash Formation (DF) which has juvenile signatures and Late Proterozoic model ages, and schists of the pericratonic Aishihik Metamorphic Suite (AMS), part of the Yukon Tanana terrane, with ancient continental crust source and Late Archean model ages. The KMA has intermediate $\epsilon_{Nd}(0)$ values of -4 and T_{DM} of 1.3 Ga, indicative of

homogeneous mixing of ancient and juvenile material.

A possible tectonic model for the evolution of the KMA involves deposition of fine grained pelitic sediments in a backarc basin proximal to a volcanic arc and distal to an ancient continent. Late Cretaceous eastward motion of the Kula plate resulted in collapse of the basin and oblique eastward subduction, with a left-lateral strike-slip component, underneath the North American continental margin (AMS). Sediments of the KMA and parts of the oceanic crust experienced ductile deformation and high P/low T metamorphism during subduction and were added to the upper plate.

Change of plate motion in the latest Cretaceous resulted in Early Eocene sill-like intrusion of the RRB along the suture between the KMA and AMS.

Continuous northward plate motion caused rapid late Eocene uplift of the KMA and juxtaposition with the DF and INS.

ACKNOWLEDGEMENTS

Dr. Philippe Erdmer is thanked for introducing me to the exciting geology of the Northern Canadian Cordillera. His relentless support and guidance throughout the course of my Ph.D. thesis is sincerely appreciated. The Yukon Geology Program, formerly the Yukon Geoscience Office, in Whitehorse provided valuable logistical support and is thanked for usage of facilities and field equipment, as well as sharing helicopter time. In the field discussions of the KMA and AMS with Dr. Steve Johnston of the Yukon Geoscience Office and of the Dezadeash Formation with Dr. Grant Lowey are sincerely appreciated. Important geochronological data was provided by Dr. Jim Mortensen of the University of British Columbia. Together with his thorough knowledge of the geology of the southwestern Yukon, it helped to improve this thesis. Able assistance and companionship in the field was provided by Rob Brown (1993), Kevin Deck (1994) and Brys Francis (1995). The Bayshore Restaurant along the Alaska Highway at the southwestern end of Kluane Lake always welcomed "dirty" geologists and served some of the best food north of latitude 60.

The members of my supervisor committee, Dr. Tomas Chacko, Dr. Robert Creaser and Dr. Karlis Muehlenbachs are thanked for guidance during the my Ph.D. program. I am very thankful to Dr. Thomas Chacko for lengthy discussions on metamorphic petrology and geothermobarometry. Introduction to the unstable world of radiogenic isotopes by Dr. Creaser was fundamental in developing ideas on the origin of the Kluane metamorphic assemblage. It could not have been done without them. Dr. Robert Luth is thanked for help on petrochemical problems.

I am also grateful for discussions with other geologists at various meetings. In particular I would like to thank Dave Brew (USGS Menlo Park), Carol Evenchick (GSC Vancouver), Paul Williams (University of New Brunswick) and Lincoln Hollister (Princeton University). Even if these

discussions were short, they provided me with better understanding and helped to improve my thesis.

Geochemical analyses were provided by Washington State University. Oxygen isotope determinations of the olivine serpentinites were undertaken by Dr. Fred Longstaffe of the University of Western Ontario. One ^{40}Ar-^{39}Ar analysis was done at Queen's University of Kingston, Ontario, by Karen Fallas.

The relentless help and prompt assistance of Paul Wagner of the electron microprobe lab at the Department of Earth & Atmospheric Sciences at the University of Alberta is gratefully acknowledged.

The help and friendship of my fellow graduate students at the University of Alberta in the last four and a half years made the highs and lows of graduate student life more enjoyable and bearable. I am thankful to Rob Stevens for welcoming me to Edmonton and sheltering me for the first weeks. I have learned a lot from discussions with Suman De, Karen Fallas, Steve Grant, George Morris, Dinu Pană, Rob Stevens, Steve Wetherup, and Taro Yamashita. Karen Fallas and George Morris read parts of my thesis and made valuable suggestions that helped to improve my English. Further thanks to Liane Schlickenrieder, Darlene Atkinson, Leslie Driver, Mario Houle, Kerrie-Ann Shannon, Harald Hübscher and Ruth Noronha for their friendship. But most of all I am grateful for the support and friendship of Sabrina Trupia. The next beers will be on me!

I am very grateful for the moral, and often financial, support of my friends and family in Germany, and especially my parents, Trude and Werner Mezger.

Fieldwork for this project was funded by NSERC operating grants to P. Erdmer and research grants from the Canadian Circumpolar Institute (CCI) and the Geological Society of America to the author. Several University of Alberta scholarships provided further financial support that helped to complete this project.

TABLE OF CONTENTS

CHAPTER 1 - INTRODUCTION 1
Statement of problem 2
Previous work 4
Outline of present study 5
CHAPTER 2 - ROCK TYPES AND STRATIGRAPHIC RELATIONSHIPS 7
INTRODUCTION 8
THE KLUANE METAMORPHIC ASSEMBLAGE (KMA) 8
Muscovite-chlorite-quartz schist (calcic schist) 12
Biotite-quartz schist (aluminous schist) 21
Olivine serpentinite 42
RUBY RANGE BATHOLITH 49
POST-EOCENE IGNEOUS INTRUSIONS 54
DEZADEASH FORMATION (JK_D) 56
GREENSCHIST (PMvs) 59
CHAPTER 3 - STRUCTURAL STYLES OF THE KLUANE METAMORPHIC ASSEMBLAGE 61
INTRODUCTION 62
PREVIOUS WORK 66
DUCTILE FABRICS OF THE KLUANE METAMORPHIC ASSEMBLAGE . 66
Planar fabrics 66
Linear fabrics 72
Shear-sense indicators 74
Folds 85
BRITTLE STRUCTURES 88
Faults 88
Jointing 93
STRUCTURAL ANALYSIS OF THE KMA 94
Introduction 94
Results and discussion 94

REGIONAL CORRELATION 100
EVOLUTION MODEL OF THE KMA IN THE NORTHWESTERN COAST BELT 103
D_n 103
D_{n+1} 103
D_{n+2} 103
D_{n+3} 106
D_{n+4} 107
D_{n+5} 108
CONCLUSIONS 110
CHAPTER 4 - METAMORPHIC EVOLUTION OF THE KLUANE METAMORPHIC ASSEMBLAGE 112
INTRODUCTION 113
PREVIOUS STUDIES 114
METAMORPHIC MINERAL ZONES IN THE KMA 115
Introduction 115
Metamorphic character of the KMA along traverses in the Ruby Range 121
GEOTHERMOBAROMETRY OF THE KMA 132
Introduction 132
Estimation of metamorphic pressures and temperatures using computer generated equilibria reactions 134
Results and discussion 135
Regional metamorphic temperature and pressure variations 145
P-T-t PATH VARIATIONS OF THE KMA 148
METAMORPHIC EVOLUTION MODEL OF THE SOUTHWEST YUKON 151
CONCLUSIONS 154
CHAPTER 5 - GEOCHEMICAL AND NEODYMIUM ISOTOPE SIGNATURES OF METAMORPHIC AND SEDIMENTARY ROCKS IN THE SOUTHWEST YUKON 157
INTRODUCTION 158
WHOLE ROCK GEOCHEMISTRY 160

Major elements 160
Rare earth elements 164
Trace elements 168
NEODYMIUM ISOTOPES 170
PROTOLITH PROVENANCE AND REGIONAL CORRELATION 177
Aishihik Metamorphic Suite 177
Dezadeash Formation 181
Kluane metamorphic assemblage 181
CONCLUSIONS 183
CHAPTER 6 - TECTONIC MODEL OF THE KLUANE METAMORPHIC ASSEMBLAGE 185
MODEL OF TECTONIC EVOLUTION 186
Late Jurassic (?) - early Late Cretaceous (~95 Ma) 186
Late Cretaceous (~95-70 Ma) 190
Latest Cretaceous (~72 Ma) - Early Eocene (57 Ma) 193
Early Eocene (57-55 Ma) 194
Eocene (55-40 Ma) 195
Oligocene - Holocene 196
DISCUSSION 196
Evaluation of evidence for dextral strike-slip along the Denali fault zone in the Cenozoic 196
The Denali fault zone in the southern Yukon - a Late Cretaceous suture zone with minor Eocene dextral strike-slip displacement 198
CONCLUSIONS 203
REFERENCES 204
APPENDICES 223
Appendix 1-1: NTS map index of study area 224
Appendix 2-1: Thin section sample localities and observed mineral phases . 225
Appendix 2-2: Electron microprobe analyses of Cr-muscovite ultramafic layers of the KMA 231
Appendix 2-3: Ca-Fe-Mg-rich layers in the Kluane metamorphic assemblage 232

Appendix 2-4: Age determinations of the Ruby Range Batholith 233
Appendix 2-5: Age determinations of mica schists of the KMA and phyllites of the DF 234
Appendix 2-6: Locality map of age determinations of the RRB, KMA and DF 235
Appendix 2-7: ^{40}Ar-^{39}Ar geochronology of calcic schist 94-3 236
Appendix 2-8: Muscovite and whole rock Rb-Sr isochrons of calcic schists of the Kluane metamorphic assemblage 237
Appendix 2-9: Location and $\delta^{18}O$ SMOW values of olivine serpentinites of the KMA 238
Appendix 2-10: Concordia plots of granitic dykes intruding the KMA 240
Appendix 2-11: Felsic and mafic dykes intrusive in the KMA 241
Appendix 3-1: Shear sense indicators deducted from field observations, oriented samples and oriented thin sections 243
Appendix 3-2: Mesoscopic folds in the Kluane metamorphic assemblage ... 245
Appendix 3-3: Application of SpheriStat (version 2.0) 248
Appendix 3-4: Station localities and measured structural data 250
Appendix 3-5: Rotation of lineation of the southern limb of the Ruby Range anticline around anticline fold axis 264
Appendix 3-6: Restoration of lineation and shear-sense direction to pre-F_{n+3}-folding and northeastward tilting 265
Appendix 3-7: Structural data of phyllites of the DF and greenschist PMvs between Telluride Creek and Kathleen River 266
Appendix 4-1 - Electron microprobe conditions and mineral standards 267
Appendix 4-2 - Mineral assemblages and analyzed minerals of geothermobarometry samples 268
Appendix 4-3 - Electron microprobe analyses and calculated endmembers of garnets 270
Appendix 4-4 - Electron microprobe analyses of biotite 274
Appendix 4-5 - Electron microprobe analyses of muscovite 276
Appendix 4-6 - Electron microprobe analyses of plagioclase 277
Appendix 4-7 - Electron microprobe analyses of cordierite 280

Appendix 4-8 - Electron microprobe analyses of spinel 281
Appendix 4-9 - Application of the computer program TWQ 2.02 282
Appendix 4-10 - Equilibria reactions calculated by TWQ 2.02 285
Appendix 4-11 - Compositional zoning profiles of garnets 295
Appendix 5-1 - Descriptions and locations of samples analyzed for geochemistry and Nd, Sr, ^{40}Ar-^{39}Ar isotopes 299
Appendix 5-2 - Analytical procedures for geochemistry and Nd and Sr isotope studies 300
Appendix 5-3 - Neodymium studies in the North American Cordillera 303
Appendix 5-4 - Generalized terrane map of the northern Canadian Cordillera with location of published neodymium studies 306

LIST OF TABLES

Table 3-1: Deformation events in the KMA with associated fabrics and metamorphism 104
Table 4-1: Mineral parageneses and reactions for mica-quartz schist of the KMA with increasing metamorphic grade 119
Table 5-1: Major and trace element abundances of KMA, AMS and DF 161
Table 5-2: Element ratios of mica-quartz schists of the KMA, AMS and Nisling assemblage, and slates of the DF 163
Table 5-3: Sm and Nd concentration and isotopic data for metamorphic and sedimentary rocks of the SW Yukon 173

LIST OF FIGURES

Figure 1-1: Generalized terrane map of the Canadian Cordillera 3
Figure 2-1: General geological map of the southwestern Yukon east of the Denali fault zone with accompanying legend 9
Figure 2-2: Location map of detailed maps and cross-sections 11
Figure 2-3: Outcrop photograph of muscovite-chlorite schist 14
Figure 2-4: Photomicrograph of muscovite-chlorite schist 14
Figure 2-5: Photograph and map of Ca-Fe-Mg-rich layers in the KMA 17
Figure 2-6: Photograph of intrusive contact between the Ruby Range Batholith and the Kluane metamorphic assemblage 20
Figure 2-7: Outcrop photograph of sillimanite-cordierite-biotite-quartz schist . . 25
Figure 2-8: Photomicrograph of sillimanite-cordierite-biotite-quartz schist 25
Figure 2-9: Detailed map of southern Dezadeash Range and Coast Mountains east of Dezadeash Lake 27
Figure 2-10: Detailed geological map of the Jarvis River area, west of Haines Junction 31
Figure 2-11: Photograph of cordierite-biotite-quartz schist xenolith in granodiorite in western Dezadeash Range 32
Figure 2-12: Photograph of granodiorite intrusion into sillimanite-cordierite-biotite-quartz schist of the Kluane metamorphic assemblage 35
Figure 2-13: Geology of the Nasina assemblage at north end of Talbot Arm, Kluane Lake 37
Figure 2-14: Geological map of the Klukshu Lake - Tatshenshini River area . . 40
Figure 2-15: Geological map of central Kluane Lake area with schematic geological and total magnetic field cross-section 45
Figure 2-16: Photograph of Swanson Creek ultramafic lens 46
Figure 2-17: Outcrop photograph of tonalitic gneiss north of Doghead Point ultramafic 51
Figure 2-18: Outcrop photograph of late-synkinematic fine grained biotite granite dyke intruding the KMA at Canyon Bridge, Alaska Highway 53

Figure 2-19: Photograph of feldspar porphyry dyke intruding muscovite-chlorite-quartz schist of the Kluane metamorphic assemblage, ... 55
Figure 2-20: Photomicrograph of Dezadeash Formation slate 58
Figure 2-21: Photomicrograph of Dezadeash Formation phyllite 58
Figure 3-1: Structural map of the KMA 63
Figure 3-2: Structural geology map of the area east of Kluane Lake 64
Figure 3-3: Schematic geological cross sections through the KMA 65
Figure 3-4: Photomicrograph of plagioclase porphyroblast in aluminous mica-quartz schist of the KMA 69
Figure 3-5: Photomicrograph of plagioclase porphyroblast of the calcic schist of the KMA 69
Figure 3-6: Photomicrograph of a synkinematic garnet of the KMA 71
Figure 3-7: Photomicrograph of C/S fabrics in olivine serpentinite of the Doghead Point ultramafic 71
Figure 3-8: Outcrop sketch of S_{n+3} cleavage 73
Figure 3-9: Photomicrograph of δ-type plagioclase porphyroblast in the KMA . 75
Figure 3-10: Photomicrograph of δ-type plagioclase porphyroblast in the KMA 77
Figure 3-11: Photomicrograph of mylonite of the KMA with C'-shear band . . . 77
Figure 3-12: Map with observed shear-sense in the KMA, accompanied by two stereonet plots 81
Figure 3-13: Block model interpretation of shear-sense in the KMA 82
Figure 3-14: Photomicrograph of crd-bt-qtz schist with undeformed crosscutting quartz vein overgrown by cordierite and fibrolite 84
Figure 3-15: Outcrop photograph of open F_{n+3}-fold 86
Figure 3-16: Map displaying major lineaments, dykes and faults in the KMA . . 90
Figure 3-17: Photograph of NNE-trending fault south of Killermun Lake 92
Figure 3-18: Stereographic presentation of total schistosity, mineral stretching lineation and mesoscopic fold axes of the KMA 95
Figure 3-19: Stereographic presentation of schistosity, mineral stretching lineation and mesoscopic fold axes of the northwestern and southeastern structural domains of the KMA 96

Figure 3-20: Stereographic presentation of total schistosity, mineral stretching lineation and mesoscopic fold axes of the northern and southern limb of the southeastern structural domain of the KMA 97
Figure 3-21: Generalized structural map of the southwest Yukon with regional fold axes in the KMA, Nasina and Nisling assemblages and the DF 101
Figure 3-22: Blocking temperature - geochronological age plot of the KMA .. 109
Figure 4-1: Index mineral and mineral isograd map of the KMA 116
Figure 4-2: Detailed index mineral and mineral isograd map of the KMA in the central Ruby Range 117
Figure 4-3: Natural scale metamorphic cross-sections through the KMA in the central Ruby Range 118
Figure 4-4: Petrogenetic grid applied to the KMA 120
Figure 4-5: Photomicrograph of a biotite-quartz schist of the KMA 124
Figure 4-6: Photomicrographs that show the effect of the appearance of cordierite on the texture of the biotite schist 126
Figure 4-7: Photomicrograph of grt-crd-sil-bt schist near contact with RRB .. 129
Figure 4-8: Photomicrograph of grt-crd-sil-bt schist near contact with RRB .. 129
Figure 4-9: Backscatter images of K-feldspar-bearing crd-bt schist 130
Figure 4-10: P-T diagrams of probed mica-quartz schist of the KMA 137
Figure 4-11: Geological map with calculated P-T of analyzed samples 138
Figure 4-12: Photomicrographs of garnets in grt-st-bt schist and crd-bt schist 142
Figure 4-13: Compositional cross-sections of garnets in the staurolite zone and the cordierite zone 143
Figure 4-14: Regional tilt of the KMA, RRB and AMS after Eocene thermal metamorphism 147
Figure 4-15: P-T-t paths of the Kluane metamorphic assemblage 149
Figure 5-1: K_2O/Na_2O versus SiO_2/Al_2O_3, $\sum$REE (ppm), La_N/Yb_N, Eu/Eu* plots.165
Figure 5-2: REE diagrams of the KMA, AMS, DF and average values 167
Figure 5-3: La_N/Yb_N-La/Sc, La/Sc-Th/Sc, Th-U, Zr-Th, La-Th, Ti/Zr-La/Sc diagrams 169
Figure 5-4: Tectonic setting discrimination diagrams 171

Figure 5-5: $\epsilon_{Nd}(0)$-values of the KMA, AMS and DF shown on geological map.174
Figure 5-6: ϵ_{Nd}-evolution diagram for the KMA, AMS and DF 175
Figure 5-7: $\epsilon_{Nd}(0)$ - $^{147}Sm/^{144}Nd$ diagram 176
Figure 5-8: $\epsilon_{Nd}(0)$ versus Th/Sc, La/Sc and La_N/Yb_N diagrams 178
Figure 5-9: Block diagram of published neodymium studies in northern Canadian Cordillera 179
Figure 5-10: Possible tectonic settings for the protolith of the KMA 183
Figure 6-1: Model of tectonic evolution of the KMA 187
Figure 6-2: Model of tectonic evolution of the western North American continental margin in the Late Cretaceous-Early Tertiary 202

Abbreviations used in text and appendices

Mineral phases:

ab	albite
alm	almandine
aln	allanite
alt	undefined alteration
amp	amphibole
an	anorthite
and	andalusite
ann	annite
ap	apatite
aQtz	alpha-quartz
bQtz	beta-quartz
bt	biotite
cal	calcite
cam	clinoamphibole
chl	chlorite
chr	chromite
crd	cordierite
czo	clinozoisite
dol	dolomite
en	enstatite
ep	epidote
fac	ferroactinolite
Fe-crd	Fe-cordierite
fsp	undifferentiated feldspar
grp	graphite
grs	grossular
grt	garnet
hbl	hornblende
hc	hercynite
idd	iddingsite
ill	illite
ilm	ilmenite
jar	jarosite
kfs	K-feldspar
ky	kyanite
mag	magnetite
ms	muscovite
o	opaque
ol	olivine
phl	phlogopite
pl	plagioclase
px	pyroxene
py	pyrope
rt	rutile
qtz	quartz
ser	sericit
srp	serpentine
sil	sillimanite
spn	sphene
sps	spessartine
st	staurolite
tlc	talc
tur	tourmaline
xe	xenotime
zrn	zircon

An_{30} denotes mol.% of anorthite end member in plagioclase.

X_a denotes mol% of end member component. 'a' can be expressed as component (i.e. grs) or as element (i.e. Mg).

Tectonic nomenclature:

AMS	Aishihik Metamorphic Suite
CPC	Coast Plutonic Complex
DF	Dezadeash Formation
DFZ	Denali fault zone
INS	Insular Superterrane
KMA	Kluane metamorphic assemblage
MGMB	Maclaren Glacier Metamorphic Belt
NA	North America
NS	Nisling terrane
RRB	Ruby Range Batholith

Chapter 1

Introduction

Statement of problem

The Kluane metamorphic assemblage (KMA) is a 160 km long, northwest-striking, belt of graphitic mica-quartz schist with interlayered serpentinized dunite bodies, located at the northwestern margin of the Coast Belt of the Canadian Cordillera, in the southwest Yukon (Figure 1-1). The Coast Belt, comprised of granitic and medium to high grade metamorphic rocks, is interpreted to be the result of Cretaceous subduction and/or accretion of two volcanic arcs, the Insular Superterrane (INS) to the west and the Intermontane Superterrane to the east (Gabrielse et al., 1991). The mica-quartz schists of the KMA are unique within the Coast Belt, since they comprise the most extensive homogeneous metamorphic assemblage and the only medium to high grade metamorphic rocks not of continental affinity. The lithology of the KMA is distinct from any other known metamorphic assemblage in the Cordillera.

The KMA is situated at a major boundary in the Canadian Cordillera. To the east, it is bounded by rocks of continental affinity, that comprise the Nisling terrane (Wheeler et al., 1991), thought to be part of the Yukon-Tanana terrane (Mortensen, 1992). To the west, the Denali fault zone separates the KMA from the INS, comprised mainly of the Alexander and Wrangellia terranes, Paleozoic to Cenozoic volcanic arc and oceanic assemblages that were amalgamated in Late Jurassic and accreted to the North American margin by mid-Cretaceous (Gabrielse & Yorath, 1991). The accretion of the INS resulted in mid-Cretaceous to early Tertiary granitic intrusions of the Coast Plutonic Complex (CPC) that underlie the bulk of the Coast Belt (Woodsworth et al., 1991). Metamorphic rocks occur along the western margin and as roof pendants in the CPC and are assigned to the Nisling terrane (Wheeler et al., 1991) or the Yukon-Tanana terrane (Samson et al., 1991a; Brew & Ford, 1993).

The nature and the tectonic setting of the protolith of the KMA were unclear. Despite its location at one of the major fault zones in the Cordillera and the important clues for Cordilleran tectonism that the KMA holds, no

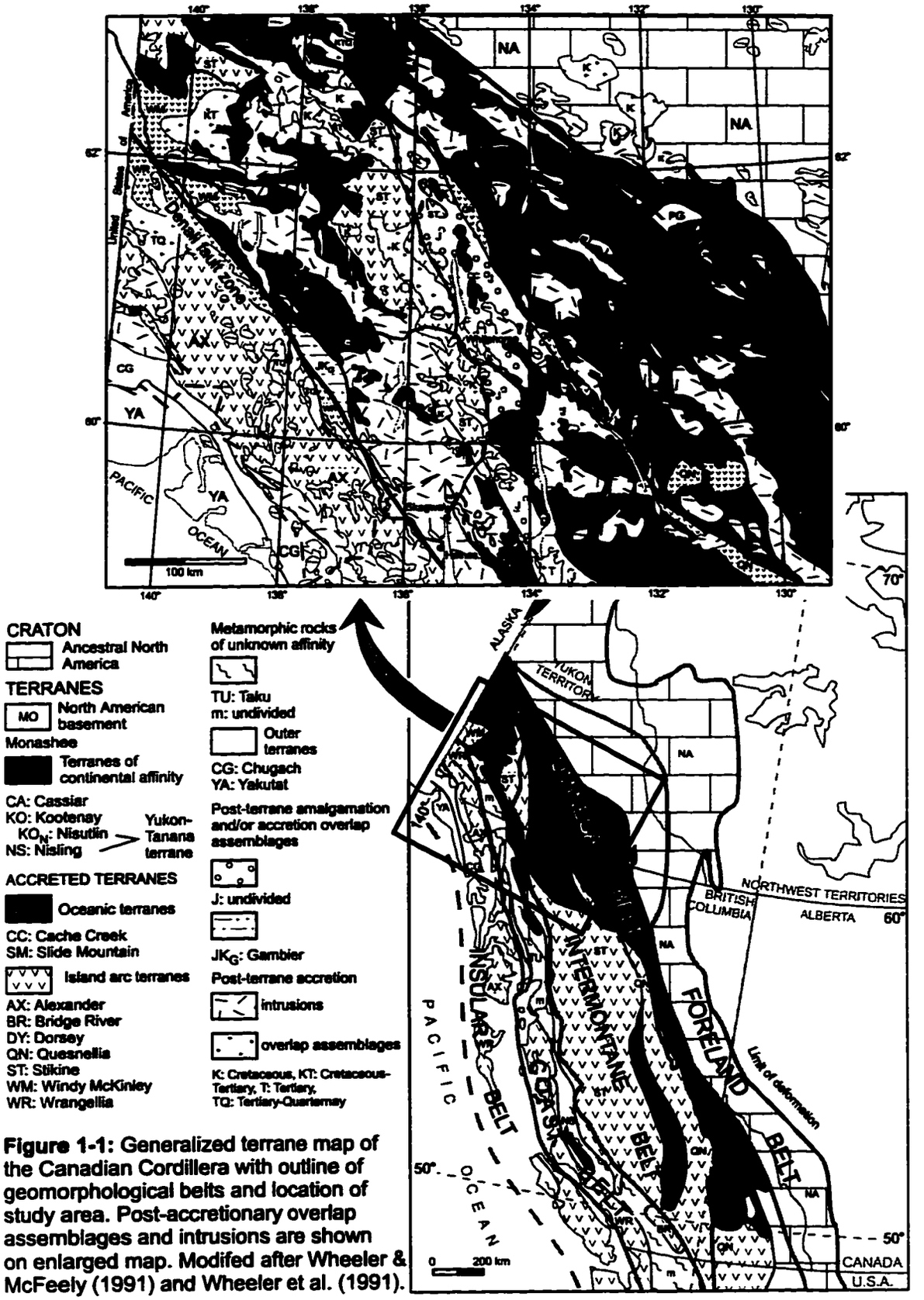

Figure 1-1: Generalized terrane map of the Canadian Cordillera with outline of geomorphological belts and location of study area. Post-accretionary overlap assemblages and intrusions are shown on enlarged map. Modifed after Wheeler & McFeely (1991) and Wheeler et al. (1991).

detailed structural study of the KMA existed prior to this study. The relationship between deformation and peak metamorphism was uncertain. Displacement estimates on bounding faults were primarily based on reconnaissance data. No geochemical or isotope data for the KMA were available to test the various models proposed.

In order to fill these gaps in knowledge, and to develop the first tectonic model of the evolution of the KMA in the framework of the Canadian Cordillera, I undertook a detailed study of the KMA.

Previous work

The term "Kluane metamorphic assemblage" was introduced by Mezger (1995) to emphasize the contemporaneous evolution of mica-quartz schists and ultramafic rocks in one assemblage. Older terms, the "Kluane Schist" of McConnell (1905), widely used by Muller (1967), Eisbacher (1976), Nokleberg et al. (1985), Erdmer (1990), Dodds (1991), and Dodds & Campbell (1992), "Ruby Range metamorphic belt" (Forbes et al. 1974, Turner et al. 1974), "Hornfelsed Schist" (Tempelman-Kluit, 1974) and "Kluane assemblage" (Erdmer, 1991; Erdmer & Mortensen, 1993), only referred to the schistose units. To avoid confusion, the older terminology will only be used in subsequent discussions if a specific point has to be made.

Prior to this study, work consisted of 1:250,000 scale regional mapping, localized structural mapping and thermometry studies, as well as detailed geochronology studies.

Early workers in the Aishihik Lake (Cockfield, 1927), Dezadeash (Kindle, 1952) and Kluane Lake (Muller, 1953a, 1953b, 1958, 1967) map areas included the metamorphic rocks that comprise the KMA in the Precambrian Yukon Group (Cairnes, 1914) or Yukon Complex (Muller, 1967), which were interpreted as metamorphosed geosynclinal sediments.

Tempelman-Kluit (1974) and Erdmer (1990, 1991) recognized the

homogeneity of the mica-quartz schist of the KMA and the orientation of its schistosity, which distinguish it from more heterogeneous metamorphic assemblages of the Nisling terrane to the north and east. A single period of deformation and metamorphism has been observed in the KMA, related to the intrusion of the Ruby Range Batholith during the Eocene, compared to multiple phases of deformation and metamorphism in the Nisling terrane assemblages (Farrar et al. 1988; Erdmer, 1991; Mortensen & Erdmer, 1992).

Forbes et al. (1974), Turner et al. (1974) and Nokleberg et al. (1985) correlated metamorphic rocks and plutonic rocks of the Ruby Range with the Susitna batholith and the Maclaren glacier metamorphic belt (MGMB) in the eastern Alaska Range. Based on this correlation, a post-Eocene dextral offset of 400 km along the Denali fault was proposed. Subsequent workers questioned the amount of displacement (Stout & Chase, 1980; Csejtey et al., 1982).

Eisbacher (1976) interpreted the mica-quartz schist of the KMA as metamorphosed equivalent of Late Jurassic-Early Cretaceous flysch sediments of the Dezadeash Formation (DF), which marks the amalgamation of the Insular Superterrane (Monger et al., 1982). The DF is separated by an alluvium covered valley from the KMA in the east. This correlation was questioned by Erdmer (1990).

Outline of present study

Mapping on a 1:50,000 scale was done in the 1993, 1994 and 1995 field seasons. Map locations are shown in Appendix 1-1. Rock samples and structural measurements were collected for petrographic, metamorphic, structural, geochemical and isotopic studies.

First order interpretation of the KMA is established by a detailed description of rock types of the KMA and their contact relationships, with discussion of possible protolith origin and comparison with adjacent

assemblages. A critical evaluation of previously stated correlations with the KMA (Forbes et al., 1974; Eisbacher, 1976; Nokleberg et al.,1985) points out existing inconsistencies. Consequently, there is no geological evidence to support the postulated 400 km post-Early Eocene offset along the Denali fault.

The following chapter on the structural geology of the KMA documents that one major ductile deformation event, which pre-dates peak metamorphism, has affected the KMA. Shear-sense indicators observed in the KMA record predominantly sinistral shear, an important implication for Cordilleran transcurrent tectonics as the adjacent Denali fault is considered to be a Cenozoic dextral strike-slip fault.

Next, the metamorphic character of the KMA is outlined by mineral isograd maps and a detailed petrographic section across strike. Evidence for thermal metamorphic overprinting of regional metamorphosed rocks of the KMA is presented. Metamorphic pressures and temperatures are established by garnet-biotite-plagioclase-muscovite and garnet-biotite-plagioclase-cordierite geothermobarometry. The metamorphic and structural results provide evidence that the KMA cannot be correlated with the DF or the MGMB.

Whole rock geochemistry and neodymium isotope studies of the KMA, the DF and the Aishihik Metamorphic Suite (Nisling terrane) are presented in Chapter 5. REE plots, discrimination diagrams, isotopic signatures and depleted mantle model ages indicate different tectonic settings for the protoliths of the three assemblages.

A tectonic model of the Kluane metamorphic assemblage is presented in Chapter 6. The results from the previous chapters are incorporated with existing data to form a new model of tectonic evolution of the North American continental margin in the Late Mesozoic and the evolution of the northwestern Coast Belt from the Late Cretaceous to the present.

Chapter 2

Rock types and stratigraphic relationships

INTRODUCTION

This study presents the first detailed description of the lithology of one of the major metamorphic assemblages of the northern Coast Belt of the western North American Cordillera. The petrography, occurrence, and contact relationships of rock types that comprise the KMA and adjacent sedimentary and igneous assemblages are discussed in this chapter. The oceanic character of the KMA distinguishes it from other metamorphic assemblages in the Coast Belt, which have more heterogeneous lithologies that indicate an origin in the proximity of an ancient continental margin. The difference between the KMA and the Maclaren Glacier Metamorphic Belt (MGMB) of the eastern Alaska Range is outlined and it is concluded that a 400 km post-Early Eocene offset along the Denali fault, as proposed by Forbes et al. (1974) and Nokleberg et al. (1985), cannot be determined by correlating these two different metamorphic assemblages.

The general geology of the southwest Yukon east of the Denali fault is shown on Figure 2-1. Figure 2-2 shows the location of detailed maps and cross-sections used in this and following chapters. Locations referred to in the text (i.e. 94-81) and mineral assemblages of sampled rocks are listed in Appendix 2-1.

THE KLUANE METAMORPHIC ASSEMBLAGE (KMA)

The KMA underlies approximately 3000 km^2 of the southern flank of the Ruby Range and the northern Dezadeash Range in the southwest Yukon. To the northeast and east it is in contact with the Ruby Range Batholith (RRB), the northwestern part of the Coast Plutonic Complex (CPC; Brew & Ford, 1993). To the southwest, the alluvium covered Shakwak valley obscures the contact between the KMA and weakly deformed volcanogenic rocks of the Wrangellia terrane, shales and phyllites of the Jurassic-Cretaceous Dezadeash Formation

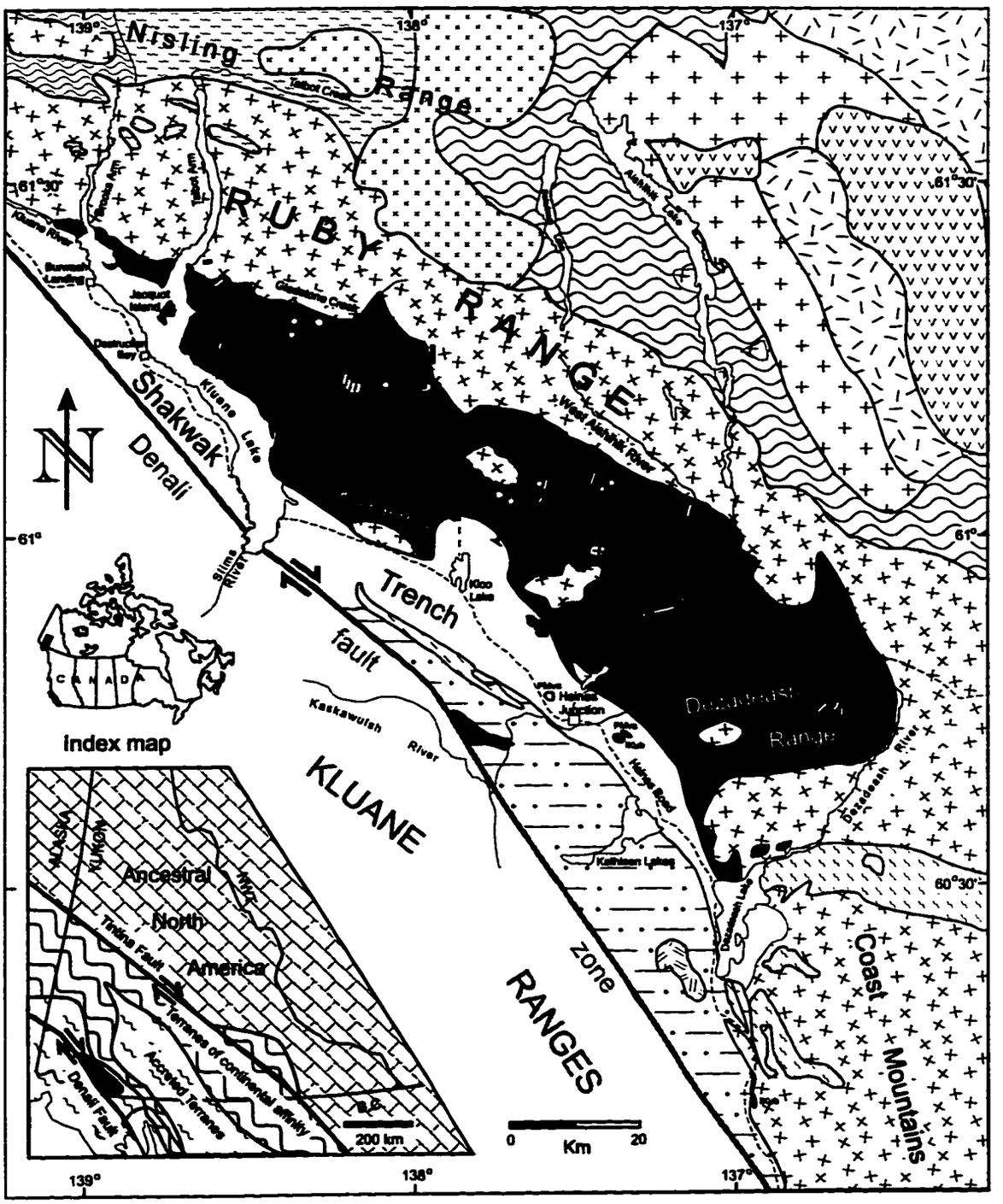

Figure 2-1: Generalized geological map of the southwestern Yukon east of the Denali fault zone with accompanying legend on next page. The Kluane metamorphic assemblage (KMA) is highlighted in grey. Geology outside of KMA is modified after Kindle (1952), Muller (1967), Tempelman-Kluit (1974), Wheeler & McFeely (1991), Dodds & Campbell (1992) and Johnston & Erdmer (1995). Index map shows the approximate setting of the study area in the tectonic framework of the northern Canadian Cordillera.

Geology of the southwest Yukon east of the Denali fault zone

Legend to accompany Figure 2-1

alluvium, glacial till

Late Jurassic - Early Cretaceous

Dezadeash Formation (JK_D)
interlayered mud-, silt- and sandstone with cross bedding, slump folds; graphitic black shale and slate; garnetiferous graphitic phyllite.

IGNEOUS ROCKS

Post-Early Eocene - Pliocene (?)

dacite, diorite, feldspar porphyry
0.5 - 4m thick, undeformed and cross cutting KMA or RRB; lines indicate known strike, dots mark occurance as float.
black: light grey porphyritic massif dacite, partly extremely altered to greenish porphyry
white: medium to fine grained equigranular dark green diorite.

Eocene

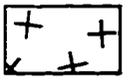

Ruby Range Batholith
equigranular massive salt and pepper biotite granodiorite, biotite-hornblende granodiorite, foliated at intrusive contact; minor amphibolite lenses in sheared contact zone, partly migmatitic; minor massive, medium grained, porphyritic augite diorite and quartzdiorite-gneiss.

Cretaceous and younger

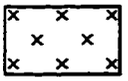

Nisling Range alaskite
medium grained, equigranular, miarolitic leucocratic granite.

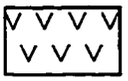

acidic tuff
brightly coloured, light-weathering acidic crystal tuff, lapilli tuff and welded tuff.

Cretaceous

mafic-ultramafic (lKub)
dark green massive, medium grained gabbro norite and serpentinized pyroxenite

Shorty Creek pluton
light grey, medium grained, biotite-hornblende granodiorite.

Early - Mid (?) Jurassic

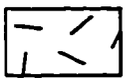

Long Lake Plutonic Suite
pink to white, leucocratic, biotite-hornblende quartz monzonite to granite.

Early Jurassic

Aishihik Batholith
coarse crystalline, equigranular, hornblende diorite and monzodiorite

METAMORPHIC ROCKS

Devonian - Cretaceous

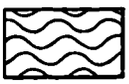

White River Assemblage
brown to black weathering mica-quartz schist minor micaceous quartzite, marble, dark green epidote-hornblende amphibolite.

Paleozoic and (?) Mesozoic

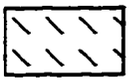

greenschist, meta-andesite (PMvs)
foliated, fine grained, pale green to greenish grey, quartzose epidote-bearing actinolite-chlorite-plagioclase schist, chlorite-plagioclase schist, actinolite schist and hornblende-quartz schist; compositional layering occaisionally observed; minor massive, greenish altered, porphyric meta-andesite.

Cambrian - Devonian

Nasina Assemblage
brown to dark grey weathering, mica-quartz schist, light grey, garnetiferous micaceous quartzite, dark blueish grey weathering, sillimanite-cordierite-bearing mica-quartz schist, marble, calc-silicate.

Late Proterozoic and Paleozoic

Aishihik Metamorphic Suite
brown to black quartzite, grey to brown weathering garnetiferous mica-quartz schist, marble, metabasite, felsic meta-igneous rocks

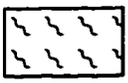

Nisling assemblage
brown weathering, garnetiferous sillimanite-cordierite-biotite-quartz schist, garnetiferous kyanite-biotite-quartz schist, minor garnetiferous amphibolite, marble, calc-silicate.

age unknown

Kluane metamorphic assemblage

purple-grey weathering, garnet-staurolite-sillimanite/andalusite-bearing graphitic biotite-plagioclase-quartz schist with graphitic plagioclase porphyroblasts;
grey-brown weathering, garnet-bearing sillimanite-cordierite-biotite-plagioclase-quartz schist, partly gneissic; minor ortho-amphibole-biotite-plagioclase-quartz schist.

blueish-grey weathering epidote-bearing graphitic muscovite-chlorite-quartz schist, with graphitic plagioclase porphyroblasts; minor lenses of bright green, epidote-amphibolite-Cr-mica-plagioclase-quartz schist and massive actinolite-Cr-mica fels.

light green, olivine serpentinite, massive or foliated lenses within the mica-quartz schists.

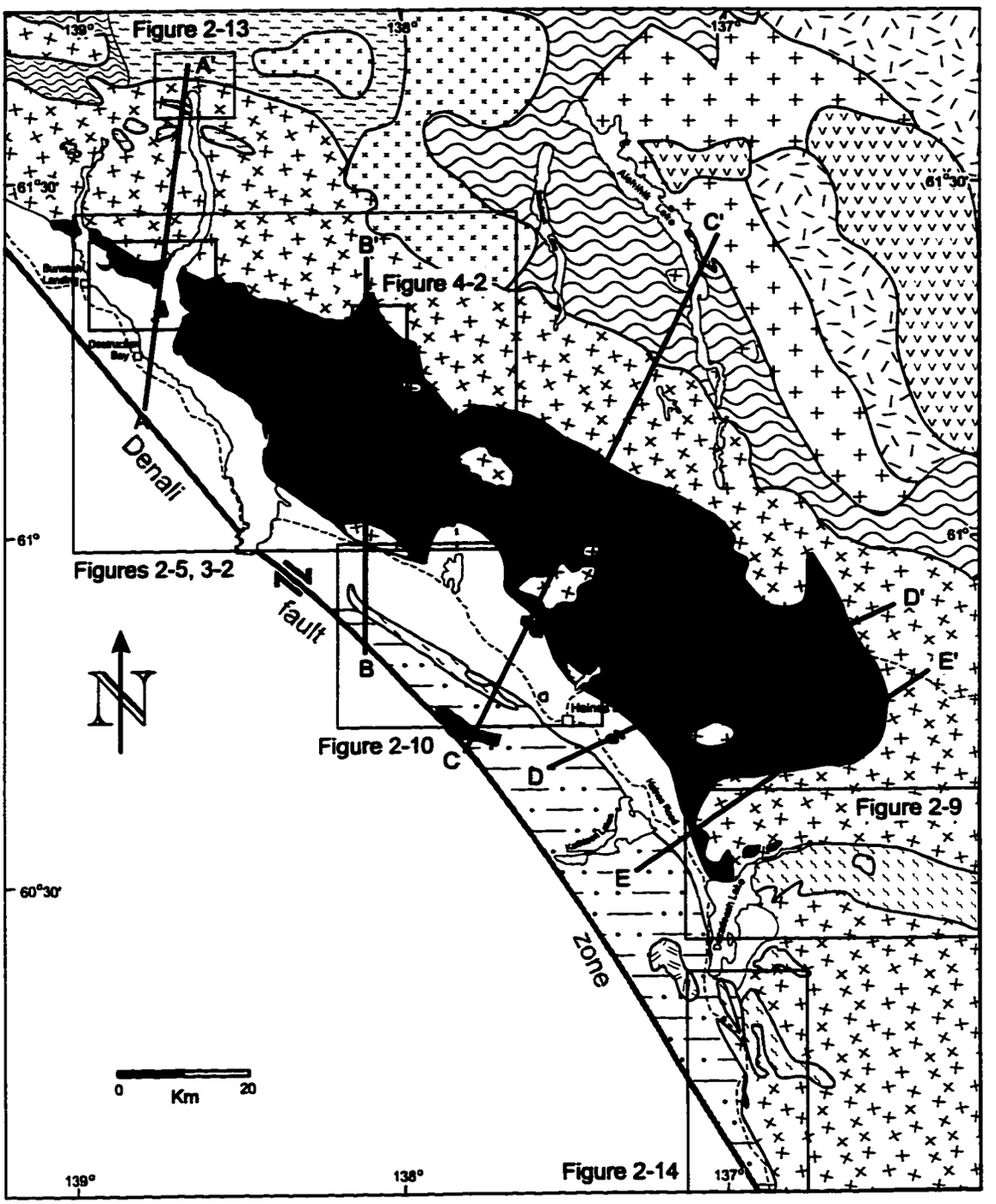

Figure 2-2: Location of detailed maps and cross-sections of Figure 3-3.

(DF) and greenschist (PMvs) that form the Kluane Ranges.

The KMA consists of three rock types that have undergone the same tectonic and metamorphic history, forming an assemblage distinct from adjacent rocks in the northern Cordillera. The two major units are an aluminous biotite-quartz schist and a calcic muscovite-chlorite-quartz schist. Olivine serpentinite bodies of various size occur along strike near the contact of the two schist units. The KMA includes the Kluane assemblage of Erdmer (1991).

Muscovite-chlorite-quartz schist (calcic schist)

The muscovite-chlorite-quartz schist (ms-chl-qtz schist) can be traced for 70 km from the south end of Talbot Arm, Kluane Lake, along the ESE-striking ridge system of the central Ruby Range to the McKinley Creek valley northeast of Kloo Lake, where it tapers out (Figure 2-1). Southeast of Kluane Lake the ms-chl-qtz schist forms the northern part of the Kluane Hills, a lower ridge system parallelling the Ruby Range south of Cultus Creek. The maximum northeast-southwest extension of the ms-chl-qtz schist is 15 km. It also underlies 4-6 km^2 of an isolated hill 12 km northwest of Haines Junction, 15 km south of its major occurrence in the Ruby Range. The ms-chl-qtz schist is equivalent to the "Kluane Schist" of McConnell (1905) and unit 2 on the Kluane Lake map area (Muller, 1967).

The schist is characterized by elongated plagioclase porphyroblasts of 0.3 to 1.0 cm length, giving the foliation plane a "knotty" surface. The porphyroblasts appear dark grey and striped, due to minute parallel graphitic inclusions (Figures 2-3, 2-4). Twinning is not commonly observed. Two different plagioclase compositions, albite (An_{10}) and oligoclase (An_{30}), are observed. However, no systematic plagioclase analysis with the electron microprobe was undertaken, so that exact compositional variation is not known.

A well developed schistosity and mineral stretching lineation is defined by 0.2 to 1.0 mm long chlorite and muscovite grains. Muscovite and chlorite constitute for 20-30 vol.% and form layers of 0.25 to 0.5 mm thickness.

Figure 2-3: Fresh rock face of the muscovite-chlorite schist of the KMA. The greenish appearance is due to abundant chlorite. Quartz-rich bands appear white. Dark grey spots with a diameter of 5 mm are plagioclase porphyroblasts with parallel layers of fine graphite (see photomicrograph of Figure 2-4), that are relics of an earlier slaty cleavage. Orientation of schistosity (S) is indicated by black line. Located at the east shore of Kluane Lake, 7 km east of Destruction Bay (93-11). Scale is in centimeter.

Figure 2-4: Photomicrograph of mylonitic calcic schist of the KMA (95-22). The elongated grey porphyroblast in the center is a plagioclase with inclusions of graphite. The foliation, defined by the platy muscovite grains (yellow interference colour), is deflected around the plagioclase. The asymmetry of the porphyroblast indicates non-coaxial progressive deformation and can be used to determine a sense of shear. The δ-type shape of the crystal suggests top to the left sense of shear. The same asymmetric fabric shape with a top to the left sense of shear is seen in Figure 2-3. Chlorite, not as abundant as muscovite, is characterized by its brown to deep blue interference colour. Note the interlayered bands of almost pure quartz (white to grey).
Scale bar: 0.5 mm. XPL (Crossed Polarized Light)

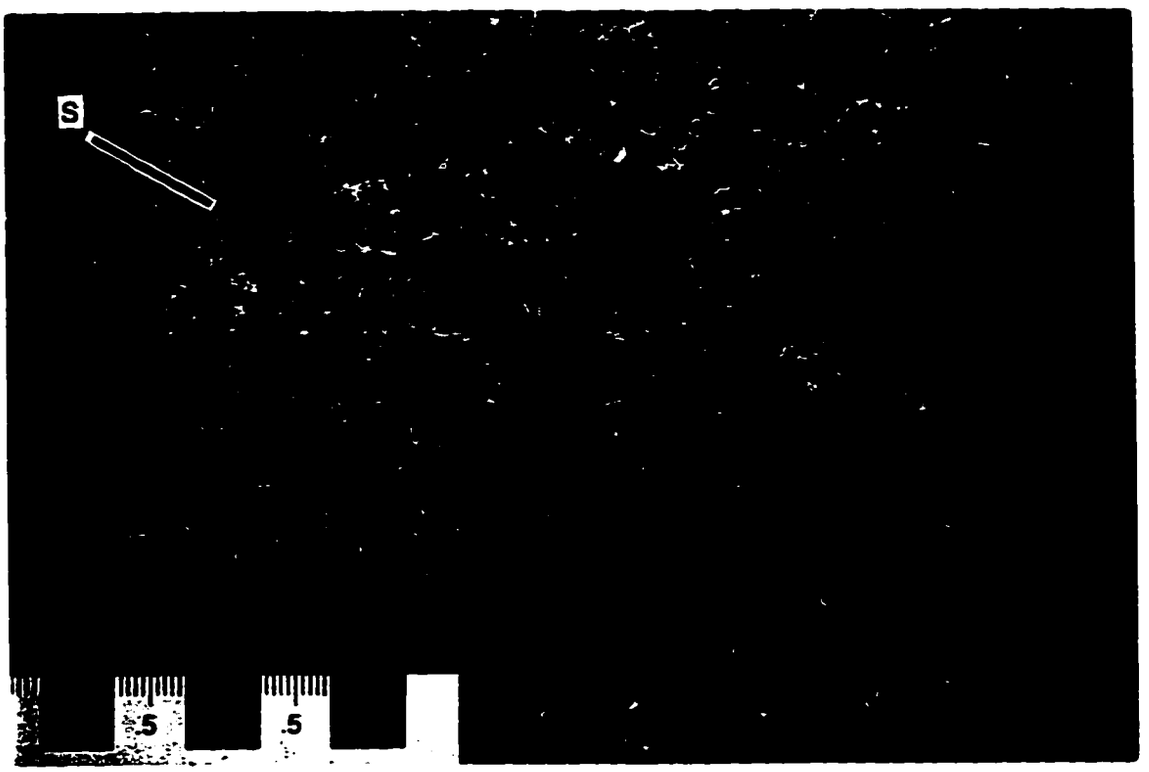

2-3

2-4

Graphitic inclusions in chlorite and muscovite are common.

Quartz (30-50 vol.%) occurs in lenses and layers of 0.5 to 1.0 mm thickness. It forms small (50 to 100 μm) grains with stable grain boundaries and uniform extinction and larger grains (250 to 500 μm) characterized by subgrains and undulous extinction.

Stubby, subhedral to euhedral, 0.25 to 1.0 mm long grains of clinozoisite and minor epidote are common in the schist and can make up to 10 vol.% of the rock. Clinozoisite overgrowth of epidote can be observed. Graphite inclusions are also common.

Brown pleochroic biotite forms 0.2 to 1.0 mm long platy grains. Replacement of chlorite and larger biotite grains that grow at random angle to foliation indicate post-deformational growth. Biotite is absent along Kluane Lake shore, but gradually increases in abundance towards the northeastern contact with the aluminous schist.

Small (250-500 μm), anhedral to subhedral garnets coexist with clinozoisite within one kilometer from the contact with the aluminous schist in the Ruby Range and the Kluane Hills (Figure 4-1). Garnets from one sample (93-64) have a spessartine-almandine composition (X_{sps}=30, X_{alm}=60, see Appendix 4-3).

Tourmaline, forming up to 1 mm long distinct tabular crystals, apatite, sphene, zircon and opaque minerals, mainly ilmenite, are common accessory minerals. Calcite is abundant in schists on Jacquot Island.

A well developed mylonitic fabric with a monoclinic symmetry and mineral stretching lineation, indicating non-coaxial progressive deformation is characteristic for the calcic schist (Figure 2-3). The significance of the asymmetric fabric shapes as shear-sense indicators is discussed in Chapter 3.

A fresh surface of the schist has a silver grey to bluish green grey appearance (Figure 2-3). Weathered rock faces appear darker.

Discontinuous, boudinaged, grass green layers of coarse grained actinolite fels, Cr-mica-actinolite schist and greenish grey Cr-ms-ab-act-ep-chl schist are interfoliated with the ms-chl-qtz schist (Figure 2-5). Actinolite can

Figure 2-5: Lake shore exposure of ms-chl schist with boudinaged thin layers of massive green actinolite-Cr-mica fels and greenish grey Cr-ms-ab-act-ep-chl schist (thick white arrow in foreground). The foliation of the schist dips to the northeast. Crosscutting quartz veins (thin white arrows) are boudinaged. Scale bar is 50 cm (foreground). The observed occurrences of the actinolite-bearing rocks and olivine serpentinite bodies in the KMA are shown on the simplified map. Light grey lines indicate possible along-strike correlation of the actinolite-bearing rocks. The olivine serpentinites are located close to the contact between the ms-chl-qtz schist and the bt-qtz schist. The location of the Denali fault is taken from Dodds & Campbell (1992).

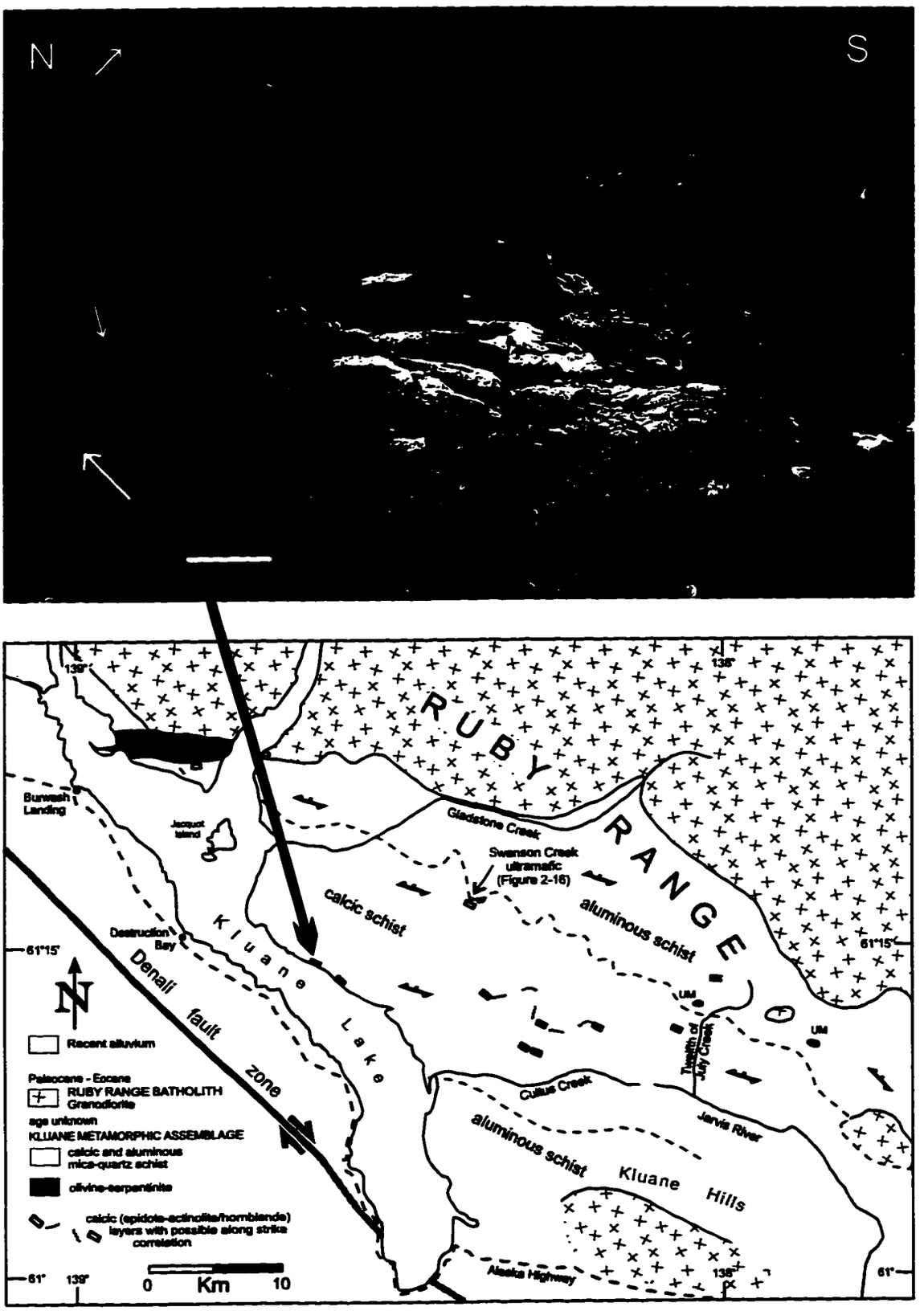
N
S
RUBY RANGE
Burwash Landing
Jacquot Island
Gladstone Creek
Swanson Creek ultramafic (Figure 2-16)
calcic schist
aluminous schist
Destruction Bay
Kluane Lake
Denali fault zone
Cultus Creek
Jarvis River
aluminous schist
Kluane Hills
Alaska Highway
61°15'
61°
139°
138°
0 Km 10
Recent alluvium
Paleocene - Eocene
RUBY RANGE BATHOLITH
Granodiorite
age unknown
KLUANE METAMORPHIC ASSEMBLAGE
calcic and aluminous mica-quartz schist
olivine-serpentinite
calcic (epidote-actinolite/hornblende) layers with possible along strike correlation

form radiating needles of 0.5 to 5 cm length. The green mica is a low Al-, high Cr-, Fe-muscovite (Appendix 2-2). Quartz, calcite and sphene are minor phases. The Cr-ms-ab-act-ep-chl schist has a texture that resembles that of the ms-chl-qtz schist. The thickness of these layers, which generally extend laterally only a few meters, is less than one meter. An exception is a five meter thick layer that be traced for over 150 m north of Cultus Creek (93-159). Three separate layers are inferred from along-strike occurrences of actinolite-bearing rocks on the southern slope of the Ruby Range (Figure 2-5 and Appendix 2-3).

K-Ar muscovite and whole rock and ^{40}Ar-^{39}Ar muscovite ages determined by Stevens et al. (1982), Farrar et al. (1988), Mortensen & Erdmer (1992) and this study range from 42.5 to 54.7 Ma (Appendices 2-5, 2-6, 2-7). K-Ar biotite ages of the Ruby Range Batholith (RRB) are similar (50-57 Ma, Appendix 2-4, Farrar et al., 1988), suggesting that the oldest ages of the KMA reflect peak metamorphism related to the intrusion of the RRB (Mortensen & Erdmer, 1992). Results of microtectonic and metamorphic studies discussed in Chapters 3 and 4 show that peak metamorphism post-dates deformation. Rb-Sr dating of muscovites from samples along Kluane Lake shore did not produce reliable data to allow age constraint on the pre-peak metamorphic fabric (Appendix 2-8). Depleted mantle model ages of 1.29 and 1.42 Ga are calculated from Nd-isotope analyses of two samples (93-156, 94-36, see Chapter 5). These ages do not represent a formation age, but a possible age of the protolith or an intermediate age resulting from mixing of different source rocks.

The ms-chl-qtz schist is structurally overlain and underlain by a bt-qtz schist. The contact with the bt-qtz schist is exposed south of Gladstone Creek and in the Kluane Hills. Muller (1967) described the contact between the two schist units as a southerly verging thrust fault. Erdmer (1991) concluded that it is not a brittle feature and the foliation of both units has a similar northeast dip. The abundance of biotite gradually increases over a few hundred meters, while chlorite and muscovite abundance decrease. In contrast, the transition from calcic clinozoisite/epidote-bearing schist to aluminous garnet-, staurolite-,

andalusite- and/or sillimanite-bearing schist is sharp. Both changes occur in the same area within the KMA, but have different origins. The calcic-aluminous contact is a change in bulk rock composition. It could be a primary sedimentary contact or a faulted contact. Later thermal overprinting from the RRB intrusion caused an increase in metamorphic grade, resulting in the transition from muscovite/chlorite to biotite schist (see Chapter 4). Whole rock geochemistry did not reveal major differences between both schist types (Table 5-1). However, only two samples from the ms-chl-qtz schist unit were analyzed and do not contain any Ca-rich mineral phase (epidote), and may not be representative for that unit. This suggests that aluminous-richer layers are also present in the predominantly calcic sequence.

The eastern margin of the calcic schist is presumed to be a fault covered by overburden in the lowland surrounding Kloo Lake. Evidence for the existence of the fault is given by structural discontinuities, change of plunge of mesoscopic fold axes and presence of south-dipping schistosity east of the fault. The informal name Kloo Lake fault is proposed and used throughout this thesis.

Two olivine serpentinite bodies are located at or close to the contact between the calcic and aluminous schist at Doghead Point on Kluane Lake and in the Ruby Range south of Gladstone Creek (Figure 2-5). The exposed contact is parallel to the foliation of the schist. No alteration of the schist, which would indicate an intrusive contact, has been observed. It is more likely that this contact is fault bounded, also implying a faulted contact between the aluminous and the calcic schist, pre-dating thermal overprinting in the Eocene.

At its eastern margin the ms-chl-qtz schist is in contact with a granodiorite that intrudes the schist diapir-like (Figure 2-6). The intrusive contact is parallel to the foliation of the schist. Sills parallel to the intrusive contact can be observed 30 m away from the contact. This suggests a primary intrusive origin of the contact and not a fault. The plug is interpreted as part of the major intrusion of the RRB, exposed 10 km further north.

Graphite, residual organic matter, and calcium-rich mineral phases

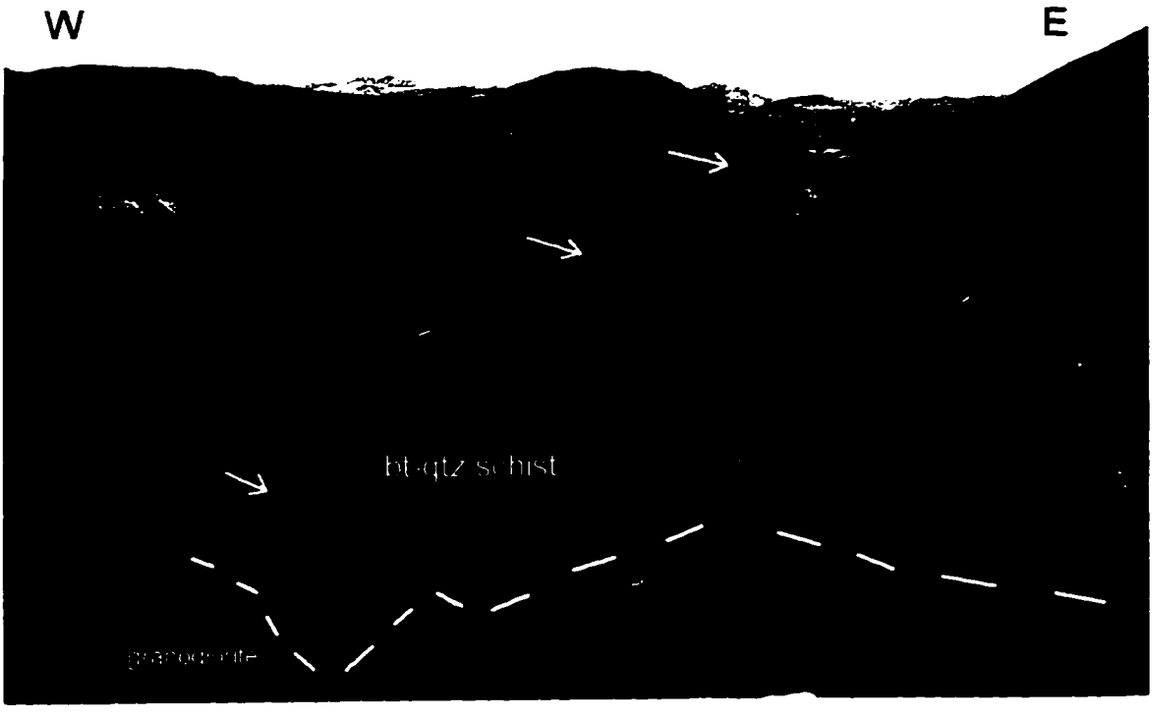

Figure 2-6: Foliation parallel intrusion of the granodiorite of the Ruby Range Batholith into the biotite-quartz schist of the KMA. Several parallel sills of the granodiorite, ranging from 0.5 to 2 m in thickness, can be observed up to 30 m away from the main intrusive body. No foliation or flow banding has been observed in the granodiorite. Killermun Lake is seen in the background. Field assistant standing on plateau in the upper right corner for scale (93-60).

suggest that the protolith of the ms-chl-qtz schist was a calcic shale, depleted in aluminum, interbedded with more aluminous layers (see Chapter 5). The absence of larger sedimentary clasts implies deposition in a quiet basin, distal to the source region.

The actinolite-rich layers have a more mafic protolith. They resemble epidote-actinolite schist of Yardley et al. (1990), which are interpreted as greenschist grade metamorphosed volcanogenic sediment or lava flow. Crenulation folds defined by small actinolite needles and preserved in albite porphyroblasts suggest a sedimentary origin, rather than lava flows. The minor occurrence of these mafic layers suggests restricted and minor source.

Biotite-quartz schist (aluminous schist)

The most common rock type of the KMA is a biotite-quartz schist which underlies approximately 75% of the study area shown on Figure 2-1. It can be traced over 160 km from the mouth of Kluane River, at the northwestern end of Kluane Lake, to the southern and eastern part of the Dezadeash Range.

The biotite-quartz schist is equivalent to the rock types described as unit A by Kindle (1952) on the northern Dezadeash map area, unit 1 south of the RRB on the Kluane Lake map area (Muller, 1967), and PPsqr in the southern part of the Aishihik Lake map area (Tempelman-Kluit, 1974).

The bt-qtz schist contains graphitic plagioclase porphyroblasts similar to those of the ms-chl-qtz schist. Biotite is the dominant sheet silicate and defines the main foliation. Muscovite and chlorite occur only as accessory minerals or are absent. Alteration of plagioclase and biotite to sericite, a fine grained muscovite, and chlorite, respectively, is common. Plagioclase also is present in the matrix. Plagioclase composition does not vary within a sample or between porphyroblast and matrix grains. Throughout the bt-qtz schist the composition ranges from An_{23} (oligoclase) to An_{36} (andesine), as determined by electron microprobe (Appendix 4-6).

Whereas the calcic schist contains Ca-rich mineral phases (clinozoisite,

epidote and calcite), common minerals of the bt-qtz schist are Al-rich mineral phases: garnet, staurolite, andalusite, sillimanite, cordierite, K-feldspar and spinel. Therefore the bt-qtz schist is also referred to as aluminous schist. The Al-rich minerals occur in zones that parallel the contact with the RRB. Their first appearances towards this contact can be traced as mineral isograds and describe increasing metamorphic grades that define a contact metamorphic aureole around the batholith (Chapter 4, Figure 4-1).

Garnets are commonly subhedral to anhedral, poikilitic, ranging from 0.25 to 10 mm in diameter. They are purple red coloured Fe- and Mn-rich, almandine-spessartine garnets (Appendix 4-3). Zoning of the grains can be determined by electron microprobe and provides important information on the pressure-temperature path during garnet growth. Rare preserved spiral shaped graphitic inclusion trails indicate synkinematic growth (Figure 3-6). Garnet rims are commonly altered to chlorite, sericite and biotite. Replacement of the garnet core by biotite can also be observed.

Staurolite occurs as subhedral, rarely euhedral, porphyroblasts (0.5-3 mm) with graphitic inclusion trails in a narrow zone throughout the Ruby Range and in the Western Dezadeash Range.

Andalusite forms anhedral to subhedral, poikilitic, colourless crystals. Inclusions of quartz and biotite are common. The grains have an average size of 0.5 to 3 mm. Andalusite appears synchronous with biotite at the muscovite-biotite boundary. Overgrowth of staurolite indicates that andalusite is formed by the breakdown of staurolite (Figure 4-5).

Sillimanite occurs as fine needles of fibrolite with lengths of less than 200 μm and widths of a few tens of μm. Fibrolite commonly nucleates in biotite and grows parallel to the cleavage of the biotite crystal (epitaxial growth, Figure 4-6), as well as in plagioclase, quartz and cordierite. In rocks with abundant sillimanite, the fibrolite needles radiate away from the margin of biotite grains into the felsic layers. Coarse sillimanite was observed only at two locations, close to the contact with the RRB (94-147c, 94-174).

In the eastern Ruby Range and the eastern and southern Dezadeash

Range Fe-rich cordierite (Appendix 4-7) forms porphyroblasts up to 3 mm in diameter (Figures 2-7, 2-8, 2-9). Inclusions of small cubes or worms of deep green coloured hercynite, a Fe-Al-spinel (Appendix 4-8) and fibrolite needles are common. Hercynite is found in samples in close proximity (generally less than 1 km) to the intrusive contact with the RRB.

K-feldspar has been identified by electron microprobe as discrete grains in the order of 100 µm in certain cordierite-bearing samples (Figure 4-9). The paragenesis with cordierite and textural evidence that potassium-feldspar grows on the expense of biotite suggest a metamorphic origin. Estimation of modal abundance of K-feldspar is difficult, since it lacks twinning, and cannot be distinguished by optical petrology from the more abundant, but also commonly untwinned, plagioclase.

Due to abundant biotite the aluminous schist is darker than the ms-chl-qtz schist, and has a purplish grey to dark brown coloured rock face, depending on the state of weathering. Large plagioclase porphyroblasts give the foliation plane a "knotty" appearance. A well developed schistosity with a monoclinic symmetry and mineral stretching lineation, similar to the fabric of the calcic schist, is characteristic of aluminous schist in the western Ruby Range and Dezadeash Range.

In the eastern Ruby Range and eastern Dezadeash Range, the schist is coarser, less well foliated and mineral lineations are absent. Quartz layers are comprised of large single crystals instead of a multitude of smaller grains or subgrains. Biotite crystals are up to one millimeter in size and overgrow the foliation plane (Figure 2-8). The coarsening is related to thermal recrystallization of quartz, plagioclase and biotite and new growth of cordierite near the contact with the RRB.

A light bluish grey coloured orthoamphibole-biotite-plagioclase-quartz schist occurs in the eastern Dezadeash Range. The orthoamphibole is Fe- and Mg-rich, a gedrite or anthophyllite, and forms poikilitic, anhedral grains, ranging in size from 0.25 to 0.75 mm. Although cordierite is abundant in the adjacent schist, it is absent in the orthoamphibole-bearing schist. The different mineral

Figure 2-7: Sillimanite-cordierite-biotite-quartz schist of the KMA in the eastern Dezadeash Range (94-275). Note the contrast in appearance to the muscovite-chlorite schist along Kluane Lake in Figure 2-3. The rock appears coarser. Compositional banding is more pronounced than in the schist of Figure 2-3. No asymmetry can be observed in the fabric. However, geochemical and isotope studies from samples close to both localities (94-36 and 94-272) show that the rocks have had a similar protolith (Chapter 5), and the different appearance is due to an increase in metamorphic grade compared to the rock in Figure 2-3.

Figure 2-8: Photomicrograph of a sillimanite-cordierite-biotite-quartz schist 2.5 km east of the location of Figure 2-7 (90-33). The rock appears gneissic, almost granoblastic in thin section. Note the contrast to the well foliated ms-chl schist in Figure 2-4. Scale is the same in both photographs.
Scale bar: 0.5 mm. XPL

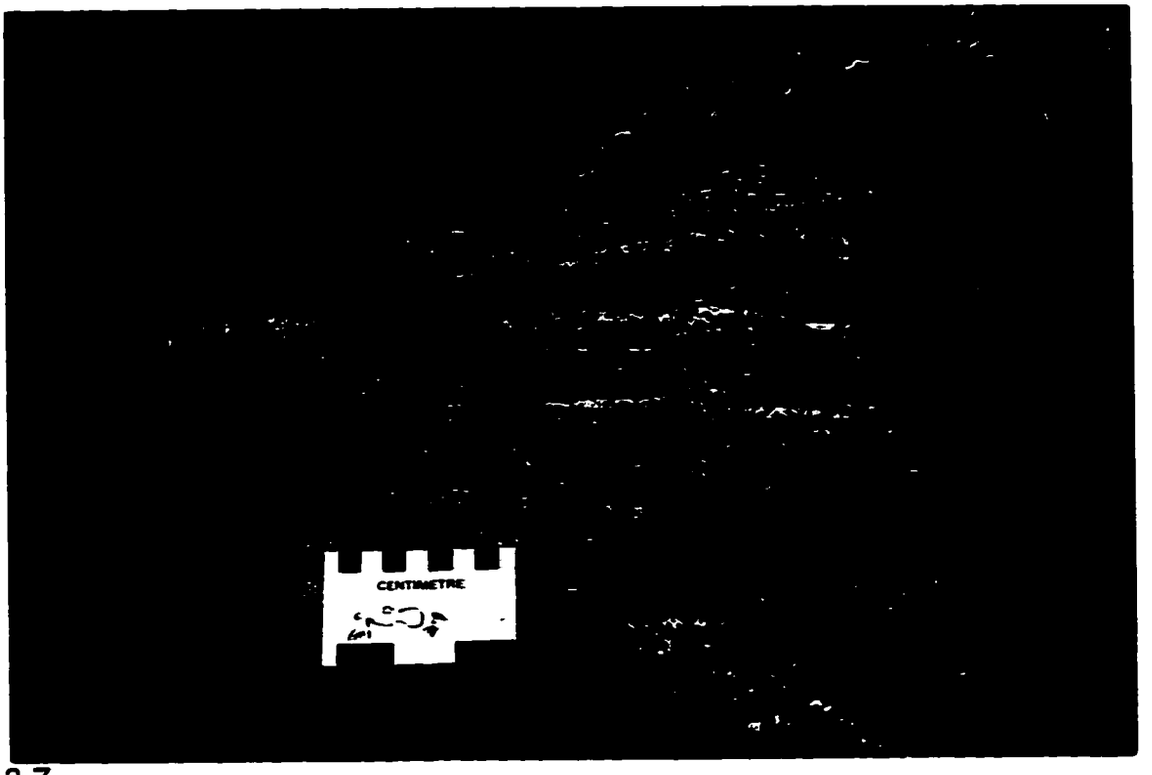

2-7

2-8

Figure 2-9: Detailed geological map of the southern Dezadeash Range and the Coast Mountains east of Dezadeash Lake. The area near Undie Creek was mapped by Erdmer (1990) and the metamorphic rocks assigned to the Nisling assemblage. The geology at the 1798 m peak and north of Undie Creek is adapted after Kindle (1952). Assumed contacts are shown as dashed lines. See Figure 2-2 for location.

DEZADEASH RANGE
KLUANE RANGES
Dezadeash Lake
702 m
1798 m
Haines Road
Alsek River
Kluane River
Dezadeash River
Aaumbo Creek
Mile Creek
Sky Creek
136°45'
137°
60°30'
2 km
112/38
LATE PROTEROZOIC - PALEOZOIC
Nisling assemblage
gamet-staurolite-biotite-quartz schist
marble, calc-silicate
EOCENE
Coast Plutonic Complex
biotite granodiorite
hornblende-biotite granodiorite
LATE JURASSIC - EARLY CRETACEOUS
Dezadeash Formation
interbedded grey sand-, silt- and mudstone
AGE UNKNOWN
Kluane metamorphic assemblage
graphitic biotite-plagioclase-quartz schist
schistosity with dip angle
schistosity and mineral stretching lineation measured on schistosity
mesoscopic fold axis
bedding with dip angle
geological contact: observed, assumed

assemblage is also reflected in its geochemistry and neodymium isotope composition, indicating an andesitic composition and juvenile isotopic signature, compared to the pelitic bt-qtz schist with its more evolved signature (Chapter 5). The orthoamphibole-bearing schist has a texture similar to the cordierite-bearing bt-qtz schist, and cannot be distinguished from the bt-qtz schist in hand samples. The contact relationship with the cordierite-bearing schist and the exact extent of the orthoamphibole-bearing schist are not known. It was observed at only one location in the eastern Dezadeash Range (94-297/1). Samples from locations 1-2 km away are cordierite-bearing bt-qtz schist. The orthoamphibole schist appears to be a local occurrence and is not shown as a separate unit on the map of Figure 2-1. The similarity of the texture with the cordierite schist and the lack of evidence for hydrothermal alteration (enrichment or depletion of mobile elements Sr, Ba, etc., see Table 5-1) suggest that the protolith of the orthoamphibole schist was a metamorphosed first cycle sedimentary rock derived from an andesitic source, rather than a metamorphosed and altered andesitic flow.

Quartz bands, from a few centimeters to half a meter thick, crosscut the ms-chl schist along the eastern Kluane Lake shore. Deformed and boudinaged quartz layers may be transposed original quartz-rich sedimentary layers or late synkinematic veins related to the early magmatic phase of the RRB (Figure 2-5). Undeformed NNE-striking veins resemble tension gashes (93-9), compatible with NNE-SSW compression in the Early Tertiary (Engebretson et al., 1995; see Chapter 3). Undeformed quartz veins crosscut by granitic dykes at the northeastern margin of the KMA, east of Aishihik River indicate pre-RRB origin of the veins (S. Johnston, pers. comm., 1994).

The contact of the aluminous with the calcic schist is described above and interpreted as a pre-peak metamorphic faulted contact between rock types of different sedimentary protoliths.

The nature of the contact between the bt-qtz schist and the two olivine serpentinite bodies is the same as described for the calcic schist above. The bt-qtz schist overlies the olivine serpentinite south of Gladstone Creek, while it

partially underlies the body at Doghead Point (Figure 2-15). Two smaller olivine serpentinites are interlayered with the bt-qtz schist. Their contacts are not exposed.

Exposed contacts of the bt-qtz schist with the main body of the RRB are parallel to the foliation of the schist. In the Ruby Range, the foliation of the schist dips north to northeast underneath the granodiorite intrusion. Similar dip of the schist underneath the intrusion is observed in the western Dezadeash Range, while the RRB dips northward underneath the bt-qtz schist in the eastern Dezadeash Range.

A weak gneissic foliation can be observed in the granodiorite up to a hundred meters away from the contact (93-32). At diapirs and plugs of the RRB within the KMA, foliation parallel and crosscutting contacts are common (Figure 2-6). Deflection of the foliation of the schist can occur near the contact (Figure 2-10). Xenoliths of the schist found the granodiorite in the southern Dezadeash Range confirm the intrusive nature of the contact (Figure 2-11).

The age of the protolith of the bt-qtz schist is not known. No detrital zircon ages are recorded. Depleted mantle model ages calculated from neodymium isotope composition range from 1.22 to 1.45 Ga for the bt-qtz schist, similar to the ages for the ms-chl-qtz schist (1.29 and 1.42 Ga). The similarities of the model ages and Nd-isotope composition for both schist types suggest that their protoliths, although one more calcic and the other more aluminous, are of the same age. The orthoamphibole-bearing bt-qtz schist has a younger model age of 720 Ma, which may represent the actual age of its protolith, as it may not have been derived from sedimentary mixing as the other bt-qtz schist and ms-chl-qtz schist samples. This is discussed further in detail in Chapter 5.

K-Ar biotite ages determined for the bt-qtz schist range from 45.4 to 61.7 Ma (Appendices 2-5, 2-6; Stevens et al., 1982; Farrar et al., 1988; Mortensen & Erdmer, 1992). U-Pb monazite and xenotime ages of schist samples near the contact with the RRB yielded ages 2 to 5 Ma older than K-Ar biotite dates, suggesting rapid cooling of 40-165° C/Ma of these rocks (Erdmer & Mortensen,

Figure 2-10: Detailed geological map of the Jarvis River area, west of Haines Junction. Note the isolated plug of diorite north of Garnet Creek. The location of two samples analyzed for geothermobarometry (Chapter 4) is also shown. The geological contacts at Mt. Decoeli are adapted from Dodds & Campbell (1992). Geology west of Kloo Lake is adapted from Muller (1967).

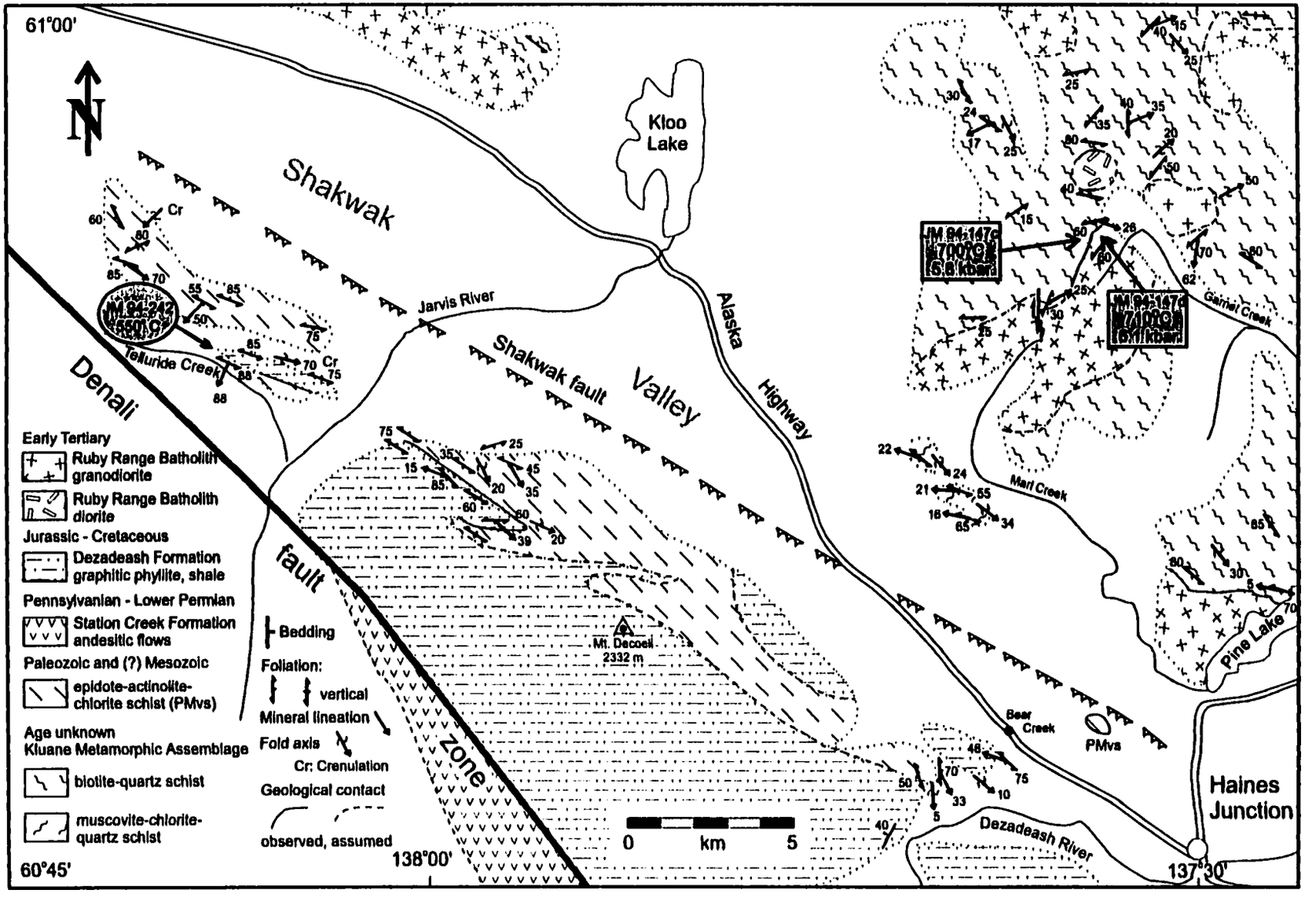
61°00'
N
Kloo Lake
Shakwak
Jarvis River
Alaska Highway
Shakwak fault
Valley
Denali
fault
Zone
Telluride Creek
Garnet Creek
Marl Creek
Pine Lake
Bear Creek
Mt. Decoeli
2332 m
PMvs
Haines Junction
Dezadeash River
0 km 5
60°45'
138°00'
137°30'
Early Tertiary
Ruby Range Batholith granodiorite
Ruby Range Batholith diorite
Jurassic - Cretaceous
Dezadeash Formation graphitic phyllite, shale
Pennsylvanian - Lower Permian
Station Creek Formation andesitic flows
Paleozoic and (?) Mesozoic
epidote-actinolite-chlorite schist (PMvs)
Age unknown
Kluane Metamorphic Assemblage
biotite-quartz schist
muscovite-chlorite-quartz schist
Bedding
Foliation:
vertical
Mineral lineation
Fold axis
Cr: Crenulation
Geological contact
observed, assumed

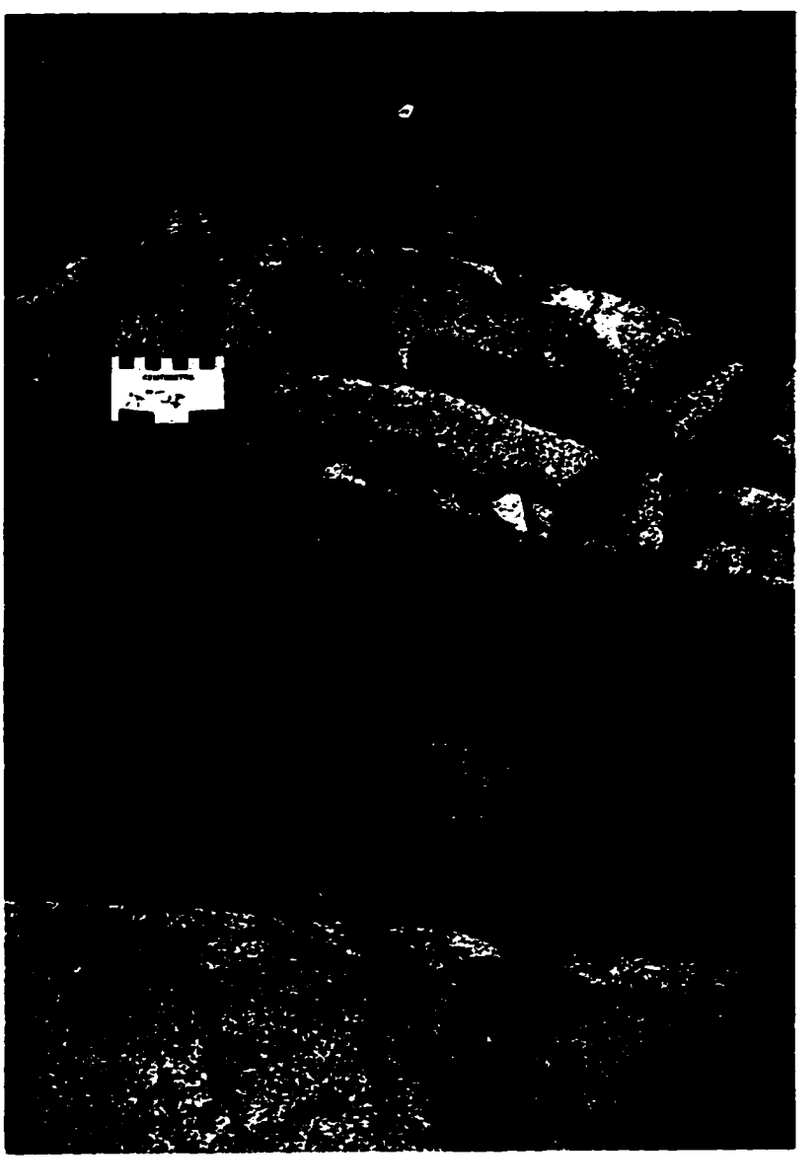

Figure 2-11: Light grey granodiorite of the Ruby Range Batholith intruding dark cordierite-biotite-quartz schist of the KMA. Note xenolith band of the schist next to the scale bar (8 cm). Southwestern slope of Dezadeash Range (95-38).

1993). Mortensen & Erdmer (1992) interpret monazite and xenotime as metamorphic in origin and their U-Pb ages date peak metamorphism of the KMA. Younger ages in the southwestern part are explained by slower cooling and/or slower rates of uplift. A K-Ar biotite age of 140 Ma as reported by Lowdon (1960) is regarded as unreliable due to low K content (Erdmer & Mortensen, 1993).

The bt-qtz schist of the KMA is derived from a homogeneous package of pelitic sediments. Abundant graphite preserved as thin layers in plagioclase porphyroblasts is residual organic matter. Almandine-spessartine garnet, staurolite, sillimanite/andalusite and cordierite are typical minerals found in medium grade metamorphosed aluminous pelitic sediments. Trace element and neodymium isotope signatures of the bt-qtz schist indicate homogeneous mixing of sediments derived predominantly from a volcanic arc source with minor detrital input from ancient continental crust (see Chapter 5). Minor occurrences of orthoamphibole-bearing schists within the aluminous schist are interpreted as metamorphosed sediments directly derived from an andesitic source, without mixing with continent-derived material. The similarity of the appearance and major mineral assemblage of the calcic and aluminous mica-quartz schist, implies similar depositional environment, with slightly different geochemical bulk composition of the source material.

The KMA has been interpreted as the metamorphosed equivalent of the Dezadeash Formation (Eisbacher, 1976). Trace element and neodymium isotope data, discussed in Chapter 5, show that the DF has more juvenile signatures than the KMA, suggesting a volcanogenic source without mixing with continent-derived material.

Erdmer (1991) proposed a faulted contact between bt-qtz schist of the KMA to the west and biotite schists of the Aishihik assemblage (equivalent to Nisling assemblage of Erdmer (1990)) to the east, east of Van Bibber Creek in the eastern Dezadeash Range. Aishihik assemblage rocks, described east of Dezadeash Lake and around Kusawa Lake, are more heterogeneous than the KMA and contain biotite schist, granitic gneiss, biotite granodiorite gneiss,

amphibolite and minor quartzite, marble and calc-silicate (Erdmer, 1990, 1989). In light of recent field studies and detailed thin section analyses the existence of a contact between the KMA and the Aishihik assemblage in the Dezadeash Range cannot be supported:

(1) The mineral assemblage of the KMA in the easternmost Dezadeash Range is similar to cordierite-bearing KMA schists in the eastern Ruby Range, with the exception of orthoamphibole-bearing schist described above. The rocks are brownish grey weathering coarse grained sillimanite-cordierite-biotite schist, resembling cordierite-biotite schist found in roof pendants in the southern Dezadeash Range (Figures 2-7, 2-8).

(2) Coarsening of the schist towards the east is attributed to static recrystallization in proximity of the contact with the RRB and obscures foliation (see Chapter 4).

(3) Quartzite, marble and calc-silicate described by Erdmer (1991), as typical of the east, were not found at this location.

(4) A small (1 km^2) strongly foliated granodiorite plug, not reported by Erdmer (1991), is found close to the proposed contact. Xenoliths of the crd-sil-bt schist are found at the margin of the intrusion. The intrusive contacts are sharp and no migmatization of the schist is observed. (Figure 2-12).

(5) Whole rock geochemistry and neodymium studies do not indicate major lithological changes within the eastern Dezadeash Range (Chapter 5).

The mica-quartz schists of the KMA are distinct from all other metamorphic assemblages north and southeast of the RRB, and roof pendants within the RRB north of Kluane Lake. These assemblages are, from northwest to southeast, the White River Assemblage, Nasina Assemblage, Aishihik Metamorphic Suite (AMS), and the Nisling assemblage (Figure 2-1). These assemblages contain a variety of rock types, including mica-quartz schist, micaceous quartzite, quartzite, calc-silicate, marble, amphibolite (Muller, 1967; Erdmer, 1990; Wheeler & McFeely, 1991; Johnston & Timmerman, 1993a). The AMS also includes metabasite and meta-igneous rocks and is correlated in

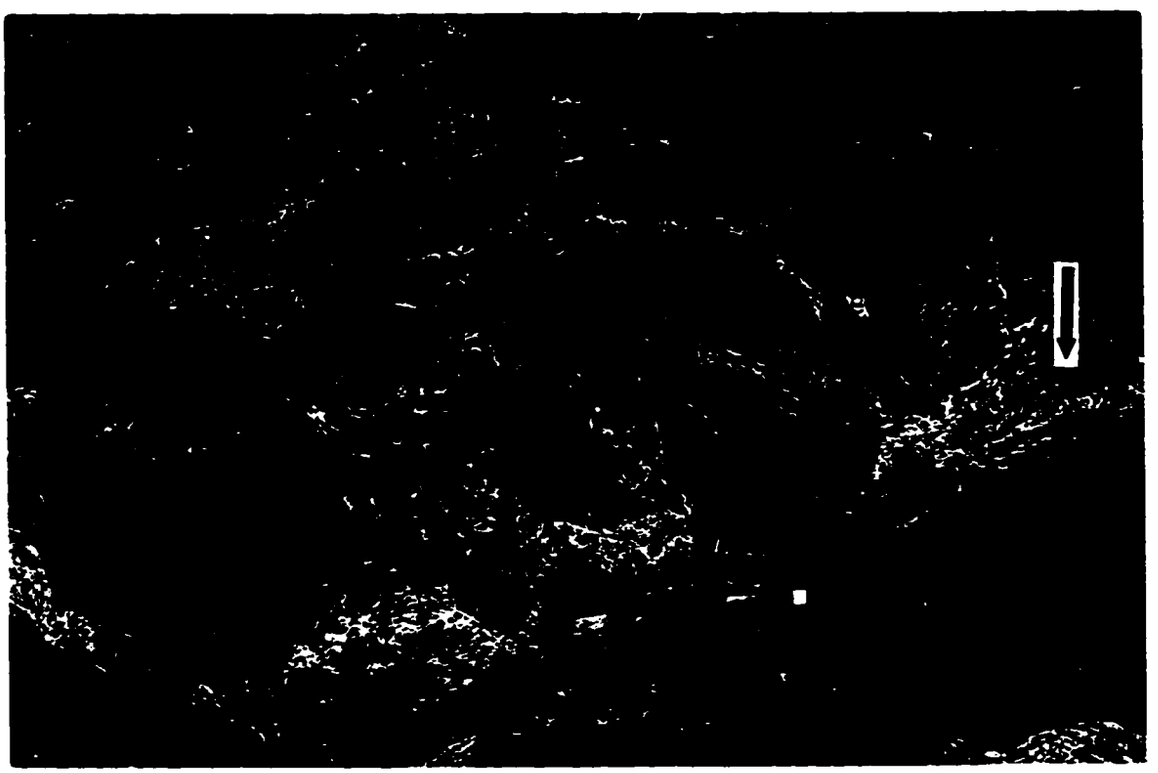

Figure 2-12: Intrusive contact between sillimanite-cordierite-biotite-quartz schist of the KMA and medium grained bluish grey granodiorite in the eastern Dezadeash Range (94-276). The contact is generally sharp. The igneous intrusion occurred along existing foliation plane or along fractures. The host schist is not migmatized. Reaction rims in the host rock are not observed. The fold in the left hand corner apparently pre-dates the intrusion. Arrow points at flow banding, dark mafic layers and leucocratic bands in the granodiorite.

part with the Nisling and the Nasina assemblages (Johnston & Timmerman, 1993a). Muller (1967) included the Nasina Assemblage, exposed north of the RRB, in the same unit 1 with the bt-qtz schist of the KMA. Intercalated layers of mica-quartz schist, micaceous quartzite, marble and calc-silicates were observed during mapping for this study, establishing the lithologic differences between the Nasina Assemblage and the KMA (Figure 2-13). The Nasina and Nisling assemblages and the AMS are interpreted as Late Proterozoic to Paleozoic continental margin and off-shelf sediments, associated with the pericratonic Nisling terrane (Erdmer, 1990; Wheeler & McFeely, 1991; Johnston & Timmerman, 1993a). Geochemical and neodymium isotope studies of mica-quartz schists from the AMS confirm their mature provenance (Chapter 5). The White River Assemblage is associated with Paleozoic-Mesozoic oceanic assemblages (Wheeler & McFeely, 1991).

Metamorphic rocks exposed along the western part of the Coast Mountains, south of Dezadeash Lake and in northern British Columbia, are mapped as "unit 1" by Kindle (1952) on the Dezadeash map area and "Msm" on the Tatshenshini map area (Dodds & Campbell, 1992). These metamorphic rocks are assigned to the "Kluane Schist" by Eisbacher (1976) and Dodds & Campbell (1992). However, they differ in petrology from the bt-qtz schist of the KMA. Metamorphic rocks south and southeast of Dezadeash Lake are generally graphite-free garnetiferous biotite quartzites. Feldspar occurs only as a minor phase. Kyanite-staurolite-garnet assemblages in biotite schists southeast of Dezadeash Lake indicate that these rocks experienced high P/high T conditions unlike the KMA (Chapter 4). 50 meter thick marble bands, interlayered with a biotite schist, are observed south of Klukshu Lake (Figure 2-14). Quartzite and marble are characteristic for the Nisling assemblage, but are absent in the KMA. Whole rock major element geochemistry of a garnetiferous biotite quartzite east of Dezadeash Lake (94-358) also suggests a continental provenance for these metamorphic rocks (Chapter 5). The metamorphic assemblages south of Dezadeash Lake are part of the Nisling assemblage of Erdmer (1990) and not correlative with the KMA as Eisbacher (1976) proposed.

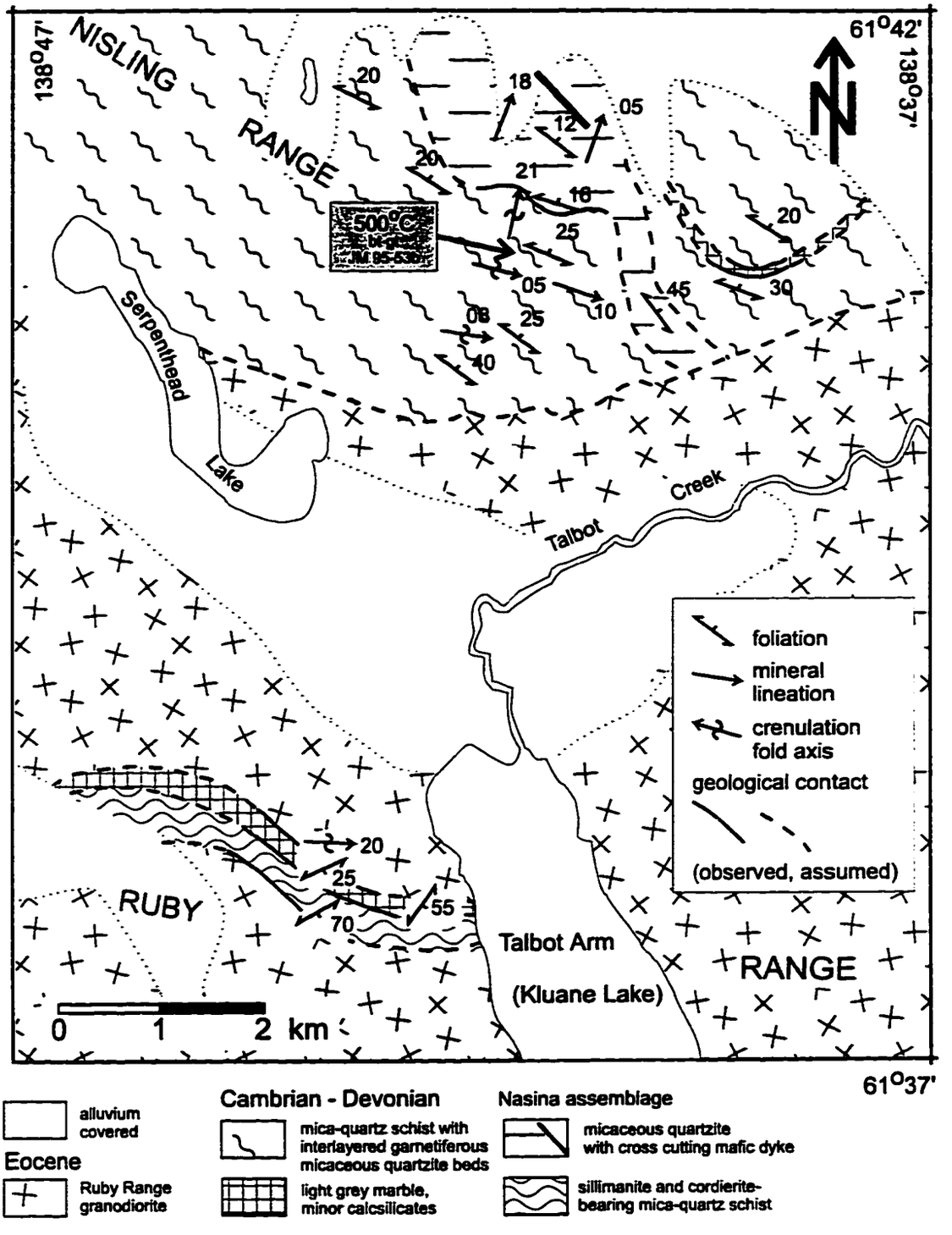

Figure 2-13: Geology of the Nasina Assemblage at the north end of Talbot Arm, Kluane Lake. Location of biotite-garnet thermometry sample is shown. See discussion in Chapter 4. Geology partly modified after Muller (1967).

A ky-st-grt-bt schist structurally overlies phyllites of the Dezadeash Formation east of Klukshu Lake (Figure 2-14). Mineral stretching lineation and shear-sense indicators in the underlying DF phyllite imply a westward thrusting of the high grade assemblage over the DF (Figure 2-21).

Detailed mapping and petrographic analyses show that a contact between the DF and the KMA, as inferred by Eisbacher (1976) does not exist south of Dezadeash Lake and his hypothesis that the KMA is metamorphosed DF, based on the lower metamorphic grade of the KMA in the south, cannot be supported by field evidence and geochemical and isotopic data (Chapter 5).

The KMA has been correlated with the Maclaren Glacier metamorphic belt (MGMB) in the eastern Alaska Range by Forbes et al. (1974), Turner et al. (1974) and Nokleberg et al. (1985). This correlation implies a dextral offset along the Denali fault of about 400 km. Comparison between the KMA and the Maclaren Glacier metamorphic belt shows that rock types, and structural and metamorphic history of both assemblages are different and do not support a correlation:

1) The MGMB, which comprises three mappable belts of argillite and metagraywacke, phyllite, schist and amphibolite, is more heterogeneous than the KMA.

2) The East Susitna batholith, which is interpreted as the equivalent of the RRB by Nokleberg et al. (1985), north of the MGMB, has a pervasive schistosity of Eocene age. The RRB is undeformed, with the exception of an early stage sheared diorite near Doghead Point, and has developed flow banding near some contacts with the KMA.

3) The Meteor Peak fault, a faulted intrusive contact, between the East Susitna batholith and the MGMB, is truncated by the Denali fault to the east. No evidence of major faulting along the contact between the KMA and the RRB is observed in the Ruby Range.

4) Structural and metamorphic analyses of the KMA discussed in Chapters 3 and 4 show that deformation pre-dates peak metamorphism, contrary to

Figure 2-14: Geological map of the Klukshu Lake - Tatshenshini River area in the southern Yukon. The contact of the Coast Plutonic Complex (CPC) with the Dezadeash Formation west of the Haines Road, south of Klukshu Lake has been reported by Lowey (pers. comm., 1995). Location of the Shorty Creek pluton is from Dodds & Campbell (1992). K-Ar and Rb-Sr ages of the CPC are from Farrar et al. (1988) and LeCouteur & Tempelman-Kluit (1976), respectively. The K-Ar (whole rock) ages of the DF are from Lowey (pers. comm., 1995). Location of Figure 2-21 is also shown.

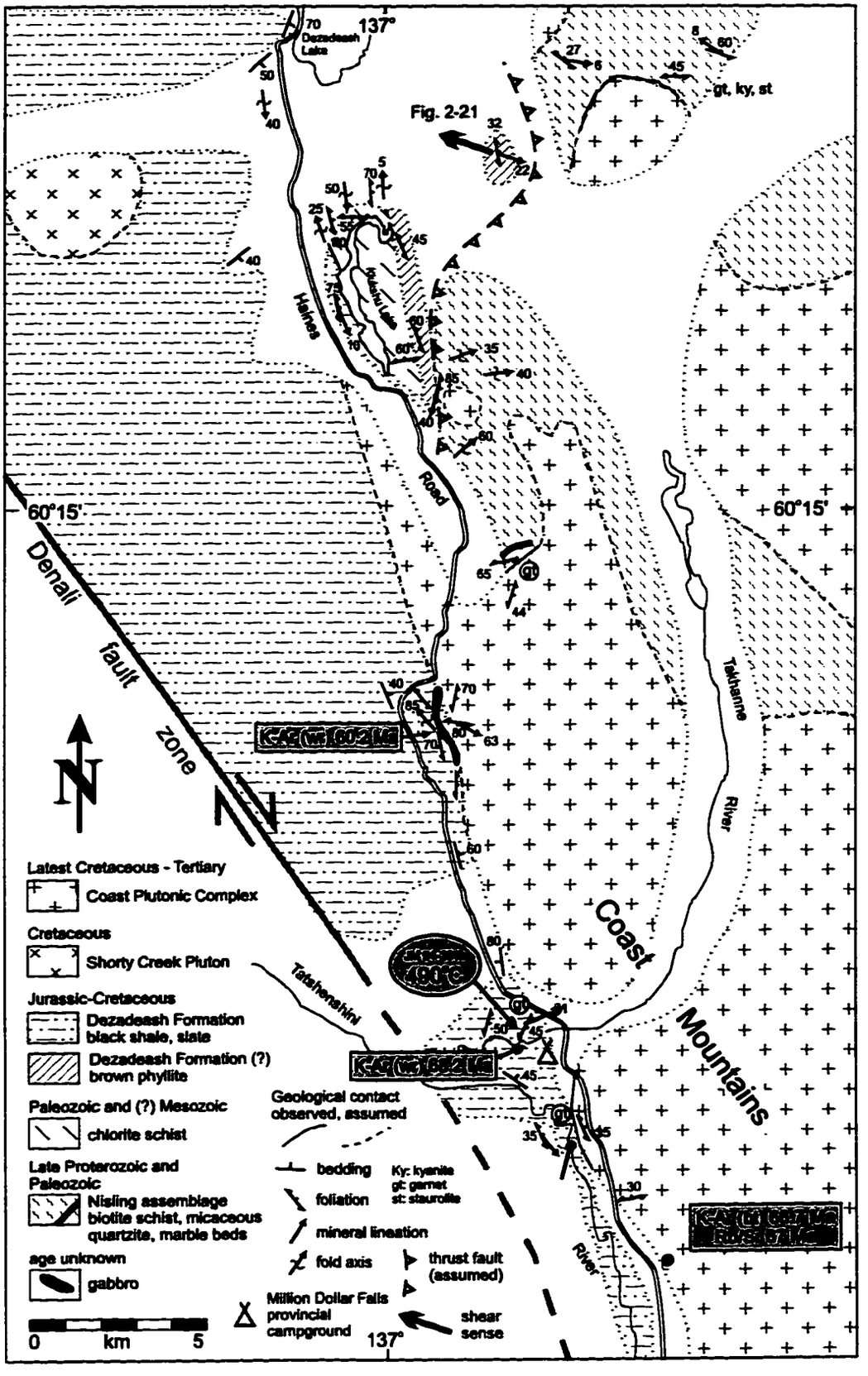
137°
Dezadeash Lake
Fig. 2-21
gt, ky, st
Haines
Haines Road
Kluane Lake
60°15'
Denali fault zone
Tatshenshini
Alsek River
Coast Mountains
Latest Cretaceous - Tertiary
Coast Plutonic Complex
Cretaceous
Shorty Creek Pluton
Jurassic-Cretaceous
Dezadeash Formation black shale, slate
Dezadeash Formation (?) brown phyllite
Paleozoic and (?) Mesozoic
chlorite schist
Late Proterozoic and Paleozoic
Nisling assemblage biotite schist, micaceous quartzite, marble beds
age unknown
gabbro
Geological contact observed, assumed
bedding
foliation
mineral lineation
fold axis
thrust fault (assumed)
shear sense
Ky: kyanite
gt: garnet
st: staurolite
Million Dollar Falls provincial campground
0 km 5

Nokleberg et al.'s (1985) observations in the MGMB.

5) Deformation and metamorphism of the schists of the MGMB is related to synkinematic tonalite intrusions along localized shear zones (Valdez Creek shear zone) of Late Cretaceous (68-74 Ma) age (Davidson, 1989; Davidson et al., 1992). No equivalent tonalite bodies were observed within the KMA.

These points strongly suggest that the KMA in the southwest Yukon and the MGMB in south-central Alaska cannot be correlated, removing a major evidence for 400 km dextral displacement along the Denali fault during post-Eocene time, as proposed by Nokleberg et al. (1985). Although major dextral offset along the Denali fault cannot be disproved, the lack of strong geological evidence requires reevaluation of the role of strike-slip along the Denali fault (see Chapter 6).

Metamorphic assemblages in southeast Alaska, located on the western margin of the Coast Belt and as roof pendants within the CPC are labelled "m - undivided metamorphic rocks", just as the KMA, by Wheeler et al. (1991). Studies by Brew & Ford (1984), Berg et al. (1978), Brew & Grybeck (1984), Himmelberg et al. (1984) and Brew et al. (1985) show that these assemblages are more heterogeneous than the KMA, consisting of interlayered biotite schists, biotite gneiss, amphibolite, quartzite, calc-silicate and marble. Fossils found in lower grade carbonates southeast of Skagway were identified as middle to upper Triassic in age (Brew et al., 1985). Thick homogeneous mica-quartz schist assemblages and olivine serpentinites that characterize the KMA have not been observed. Brew et al. (1991) included these metamorphic rocks in the "Yukon prong" terrane, the equivalent of the Nisling terrane, to indicate that they are derived from ancestral North American margin. Neodymium isotope studies by Samson et al. (1991a) near Tracy Arm support the idea of rocks derived from ancient crust on the western flank of the Coast Belt.

Erdmer & Mortensen (1993) correlate the KMA bt-qtz schist with "distinctive graphitic phyllites, chlorite-epidote-plagioclase schist and phyllite"

on Admiral Island, part of the Admiral Island metamorphic belt of Brew et al. (1992). The original mapping report by Loney (1964) list chlorite-epidote-calcite phyllite or schist with interbedded marble lenses and larger beds, phyllitic slate and greenschist as part of the Gambier Bay Formation. Graphitic phyllite as mentioned by Brew et al. (1992) is not listed. A correlation of the KMA with the Gambier Bay Formation, based solely on lithology, is not strong, and should be regarded with caution.

The mica-quartz schists of the KMA are unique within the Coast Belt of the Canadian Cordillera. The KMA is the most extensive homogeneous metamorphic assemblage and the only medium to high grade assemblage allochthonous to a continental margin. It is distinguished by its lithology and isotopic signature from any other studied metamorphic assemblage in the Cordillera.

Olivine serpentinite

Four ultramafic bodies are observed interlayered with the mica schists of the KMA. They occur for 60 km along strike in the Ruby Range from Doghead Point, northeast of Burwash Landing, to north of Kloo Lake. They vary in size from a width of few tens of meters (Erdmer, 1990) to 15 km and a structural thickness of more than 1 km (Figure 2-5). The two larger bodies in the west form distinct positive magnetic anomalies on the aeromagnetic map (GSC, 1969). Muller (1967) and Erdmer (1990) recognized ultramafic bodies in the mica-quartz schist, but did not map them as separate units.

The ultramafics are serpentinized dunites consisting of varying amounts of Mg-rich olivine (Fo=90, determined by electron microprobe, 10-80 vol.%), serpentine (15-60 vol.%), talc (0-40 vol.%), and iddingsite, magnetite, chromite and pentlandtite (5-10 vol.%), as well as traces of calcite. Olivine is preserved in rounded pods up to 1 cm long, with mesh-like inclusions of chromite overgrown by chromium-magnetite (Figure 3-7).

Abundant serpentinite gives the rock a light greenish appearance and a

soapy touch results from abundant talc.

A well developed foliation defined by aligned serpentine grains characterizes the larger olivine serpentinite at Doghead Point. The foliation dips steeply to the north, parallel to the orientation of the underlying mica-quartz schist. C/S fabrics that indicate progressive non-coaxial deformation and can be used as shear sense indicators are common (Figure 3-7). Talc crystals are randomly oriented and post-date deformation.

0.5 m thick layers of boudinaged and altered gabbronorite, parallelling the foliation of the serpentinite, were observed at one location (94-20). Orthopyroxene in the gabbronorite is partly replaced by clinoamphibole.

The foliated serpentinite at Doghead Point has an estimated structural thickness exceeding 1000 m and can be traced over 15 km along east-west strike (Figure 2-15). Steeper dipping foliation at its northern margin and the lack of a distinct magnetic low to the north of the ultramafic, suggest that the ultramafic body has a wedge-like shape not extending much into depth beyond its surface exposure to the north.

The three smaller olivine serpentinite lenses in the Ruby Range are not foliated. Talc is an abundant phase in the serpentinite at the margin of the body. The serpentinite at Swanson Creek appears as a 150-200 m thick and 1 km wide lens (Figure 2-16), which can be recognized as a positive magnetic anomaly (GSC, 1969). The other occurrences are much smaller, since they do not form noticeable anomalies on the aeromagnetic maps which are compiled from 750 m spaced flights.

As described in the previous section, the olivine serpentinites are interfoliated within the mica-quartz schists of the KMA, with the contact being parallel to the fabric of the schist. The similar orientation of the mica-quartz schist and the serpentinite at Doghead Point suggests an emplacement of the ultramafic prior to deformation. At the northern margin of the Doghead Point body, the ultramafic is in contact with gneissic quartz diorite and tonalite associated with the RRB (Figure 2-15). The ultramafic is less serpentinized and olivine crystals appear fresh, implying new growth of olivine as a result of

Figure 2-15: Detailed geological map with magnetic and geological cross-section of central Kluane Lake area. Cross-section AA-AA' shows the geology and total magnetic field of the Doghead Point olivine serpentinite. Foliation of the schist and the serpentinite is indicated by the sketched lines. The wedge-shaped body of the ultramafic is inferred from the magnetic anomaly. See text for discussion.

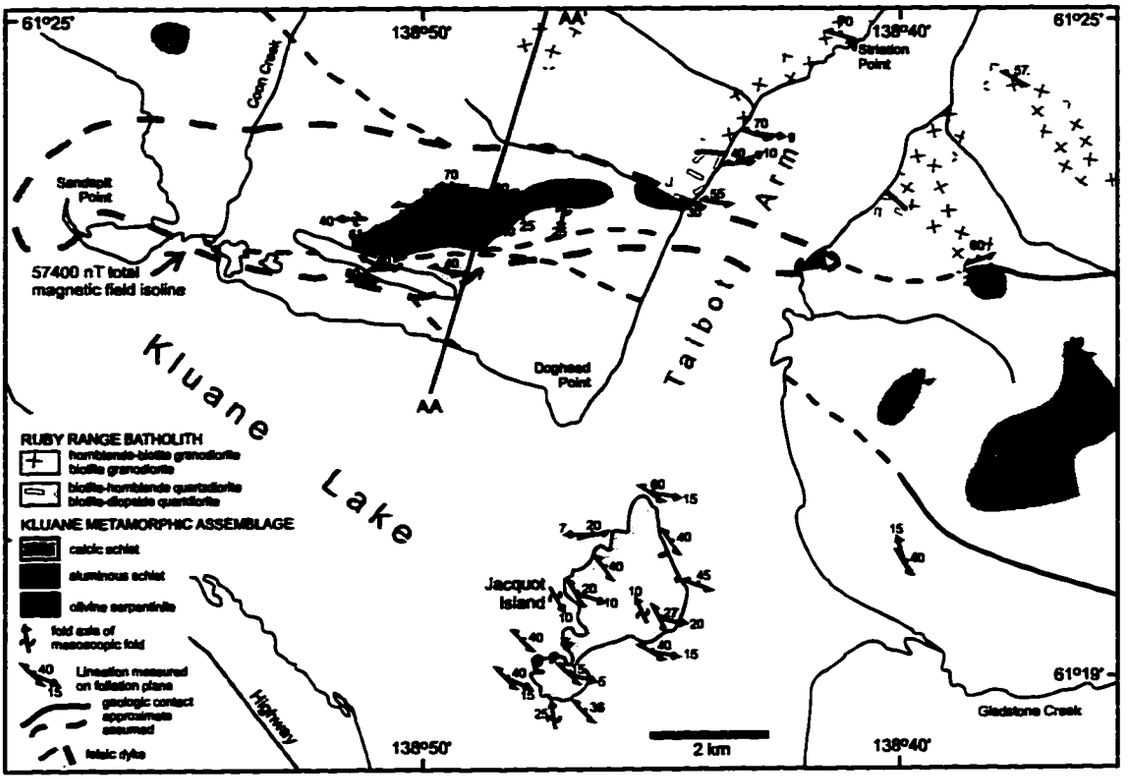
61°25'
138°50'
AA'
138°40'
61°25'
Coen Creek
Sandspit Point
57400 nT total magnetic field isoline
Kluane Lake
Talbot Arm
Dogshead Point
Jacquot Island
Setsion Point
Gladstone Creek
61°19'
Highway
2 km
RUBY RANGE BATHOLITH
hornblende-biotite granodiorite
biotite granodiorite
biotite-hornblende quartzdiorite
biotite-diopside quartzdiorite
KLUANE METAMORPHIC ASSEMBLAGE
calcic schist
aluminous schist
olivine serpentinite
fold axis of mesoscopic fold
Lineation measured on foliation plane
geologic contact approximate assumed
felsic dyke

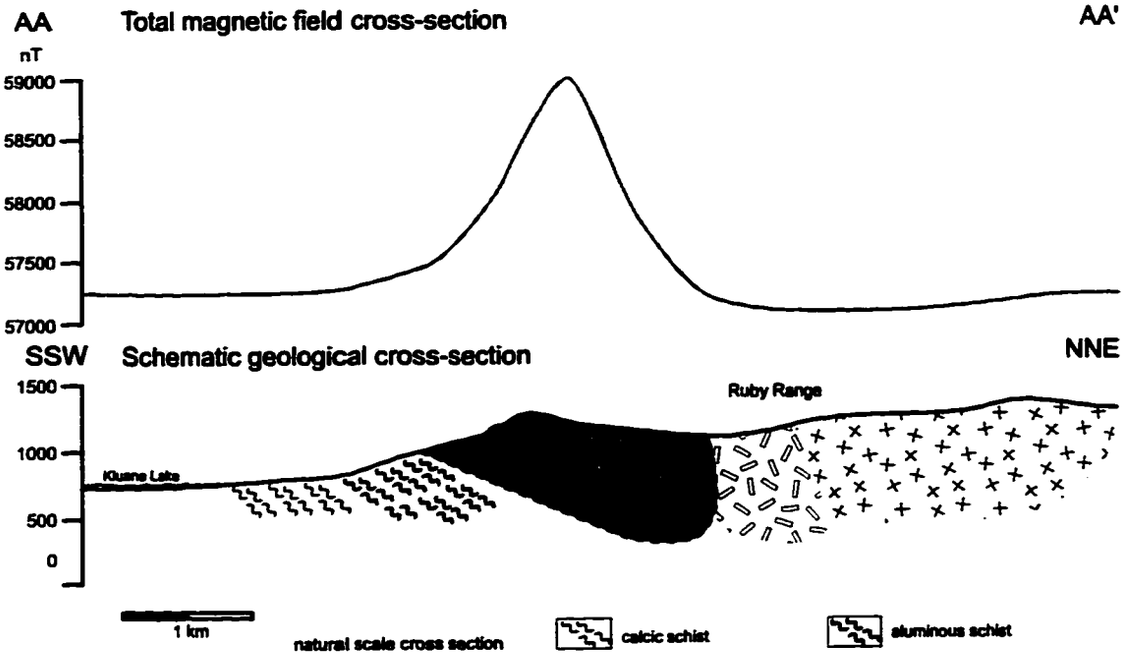
AA
Total magnetic field cross-section
AA'
nT
59000
58500
58000
57500
57000
SSW
Schematic geological cross-section
NNE
1500
1000
500
0
Ruby Range
Kluane Lake
1 km
natural scale cross section
calcic schist
aluminous schist

Figure 2-16: View of the Swanson Creek olivine serpentinite lens in the Ruby Range from a nearby ridge. The ultramafic (light grey) is situated at the contact between the calcic schist of the KMA to the south and the aluminous schist to the north. The contact between serpentinite and schist is foliation parallel, as seen by the parallelism with the thin lines that trace the schistosity of the schist. The scale bar refers to the ridge with the ultramafic. See map of Figure 2-5 for location.

contact metamorphism. The rock still has a foliation, but appears more massive in general. This supports a proposed post-deformational emplacement of the RRB.

The ages of the olivine serpentinites are not known. The similar attitude of foliation in the mica-quartz schist and the Doghead Point ultramafic and new growth of olivine at the contact with the RRB suggest that the ultramafic and the schist were juxtaposed prior to deformation that preceded the Early-Eocene intrusion of the RRB.

Oxygen isotope studies of the olivine serpentinite show that $\delta^{18}O$-values from the core zone of the two larger ultramafic bodies at Doghead Point and Swanson Creek range between 6.1-6.7‰, similar to values from ophiolitic serpentinites (Appendix 2-9; Hoffman et al., 1986; Muehlenbachs, 1986). The pristine values indicate a small water/rock ratio during serpentinization, but not necessarily an ophiolitic origin (K. Muehlenbachs, pers. comm., 1996).

Oxygen isotope data obtained from the smaller serpentinite bodies have elevated $\delta^{18}O$-values of +11‰, indicating interaction with metamorphic fluids, that generally have a $\delta^{18}O$-range from +13 to +20‰. (Muehlenbachs, 1986).

The juxtaposition of ultramafics and the sedimentary protolith of the KMA can be accomplished by intrusion of the ultramafic into the sediment ("Alaskan-type") or by interleaving of disrupted lower portions of oceanic crust ("Alpine-type") (Taylor, 1967; Patton et al., 1994).

"Alaskan-type" ultramafics are concentrically zoned with a dunite core and pyroxenite shells. They are generally intruded into gabbros and interpreted as the result of magma fractionation (Taylor, 1967; Himmelberg et al., 1985; Patton et al., 1994). Zoned ultramafic bodies occur along a 560 km narrow belt southwest of the Coast Plutonic Complex (Patton et al., 1994), and are observed as Early Cretaceous intrusions into the DF (Pyroxenite Creek Ultramafic Complex; Sturrock et al., 1980). Similarly, an unnamed massive serpentinized pyroxenite at the western slope of the Dezadeash Range, 10 km east of Haines Junction (95-13), may also be interpreted as an "Alaskan-type" ultramafic.

In the central and eastern Alaska Range, fault-bounded narrow slivers of serpentinite, serpentinized dunite and peridotite are located north and south and parallel to the Denali fault zone (DFZ) (Patton et al., 1994). Some of those ultramafics are associated with flysch deposits and mica schists. Age constraints for the ultramafics are vague and range from middle Paleozoic to Triassic (Patton et al., 1994). They are interpreted as "Alpine-type" ultramafics, remnants of an ocean basin, possibly the basement of Wrangellia, that collapsed during subsequent accretion (Nokleberg et al., 1985, Patton et al., 1994).

Complete ophiolite sequences are only observed in the Chulitna terrane of the eastern Alaska Range, south of the DFZ, where a complete Upper Devonian ophiolite is disrupted by north-dipping thrust faults and serpentinite lenses occur as thin (<1 km thick, 20-25 km wide) slivers (Jones et al., 1980), and on Admiral Island in southeastern Alaska (Berg & Jones, 1974).

For most ultramafics in the Coast Belt or the Alaska Range, however, a distinctive origin cannot be determined (Patton et al., 1994). A number of small ultramafic bodies, ranging from tens of meters to eight kilometers in length, with a compositional variety of dunite, pyroxenite, peridotite, serpentinite and harzburgite, are reported within the CPC. These ultramafics are strongly foliated and situated in gneiss roof pendants of the CPC, pre-dating its Late Cretaceous-Eocene intrusion. Grybeck et al. (1977) and Brew & Grybeck (1984) correlate them with the other "Alaskan-type" ultramafic intrusions in southeastern Alaska.

Although the serpentinized dunites of the KMA are not part of a complete ophiolitic sequence, a tectonic "Alpine-type" emplacement of the ultramafic bodies into the mica-quartz schist is supported by:

1) foliation parallel contact between schist and ultramafic;
2) lack of evidence of thermal overprinting of the schist at the contact;
3) location of the ultramafics along strike at or close to the boundary between the aluminous and the calcic schist;
4) homogeneous composition of the serpentinized dunites, indicating that

they are derived from a similar magma and may be disrupted parts of one large body;

5) no zoning observed within the ultramafic bodies;

6) no intrusive relation with gabbros.

7) the gneissic quartz diorite and tonalite in contact with the Doghead point ultramafic are interpreted as an earlier more mafic phase of the RRB, instead of being genetically related to the ultramafics (see next section).

The tectonic setting and composition of the KMA ultramafics are very similar to that of the "Alpine-type" ultramafics in the central and eastern Alaska Range. If their interpretation as remnants of oceanic crust is correct, then the distribution of elongated fault-bounded ultramafic bodies near the DFZ strongly suggests that it marks a major suture zone, characterized by the collapse of an oceanic basin, ranging from the Alaska Range in Alaska to the Ruby Range in the Yukon. Accretion of the sediments of the collapsing basins to the North American margin included slivers of disrupted portions of the lower oceanic crust.

RUBY RANGE BATHOLITH (RRB)

The Ruby Range Batholith (RRB) (Muller, 1967) is a narrow, more than 200 km long, northwest-trending intrusion that underlies the Ruby Range in the southwest Yukon. It is the northernmost element of the CPC, which extends 1750 km from southern British Columbia to the Yukon-Alaska border (Brew & Ford, 1993). The RRB is equivalent to the Coast Intrusion of Kindle (1952) and the Ruby Range Granodiorite of Tempelman-Kluit (1974).

The RRB is composed of equigranular, fine to medium grained "salt and pepper" granodiorite. Hornblende-biotite granodiorite is the most common type, with minor hornblende granodiorite and biotite granodiorite. The major felsic minerals are quartz and plagioclase. Pyrope-almandine garnets are present

near the contact with the bt-qtz schist of the KMA at the Garnet Creek plug (Figure 2-10). Garnet grain size varies from 0.5 mm to 5 mm. Assimilation of some pelitic schist during the emplacement of the granodiorite may account for the presence of garnets.

The texture of the granodiorite is generally massive. At the contact with metamorphic rocks of the KMA and the Nasina assemblage, which is intrusive and generally parallel to the fabric of the country rock, a parallel alignment of biotite and hornblende is present. This weak foliation is interpreted as a primary flow structure, where platy and elongated mafic minerals were aligned during the emplacement of the batholith. The width of the foliated contact granodiorites ranges from a few metres up to 100 m.

A 1 km^2 plug of massive medium grained porphyritic augite diorite is observed northwest of Haines Junction (Figure 2-10).

Fine grained, dark greenish grey to brown, equigranular, gneissic quartz diorite to tonalite with variable assemblage of mafic minerals (hornblende and biotite, diopside and biotite, and hornblende) is exposed along the western shore of Talbot Arm, north of Doghead Point (Figures 2-15, 2-17), at the contact with the olivine serpentinite. Mafic minerals comprise 35-60 vol.% of these rocks. The felsic minerals are plagioclase (30-50 vol.%) and quartz (10-20 vol.%). K-feldspar has not been observed. The rocks have a distinct foliation, mineral stretching lineation and compositional banding. The quartz diorite/tonalite is intruded by sills of massive medium to coarse-grained granodiorite.

A genetic relation of these tonalitic gneisses with the ultramafic, defining a mafic shell around the serpentinite, similar to "Alaskan-type" intrusions, is regarded unlikely, since these shells are comprised by more mafic rocks (pyroxenite, gabbro) than the quartz diorite/tonalite present. Also, the occurrence of a massive undeformed dioritic intrusion within the biotite schist of the KMA suggests that the diorite and the gneissic quartz diorite/tonalite represent an earlier more mafic phase of the RRB.

Biotite and hornblende K-Ar and Rb-Sr ages of the major body of the

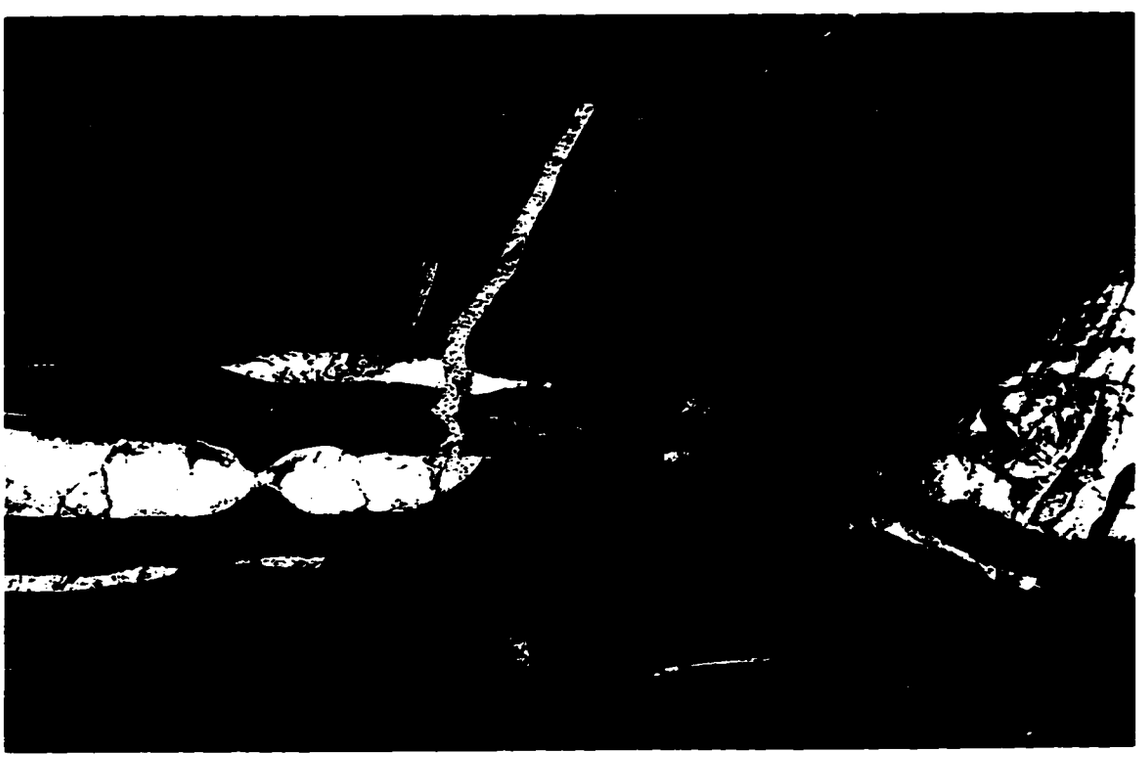

Figure 2-17: Well foliated, fine grained, blueish grey tonalitic gneiss with boudinaged quartz layers. A 2 cm thick granitic dyke, related to larger sills fifty meters away, cuts the diorite and the quartz boudins without any obvious deformation. The tonalite is interpreted as an earlier mafic phase that preceded the main felsic intrusion of the Ruby Range Batholith. Outcrop is located north of olivine serpentinite at Doghead Point (94-26). Rock hammer (32 cm) for scale.

RRB range from 53 to 58 Ma (Appendices 2-4, 2-6; LeCouteur & Tempelman-Kluit, 1976; Farrar et al., 1988). Biotite K-Ar geochronology of two smaller intrusions within the KMA, west of Kloo Lake and at Pine Lake, yield similar ages of 58 and 50.6 Ma, respectively. An undeformed granitic dyke, intruding the bt-qtz schist of the KMA at the Canyon Bridge along the Alaska Highway (94-81), has U-Pb zircon and monazite ages of 54.6 Ma (Appendices, 2-6, 2-10; Mortensen, unpublished data, 1996). U-Pb zircon ages of 71.8 Ma are obtained from a deformed fine grained biotite granite dyke in an outcrop less than one hundred meters away (Figure 2-18, Appendices 2-6, 2-10; J. Mortensen, unpublished data, 1997).

U-Pb zircon ages from hornblende diorite at the northern margin of the RRB at the south end of Aishihik Lake and from hbl-bt granodiorite at the southern margin of the RRB south of Aishihik Lake range from 69-78 Ma and 70-90 Ma, respectively, while a granitic sample from the central part of the batholith yielded U-Pb zircon age of 55.8 Ma (Appendices 2-4, 2-6; Johnston, 1993).

The two age groups suggest an early, more mafic (?), intrusive period in the Late Cretaceous, while the main granodiorite body of the RRB intruded in the Early Eocene. Magmatic activity from 55 to 70 Ma is also reported from the tonalites of the Great tonalite sill at the western margin of the CPC in southeastern Alaska (Gehrels et al., 1992).

Latest Cretaceous ages are also reported from granodiorite of the Coast Plutonic Complex (CPC) near the Yukon-British Columbia border along the Haines Road (Rb-Sr and K-Ar biotite: 67 and 66.7 Ma, respectively, LeCouteur & Tempelman-Kluit. 1976; Farrar et al., 1988).

The RRB dips northeastward underneath the Nasina Assemblage and the AMS in the north, and is underlain to the southwest by the KMA. The RRB is interpreted as an Eocene (50-58 Ma) synmetamorphic and syntectonic sill by Erdmer & Mortensen (1993). The exposure of the smaller intrusions with similar composition and K-Ar ages at the southwestern margin of the KMA possibly trace a second sill, partly covered, parallel to the one underlying the Ruby

Figure 2-18: Outcrop photograph of a boudinaged fine grained biotite granite dyke (dark grey underneath rock hammer) in the cordierite-sillimanite-biotite-quartz schist near the eastern margin of the KMA. U-Pb zircon ages of 68-72 Ma and 55.6 Ma were obtained from zircon and monazite fractions, respectively (Mortensen, unpublished data, 1997). See text for discussion. Sample location is at the Aishihik River, near the Canyon Bridge on the Alaska Highway (94-81). Rock hammer for scale. Photo courtesy of Jim Mortensen, University of British Columbia.

Range to the north. Both sills can be interpreted as large apophyses of the main body of the CPC south of the Dezadeash Range.

POST-EOCENE IGNEOUS INTRUSIONS

Felsic and mafic igneous intrusions are common in the KMA and the RRB (Figure 2-1, Appendix 2-11). Felsic dykes can be found on the eastern shore of Kluane Lake and on Jacquot Island, where they occur in ENE- and SSE- trending swarms of two or three parallel dykes, spaced tens or a few hundred meters apart. They are massive feldspar porphyries of dacitic composition. Centimeter-sized phenocrysts of plagioclase, with minor hornblende, biotite and miarolitic quartz occur in a fine grained groundmass of quartz, plagioclase and biotite. Unaltered dyke rocks have a bluish grey appearance, while altered dykes are light greenish brown. The dykes vary in thickness from 10 cm to 7 m. They are undeformed, generally vertical, crosscutting the ms-chl-qtz schist and the olivine serpentinite and deflecting the foliation of the schist during emplacement (Figure 2-19).

Mafic dykes are fine grained holocrystalline, equigranular hornblende or hornblende-biotite diorites, with minor porphyric andesites. The dykes are found predominantly along strike at the northern margin of the KMA, trending N-NNE. The mafic dykes are generally vertical, crosscutting the biotite schist, and have a width of 2 to 7 meters. A swarm of four parallel dykes, spaced 400 m apart, was observed north of Cultus Creek (93-179, 93-181).

Dacitic and dioritic dykes also crosscut the RRB at Kluane Lake and in the Ruby Range east of Gladstone Creek.

The mafic and felsic dykes post-date the Eocene emplacement of the RRB. They are the southern part of a north-trending set of rhyolitic, feldspar porphyry dyke swarms that intrude metamorphic assemblages and Mesozoic and early Tertiary igneous rocks (Muller, 1967; Tempelman-Kluit, 1974; Johnston & Timmerman, 1993a), along 250 km, from the Shakwak Trench in

Figure 2-19: Vertical, undeformed, altered feldspar porphyry dyke, intruding northeast-dipping ms-chl-qtz schist on the eastern Kluane Lake shore (94-38). Flow banding can be observed in the lighter coloured dyke at the contact with the dark grey ms-chl schist. The thickness of the dyke varies from 3 to 5 m along the outcrop (see dotted line of contact).

the south to the Yukon River in the north.

Geochronological data for these dykes is not available. Tempelman-Kluit (1974) and Johnston & Timmerman (1993a) propose early Tertiary emplacement, related to the RRB and similar early Tertiary intrusions. North-trending rhyolitic to basaltic dykes are reported from the Kluane Ranges southwest of Kluane Lake, where they crosscut mid-Miocene conglomerates of the Amphitheater Formation (Eisbacher & Hopkins, 1977). K-Ar whole rock ages of 6-16 Ma are reported for several dykes (Stevens et al., 1982). Since the juxtapostion of the Insular Superterrane with the KMA had happened by Early Oligocene (see Chapter 6), it is possible that the dykes crosscutting the Amphitheater Formation are coeval with dykes in the KMA and the AMS, suggesting a Miocene age for these dykes.

The predominantly north-trending orientation of the dykes intruding the metamorphic assemblages can be related to extensional fractures resulting from northward movement of the Pacific plate relative to North America, which also caused dextral motion along the Denali fault zone (Eisbacher & Hopkins, 1977; see Chapter 3).

DEZADEASH FORMATION (JK_D)

The late Jurassic-Early Cretaceous Dezadeash Formation (DF) consists of generally undeformed, interbedded sandstones and shales with minor conglomerates, limestone, interpreted as flysch sediments of volcanogenic origin (Eisbacher 1976). It is equivalent with the Dezadeash Group of Kindle (1952).

At its northern and eastern margin of exposure the DF occurs as a fine to medium grained graphitic ms-bt-chl-qtz phyllite. Euhedral spessartine-rich garnets and "knotty schist" indicate low grade metamorphism (Figure 2-20). The width of that phyllitic zone varies from less than 100 m at Klukshu Lake and Motherall Creek up to 3 km at Takhanne River (G. Lowey, pers. comm.,

Figure 2-20: Photomicrograph of a "knotty schist", a slate of the Dezadaesh Formation in the Takhanne river valley at Million Dollar Falls campground, along Haines Road in the southern Yukon (95-26). The porphyroblasts consist of fine grained muscovite. Biotite, quartz and muscovite make up the matrix. The contact of the DF with the Coast Plutonic Complex is a few hundred meters to the east.
Scale bar: 2 mm. XPL

Figure 2.21: Photomicrograph of coarse grained garnetiferous hornblende-biotite phyllite assigned to the Dezadeash Formation southeast of Dezadeash Lake (95-37). The phyllite is structurally overlain by a kyanite-staurolite-garnet schist. Curved inclusions in the hornblende porphyroblast (black arrow) and domino structures of the biotite porphyroblast (white arrow) imply top to the left shear. See Figure 2-14 for loaction.
Scale bar: 2 mm. XPL

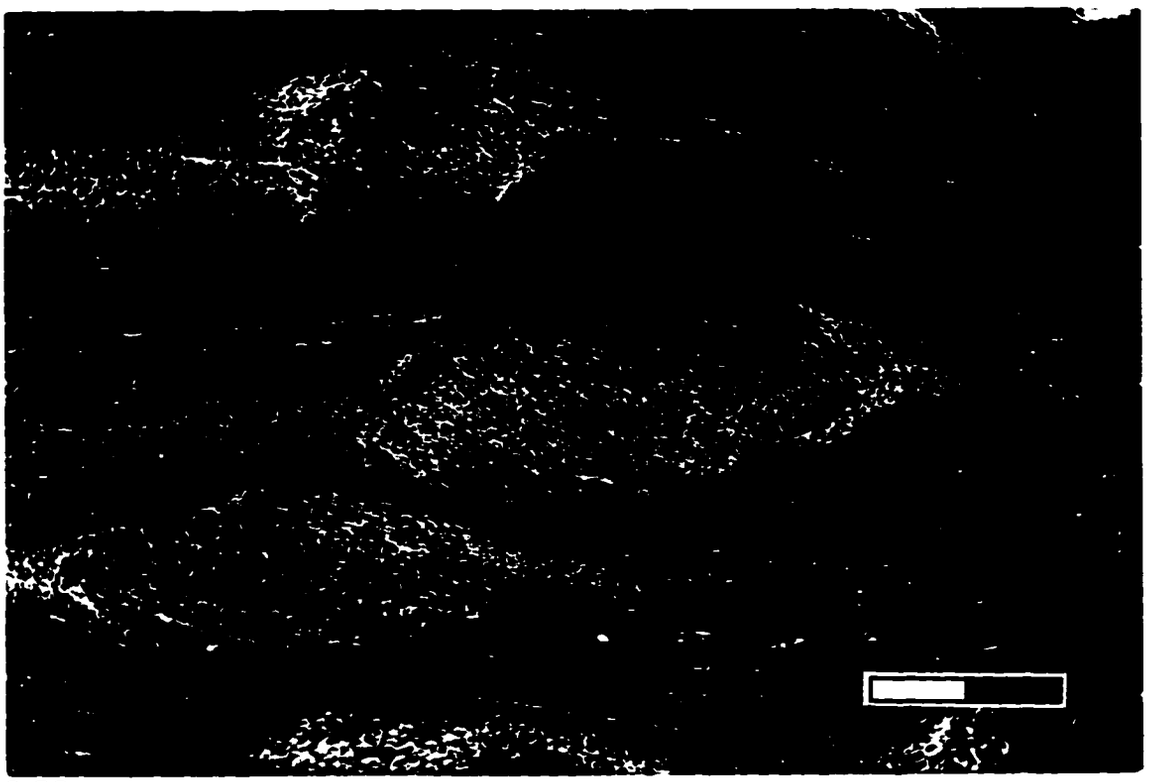

2-20

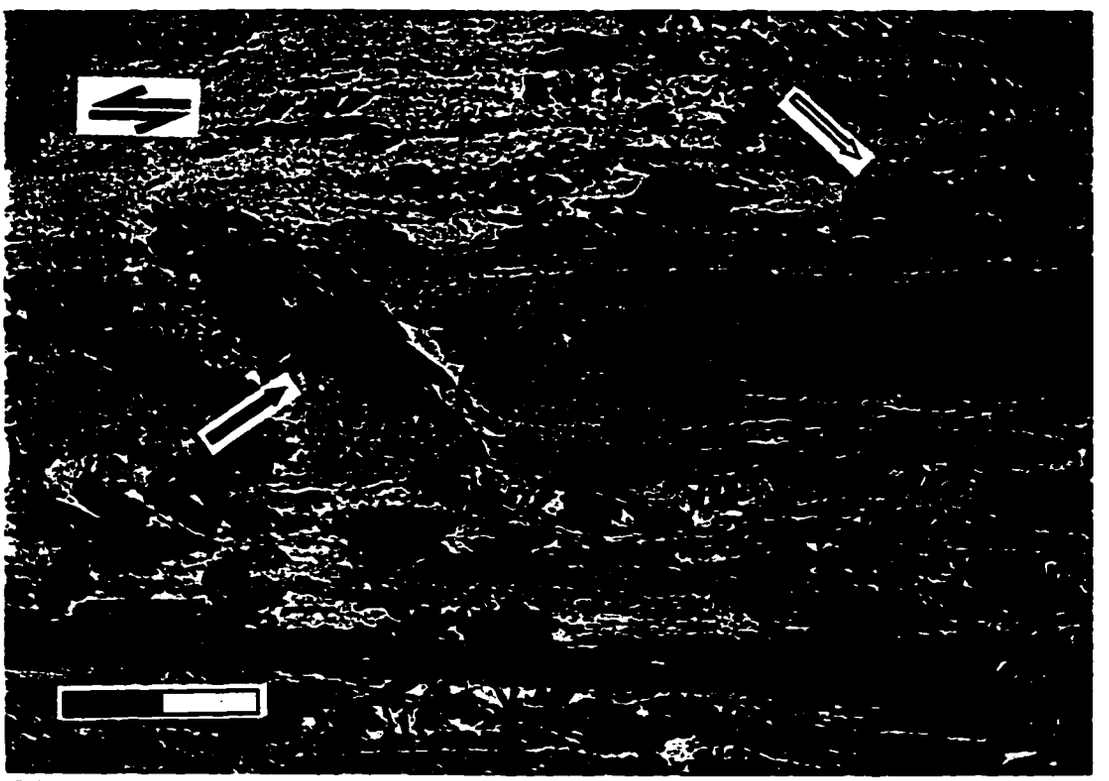

2-21

1995) to the south.

The DF overlies a narrow band of chlorite-actinolite-schist (PMvs of Dodds & Campbell, 1992) (Figure 2-9). Andesitic clasts within the DF, and interbedded phyllite and chlorite-actinolite schist suggest a primary sedimentary contact (Eisbacher, 1976; Bremner, 1990).

East of Klukshu Lake the DF is in a presumed faulted contact with the Nisling assemblage, as mentioned above (Figures 2-15, 2-21).

South of Klukshu Lake the DF dips eastward underneath the Coast Plutonic Complex. The contact is shown on the map by Kindle (1952) as a fault. A K-Ar whole rock age of 68.2 Ma of a DF phyllite at Takhanne River valley (G. Lowey, pers. comm., 1995) is similar to K-Ar biotite (66.7 Ma, Farrar et al., 1988) and Rb-Sr (67 Ma, LeCouteur & Tempelman-Kluit, 1976) ages of granodiorite of the CPC, suggesting an intrusive contact. However, the whole rock age of the phyllite has to be regarded with caution (J. Mortensen, pers. comm., 1997).

The interpretation of the DF as the immediate protolith of the KMA, as proposed by Eisbacher (1976), cannot be accepted in light of the evidence presented in this chapter and Chapter 5.

GREENSCHIST (PMvs)

A fine grained greenschist of variable composition (pl-chl-ep-qtz, hbl-ep-qtz, hbl-pl-ep-chl-qtz), forms a 100 km long and maximal 2 km wide discontinuous belt from the south end of Kluane Lake to Klukshu Lake (Figure 2-1). It crops out northeast and east of the DF. The greenschist is equivalent with unit PMvs of Dodds & Campbell (1992). Kindle (1952) misinterpreted these rocks as peridotite or serpentinite (unit 5), west of Haines Junction, or assigned them to the "Yukon Group", which also included the KMA bt-qtz schist.

The greenschist has developed a foliation that parallels compositional

layering. Distinct compositional layering with plagioclase and hornblende clasts, observed in some samples, suggests that the protolith is a weakly metamorphosed andesitic tuff. A massive dark greenish grey andesite occurs 2 km east of Bear Creek Motel on the Alaska Highway (Figure 2-9).

No radiometric ages have been determined for the greenschist. Since it underlies the DF north of Dezadeash Lake, and is presumably the depositional base of the DF (see above; Eisbacher, 1976), its minimum age is pre-Late Jurassic.

Chapter 3

Structural styles of the Kluane metamorphic assemblage

INTRODUCTION

Well developed schistosity and mineral stretching lineation in mica-quartz schist reflecting ductile deformation of the KMA are described and their regional tectonic significance is discussed in the first part of this chapter. Microtectonic analyses show that the KMA schists are mylonites characterized by a distinct monoclinic shape symmetry, indicative of intensive ductile deformation (Passchier & Trouw, 1996). Shear-sense obtained from δ-type porphyroclasts records consistent oblique slip with westward-directed hangingwall up motion. This is the first reported evidence of ductile deformation in the North American Cordillera indicating late Mesozoic sinistral motion along the North American continental margin as postulated by Monger et al. (1994).

The structural geology of the KMA is shown on an overview map (Figure 3-1), a detailed map of the Kluane Lake region (Figure 3-2) and in several cross-sections (Figure 3-3). A proposed early Tertiary deep seated fault divides the KMA into a northwestern and southeastern domain. Computer aided stereographic analysis, presented in the second part of the chapter, documents that the orientation of mesoscopic folds is parallel to an ESE-plunging regional anticline. Similarly oriented local and regional folds are observed in adjacent metamorphic assemblages of the Nisling terrane (NS) and in unmetamorphosed shales and slates of the Dezadeash Formation (DF), suggesting a regional NNE-directed compression.

The chapter concludes with a tectonic evolution model that incorporates previously unpublished geochronological data and metamorphic results from Chapter 4. The model proposes Late Cretaceous underplating of the KMA along a sinistral oblique slip fault underneath the North American continental margin. Non-coaxial progressive deformation coeval with high pressure-low temperature metamorphism is evident in rare synkinematic grossular-rich garnets. Latest Cretaceous emplacement age (72 Ma) of a late synkinematic granitic dyke provides a minimum age of deformation of the KMA.

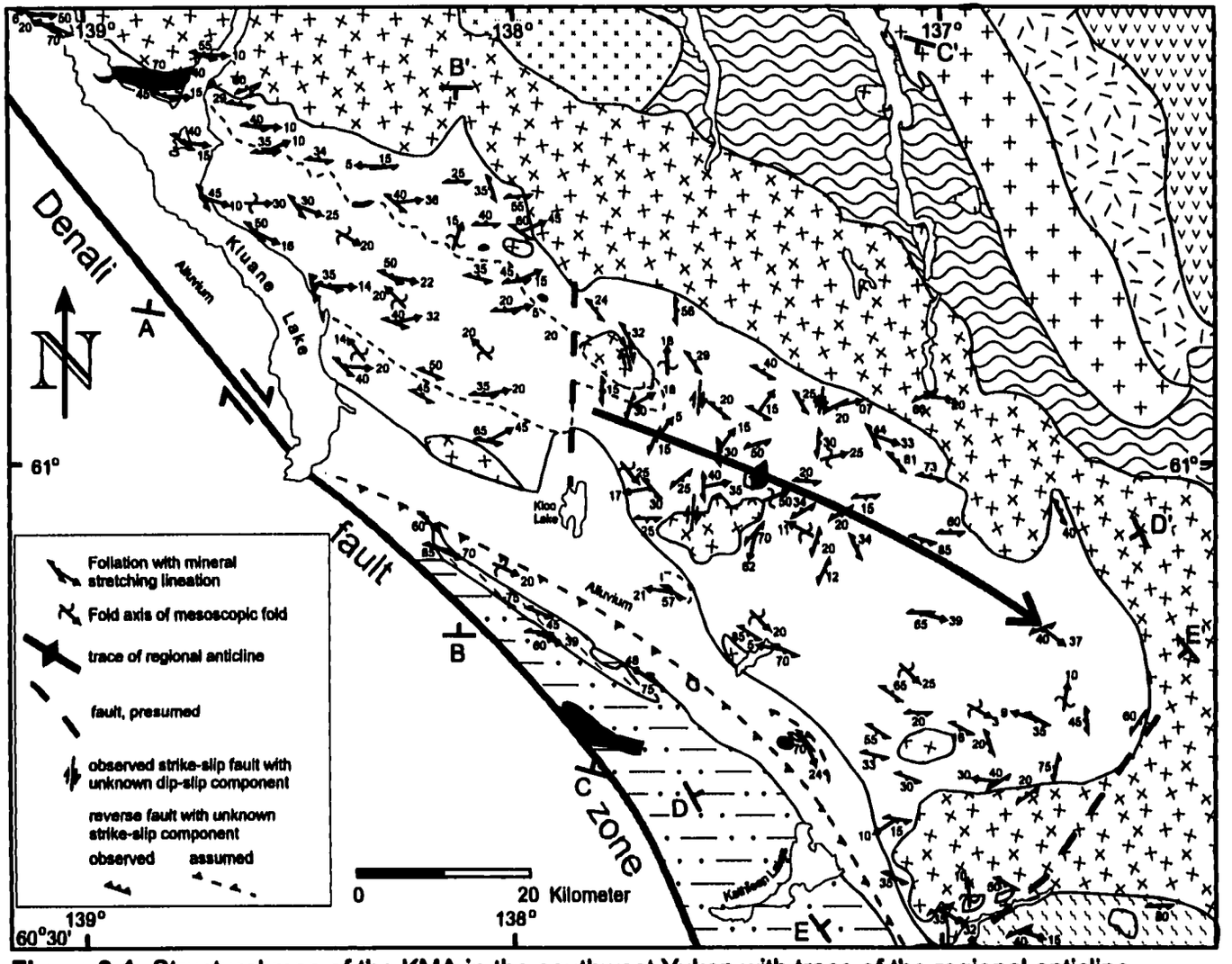

Figure 3-1: Structural map of the KMA in the southwest Yukon with trace of the regional anticline. Geology is the same as in Figure 2-1, except for the KMA, which is shown in white. Letters indicate location of cross-sections shown on Figure 3-3. Trace of Denali fault after Dodds & Campbell (1992).

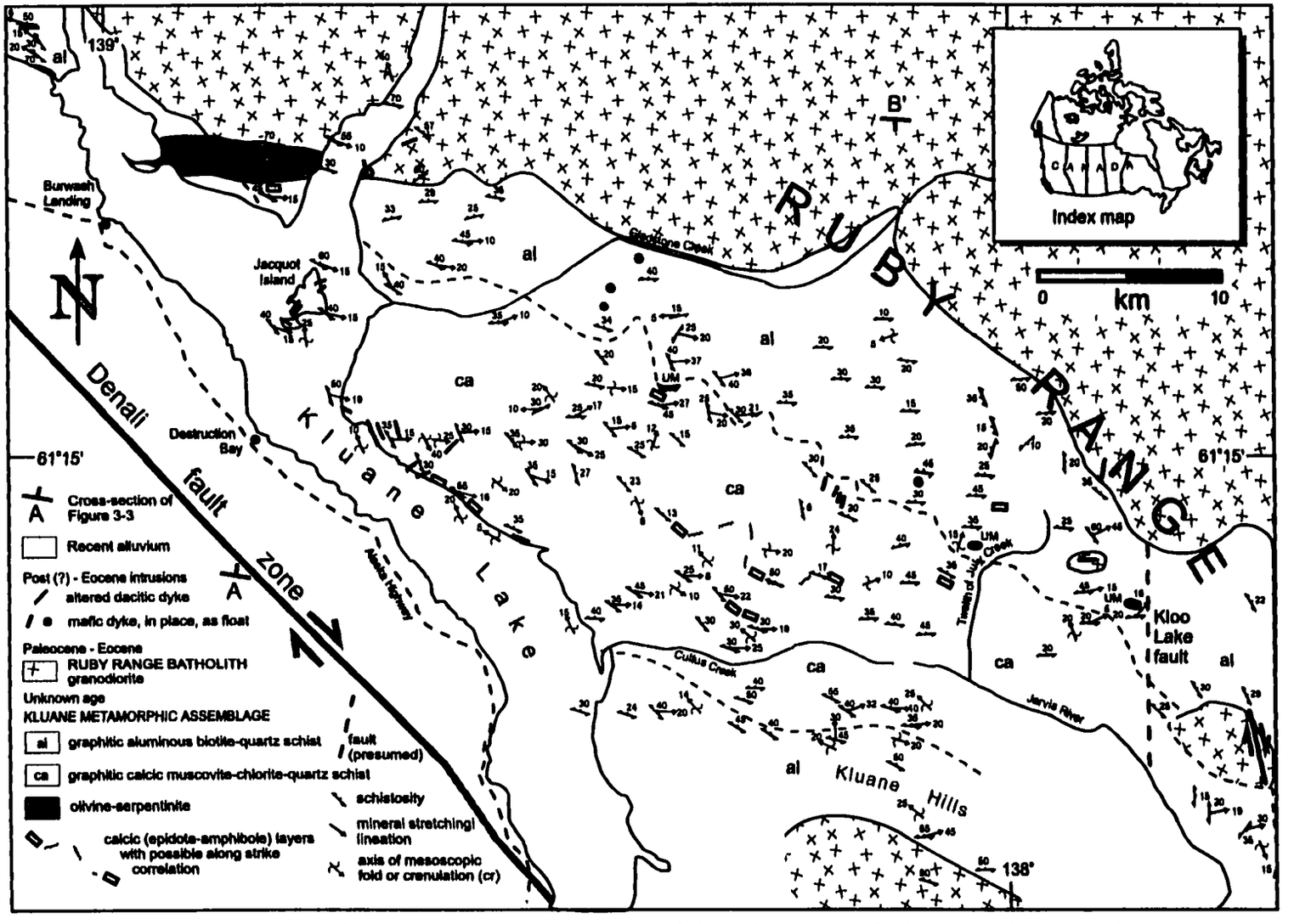

Figure 3-2: Structural map of the northwestern domain of the KMA east of Kluane Lake. Note homogeneous moderately north- to northeast-dipping schistosity west of Kloo Lake fault.

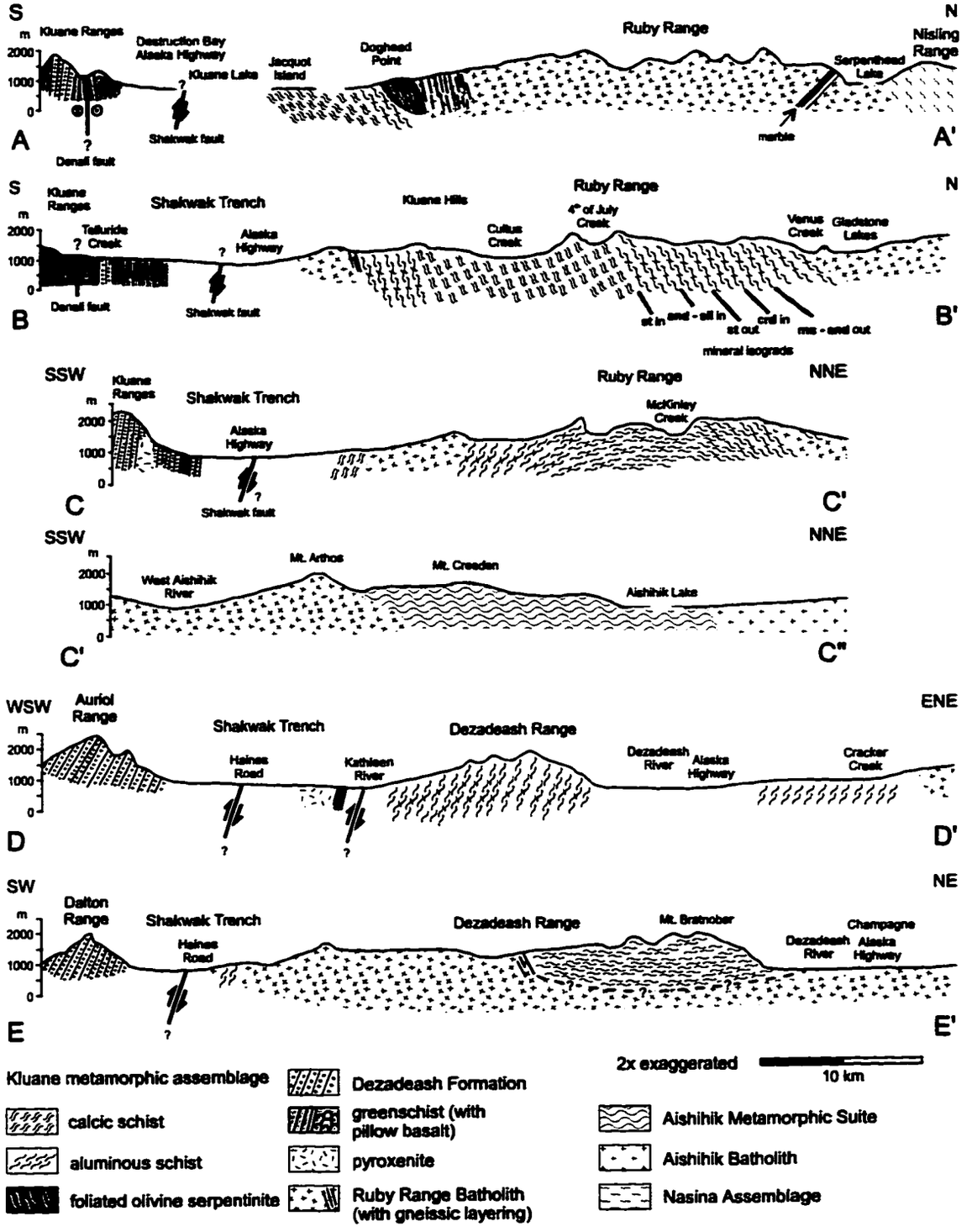

Figure 3-3: Schematic geological cross-sections through the KMA and adjacent assemblages in the Ruby Range and the Dezadeash Range, from northwest (A-A') to southeast (E-E'). See text for discussion.

PREVIOUS WORK

Workers who previously studied the KMA northeast of Kluane Lake noted the uniform north-dipping schistosity (McConnell, 1905; Muller, 1967; Tempelman-Kluit, 1974; Erdmer, 1990). McConnell (1905) recognized that the schists dip more steeply and are in part overturned near the eastern contact with the batholith. He assigned south-dipping schists at the base of the St. Elias Mountains to the "Kluane Schist" and suggested that the KMA forms a large anticline, whose hinge zone has been eroded during the formation of the Shakwak valley. Although field work carried out for this project did only find greenschist and phyllite of the DF, instead of KMA-type schists at McConnell's locality (Telluride Creek, see Figure 2-10), field observations and structural analysis presented below support McConnell's model that the orientation of schists of the KMA defines a regional anticline in the eastern part.

Southwest-verging open to isoclinal folds, asymmetrical crenulation and small folds with an axial-planar northeast-dipping cleavage were observed at the Kluane Lake shore and in the Kluane Hills (Erdmer, 1990, 1991). Tempelman-Kluit (1974) noted that schistosity is masked and linear elements are obliterated by thermal overprinting of regional metamorphosed rocks. U-Pb, K-Ar, ^{40}Ar-^{39}Ar geochronology of mica-quartz schist record ages of 39-61 Ma, interpreted as peak metamorphic and cooling ages related to the intrusion of the RRB and constraining the development of the schistosity in the KMA to pre-Early Eocene (Erdmer & Mortensen, 1993).

DUCTILE FABRICS OF THE KLUANE METAMORPHIC ASSEMBLAGE

Planar fabrics

Parallel graphitic layers in plagioclase porphyroblasts are relics of an early slaty cleavage. Rare crenulation cleavage preserved in some

porphyroblasts show that this cleavage was formed by transposition of an older foliation, possibly bedding (Figure 3-4). Since no primary sedimentary structures are preserved to confirm that this older foliation represents original bedding, it is referred to as S_n, while the prominent parallel graphitic layers are called S_{n+1}.

S_{n+1} is commonly identified only in thin sections (Figures 3-4, 3-5), except when large porphyroblasts can be observed on unaltered rock faces along the Kluane Lake shore (Figure 2-3). The graphitic inclusion trails are generally curved, implying a synkinematic growth of the porphyroblasts (Figure 3-5; Passchier & Trouw, 1996). Continuation of S_{n+1} layers from plagioclase porphyroblasts into surrounding mica grains is observed in some samples. S_{n+1} in the mica grains is also parallel to the major schistosity S_{n+2}, suggesting that S_{n+2} has developed parallel to the earlier cleavage S_{n+1} (Figure 3-4). S_{n+1} is also observed in rare synkinematic garnets (Figure 3-6).

The major fabric observed in the schists of the KMA is a spaced schistosity S_{n+2}. The cleavage domains which define the foliation plane S_{n+2} are comprised of parallel aligned muscovite, chlorite and biotite grains, ranging from 0.2 to 2 mm in length. Microlithons contain plagioclase porphyroblasts and quartz (Figure 2-4). Microlithons are generally thicker than cleavage domains, but individual thickness can vary within a single sample from less than 200 µm to more than 2 mm. The transition between microlithon to cleavage domain is discrete (domainal spaced foliation). Quartz bands commonly appear lenticular, boudinaged, with thinning at the necks. Compositional layering can be observed with the unaided eye in some outcrops (Figure 2-7). Approaching the contact with the RRB, rocks of the KMA have a more gneissic appearance (Figure 2-8). This is due to coarsening of the grain size, overgrowth of the S_{n+2} foliation plane and new growth of cordierite, a result of thermal recrystallization caused by the intrusion of the RRB.

S_{n+2} schistosity is also developed in the olivine serpentinite at Doghead Point, where it is defined by serpentine (Figure 3-7). Parallelism between the schistosity in the serpentinite and nearby ms-chl schist implies

Figure 3.4: Photomicrograph of aluminous mica-quartz schist from the northwestern part of the KMA (94-346). Two foliation generations, original bedding (?) S_n and a slaty cleavage S_{n+1} are distinguished by graphitic layers in a plagioclase porphyroblast. S_{n+1} is approximately parallel to the schistosity in this sample, which is oriented parallel to the long axis of the picture. The continuation of from the plagioclase porphyroblast into the biotite grains suggests that the rock has not experienced significant deformation.
Scale bar: 0.5 mm. XPL

Figure 3.5: Photomicrograph of a plagioclase porphyroblast of the calcic schist of the KMA. The graphitic inclusions in the grain are curved towards the rim of the plagioclase, indicating a counterclockwise rotation of the grain during growth. Sample location is from the eastern Kluane Hills (90-37).
Scale bar: 0.5 mm. XPL

3-4

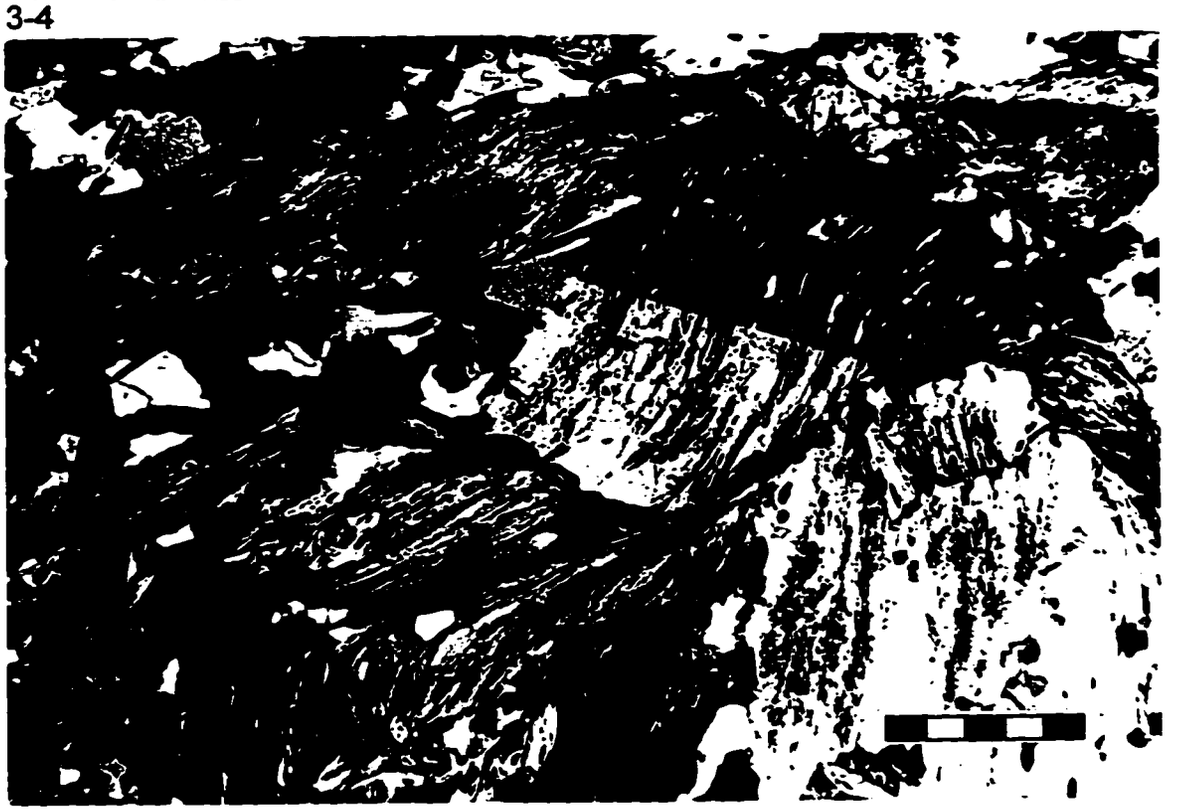

3-5

Figure 3-6: Photomicrograph of a garnet (center) of the aluminous schist near the contact with the calcic schist (93-183). Curved graphitic inclusion trails in the garnet crystal are remnants of an earlier foliation (S_{n+1}) and indicate a clockwise rotation of the garnet during growth. S_{n+1} does not continue outside the garnet. The garnet is rimmed and partly embayed by staurolite (st) and biotite (brown). Graphitic layers in the staurolite crystals do not show a preferred orientation and suggest a static overgrowth by staurolite.
Scale bar: 0.5 mm. PPL

Figure 3-7: Photomicrograph of an olivine serpentinite from the Doghead Point ultramafic body (94-20b). The schistosity (C) is defined by platy alignment of serpentine (bluish grey to whitish needles) in the microlithons, parallel to the long axis of the photograph. S-planes are developed in the 3 mm wide zone between zones of more intense shearing. Sense of shear is top to the left. The light yellow mineral is talc. Olivine porphyroclasts are characterized by bright yellow, red and green colours and a web-like alteration to opaque minerals, magnetite and chromite (center of picture).
Scale bar: 2.0 mm. XPL

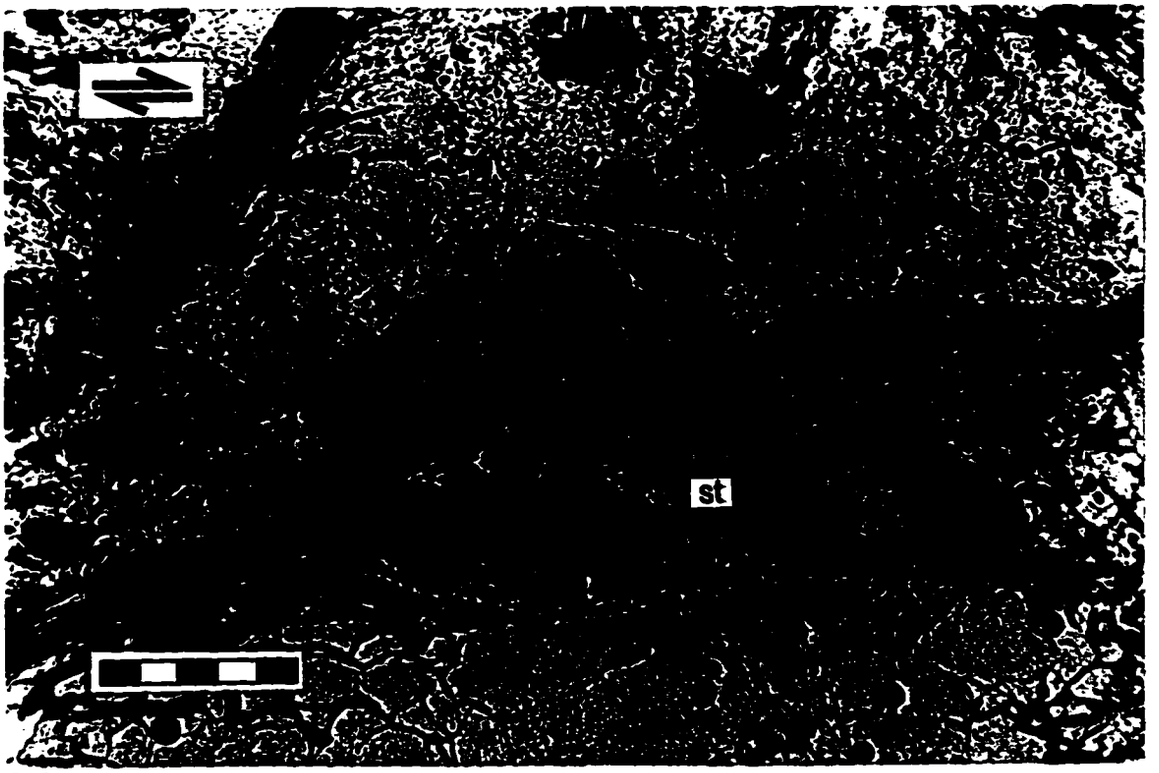

3-6

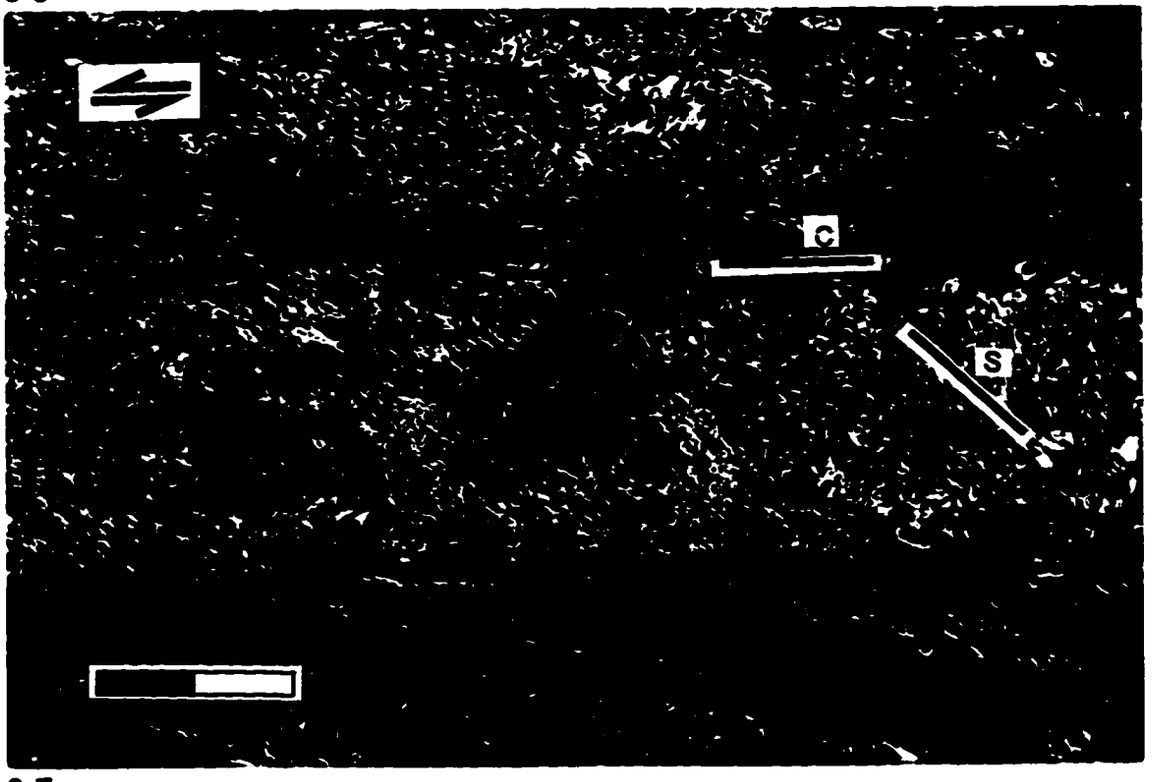

3-7

contemporaneous development of the fabric in both rock types (Figure 2-18). No planar fabric is developed in the smaller serpentinite bodies.

The general attitude of S_{n+2} in the western Ruby Range remains unchanged over tens of kilometers, along and across strike, dipping moderately (15-45°) north to northeast (Figures 3-1, 3-2, 3-3). East of Kloo Lake the attitude changes to easterly dips and to steeper (55-85°) southernly dips in the Dezadeash Range. A detailed discussion of the structural data is presented below.

Locally, a secondary foliation S_{n+3} is developed in the mica-quartz schist and in the olivine serpentinite at Doghead Point. This foliation is axial planar to mesoscopic F_{n+3}-folds and millimeter-scale F_{n+3}-crenulation folds. The cleavage is generally only observed in the immediate fold hinges. However, not all F_{n+3}-folds have developed a S_{n+3}-cleavage. The spacing of the cleavage ranges from 1 mm to several centimeters. Thin section analyses show the foliation is defined by preferred orientation of new mica crystals. The cleavage is generally better developed in the olivine serpentinite at Doghead Point than in the mica-quartz schist. Rare good exposure at the Kluane Lake shore show that S_{n+3} strikes subparallel to the main foliation S_{n+2}, but dips steeper to the north. The outcrop sketch in Figure 3-8 shows the localized character of S_{n+3}, indicating inhomogeneous deformation at outcrop scale. Due to its limited occurrence S_{n+3} does not form a pentrative foliation and is not mappable.

Linear fabrics

A distinct mineral stretching lineation L_{n+2} can be observed on the S_{n+2}-plane. It is defined by an elongated alignment of mica or chlorite minerals and is best developed in ms-chl schist along the Kluane Lake shore. At sample and outcrop scale the orientation of the mineral stretching lineation is consistent. Where observed in the KMA, the orientation of L_{n+2} is homogeneous, generally plunging gently (5-20°) to NE-ESE or WNW (Figures 3-1, 3-2). L_{n+2} is also developed in the foliated olivine serpentinite at Doghead Point.

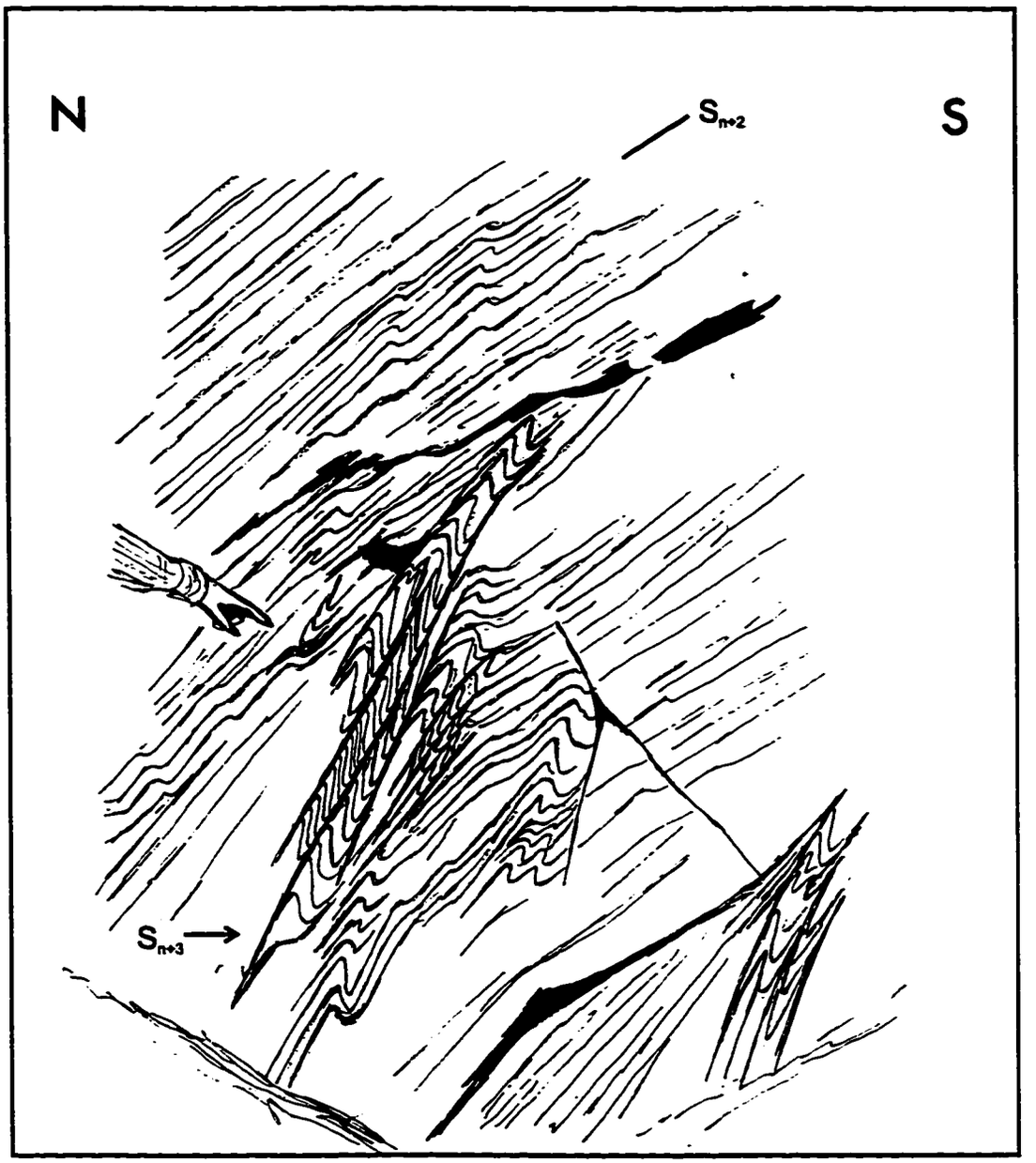

Figure 3-8: Outcrop sketch of a 10 centimeter-spaced crenulation cleavage S_{n+3} in a north dipping muscovite-chlorite schist. The crenulation is developed irregularly and dies out at the top and the bottom of the sketch. The dip direction of both S_{n+2} and S_{n+3} is similar. The view plane is approximately perpendicular to the strike of the schist. Location of outcrop is at the eastern shore of Kluane Lake, south of Cultus Creek (94-33). Hand of field assistant for scale.

L_{n+2} is harder to distinguish in cordierite-bearing rocks, and non-existing near the contact with the RRB. It is obliterated by static growth of minerals during post-deformational thermal overprinting, concurrent with coarsening of grain size and gneissification.

It can be observed that samples with well developed mineral stretching lineation generally have a distinct monoclinic symmetry that can be used as a shear-sense indicator. Since a mineral stretching lineation is regarded as indicator of progressive deformation (Hanmer & Passchier, 1991), L_{n+2} is contemporaneous with the asymmetrical fabrics described in the previous section. The distinct monoclinic fabric observed in sections parallel to L_{n+2} and the lack of them in sections perpendicular to the lineation support this assumption.

A second lineation L_{n+3} traces the fold hinges of small crenulation folds F_{n+3} on the foliation plane. This lineation was developed concurrently with the crenulation cleavage S_{n+3}. It occurs only locally and is not mappable.

Shear-sense indicators

A distinct asymmetry of the schistosity S_{n+2} can be observed in thin section (Figures 2-4, 3-9, 3-10, 3-11) and outcrop (Figure 2-3), indicating progressive non-coaxial deformation of the schist. Alternating quartz- and mica-rich layers define a mylonitic foliation parallel to S_{n+2}. The plagioclase porphyroblasts behaved as kinematic porphyroclasts, since they ceased growing in the early stage of metamorphism and acted as passively rotated clasts during most of the major deformation period. With a variable porphyroclast content of 15-35 vol.% in a fine grained mica-quartz matrix, schists of the KMA are mylonites or mesomylonites, using the classification of Spry (1969).

Mica grains that define the S_{n+2}-foliation are deflected around plagioclase porphyroclasts with a δ-type shape. δ-type porphyroclasts are a special type of mantled porphyroclasts, where recrystallized plagioclase of the

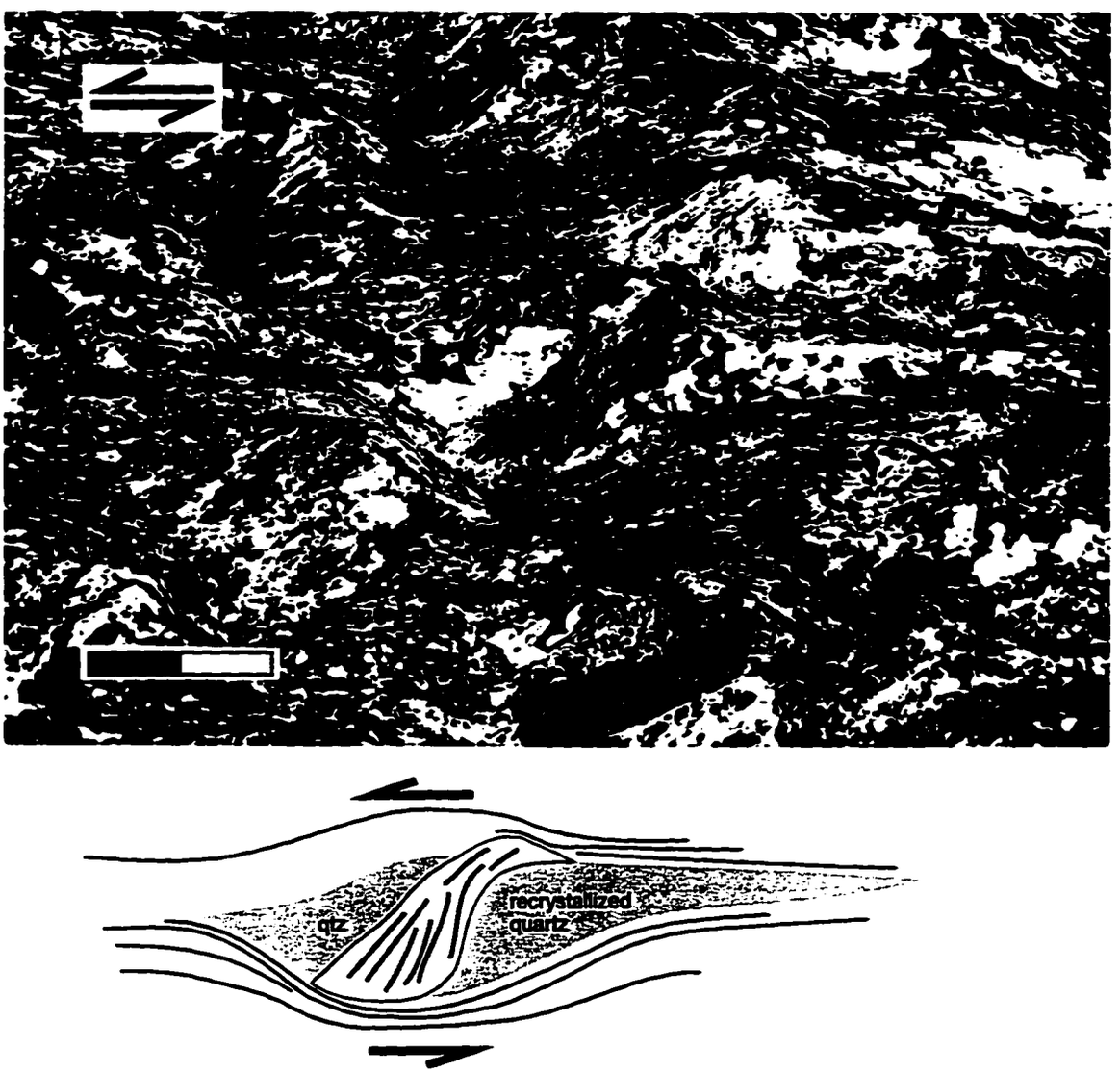

Figure 3-9: Elongated δ-type plagioclase porphyroclast (center) indicating non-coaxial progressive deformation with a top to the left sense of shear (Passchier & Trouw, 1996). Quartz grains are recrystallized in the pressure shadows. Thin section is cut parallel to mineral stretching lineation and perpendicular to schistosity.
Scale bar: 2 mm. XPL

Figure 3-10: Two δ-type plagioclase porphyroclasts indicating top to the right (clockwise) sense of shear. Deflection of the foliation between the two grains give local antithetic shear. This shear is not penetrative, as it is restricted to the zone between two porphyroclast. The foliation to the right of the center grain is aligned to the main schistosity (parallel to long axis of photograph) at the right margin, indicating that the deflection is only caused by the porphyroclast, and not by C'-shear bands, which would indicate opposite sense of shear. The upper part of the photograph is devoid of porphyroclast and no deflection of the foliation is noticed. Pressure solution along the deflected foliation (white arrow) forming stylolites, implies top left to lower right maximum stress direction, in agreement with a top to the right sense of shear. Sample is from the calcic schist on Jacquot Island (94-12). Thin section is cut parallel to mineral stretching lineation and perpendicular to schistosity.
Scale bar: 2 mm. PPL

Figure 3-11: Fine grained mylonite of the calcic schist unit northwest of Haines Junction (95-22). Notice that a C'-shear band is developed above the two center right δ-type plagioclase porphyroclasts (white arrow). C'-shear bands are rarely observed in the KMA and probably restricted to fine grained samples (compare the porphyroclasts in this sample to those in Figures 3-7 and 3-8, which have the same scale) and also indicate higher strain.
Scale bar: 2 mm. PPL

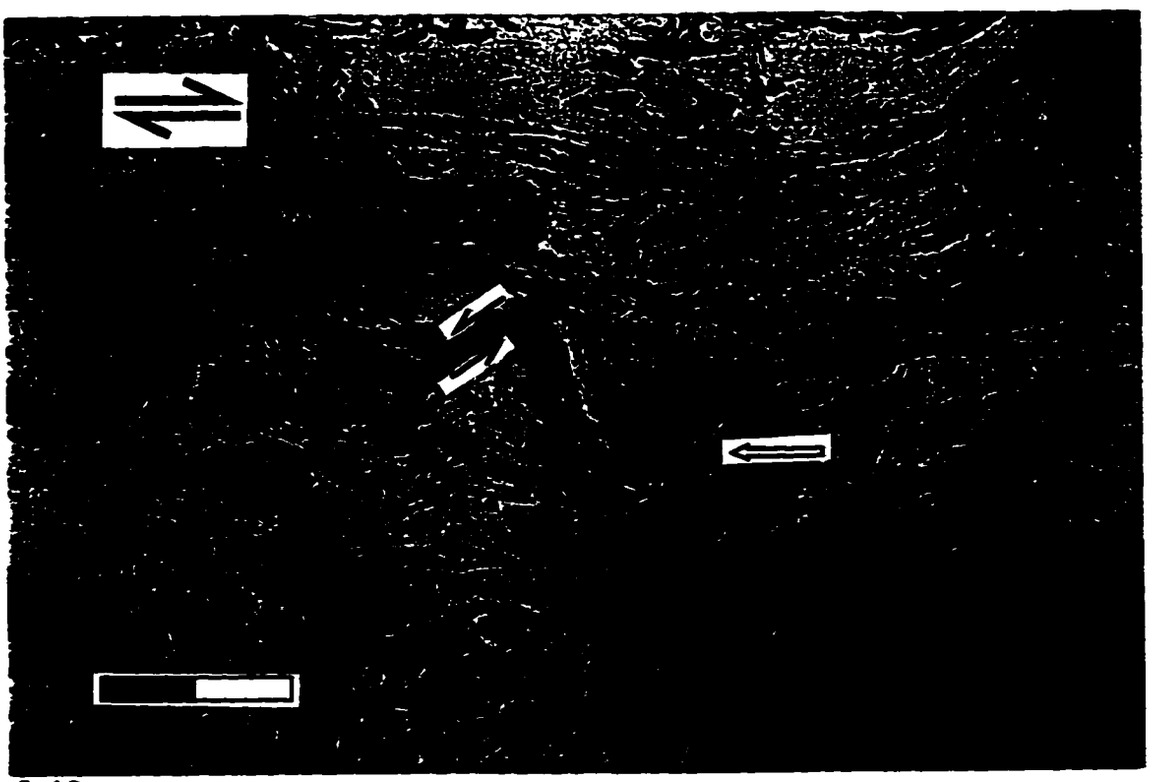

3-10

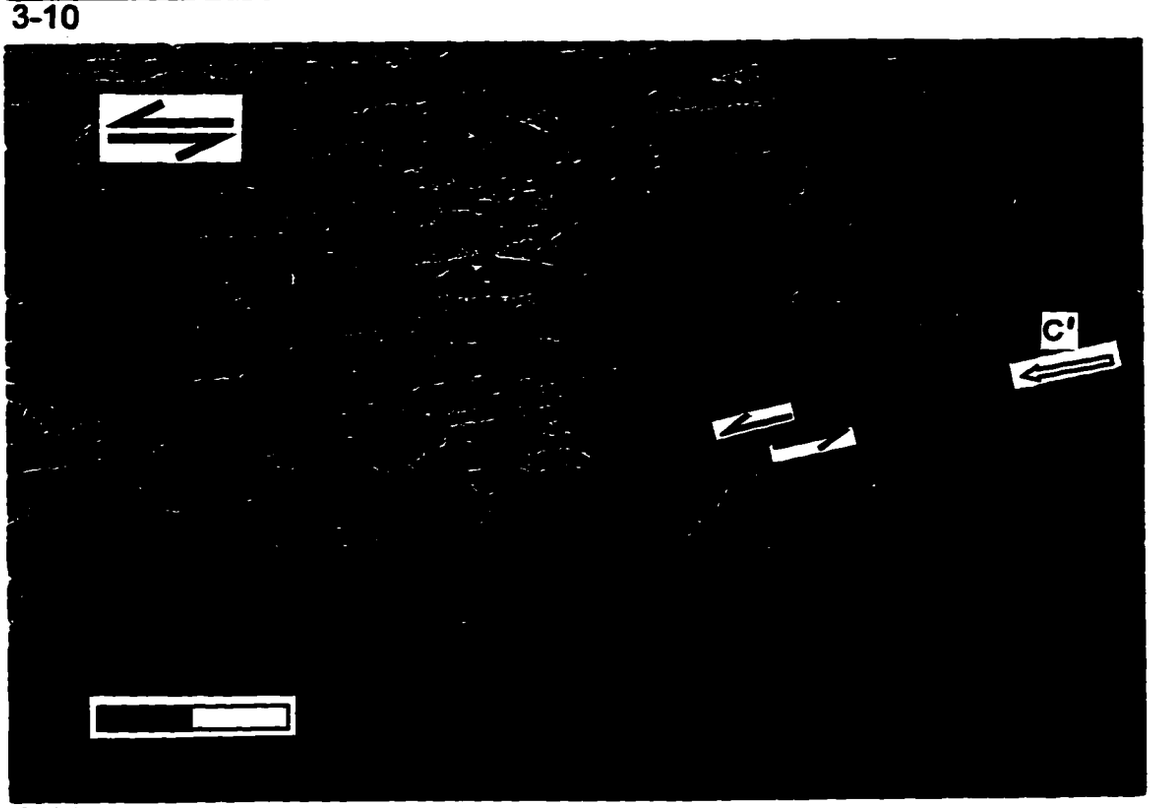

3-11

clast forms wings with a monoclinic shape symmetry, that can be used as a shear-sense indicator (Figures 2-4, 3-9, 3-10). δ-type porphyroclasts are indicative of high strain mylonites (Passchier & Trouw, 1996). Most analyzed KMA schist samples contain δ-type porphyroclasts. A large concentration of these clasts in a thin section give the impression that shear band cleavages are developed. The rotation of neighbouring clasts results in local antithetic shear near the contact of two clasts (Figure 3-10). However, the apparent shear bands are not penetrative on thin section scale and are not developed in porphyroclast-free zones. Figure 3-10 shows that S_{n+2} is being deflected around a single porphyroclast and the magnitude of deflection decreases with distance from the clast.

Shear band cleavages, C/S fabrics (Berthé et al., 1979) and C'-shear bands (Passchier & Trouw, 1996), are rarely observed and may be related to slightly higher strain and/or smaller porphyroclasts (Figure 3-11). In cases where shear band cleavage is observed, the sense of shear is the same as indicated by δ-type clasts of that rock. Oblique foliation of quartz in mm-wide quartz layers distinguished in a few samples and rare spiral-shaped inclusion trails of S_{n+2} in garnet porphyroblasts provide the same sense of shear. In any given sample the shear-sense obtained from porphyroclasts or shear bands is consistent on the scale of the thin section.

Asymmetrical fabrics are also observed in the foliated olivine serpentinite at Doghead Point (Figure 3-7). Narrow shear zones, 0.25-1 mm wide, parallel to the dominant foliation S_{n+2}, separate wider zones (1-3 mm) of oblique grain shape foliation defined by serpentine crystals. The angle between the foliation S_{n+2} and the oblique serpentine grains is 35-45°. The orientation of foliation, lineation and the sense of shear is similar to that of the adjacent ms-chl schist. The described fabric resembles C/S fabrics reported by Norrell et al. (1989) from partly serpentinized peridotites of the Josephine ophiolite in northern California. The formation of the C/S fabrics indicate a maximum T of 550°C, the upper stability limit of serpentine (Norrell et al., 1989). Geothermobarometry of a nearby sample (94-47) yields a temperature 540°C

(see Chapter 4).

The sense of shear shown on Figure 3-12 and listed in Appendix 3-1 was primarily determined from thin section or polished rock slabs, along sections parallel to the mineral stretching lineation and perpendicular to the foliation (Passchier & Trouw, 1996). Only those samples which provided unambiguous sense of shear were considered.

Reliable kinematic indicators observed in outcrops are rare and include transposed quartz veins and centimeter-scale winged porphyroclasts.

Sense of shear observed in schists of the KMA is shown as direction of hangingwall motion on a map and as vectors and slip linears on stereonets on Figure 3-12. The motion of the hangingwall is similar in the western part of the KMA, generally towards west. At the southwestern flank of the KMA, the orientation of the mineral stretching lineation is subparallel to the assumed strike of the Denali fault and hangingwall motion is to the WNW. Further to the east and northeast, towards the contact with the RRB, the lineation changes to a NE-SW direction, with motion of hangingwall towards southwest. Shear-sense indicators are rare in the eastern Ruby Range and the Dezadeash Range, due to thermal overprinting caused by the intrusion of the RRB during the Early Tertiary (see Chapter 4).

The stereonets show a consistent westward-directed hangingwall up oblique slip. Oblique westward thrusting is in contrast with vertical right-lateral strike-slip assigned to the Denali fault to the southwest (Dodds, 1991). Absence of vertical slip planes in the KMA implies that no steep strike-slip faults or shear zones transect the KMA. Therefore west-directed ductile hangingwall motion observed in the KMA is not the result of right-lateral strike-slip along the Denali fault, but indicates oblique underplating of the KMA under the WNW-trending (in current reference frame) North American continental margin, as represented by the AMS, during eastward motion of the Kula plate in the Cretaceous (Figure 3-13; Engebretson et al., 1995). The consistent sense of shear and the lack of regional strain gradients in the KMA suggest

Figure 3-12: Map of the KMA with observed shear-sense indicators. Black arrows point in direction of hangingwall motion, deduced from oriented thin sections. Location of samples and types of shear-sense indicators are listed in Appendix 3-1. Stereographic upper and lower hemisphere projection of shear-sense indicators is shown in upper right corner. Slip linears, which show hangingwall motion as arrows on pole of foliation containing the mineral stretching lineation (Hoeppner, 1955), are displayed in lower left corner. The trace of the Denali fault is after Dodds & Campbell (1992).

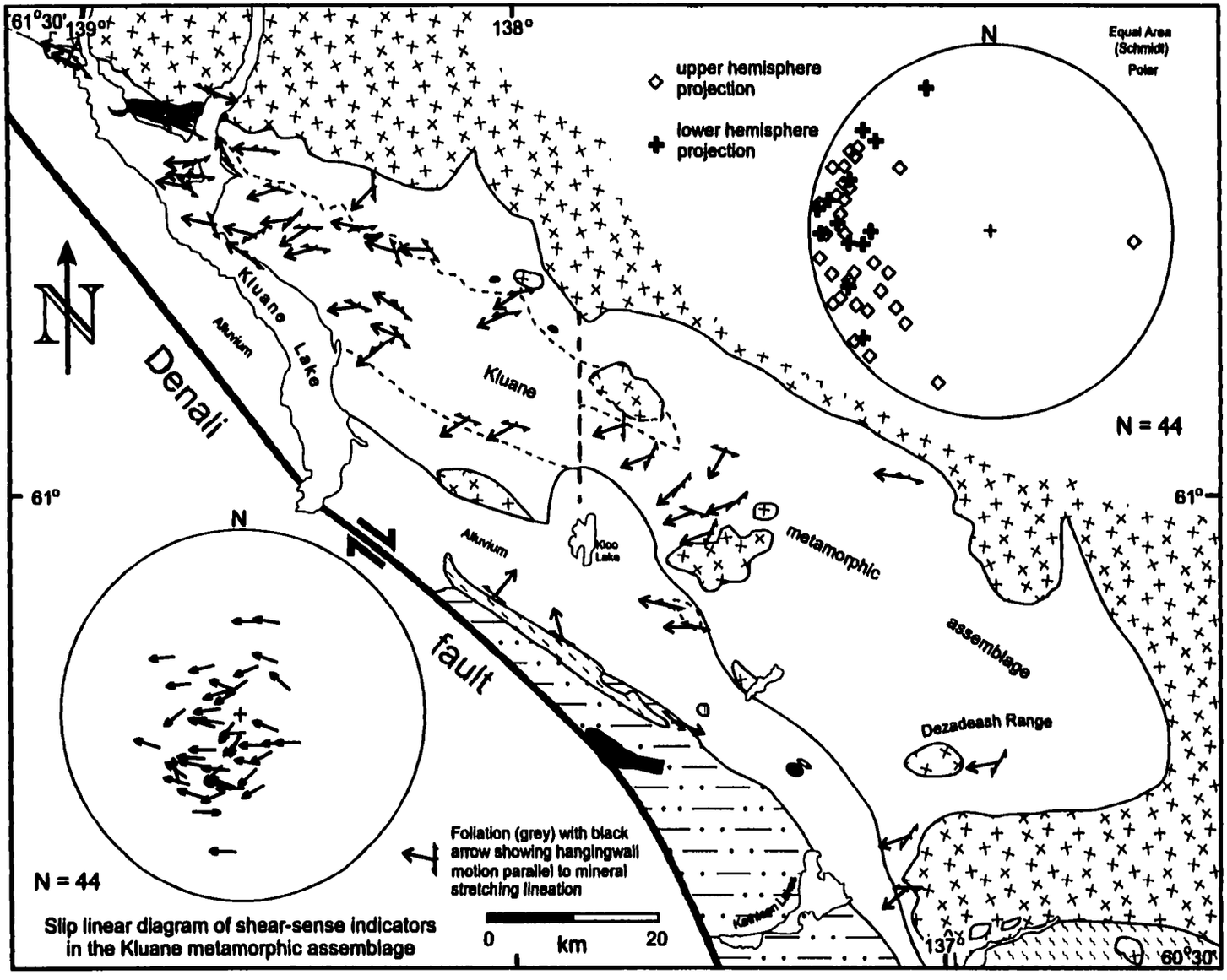
61°30'
139°
138°
N
Equal Area
(Schmidt)
Polar
upper hemisphere
projection
lower hemisphere
projection
Kluane Lake
Alluvium
Kluane
Denali
fault
N = 44
61°
Alluvium
Kloo
Lake
metamorphic
assemblage
Dezadeash Range
Foliation (grey) with black
arrow showing hangingwall
motion parallel to mineral
stretching lineation
N = 44
Slip linear diagram of shear-sense indicators
in the Kluane metamorphic assemblage
0
km
20
137°
60°30'

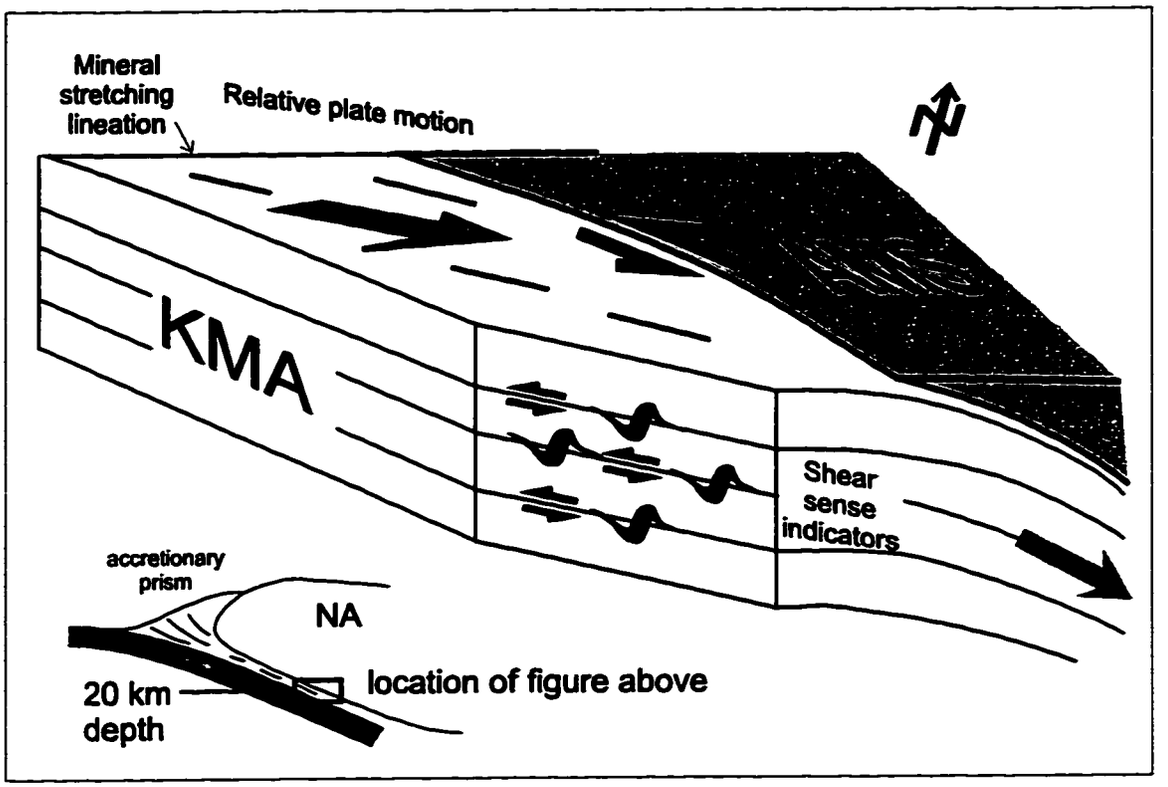

Figure 3-13: Tectonic interpretation of shear-sense indicators in the KMA. Homogeneous hangingwall up sense of shear is compatible with underplating of the KMA underneath the North American continental margin, represented by the AMS. Schistosity of both assemblages currently dip to the NNE. The mineral stretching lineation, which is assumed to lie in the direction of shear direction (Hanmer & Passchier, 1991), is at low angle with continental margin (~ 30°), resulting in oblique slip with a left-lateral horizontal component. Eastward motion of the Kula plate, between ~80-95 Ma (Engebretson et al., 1995), resulted in the collapse and subduction of the oceanic basin onto which the KMA was deposited, and eastward underthrusting of the KMA underneath North America. The block diagram displays the presently exposed erosional surface. The actual accretion to the upper plate (AMS) and ductile deformation of the KMA occurred at depths of 20 km (see small sketch).

that the KMA was deformed as a whole. Local narrow high strain shear zones were not observed in the field. However, it is possible that some may exist that may not have been noticed, since sampling occurred on a kilometer scale and continuous outcrop exposure is not always realized.

The magnitude of finite strain and the amount of extension during deformation are hard to determine, since no objects of known shape exist on which deformation can be measured. Also, the deformed KMA schists do not represent a complete shear zone, since no undeformed wall rocks exist from which a strain gradient could be determined.

Consistent strain of the mylonized schist and a possible depth of syndeformational metamorphism of approximately 20 km (see Chapter 4), suggest that the oceanic sedimentary protolith of the KMA was accreted to the base of an overriding plate (AMS) during eastwards subduction, similar to models proposed by Karig (1974, 1982).

The age of the asymmetric fabric and thus the age of the deformation D_{n+2} cannot be dated directly. The presence of synkinematic garnets (Figure 3-6) and undeformed crosscutting quartz veins overgrown by sillimanite and cordierite (Figure 3-14) show that peak metamorphism post-dates peak deformation. K-Ar and ^{40}Ar-^{39}Ar ages of 39-60 Ma record cooling through the 280°C and 350°C blocking temperature for argon in biotite and muscovite, respectively (Erdmer & Mortensen, 1993). An ^{40}Ar-^{39}Ar muscovite age of 51.1 ±0.5 Ma was obtained from a sample of the lowest metamorphic grade on Jacquot Island (94-3, Appendix 2-7). A late-synkinematic boudinaged fine grained biotite granite dyke from the eastern part of the KMA recorded U-Pb zircon ages of 68.4±0.2 Ma and 71.8±0.2 Ma and U-Pb monazite age of 55.6±0.6 Ma (Figure 2-18; Appendix 2-10; Mortensen, unpublished data, 1997). The older age represents the emplacement age of the dyke, while the younger age reflects thermal overprinting in the Eocene. The blocking temperature of monazite (~700°C; Heaman & Parrish, 1991) is close to the peak temperature obtained from a sample taken from an outcrop nearby (94-

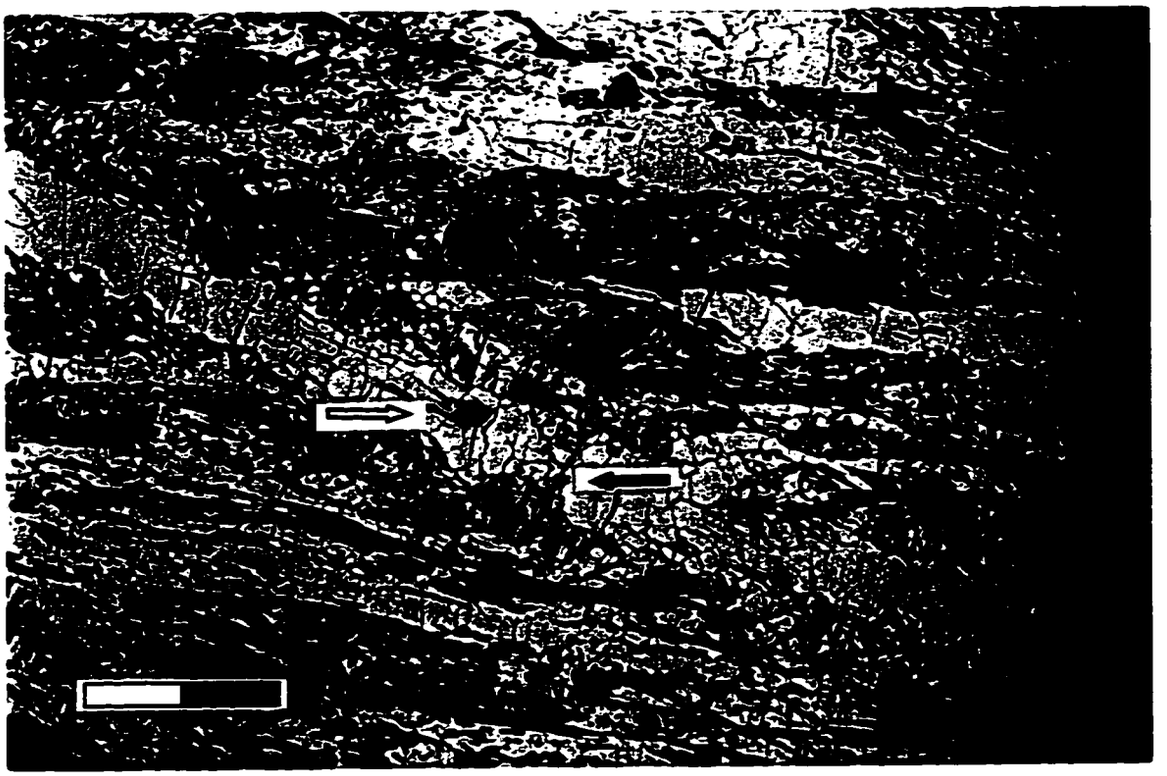

Figure 3-14: Photomicrograph of a cordierite-biotite-quarz schist north of Garnet Creek. A well defined schistosity, parallel to the long axis of the photograph, is crosscut by a small quartz vein. The vein does not appear to be deformed. In the center of the picture, the vein is overgrown by cordierite (black arrow), recognized by its higher relief and a yellowish brown altered rim. To the left fibrolitic sillimanite (white arrow) nucleates in the quartz vein. This indicates that peak metamorphism is postkinematic. (94-146).
Scale bar: 2 mm. PPL

81, 660°C). An undeformed granitic dyke from an outcrop nearby yielded U-Pb zircon and monazite ages of 54.6±0.2 Ma and 54.7±0.9 Ma, respectively (Appendix 2-10; Mortensen, unpublished data, 1996). These ages indicate that ductile deformation of the KMA took place as late as Late Cretaceous, but had ceased by early Tertiary. No direct geological evidence is given for the maximum age of deformation. However, the lack of high P/high T mineral assemblages suggests that deformation and associated high P metamorphism of presently exposed KMA schist did not occur over an exceedingly long period (20-30 Ma, see Chapter 4).

Folds

Crenulation folding of assumed original bedding S_n is preserved in some plagioclase porphyroblasts (Figure 3-4). Since these are found in thin sections of only a few samples, and the host grains were subject to deformation, the orientation of F_{n+1}-fold axes cannot be determined.

Curvature of the graphite layers representing S_{n+1} in plagioclase porphyroblasts is interpreted as the result of synkinematic growth of the porphyroblast during non-coaxial progressive deformation, and does not reflect folding (Figure 3-5).

In outcrop, S_{n+2}-foliation can appear wavy, forming gentle folds with amplitudes of 10 cm and wavelengths of 1-2 m. When more distinct folding is developed, open folds with wavelength ranging from several centimeters to 10 m and amplitudes of a few centimeters to 3-4 m are most common (Figure 3-15, Appendix 3-2). However, observed tightness of folds covers the whole spectrum from open to isoclinal. Fold shapes vary from symmetrical to slightly asymmetrical, upright to steeply inclined. Recumbent folds are less common and occur predominantly in the Dezadeash Range. Asymmetrical folds are often disharmonic, and their limbs sheared off. West to southwest vergence of the folds is slightly dominant. The majority of the folds can be classified as parallel or 1b type folds (Ramsey, 1967). Second-order folds, from millimeter-

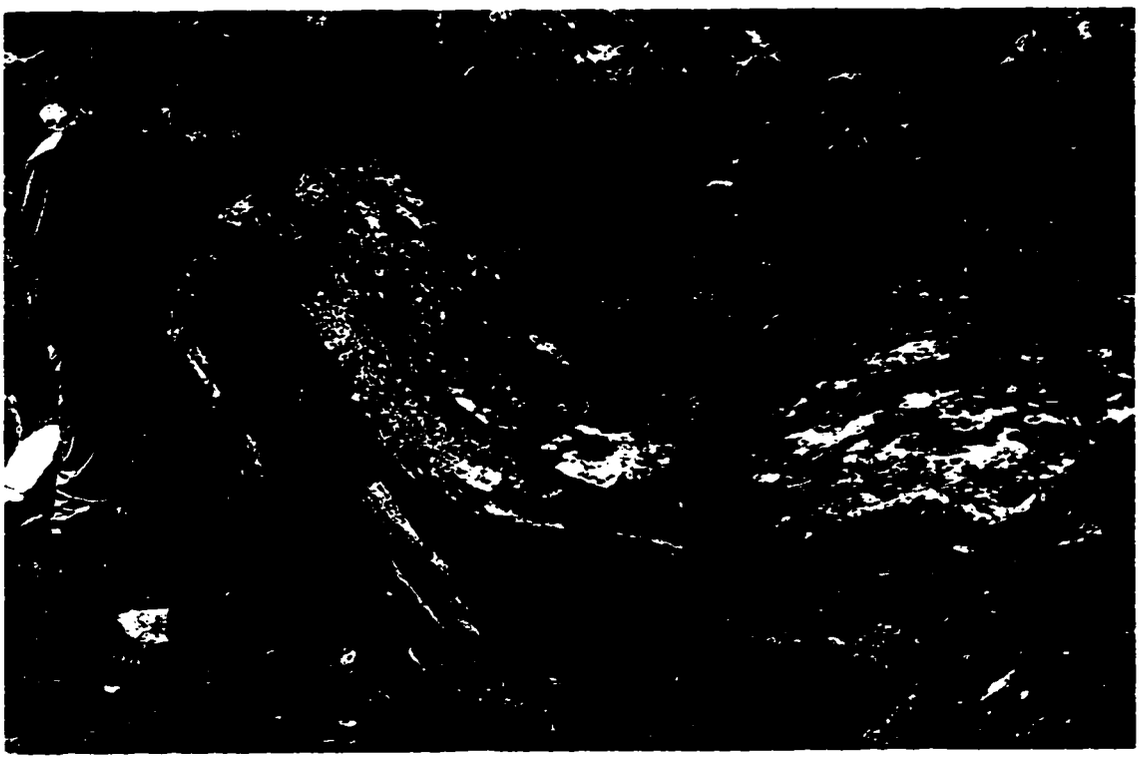

Figure 3-15: Mesoscopic open F_{n+3}-fold in muscovite-chlorite schist of the KMA on a ridge east of Cultus Bay, Kluane Lake (93-23). The fold axis plunges moderately to the north (350/25). The fold has an amplitude of 1 m and a wavelength of 3 m. S_{n+2}-schistosity in the area dips moderately to the north east. P. Erdmer for scale.

scale crenulations to larger structures with amplitudes of 5 cm and wavelengths of 10-15 cm are commonly developed on the limbs of upright open folds. Crenulation folding with the same axis orientation can also occur without larger folds.

Locally, a crenulation cleavage S_{n+3} has formed in the hinge zones of F_{n+3}-folds (see previous section).

Mesoscopic F_{n+3}-folds effect only layers with thickness in the order of a few meters. These folds are not penetrative on a regional or even at outcrop scale. In the northwestern Dezadeash Range mesoscopic folding is common in an area of several square kilometers.

The orientation of F_{n+3}-fold axes are similar, suggesting the same deformation event. Fold axes plunge shallowly towards southeast or northwest throughout the whole KMA (Figures 3-1, 3-2).

In the southeastern part of the KMA, in the eastern Ruby Range and in the Dezadeash Range, S_{n+2}-schistosity is folded into a 20 km wide ESE-plunging anticline (Figures 3-1, 3-3). An along-strike change from generally north- to south-dipping schistosity is observed east of Kloo Lake. Although there is no field evidence for faulting, the area being underlain by a 10 km wide lowland around Kloo Lake, the structural change from north-dipping homocline west of Kloo Lake to an anticline east of the lake is best explained by a fault (Figure 3.1). However, near the Killermun plug to the north, orientation seems to be continuous. The nature of the proposed fault is not known and the fault remains a conjecture.

Stereographic analyses presented in the following section show that the attitude of the regional fold axis, derived from foliation data east of the presumed fault, is virtually identical with that of mesoscopic fold axes (Figure 3-19). It is therefore inferred that regional scale folding and local mesoscopic folds are part of the same deformation event. The WNW-ESE trend of the F_{n+3}-fold axes indicates NE-directed compression. Although F_{n+3}-folding cannot be dated directly by geochronology, folding of S_{n+2} and higher peak metamorphic pressures on the southern south-dipping limb, suggest that F_{n+3} occurred after

peak deformation in the latest Cretaceous and before the emplacement of the RRB in the Early Eocene.

Variations of the dip direction of S_{n+2} over several hundred meters to a few kilometers can be attributed to deflection near the contact with the RRB or associated plugs within the KMA (Figures 2-9, 2-10).

BRITTLE STRUCTURES

Faults

The lithological homogeneity of the KMA and the absence of distinct marker horizons make identification of faults difficult. As a result most published maps show very few faults, if any, within the KMA (Kindle, 1952; Muller, 1967; Tempelman-Kluit, 1974). The faults shown on the Dezadeash map sheet are inferred from aerial photographs and are not supported by geological evidence (Kindle, 1952). Fieldwork carried out for this project did not find any evidence for faulting at the given locations.

Faults are proposed by Muller (1967) at the contact between the calcic and aluminous schist in the Ruby Range and by Erdmer (1990) in the eastern Dezadeash Range, where the KMA is assumed to be in contact with the Nisling assemblage. The probability of those structures is discussed in Chapter 2, where it is concluded that the contact in the Ruby Range presents a syndeformational or primary sedimentary contact, while the contact in the Dezadeash Range does not exist.

During work for this study only five faults within the KMA could be identified from geological evidence in the field (Figure 3-16). Two undeformed crosscutting dykes are offset by north-trending faults north of McKinley Creek valley in the northeastern Ruby Range (93-137, 94-119). The faults show apparent right-lateral strike separation of 5 m and 20-25 m, respectively. The dip of the fault plane is not known. A right lateral north-trending fault with a strike separation of approximately one kilometer is inferred from offset of the

Figure 3-16: Major lineaments in the Kluane Metamorphic Assemblage. Valleys are shown as thick grey lines, dykes as thin grey and black lines and lines with arrows represent faults with known along strike displacement. The major lineaments in the Ruby Range Batholith are the Three Guardsmen (1) and the Dezadeash River (2) lineaments. The nature of the Three Guardsmen lineament is not known. The Dezadeash River is thought to be the location of a tear fault that juxtaposes rocks of the KMA, from Nisling assemblage rocks to the southeast that were at higher structural levels during Eocene metamorphism.
Rose diagrams of the dykes are shown on the inset in the upper right corner. The relationship between conjugate Riedel shears (R, R'), P-shears, extension fractures with faulting and major stress direction σ_1 is shown on the sketch in the lower left corner (modified after Twiss & Moores, 1992). The strike of the majority of the observed dykes lies perpendicular to the extensional direction. The north-trending valleys and observed faults can be correlated with Riedel shears that became active after the dyke emplacement in a more brittle environment. The southeast-trending linears are subparallel to the Denali fault and may represent dextral faults with unknown offset.

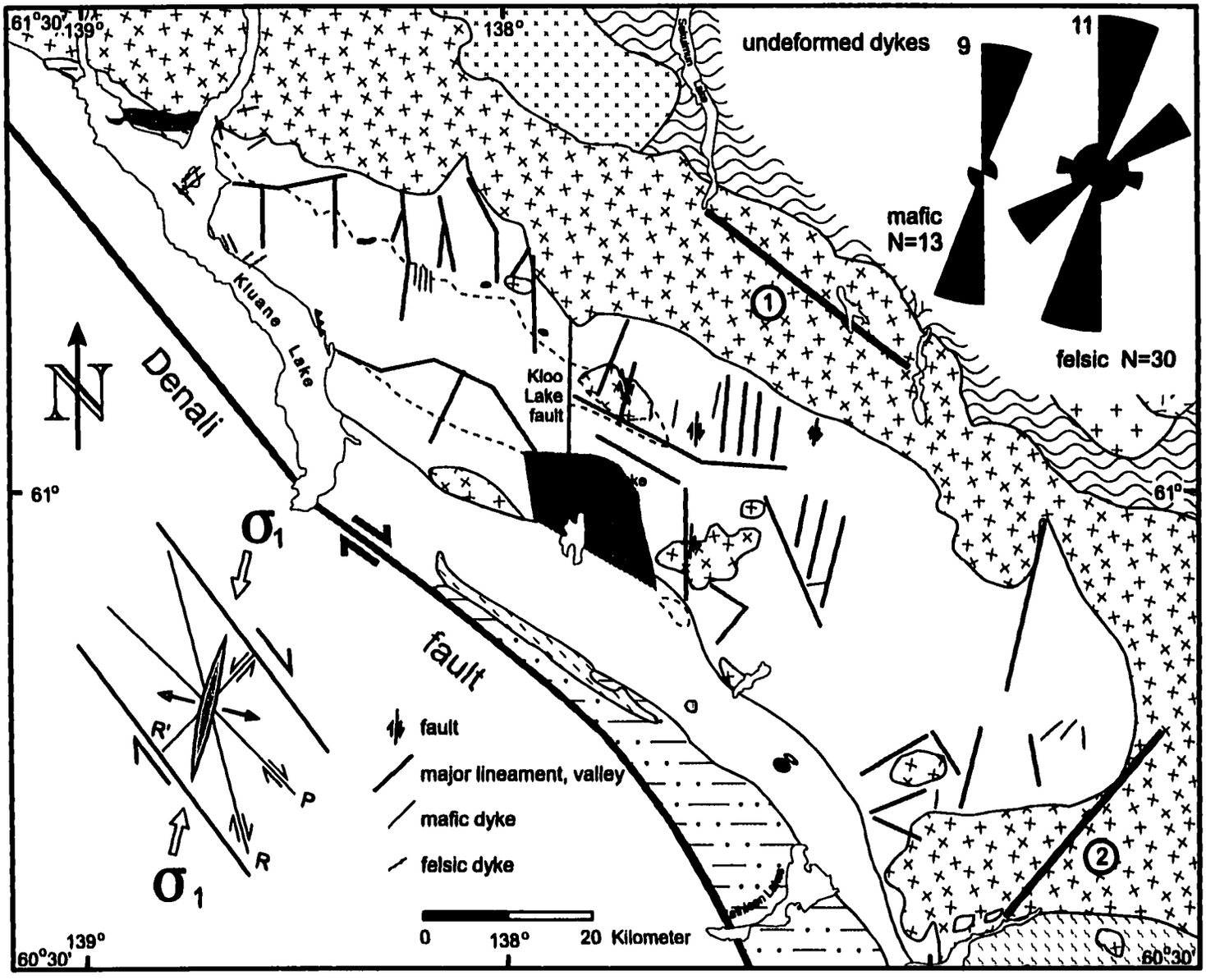
61°30'
139°
138°
undeformed dykes
9
11
mafic
N=13
felsic N=30
Kluane Lake
Kloo
Lake
fault
Denali
fault
61°
σ1
σ1
R'
P
R
fault
major lineament, valley
mafic dyke
felsic dyke
0
138°
20 Kilometer
60°30'
139°
60°30'
1
2

contact between the KMA and a granodiorite plug at the headwaters of Marl Creek (Figure 2-10).

A more prominent fault, located south of Killermun Lake also displaces the KMA-RRB contact (Figure 3-17). The fault strikes SSE and has an apparent right-lateral strike separation. The amount of displacement and the nature of the fault could not be determined. A well preserved fault scarp can be traced along the slope of the ridge. Since the valley was formed during the latest glaciation period, the McConnell glaciation (~10 ka; Bostock, 1966), the presence of fault scarps suggests that the fault has been active during the Holocene.

A north-striking steep dipping reverse (?) fault offsetting the muscovite-chlorite schist can be seen on a ridge at the eastern Kluane Lake shore, between Cultus and Thorsen Bay (94-33). A well preserved fault scarp indicates recent displacement in the order of five meters.

Two faults for which there is no direct field evidence are proposed on the basis of structural and metamorphic data. A north-trending fault in the Kloo Lake area, dividing the KMA into a northwestern and southeastern structural domain, is inferred from structural discontinuity. Also, the apparent tapering of the calcic schist in the east may be caused by truncation along the proposed fault. East of the fault the calcic schist crops out just south of the Killermun Lake plug. In the eastern domain mesoscopic F_{n+3}-folds plunge to the ESE, while they plunge WNW in the western domain. Peak metamorphic pressures along the upper contact of the KMA do not show a significant gradient to support post-metamorphic tilting of the eastern domain or large vertical displacement between the domains (Figure 4-11). This constricts the timing of faulting to the period immediately prior to the intrusion of the RRB.

A NNE-striking tear fault is assumed to lie in the Dezadeash River valley. Indirect evidence for the presence of a fault is given by the steep slope of the mountains flanking the valley. The fault is necessary to juxtapose the KMA in the Dezadeash Range which record higher pressures during Eocene metamorphism with Nisling assemblage rocks east of Dezadeash Lake that

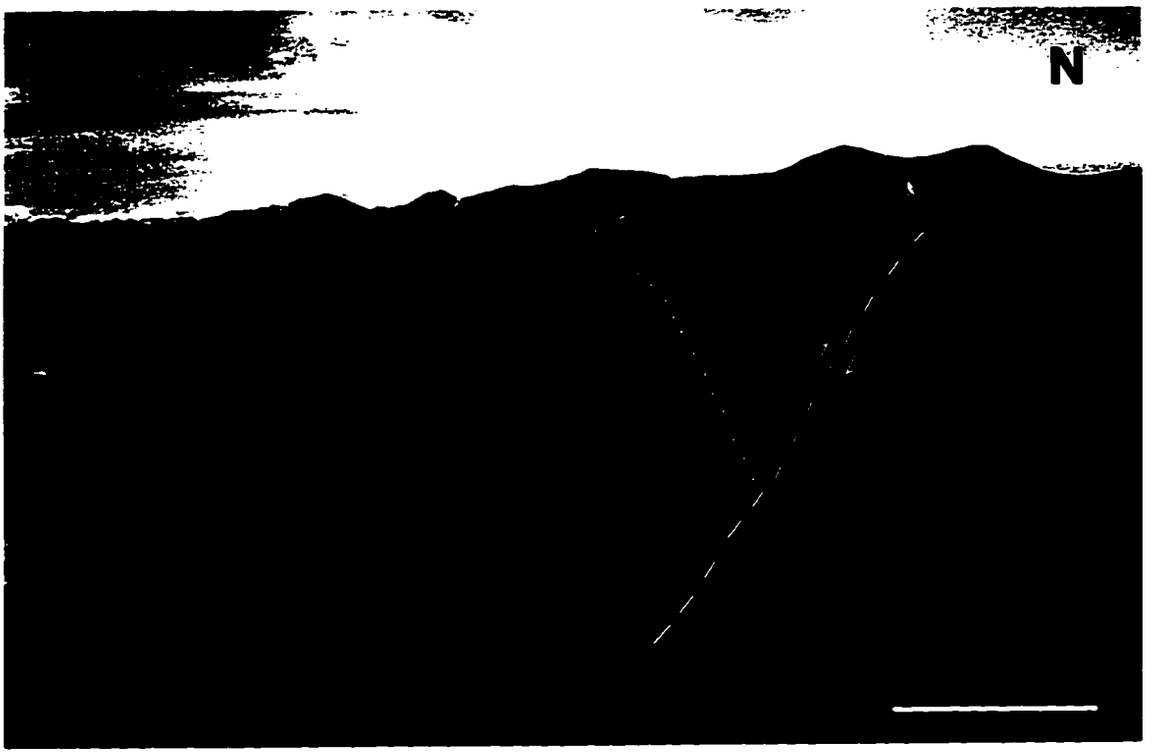

Figure 3-17: One of few observed brittle faults. The contact between the granodiorite of the Ruby Range Batholith and the biotite-quartz schist of the KMA (dotted line) south of Killermun Lake (93-67) does not continue to the foot of the mountain. A north-trending fault can be traced along a little scarp (to the right of the dashed line). The apparent displacement and the fault scarp suggests an oblique slip fault. The bush covered talus at the foot of the mountain hides any trace of the contact. Thin white lines indicate orientation of foliation of the schist. Scale bar equals 200 m.

experienced only weak metamorphic overprinting in the Eocene. The exhumed KMA rocks reflect greater depth, and were likely juxtaposed with the Nisling assemblage along a tear fault during more extensive uplift of the KMA compared to the Nisling assemblage (Figure 3-1).

The strike of the faults parallels major valleys in the Ruby Range and the undeformed mafic dykes (Figure 3-16). Narrow north-trending depressions are also occupied by Aishihik Lake, Sekulmun Lake, Talbot and Brooks arms of Kluane Lake, Aishihik River and Brooks Creek. Compared to a stress pattern with a right-lateral Denali fault as a reference, north-trending structures are close to the orientation of a right-lateral Riedel shear (Figure 3-16). The major compressional stress σ_1 would strike 15°, as a result of northward subduction of the Yakutat block underneath the St. Elias Mountains (Horner, 1983).

Jointing

Jointing is common in the schist, although it is not a striking feature. Joint planes are generally vertical and perpendicular to the overall strike of the foliation of the schist. The spacing is irregular and in the range of tens of centimeters to a few meters. Well developed jointing can be observed on a ridge north of the McKinley Creek valley in the eastern Ruby Range (94-108, 109). There, vertical joint planes, striking 10° and 100°, spaced less than one meter, have developed in a shallow NNE-dipping biotite-quartz schist. A 20°-striking, vertical, fine grained granodiorite dyke cross-cuts the schist. Moderately (40-50°) southeast- and north-dipping joint planes are also observed in the same outcrop. The origin of jointing is probably related to the latest stage of uplift of the KMA.

STRUCTURAL ANALYSIS OF THE KMA

Introduction

Statistical analysis of structural data can provide information on regional structural trends that may be overprinted by local variations. Structural data is planar or linear and is commonly represented by stereographic projections (Schmidt, 1925; Bucher, 1944). Foliation, lineation and fold axes data collected in the KMA was analyzed by using SpheriStat 2.0, a Windows-based software program which produces stereoplots, circular rose diagrams and maps, calculates principle directions and provides a number of structural analyses (Pangaea Scientific, 1995). Stereoplots shown in Figures 3-18, 3-19 and 3-20 are lower hemisphere projections using an equal area Schmidt net. Density contours are calculated by the Gaussian counting method. The statistical methods are described in Appendix 3-3 and the structural data are listed in Appendix 3-4.

The following results are not intended to represent a quantitative structural analysis. The availability of structural data depends on outcrop density, which can vary throughout the area underlain by the KMA. Spatial averaging of the data was not attempted.

Results and discussion

Figure 3-18 represents the total structural data collected in the KMA: 583 S_{n+2}-foliation, 149 L_{n+2}-mineral stretching lineation and 143 F_{n+3}-fold axes measurements. The foliation data forms a moderately developed cluster with girdle (modified Flinn diagram analysis by SpheriStat). A major maximum coincides with the E_3-eigenvector. The E_1-eigenvector, which represents regional fold axis, has an orientation of 104/08. The trace of the fold axis shown on the regional map on Figure 3.1 and on cross section C-C' (Figure 3-3), approximated from the location of the hinge zone, trends slightly more to the southeast (115°). Fold axes data display two maxima, one shallowly SE-

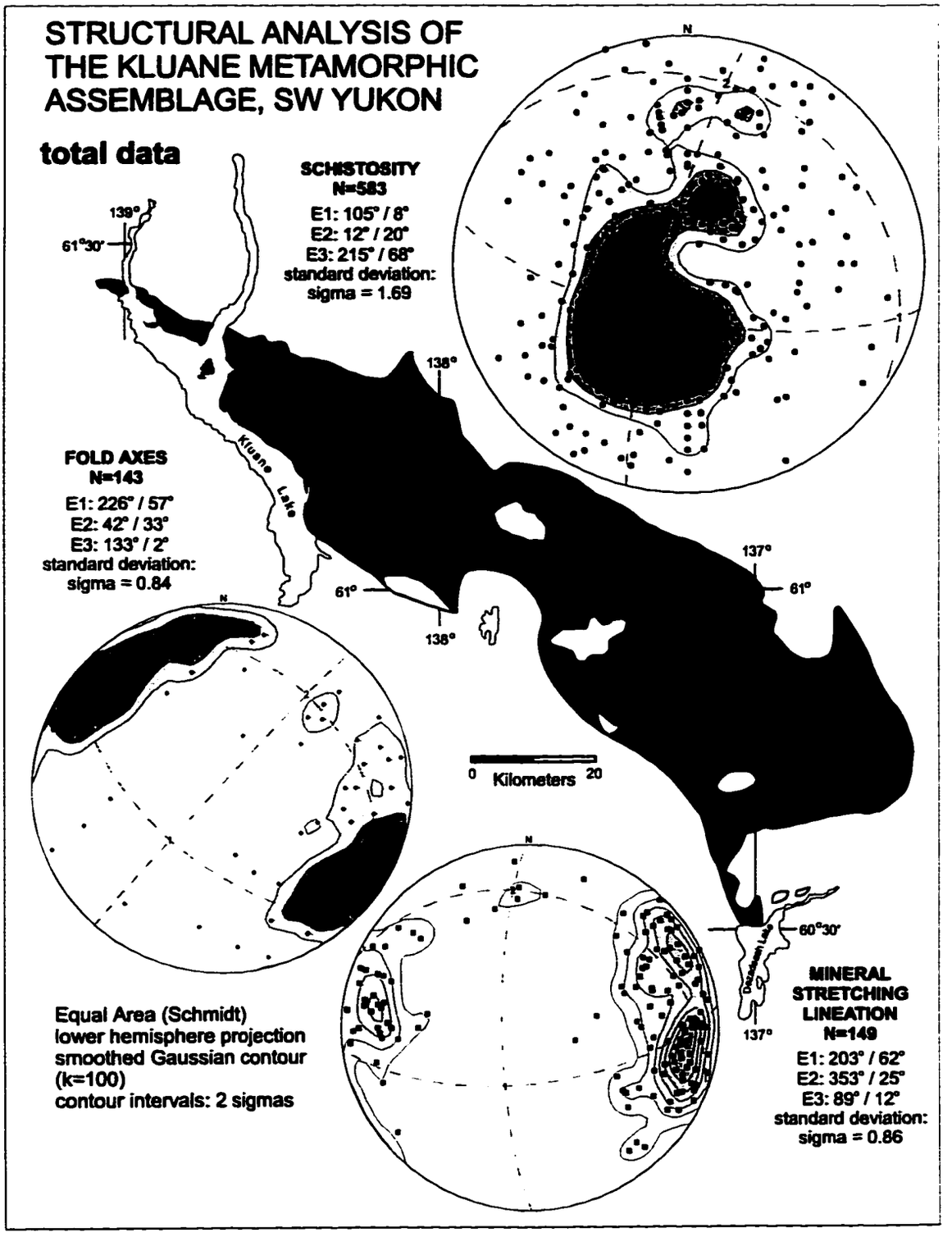

Figure 3-18: Stereographic presentation of total S_{n+2}-schistosity, L_{n+2}-mineral stretching lineation and F_{n+3} mesoscopic fold axes data of the KMA.

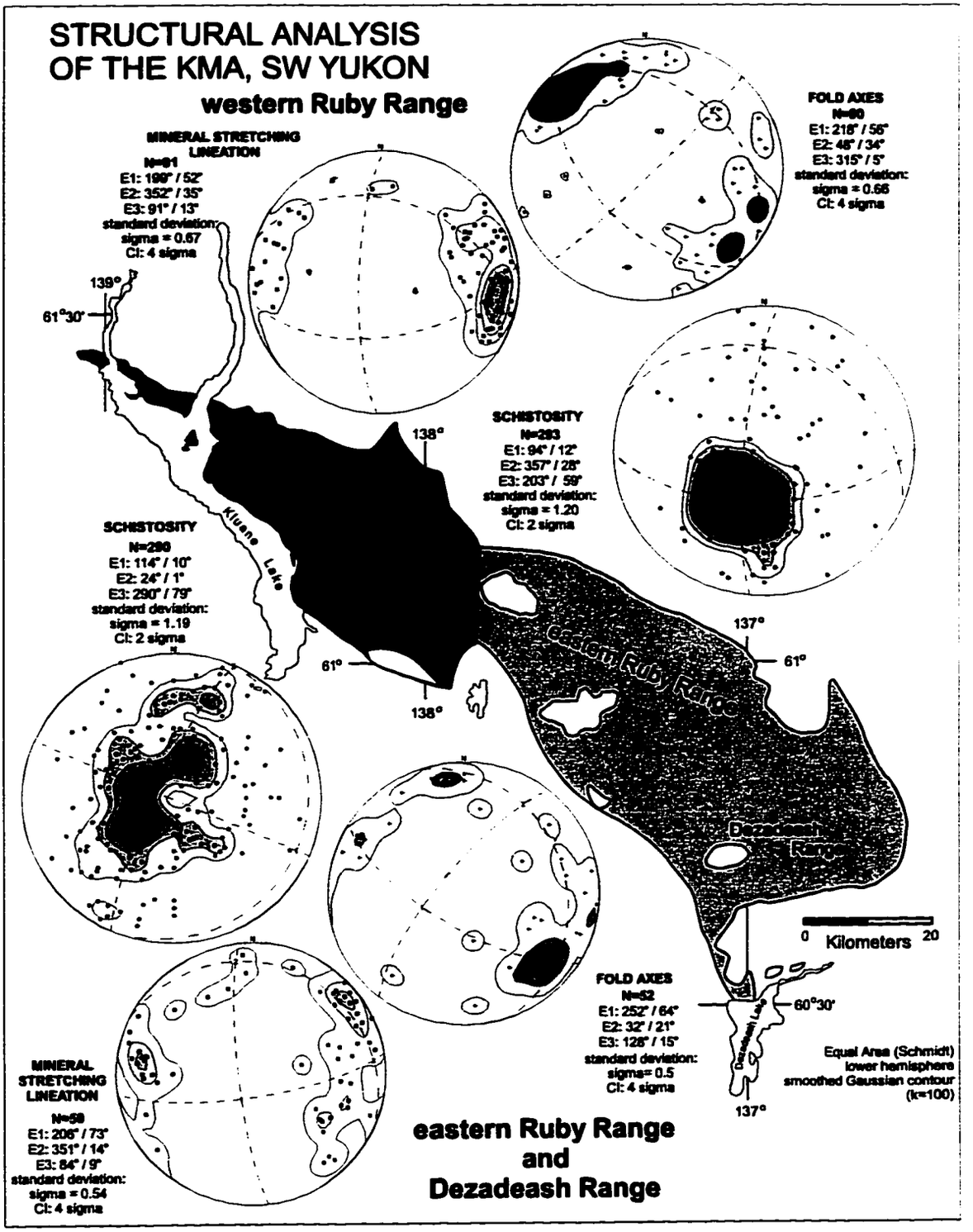

Figure 3-19: Stereographic presentation of S_{n+2}-schistosity, L_{n+2}-mineral stretching lineation and F_{n+3} mesoscopic fold axes data of the northwestern and southeastern structural domains of the KMA.

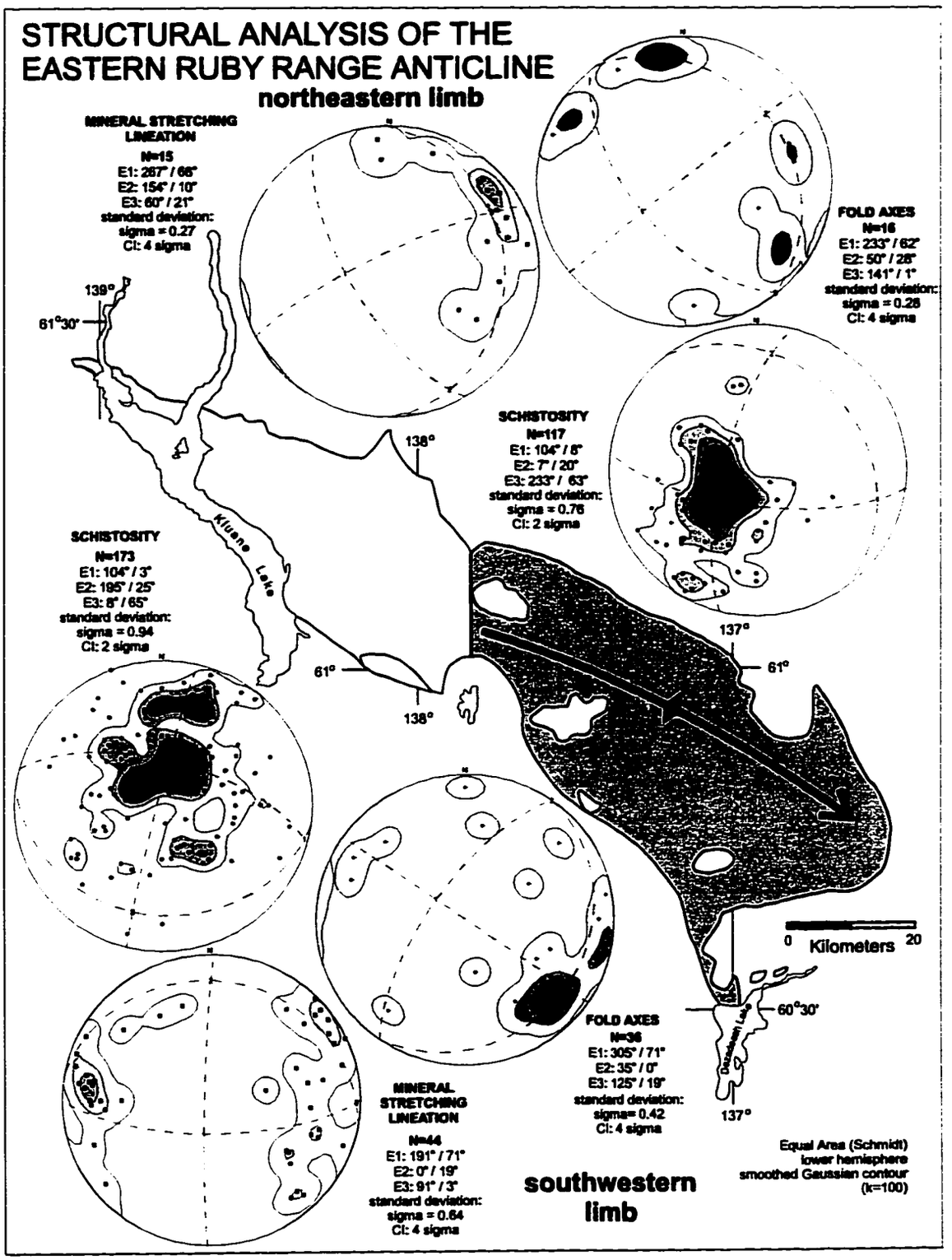

Figure 3-20: Stereographic presentation of S_{n+2}-schistosity, L_{n+2}-mineral stretching lineation and F_{n+3} mesoscopic fold axes data for the northeastern and southwestern limb of the Ruby Range anticline.

plunging, the other shallowly NW-plunging. Mineral stretching lineation data cluster at low angles in the east, east-northeast and west.

It has been noted above that regional folding is observed only in the eastern part of the KMA. The KMA is subdivided into a northwestern and a southeastern domain, on the assumption that a fault is located in the Kloo Lake lowlands (see above).

Schistosity of the northwestern domain forms a moderately developed cluster, presenting a NNE-dipping homocline, as observed by the earliest workers (Figure 3-19; McConnell, 1905). A regional anticline in the southeastern domain is reflected in the moderately developed girdle with cluster. E_1 (114/10) of the schistosity is close to the maximum eigenvalue E_3 (128/15) of the mesoscopic fold axes, strongly suggesting that regional and local folding are related. This was not evident from field data.

Fold axes of the northwestern domain plunge shallowly to the northwest or southeast. No regional variation is observed, as both orientations are represented in single outcrops. The difference between the maxima of both domains is minimal (E_3 northwest: 315/05, E_3 southeast: 128/15) and data of both domains overlap.

Mineral stretching lineation in the western domain has a well developed cluster, with a shallow east-plunging maximum (91/13), coinciding with E_1 of the schistosity in that domain. This reflects the general observation in the field that strike of foliation and plunge of lineation are subparallel. But similar to the fold axis pattern, mineral stretching lineation does not vary significantly between both domains, their maxima being virtually identical (E_3 northwest: 94/12, E_3 southeast: 89/09). A minor northeastern maximum is observed in both domains, and especially in the northern flank of the anticline (Figures 3-19, 3-20). This is interpreted as an original regional deviation, since it stretches from the eastern Kluane Lake shore diagonal across the domain boundaries to the western margin of the KMA.

Wider scattering of structural data in the eastern domain can be explained by several granodiorite plugs or diapirs of the RRB within the KMA

that deflect the foliation locally. Except for the southernmost area in the Kluane Hills no RRB intrusions are observed in the western domain.

Structural data of the northeastern and southwestern limb of the anticline in the eastern domain are shown on Figure 3-20. The most notable difference, apart from the dip direction of the foliation, which defines the limbs, is the absence of westerly trending lineation on the northern limb.

The influence of the regional folding on the orientation of the mineral stretching lineation on the southern limb was tested by clockwise rotation of the lineation of 60° around an axis of 115/10, the approximate attitude of the regional fold axis. The result after rotation does not differ much from the original orientation. E_3 changes from 91/03 to 288/14 (Appendix 3-5).

A similar test was made with shear-sense indicators on the southwestern limb. Generally, the sense of hangingwall motion does not change after the planes containing the mineral stretching lineation were rotated around the regional fold axes, so that they approach a northerly dip of approximately 30°. The direction of motion, measured along the trend of the mineral stretching lineation varies only by 10-20° (Figure 3-20, Appendix 3-6). Therefore, it is not necessary to restore shear-sense direction on the southwestern limb to pre-folding orientation. The important conclusions of statistical analysis of structural data of the KMA can be summarized:

1) A subdivision of the KMA into a northwestern and a southeastern domain along a presumed north-trending fault as suggested by structural discontinuity is supported by stereographic analysis.
2) In the southeastern domain E_3 of mesoscopic F_{n+3}-folds and E_1 of S_{n+2}-foliation have identical shallowly plunging ESE-trends, suggesting that both are results of the same deformation event.
3) The trend of the regional fold axis, E_1 of S_{n+2}-foliation, is similar to the trace of the hinge zone on the map.
4) Northeasterly trending mineral stretching lineation occurs in all domains along Jarvis River-McKinley Creek and can be interpreted as regional deviation during underplating of the KMA.

5) The direction of shear-sense has not been changed significantly on the southern limb by folding and tilting of the regional anticline.

REGIONAL CORRELATION

Certain structures of the metamorphic assemblages of Nisling terrane affinity and the DF bear similarities to those of the KMA, providing important information on the tectonic evolution of the Coast Belt-Insular Belt boundary.

The orientation of schistosity of the metamorphic assemblages east of the Denali fault, the KMA and the AMS and Nisling assemblage define a large ESE-plunging anticline, with the KMA in its core zone (Figures 3-3, 3-21). The anticline can be traced from the north end of Kluane Lake to Kusawa Lake, 200 km to the southeast.

Mesoscopic open folds and crenulation folds with moderately ESE- to SE-plunging fold axes are common in biotite-quartz schist of the Nisling assemblage east of Dezadeash Lake and in the Kusawa Lake area, 40 Km further east. Regional folding in the same area has a similar orientation (Erdmer 1989, 1990).

WNW-trending regional open folds are also reported in the Dezadeash Formation of the Auriol Range, where they are superimposed on northerly trending folds (Eisbacher, 1976). Mesoscopic southwest-verging open folding with wavelengths of a few meters and millimeter-scale crenulation folds in the DF and greenschist units in the Jarvis River area plunge shallowly to moderately southeast (Figure 2-10, Appendix 3-7).

The similar orientation of regional folding and local mesoscopic folds within the KMA, Nisling assemblage and the DF suggest a common origin in a NNE-directed stress field. In the metamorphic assemblages regional and mesoscopic folding overprint older penetrative foliation. Since the metamorphic assemblages in the eastern part are found as roof pendants within the generally undeformed granodiorites of the CPC, this folding event, F_{n+3} in the

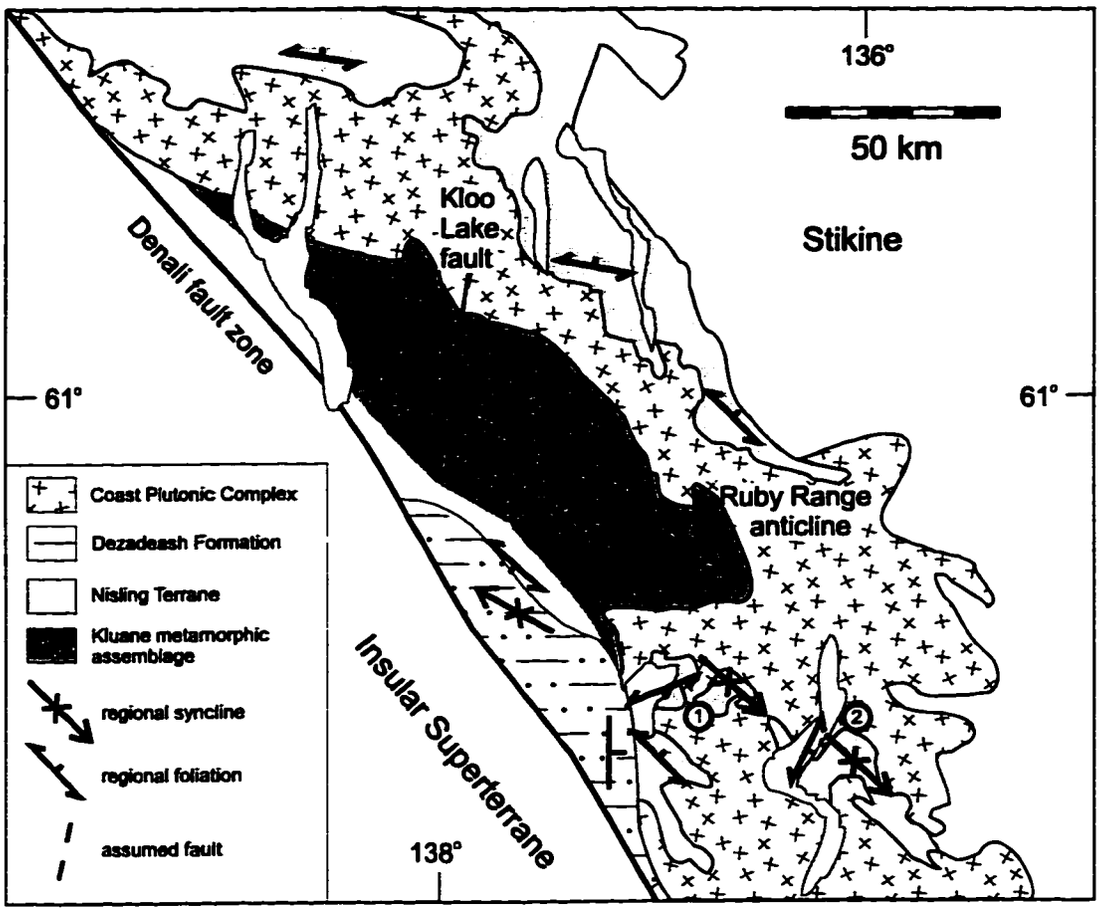

Figure 3-21: Generalized structural map of the southwest Yukon with metamorphic assemblages outlined in grey. Regional trend of foliation, mesoscopic and regional fold axes are shown. The regional foliation in the metamorphic assemblages define a ESE-plunging regional anticline, the so called Ruby Range anticline with the KMA in its core. The area east of Dezadeash Lake and the Kusawa Lake region are indicated by (1) and (2), respectively. Geology modified after Wheeler & McFeely (1991). Nisling terrane structural data after Tempelman-Kluit (1974), Erdmer (1989) and Johnston & Timmerman (1993b). Structural data from the DF after Eisbacher (1976).

KMA, is older than the major magmatic phase of the Coast Plutonic Complex.

Mineral stretching lineation in phyllitic rocks associated with the DF at the footwall of a west-verging thrust that puts high P/high T kyanite-garnet-staurolite schist structurally over the DF (Chapter 2) plunges ESE, similar to the attitude of the lineation L_{n+2} in the KMA. Shear-sense obtained from synkinematic hornblende porphyroblasts indicate hangingwall up motion or thrusting towards WNW, in agreement with the shear direction in the KMA. NNE-trending folds in the DF at Klukshu Lake (Figure 2-15) and in the Auriol Range (Eisbacher, 1976) are interpreted as having formed in response to westward directed stress, related to the thrusting of the Nisling assemblage onto the DF. The age of this event is pre-Early Paleocene (see Chapter 2).

Northerly trending feldspar porphyry dyke swarms can be observed from the Shakwak valley 250 km north towards the Yukon River crosscutting metamorphic assemblages and Mesozoic and early Tertiary igneous rocks (Chapter 2; Muller, 1967; Tempelman-Kluit, 1974; Johnston & Timmerman, 1993a). In the Kluane Ranges northerly trending subvolcanic rhyolitic to basaltic dykes are interpreted as feeder dykes associated with the Miocene Wrangell Plutonic Suite (Eisbacher & Hopkins, 1977; Dodds & Campbell, 1992). The dykes crosscut the mid-Oligocene Amphitheater Formation and yield K-Ar whole rock ages of 6-16 Ma (Eisbacher & Hopkins, 1977; Stevens et al., 1982).

North-trending fractures in conglomerates of the Amphitheater Formation and a Holocene fault were reported by Eisbacher & Hopkins (1977).

North-trending brittle structures and dykes in the DF, KMA and the AMS are compatible with continuous north-south stress field from Oligocene to Holocene, related to northward motion of the Pacific plate relative to North America.

EVOLUTION MODEL OF THE KMA IN THE NORTHWESTERN COAST BELT

The deformation events observed in the KMA are summarized on Table 3-1 and in the following evolution model of the northwestern Coast Belt in the Yukon. The direction of plate motion and the orientation of continental margins mentioned below refer to present day reference frame.

D_n

Deposition and diagnesis of the protolith of the KMA occurred in a quiet backarc basin proximal to an island arc and distal to a mature source region (North America ?) (see Chapter 5). Crenulated graphite layers in plagioclase porphyroblasts are interpreted as original bedding S_n. The age of deposition and formation of S_n is not known.

D_{n+1}

A slaty cleavage S_{n+1} developed as a crenulation cleavage in the shale. Rare F_{n+1}-crenulation folds are preserved in plagioclase porphyroblasts. S_{n+1} is defined by parallel graphitic layers in plagioclase and garnet porphyroblasts. Larger fold structures which may be related to S_{n+1} are not observed. Regional subgreenschist burial metamorphism accompanies D_{n+1}.

D_{n+2}

S_{n+2}-schistosity overprinted the slaty cleavage S_{n+1}. Parallel S_{n+1} and S_{n+2} in less deformed schist suggest that D_{n+1} and D_{n+2} are not completely separate events, but the result of a continuous deformation under increasing metamorphic pressures and temperatures. Well developed S_{n+2}-foliation in the large olivine serpentinite body at Doghead Point implies that the ultramafic bodies were structurally juxtaposed with the calcic and aluminous schists during the early stage of S_{n+2} development.

This juxtaposition was the result of tectonical interleaving of the KMA during accretion and underplating underneath the North American continental

Table 3-1: Deformation events in the KMA with associated fabrics and metamorphism

Event[1]	Foliation	Lineation	Folding	Fabric / Structure	Metamorphism	Stress field[2]	Age
D_n	S_n	-	-	original bedding (?)	diagenesis	?	?
D_{n+1}	S_{n+1}	-	F_{n+1}	slaty cleavage	M_1 subgreenschist grade	?	
D_{n+2}	**S_{n+2}**	**L_{n+2}**	-	δ-type porphyroclasts schistosity, mineral stretching lineation	M_1 regional greenschist grade	E-W	Late Cretaceous
D_{n+3}	S_{n+3}	L_{n+3}	F_{n+3}	local mesoscopic folds, regional ESE-plunging anticline	-	NNE-SSW	Latest Cretaceous to Early Tertiary
D_{n+4}	-	-	-	gneissification	M_2 contact metamorphism amphibolite to granulite grade	NNE-SSW	Early Eocene (57 Ma)
D_{n+5}	-	-	-	north-trending dykes, north-trending steep (?) faults	-	N-S	post-Early Eocene-post-Pleistocene

1: Major deformation or metamorphic events are outlined in bold.
2: Motion of Kula plate relative to North American plate in current reference frame (after Engebretson et al., 1995).

margin represented by the AMS. Fine grained basal sections of oceanic sediments can be underthrusted and accreted to the upper plate at greater depth than clastic trench fill, which is being removed by offscraping in the early phase of subduction (Karig, 1974, 1982). As a result, the sediments experience high P metamorphism and ductile deformation (Karig & Sharman, 1975; Moore, 1989). Topographic irregularities in the downgoing slab may cause offshearing of slivers of oceanic crust, which are then being added to the previously accreted oceanic sediments and are preserved as serpentinites (Karig & Sharman, 1975). Lack of foliation in the smaller olivine serpentinites is explained by strain deflection around the more rigid massive ultramafic bodies, behaving as large boudins in the more plastic schistose matrix.

With continuous deformation the schist was moderately mylonized. As a result of progressive non-coaxial deformation a mineral stretching lineation L_{n+2} and a monoclinic fabric, defined by δ-type plagioclase porphyroclasts, were developed (Passchier & Trouw, 1996). Curved graphitic inclusion trails in plagioclase porphyroblasts indicate that the development of the mylonitic fabric began during early stage of metamorphism. Maximum depth of approximately 20-22 km attained during underplating is preserved in grossular-rich cores of synkinematic garnets (see Chapter 4). Consistent east-plunging L_{n+2} and hangingwall up sense of shear over 130 km along strike indicates homogeneous deformation of the KMA across its total structural thickness of 12 km.

Westward hangingwall up movement requires a eastward motion of the plate that carried the KMA, which is provided by the Kula plate from ~95-~80 Ma (Engebretson et al., 1995). While the KMA-AMS interaction resulted in left-lateral oblique slip along the WNW-trending North American continental margin, further south, the NA continental margin trends northerly, resulting in a straight convergence with westward thrusting of the North American Nisling assemblage onto the DF and the development of north-trending folding of the DF. The minimum age for deformation in the KMA and overthrusting of the DF is ~70 Ma, the emplacement age of a late syndeformational biotite granite dyke

intruding the KMA and cooling ages of the CPC at an intrusive contact (Figure 2-15).

Late Early Cretaceous U-Pb titanite ages (109 Ma; Mortensen, pers. comm., 1996) of the Shorty Creek Pluton which crosscuts NNE-trending regional folds in the DF, indicate that the folding event in the DF is as old as Early Cretaceous (Eisbacher, 1976; Evenchick, 1995). However, this does not necessarily preclude a later thrusting event at the eastern margin. The NNE-trending folds are interpreted as outgrowth of syndepositional slump folds (Eisbacher, 1976), implying folding shortly after deposition of the DF (135 Ma), responding to ESE-WNW compression. This may have lasted until the latest Cretaceous and resulted in development of a WNW-directed thrust further east. The relative motion of the Kula plate to the southeast from 150 Ma, and to the east from 95-80 Ma allows prolonged ESE-WNW compression (Engebretson et al., 1995).

A maximum age for underplating of the KMA is given by Late Jurassic (~160 Ma) burial of the AMS (Johnston et al., 1996). Evidence from metamorphic studies suggests that presently exposed rocks of the KMA did not remain at high pressures for an extensive period, since no high P/high T mineral assemblages are observed (see Chapter 4). However, it does not preclude earlier underplating of KMA-associated rocks, as these rocks may remain buried.

D_{n+3}

ESE-SE-trending mesoscopic and regional folds are common south of the RRB, and can be observed in the KMA, Nisling assemblage schist east of Dezadeash Lake and in the DF (Figures 2-10, 2-15, 2-18, 3-1, 3-21). F_{n+3}-folds are less common in metamorphic assemblages north of the RRB, and only observed in the Nasina Assemblage at the north end of Talbot Arm (Figure 2-14), and in the White River Assemblage along the Shakwak Valley.

After correction for northeastward tilting of the KMA (see D_{n+4} below), F_{n+3} -folds verge to the southwest. F_{n+3} developed in response to a change in

the motion direction of the Kula plate from east to NNE. F_{n+3}-folds in the KMA are developed locally and affect only meter thick layers. Tight folds are commonly sheared off at their base. No penetrative ductile fabric is related with D_{n+3}. This suggests that the amount of strain that was absorbed by the KMA schist was less than during D_{n+2}, and resulted mainly in the formation of a regional anticline.

Timing of D_{n+3} is constricted by latest ductile deformation of the KMA at ~70 Ma and the intrusion of the RRB at 57 Ma (Erdmer & Mortensen, 1993), slightly younger than the beginning of NNE motion of the Kula plate at ~80 Ma (Engebretson et al., 1995). Presence of F_{n+3}-folds in roof pendents of the Nasina and Nisling assemblages in the undeformed RRB, deflection of F_{n+3}-fold axes and brittle deformation of F_{n+3}-folds near the intrusive contact (Figure 2-12) suggest that D_{n+3} preceded the intrusion of the RRB.

D_{n+4}

Continuation of N-NNE motion of the Kula plate resulted in faulting along the Kloo Lake fault with eastward tilting of the KMA and the metamorphic assemblages to the east, followed immediately by sill-like intrusion of the major body of the RRB along the suture between the KMA and the AMS. The resulting contact aureole is wide in the KMA, but relatively narrow in the Nisling terrane assemblages to the north and south, suggesting that the KMA was situated at greater structural depth. Increasing metamorphic pressures and younger cooling ages of the KMA to the southwest also suggest that the KMA was at structurally lower levels than the AMS to the north. A post-metamorphic northeast tilt of 15° can be calculated from metamorphic pressure gradients (see Chapter 4). Assuming a similar NNE dip of 30° of the schistosity for the KMA and AMS and a foliation-parallel intrusion of the RRB, the batholith intruded at an angle of 15° dipping to the NNE (Figure 4-14; Johnston & Timmerman, 1993b).

A second structurally lower sill, which is to a large extend covered, is situated at the base of the KMA on the northeast flank of the Shakwak valley.

U-Pb geochronology of the KMA and intruding granitic dykes and K-Ar cooling ages of the RRB, indicate that the main body of the RRB was emplaced at 55-58 Ma (see Chapter 2; Erdmer & Mortensen, 1993). D_{n+4} did not result in a major deformation.

D_{n+5}

Rapid cooling of the northern KMA (184°C/Ma) indicate that uplift ensued immediately after the intrusion of the RRB (Figure 3-22). Cooling rates of the structurally lower levels of the KMA in the southwest are much slower (24°C/Ma), reflecting slower uplift. The uplift was the result of underplating of the Insular Superterrane underneath the KMA. The fault along which juxtaposition took place is covered by thick glacial till of the Shakwak Trench, so that the nature of the fault is not known. Similar metamorphic pressures along the northern margin of the KMA (see Chapter 4) imply that it was uplifted as a homogeneous block with an axis that parallels the strike of the schistosity (WNW). A NNE-trending tear fault, located in the steep Dezadeash River valley, juxtaposed deep level KMA rocks with Nisling assemblage rocks that were at higher structural level during early Tertiary metamorphism.

The amount and timing of right-lateral displacement along the Denali fault zone (DFZ) is a matter of conjecture (Chapter 2; Dodds, 1991). Southeast-striking steep shear zones, interpreted as strands of the Denali fault cut Pennsylvanian to Triassic strata of the Wrangellia terrane in the Kluane Ranges, but were not observed transecting the KMA (Eisbacher, 1976; Dodds & Campbell, 1985). A number of authors (Forbes et al., 1974; Turner et al., 1974; Eisbacher, 1976; Nokleberg et al., 1985) infer an offset of 300-400 km in the Eocene (40-55 Ma) during the rapid final subduction of the Kula plate underneath North America. These large offset estimates were based on correlation of similar metamorphic and igneous assemblages on both sides of the fault, without existence of detailed geological data. Detailed studies along the McKinley strand of the DFZ in the eastern Alaska Range (Reed & Lanphere, 1974; Csejtey et al., 1982) and tectonic modelling (Stout & Chase,

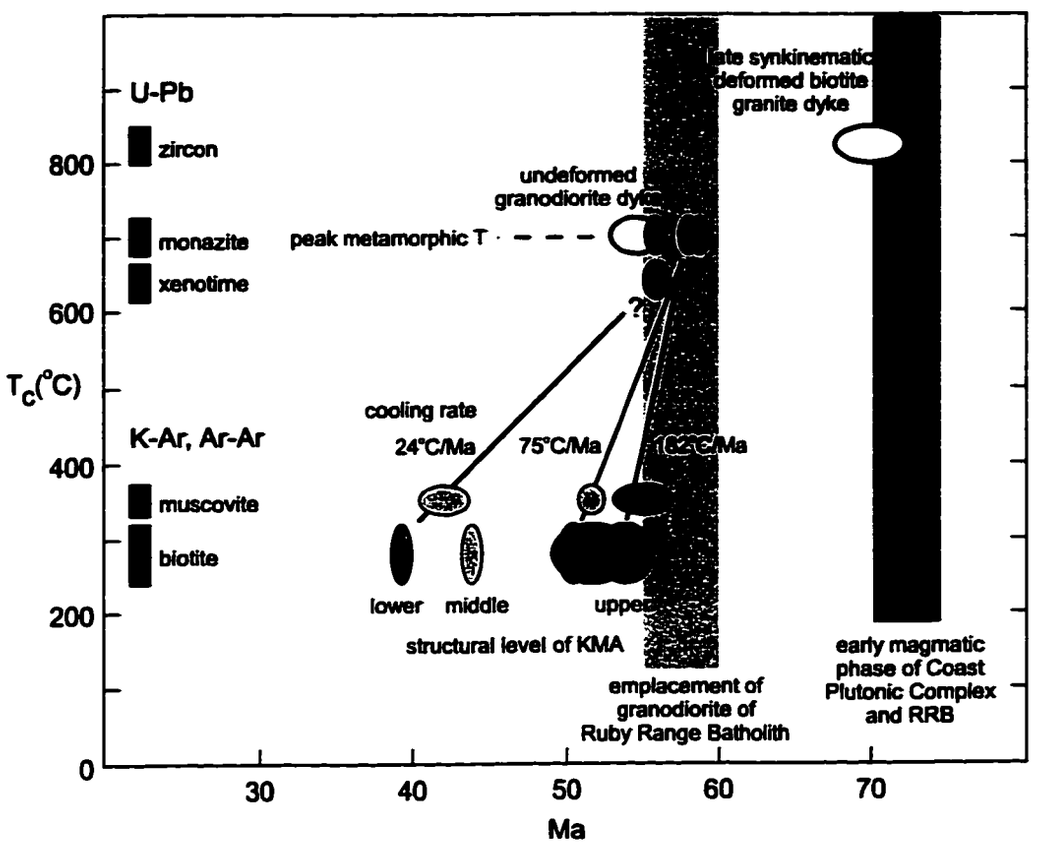

Figure 3-22: Blocking temperature (T_c) versus geochronological age determination of U-Pb zircon, monazite and xenotime, K-Ar (dark grey) and ^{40}Ar-^{39}Ar (light grey) muscovite and biotite. Cooling rates are presented for various KMA samples from the upper and lower structural level of the KMA. Black bars represent uncertainties of Tc (after Heaman & Parrish, 1991). Width of ellipsoid reflects uncertainty of age determination. Radiogenic data from Farrar et al. (1988), Mortensen & Erdmer (1992) and this study.

1980) suggested that Cenozoic dextral offset along the DFZ may amount to only 10-90 km.

It is questionable that coeval rapid uplift of the KMA, which requires northward underplating or southward thrusting, could have been accomplished if a major steep strike-slip fault was located outboard the unroofing KMA. Current seismic activities are restricted to the Duke River and Totschunda fault zones to the southwest (Horner, 1983).

Coinciding with post-Early Eocene uplift is the emplacement of rhyolitic to andesitic north-trending dykes throughout the KMA and AMS in the Oligocene to mid-Miocene (?) (Eisbacher & Hopkins, 1977; Stevens et al., 1982).

The fault that juxtaposed high grade metamorphic rocks of the KMA against low grade rocks of the Insular Superterrane and DF in the south may have been transformed into a steep southwest-dipping reverse fault, as a result of NNW-ward subduction of the Pacific plate underneath North America (Lowe et al., 1994). Alternatively, the Shakwak valley is the site of a Pliocene graben, along which the southwall with the St. Elias Mountains continues to rise (Tempelman-Kluit, 1980).

North-trending brittle dextral (?) faulting in the KMA has been active into the Holocene, evident in well preserved fault scarps (Figure 3-17).

CONCLUSIONS

Mylonitic rocks of the Kluane metamorphic assemblage record two major deformation phases that can be related to the direction of motion of the Kula plate:

1) Late Mesozoic eastward movement of the Kula plate (Engebretson et al., 1995), relative to the North American craton, resulted in oblique left-lateral slip along the North American continental margin, represented by the AMS. During

this period of oblique convergence the KMA was accreted onto North America by underplating the AMS, resulting in the development of a mylonitic fabric in the KMA with homogeneous westward hangingwall up sense of shear. Timing of accretion is confined by Middle Jurassic high pressure metamorphism of the AMS, eastward motion of the Kula plate (~95-80 Ma) and latest Cretaceous synkinematic granitic dykes intruding the KMA.

The existence of sinistral strike-slip along the North American continental margin, as postulated by Rubin & Saleeby (1991) and Monger et al. (1994), at the time of accretion of the KMA is likely. However, since the KMA represents only the deep seated ductile part of a subduction zone, any evidence of brittle faulting was eroded during subsequent unroofing. Likewise, turbidites and mélanges, the upper portion of an associated accretionary prism, are also not preserved.

2) Change of relative motion of the Kula plate from east to NNE during the latest Cretaceous resulted in ESE-trending, predominantly southwest-verging folding in the metamorphic assemblages and sedimentary strata at the continental margin of North America. Subsequent sill-like intrusion of the RRB, a Late Cretaceous-early Tertiary apophysis of the CPC, overprinted the suture between the AMS and the KMA. Post-Early Eocene fast northward motion and consumption of the Kula plate led to northerly underplating of the KMA by the DF and Alexander terrane to the south, resulting in differential uplift of the KMA with a relative northward tilting of the metamorphic assemblages. Right-lateral strike-slip faults may have developed in the Insular Superterrane in front (outboard) of the late Cretaceous suture zone.

Chapter 4

Metamorphic evolution of the Kluane metamorphic assemblage

INTRODUCTION

The importance of mineral assemblages as indicators of metamorphism was first recognized by Rosenbusch (1877), who observed distinct mineral parageneses in slates around granites in the European Vosges. The appearance of new minerals, designated as index minerals, towards an intrusive contact, first described by Barrow (1893), and the definition of metamorphic facies (Eskola, 1915) and metamorphic grade (Tilley, 1924) allow qualitative statements on prevailing temperatures during metamorphism. The pressure (P) and temperature (T) dependence of mineral equilibria reactions are determined by thermodynamics, and allow for the development of petrogenetic grids, which show these reactions in P-T space (e.g. Spear & Cheney, 1989; Powell & Holland, 1990), and provide more quantitative P-T estimations from observed mineral assemblages. Thus, the P-T conditions during metamorphism can be approximated by thorough petrographic studies. Geothermobarometry is the calculation of P and T by using electron microprobe chemical analyses of mineral phases in conjunction with computer software programs, such as TWQ 2.02 (Berman, 1996).

The first part of this chapter summarizes previous studies on metamorphism in the Kluane metamorphic assemblage (KMA). Next, a detailed petrographic study along an exemplary section of the KMA describes textural relationships between mineral phases and help to define mineral isograds and metamorphic zones. The mineral isograds outline a contact metamorphic aureole parallel to the contact with the Ruby Range Batholith (RRB) with an inverted metamorphic gradient. Geothermobarometric studies on 22 samples are presented in the third part of this chapter. As a result two major metamorphic events can be distinguished in the KMA, an earlier syndeformational low T/high P metamorphism and a high T/low P event, which can be correlated to the Late Cretaceous-Early Tertiary emplacement of the RRB. The P-T-t evolution of the KMA defines a clockwise path, characteristic of an underthrusting or underplating event, followed by relatively fast uplift and

subsequent thermal overprinting in the Paleocene/Eocene. Higher P and younger ^{40}Ar-^{39}Ar cooling ages in structurally lower parts in the southwest indicate that the KMA experienced northward tilting during post-Early Eocene uplift.

Comparison with adjacent pericratonic metamorphic assemblages of Nisling terrane affinity suggests that the KMA was accreted to North America between post-Mid Jurassic to Late Cretaceous.

PREVIOUS STUDIES

Muller (1967) observed an increase of metamorphic grade in mica-quartz schists of the KMA from greenschist to amphibolite grade towards the contact with the Ruby Range batholith. Tempelman-Kluit (1974) recognized that regionally metamorphosed schists (hornfels unit PPsqr) in the southern Aishihik Lake area were thermally overprinted. Whether this occurred during two distinct metamorphic events or was the result of regional metamorphism with a late thermal event remained ambiguous. A prograde sillimanite-grade overprint of the bt-qtz schist, with temperatures of 530-660°C, increasing towards the contact with the Ruby Range Batholith (RRB), was reported by Erdmer (1991).

A decrease in metamorphic grade of the KMA towards the south was suggested by Eisbacher (1976), in agreement with his interpretation of the KMA as a metamorphosed equivalent of the Dezadeash Formation (DF). Eisbacher's descriptions are vague, however, and the lower grade schist, is more likely a coarse-grained phyllite of the DF, as discussed in Chapter 2 (Figures 2-15, 2-21), instead of a biotite-quartz schist with KMA affinity.

K-Ar and ^{40}Ar-^{39}Ar ages obtained from mica-quartz schists of the KMA range from Paleocene to Eocene, and are interpreted as cooling ages related to the Late Paleocene to Eocene (50-57 Ma) intrusion of the RRB (Erdmer & Mortensen, 1993; see Chapter 2). The oldest ages (50-55 Ma) were obtained

in rocks close to the contact with the batholith to the north, and younger ages (39-43 Ma), at the eastern shore of Kluane Lake, indicating slower cooling in the southwest (Appendix 2-5, Erdmer & Mortensen, 1993). An earlier radiometric K-Ar age of 140 Ma (Lowdon, 1960) of the KMA is regarded as unreliable due to low K-content of the analyses (Erdmer & Mortensen, 1993). These studies date contact metamorphism at 50-55 Ma.

METAMORPHIC MINERAL ZONES IN THE KMA

Introduction

Mineral assemblages described in this study were obtained by optical microscopy and electron microprobe analyses of over 150 thin sections of samples collected by P. Erdmer and the author during field work from 1989 to 1995. Due to the small grain size, definitive identification of most diagnostic minerals in the field, with the occasional exception of garnet, was generally precluded. Mineral assemblages and sample location of all thin sections are listed in Appendix 2-1. Metamorphic indicator minerals and index mineral isograds for the whole KMA are shown on a regional map (Figure 4-1), as well as a detailed map area in the Ruby Range (Figure 4-2), with accompanying cross-sections (Figure 4-3).

Observed mineral assemblages and the appropriate reactions from one zone to another are listed on Table 4-1. The reactions are based on the petrogenetic grid of Spear & Cheney (1989) and Powell & Holland (1990) as quoted in Spear (1993) and Bucher & Frey (1994), respectively. It involves reactions in the CAS-HC (CaO, Al_2O_3, SiO_2, H_2O, CO_2), FASH (FeO, Al_2O_3, SiO_2, H_2O), KFASH (K_2O, FeO, Al_2O_3, SiO_2, H_2O), KFNASH (K_2O, FeO, Na_2O, Al_2O_3, SiO_2, H_2O) and KFMASH (K_2O, FeO, MgO, Al_2O_3, SiO_2, H_2O) systems (Figure 4-4). Additional components can change the location of individual equilibria on the petrogenetic grid. Sufficient MnO and CaO, which are not considered in the systems above, can significantly lower the first occurrence of

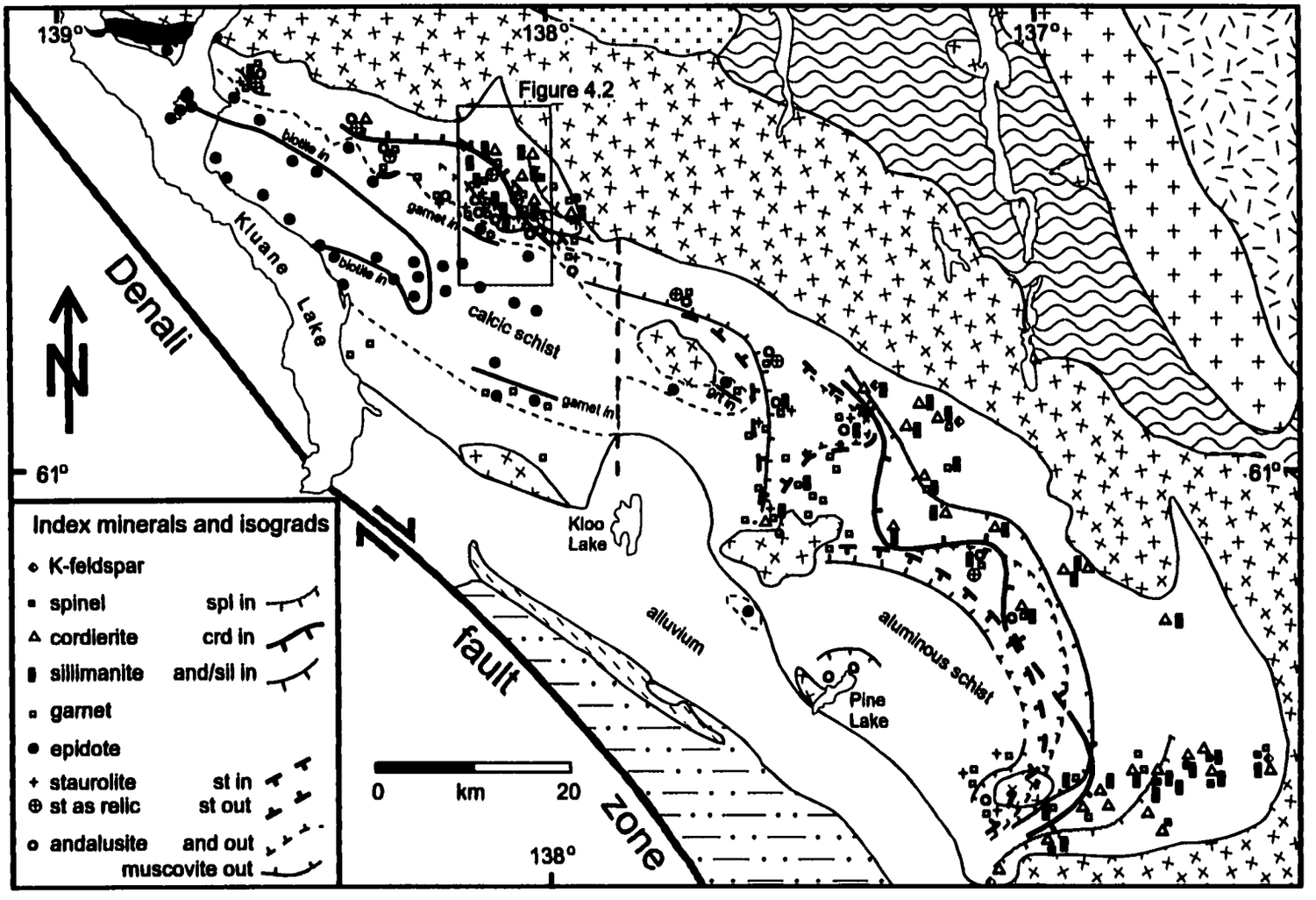

Figure 4-1: Index mineral and mineral isograd map of the KMA. Mineral isograds mark the first prograde appearance or the upper stability field of a diagnostic metamorphic mineral. The location of detailed map on Figure 4-2 is also shown. Geology outside the KMA is the same as in Figure 2-1.

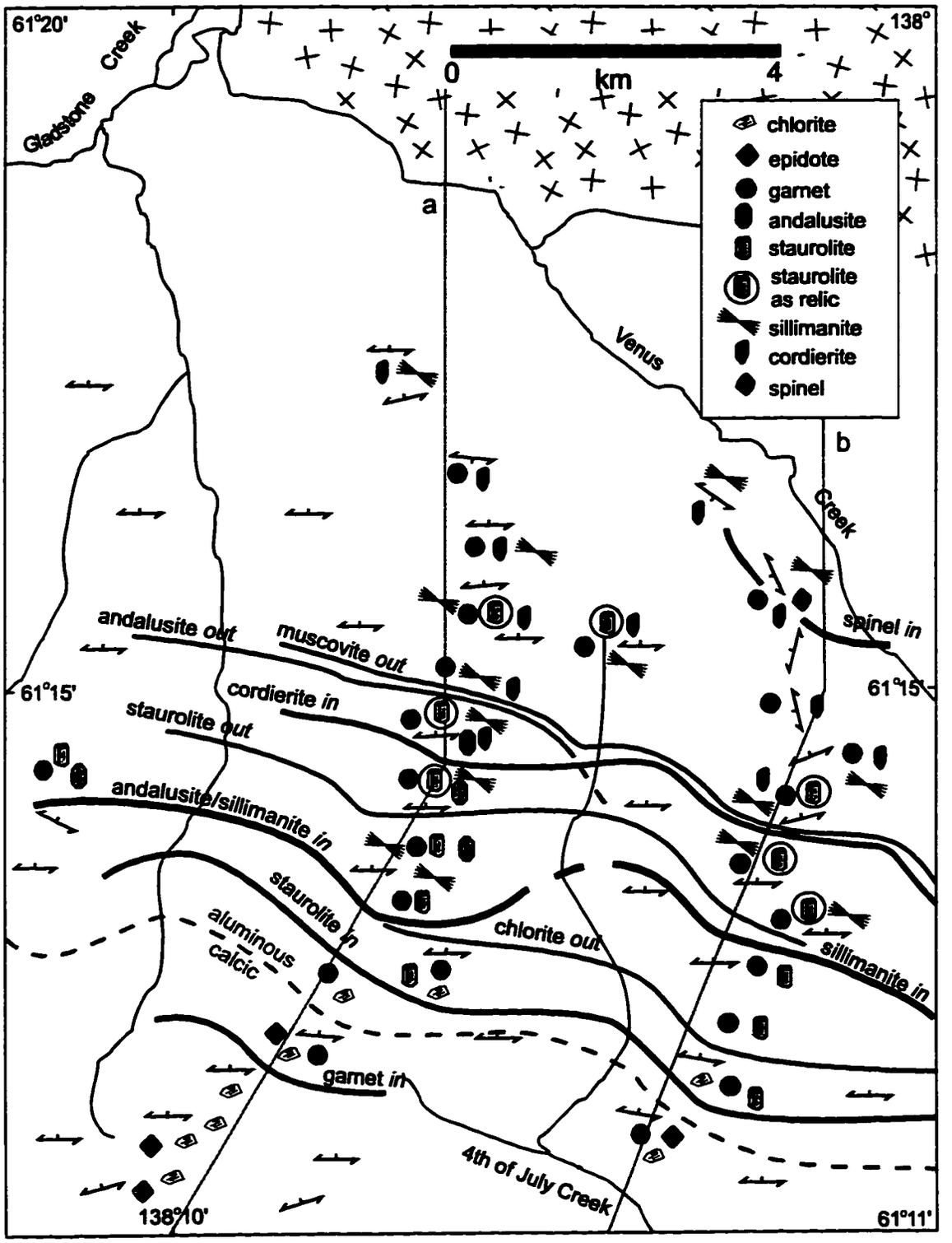

Figure 4-2: Detailed index mineral and mineral isograd map of the KMA in the central Ruby Range (see Figure 4-1 for location). Dashed line marks the approximate lithological boundary between calcic schists of the KMA to the south and aluminous schists to the north. Grey lines mark the locations of cross-sections of Figure 4-3.

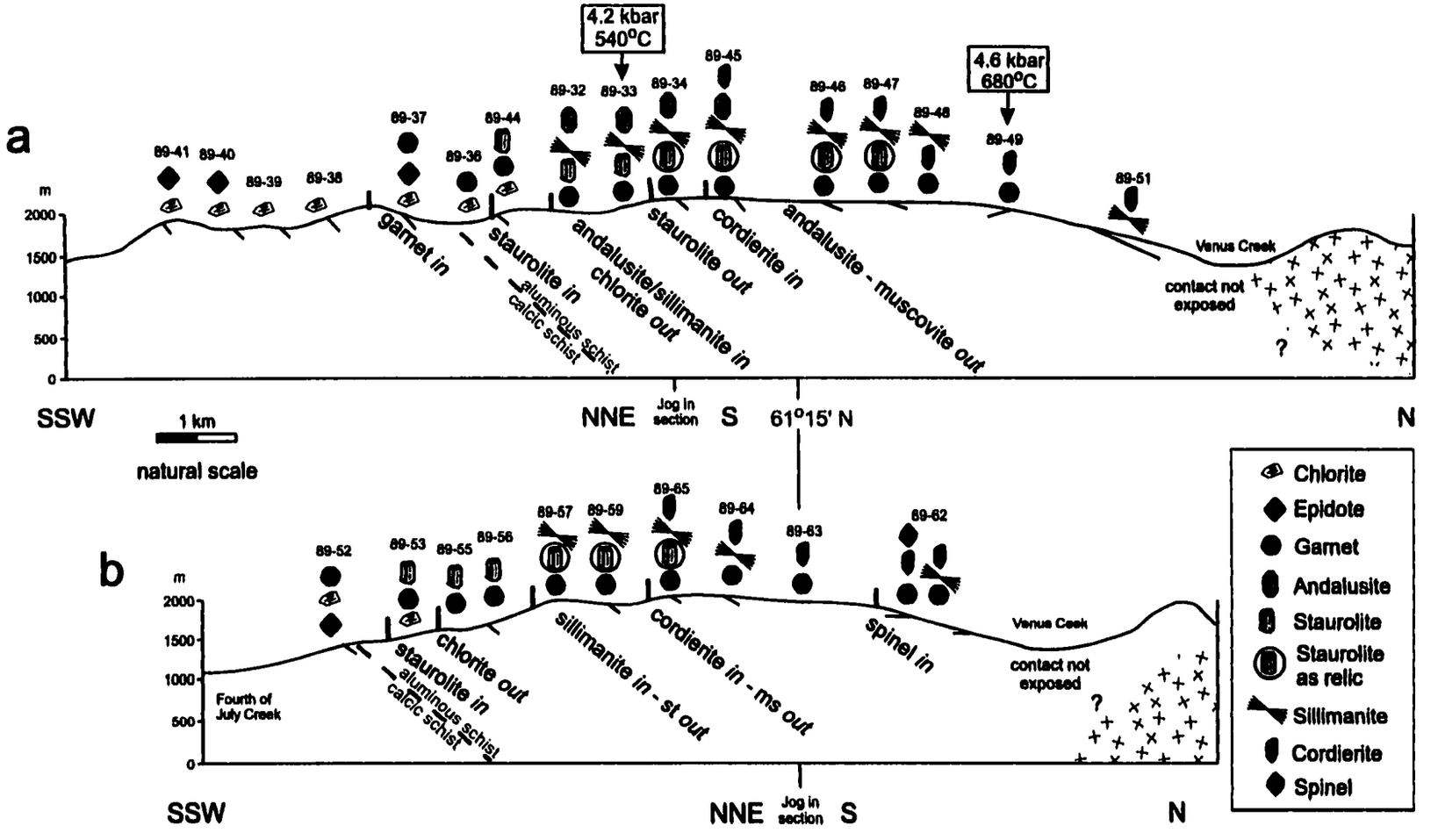

Figure 4-3: Two natural scale cross-sections in the central Ruby Range. Sections are oriented perpendicular to the strike of the KMA. The two sections are parallel, and approximately 4 km apart. Location of the sections are shown on Figure 4-2. The numbers indicate individual samples. Their mineral assemblage is listed in Appendix 2-1. Dip of foliation is indicated by short black lines. Geothermobarometry data is taken from Figures 4-10 and 4-11.

Table 4.1: Mineral[1] parageneses and reactions for mica-quartz schist of the KMA with increasing metamorphic grade

calcic sequence:	***reactions[2]:***	
ms, chl, ep/czo, cal, kfs (?)		
↓	(1)	8 kfs + 3 chl = 5 ann + 3 ms + 9 qtz + 4 H_2O
bt, ms, chl, ep/czo, cal		
↓	(2)	2 czo + 3 qtz + 5 cal = 3 grs + H_2O + CO_2
grt, bt, ms, chl, ± ep/czo		
aluminous sequence:		
grt, bt, ms, chl		
↓	(3)	ms + qtz + grt + chl = st + bt + H_2O
st, grt, bt, ms		
↓	(4)	75 st + 312 qtz = 100 alm + 575 and/sil + 150H_2O
	(5)	st = grt + bt + and/sil
sil/and, st, grt, bt ± ms		
↓	(6)	and = sil
sil, and, st, grt, bt ± ms		
	(7)	2 bt + 6 ms + 15 qtz = 3 crd + 8 kfs + 8 H_2O
↓	(8)	2 alm + 4 and/sil + 5 qtz + n H_2O = 3 Fe-crd
	(9)	6 and/sil + 2 bt + 9 qtz = 3 Fe-crd + 2 kfs + 2 H_2O
crd, **kfs**, sil, bt ± grt, ms		
↓	(10)	2 sil + alm = Fe-crd + hc
spl (hc), crd, kfs, sil, bt ± grt		
↓	(11)	bt + sil = crd + grt
grt, crd, kfs, spl (hc), sil, bt		

Phases in bold appear for the first time, phases underlined are being consumed.

Reaction (1) applies for the KFNASH system: K_2O, FeO, Na_2O , Al_2O_3, SiO_2, H_2O.
Reaction (2) applies for the CAS-HC system: CaO, Al_2O_3, SiO_2, H_2O, CO_2
Reaction (4) applies for FASH system: FeO, Al_2O_3, SiO_2, H_2O.
Reactions (8), (9) apply for the KFASH system: K_2O, FeO, Al_2O_3, SiO_2, H_2O.
Reactions (3), (5), (7), (10), (11) apply for the KFMASH system: K_2O, FeO, MgO, Al_2O_3, SiO_2, H_2O.

1: Plagioclase and quartz are present in all assemblages.
2: Reactions (1), (2), (4), (5), (6), (7), (8), (9) are taken from Bucher & Frey (1994); reactions (3) and (11) from Spear & Cheney (1989) are not balanced (see p. 345 in Spear (1993)), reaction (10) from Chacko (pers. comm., 1997).

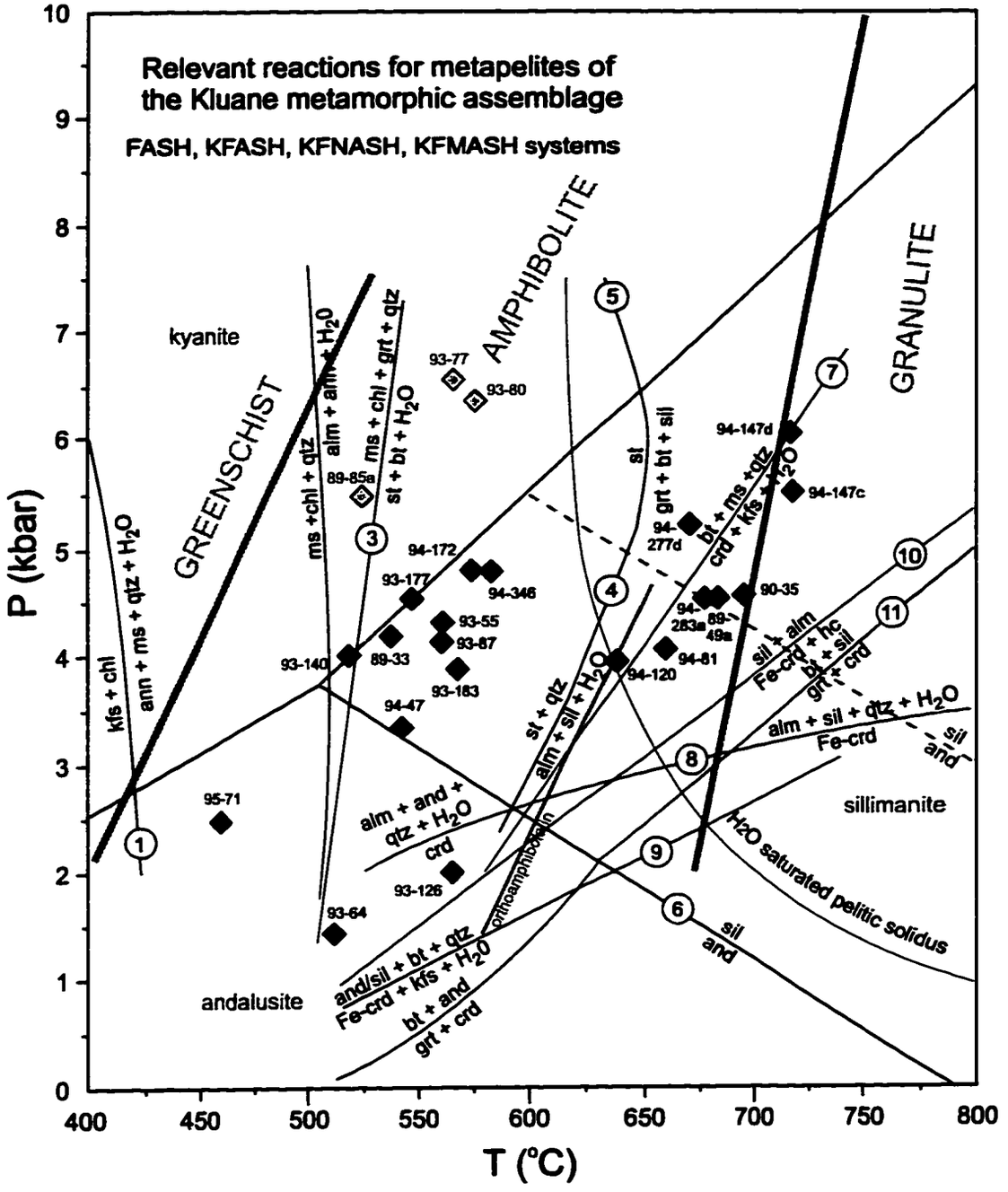

Figure 4-4: Petrogenetic grid applied to mica-quartz schist of the KMA. Equilibrium reactions are taken from Bucher & Frey (1994) and Spear & Cheney (1989). Note that Mn- and Ca-bearing phases are not included in the reactions. Reaction numbers refer to Table 4-1. Diamonds represent P-T estimates for samples analyzed in this study. Aluminosilicate triple point is taken from Holdaway & Mukhopadhyay (1993). Dashed line marks andalusite-sillimanite reaction after Richardson et al. (1969). H_2O-saturated pelitic solidus curve after Spear (1993). Facies division is after Bucher & Frey (1994).

garnet from ~500°C in a Fe-rich system to 450°C (Bucher & Frey, 1994; Spear, 1993).

At best these reactions are valid as a general guide and have to be evaluated together with as many other equilibria as possible, especially if a substantial amount of additional components (CaO, MnO) is present.

Tilley (1924) originally defined the term "isograd" as a line joining points of similar P and T. Such a definition assumes detailed thermodynamic knowledge of minerals and mineral reactions and is unrealistic given the scope of the present study. Instead the term "isograd", as used in this study, marks the first observance, in a prograde sense, of a new mineral or mineral assemblage, drawn as a line on the map to provide a general, if incomplete, overview of the mineral parageneses. In addition, the disappearance of a mineral phase due to a prograde reaction can be shown on the map as an "upper stability" isograd.

Metamorphic character of the KMA along traverses in the Ruby Range

The metamorphic character of the KMA can best be described along two SSW-NNE sections in the Ruby Range, that cover approximately 14 km of surface exposure of the KMA across strike, from the lowest grade rocks near the Kluane Lake shore to the highest grade assemblages near the contact with the RRB at Venus Creek (Figures 4-2, 4-3). The schist of the KMA in that area has a homogeneous N-NNE dipping schistosity and strikes approximately parallel to the contact with the RRB. Although the intrusive contact is not exposed in that area, there is evidence elsewhere in the Ruby Range that the RRB overlies the KMA.

Along the eastern Kluane Lake shore and on Jacquot Island, epidote-bearing chlorite-muscovite schist, as described in Chapter 2, represents the lowest metamorphic grade in the KMA. Prograde biotite first appears growing folioform on chlorite, and with decreasing distance to the intrusive contact of the RRB increases in abundance, growing more randomly. Biotite crystals

overgrowing the foliation are common, implying post-kinematic growth. Biotite is formed by the breakdown of potassium feldspar and chlorite at approximately 400°C (reaction (1), Table 4.1; Bucher & Frey, 1994). Simultaneous with biotite abundance increasing from <1 to 5 vol.%, 13 km away from the contact with the RRB, the chlorite/muscovite ratio decreases, as biotite and muscovite are products of the chlorite-consuming reaction (1).

In Al-rich pelites, chloritoid would be the next mineral to form in a prograde metamorphic sequence. However, chloritoid is absent in the ms-chl schist, which can be attributed to the deficiency of aluminum in the calcic unit of the KMA.

Coexisting clinozoisite and garnet are found in a narrow zone (~1 km) near the calcic-aluminous schist contact (Figure 4-2, 4-3). Ca-rich garnet (grossular) can be produced by the breakdown of clinozoisite and calcite according to reaction (2). Garnet, clinozoisite, biotite, muscovite, chlorite, plagioclase and quartz represent the highest grade mineral assemblage observed in the calcic schist of the KMA.

The first mineral assemblage observed in the aluminous schist consists of garnet, biotite, chlorite, muscovite, plagioclase and quartz. Biotite overgrowth of the foliation plane results in a more gneissic appearance of the schist.

The first prograde appearance of staurolite, 9 km away from the contact with the RRB, indicates that the lower amphibolite facies (~520°C) is reached. Abundant subhedral to euhedral, 0.25-1 mm long, stubby staurolite crystals, with common twinning and zoning, occur within a 2 km wide zone. Not far behind the first prograde occurrence of staurolite, the abundance of biotite increases, while muscovite is reduced to an accessory phase and chlorite disappears completely. Beyond the staurolite-isograd, chlorite occurs only as a retrograde alteration product of biotite. Staurolite and biotite are formed by the breakdown of chlorite, muscovite and garnet, according to reaction (3).

Andalusite and sillimanite appear simultaneously on the western section of Figure 4-3. Andalusite forms large poikilitic porphyroblast, with abundant inclusions of biotite and graphite. Sillimanite grows as small acicular fibrolite

needles. Fibrolite generally nucleates in biotite and grows parallel to its cleavage (Figure 4-6a). Outside biotite grains the fibrolite needles generally fan out and display no preferred growth orientation. Concurrent with a steep increase in the abundance of sillimanite and andalusite, from <1 to 5-10 vol.%, over less than one kilometer along the section in Figure 4-3, the staurolite abundance experiences a sharp decline. Over the next 3-4 km staurolite is mantled by andalusite (Figure 4-5) and restricted to small (< 250 μm) anhedral and embayed relics within andalusite grains. This suggests that andalusite was formed as a product of staurolite breakdown (reactions (4) and (5)).

P-T constraints can be obtained from the breakdown of staurolite to form andalusite and coexisting sillimanite, but depend on the Al_2SiO_5-triple point chosen. This assemblage would plot at 2.5 kbar and 600°C, using the Holdaway & Mukhopadhyay (1993) model and at 4.5 kbar and 630°C after the Richardson et al. (1969) model (Figure 4-3). Spear (1993) suggested that the later model may represent the triple point for fibrolitic sillimanite. Estimated pressure of a nearby sample (4.5 kbar, 89-49a, see below) are similar to Richardson et al.'s (1969) triple point.

Fibrolite growth at the rim of andalusite (Figure 4-5) indicates a replacement of andalusite by fibrolite due to increasing metamorphic temperature (reaction (6)). Coexisting andalusite and fibrolite are observed along 2.5 km on the western section. No andalusite was observed in the eastern section, where temperature and/or pressure exceeded the stability field of andalusite. Here, staurolite relics are commonly mantled by plagioclase or, at higher grade, by cordierite.

The first prograde cordierite appearance coincides with the breakdown of andalusite in the western section, and a decrease in biotite abundance from 30 to less than 5 vol.% along the next two kilometers. Biotite grains are embayed and do not form continuous bands along the foliation plane. These observations suggest that biotite is consumed in a cordierite-forming reaction (Figure 4-6). Sillimanite abundance is also negatively correlated with the amount of cordierite in a sample. Some cordierite-rich samples do not contain

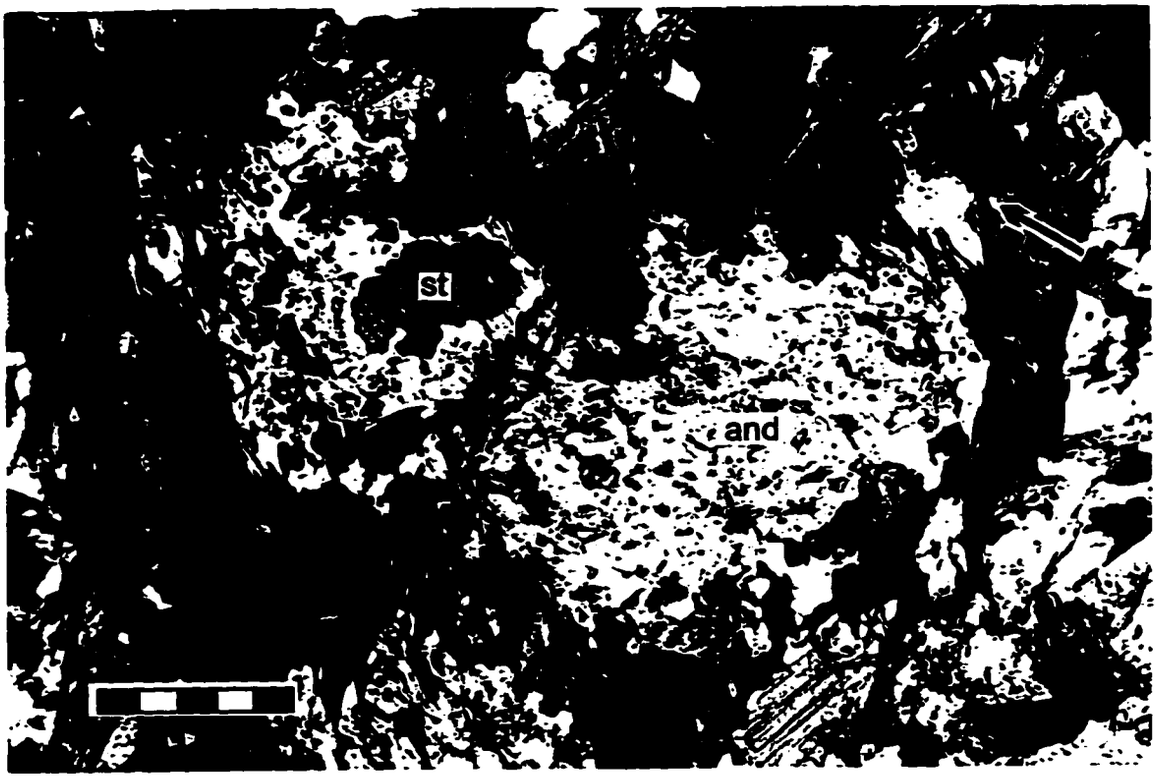

Figure 4-5: Photomicrograph of a biotite-quartz schist of the KMA in the Ruby Range (89-34a). 1.5 km after the first prograde appearance of andalusite and sillimanite (as acicular fibrolite) staurolite occurs only as relics mantled by andalusite. This suggests that staurolite is being consumed by an andalusite forming reaction ((4) and/or (5), see text for discussion). In contrast to the embayed crystals in this sample, staurolite is more abundant and forms euhedral porphyroblasts in samples further away from the RRB. Fibrolite needles (arrow) growing at the rim of andalusite imply replacement of andalusite due to increasing temperature towards the contact with the RRB. *Scale bar: 0.5 mm. XPL*

Figure 4-6: Photomicrographs that show the effect of the appearance of cordierite on the texture of the biotite schist of pelitic KMA schist of the Venus Creek section (Figure 4-3). **a)** Biotite grains in this andalusite-sillimanite-staurolite-bearing biotite-quartz schist (89-34a, same as in Figure 4-5) are large and define the foliation (top right to lower left). Fibrolite nucleates epitaxial in biotite in the upper left corner (arrow). **b)** In this sample (89-45), which is shown at the same scale, cordierite, recognizable by yellow alteration rims, replaces biotite and sillimanite (reactions (7), (8), (9)). In the cordierite-rich central portion of the section biotite grains are small and embayed, and do not define continuous layers as in the cordierite-absent section shown in a). Fibrolite is abundant in cordierite absent parts (top of section), but found only as inclusions in cordierite in the cordierite-rich areas.
Scale bars: 0.5 mm. PPL

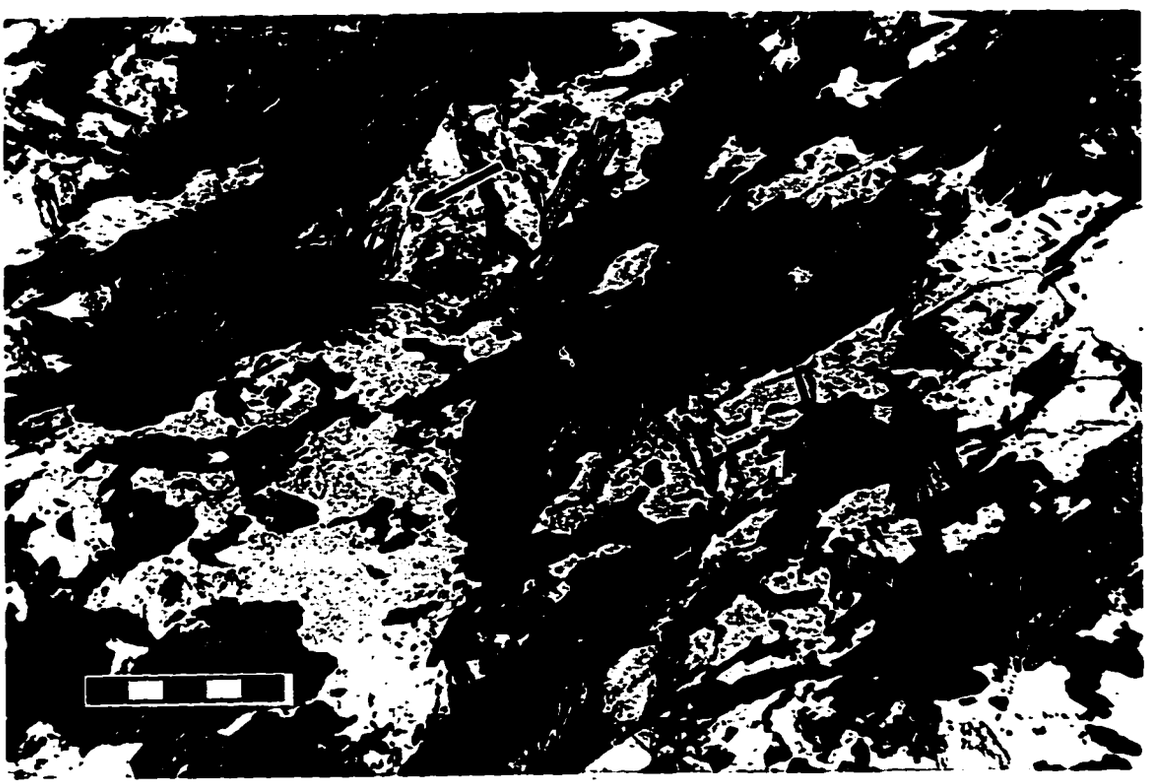

a)

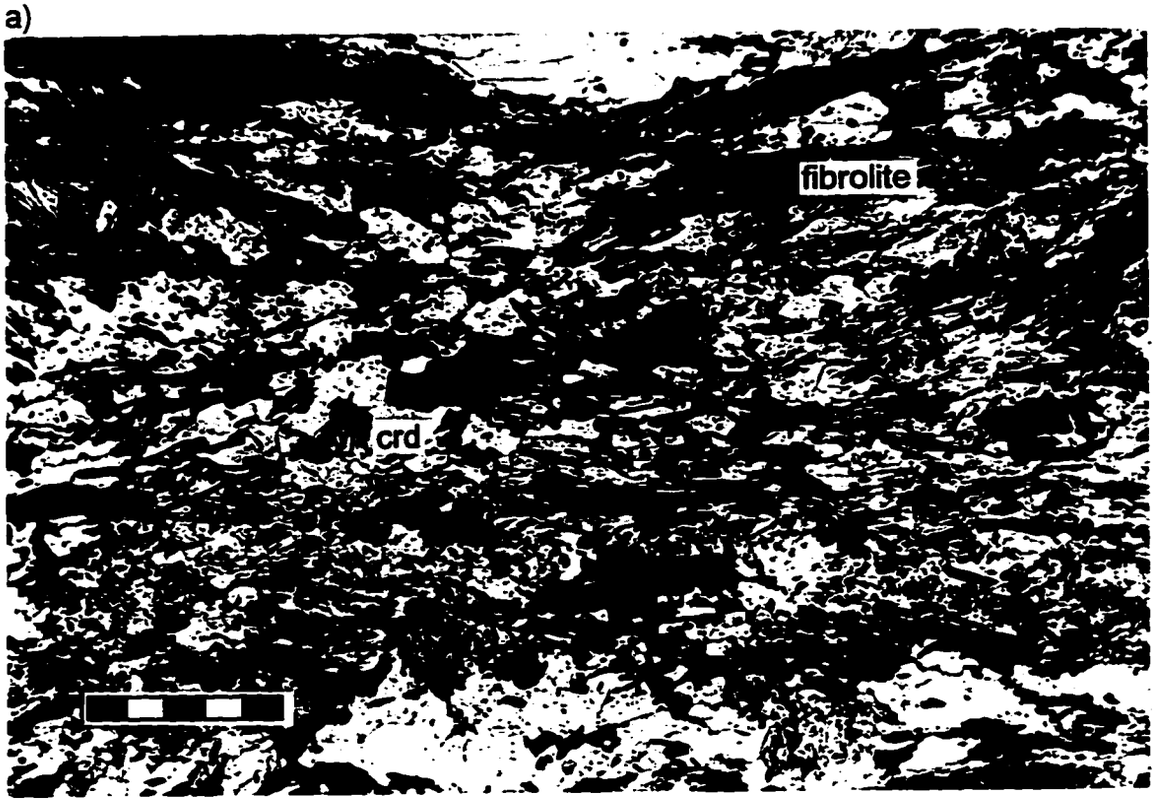

b)

any sillimanite at all. Cordierite in contact with or enveloping garnets is common (Figure 4-7). According to these textural relations, cordierite can be the product of the breakdown of muscovite and biotite (reaction (7)), almandine garnet and sillimanite (reaction (8)), or sillimanite and biotite (reaction (9)).

Reaction (8) probably has contributed most of the cordierite. In the eastern Dezadeash Range, garnet, being consumed in reaction (8), is absent in a 8-10 km wide zone in the cordierite-biotite schist (Figure 4-1). The absence of K-feldspar, a product of reactions (7) and (9), as a major phase in most cordierite-bearing samples suggests that these reactions are only minor contributors to cordierite. K-feldspar, which has not developed twinning, can be distinguished from plagioclase by EDS (Energy Dispersive Spectrometry) analyses with an electron microprobe, and was only observed as a major phase in the eastern Dezadeash Range (90-35, Figure 4-9) and the eastern Ruby Range (94-120). However, no systematic search for K-feldspar was undertaken for most samples, so that the extent of K-feldspar and thus the contributions of reactions (7) and (9) are not exactly known.

Also, the scarcity of muscovite (<2 vol.%), a major reactant in reaction (7), indicates that the reaction is only a minor contributor to cordierite, which makes up an average of 10 vol.% of the schist.

Reactions (8) and (9), which include only the Fe-end member of cordierite, plot at lower P than the estimated P calculated for cordierite-bearing samples (Figure 4-4). However, the analyzed cordierite grains contain a substantial amount of Mg (X_{Mg}≈60), which increases the stability field of cordierite towards higher P. P estimates of 4-4.5 kbar at 675°C (Figure 4-4) are close to the location of reaction (8) with X_{Mg}≈60 according to Holdaway & Lee (1977).

The cordierite-forming reaction (7) consumes muscovite completely so that primary muscovite is generally absent in cordierite-bearing schists. A muscovite-out isograd can be traced close to the cordierite-in isograd (Figures 4-2 and 4-3). Fine grained muscovite growing at the rim of cordierite is the product of retrograde alteration of cordierite, known as pinitization. Poikilitic

Figure 4-7: Photomicrograph of garnet-cordierite-sillimanite-biotite schist, within 2 km of the contact with the RRB at the Venus Creek section (89-62a, Figure 4-3). The corroded and embayed rims of garnet (grey with dark inclusions), partly mantled by cordierite (arrow), suggest that garnet is being consumed by the cordierite producing reaction (8) (see text).
Scale bar: 0.5 mm. PPL

Figure 4-8: Photomicrograph of a sillimanite-garnet-cordierite-biotite schist of the KMA within one kilometer of the contact with the RRB near Twelfth of July Creek (94-174). A garnet (center), dark green hercynite (black arrow) and colourless coarse sillimanite (white arrow) are found within a large colourless, low relief cordierite porphyroblast, occupying most of the photomicrograph. The embayed rim of the garnet crystal and the presence of sillimanite predominantly as inclusions in cordierite, indicate that both phases are being consumed by a cordierite-forming reaction. See text for discussion.
Scale bar: 0.5 mm. PPL

4-7

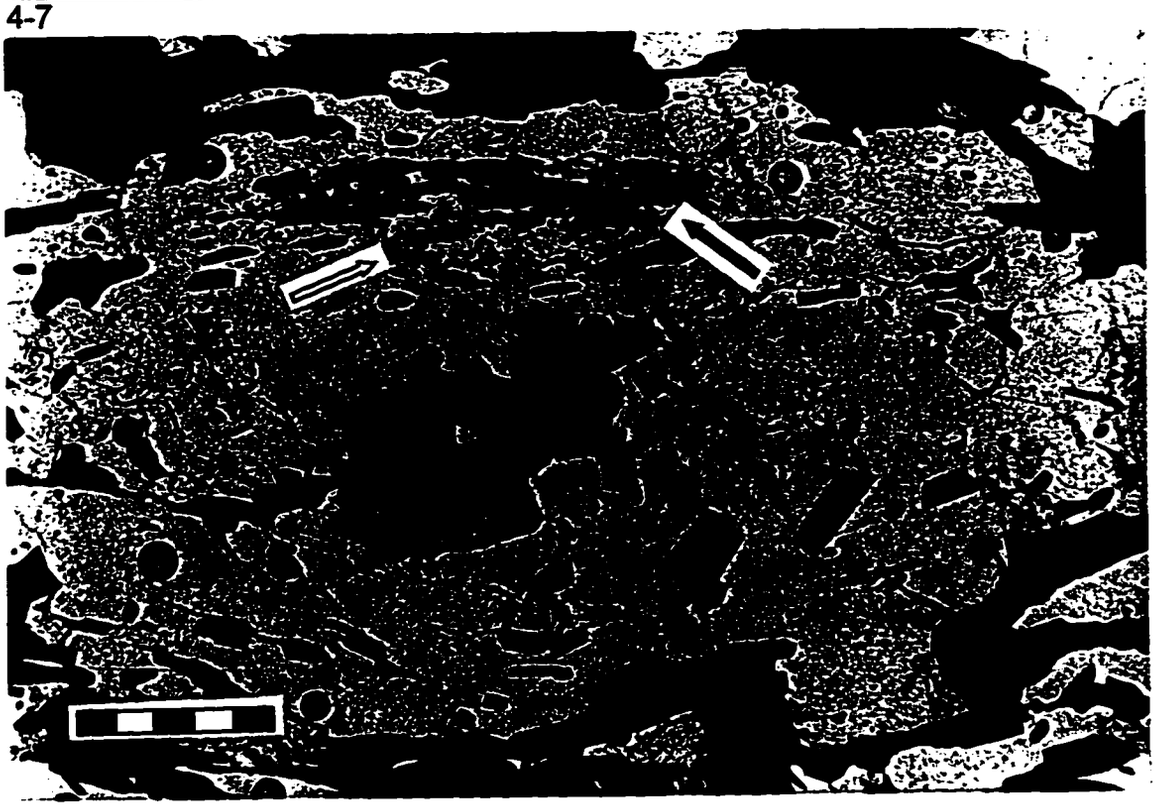

4-8

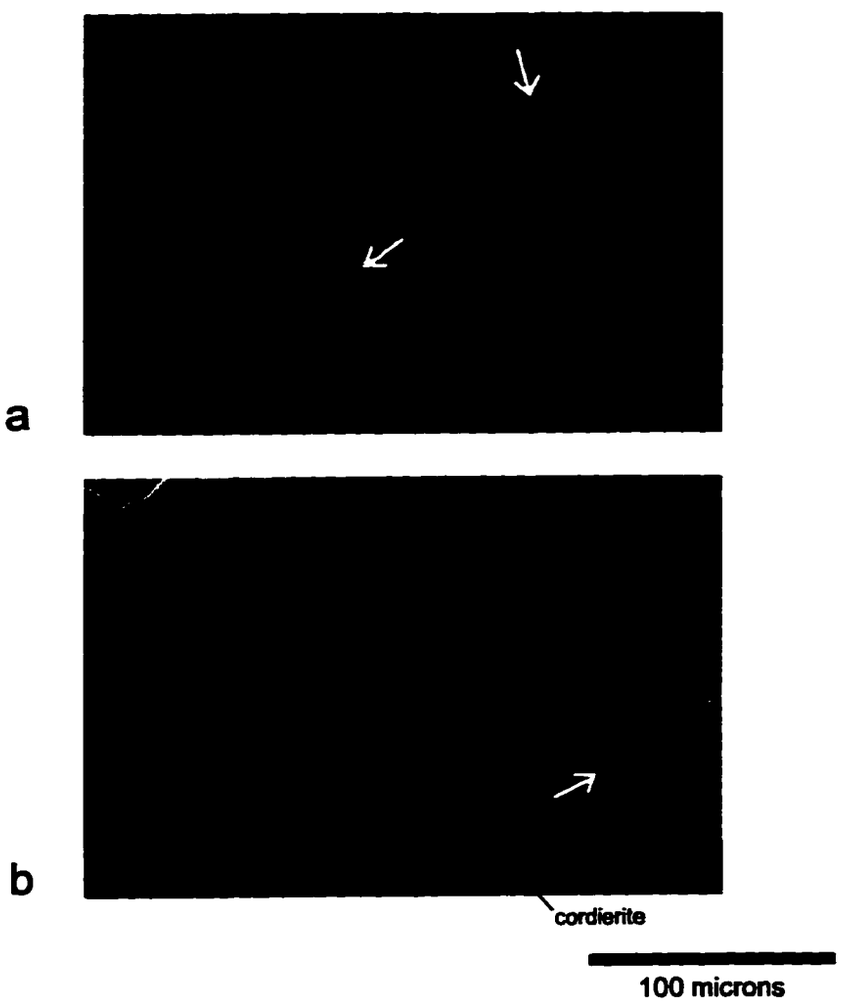

Figure 4-9: Backscatter images of K-feldspar-bearing cordierite-biotite schist of the Kluane metamorphic assemblage in the eastern Dezadeash Range (sample 90-35). **a)** K-feldspar (medium grey) grows at the expense of biotite (light grey), obvious in the embayments of K-feldspar in the biotite grain (white arrow). The black shading represents quartz. **b)** K-feldspar and cordierite (dark grey) are in contact with biotite. The white arrow indicates where cordierite is consuming biotite. This textural evidence shows that cordierite and K-feldspar are formed by the consumption of biotite (and muscovite, not shown here), according to reaction (6), implying T above 600°C. The rectangular patterns in the images are due to reproduction limitations.

texture of millimeter-sized muscovite crystals, commonly overgrowing cordierite and biotite, observed in cordierite-biotite-rich rocks in the eastern Dezadeash Range, is also interpreted as indication of retrograde metamorphic growth.

Close to the contact with the RRB, hercynite, a Fe-Al-spinel, can be observed in the core of cordierite. It occurs first as equigranular, 10-20 μm euhedral cubes or worms, and forms larger and more coherent grains closer to the intrusive contact (Figure 4-8). The presence of anhedral garnet inclusions in some cordierite crystals and fibrolite commonly surrounding hercynite within the cordierite suggest that the spinel is formed by a garnet and sillimanite-consuming reaction (10) (T. Chacko, pers. comm., 1997):

$$2\ sil + alm = Fe\text{-}crd + hc.$$

For sample 90-35 TWQ calculates this reaction at 700°C and 4 kbar. This is in good agreement with the P-T estimates of 690°C and 4.6 kbar obtained from the grt-crd-ms-pl assemblage of the same sample (Figure 4-3).

The highest grade assemblage realized in the KMA is found in the eastern Dezadeash Range, and consists of cordierite, sillimanite, K-feldspar, biotite, hercynite (nucleating in crd) and garnet (Figures 4-8, 4-9). This assemblage is characteristic of the lowermost granulite facies. The garnet, poikilitic and inclusion-free, is likely a prograde formation, possibly formed by the biotite- and sillimanite-consuming reaction (11).

Parallelism of mineral isograds with the exposed contact of the RRB and increasing metamorphic grade towards the contact strongly suggest that the above described metamorphic sequence is the result of contact metamorphism related to the intrusion of the RRB during Paleocene-Eocene time. The individual isograds are generally parallel and do not cross each other, with the exception of the andalusite-out isograd. As coexisting andalusite and sillimanite/fibrolite occur in several locations, a slight temperature variation has a large impact on the trace of the andalusite isograd.

The increase in metamorphic grade from structurally lower towards structurally higher rocks near the contact with the RRB indicates an inverted

metamorphic gradient on the underside of the batholith. A normal metamorphic gradient can be observed at the southern end of Kluane Lake in the Kluane Hills. However, there the peak metamorphic grade (garnet zone) is less than in the Ruby Range (cordierite zone). From this is can be deduced that metamorphism in the KMA is caused by an overlying batholith, the RRB, and by a smaller underlying sill.

The thickness of the contact aureole, beginning with the staurolite isograd, measured perpendicular to the contact with the RRB, and assuming an average dip of 35° of the KMA to the north, and a north-dipping sill-like RRB, is approximately 4-5 km at the Venus Creek section. The relative great depth of emplacement of the RRB (ca. 12 km, see next section) and a, prior to the intrusion, already hot KMA are major factors that cause the relative thick contact aureole.

In the eastern Ruby Range and the Dezadeash Range, the mineral isograds are deflected by larger intrusions of the RRB within the KMA, effectively widening the high grade assemblages towards the southeast. The surface width of the cordierite zone of 10-20 km in the southeast is probably caused by igneous rocks of the RRB that underlie the KMA, but are not exposed, rather than representing the actual thickness of the contact aureole. In the western Ruby Range the surface of the mineral isograds is approximately parallel to schistosity of the KMA, as the KMA underlies the RRB. In the central Ruby Range and the Dezadeash Range, where isograds are deflected by intrusive plugs of the RRB, they probably cross structural fabrics.

GEOTHERMOBAROMETRY OF THE KMA

Introduction

The mineral parageneses described in the previous section are good indicators of the metamorphic grade of the KMA. Although metamorphic

temperatures are well constrained by mineral equilibria, the steep slope of most equilibria reactions does not provide good evaluation of metamorphic pressures (Figure 4-4). Quantitative estimates of P and T can be obtained by geothermobarometry. Geothermobarometry utilizes the compositional changes of certain minerals with changing P-T conditions to calculate prevailing pressure and temperature during crystal formation (Spear, 1993).

Geothermometers are based on exchange reactions, which involve cation exchange between coexisting minerals, without producing or consuming a new phase. These reactions are pressure insensitive, due to negligible volume changes. The most common geothermometer for metapelites is based on Fe-Mg exchange between garnet and biotite (reaction (12); Thompson, 1976):

phl + alm = ann + py.

Net-transfer reactions are used as geobarometers. These reactions produce and consume mineral phases, and are often associated with large volume changes, thus providing better barometers (Spear, 1993). A common barometer for metapelites involves the formation of **G**rossular, **A**luminosilicates and quartz (**S**) from anorthite (**P**), known as GASP (reaction (14); Ghent, 1976):

grs + 2 sil/and/ky + qtz = 3 an.

Uncertainties in pressures and temperatures calculated from these reactions result from uncertainties in the microprobe analyses, the P-T location of the end-member reaction, and activity-composition models for minerals showing solid solution. Kohn & Spear (1991a, b) provide a detailed discussion of the total P-T uncertainty expected from a combination of all these sources as well as the fraction of the total uncertainty attributable to each source. They estimate total uncertainties of about ±3 kbar and ±75°C (1σ) for P-T estimates obtained using the garnet-biotite thermometer and GASP barometer. Importantly, only a small fraction (~5-10%) of this total uncertainty is attributable to uncertainties in the microprobe analyses. This observation is

significant, because it shows that P-T *differences* between samples are resolvable to about ±300 bars and ±10°C provided that the same set of thermometers and barometers, and a consistent set of calibrations and activity-composition models are used for all samples.

22 samples of garnet-bearing biotite-quartz schist of the KMA and one micaceous quartzite of the AMS (PAMfs of Johnston & Timmerman, 1993a, b) were selected for geothermobarometry. In addition two phyllites of the DF and a micaceous quartzite of the Nasina Assemblage were analyzed for geothermometry.

The criteria for the selection were based on a representative coverage of the KMA, the influence of the RRB intrusion on the country rock, the lack of retrograde alteration of minerals, and the presence of the appropriate mineral assemblage for geothermobarometry. The ideal mineral paragenesis in metapelitic rocks includes garnet, biotite, plagioclase and muscovite or cordierite. Coexisting staurolite and aluminosilicate phases help constrain P and T estimates. Quality and accuracy of geothermobarometric studies depend on a maximum mineral paragenesis. For that reason and due to field circumstances, the whole area underlain by the calcic schist, does not contain the essential garnet and is therefore not suitable for geothermobarometry.

Once selected, the mineral composition of garnet, biotite, muscovite, cordierite and plagioclase of each sample was determined by electron microprobe (type ARL-SEMQ and JEOL JXA-8900R) at the University of Alberta. Descriptions of the equipment and the mineral standards, as well as the probed samples, are given in Appendices 4-1 and 4-2, respectively. Microprobe results of the probed minerals are listed in Appendices 4-3 through 4-8.

Estimation of metamorphic pressures and temperatures using computer generated equilibria reactions

Pressure and temperature were estimated from intersections of mineral

equilibria calculated by the computer program TWQ (version 2.02) (Berman, 1996). TWQ (Thermobarometry With estimation of EQuilibrium state) calculates the P-T position of these equilibria using an internally consistent set of thermodynamic data for end member phases and activity-composition relationships for minerals showing solid solution. The convergence of all possible reaction curves in a single point in P-T space is regarded as the equilibration point of all minerals involved (Berman, 1991). Therefore the tightness of the intersections can be regarded as an indicator of the quality of the state of equilibrium reached in the specific sample. It is not to be confused with the uncertainty. No specific uncertainties are given for the intersections (see above for discussion on errors in geothermobarometry). Reproducibility and similar results with comparable samples as well as correlation with observed mineral parageneses are regarded as an indication of the accuracy of the technique. Average pressures and temperatures for each sample are shown on a P-T grid on Figure 4.10 and in map form on Figure 4-11. The application of the computer program TWQ 2.02 is described in Appendix 4-9.

Results and discussion

Equilibria reactions for garnet core and rim compositions in combination with average biotite or matrix biotite, were calculated for all samples graphically, as shown in Appendix 4-10. According to the mineral phases present, the garnet-biotite-muscovite-plagioclase geothermobarometer was applied on samples from the staurolite zone, and a garnet-biotite-plagioclase-cordierite thermobarometer for cordierite-bearing samples that do not contain any primary muscovite. Garnet rim and matrix biotite values generally do not provide such tight intersections as do garnet rim-contact biotite points, which come closest to an actual state of equilibrium within each sample. However, re-equilibration of biotite in contact with garnet during cooling will result in lower T than peak metamorphic T. The generally wider scattered intersections of garnet core and average values suggest that these points are not in

Figure 4-10: Pressures and temperatures of mica-quartz schist of the Kluane metamorphic assemblage and one granodiorite of the Ruby Range Batholith (94-147d) averaged from equilibria reaction intersections, shown on the right diagram, calculated by TWQ 2.02 (Berman, 1996). Sample symbols refer to mineral assemblage observed in thin sections of analyzed samples. Staurolite was not considered in the calculations, but its presence in probed samples provides independent information on the accuracy of P-T data. Note that staurolite is constrained to its stability field (after Spear, 1993) and cordierite is only present in higher temperature assemblages. See text for discussion on methodology and Appendix 4-9 for description of computer program. The right P-T diagram displays the triangles calculated by TWQ 2.02 (Berman, 1996), that were used to estimate P and T for each sample. No triangles are shown for the samples shown in grey on the left diagram (93-77, 93-80), as their spread is very large and exceeds the scale of the diagram. See Appendix 4-10 for their equilibria reaction diagrams. Aluminosilicate triple point, H_2O-saturated pelitic solidus curve and facies division are after Holdaway & Mukhopadhyay (1993), Spear (1993) and Bucher & Frey (1994), respectively. Dashed grey line marks the location of the andalusite-sillimanite reaction after Richardson et al. (1969).

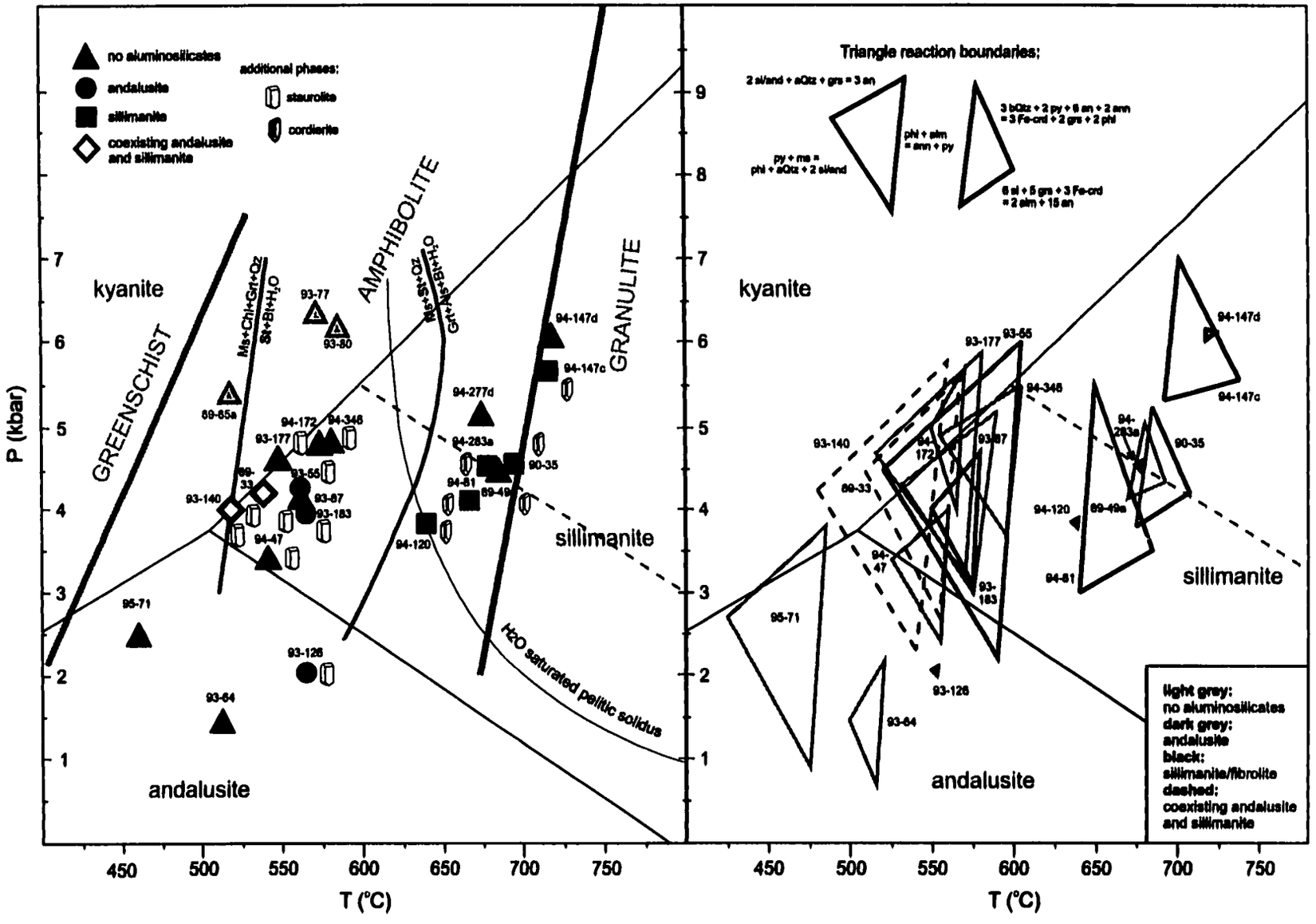
no aluminosilicates
andalusite
sillimanite
coexisting andalusite and sillimanite
additional phases:
staurolite
cordierite
kyanite
andalusite
sillimanite
GREENSCHIST
AMPHIBOLITE
GRANULITE
Ms+Chl+Grt+Qz = St+Bt+H2O
Ms+St+Qz = Grt+Als+Bt+H2O
H2O saturated pelitic solidus
93-77
93-80
89-65a
94-172
94-346
93-177
93-55
93-140
89-33
93-87
93-183
94-47
95-71
93-126
93-64
94-277d
94-283a
90-35
94-81
89-49a
94-120
94-147d
94-147c
P (kbar)
T (°C)
Triangle reaction boundaries:
2 sil/and + aQtz + grs = 3 an
phl + sim = ann + py
py + ms = phl + aQtz + 2 sil/and
3 bQtz + 2 py + 6 an + 2 ann = 3 Fe-crd + 2 grs + 2 phl
6 sil + 5 grs + 3 Fe-crd = 2 sim + 15 an
light grey: no aluminosilicates
dark grey: andalusite
black: sillimanite/fibrolite
dashed: coexisting andalusite and sillimanite

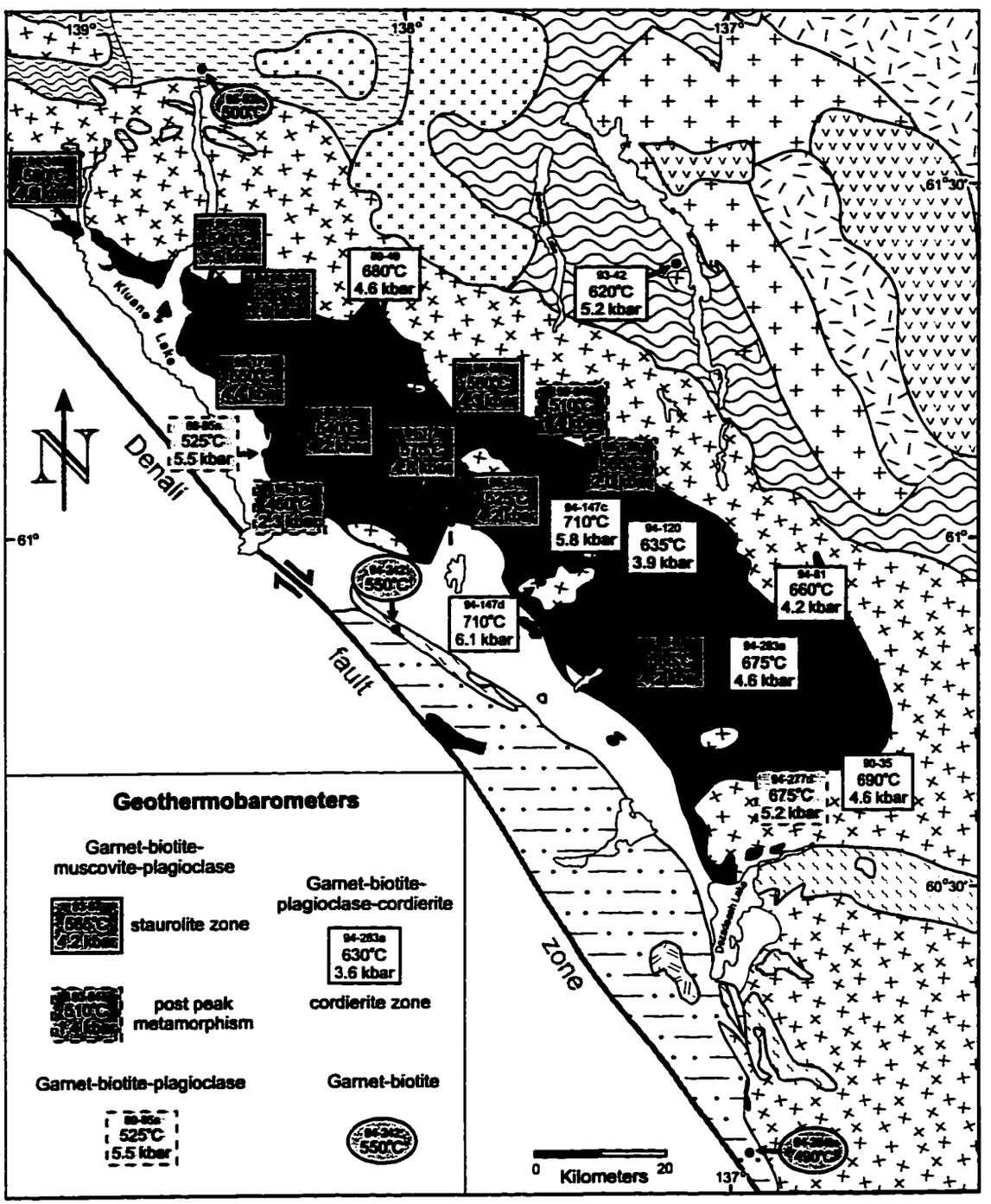

Figure 4-11: Geological map with pressure and temperature estimated from equilibria calculated by TWQ (2.02) and displayed on P-T diagrams on Figures 4-4 and 4-10. Only samples with good reaction intersections are shown. See text for detailed discussion. Geology is the same as on Figure 2-1.

equilibrium, therefore P-T estimations for garnet core values are meaningless. The P-T spread used in the following discussion describes the tightness of the equilibria reactions intersections and is not to be confused with error or uncertainty.

Most samples of the bt-qtz schist of the KMA cluster in two areas in P-T space (Figure 4-10). These clusters can be correlated with index mineral zones, garnet composition and geographic location. Samples that plot near the aluminosilicate triple point, at 4 kbar and 550°C, are from the staurolite zone. There is good agreement between P-T estimates presented in Figure 4-10 and observed mineral parageneses. All samples that plot in the staurolite stability field shown on Figure 4-4 contain several weight percent staurolite. Andalusite and fibrolite are common accessory phases. Outcrops in the vicinity of aluminosilicate-free samples contain either andalusite or fibrolite, or as in the case of 94-47, both phases. The staurolite bearing samples have a P-T spread from ±0.7-1.9 kbar and ±15-40°C. Two of the samples (93-77 and 93-80) that are shown in grey on Figure 4-4 have average P and T of 6.5 kbar and 575°C, which places them in the kyanite field. However, kyanite has not been observed, and a spread of ±3 kbar and ±75°C of the equilibria reactions, suggest that the probed mineral phases of these samples were not in equilibria.

A second cluster of samples lies within the cordierite stability field at 4 kbar and 675°C, corresponding to a depth of 12 km (Figure 4-10). All samples are from the cordierite zone of the KMA, and most of them contain cordierite, as well as abundant sillimanite. The absence of staurolite is in agreement with the location of the samples outside the staurolite stability field. Reaction intersections obtained from cordierite-bearing samples are generally tighter than those from staurolite zone samples, with some intersecting at one spot (94-120, 94-283a, Appendix 4-10), suggesting that the probed phases in one sample come close to a chemical equilibrium. Sample 94-81 yields a tight intersection (3.3 kbar, 630°C) by using muscovite, while a wider scattered intersection (4.2 and 660°C) results from using cordierite instead (Appendix 4-

10). The cordierite P-T estimate is similar to other samples along strike and is thought to represent the peak metamorphic conditions, while the muscovite P-T is due to re-equilibration during uplift.

The P-T estimates from the cordierite-bearing samples plot at higher T than the solidus curve for water saturated metapelites. However, the samples do not show signs of migmatization, suggesting that these rocks were water undersaturated during peak metamorphism.

The staurolite and cordierite zone samples have distinct garnet compositions. Photomicrographs, compositional zoning profiles of garnets and calculated equilibria reactions for garnet rims from the staurolite and cordierite zone in the Dezadeash Range are shown on Figures 4-12 and 4-13. The garnet from a staurolite-bearing schist (93-80) appears cloudy, due to minute graphitic inclusions. Its rim is corroded and embayments are abundant (Figure 4-12a). Biotite and staurolite in contact with the garnet suggest it is being consumed to form staurolite and biotite according to reaction (3). An electron microprobe profile across the garnet shows distinct compositional zonation of the grain (Figure 4-13a, also see Appendix 4-11). Fe and Mg increase, while Ca, Mn and the Fe/(Fe+Mg)-ratio decrease towards the rim. The compositional change reflects changing P-T conditions or a change in bulk composition during the growth of the garnet. This zoning pattern is known as growth zoning and is commonly observed in greenschist and amphibolite grade rocks (Spear, 1993). Preserved growth zoning indicates that the sample has not been heated long enough above 600°C, at which chemical diffusion is sufficiently rapid enough to homogenize the composition of garnets over hundreds of μm. The "bell-shaped" profile with decreasing Ca towards the rim is typical of heating following decompression (Spear, 1993).

In contrast, garnets from the cordierite zone often are clear and poikilitic, with less altered rims (Figure 4-12b). Electron microprobe cross-sections show no compositional zoning, implying either homogenization by diffusion at temperatures above 600°C or new crystal growth (Figure 4-13b and Appendix 4-11).

Figure 4-12:
a) Photomicrograph of a garnet-staurolite-biotite schist from the western Dezadeash Range (93-80). The rim of the garnet (grey brown high relief mineral in the center) is corroded. Embayments of biotite, obvious in the upper parts of the photograph, and staurolite (st) in contact with the garnet on the right side, suggest that the garnet is being consumed to form staurolite and biotite, according to reaction (2). As a result, the garnet rim is not in equilibria with other minerals. The calculated equilibria reactions have a wide spread (Figure 4-13a).
Scale bar: 0.5 mm. PPL
b: Photomicrograph of a poikilitic, inclusion-free garnet of a cordierite-biotite-quartz schist in the eastern Dezadeash Range (90-35). The garnet is clear, lacking the graphitic inclusions of the garnet in a). The margin is not embayed or corroded. To the right, the garnet is growing into biotite, apparently consuming it, according to reaction (10). The same can be observed in the lower part of the garnet, where it overgrows a biotite crystal. This garnet is part of the highest T assemblage found in the KMA, which includes garnet, cordierite, K-feldspar (Figure 4-9), biotite and sillimanite, as well as hercynite-nuclei in cordierite. The resulting equilibria reaction intersection is relatively tight (Figure 4-13b).
Scale bar: 0.2 mm. PPL

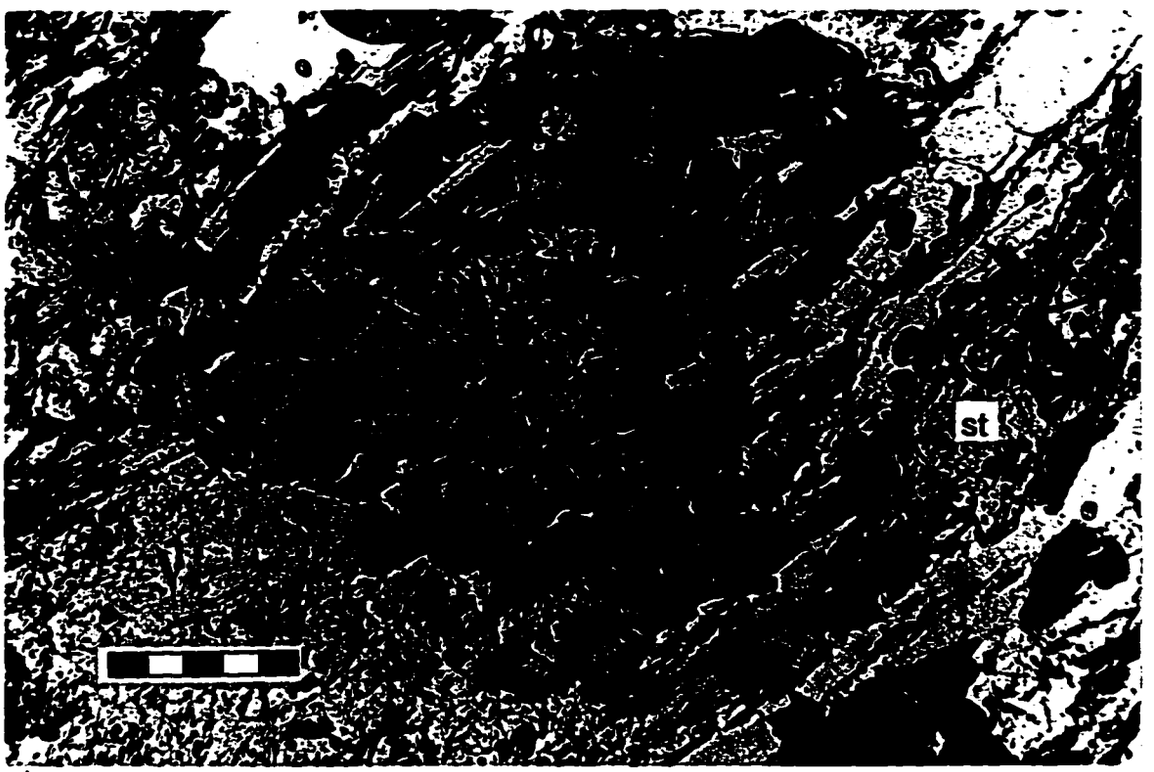

a)

b)

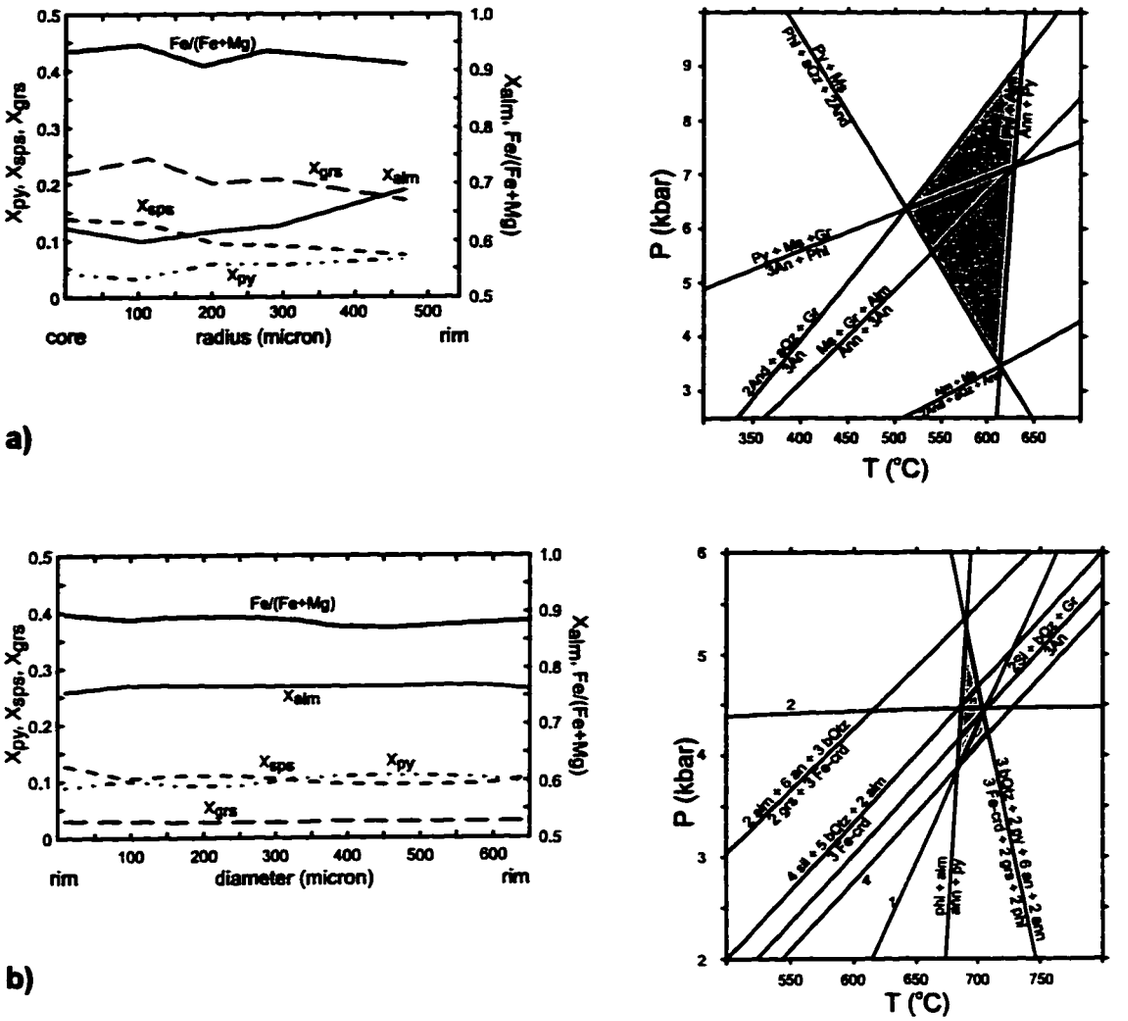

Figure 4-13: Compositional cross-sections of garnets and equilibria reactions curves calculated by TWQ for two samples in the Dezadeash Range. **a)** 93-80 is from a staurolite-bearing biotite schist. Altered rims, embayments in the crystal and staurolite in contact with garnet (Figure 4-12a) indicate that the grain is consumed by the staurolite producing reaction (2). As it is consumed, the garnet rim does not represent the current P-T conditions, and resulting equilibria reaction curves (right diagram) show a wide spread. The "bell-shaped" curve of grossular indicates heating following decompression. The preserved growth zoning pattern implies that the garnet was not sufficiently heated above 600°C for diffusion to homogenize the grain. **b)** The garnet of sample 90-35, a sillimanite-cordierite-biotite schist, shows a homogeneous garnet composition, implying temperatures above 600°C. The garnet is either totally homogenized due to diffusion or, as in this case, a second generation garnet (see Figure 4-12b and text for discussion). The low grossular- and spessartine-components are also indicative of high temperature garnets. The tighter intersection of the equilibria reaction curves suggests that the analyzed mineral phases were in a better equilibrium than in the sample of the staurolite zone. Note that in **a)**, the compositional cross-section is from core to rim, while in **b)** it is from rim to rim. Also note the different scale of the P-T diagrams.

Staurolite zone garnet cores have a higher Ca-content (~X_{grs}=15-30) compared to X_{grs}=3-5 for the cordierite zone garnets, indicating higher metamorphic pressures or lower temperatures during the formation of the core (Spear, 1993). A higher Mn-content (X_{sps}=15-30 versus X_{sps}=5-15), and higher Fe/(Fe+Mg) ratio of the same garnet cores also indicate lower temperature conditions than cordierite zone garnets.

Garnets of the staurolite zone were being consumed by the formation of staurolite, whereas in the cordierite zone renewed garnet growth occurred due to the breakdown of staurolite or garnet compositions were homogenized by diffusion. As a result, it is to be expected that equilibria reactions of cordierite zone garnets have in general tighter intersections. Their rim composition is believed to be closer to peak metamorphic conditions than the partly corroded rims of the staurolite zone garnets. This explains in part the temperature gap between the staurolite and cordierite zone samples. Calculated temperatures of aluminosilicate-bearing samples of the staurolite zone are 50-100°C lower than the peak T indicated by the aluminosilicates, which form by the breakdown of staurolite, as described in the previous section.

The cores of staurolite zone garnets preserve earlier high P/low T conditions, while the homogenized cordierite zone garnets represent peak metamorphic conditions. However, as the garnet cores are not in equilibrium with the other phases (plagioclase, biotite and muscovite), which re-equilibrate much faster than garnet, calculation of reaction equilibria using garnet core values result in widely scattered intersections (Appendix 4-10). P-T estimates based on the location of these equilibria would be meaningless.

The highest P and T, 6 kbar and 710°C, were obtained from a grt-crd-bt-qtz schist and a garnetiferous granodiorite of the RRB plug near Garnet Creek. Both samples (94-147c and 147d) are located close to the intrusive contact (Figure 2-10). The garnets are exceptionally large (1.5-2 mm), euhedral, clear, and relatively Fe-rich. The schist sample also contains coarse sillimanite, which is otherwise uncommon in the KMA. Cordierite from the schist sample has the highest Mg-content (X_{Mg}=68) of all probed KMA samples. Reaction equilibria

intersections of both samples are similar. The high P and T of these samples imply a crystallization at greater depth (~18 km) than those of other cordierite zone samples, at the contact with the top of the structurally deeper sill (see Chapter 2). Assimilation of some pelitic schist during the emplacement of the granodiorite may account for the presence of garnets in the granodiorite.

Mn-rich (X_{sps}=25-30), clear, small (150-300 μm), euhedral garnets, with low P (1.4-2.3 kbar) and low to medium T (460-565°C) were found east of the Killermun Lake plug of the RRB (93-64, 93-126/1) and in the western Kluane Hills (95-71). The Killermun Lake samples lie in the staurolite field, but garnets are small and, unlike other staurolite zone garnets described above, have no zonation. They indicate formation at higher structural levels during uplift.

The western Kluane Hills sample (95-71) contains a small euhedral, Mn-rich (X_{sps}=25), garnet that crystallized at relative lower P and T of 2.3 kbar and 460°C, respectively (Appendix 4-10). The garnets in these three samples cannot be related to any known metamorphic event and may reflect local thermal events or anomalies during uplift.

In contrast, a sample near the Kluane Lake shore (89-85a), 2.5 km west of 95-71, contains garnets that are similar to the staurolite zone garnets. The grains appear corroded, display growth zoning and have Ca-rich (X_{grs}=24) cores (Appendix 4-11). The P and T obtained from this sample, 5.5 kbar and 525°C, have to be regarded with some caution, since they are derived from only two independent reactions, which do not constrain P very well (Appendix 4.8). However, the intersection of reactions (12) and (14) is in the same P range as those of other staurolite zone garnets, suggesting formation at similar high P/low T conditions.

Regional metamorphic temperature and pressure variations

The confinement of the probed samples to garnet-bearing staurolite and cordierite zones within the aluminous portion of the KMA, generally limits comparison to samples along strike. Since the metamorphic character of the

KMA is dominated by a large contact aureole, T estimates obtained through thermometry can be correlated with mapped mineral isograds. T increases from 525°C at Kluane Lake (89-85a) to 680°C near the intrusive contact (89-49a). The highest T of 710°C were recorded in samples immediately near an intrusive contact (94-147c, d). Along strike, an increase from 580°C at the north end of Kluane Lake (94-346) to 690°C in the eastern Dezadeash Range (90-35) can be observed. A southeastward increase in T can be explained by the massive nature of the Coast Plutonic Complex (CPC) east of the Dezadeash Range, which provided a larger heat source than the comparably thin sill-like body of the RRB in the Ruby Range.

There is little variation between P estimates along strike (Figure 4-11). Although equilibria intersections of staurolite samples are more scattered, the intersection triangles all overlap in the 3.5-5 kbar range. Although P-T conditions during garnet core growth cannot be calculated, the similarity in core composition may indicate similar P-T ranges of the samples.

Cordierite zone samples that reflect peak metamorphic conditions, show no variation in P along strike. Samples 100 km apart (89-49 and 90-35) were equilibrated at the same P and T. These samples are at the northeastern exposed margin of the KMA, close to the contact with the RRB.

A P-gradient across strike can be obtained from 94-120 (3.9 kbar) near the northeastern contact with the RRB, and 94-147c (5.8 kbar) and 94-147d (6.1 kbar), 20 km to the southwest, closer to the structural base of the KMA. The difference of approximately 2 kbar across strike indicates that the samples in the southwest represent rocks that were equilibrated at 6 km greater depth than those near the intrusive contact to the northeast. The resulting P-gradient of 0.1 kbar/km is equivalent to a depth gradient of 0.3km/km and requires post-peak metamorphic northward tilting of the assemblage in that area of 15° (Figure 4-14).

The apparent lack of P-variation along strike indicates that the present erosional surface was at the same depth during peak metamorphism. The KMA behaved as a rigid block in during subsequent uplift and northward tilting.

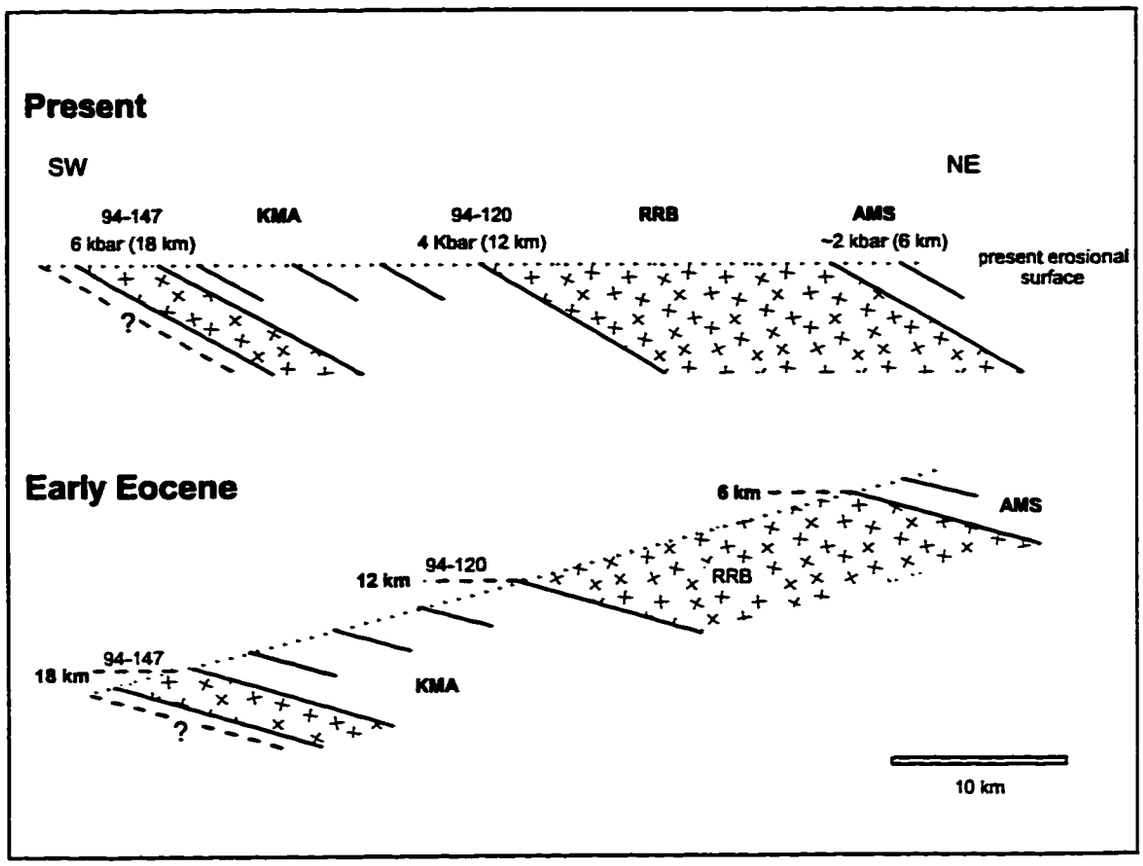

Figure 4-14: Peak metamorphic pressures of samples of the KMA and the RRB in the Ruby Range suggest that samples from the exposed structural base of the KMA were equilibrated at greater depth than samples near the intrusive contact with the RRB in the north. The original structural levels during the emplacement of the RRB can be restored by calculating a pressure gradient. See text for discussion.

P-T-t PATH VARIATIONS OF THE KMA

The different P and T ranges recorded in the KMA document two major metamorphic events, an older regional high P/low T event M_1, and a younger contact metamorphic low P/high T event M_2. Possible P-T-t paths for samples representative of the high T assemblage near the contact with the RRB, and samples of the low grade schists along the Kluane Lake shore are shown in Figure 4-15.

The first metamorphic event M_1 is coeval with deformation $D_{n+2,}$ resulting in the development of the S_{n+2}- and L_{n+2}-fabrics and regional upper greenschist grade metamorphism that reached the garnet zone in the aluminous sequence. The maximum T is given by the first prograde appearance of staurolite at approximately 525°C at 4-5 kbar (Figure 4-4). Prevailing P-T during growth of cores of staurolite zone garnets can be approximated by the composition of the garnet cores. An average garnet core composition of X_{grs}=20, X_{py}=5, X_{alm}=60 and X_{sps}=10 is located at 7 kbar and 500°C on P-T composition diagrams for garnets in pelitic schist (Figure 17-10 in Spear, 1993). However, this is just an approximation and should not be considered as accurate as P-T estimates from reaction equilibria calculations. 7 kbar equals a depth of approximately 21 km. A high P/low T metamorphism is typical for accreted rocks during underplating, resulting in a deflection of the geotherm towards depth (Platt, 1986).

The timing of M_1 is unclear, since radiometric dates show that the cooling ages of the KMA were reset by the intrusion of the RRB, or the KMA did not undergo cooling below 280-350°C, the closure temperatures of argon in biotite and muscovite, before Eocene. Rb-Sr dating of muscovite, which provides higher closure temperatures (500°C) proves to be inconclusive. An isochron calculated for muscovite and whole rock samples of lower grade ms-chl schist yield an age of 57.5 ± 7.2 Ma, with a large deviation (MSWD 67.2) and therefore cannot be regarded as reliable (Appendix 2-7). Concordant zircons of a late-synkinematic granitic dyke (location of 94-81) yield an age of

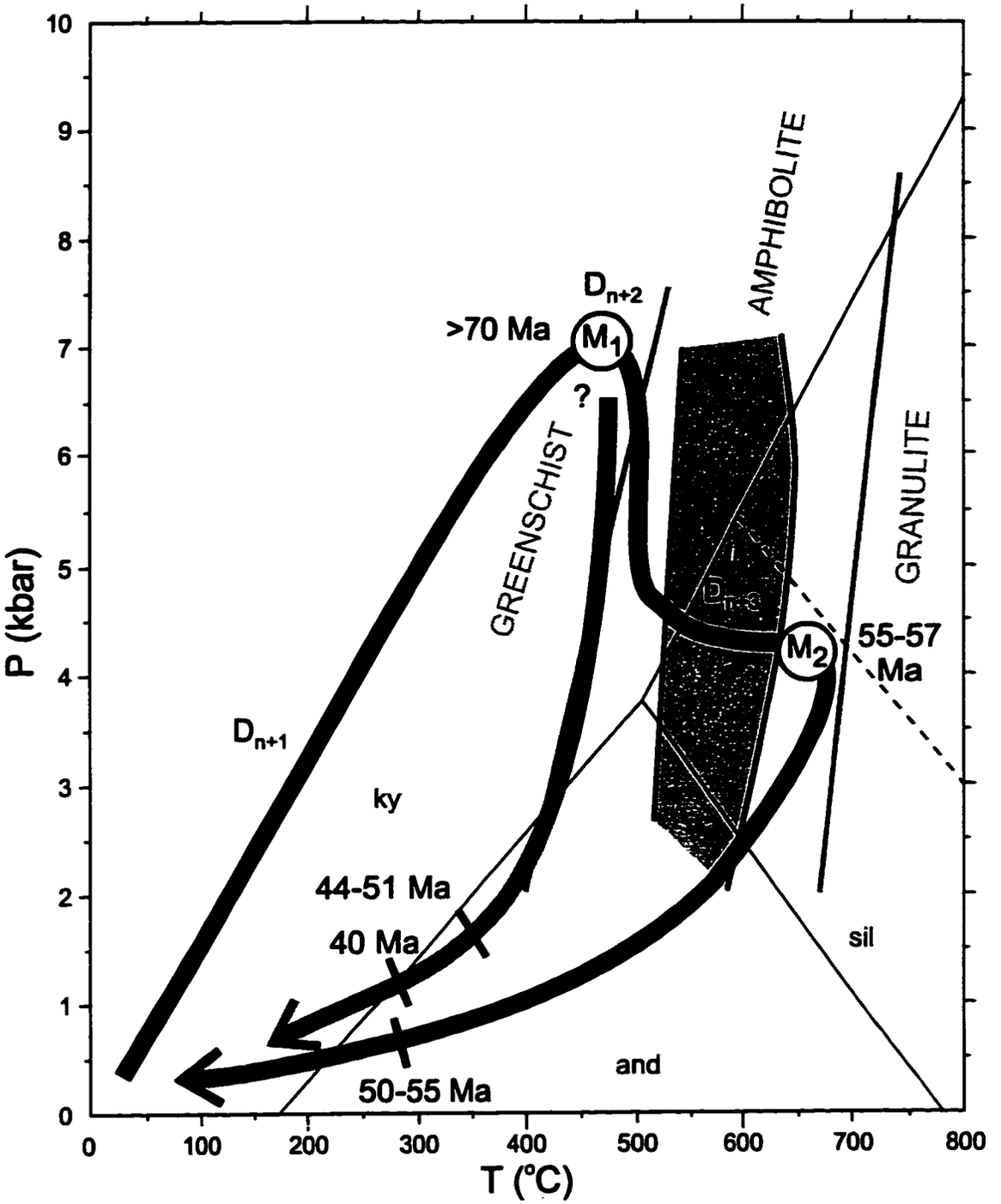

Figure 4-15: P-T-t paths with observed metamorphic events for the KMA close to the contact with the Ruby Range Batholith (black line) and further away from it (grey line). The periods of major deformation are shown. Ages represent time at which rocks have undergone cooling through blocking temperature (after Erdmer & Mortensen, 1993). Minimum age of 70 Ma is from late synkinematic granitic dyke intruding the KMA (Mortensen, unpublished data, 1997). The staurolite stability field is shown in grey.

71.8 Ma, which can be regarded as a minimum age for D_{n+2} and M_1 (Appendices 2-5, 2-6; Mortensen, unpublished data, 1997).

The absence of high P/ high T mineral assemblages in the KMA implies that the assemblage did not stay long enough at this depth for the geotherm to relax and T to increase. However, quantification of the duration at higher P cannot be made without geochronological evidence, since too many unknown factors, such as the rate of heat flow and the nature of the geotherm prior to underplating, as well as the thickness of the material that was underplated and the duration of subduction and underplating of cooler material, all influence the perturbation of the geotherm. Estimates for the duration of the presently exposed KMA at depths in excess of 20 km are in the order of 10-30 Ma, from comparison with studies in the Alps (Rubie, 1984) and models (England & Thompson, 1984).

Shortly after reaching peak P during M_1 isothermal (?) decompression is followed by an apparent isobaric heating event M_2 at 4-4.5 kbar, corresponding to a depth of 12-13 km, at the northern margin of the KMA. Replacement of andalusite by sillimanite, observed in samples along the Venus Creek sections discussed above indicate an apparent isobaric heating path preserved at the current erosional surface. The above mentioned pressure gradient of 0.1 kbar/km across strike further to the east, would imply an increase of 1 kbar towards the south end of the Venus Creek transect. This difference is too small to be distinguished by petrographic methods.

Radiometric and petrographic studies discussed above strongly suggest that M_2 is the result of the intrusion of the RRB in the Late Cretaceous to early Tertiary. Overprinting of earlier schistosity and lineation indicates that no significant deformation was related with the M_2-event.

As the thermal effect of M_2 decreases with distance to the intrusive contact, so is M_2 less evident in the mineral assemblages. The grey arrow in Figure 4-15 outlines a decompression path for lower grade rocks of the KMA. Absence of staurolite in samples of the aluminous schist near Kluane Lake (89-85a) suggests that these rocks did not experience substantial T increase after

peak P conditions. Chlorite overgrowing foliation in the lowest grade ms-chl schists along Kluane Lake may indicate retrograde formation of chlorite from biotite. Younger ^{40}Ar-^{39}Ar ages of 40 Ma, reported by Mortensen & Erdmer (1992) for the lower grade rocks, are interpreted as slower cooling of the rocks near Kluane Lake, which would provide more time for retrograde reactions to take place.

METAMORPHIC EVOLUTION MODEL OF THE SOUTHWEST YUKON

The metamorphic evolution of the former continental margin is preserved in the pericratonic assemblages associated with the Nisling terrane, the Aishihik Metamorphic Suite (AMS), the Nasina assemblage and the Nisling assemblage.

Triassic (?) greenschist grade regional syndeformational metamorphosed rocks of the AMS were thermally overprinted by the Early Jurassic (186 ± 2.8 Ma) intrusion of the Aishihik Batholith (Johnston et al., 1996). High pressure assemblages (staurolite-kyanite) and geobarometry in the AMS indicate pressures of 8-10 kbar, corresponding to a depth of emplacement of the Aishihik Batholith at 30 km. Similar high P assemblages are common in Nisling assemblage schists east and southeast of Dezadeash Lake (Figures 2-9 and 2-15). Garnets of the AMS and Nasina Assemblage (93-42, 95-53b) have distinct compositional zoning, with "bell-shaped" Mn- and Ca-profiles, and grossular- and spessartine-rich (X_{grs}=25, X_{sps}=10-15) cores similar to garnets of the staurolite zone of the KMA (Appendix 4-11). Garnets of the AMS and the Nasina Assemblage are larger (up to 1 cm) than those in the KMA and display "snowball" inclusion trails, indicating synkinematic growth. Calculated P of 5.2 kbar for one AMS sample (93-42) is comparable to staurolite zone KMA samples (4-5 kbar, Appendix 4-10). However, this P is much lower than the 8-10 kbar reported by Johnston & Erdmer (1995a), and may reflect re-equilibration during uplift. A direct correlation between this

sample and the staurolite zone samples of the KMA should be cautioned. Likewise, the relatively low garnet rim T of 500°C recorded in the micaceous quartzite of the Nasina Assemblage is interpreted as a result of re-equilibration in cooler conditions during exhumation of the assemblage (Appendix 4-10).

It is possible that the KMA was already accreted to the continental margin represented by Nisling terrane assemblages. The contact aureole of the Aishihik Batholith is only 10 km wide (Johnston & Erdmer, 1995a) and the intrusion may have thermally effected only the AMS and not the KMA. However, recorded pressures in the AMS increase towards south, away from the contact with the Aishihik Batholith, implying that the KMA, if underlying the AMS at that time, would be at greater depth, and should record greater pressures. P-T results available for the KMA suggest that this was not the case.

Johnston et al. (1996) report that the AMS experienced rapid uplift after the intrusion of the Aishihik Batholith, as evident in the low level (<6 km) emplacement of the Long Lake plutonic suite (185.6±2 Ma), followed by another period of burial in the Middle Jurassic, as indicated by K-Ar ages of 165 Ma. It is after this late Middle Jurassic burial that the KMA was likely accreted to the continental margin. An earlier accretion can be ruled out for the following reasons:

1) the KMA records only one deformational and two metamorphic events, compared to two and four, respectively, for the AMS (Johnston et al., 1996);
2) there is no indication of repeated uplift and burial in the KMA as in AMS;
3) geochronology and petrography records only one high T event, related to the intrusion of the RRB (Mortensen & Erdmer, 1992);
4) no pre-Late Cretaceous intrusive events have been observed in the KMA.

The accretion of the KMA onto the continental margin of North America must have taken place before the latest Cretaceous (71.8 Ma) intrusion of the syndeformational dyke, and possibly already during mid-Late Cretaceous, as indicated by U-Pb zircon ages of 78-87 Ma from marginal phases of the RRB in

the Aishihik Lake area (Johnston, 1993). High T andalusite-cordierite-sillimanite assemblages are found near contacts with the RRB in the KMA and the pericratonic AMS, Nisling and Nasina assemblages, identifying the RRB as a "stitching pluton" (Figures 2-14, 2-15). The relative thick (~5 km) contact aureole observed in the Ruby Range, compared to thinner aureoles in the AMS (<1 km, S. Johnston, pers. comm., 1996) and in the Nisling assemblage east of Dezadeash Lake, indicates that the KMA was at greater crustal depth, probably in part underlying the pericratonic terranes to the north and east. Depth of emplacement for the RRB at the exposed contact with the AMS is believed to be 2-3 kbar (S. Johnston, pers. comm., 1996).

The intrusive contacts of the DF and Nisling assemblage with the CPC south of Dezadeash Lake are shallow level, as indicated by the lack of thermal overprinting of kyanite-staurolite-garnet assemblages in the Nisling assemblage, and by the presence of "knotty schist" (Figure 2-20) and low T garnets (X_{sps}=50), recording T of 490°C (94-204b, 94-237; Appendices 4-10, 4-11) in phyllites of the DF at Million Dollar Falls campground (Figure 2-15). K-Ar ages of 66-68 Ma, obtained from the phyllite and from granodiorites of the CPC (LeCouteur & Tempelman-Kluit, 1976; G. Lowey, pers. comm., 1995), suggest that the DF was already attached onto North America by the latest Cretaceous. Since the KMA is situated between the pericratonic metamorphic assemblages in the east and northeast and the DF in the southwest, the minimum age for the accretion of the KMA onto the continental margin is 68 Ma, unless the spatial relations between assemblages east of the Denali fault have changed significantly since the emplacement of the RRB and CPC.

No major metamorphic event post-dating the Late Cretaceous-Early Tertiary intrusion of the RRB/CPC is observed in the plutonic and metamorphic assemblages of the southwest Yukon. Cooling ages from 68 to 40 Ma record final uplift of these assemblages through the 280-350°C geotherm range (LeCouteur & Tempelman-Kluit, 1976, Mortensen & Erdmer, 1992). The juxtaposition of low-grade DF to the southwest with medium to high-grade KMA

north and northeast occurred along a southwest-verging thrust or reverse fault, coeval with the relative northward tilting that brought structural lower levels of the KMA to the present surface.

CONCLUSIONS

1) Two major metamorphic events are recorded in aluminous schists of the KMA:

M_1: Syndeformational high P/low T regional metamorphism, which is preserved in Ca-rich cores of garnets that display compositional zoning. Inclusion trails in some garnets indicate synkinematic growth. No staurolite is identified with M_1, limiting the maximum T to approximately 525°C, equivalent to upper greenschist grade.

M_2: A thermal event that overprinted existing foliation and lineation and resulted in coarsening of the grain size. Mineral assemblages associated with M_2 define a metamorphic aureole with an inverted metamorphic grade around the exposed contact with the RRB, suggesting that the emplacement of the RRB resulted in the thermal metamorphism. The thickness of the metamorphic aureole is estimated to exceed 5 km in the Ruby Range. Peak assemblages of cordierite-K-feldspar-sillimanite-garnet near the contact indicate that the lower granulite grade was reached. Garnets in high T assemblages have no compositional zoning, which is caused by diffusional homogenization at T over 600°C. No major deformation is associated with M_2.

2) Geothermobarometry of the KMA distinguishes two P-T ranges, related to the two metamorphic events. P and T of 4-5 kbar and 550°C are recorded in samples that contain garnets equilibrated under peak P conditions. Actual peak P is thought to be in the order of 7 kbar, as implied by grossular-rich garnet cores. However, since garnet cores are not in equilibrium with other phases, reliable P-T calculations are not possible. P-T estimates of high T assemblages

record 4-4.5 kbar and 635-690°C, in good agreement with observed mineral assemblages.

3) A clockwise P-T-t path can be reconstructed for the KMA. The high P event M_1 represents burial of a relative cool pelitic assemblage. This burial was likely related to underthrusting or underplating of the KMA underneath the North American continental margin, represented by Nisling terrane assemblages. Minimum depth of burial was 20 km, but grossular-rich garnet cores suggest that the actual depth could have been greater. The lack of distinct P gradients suggests that the present erosional surface exposes rocks from the same depth. Timing of M_1 is constrained by late-Middle Jurassic (165 Ma) metamorphism of the AMS and beginning of the igneous activity of the RRB in Late Cretaceous (70-90 Ma; Johnston, 1993) marks the stitching the KMA and DF onto the continental margin. Absence of high P/high T mineral assemblages in the KMA suggests that M_1 is not older than latest Early Cretaceous.

The proposed clockwise P-T-t path of the KMA is similar to Alpine-type P-T-t paths, where isothermal decompression is interpreted as rapid exhumation due to underplating (Platt, 1986) or as a change from subduction of oceanic crust to collision of island arcs or continental crust (Ernst, 1988). Beginning of underplating of the INS (?) underneath the KMA, resulting from a change in plate motion of the Kula plate from east to NNE in the latest Cretaceous, provide a mean for a rapid Paleocene uplift prior to the intrusion of the RRB (see Chapter 3).

Geochronology yields cooling ages for the KMA (39-61 Ma) similar to the assumed crystallization age of the RRB (50-57 Ma) indicating that M_2 occurred in the Late Paleocene to Early Eocene. Maximum depth of emplacement of the RRB, as recorded in structural lower units of the KMA, is 18 km. The main portion of the RRB intruded the KMA at depth of 12 km.

4) Wider RRB-related contact aureoles in the KMA compared to the AMS

indicate a greater crustal depth of the KMA at the time of emplacement of the RRB. An approximated P-gradient of 0.1 kbar/km, from the southern contact of the AMS (2 kbar) to the structural lower levels of the KMA (6 kbar) is obtained from geothermobarometry. Therefore, a post-peak metamorphic northward tilting of 15° is required to bring these rocks to the present erosional surface. The RRB was emplaced along the contact between the KMA and the AMS, at a shallower angle (15°) than observed at the presently exposed contacts (~30°). Younger argon cooling ages (~40 Ma) reported for structurally lower schists of the KMA at the Kluane Lake shore, compared to schist near the contact with the RRB in the north (~55 Ma) are compatible with the tilt.

5) The KMA has been correlated with the Maclaren Glacier Metamorphic Belt (MGMB) in the eastern Alaska Range, which has led several authors to suggest a post-Eocene dextral offset of 400 km along the Denali fault (Forbes et al., 1974; Nokleberg et al., 1985). Peak metamorphism in the MGMB is only up to middle amphibolite facies and coeval with deformation. The deformation, dated to the early Eocene (57 Ma), also resulted in the development of a penetrative foliation in the East Susitna Batholith (70 Ma), which was previously correlated with the RRB (Forbes et al., 1974; Nokleberg et al. 1985). Deformation and metamorphism in the eastern Alaska Range is interpreted to have occurred during faulting along the Denali fault (Nokleberg et al., 1985). Together with stratigraphic differences discussed in Chapter 2, the different deformation-metamorphism histories, post-deformational peak metamorphism in the KMA versus lower grade syndeformational peak metamorphism in the MGMB, suggest that a correlation between these metamorphic assemblages in eastern Alaska and in the southwest Yukon is not justified. Consequently, it cannot be used as geological evidence to support the postulated 400 km right-lateral offset along the Denali fault.

Chapter 5

Geochemical and neodymium isotope signatures of metamorphic and sedimentary rocks of the southwest Yukon

INTRODUCTION

Establishment of the tectonic affinity and protolith provenance of metamorphosed sedimentary rocks are important aspects in the development of a tectonic model for the northwestern Coast Belt, which marks the boundary between terranes with North American affinity to the east and accreted suspect terranes to the west. The distinct lithology and metamorphic and deformational history of the KMA, that set it apart from the Nisling/YTT-assemblages to the east and the Insular Superterrane (INS) and associated overlap assemblages (DF) to the west, has been discussed in detail in the previous chapters. However, as metamorphism and deformation have obliterated any primary mineral assemblages, sedimentary features or fossils, a correlation of protoliths of the KMA with North American terranes or volcanic arc terranes can neither be concluded nor excluded on basis of the results presented in the previous chapters alone. The difficulty of distinguishing between different medium to high grade metasedimentary rocks was clear in the earlier part of geological exploration in the southwest Yukon when all metamorphic rocks were assigned to the "Yukon Group" (see Cairnes, 1914; Kindle, 1952; Muller, 1967; Tempelman-Kluit, 1974).

Geochemical and isotopic studies can help distinguish protolith provenances of sedimentary and metasedimentary rocks and place constraints on the depositional tectonic setting. Major element geochemistry as source rock indication is limited due to mobility of Na, Ca and K during weathering and metamorphism (Taylor & McLennan, 1985). Rare earth elements (REE: La-Lu) and other trace elements, such as Y, Th, Zr, Hf, Nb, Ti, Sc and Co, are best suited for provenance determination, since they are considered immobile during sedimentation and metamorphism, and are transported quantitatively into clastic sedimentary rocks (Bhatia, 1985; Taylor & McLennan, 1985; Bhatia & Crook, 1986). They are also good provenance indicators for medium grade metamorphic rocks like the KMA and AMS, since mobility of these trace

elements and REE does not appear to be increased until granulite grade metamorphism (Bhatia, 1985). The ratios between elements that are compatible (V, Sc, Co) and incompatible (LREE: La-Sm and Th) during differential crystallization can be used to further distinguish sedimentary protolith provenance (Bhatia & Crook, 1986). Increasing abundance of trace elements that are concentrated in heavy minerals, such as Zr, indicate multiple recycling phases and increasing sedimentary maturity of the protolith (Bhatia & Crook, 1986). Normalized REE plots, La-Th, La-Th-Sc, Ti/Zr-La/Sc and Th-Sc-Zr/10 diagrams are good discriminatory plots to distinguish different tectonic settings (Taylor & McLennan, 1985; Bhatia & Crook, 1986).

The nature of the source region and terrane relationships can be further constrained by Nd isotope analyses, which yield average crustal residence ages, also called depleted mantle model ages (T_{DM}), of the various protolith components involved (McLennan & Hemming, 1992). Nd isotope studies also provide information on the isotopic evolution of the protolith (DePaolo, 1988), as well as on the homogeneity of mixing during sedimentation (Frost & Coombs, 1989). Model ages obtained from Nd isotope signatures do not reflect the depositional age of the protolith (Faure, 1986), but the average crustal residence age of the provenance.

Combined geochemical and Nd isotope studies are important tools to constrain tectonic setting and possible protolith provenance of metamorphic assemblages, as demonstrated by Creaser et al. (1997), in the Teslin tectonic zone (TTZ) of the southern central Yukon.

This chapter presents the first detailed geochemical and Nd isotope study of metamorphic and sedimentary rocks of the northwestern Coast Belt of the Canadian Cordillera. Previous studies by Eisbacher (1976) and Tempelman-Kluit & Currie (1978) analyzed only selected major element distribution in the KMA and DF and precious metal content in the KMA, respectively. For this study 11 samples of bt-qtz schist of the KMA (for 3 samples only major elements), two slates of the DF and four samples of mica-

quartz schist of the AMS correlated with the Nisling assemblage (units PAMqb and PAMfs of Johnston & Timmerman, 1993a, b), provided by Steve Johnston from the Yukon Geoscience Office, one biotite-quartz schist sample (major elements only) of the Nisling assemblage (NS) were selected. Sample descriptions and locations are listed in Appendix 5-1. Analytical procedures are described in Appendix 5-2. Major and trace element abundance and element ratios of the analyzed samples are shown on Tables 5-1 and 5-2. Neodymium isotopic data is listed on Table 5-3.

Trace element and Nd isotope signatures of the KMA, AMS and DF show that they have distinct protolith provenances. The DF has juvenile signatures and young crustal residence ages corresponding to an origin at or near an volcanic island arc, while evolved signatures and Late Archean crustal residence ages of the AMS suggest an ancient cratonic source. Geochemical and isotopic signatures of the KMA are intermediate between the DF and AMS, indicating relatively homogeneous mixing of predominantly juvenile with minor evolved sedimentary sources. Local occurrence of orthoamphibole schist within the KMA displaying strongly juvenile character suggests relative proximity to a volcanic arc. The overall intermediate signatures of the KMA imply the existence of a backarc basin outboard the North American continental margin in the Cretaceous, that collapsed during the accretion of the INS onto NA in the Late Cretaceous.

WHOLE ROCK GEOCHEMISTRY

Major elements

KMA and AMS samples show a similar range of SiO_2 content from 59 to 75 wt.%, which also includes the DF (63 %) and NS (65 %) samples (Table 5-1). The range in SiO_2 content in the AMS and KMA is due to quartz-rich layers of variable thickness that are commonly observed in the schists (Chapter 2). The four assemblages are indistinguishable by their SiO_2/Al_2O_3 ratio, ranging

Table 5-1: Major and trace element abundances of mica-quartz schists of the KMA, AMS and Nisling assemblage and slates of the DF

Kluane metamorphic assemblage											
Major elements:											
(weight %)	**90-39**	**93-96**	**93-136**	**93-156**	**94-36**	**94-82**	**94-115**	**94-272**	**94-297/1**	**94-346**	**94-387**
SiO_2	62.21	64.41	70.11	63.34	64.49	65.58	65.46	64.55	61.14	59.20	66.14
Al_2O_3	17.40	19.30	14.77	18.54	16.36	16.33	17.39	16.77	17.37	16.31	16.84
TiO_2	0.89	0.90	0.73	0.94	0.84	0.84	0.86	0.86	0.77	1.17	0.83
FeO	7.20	6.48	5.42	6.43	6.15	6.38	6.35	6.21	6.59	8.01	5.69
MnO	0.10	0.11	0.09	0.09	0.07	0.09	0.12	0.11	0.09	0.10	0.12
CaO	2.11	1.16	1.67	0.94	0.92	2.23	1.83	2.99	5.41	2.62	2.07
MgO	3.86	2.95	2.24	2.61	3.26	2.64	2.45	2.22	3.81	3.10	2.20
K_2O	2.83	3.06	2.02	2.88	1.33	2.22	2.28	2.28	1.48	2.80	1.92
Na_2O	2.47	1.69	2.25	2.35	4.21	2.34	2.20	3.03	3.22	3.37	2.63
P_2O_5	0.21	0.09	0.12	0.20	0.11	0.15	0.23	0.56	0.33	0.15	0.16
Total	99.10	100.14	99.43	98.32	97.95	98.80	99.17	99.58	100.21	98.83	98.60
Trace elements (ppm):											
Ba		1309	708	918	451	787		704	487	847	
Rb		96.7	67.4	93.4	42.0	69.9		79.3	39.6	87.4	
Cs		4.16	3.75	4.72	2.46	4.18		3.79	1.37	5.74	
Sr*		235	250	224	194	280		344	634	379	
Pb		7.25	13.36	13.50	6.11	14.43		14.28	19.46	13.32	
Th		7.78	5.25	6.78	5.76	5.68		6.85	1.25	4.76	
U		2.77	2.14	2.24	2.14	1.98		2.28	0.91	2.18	
Zr*	138	171	141	167	137	152	155	170	98	174	155
Nb	11.3	13.6	10.39	12.92	10.55	10.26	12.8	11.84	5.76	13.35	11.6
Hf		4.82	3.61	4.70	3.76	4.23		4.48	2.21	4.68	
Ta		1.24	0.81	0.91	0.78	0.79		0.83	0.51	0.95	
Y		24	21	24.79	23.41	22.29		41	18	28.97	
La		25.56	21.53	23.34	23.10	23.57		29.62	10.62	20.87	
Ce		50.56	41.42	44.78	43.76	45.14		59.27	21.51	41.60	
Pr		5.61	4.82	5.13	4.96	5.17		7.05	2.73	5.04	
Nd		22.06	19.38	20.80	19.84	21.05		28.97	12.33	21.55	
Sm		5.00	4.35	4.89	4.73	4.70		7.47	3.26	5.48	
Eu		1.06	1.13	1.16	1.35	1.34		1.78	1.12	1.66	
Gd		4.39	3.67	4.36	4.58	4.33		7.0	3.04	5.30	
Tb		0.75	0.62	0.73	0.78	0.71		1.31	0.53	0.89	
Dy		4.44	3.65	4.43	4.53	4.18		7.81	3.22	5.47	
Ho		0.94	0.76	0.92	0.93	0.83		1.53	0.66	1.11	
Er		2.68	2.15	2.70	2.50	2.31		4.18	1.89	3.00	
Tm		0.37	0.30	0.42	0.36	0.35		0.53	0.25	0.43	
Yb		2.54	1.98	2.67	2.21	2.33		3.26	1.63	2.75	
Lu		0.42	0.32	0.43	0.35	0.37		0.49	0.27	0.43	
Sc*	18	19	17	18	11	10	13	20	19	15	17
V*	187	181	155	187	195	177	173	171	160	241	169
Cr*	122	113	115	95	135	135	119	111	38	173	118
Ni*	44	23	34	31	60	43	58	40	22	65	62
Cu*	150	17	16	34	77	58	136	34	68	11	77
Zn*	123	138	116	116	96	123	119	109	92	192	116
Ga*	19	24	14	21	21	18	20	20	19	15	17

Major element analyses performed by XRF. Trace elements denoted with * performed by XRF, all others by ICPMS. Analyses were made at Washington State University.

Table 5-1 (continued):

	Dezadeash Formation		Aishihik Metamorphic Suite				Nisling	Average			Continental Crust[1]	
								KMA	DF	AMS	Upper	Bulk
Major elements:												
(weight %)	94-190	94-204b	93-16	93-67	93-14	93-42	94-358					
SiO_2	62.84	62.86	63.71	74.49	59.46	62.73	64.77	64.26	62.85	65.10	66.0	57.3
Al_2O_3	17.01	17.99	17.91	13.74	18.84	20.25	15.99	17.22	17.50	17.69	15.2	15.9
TiO_2	0.65	0.77	0.95	0.61	1.14	0.84	0.80	0.88	0.71	0.89	0.5	0.9
FeO	5.18	6.08	6.39	4.36	6.85	5.97	6.59	6.45	5.63	5.89	4.5	9.1
MnO	0.09	0.12	0.07	0.05	0.10	0.09	0.07	0.10	0.10	0.08	-	-
CaO	3.13	3.49	0.94	0.56	2.22	0.82	1.21	2.18	3.31	1.14	4.2	7.4
MgO	2.22	2.42	2.27	1.60	2.36	2.05	5.20	2.83	2.32	2.07	2.2	5.3
K_2O	4.01	2.30	5.28	3.42	4.87	4.79	2.71	2.28	3.16	4.59	3.4	1.1
Na_2O	2.70	4.09	1.44	1.03	2.34	1.08	1.82	2.71	3.40	1.47	3.9	3.1
P_2O_5	0.13	0.16	0.17	0.07	0.11	0.12	0.18	0.21	0.14	0.12	-	-
Total	97.96	100.27	99.13	99.94	98.30	98.74	99.24	99.10	99.12	99.03	99.9	100.1
Trace elements (ppm):												
Ba	1112	918	940	641	2522	826		776	1015	1232	550	250
Rb	88.9	57.6	211.4	128.1	136.7	166.8		72.0	73.3	160.6	112	32
Cs	2.78	2.82	6.88	3.86	5.00	4.52		3.77	2.80	50.7	3.7	1.0
Sr*	320	481	153	170	191	126		318	401	160	350	260
Pb	13.16	11.50	17.73	17.91	15.16	28.30		12.96	12.33	19.76	20	8.0
Th	1.63	2.96	15.68	15.74	14.72	16.18		5.51	2.30	15.58	10.7	3.5
U	1.13	1.81	3.30	2.66	2.73	3.28		2.08	1.47	2.99	2.8	0.91
Zr*	82	134	236	248	236	147	130	151	108	217	190	100
Nb	4.83	7.00	31.88	14.77	27.41	20.24	11.1	11.30	5.92	23.58	-	-
Hf	2.00	3.55	6.87	7.16	7.10	4.29		4.06	2.78	6.36	5.8	3.0
Ta	0.51	0.56	2.32	1.15	1.82	1.40		0.85	0.54	1.67	2.2	1.0
Y	18	29	36.05	24.35	28.36	37.69		25.43	23.50	31.61	22	20
La	8.76	14.29	59.78	44.67	23.15	64.18		22.29	11.53	47.95	30	16
Ce	19.53	28.39	108.16	85.95	49.41	120.21		43.51	23.96	90.93	64	33
Pr	2.60	3.75	11.72	9.01	5.22	13.21		5.06	3.18	9.79	7.1	3.9
Nd	11.59	16.54	44.31	33.48	20.55	49.77		20.75	14.07	37.03	26	16
Sm	2.73	4.56	8.91	6.50	4.66	9.94		4.99	3.65	7.50	4.5	3.5
Eu	0.67	1.22	1.60	1.28	1.23	1.68		1.33	0.95	1.45	0.88	1.1
Gd	2.95	4.55	7.22	4.97	4.05	7.98		4.59	3.75	6.06	3.8	3.3
Tb	0.51	0.82	1.16	0.78	0.76	1.22		0.79	0.67	0.98	0.64	0.60
Dy	2.99	5.22	6.83	4.52	4.97	7.15		4.72	4.11	5.87	3.5	3.7
Ho	0.60	1.08	1.36	0.90	1.07	1.40		0.96	0.84	1.16	0.8	0.78
Er	1.72	3.15	3.61	2.39	3.02	3.72		2.68	2.44	3.19	2.3	2.2
Tm	0.23	0.43	0.53	0.36	0.46	0.53		0.38	0.33	0.47	0.33	0.32
Yb	1.51	2.81	3.35	2.21	2.79	3.28		2.42	2.16	2.91	2.2	2.2
Lu	0.24	0.46	0.52	0.34	0.43	0.48		0.39	0.35	0.44	0.32	0.30
Sc*	16	21	14	8	18	17	12	16	19	14	11	30
V*	127	195	89	55	122	102	168	181	161	92	60	185
Cr*	55	54	62	34	77	57	291	116	55	58	35	105
Ni*	47	29	37	24	15	35	170	44	38	28	20	75
Cu*	60	8	14	4	32	22	39	62	34	18	25	60
Zn*	75	106	108	61	75	103	155	122	91	87	71	80
Ga*	16	27	24	18	26	28	19	20	22	24	17	18

Major element analyses performed by XRF. Trace elements denoted with * performed by XRF, all others by ICPMS. Analyses were made at Washington State University.
(1) "Upper continental crust" from table 2.15 in Taylor & McLennan (1985), "bulk continental crust" from table 3.5 in Taylor & McLennan (1985).

Table 5-2: Element ratios of mica-quartz schists of the KMA, AMS and Nisling assemblage, and slates of the DF

	Kluane metamorphic assemblage										
	90-39	93-96	93-136	93-156	94-36	94-82	94-115	94-272	94-297/1	94-346	94-387
SiO_2/Al_2O_3	3.58	3.34	4.75	3.42	3.95	4.02	3.76	3.85	3.52	3.23	3.87
K_2O/Na_2O	1.15	1.81	0.90	1.23	0.32	0.95	1.04	0.75	0.46	0.83	0.73
MgO+FeO	10.88	9.43	7.66	9.04	9.41	9.02	8.80	8.43	10.40	11.11	7.89
CIA[1]	70.1	76.6	71.3	75.0	71.7	70.6	73.4	66.9	63.2	67.6	71.8
Rb/Sr		0.41	0.27	0.42	0.22	0.25		0.23	0.06	0.23	
Total REE		126.38	106.6	116.89	113.98	116.38		160.28	63.06	115.58	
LREE/HREE		6.58	6.80	5.94	5.94	6.47		5.07	4.39	4.88	
La/Yb		10.06	10.87	8.78	10.45	10.12		9.09	6.52	7.59	
La_N/Yb_N[2]		6.80	7.35	5.93	7.06	6.84		6.14	4.40	5.13	
Eu/Eu^*[3]		0.69	0.86	0.77	0.89	0.91		0.75	1.09	0.94	
Gd_N/Yb_N		1.40	1.50	1.33	1.68	1.51		1.74	1.51	1.56	
Sm/Nd		0.23	0.22	0.24	0.24	0.22		0.26	0.26	0.25	
Th/U		2.81	2.45	3.03	2.69	2.87		3.00	1.37	2.18	
La/Th		3.29	4.10	3.46	4.01	4.15		4.32	8.50	4.38	
Hf/Yb		1.90	1.82	1.76	1.70	1.82		1.37	1.36	1.70	
La/Sc		1.35	1.27	1.47	2.10	2.36		1.48	0.56	1.39	
Th/Sc		0.41	0.31	0.42	0.52	0.57		0.34	0.07	0.32	
Cr/Th		14.52	21.90	14.01	23.44	23.77		16.20	30.40	36.34	

	Dezadeash Formation		Aishihik Metamorphic Suite				Nisling	Average			Continental Crust	
	94-190	94-204b	93-16	93-67	93-14	93-42	94-358	KMA	DF	AMS	Upper	Bulk
SiO_2/Al_2O_3	3.69	3.49	3.56	5.42	3.16	3.10	4.08	3.73	3.59	3.68	4.34	3.60
K_2O/Na_2O	1.49	0.56	3.67	3.32	2.08	4.44	1.49	0.92	1.02	3.38	0.87	0.35
MgO+FeO	7.40	8.50	8.66	5.96	9.21	8.02	11.79	9.28	7.95	7.96	6.70	14.40
CIA[1]	63.4	64.5	70.0	73.3	66.6	75.2	73.5	70.6	64.0	71.1	56.9	57.8
Rb/Sr	0.28	0.12	1.38	0.75	0.72	1.32		0.23	0.18	1.00	0.32	0.12
Total REE	56.63	87.27	259.06	197.36	121.77	284.75		114.83	71.95	215.73	146.37	86.90
LREE/HREE	4.21	3.65	9.47	10.91	5.87	9.99		5.71	3.85	9.16	9.47	5.53
La/Yb	5.80	5.09	17.84	20.21	8.30	19.57		9.21	5.34	16.49	13.64	7.27
La_N/Yb_N[2]	3.92	3.44	12.06	13.66	5.61	13.22		6.22	3.61	11.14	9.21	4.91
Eu/Eu^*[3]	0.72	0.82	0.61	0.69	0.87	0.58		0.86	0.78	0.66	0.65	0.99
Gd_N/Yb_N	1.58	1.31	1.75	1.82	1.18	1.97		1.54	1.41	1.69	1.40	1.22
Sm/Nd	0.24	0.28	0.20	0.19	0.23	0.20		0.24	0.26	0.20	0.17	0.22
Th/U	1.44	1.64	4.75	5.92	5.39	4.93		2.65	1.56	5.21	3.82	3.85
La/Th	5.37	4.83	3.81	2.84	1.57	3.97		4.04	5.04	3.08	2.80	4.57
Hf/Yb	1.32	1.26	2.05	3.24	2.54	1.31		1.68	1.28	2.19	2.64	1.36
La/Sc	0.55	0.68	4.27	5.58	1.29	3.78		1.40	0.62	3.36	2.73	0.53
Th/Sc	0.10	0.14	1.12	1.97	0.82	0.95		0.35	0.12	10.9	0.97	0.12
Cr/Th	33.74	18.24	3.95	2.16	5.23	3.52		21.05	23.91	3.72	3.27	30.0

1: CIA (Chemical Index of Alteration): $Al_2O_3/(Al_2O_3$+ silicate $CaO+Na_2O+K_2O)\times100$;

2: normalized to chondritic values La_N=La/0.367, Yb_N=Yb/0.248 ;

3: Eu/Eu*: $Eu_N/sqrt(Sm_N \times Gd_N)$, Eu_N=Eu/0.087, Sm_N=Sm/0.231, Gd_N=Gd/0.306 (chondritic normalizing factors) (Taylor & McLennan, 1985).

from 3 to 6 (Table 5-2). K_2O/Na_2O ratios of 2 to 4.5 for the AMS and NS and 0.45 to 1.8 for the KMA and DF samples assign them to the lithic arenite field and greywacke field of Pettijohn et al. (1987), respectively (Figure 5-1a). This may indicate a higher sedimentary maturity of AMS and NS samples compared to the KMA and DF.

The weathering index CIA and the combined MgO+FeO% of individual samples overlap for all four assemblages and cannot be used to discriminate between them (Table 5-2).

Although major element geochemistry is able to distinguish the pericratonic assemblages (AMS, NS) from the KMA and DF, it cannot discriminate between KMA and DF. This fact may be one reason why Eisbacher (1976) correlated the KMA with the DF. However, trace element and isotopic data described below clearly establishes distinct protoliths for both rock types.

Rare earth elements

Geochemical differentiation of the protolith of a sedimentary rock is reflected by its REE characteristics. Sediments derived from a highly differentiated protolith will have higher total REE abundance, a stronger enrichment of LREE (La-Sm) over HREE (Gd-Yb), as expressed in the HREE/LREE or La_N/Yb_N ratios, and a more negative Eu-anomaly, expressed in the Eu/Eu* ratio (see footnotes in Table 5-2 for definitions), compared to sediments derived from a more primitive, less differentiated source (Taylor & McLennan, 1985). The maturity of AMS, KMA and DF samples can be correlated with these three REE characteristics, as shown on K_2O/Na_2O versus total REE abundance, La_N/Yb_N and Eu/Eu* ratios (Figures 5-1b, 5-1c).

Normalized REE plots are shown for individual samples of each assemblage (Figures 5-2a-c) and combined averages for comparison with the upper and bulk continental crust models (Figure 5-2d).

DF samples have moderate Eu-anomalies (0.72 and 0.82), the least

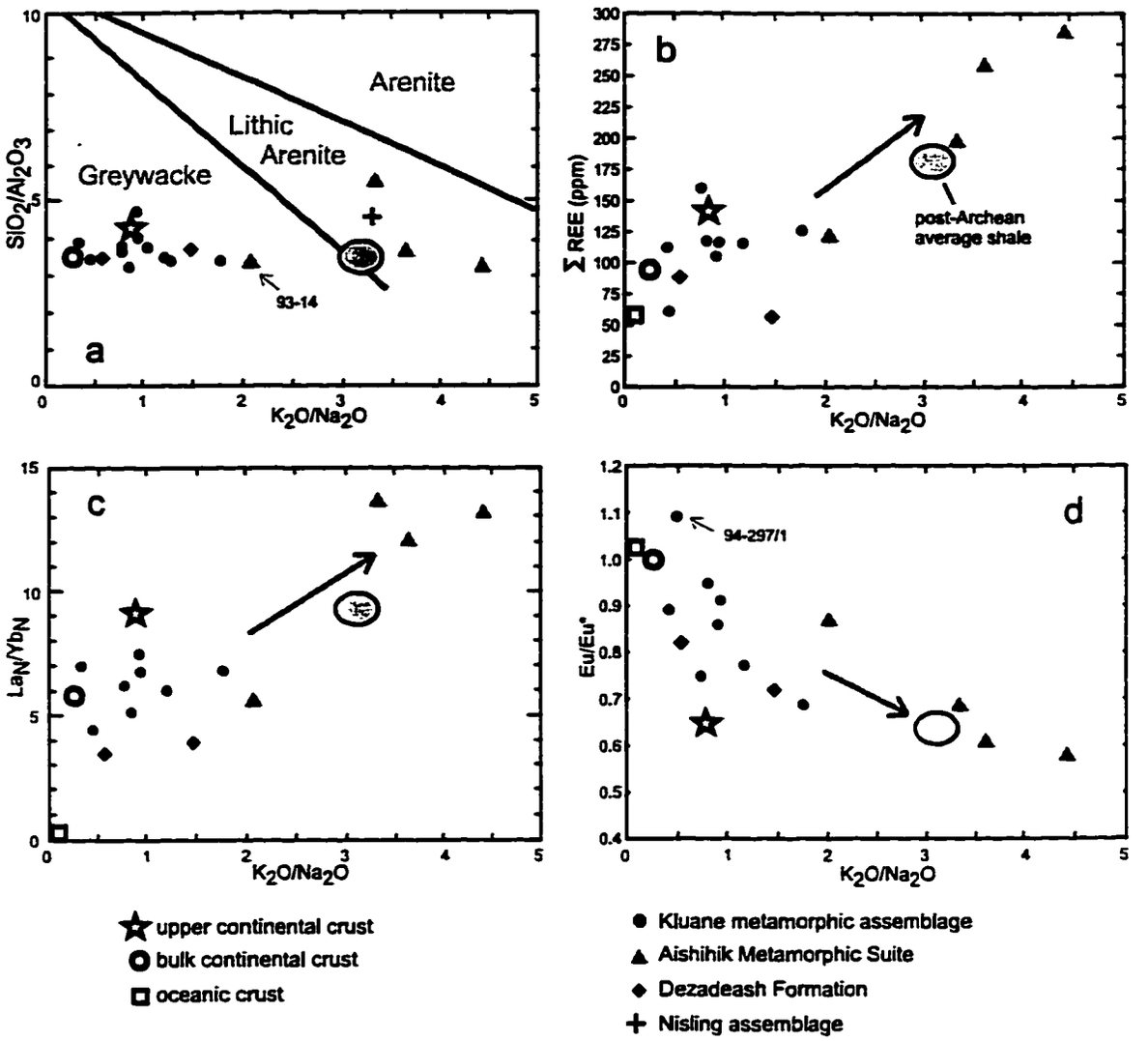

Figure 5-1: a) SiO_2/Al_2O_3 versus K_2O/Na_2O diagram for KMA, AMS, Nisling assemblage metasedimentary rocks and Dezadeash Formation sediments. Greywacke, lithic arenite and arenite fields from Pettijohn et al. (1987). **b-c)** A weak positive correlation between K_2O/Na_2O versus La_N/Yb_N and total REE can be observed, with AMS samples plotting in the evolved corner. KMA and DF samples occupy a similar K_2O/Na_2O field and are indistinguishable. **d)** K_2O/Na_2O versus Eu/Eu* plot has a negative correlation. AMS samples plot at the higher K_2O/Na_2O and the lower Eu/Eu* ratio end, indicative for more evolved crustal rocks. Note that one AMS sample (93-14) is near the KMA field. The arrow points in the direction of increasing differentiation. Upper continental and bulk continental crust, oceanic crust and post-Archean average shale values are from Taylor & McLennan (1985).

Figure 5-2: a) REE plot of DF slates. Both samples are similar to the bulk continental composition, but show a slightly negative Eu-anomaly. **b)** REE plot of AMS biotite-quartz schists. The samples have similar patterns as the upper continental crust average. **c)** REE plot of KMA mica-quartz schists. Except for sample 94-297/1, which displays positive Eu-anomaly and shallow slope, they display an intermediate signature between upper continental crust (solid black line) and bulk continental crust composition (solid grey line). **d)** Average REE values of KMA, AMS and DF show that each assemblage can be distinguished by its REE pattern. Upper continental and bulk continental crust, as well as chondritic normalizing factors are from Taylor & McLennan (1985). Note the change in logarithmic scale.

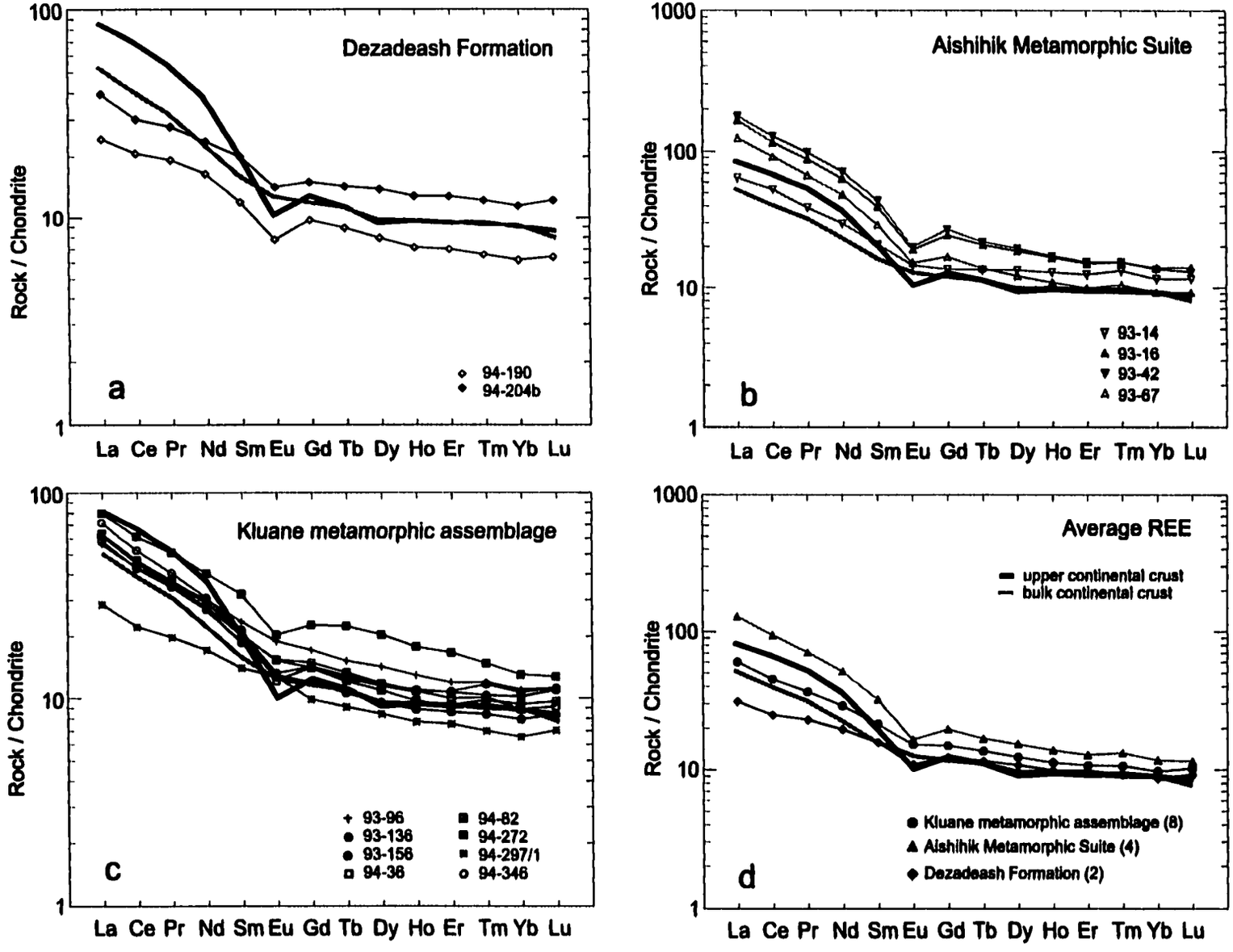
Dezadeash Formation
Rock / Chondrite
100
10
1
a
94-190
94-204b
La Ce Pr Nd Sm Eu Gd Tb Dy Ho Er Tm Yb Lu
Aishihik Metamorphic Suite
1000
b
93-14
93-16
93-42
93-67
Kluane metamorphic assemblage
c
93-96
93-136
93-156
94-36
94-82
94-272
94-297/1
94-346
Average REE
upper continental crust
bulk continental crust
d
Kluane metamorphic assemblage (8)
Aishihik Metamorphic Suite (4)
Dezadeash Formation (2)

LREE-enrichment (La_N/Yb_N ~3.6) and total REE abundances close to the bulk continental crust average (Table 5-2; Taylor & McLennan, 1985). REE patterns of the DF are similar to the bulk continental crust, with the exception of a moderately negative Eu-anomaly (Figure 5-2a). Phanerozoic first-cycle volcanogenic sediments derived from andesites or basalts of magmatic island arcs do not display a negative Eu-anomaly (Taylor & McLennan, 1985). The modest negative Eu-anomalies observed in the DF indicate a slightly more felsic source.

The most evolved characteristics are displayed by three AMS samples with a strong negative Eu-anomaly (~0.6-0.7), La_N/Yb_N of 12 to 13 and high REE totals (120-280 ppm). Sample 93-14 has more juvenile signatures than other AMS samples with a less pronounced Eu-anomaly (0.87) and less enrichment in LREE (La_N/Yb_N: 5.6). Their REE pattern is similar to post-Archean sediments derived from a felsic upper continental crust (Figure 5-2b, Taylor & McLennan, 1985).

KMA samples show patterns and characteristics that are intermediate between the evolved AMS and the more primitive DF (Figures 5-1, 5-2c). Eu/Eu* ranges from 0.69 to 1.09 and LREE are moderately enriched over HREE (La_N/Yb_N: 4.4-7.3) (Figure 5-2c). REE abundance ranges from 63-160 ppm. The lowest REE abundance, the least LREE enrichment of the KMA samples and a positive Eu-anomaly is obtained from the orthoamphibole-rich schist 94-297/1.

Trace elements

Trace elements that are considered good provenance indicators, Th, Zr, Ti and Sc (Bhatia & Crook, 1986), combined with REE, generally display a linear correlation between relative primitive DF and strongly evolved AMS samples. The KMA samples occupy the field between the AMS and DF (Figure 5.3). AMS samples have La/Sc 1.3-5.6 and Th/Sc 0.8-2 near or above the upper continental crust average, while lower ratios of the DF (La/Sc 0.6, Th/Sc

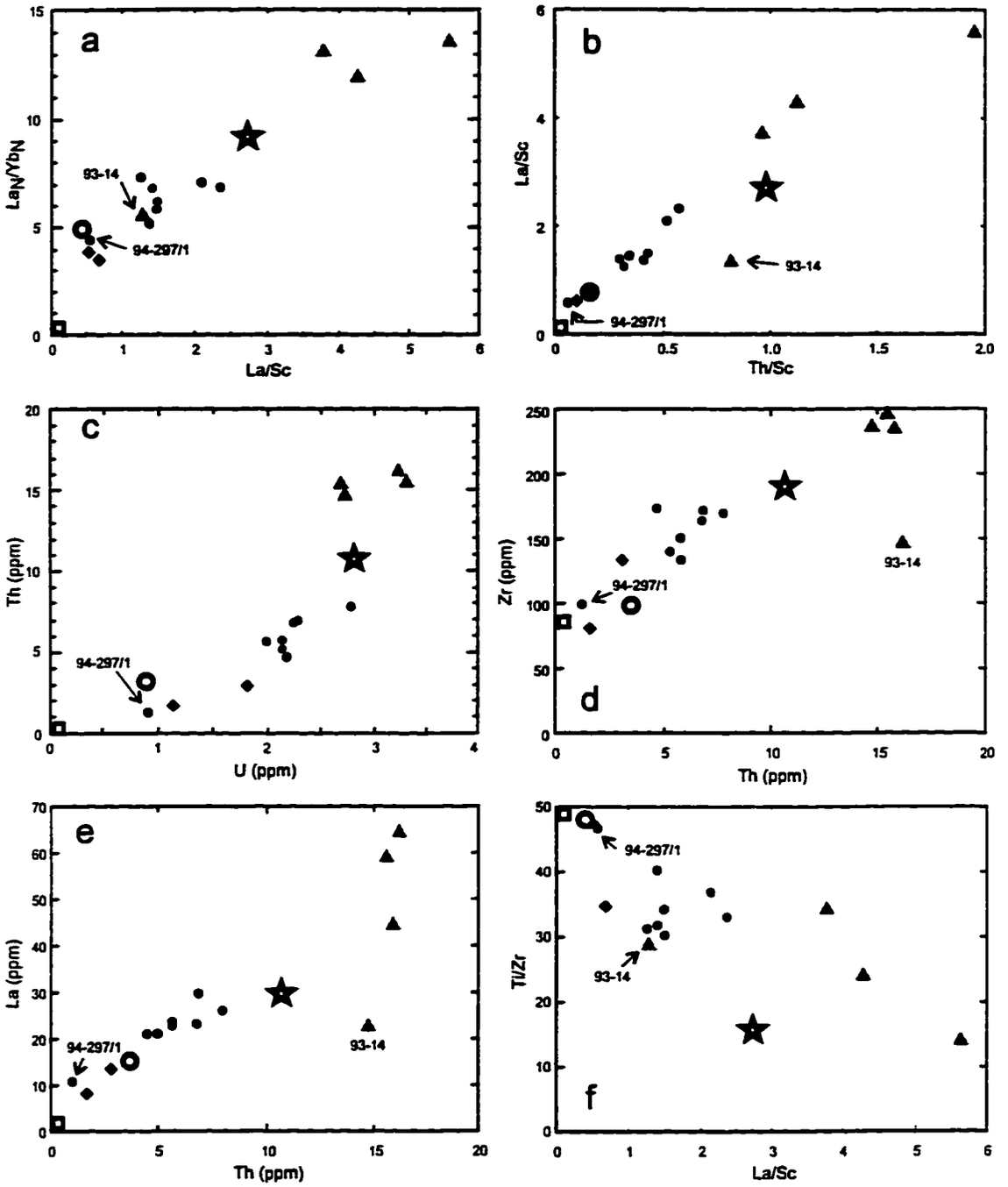

Figure 5-3: Relationship between REE and Sc, Th, U, Ti and Zi. The three assemblages are easily distinguished in the various plots. DF samples plot close to the bulk continental crust composition on the La/Sc versus La_N/Yb_N (a) and Th/Sc (b) diagrams. Note that KMA sample 94-297/1 plots close to the DF. AMS samples lie near the average upper continental crust, except 93-14, which is either off a linear correlation trend (b, d, e) or in the KMA field (a, f). Symbols and source are the same as in previous figures.

0.12) are similar to the bulk continental crust. KMA samples have ratios between upper and bulk continental crust (La/Sc 1.3-2.1, Th/Sc 0.3-0.5) (Table 5-2, Figure 5-3). Exceptions are the orthoamphibole schist of the KMA (94-297/1), which falls in the DF field and AMS sample 93-14 which plots close to the KMA in several diagrams (Figure 5-3) .

On La-Sc-Th and Th-Zr/10-Sc ternary diagrams DF samples and KMA sample 94-297/1 plot near the bulk continental crust or within the 'oceanic arc' field of Bhatia & Crook (1986), AMS samples near the upper continental crust average, within the 'continental margin' and 'continental arc' fields, while the KMA samples plot between both averages within the 'continental arc' field (Figure 5-4).

REE and trace element signatures may then recognize two geochemical end members, an evolved felsic continental crust source of the AMS and a more juvenile, basaltic to andesitic source of the DF. The possibility of mixing of both sources to form the intermediate KMA will be discussed with Nd isotope signatures below. The data presented above clearly shows that the KMA is not simply higher metamorphosed DF as suggested by Eisbacher (1976), but derived from a different sedimentary protolith. The two samples of the calcic schist of the KMA (93-156, 94-36) are geochemically indistinguishable from samples of the aluminous schist, suggesting that the two samples which do not contain epidote, the typical calcic mineral phase of the calcic schist, may be more aluminous portions within the calcic schist, and not representative of that sequence (see Chapter 2).

NEODYMIUM ISOTOPES

Neodymium isotope analyses stress the distinct protolith provenances of the KMA, AMS and DF, that is already suggested by their geochemical characteristics and help to further constrain possible source regions. Nd-

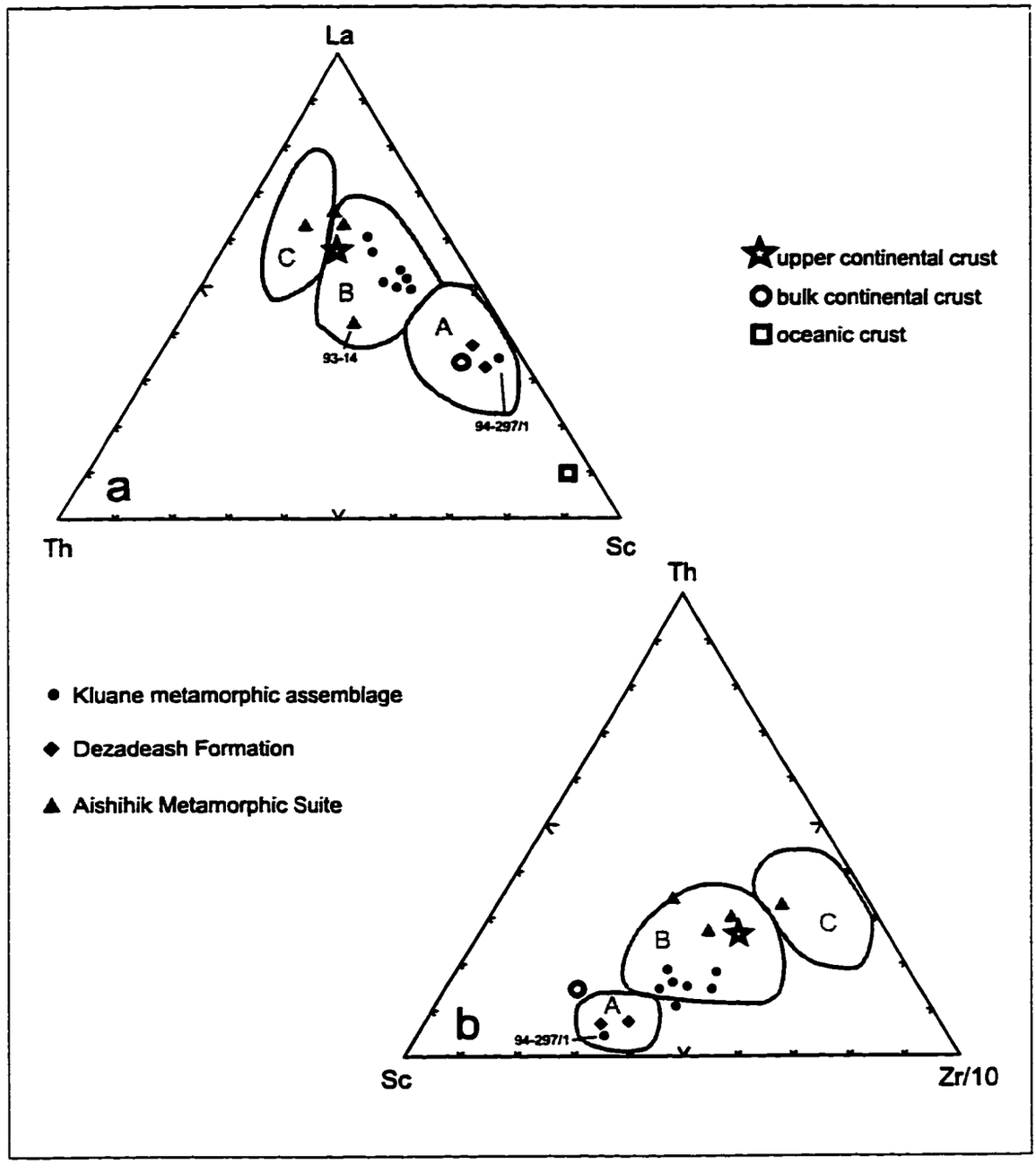

Figure 5-4: a, b) Tectonic setting discrimination diagrams for clastic sediments after Bhatia & Crook (1986) plot the DF samples and KMA sample 94-297/1 in the oceanic arc field (A) near the bulk continental crust composition, KMA in the continental arc (B) and AMS in both the continental arc (B) and continental margin fields (C). Upper continental, bulk continental and oceanic crust values are from Taylor & McLennan (1985).

isotope characteristics are reported as present day "epsilon parameter" $\epsilon_{Nd}(0)$ (DePaolo & Wasserburg, 1976), since the depositional ages of the KMA and the AMS are not known. Nd isotopic signatures are listed on Table 5-3 and shown on a map on Figure 5-5. Their isotopic evolution through time is plotted on Figure 5-6.

The four AMS samples have strongly negative $\epsilon_{Nd}(0)$ ranging from -20.5 to -27.9 and latest Archean model ages of 2.52 to 2.69 Ga, indicating an ancient crust source. Similar model ages and $\epsilon_{Nd}(0)$ are reported from the Precambrian basement of the Canadian shield in Alberta and British Columbia (Frost & O'Nions, 1984; Thériault & Ross, 1991).

The DF slates are characterized by higher $\epsilon_{Nd}(0)$-values of +1.6 and +2.2, suggesting a relative juvenile protolith, and younger Late Proterozoic model ages (T_{DM} 0.92 and 0.94 Ga). Initial ϵ_{Nd}-values for the time of the deposition of the DF (~ 140 Ma; Eisbacher, 1976) are +2.6 and +3.0. These values are similar to those observed in sediments of Wrangellia and Alexander terranes to the west (Samson et al., 1989; Samson et al., 1990b).

Mica-quartz schists of the KMA record little $\epsilon_{Nd}(0)$-variation, ranging from -5.6 to -1.4, unrelated to geographic location (Figure 5.5). These values may imply a mixture between a juvenile and an ancient source. T_{DM} varies from 1.45 to 1.17 Ga, intermediate between AMS and DF values, with the exception of the orthoamphibole schist 94-297/1, which has the most juvenile signature of all analyzed samples, $\epsilon_{Nd}(0)$ of +3.9, and the youngest T_{DM} of 0.72 Ga. Its distinct geochemical character is described in the previous section.

The $^{147}Sm/^{144}Nd$ ratio is negatively correlated with $\epsilon_{Nd}(0)$. The most evolved AMS samples have $^{147}Sm/^{144}Nd$ ratios ranging from 0.104 to 0.119, while the DF slates have ratios of 0.142 and 0.148. $^{147}Sm/^{144}Nd$ ratios of KMA samples vary from 0.123 to 0.144 (Figure 5-7). Although sample 93-14 has a negative ϵ_{Nd}-value of -20.5 and Late Archean T_{DM} of 2.52 Ga, comparable with other AMS samples, it has a high $^{147}Sm/^{144}Nd$ ratio, close to KMA samples with more evolved signatures. Its anomalous position within the AMS is also obvious in the relationship between ϵ_{Nd} and the La_N/Yb_N ratio, which reflects the

Table 5-3: Sm and Nd concentration and isotope data for metamorphic and sedimentary rocks of the SW Yukon

Sample	Stratigraphic age	Sm (ppm)	Nd (ppm)	$^{147}Sm/^{144}Nd$ [1]	$^{143}Nd/^{144}Nd$ [2]	$\epsilon_{Nd}(0)$ [3]	$\epsilon_{Nd}(T)$ [4]	T_{DM}(Ga) [5]
Kluane metamorphic assemblage								
93-96		4.86	23.53	0.1250	0.512422 ± 7	-4.2		1.27
93-136		4.19	20.52	0.1234	0.512352 ± 9	-5.6		1.37
93-156		4.54	21.91	0.1253	0.512415 ± 12	-4.4		1.29
94-36		4.22	19.58	0.1303	0.512383 ± 9	-5.0		1.42
94-82		4.18	20.65	0.1225	0.512468 ± 11	-3.3		1.16
94-272		7.24	31.83	0.1375	0.512437 ± 9	-3.9		1.45
94-297/1		3.00	12.57	0.1444	0.512836 ± 9	+3.9		0.72
94-346		4.87	21.08	0.1400	0.512569 ± 11	-1.4		1.22
Dezadeash Formation								
94-190	~140 Ma	2.91	12.37	0.1421	0.512719 ± 12	+1.6	+2.6	0.94
94-204b	~140 Ma	4.32	17.76	0.1479	0.512748 ± 10	+2.2	+3.0	0.96
Aishihik Metamorphic Suite								
93-16		8.62	48.61	0.1072	0.511344 ± 13	-25.2		2.59
93-67		6.11	35.57	0.1038	0.511209 ± 10	-27.9		2.69
93-14		4.25	21.58	0.1190	0.511589 ± 9	-20.5		2.52
93-42		9.39	53.08	0.1070	0.511291 ± 16	-26.3		2.66

1: Precision estimated at ± 0.1 % based on repeat measurements of natural samples and international standards (BCR-1 $^{147}Sm/^{144}Nd$ = 0.1378).

2: Figures in parenthesis are within-run uncertainties quoted as 2σ. Estimates of external reproducibility are ± 0.000016, based on in-house and international standards (La Jolla=0.511848 ± 8, BCR-1=0.512634 ± 9).

3: $\epsilon_{Nd}(0) = [(^{143}Nd/^{144}Nd_{meas}/^{143}Nd/^{144}Nd_{Chur}-1)\times10^4]$; present day $^{143}Nd/^{144}Nd_{Chur}$=0.512638, normalized to $^{146}Nd/^{144}Nd$=0.7219 (DePaolo & Wasserburg, 1976).

4: T=140 Ma

5: $T_{DM} = 1/\lambda \times \ln[(^{143}Nd/^{144}Nd_{meas}-^{143}Nd/^{144}Nd_{mantle})/(^{147}Sm/^{144}Nd_{meas}-^{147}Sm/^{144}Nd_{mantle})+1]$ (DePaolo, 1981); with Goldstein et al. (1984) values for $^{143}Nd/^{144}Nd_{mantle}$= 0.513163 and $^{147}Sm/^{144}Nd_{mantle}$= 0.2138.

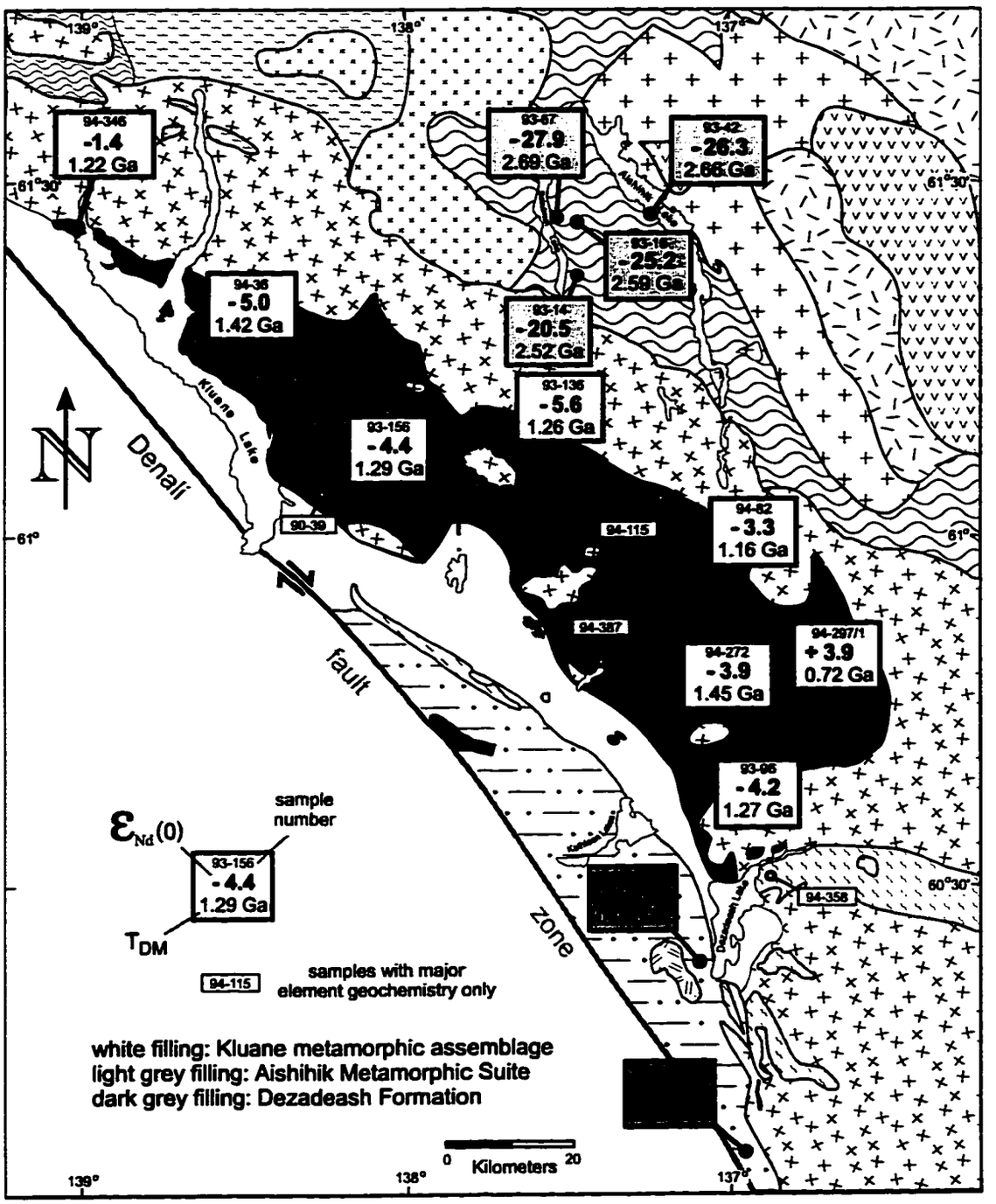

Figure 5-5: Neodymium signatures of the KMA (white), DF (dark grey) and AMS (light grey). Isotopic data are listed in detail on Table 5-3. Locations of samples analyzed for major element geochemistry only are also shown. Geology is the same as on Figure 2-1.

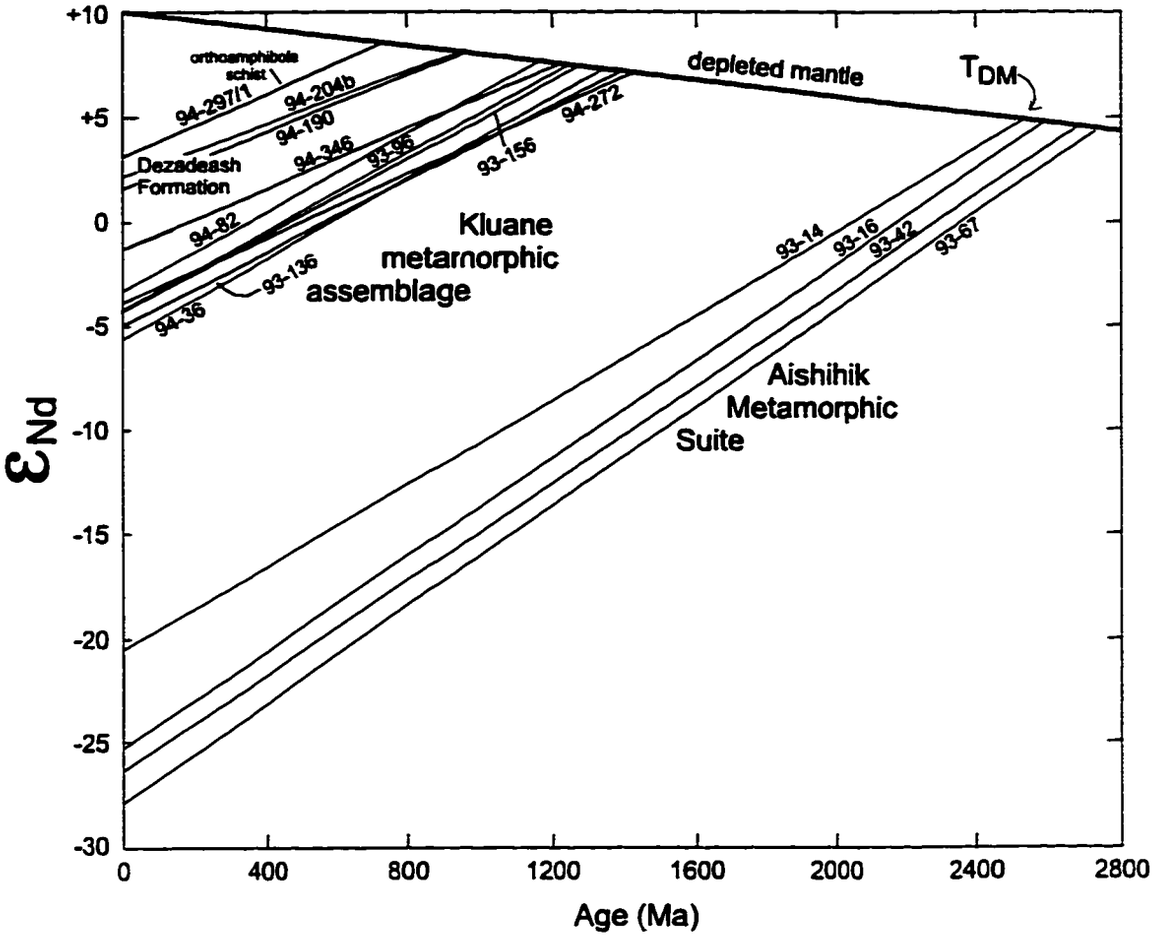

Figure 5-6: Evolution of ϵ_{Nd} through time for analyzed samples of the KMA, AMS and DF. The depleted mantle model is after Goldstein et al. (1984). Note that the orthoamphibole schist sample of the KMA (94-297/1) plots above the DF samples. AMS samples are characterized by their Late Archean model ages.

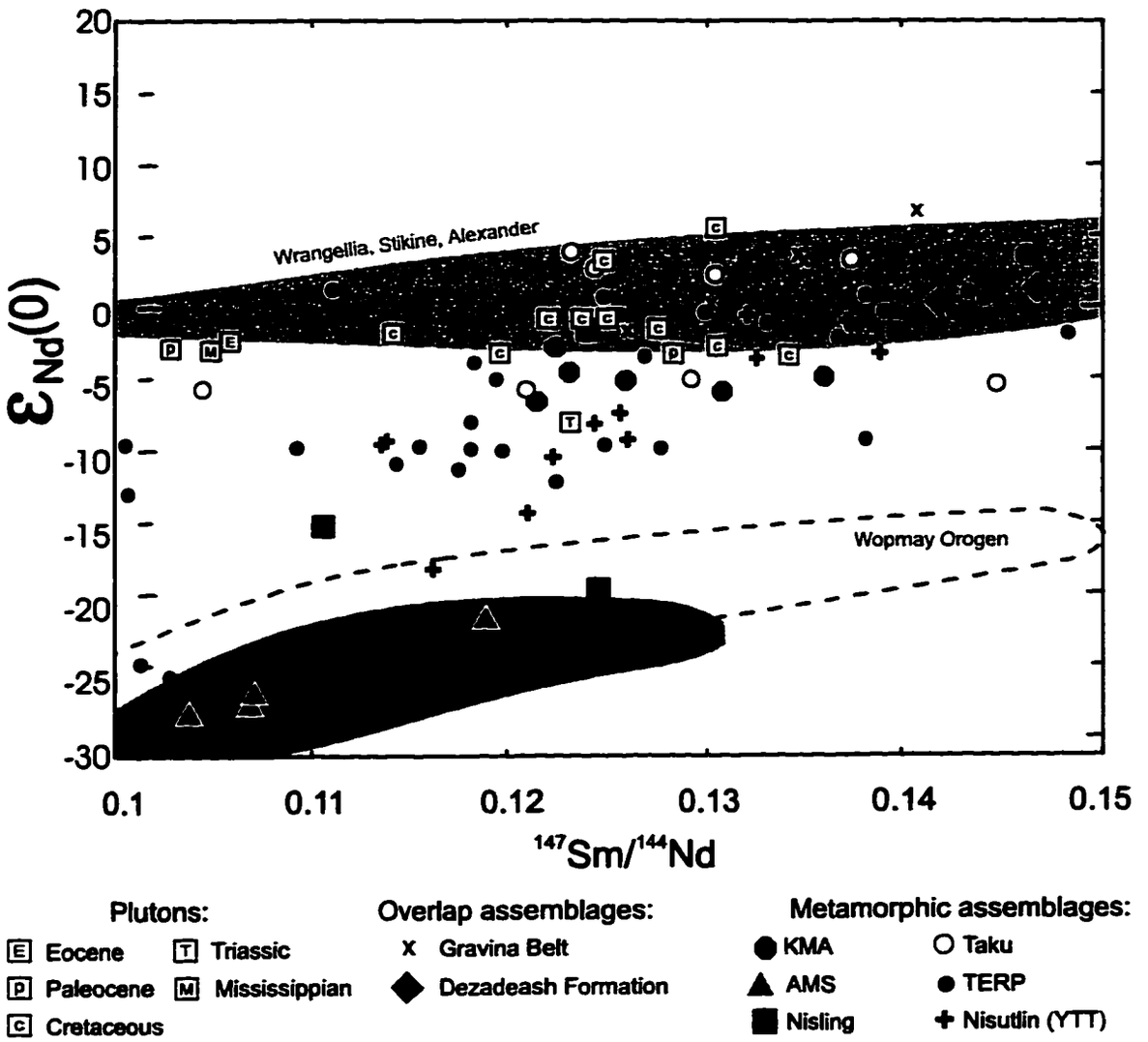

Figure 5-7: $\varepsilon_{Nd}(0)$ versus $^{147}Sm/^{144}Nd$ of the KMA, DF and AMS samples in comparison with previously published data of the northern Canadian Cordillera. The DF samples fall in the field for sediments and igneous rocks of the Alexander, Wrangellia and Stikine terranes (Samson et al., 1989, 1990b). The AMS plot in the same field as Archean igneous rocks of the Alberta basement (Thériault & Ross, 1991) and similar to some Archean igneous rocks of the Wopmay Orogen (Bowring & Podosek, 1989). Plutons are from the Coast Plutonic Complex (Samson et al., 1991a). Other metamorphic assemblages are from Creaser et al. (1997) (Nisutlin, YTT), Jackson et al. (1991) (Nisling) and Samson et al. (1991b) (Taku, TERP: Tracy Arm, Endicott Arm, Ruth and Port Hughton terranes). Gravina Belt data are from Samson et al. (1991b). See text for discussion and Appendix 5-4 for location.

steepness of the REE curve and is therefore an indication how evolved a certain sample is (Figure 5-8a). Negative correlations of ϵ_{Nd} with Th/Sc and La/Sc plot AMS near the Precambrian continental crust and DF close to average island arc volcanics, while the KMA forms a cluster in an intermediate field close to the DF (Figures 5-8b, 5-8c). The location of the KMA samples on or near a line that connects AMS and DF may indicate formation of the KMA by mixing AMS with DF or their protoliths (Figure 5-8).

PROTOLITH PROVENANCE AND REGIONAL CORRELATION

The study of neodymium isotope system is a fairly young field, pioneered among others by McCulloch and Wasserburg (1978), who presented the first comprehensive study of rocks from the major cratonic provinces in the world. Although studies in the North American Cordillera are still in an incipient state, available data is sufficient to establish first order relationships. The published work is summarized in Figures 5-7 and 5-9, Appendix 5-3 and shown in geographic relation on the terrane map of the northern Canadian Cordillera (Appendix 5-4).

Aishihik Metamorphic Suite

Trace element geochemistry, strongly negative $\epsilon_{Nd}(0)$-values and depleted mantle model ages of Late Archean age suggest an ancient cratonic protolith for the analyzed biotite-quartz schists of the AMS. The AMS has been correlated with continent marginal sediments of the Nisling assemblage, part of the Nisling Terrane (Wheeler & McFeely, 1991; Mortensen, 1992; Johnston & Erdmer, 1995). Plutonic and volcanic rocks from the Precambrian basement of the Canadian shield in Alberta and British Columbia yield model ages of 2.46 to 2.83 Ga and recalculated $\epsilon_{Nd}(0)$ of -27 (Frost & O'Nions, 1984; Thériault & Ross, 1991). Volcanic and plutonic rocks of the Wopmay Orogen in the

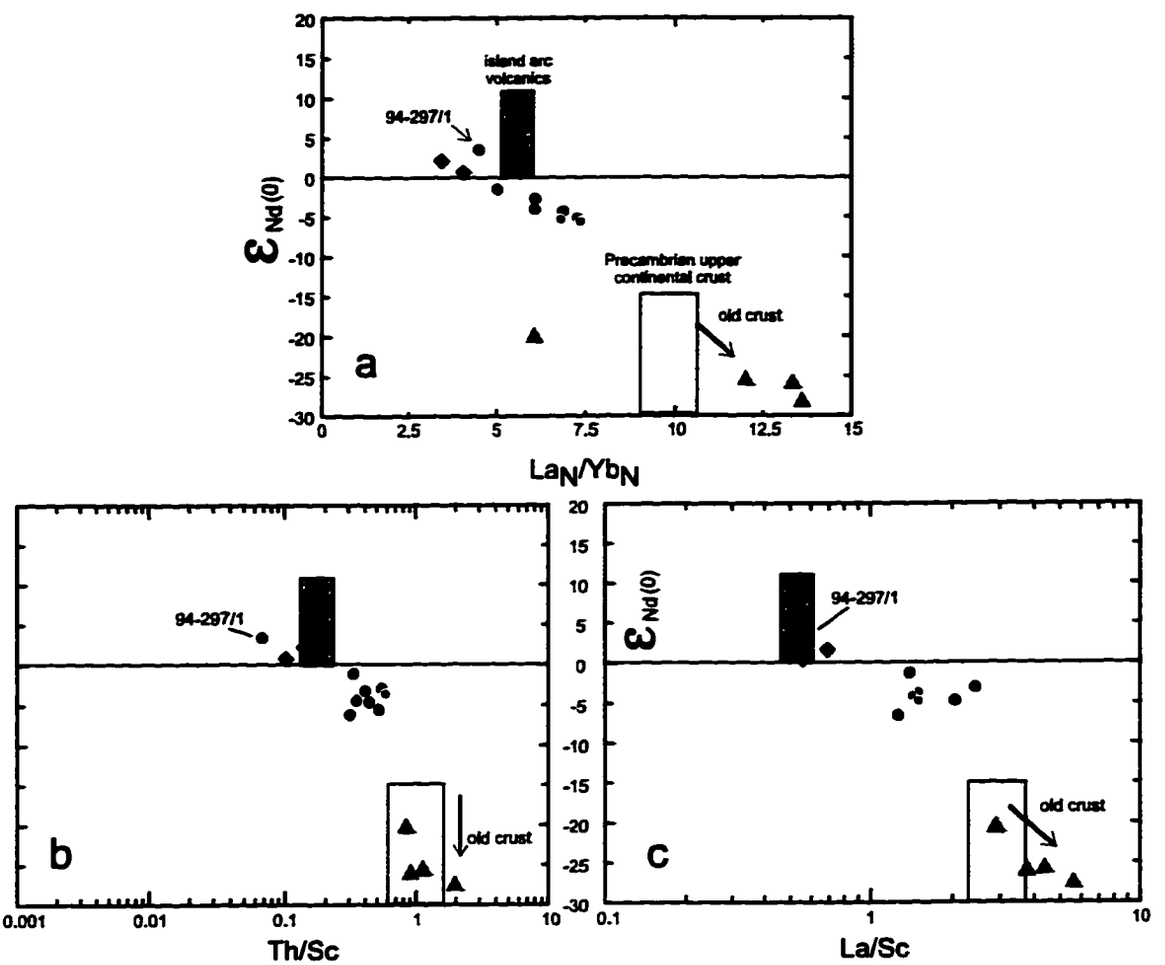

Figure 5.8: a-c) $\varepsilon_{Nd}(0)$ versus Th/Sc, La/Sc and La_N/Yb_N. AMS samples plot near the Precambrian upper continental crust field, while DF samples plot close to the island arc volcanics. KMA orthoamphibole schist (94-297/1) plots in the DF field. KMA samples lie on a line that joins DF and AMS, implying a possible origin of the KMA by mixing protoliths of the DF and AMS. The symbols are the same as in previous figures. Average present day volcanic island arc Nd signature is after Faure (1986). Precambrian upper continental crust range is adapted from Taylor & McLennan (1985) and McLennan & Hemming (1992).

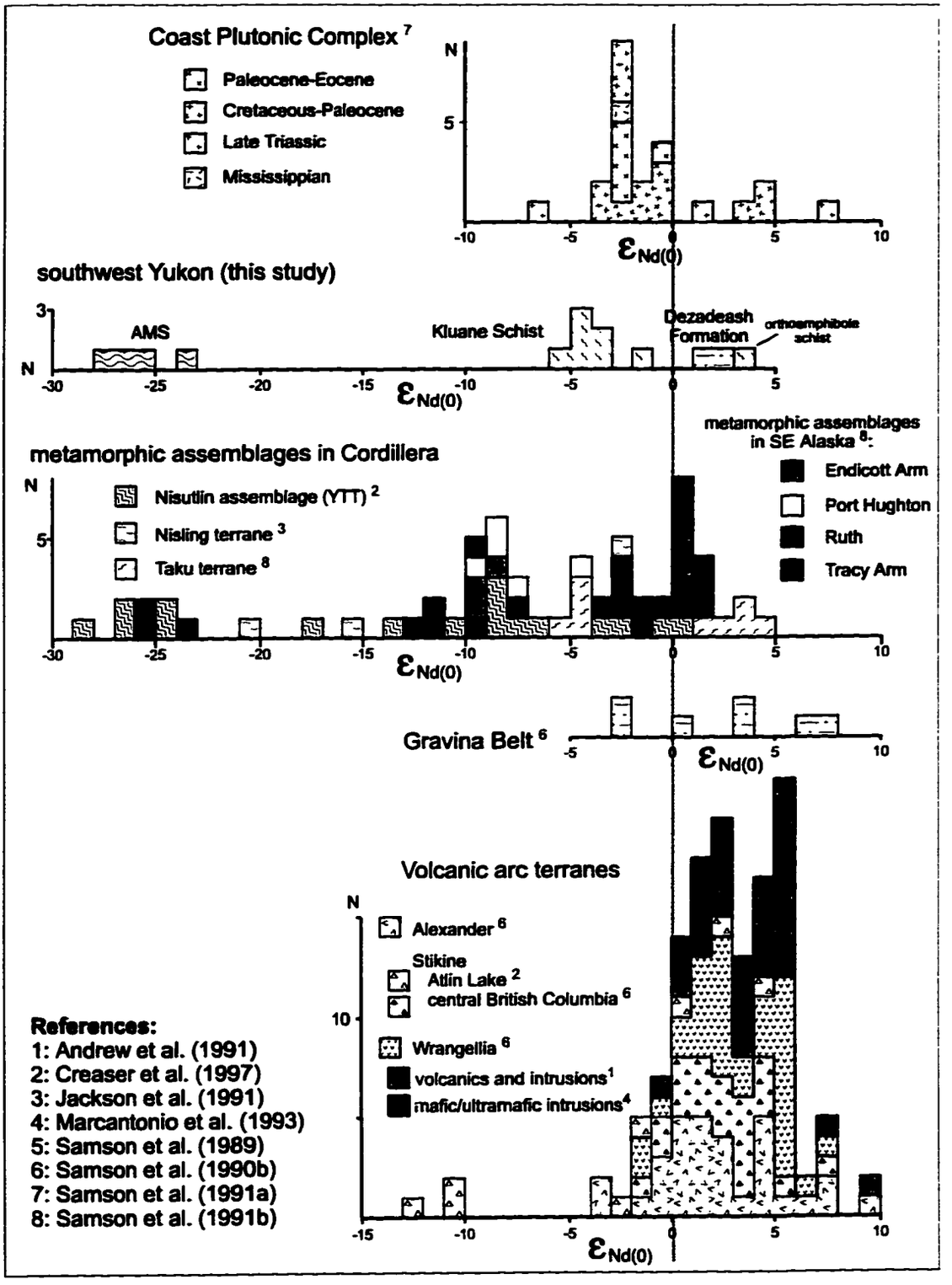

Figure 5-9: Block diagram of previously published Nd isotopic studies of metamorphic, igneous and and sedimentary rocks of the Canadian Cordillera in comparison with the KMA, DF and AMS of this study. See Appendices 5-3 and 5-4 for detailed description.

Northwest Territories have an average $\epsilon_{Nd}(0)$ of -25 and model ages between 2.4 and 2.0 Ga (Bowring & Podosek, 1989). These results are generally similar with AMS and therefore represent possible source regions on the North American continent. AMS and basement rocks overlap in the same field on a $\epsilon_{Nd}(0)$-$^{147}Sm/^{144}Nd$ diagram (Figure 5-7).

Studies of plutonic and metamorphic rocks the Yukon Tanana terrane (YTT) of eastern Alaska are few, but also report negative $\epsilon_{Nd}(0)$ of -27 to -16 and model ages of 1.9 to 2.3 Ga, similar to AMS values (McCulloch & Wasserburg, 1978; Aleinikoff et al., 1981; Bennett & Hansen, 1988).

Elsewhere, metamorphic assemblages assigned to the YYT, the Tracy Arm, Endicott Arm, Port Houghton and Ruth assemblages (TERP, informal terminology) at the western margin of the Coast Plutonic Complex in southeastern Alaska, and the Nisutlin assemblage in the TTZ in southern central Yukon, have yielded $\epsilon_{Nd}(0)$-values of -28 to +2 and model ages of ~0.6 to 2.8 Ga (Figures 5-7, 5-9; Appendices 5-3, 5-4; Samson et al., 1991b; Creaser et al., 1997). The range of isotopic signatures and model ages is interpreted as mixing of Late Archean to Cambrian sources, supported by 0.5-3.0 Ga detrital zircon ages for the TERP assemblages (Gehrels et al., 1991a; Samson et al., 1991b) or mixing of magmatic arc and ancient NA continental crust in the Nisutlin assemblage (Creaser et al., 1997). Nd isotopic and REE signatures and model ages of the most evolved Nisutlin and TERP samples are very similar to the AMS (Figures 5-7, 5-9; Appendix 5-3), suggesting a common protolith source. However, this does not necessarily imply the same depositional age for these metamorphic assemblages, as a multiple recycling and depositional phases cannot be distinguished in medium grade metamorphic rocks.

Taking the limited number and spatial distribution of the analyzed AMS samples into consideration, it can be concluded that, unlike in other metamorphic assemblages of the YTT, the AMS may have derived its detritus from an ancient continental crust source, without mixing of more primitive or post-Late Archean sources.

Dezadeash Formation

The DF has been correlated with the Late Jurassic-Early Cretaceous Gravina-Nutzotin Belt, consisting of flysch sediments derived from an oceanic island arc that mark the amalgamation of the Wrangellia and Alexander terranes to form the INS during the Jurassic (Monger et al., 1991). $\epsilon_{Nd}(0)$-values of shale and phyllite samples of the Gravina Belt in southeastern Alaska are slightly negative (-2), but yield the same T_{DM} of 900 Ma as the DF samples (Samson et al., 1991b). Figures 5-7 and 5-9 show that the isotopic signature of the DF is indistinguishable from sedimentary and igneous rocks of Wrangellia and Alexander terranes, which range in age from Cambrian to Cretaceous in age and have $\epsilon_{Nd}(0)$ values of -4 to +10, and are interpreted as derived from a juvenile mantle source (Samson et al, 1989, 1990b; Andrew et al., 1991).

The isotopic compatibility of the DF with Wrangellia and Alexander terranes and other Gravina-Nutzotin Belt assemblages suggests that the DF was derived completely from the INS. The positive ϵ_{Nd}-values indicate that little or no sediment from an ancient cratonal source was incorporated sufficiently enough to affect the isotopic signature of the DF.

Kluane metamorphic assemblage

Geochemical and isotopic signatures of the mica-quartz schists of the KMA show that it is a very homogeneous sequence, compared to other metamorphic assemblages associated with the Nisling terrane and the Yukon-Tanana terrane in the Yukon and southeast Alaska described above. The present location of the KMA, between juvenile rocks of the DF in the west and highly evolved metamorphic rocks of the AMS to the east, may suggest deposition in a basin behind a volcanic island arc to the west, but not isolated from an ancient continental source to the east, to account for the slightly negative values. Alternatively, the KMA could have been completely derived from older, more mature parts of the INS. However, the oldest known rocks of the Alexander terrane (upper Precambrian; Souther, 1991) and T_{DM} model

ages of ~900 Ma (Samson et al., 1991b) are much younger than model ages of the KMA (1.2-1.5 Ga), which does not support a single volcanic arc source region for the KMA.

The relative juvenile signature of the orthoamphibole schist 94-297/1, with $\epsilon_{Nd}(0)$ of +3.9 and T_{DM} of 720 Ma, compatible with those from igneous rocks of Wrangellia and Alexander (Samson et al., 1989, 1990b), can be interpreted as metamorphosed sediment derived from an andesitic source. Andesitic volcanism is common in the adjacent Alexander terrane, and occurs as andesitic flows southwest of Dezadeash Lake (Cambrian Field Creek Volcanics, Dodds & Campbell, 1992).

As shown on the diagrams of Figure 5-8, it is possible to derive the KMA by mixing of the DF with the AMS. However, given the distinct metamorphic and deformation histories of these three assemblages (see Chapters 3 and 4), the location of the KMA along a major crustal boundary, and unknown pre-Late Cretaceous history of the KMA, such a simple correlation should be cautioned. Nevertheless, the isotopic and REE signatures imply the possibility that the KMA has derived its detritus from sources similar, if not the same, to that of the AMS (NA) and the DF (INS).

Several tectonic settings can be envisioned that would allow mixing of material from juvenile and ancient crustal sources (Figure 5-10). A model where detritus from a volcanic arc to the west and an ancient continent to the east were transported into a backarc basin and thoroughly mixed best represents the present geological setting (Figure 5-10a). Alternatively, the protolith of the KMA could have been deposited in a forearc basin west of a volcanic arc with continental detritus transported trench-parallel from a source north or south of the volcanic arc (Figure 5-10b). However, the KMA is accreted directly onto North America and no remnants of the intervening volcanic arc can be observed. The missing arc is difficult to explain with any tectonic processes. A third possibility would be a forearc basin setting where the volcanic arc is situated in the west and the continent in the east, similar to the first model, except that a westward subduction underneath the volcanic arc

occurs (Figure 5-10c). To explain the underplating of the KMA underneath North America, a reversal of subduction is necessary. There is no evidence that such an event took place.

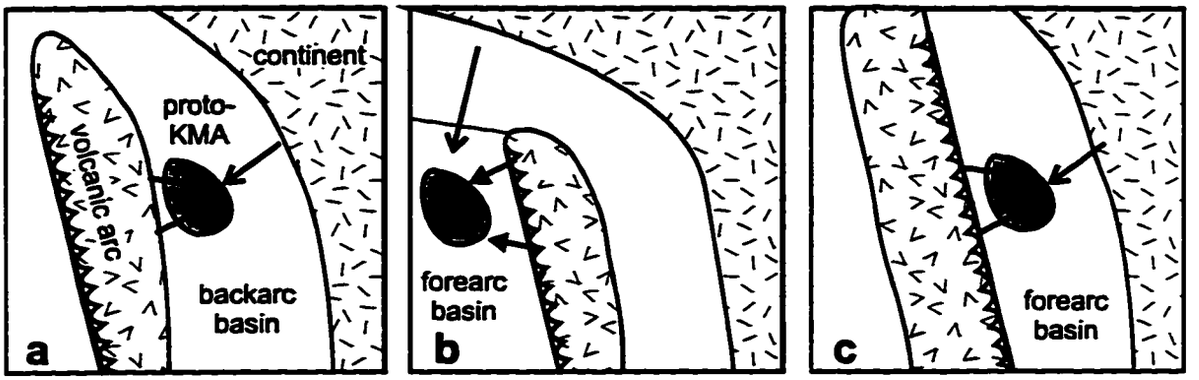

Figure 5-10: Possible tectonic settings for the protolith of the KMA. See text for discussion.

CONCLUSIONS

1) Two metamorphic assemblages (AMS, KMA) and a Late Jurassic-Early Cretaceous flysch formation (DF) situated at the northwestern margin of the Coast Belt of the Canadian Cordillera can be distinguished by their trace element, REE and neodymium isotope signatures, suggesting that their current spatial proximity is the result of tectonism.

2) Negative $\epsilon_{Nd}(0)$ of -28 to -21 and Late Archean crustal residence ages (~2.6 Ga) of the AMS indicate a single detrital source from an ancient evolved continental crust. The isotopic and geochemical signatures are compatible with other metamorphic assemblages associated with the pericratonic YTT and the Precambrian basement of the Canadian shield, suggesting a protolith derived from the ancient North American continent.

3) Trace and REE element signatures, juvenile $\epsilon_{Nd}(0)$-values (2.5-3.0) and late-Middle Proterozoic model ages (950 Ma) of the weakly metamorphosed slates of the DF suggest a juvenile volcanic island arc protolith, most likely the INS, which has compatible isotopic signatures (Samson et al. 1989, 1991b).

4) The KMA, situated between the AMS to the northeast and the DF to the south, has intermediate isotopic signatures ($\epsilon_{Nd}(0)$ ~-1.3 to -5.6, T_{DM} 1.2-1.5 Ga), that cannot be correlated to any single source region, and are interpreted as mixing of ancient Archean (?) continental crust with more juvenile sources. Possible sources include the AMS and DF. However, the unknown spatial relations between the three assemblages prior to the accretion of the KMA and DF onto the North American continental margin make a direct correlation very speculative. It is more likely that the KMA has similar, if not necessarily the same, protoliths as the DF and AMS. Restricted occurrence of an orthoamphibole schist with distinct primitive geochemical and isotopic signatures indicates a single andesitic source, possibly derived from the INS. The homogeneity of trace element and Nd isotope characteristics of the KMA suggest that the original sediments received a constant ratio of juvenile and mature detritus throughout the duration of the deposition, prior to the accretion of the KMA onto NA in the Late Cretaceous (see Chapter 3). A possible tectonic setting of the sedimentary protolith of the KMA is a backarc basin distal to a continental source and in the proximity of a volcanic island arc.

5) The distinct protolith provenances prove that the KMA is not simply the metamorphosed equivalent of the DF as suggested by Eisbacher (1976).

6) The juvenile character of sample 94-297/1 from the eastern Dezadeash Range support the suggestion brought forward in Chapters 2 and 4 that a contact between the KMA and pericratonic rocks of the Nisling terrane does not exist in the eastern Dezadeash Range, as proposed by Erdmer (1991).

Chapter 6

Model of tectonic evolution of the Kluane metamorphic assemblage

MODEL OF TECTONIC EVOLUTION

The geology and the structural, metamorphic, geochemical and isotope characteristics of the Kluane metamorphic assemblage (KMA) are incorporated into a model of evolution for the northwestern Coast Belt of the Canadian Cordillera. The model is illustrated in Figure 6-1.

Late Jurassic (?) - early Late Cretaceous (~100 Ma)

Geochemical and petrological studies indicate that the rocks of the KMA (graphitic quartzose pelites (aluminous sequence) and graphitic calcareous clays (calcic sequence)), are predominantly of sedimentary origin. The lack of recognizable lithic fragments and the presence of fine graphitic layers in feldspar porphyroblasts, interpreted as original bedding, suggest that the protolith was a fine grained sediment. Consistent ϵ_{Nd}-values throughout the KMA imply homogeneous mixing between juvenile volcanic arc and ancient continental sediment sources (Figure 6-1a). Schists with more juvenile signatures indicate a protolith derived directly from an andesitic source. The mixing of sediments derived from a juvenile and ancient continental source is interpreted to have taken place in a backarc basin setting. Other possible tectonic settings, such as deposition in a forearc basin are considered less likely, since no evidence for a remnant arc between KMA and NA exists. Olivine serpentinite bodies interlayered with the schists in the KMA support a backarc basin model, the serpentinites derived from oceanic crust. The occurrence of ultramafic rocks along a contact between calcic and aluminous schists, similar fabrics developed in schist and serpentinites, and the lack of compositional zoning within ultramafic rocks support a tectonic ("Alpine-type") instead of an intrusive ("Alaskan-type") origin for the serpentinites.

Isotopic character of the KMA and presence of minor metamorphosed volcanoclastic layers within the schist indicate proximity of the depositional basin to an active volcanic arc, but also indicate contribution of sediment from

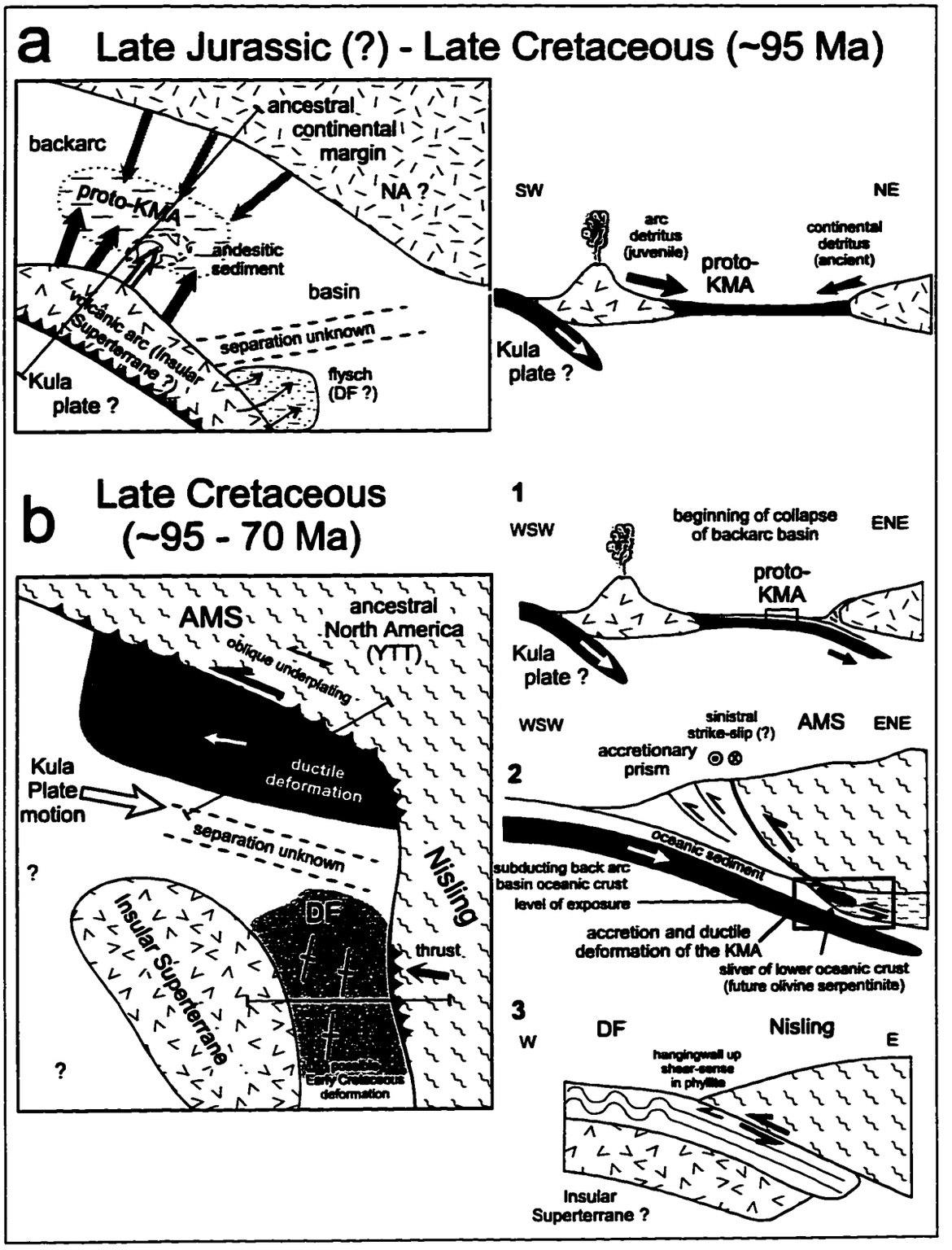

Figure 6-1: Schematic model of tectonic evolution of the Kluane metamorphic assemblage and adjacent terranes in the southwestern Yukon. See text for discussion.

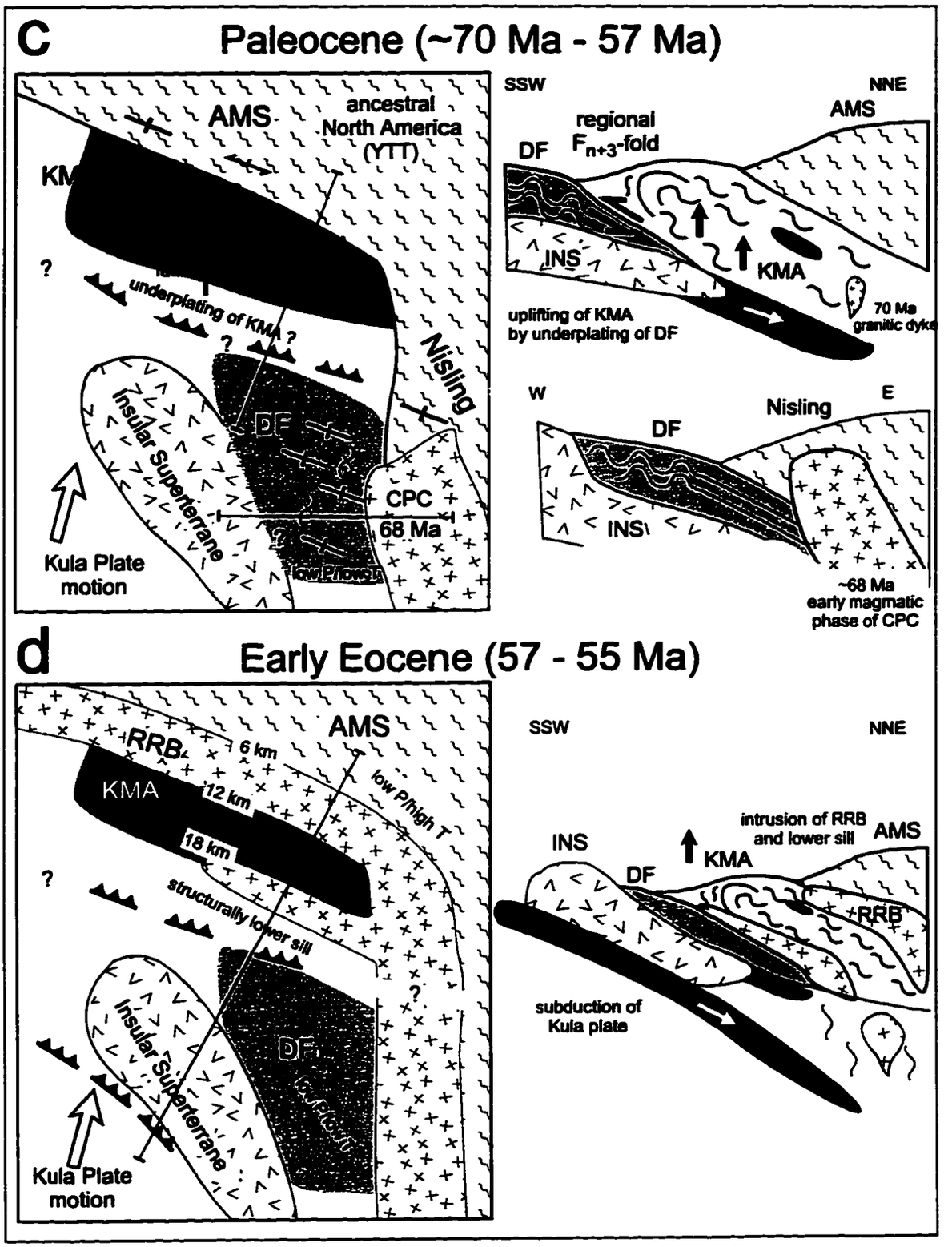

Figure 6-1 (continued): Schematic model of tectonic evolution of the Kluane metamorphic assemblage and adjacent terranes in the southwestern Yukon. See text for discussion.

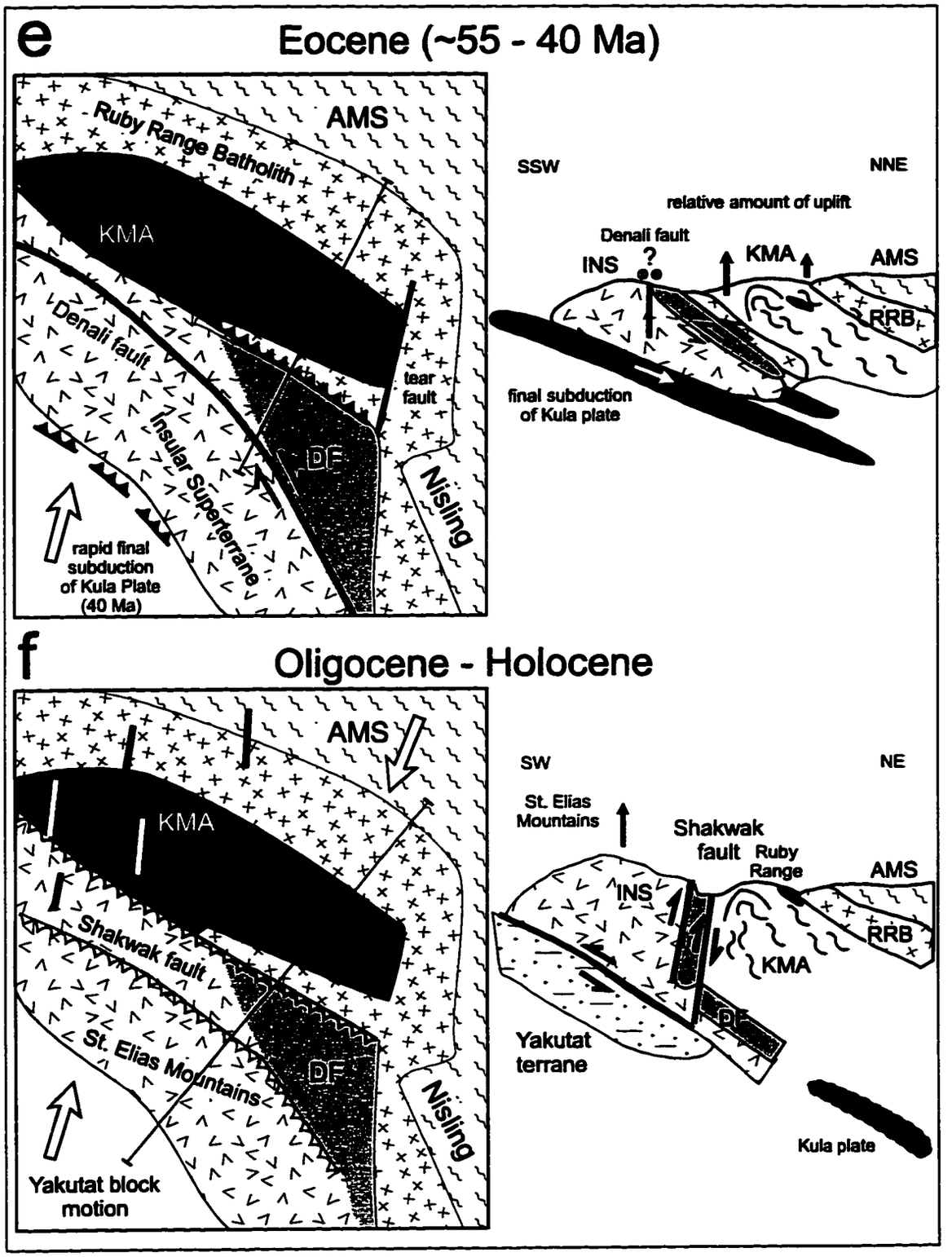

Figure 6-1 (continued): Schematic model of tectonic evolution of the Kluane metamorphic assemblage and adjacent terranes in the southwestern Yukon. See text for discussion.

an ancient continental margin. Several authors (Csejtey et al., 1982; Plafker et al., 1989) have postulated an oceanic basin of uncertain width between the Insular Superterrane (INS) and North America (NA) in the Jurassic-Cretaceous, into which the Late Jurassic-Early Cretaceous flysch derived from the Gravina-Nutzotin arc of the INS were deposited eastward into the basin. Workers in southeast Alaska and British Columbia have questioned the existence of oceanic crust in the basin and suggested intra-arc rifting instead (McClelland et al., 1992; van der Heyden, 1992). The schists and ultramafic rocks of the KMA provide evidence for the existence of an extensive and/or long-lived backarc basin between NA and the INS. A small basin, as proposed for the southern Cordillera (McClelland et al., 1992), would have resulted in a greater lithological and isotopic variety, reflecting varied detrital input from ancient and juvenile sources, such as reported from the Nisutlin assemblage of the Teslin tectonic zone (Creaser et al., 1997). The amount of *exposed* KMA, with a structural thickness of 12 km and an along-strike extent of approximately 160 km, requires a basin of a few hundred kilometers width to allow consistent long-term sedimentation of homogeneously mixed detritus. A precise estimate cannot be made, since the necessary width of the basin to allow homogeneous mixing depends on the amount of clastic input, which is a factor of the age of the continental margin, the size of the magmatic arc and the depth of the basin. Modern analogues may be the Japan basin or the Aleutian basin. The flysch of the DF may be arc-proximal sediments deposited in the same basin (Eisbacher, 1976).

Late Cretaceous (~95-70 Ma)

Southeast motion of the Kula plate during the Early Cretaceous (Engebretson et al., 1995) resulted in sinistral strike-slip along the Wrangellia-Alexander terrane boundary in the INS (Plafker et al., 1989), while the marginal basin between the INS and NA remained stable. The collapse of the basin started when the Kula plate changed from southeastward to eastward motion

at around 95 Ma (Engebretson et al., 1995). Eastward subduction of the oceanic crust underneath AMS at the North American continental margin began (Figure 6.1b, section 1). 84-95 Ma old andesites and rhyolites of the Montana Mountain volcanic complex near Carcross (Hart, 1993) may be part of the magmatic arc that developed in response to the eastward subduction of the backarc basin. Alternatively, Late Cretaceous magmatic arc plutons could have been eroded during subsequent uplift or assimilated by the extensive Early Eocene plutonism of the Coast Plutonic Complex (CPC; Woodsworth et al., 1991) east of the KMA.

The fine grained sediments of the proto-KMA entered the subduction zone and were transported to a depth of at least 20 km where they were accreted to the upper plate represented by the AMS. Several authors (Karig, 1974, 1982; Karig & Sharman, 1975; Moore, 1989) have suggested that fine grained pelagic sediments, forming the lower sedimentary layers on the oceanic crust, can be transported on the downgoing plate and added to the base of the upper plate. Meanwhile overlying clastic trench fill is being removed before entering the subduction zone and is added to the accretionary prism (Figure 6-1b, section 2). This observation is compatible with the homogeneous isotopic character of the KMA. The proto-KMA was covered by younger sediments and did not receive any detritus when it entered the subduction zone. Topographic irregularities on the downgoing plate, such as horst and graben structures, or sea mounts, provide the means of shearing off parts of the oceanic crust and adding them to the accreted oceanic sediments (Karig & Sharman, 1975). This can explain the presence of the disrupted lens-shaped ultramafic bodies within the schists of the KMA. The present 12 km thickness of the KMA is probably the result of structural stacking due to addition of newly underplated material.

During subduction and underplating at the base of NA, the KMA experienced ductile deformation and high P/low T metamorphism. The parallel alignment of slaty cleavage with schistosity suggests that both developed during continuous deformation under increasing strain and pressure. Distinct

mineral stretching lineations and mylonization of the schist indicate progressive non-coaxial deformation. The consistent westward hangingwall up sense of shear at a small angle with the strike of the foliation, and the general northeast-dipping foliation of the KMA and the AMS north of the RRB indicate oblique eastward underplating of the KMA underneath the AMS (Figure 6-1b). This resulted in left-lateral displacement along the WNW-trending ancestral NA continental margin. However, since the exposed suture between the AMS and KMA represents the deep seated part of a subduction zone, evidence for coeval sinistral strike-slip faults at higher structural levels, as proposed by Mezger & Creaser (1996), is unlikely to have been preserved as it would have been destroyed by erosion during uplift.

Underplating of the KMA is constrained by early Middle Jurassic (~187 Ma) high P/high T metamorphism of the AMS (Johnston et al., 1996), which has not been observed in the KMA, and a latest Cretaceous (72 Ma) late synkinematic dyke intruded into the KMA (Mortensen, unpublished data, 1997). Absence of high T minerals, such as kyanite, which would indicate isobaric heating of the originally cool KMA slab, indicates that maximum age of deformation of the exposed rocks of the KMA is not older than 90-100 Ma. The absence of Late Jurassic to pre-Late Cretaceous plutons on ancestral NA in the southwest Yukon precludes significant eastward subduction underneath NA during that time (Woodsworth et al., 1991).

Shear-sense indicators in phyllites on the eastern margin of the DF record similar WNW hangingwall up motion as the mylonitic schist in the KMA to the north and suggest westward thrusting of high P/high T schists of the NS onto the DF (Figure 6-1, section 3). South of the KMA, eastward motion resulted in orthogonal plate convergence, as the ancestral NA margin strikes south. While schists of the KMA reflect ductile deformation at a depth of ~20-22 km, the exposed eastern thrust fault of the low grade slaty and phyllitic DF implies a contact at higher structural levels at a depth of a few kilometer.

The time window for accretion of DF onto NA is restricted by the youngest depositional age of 135 Ma for the DF (Early Cretaceous; Eisbacher,

1976) and by radiometric ages of 68 Ma for the intrusive contact of the DF with the plutons of the CPC (LeCouteur & Tempelman-Kluit, 1976; Lowey, pers. comm., 1995). NNE-trending folds cut by a late Early Cretaceous pluton (108 Ma, Mortensen, pers. comm., 1996) suggest that thrusting of the NS may have happened as early as late Early Cretaceous (Eisbacher, 1976).

Mid-Cretaceous westward thrusting of NA onto the INS is proposed along 1200 km in southeastern Alaska and British Columbia causing high P/low T metamorphism of Gravina belt sediments (Rubin et al., 1990; McClelland et al., 1992). Crosscutting plutons constrain deformation and metamorphism to the interval 90-115 Ma (McClelland et al., 1991, 1992). McClelland et al. (1992) and van der Heyden (1992) interpreted mid-Cretaceous thrusting as intra-plate shortening, rather than collapse and subduction of a marginal basin between INS and the Stikine terrane, along the NA continental margin during the Cretaceous. The implications of these two different tectonic settings for the evolution of the North American margin are discussed below.

Paleomagnetic studies in southern British Columbia suggest 2000 km of Late Cretaceous-Early Tertiary dextral motion has taken place between the eastern Coast Belt and the Intermontane Belt (Wynne et al., 1995; Irving et al., 1996). Late Cretaceous eastward subduction beneath NA in the southern Yukon (this study) and lack of dextral northwest-trending faults or shear zones in the Coast Belt of the southern Yukon (Tempelman-Kluit, 1974; Johnston & Timmerman, 1993a; this study) do not support large amount of dextral motion within the Coast Belt or at its eastern margin in the southern Yukon during the Late Cretaceous.

Latest Cretaceous (~72 Ma) - Early Eocene (57 Ma)

A change from east to NNE-motion of the Kula plate in the latest Cretaceous resulted in ESE-trending regional folding of the metamorphic assemblages and the DF (Figure 6-1c). Locally developed WSW-verging mesoscopic F_{n+3}-folds are interpreted as contemporaneous with uplift of the

KMA. Uplift was accomplished by underplating of the remaining backarc basin and the approaching DF and INS underneath the KMA. The first magmatic phase is marked by the late synkinematic dyke crosscutting the KMA (70 Ma) and the intrusion of the CPC into the DF at Million Dollar Falls campground at ~68 Ma. A small undated tonalitic gneiss at the northern margin of the KMA at Kluane Lake (Doghead Point) is cut by undeformed granodiorites of the RRB. The tonalite is interpreted as a mafic precursor of the RRB, possibly related to a 69-78 Ma old quartz diorite at the northern margin of the RRB near Aishihik Lake (Johnston, 1993) and similar to tonalite bodies along the western margin of the CPC in southeastern Alaska. These tonalite bodies, referred to as the Great Tonalite Sill (Gehrels et al., 1991b), are interpreted as deep (15-20 km) sill-like intrusions along a steep dipping shear zone, the LeConte Bay shear zone, which has developed along the former suture zone between INS and NA (McClelland et al., 1991). The tonalites range in age from 57-83 Ma, and are succeeded by undeformed granodiorites of the CPC (Gehrels et al., 1991).

Early Eocene (57-55 Ma)

Continuing NNE-compressive motion along the Kloo Lake fault resulted in eastward tilting of the KMA, immediately followed by emplacement of the granodiorites that comprise the major portion of the RRB along the suture between the KMA and the AMS (Figure 6-1d). Fabric-parallel intrusive contacts with the northeast-dipping KMA and AMS suggest that the batholith intruded in a sill-like fashion (Erdmer & Mortensen, 1993) dipping 15° to the NNE. The batholith has a minimum thickness of 5 km and can be traced for 200 km to the WNW. A shorter, 70 km long structurally lower sill is inferred from several granodiorite exposures at the base of the KMA. The sill is only partially exhumed and was probably emplaced along the faulted contact of the KMA with the DF to the south. The RRB and the unnamed sill to the south are northernmost portions of the granodiorites of the CPC, intruded at shallow levels (6-12 km) as a result of increased speed of subduction of the Kula plate

in the late Paleocene (Erdmer & Mortensen, 1993; Engebretson et al., 1995).

The Early Eocene crystallization of the RRB resulted in a 5 km thick contact aureole in the KMA. Thermal overprinting was strong enough to reset radiometric ages and partly anneal existing fabrics. Peak metamorphic temperatures reached 650-700°C, uppermost amphibolite grade to lower granulite grade. Garnet, sillimanite, cordierite, K-feldspar and spinel characterize the highest grade metamorphic mineral assemblage. The metamorphic gradient is inverted, as it decreases to upper greenschist grade in the structurally lower section of the KMA. In the overlying AMS, contact metamorphism related to the RRB resulted only in a few hundred meter wide contact aureole, which did not reset radiometric age dates (Johnston et al., 1996). Geothermobarometry indicates depths of 12 and 18 km for the top and the base of the KMA during the emplacement of the RRB. No major deformation of the KMA or the AMS resulted from the emplacement of the RRB.

Eocene (55-40 Ma)

The upper structural panel of the KMA was exhumed rapidly after the emplacement of the RRB by northward underplating by the DF/INS (Figure 6-1e). In the southwest, where the KMA was 6 km deeper than near the contact with the RRB, the schist cooled through the 280°C isotherm at 40 Ma, 16 Ma later than at the northern contact. A relative northward tilting of the KMA by 15° is necessary to account for the current levels of exposure. Similar peak metamorphic pressures along strike of the KMA imply that the tilt axis is parallel to the strike of the schistosity. The rapid uplift of the KMA was enhanced by increased speed in the northward motion of the Kula plate, which was finally consumed at 40 Ma (Engebretson et al., 1995).

Major southeast-striking strike-slip faults are not observed cutting the KMA. Shear zones of unknown age, interpreted as strands of the Denali fault, are observed within Pennsylvanian-Triassic strata of the Wrangellia terrane in

the Kluane Ranges (Dodds & Campbell, 1992; T. Bremner, pers. comm., 1993; White, 1997). Together with the lack of compatible metamorphic assemblages west of the Denali fault, this observation strongly suggests that the KMA is not truncated to the southwest by strike-slip faults, but by dip-slip faults.

Oligocene - Holocene

The disappearance of the Kula plate by the end of the Eocene led to new plate configurations. Oblique convergence of the northwest moving Pacific plate, resulted in north-trending dykes of (possible) Miocene age that intrude the INS, KMA and AMS (Tempelman-Kluit, 1974; Eisbacher & Hopkins, 1977; Stevens et al., 1982, Johnston & Timmerman, 1993a). The cessation of exhumation of the KMA can be attributed to reduced north-south compression and northward tilting of the KMA, rotating the overturned southern limb of the Ruby Range anticline to normal upright position (Figure 6-1e). Steep southward dipping foliation of the KMA and the DF enabled to change motion along the fault plane from a south-verging thrust into a steep north-verging reverse fault with the southern hangingwall moving up (White, 1997).

DISCUSSION

Evaluation of evidence for dextral strike-slip along the Denali fault zone in the Cenozoic

Based upon correlation of similar assemblages along the Denali fault zone (DFZ), major Cenozoic dextral displacement along the DFZ, ranging from 150-400 km, has been postulated by several authors (Forbes et al., 1974; Turner et al., 1974; Eisbacher, 1976; Hudson et al., 1982; Nokleberg et al., 1985). Others have interpreted the DFZ as a major Late Cretaceous collision zone with only minor (~10 km) dextral offset (Csejtey et al., 1982).

This study has shown that the Maclaren Glacier Metamorphic Belt

(MGMB) of the eastern Alaska Range can not be correlated with the KMA. Although these results do not disprove a 400 km dextral displacement along the DFZ as proposed by Nokleberg et al., (1985), they do remove a major evidence.

Based on correlation of Late Jurassic-Early Cretaceous flysch sediments of the Nutzotin Mountains sequence with the Dezadeash Formation, and Upper Triassic strata of the Chilkat Peninsula, southeast Alaska, with similar strata in the Wrangell Mountains, Eisbacher (1976) and Plafker et al. (1989) proposed 300-350 km dextral offset along the DFZ. Along the southern continuation of the DFZ, the Chatham Strait fault, Hudson et al., (1982) only inferred 150 km of dextral offset. It is beyond the scope of this study to evaluate the validity of these correlations, but they should be regarded with extreme caution. Detailed studies of assemblages on both sides of the fault are necessary to determine possible tectonic correlations. Also, the discrepancy in the apparent offset along the same fault zone (350 and 150 km), shows the weakness of fault displacement determinations based on correlation of similar assemblages on opposite sides of a fault zone. Even if these assemblages were part of one unit that was disrupted by the fault, only the apparent strike-slip offset can be observed. The amount of offset is dependent on outcrop exposure, vertical motion along the fault, which can result in differential erosion, and independent faulting within one fault block. In the case of the Denali fault and the Chatham Strait fault none of these factors can be estimated since the faults are covered by glacial till or water, respectively.

Based on similar Late Jurassic-Early Cretaceous stratigraphy and mid-Cretaceous granodiorite intrusions, Eisbacher (1976) correlated the DF with the Nutzotin Mountain sequence. However, subsequent authors (Plafker et al., 1989; Stanley et al., 1990) have postulated a ~1500 km long flysch basin along the western margin of North America in the mid-Cretaceous. Mid-Cretaceous granodiorite intrusions were also observed in the flysch strata of southeastern Alaska (McClelland et al., 1992). Considering the length of this flysch basin and the similarity of its Late Jurassic-Early Cretaceous strata, a correlation between

two preserved flysch sequences has to be regarded with caution.

Further evidence that question major dextral displacement along the DFZ are: 1) lack of Pleistocene to Holocene lateral displacement on the DFZ east of the Totschunda fault (Richter & Matson, 1971; Clague, 1979), 2) minor (~10 km) right-lateral offset of metamorphic mineral isograds in the MGMB along the McKinley segment of the DFZ (Csejtey et al., 1982), 3) only 38 km offset along the McKinley segment since early Oligocene (38 Ma, Reed & Lanphere, 1974), 4) no activity along the Hines Creek segment of the DFZ since the Late Cretaceous (95 Ma, Wahrhaftig et al., 1975) and 5) uplift of Mt. Denali south of the McKinley segment in excess of 8 km in the last 6 Ma as determined by apatite fission-track analyses (Fitzgerald et al., 1993).

The Denali fault zone in the southern Yukon - a Late Cretaceous suture zone with minor Eocene dextral strike-slip displacement

A tectonic model is proposed which incorporates the tectonic and metamorphic evolution of the KMA described in this study with new plate motion estimates for the Kula plate (Engebretson et al., 1995) and previously published data. This model postulates northward motion of the INS along a mid-Cretaceous suture and the closure of an oceanic basin in the southern Yukon and south-central Alaska without evoking major Cenozoic dextral motion along the DFZ. The model is illustrated in Figure 6-2.

Mid-Cretaceous (90-100 Ma) collision of the INS with NA resulted in the collapse of an intervening marginal basin and westward thrusting of NA onto the INS along a 1200 km long zone (Rubin et al., 1990; McClelland et al., 1992). Lack of evidence for underlying oceanic crust may imply that the collapsed basin was associated with intra-arc rifting (Rubin et al., 1990). Syndeformational tonalite bodies were emplaced along the shear zone (Rubin et al., 1990).

This study has shown that, contemporaneous with westward thrusting in the southeastern Alaska and British Columbia, eastward oblique subduction of

the backarc basin, into which the KMA was deposited, underneath NA occurred in the southern Yukon (Figure 6-2a). Both eastward subduction in the southern Yukon, and westward thrusting of NA onto the INS, are compatible with eastward motion of the Kula plate in the early Late Cretaceous (Engebretson et al., 1995). Since the eastward subduction of the backarc basin continued until the latest Cretaceous, the INS either remained outboard of the subduction zone at that time or was located further south.

Sinistral strike-slip faults were likely developed at structurally higher levels of overriding NA plate as a result of oblique subduction. Due to subsequent unroofing of the subduction zone, no evidence of sinistral faulting is preserved. Earlier sinistral faulting is postulated for the south-central Coast Belt in southern British Columbia during Middle Jurassic-Early Cretaceous (Monger et al., 1994). It is unclear if strike-slip faulting along the North American continental margin in the southern Yukon was active at that time or if it occurred outboard the volcanic arc that enclosed the backarc basin.

Change of motion of the Kula plate from east to NNE in the latest Cretaceous (Engebretson et al., 1995) juxtaposed the INS and DF with the KMA (Figure 6-2b). The backarc basin finally collapsed when the INS and the DF were underthrust beneath the KMA, causing uplift of the KMA by >5 km. Northward motion of the already accreted INS occurred along the Coast shear zone, the former suture between the INS and NA (Hollister et al., 1997). Coeval collapse of an oceanic basin in south-central Alaska, evident in underplated mesozoic flysch beneath NA (Stanley et al., 1990) and "Alpine-type" ultramafics along the suture (Patton et al., 1994), suggest that a single backarc basin may have existed along the southern continental margin of south-central Alaska and the southern Yukon.

Rapid subduction of the Kula plate in the Early Eocene (Engebretson et al., 1995) resulted in the emplacement of the granodiorites of the CPC along the suture zone between INS and the North American continental margin (McClelland et al., 1992; Erdmer & Mortensen, 1993). Early Tertiary granites are also observed along the INS-NA suture in south-central Alaska (Csejtey et

al., 1982).

Subduction of successively younger, and therefore more buoyant, Kula plate underneath the INS resulted in rapid removing of 12-18 km of crustal material overlying the KMA, exhuming the Late Cretaceous subduction zone. The youngest K-Ar cooling ages in the KMA (≈39 Ma; Erdmer & Mortensen, 1993) are coeval with the final subduction of the Kula plate at ~40 Ma (Engebretson et al., 1995), suggesting that exhumation of the KMA ended with the disappearance of the Kula plate.

Evidence for right-lateral strike-slip has neither been found at the southern margin of the KMA, nor along the contact between the KMA and the INS and DF. Shear zones within the INS and at the basal contact of the DF suggest only minor dextral (?) strike-slip displacement (White, 1997). Eocene-Oligocene clastic sediments of the Amphitheatre Formation, deposited in small pull-apart basins near the trace of the DFZ and the Duke River fault in the INS (Ridgway et al., 1992), may indicate dextral strike-slip motion of 10-35 km during Eocene-Oligocene time.

Rearrangement of plate configuration and NNW-directed motion of the Pacific plate resulted in underplating of the Yakutat terrane beneath the INS (Engebretson et al., 1995) and rapid uplift of the St. Elias Mountains in the INS (Horner, 1983). Vertical normal or reverse fault motion of the Shakwak fault overprints earlier strike-slip movement along the Denali fault (White, 1997). The lack of post-Early Oligocene evidence for strike-slip displacement along the INS-NA suture suggests that dextral displacement has to be accommodated by faults to the west, e.g. the Fairweather fault (Dodds, 1991) or the Totschunda fault, which joins the DFZ in eastern Alaska (Horner, 1983).

On the base of northeast-trending lineaments and sinistral faults Page et al. (1995) proposed a 300 km wide dextral shear zone between the DFZ and the Tintina fault. The faults are interpreted as boundaries of individual blocks which are inferred to rotate clockwise during dextral motion along the Denali and Tintina faults. However, northeast-striking sinistral faults are not observed between the DFZ and Tintina fault in the Yukon (Tempelman-Kluit, 1974; this

study), suggesting that very little dextral motion is taking place along the DFZ east of the Totschunda fault. The continuation of lineaments south of the Denali fault in central Alaska (see figure 2 of Page et al., 1995) may imply that the observed seismicity can be explained without evoking a dextral shear zone between the DFZ and the Tintina fault.

The tectonic model presented here describes two different tectonic settings for the western North American continental margin in Cretaceous. In the southern Cordillera a relatively narrow flysch basin deposited in an intra-arc setting (?) collapsed during the early Late Cretaceous when NA was thrust westward over the INS (Rubin et al., 1990). In the southern Yukon and south-central Alaska, a large (~200-400 km) backarc basin with oceanic crust existed and was subducted underneath NA. The Late Cretaceous change of Kula plate motion resulted in dextral strike-slip of the already accreted INS along the Coast shear zone (Hollister et al., 1997) resulting in the collapse of the backarc basin. No dextral strike-slip along the Denali fault in the Yukon is necessary to explain tectonic configurations. Small amount of dextral offset (10-35 km) is possible during the time of rapid northward motion of the Kula plate (55-40 Ma).

The model provides two important constraints on the fault displacement in the Coast Belt of the North American margin:

1) Latest Cretaceous dextral displacement and northward motion of the INS along the Coast shear zone is necessary to explain the collapse of a larger backarc basin and the exhumation of the KMA in the southern Yukon. The amount of motion is uncertain, and can vary from less than 100 km to several hundred kilometers (Hollister et al., 1997).

2) Dextral motion along the Denali fault in the Yukon is restricted to the Late Eocene-Early Oligocene and did not exceed 30 km. This model proposes that the Denali fault in the Yukon is a major Late Cretaceous continent-volcanic arc suture zone with only minor strike-slip motion, as suggested by previous studies (Csejtey et al., 1982).

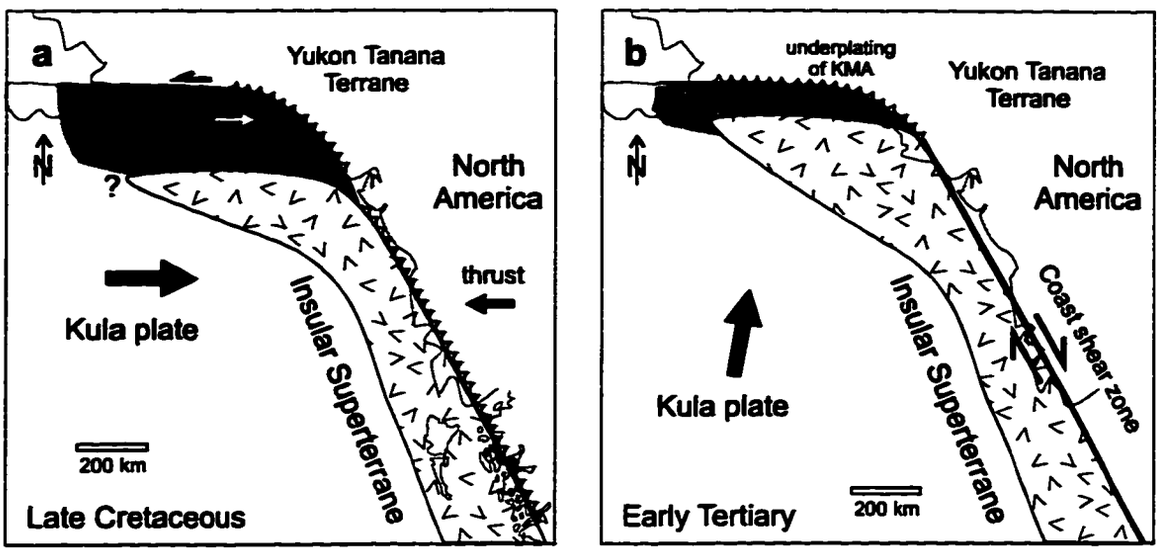

Figure 6-2: Speculative tectonic evolution model of the North American continental margin in the Late Cretaceous (a) and the Early Tertiary (b), based on plate motion model of Engebretsen et al. (1995), and work by Rubin et al. (1990), McClelland et al. (1992) and Hollister et al. (1997) in southeastern Alaska, and Csejtey et al. (1982) and Plafker et al. (1989) in south-central Alaska, as well as this study. See text for discussion.

CONCLUSIONS

The Kluane metamorphic assemblage is distinct in its lithology and metamorphic history from any other metamorphic assemblage in the Western North American Cordillera. Structural, petrographic, isotopic, geochemical and thermobarometric studies show that:

1) The sedimentary protolith of the KMA was derived from the mixing and homogenization of juvenile and ancient continental crust sources and, most likely, was deposited in a backarc basin between North America and the Insular Superterrane.

2) The KMA experienced syndeformational high P/low T metamorphism resulting from eastward subduction and underplating underneath the Aishihik Metamorphic Suite of the North American continental margin in the Late Cretaceous.

3) The change in plate motion of the Kula plate during the latest Cretaceous resulted in underplating of the KMA by the Insular Superterrane and the Dezadeash Formation.

4) Contact metamorphism, due to the Early Eocene intrusion of the RRB at a depth of 12 km, resulted in high T thermal overprinting producing a wide contact aureole and resetting radiogenic ages in the whole KMA.

5) The distinct lithologic and metamorphic character of the KMA does not support correlation with other metamorphic assemblages west of the Denali fault. Previous estimates of dextral strike-slip displacement based on such correlations are not supported by geological evidence. It is concluded that the Denali fault developed along an earlier suture zone between island arc terranes and the ancient American continental margin, possibly without any major dextral strike-slip movement.

REFERENCES

Aleinikoff, J. N., Dusel-Bacon, C., Foster, H.L. & Futa, K. (1981): Proterozoic zircon from augen gneiss, Yukon-Tanana Upland, east-central Alaska.- *Geology* **9**, pp. 469-473.

Andrew, A., Armstrong, R. L. & Runkle, D. (1991): Neodymium-strontium-lead isotopic study of Vancouver Island igneous rocks.- *Can.J.EarthSci.* **28**, pp. 1744-1782.

Aranovich, L. Y. & Berman, R. G. (1996): Optimized standard state and mixing properties of minerals: II. Comparison, predictions, and applications.- *Contrib.Min.Petrol.* **126**, pp. 25-38.

Arth, J. G., Barker, F. & Stern, T. W. (1988): Coast batholith and Taku plutons near Ketchikan, Alaska: Petrography, Geochronology, Geochemistry and Isotopic character.- *Amer.J.Sci* **288 A**, pp. 461-489.

Barrow, G. (1893): On an intrusion of muscovite biotite gneiss in the S.E. Highlands of Scotland and its accompanying metamorphism.- *Q.J.Geol.Soc.Lond.* **49**, pp. 330-358.

Bennett, V. C. & Hansen, V. L. (1988): Neodymium isotope similarities between the Yukon-Tanana terrane, Yukon Territory and continental North America.- *Geol.Soc.Am.Abstr. Programs* **20**, p. A111.

Berckhemer, H. (1990): Grundlagen der Geophysik.- Wissenschaftliche Buchgesellschaft, Darmstadt, 201 p.

Berg, H.C. & Jones, D.L. (1974): Ophiolite in southeastern Alaska.-*Geol.Soc.Am.Abstr. Programs* **6**, p. 144.

Berg, H. C., Elliott, R. L., Smith, J. G. & Koch, R. D. (1978): New Geological Map of Ketchikan and Prince Rupert quadrangles, southeastern Alaska.- *in:* Johnson, K. M. (ed.): The United States Geological Survey in Alaska. Accomplishments during 1977.- *U.S.Geol.Surv.Circular* **772-B**, pp. 82-83.

Berman, R. G. (1991): Thermobarometry using multiequilibrium calculations: a new technique,

with petrologic applications.- *CanMineral.* **29**, pp. 833-855.

Berman, R. G. (1996): TWQ (version 2.02).

Berman, R. G. & Aranovich, L. Y. (1996): Optimized standard state and mixing properties of minerals: I. Model calibration for olivine, orthopyroxene, cordierite, garnet, and ilmenite in the system FeO-MgO-CaO-Al_2O_3-TiO_2-SiO_2.- *Contrib.Min.Petrol.* **126**, pp. 1-24.

Berthé, D., Choukroune, P. & Jegouzo, P. (1979): Orthogneiss, mylonite and non coaxial deformation of granites: the example of the South Armorican Shear Zone.- *J.Struct.Geol.* **1**, pp. 31-42.

Bhatia, M. R. (1985): Rare earth elements geochemistry of Australian Paleozoic graywackes and mudrocks: Provenance and tectonic control.- *Sediment.Geol.* **45**, pp. 97-113.

Bhatia, M. R. & Crook, K. A. W. (1986): Trace element characteristics of graywackes and tectonic setting discrimination of sedimentary basins.- *Contrib.Mineral.Petrol.* **92**, pp. 181-193.

Bostock, H. S. (1966): Notes on glaciation in central Yukon Territory.- *Geol.Surv. Can.Paper* **65-36**, 18p.

Bowring, S. A. & Podosek, F. A. (1989): Nd isotopic evidence from the Wopmay Orogen for 2.0 - 2.4 Ga crust in western North America.-*EarthPlanet.Sci.Let.* **94**, pp. 217-230.

Bremner, T. (1990): Dezadeash map-area (NTS 115 A).- *in:* Morison, S. R. (ed.): Yukon Exploration 1989.- *Indian and Northern Affairs Canada*, pp. 97-99.

Brew, D. A. & Drew, L. J., Schmidt, L. M., Root, D. H. & Huber, D. F. (1991): Undiscovered locatable mineral resources of the Tongass National Forest and adjacent areas, southeastern Alaska.- *U.S.Geol.Surv.Open-File Report* **91-10**, 370 p.

Brew, D. A. & Ford, A. B. (1984): The northern Coast plutonic metamorphic complex, southeastern Alaska and northwestern British Columbia.- *in:* Conrad, W. L. & Elliott, R. L. (ed.): The United States Geological Survey in Alaska. Accomplishments during 1981.- *U.S.Geol.Surv. Circular* **886**, pp. 120-124.

Brew, D. A. & Ford, A. B. (1993): The Coast Plutonic-Metamorphic Complex between Skagway, Alaska, and Fraser, British Columbia - Geologic sketch and road log.- *in:* Johnston, S. T., Hart, C. J. R., Mihalynuk, M. G., Brew, D. A. & Ford, A. B. (ed.): The Northern Intermontane Superterrane.- fieldguide to 1993 NUNA conference, Lakeview Marina, Marsh Lake, Yukon, August 22-28, 1993, pp. 1-19.

Brew, D. A., Ford, A. B. & Garwin, S. L. (1985): Fossiliferous middle and (or) upper Triassic rocks within the Coast Plutonic Complex, southeast of Skagway.- *in:* Bartsch-Winkler, S. (ed.): The United States Geological Survey in Alaska. Accomplishments during 1984.- *U.S.Geol.Surv. Circular* **967**, pp. 86-89.

Brew, D. A. & Grybeck, D. (1984): Geology of the Tracy Arm - Ford Terror Wilderness Study Area and Vicinity, Alaska.- *in:* Mineral Resources of the Tracy Arm - Ford Terros Wilderness Study Area and Vicinity, Alaska.- *U.S.Geol.Surv.Bull.* **1525-A**, pp. 23-52.

Brew, D.A., Himmelberg, G.R., Loney, R.A. & Ford, A.B. (1992): Distribution and characteristics of metamorphic belts in the south-eastern Alaska part of the North American Cordillera- *J.metamorphic Geol.* **10**, pp. 465-482.

Bucher, W. H. (1944): The stereographic projection, a handy tool for the practical geologist.- *J.Geol.* **52**, pp. 191-212.

Bucher, K & Frey, M. (1994): Petrogenesis of Metamorphic Rocks.- 318 p., Springer-Verlag.

Cairnes, D. D. (1914): Geology of a portion of the Yukon-Alaska boundary, between Porcupine and Yukon rivers.- *Geological Survey Department of Mines Summary Report* **1912**, pp. 9-11.

Chatterjee, N. D. & Froese, E. F. (1975): A thermodynamic study of the pseudobinary join muscovite-paragonite in the system $KAlSi_3O_8$-$NaAlSi_3O_8$-AlO_3-SiO_2-H_2O.- *Am.Mineral.* **60**, pp. 985-993.

Clague, J.J. (1979): The Denali Fault system in southwest Yukon Terrritory - a geologic hazard?- *Current Research, Part A, Geol.Surv.Can.* Paper **79-1A**, pp. 169 - 178.

Clague, J. J. (1991): Structural Styles, Chapter 17.- *in:* Gabrielse, H., Yorath, C. J. (eds.): Geology of the Cordilleran Orogen in Canada, The Geology of Canada, no.4.- *Geol.Sur.Can.*, pp. 571-675.

Cockfield, W. E. (1927): Aishihik Lake District, Yukon.- *Geol.Surv.Can. Summary Report* **1926 A**, pp. 1A-13A, with accompanying map 2124.

Csejtey, B., Cox, D.P & Evarts, R.C. (1982): The Cenozoic Denali Fault System and the Cretaceous Accretionary Development of Southern Alaska.- *J.Geophys.Res.* **87**, pp. 3741-3754.

Creaser, R. A., Erdmer, P., Stevens, R. A. & Grant, S. L. (1997): Tectonic affinity of Nisutlin and Anvil assemblage strata from the Teslin Tectonic Zone, northern Canadian Cordillera: constraints from Neodymium isotope and geochemical evidence.- *Tectonics* **16**, pp. 107-121.

Davidson, C. (1989): The Maclaren Glacier metamorphic belt, south-central Alaska: a tectonometamorphic signature of the accretion of Wrangellia to the North American continent.- *Geol.Soc.Am.Abstr.Programs* **21**, p. A181.

Davidson, C., Hollister, L. S. & Schmid, S. M. (1992): Role of melt in the formation of a deep-crustal shear zone: the Maclaren metamorphic belt, south central Alaska.- *Tectonics* **11**, pp. 348-359.

DePaolo, D. J. (1981): Neodymium isotopes in the Colorado Front Range and crust mantle evolution in the Proterozoic.- *Nature* **291**, pp. 193-196.

DePaolo, D. J. (1988): Neodymium Isotope Geochemistry.- Springer-Verlag, Berlin, 187 p.

DePaolo, D. J. & Wasserburg, G.J. (1976): Neodymium isotopic variations and petrogenetic models.- *Geophys.Res.Letters* **3**, pp. 249-252.

Dodds, C. J. (1991): Denali Fault System.- in Gabrielse, H. (Comp.): Structural Styles. Chapter 17.- *in:* Gabrielse, H., Yorath, C.J. (eds.): Geology of the Cordilleran Orogen in Canada, The Geology of Canada, no.4.- *Geol.Sur.Can.*, pp. 573-674.

Dodds, C. J. & Campbell, R. B. (1992): Geology of NE Yakutat (114O) and Tatshenshini River (114P) map areas, British Columbia.- *Geol.Sur.Can.Open File* **2191**.

Eisbacher, G. H. (1976): Sedimentology of the Dezadeash flysch and its implications for strike-slip faulting along the Denali Fault, Yukon Territory and Alaska.- *Can.J.EarthSci.* **13**, pp. 1495-1513.

Eisbacher, G. H. & Hopkins, S. L. (1977): Mid-Cenozoic Paleogeomorphology and tectonic setting of the St. Elias Mountains, Yukon Territory.- *Geol.Surv.Can.* Paper **77-1b**, pp. 319-335.

Engebretson, D. C., Kelley, K. P., Burmester, R. F., Russell, R. & Blake, M. C. (1995): North American Plate Interactions Re-revisited.-*Geol.Assoc.Can.Min.Assoc.Can.Abstr.Programs* **20**, p. A 28.

England, P. C. & Thompson, A. B. (1984): Pressure-Temperature-Time Paths of Regional Metamorphism I. Heat Transfer during the Evolution of Regions of Thickened Continental Crust.- *J.Petrol.* **25**, pp. 894-928.

Erdmer, P. (1989): The Nisling Schist in eastern Dezadeash map area, Yukon.- *Current Research, Part E, Geological Survey of Canada*, Paper **89-1E**, pp. 139-144.

Erdmer, P. (1990): Studies of the Kluane and Nisling assemblages in Kluane and Dezadeash map areas, Yukon.- *Current Research, Part E, Geological Survey of Canada*, Paper **90-1E**, pp. 107-111.

Erdmer, P. (1991): Metamorphic terrane east of Denali fault between Kluane Lake and Kusawa Lake, Yukon Territory.- *Current Research, Part A, Geological Survey of Canada*, Paper **91-1A**, pp. 37-42.

Erdmer, P. & Mortensen, J. K. (1993): A 1200-km-long Eocene metamorphic-plutonic belt in the northwestern Cordillera: Evidence from southwest Yukon.- *Geology* **21**, pp. 1039-1042.

Ernst, W. G. (1988): Tectonic history of subduction zones inferred from retrograde blueschist P-T path.- *Geology* **16**, pp. 1081-1084.

Eskola, P. (1915): On the relation between chemical and mineralogical composition in the metamorphic rocks in the Orijavi region.- *Bull.Comm.Geol. de Finlande* **44**, pp. 67-225.

Evenchick, C. A. (1995): Structural evidence of Early Cretaceous sinistral displacement in the Northern Canadian Cordillera.– *GAC/MAC Program with Abstracts* **20**, p A 30.

Farmer, G. L., Barker, F. & Plafker, G. (1987): A Nd and Sr isotopic study of Mesozoic and early Tertiary Granitic rocks in southcentral Alaska.- *Geol.Soc.Am.Abstr.Programs* **19**, p. 376.

Farrar, E., Clark, A. H., Archibald, D. A. & Way, D. C. (1988): Potassium-Argon age of granitoid plutonic rocks, southwest Yukon Territory, Canada. *Isochron/West* **51**, pp. 19-23.

Faure, G. (1986): Principles of isotope geology (2nd edition).- John Wiley & Sons, New York, 589 p.

Feng, R., Kerrich, R. & Maas, R. (1993): Geochemical, oxygen, and neodymium isotope compositions of metasediments from the Abatibi greenstone belt and Pontiac Subprovince, Canada: Evidence for ancient crust and Archean terrrane juxtaposition.- *Geochim.Cosmochim.Acta* **57**, pp. 641-658.

Ferry, J. M. & Spear, F. S. (1978): Experimental Calibration of Partitioning of Fe and Mg between Biotite and Garnet.- *Contrib.Mineral.Petrol.* **66**, pp. 113-117.

Fitzgerald, P.G., Stump, E. & Redfield, T.F. (1993): Late Cenozoic Uplift of Denali and Its Relation to Relative Plate Motion and Fault Morphology.- *Science* **259**, pp. 497 - 499.

Flinn, D. (1962): On folding during three-dimensional progressive deformation.- *Geol.Soc. London Quart.Jour.* **118**, pp. 385-433.

Forbes, R. B., Smith, T. E. & Turner, D.L. (1974): Comparative petrology and structure of the Maclaren, Ruby Range and Coast Range belts: Implications for offset along the Denali fault system.-*Geol.Soc.Am.Abstr.Programs* **6**, p. 177.

Frost, C. D. & Coombs, D. S. (1989): Nd isotope character of New Zealand sediments: Implication for terrane concepts and crustal evolution.- *Am.J.Sci.* **289**, pp. 744-770.

Frost, C. D. & O'Nions, R. K. (1984): Nd evidence for Proterozoic crustal development: the Belt-Purcell Supergroup.- *Nature* **312**, pp. 53-56.

Fuhrman, M. L. & Lindsley, D. H. (1988): Ternary feldspar modelling and thermometry.- *Am.Mineral.* **73**, pp. 201-216.

Gabrielse, H., Monger, J. H. W., Wheeler, J. O. & Yorath, C. J. (1991): Part A. Morphogeological belts, tectonic assemblages and terranes.- *in:* Chapter 2 of Gabrielse, H., Yorath, C. J. (eds.): Geology of the Cordilleran Orogen in Canada, The Geology of Canada, No. 4- *Geol.Sur.Can.*, pp. 15-28.

Gabrielse, H. & Yorath, C. J. (1991): Tectonic Synthesis, Chapter 18.- *in:* Gabrielse, H., Yorath, C. J. (eds.): Geology of the Cordilleran Orogen in Canada, The Geology of Canada, No. 4- *Geol.Sur.Can.*, pp. 679-705.

Gehrels, G. E., McClelland, W. C., Samson, S. D, & Patchett, J. P. (1991a): U-Pb geochronology of detrital zircons from a continental margin assemblage in the northern Coast Mountains, southeastern Alaska.- *Can.J.Earth Sci.* **28**, pp. 1285-1300.

Gehrels, G. E., McClelland, W. C., Samson, S. D, Patchett, J. P. & Brew, D. A. (1991b): U-Pb geochronology of Late Cretaceous and early Tertiary plutons in the northern Coast Mountains batholith.- *Can.J.Earth Sci.* **28**, pp. 899-911.

Gehrels, G. E., McClelland, W. C., Samson, S. D., Patchett, J. P. & Orchard, M. J. (1992): Geology of the western flank of the Coast Mountains between Cape Fanshaw and Taku Inlet, southeastern Alaska.- *Tectonics* **11**, pp. 567-585.

Geological Survey of Canada (1969): Kluane Lake, Yukon Territory.- *Can.Geol.Surv.Geophys. Paper* **7827**.

Ghent, E. D. (1976): Plagioclase-garnet-Al_2SiO_5-quartz: a potential geobarometer-geothermometer.- *Am.Mineral.* **61**, pp. 710-714.

Goldstein, S. L., O'Nios, R. K. & Hamilton, P. J. (1984): A Sm-Nd isotopic study of atmospheric dusts and particles from major river systems.- *Earth.Planet.Sci.Let.* **70**, pp. 221-236.

Grybeck, D., Brew, D. A., Johnson, B. R. & Nutt, C. J. (1977): Ultramafic rocks in part of the Coast Range batholitic complex, southeastern Alaska.- *in:* Accomplishment in Alaska 1976, *US Geol.Surv. Circular* **751B**, pp. B82-85.

Hanmer, S. & Passchier, C. W. (1991): Shear-sense indicators: a review.- *Geol.Surv.Can. Pap.* **90-17**, 72 p.

Hart, C. J. R. (1993): B.C. - Yukon Border to Carcross to Alaska Highway.- Nuna '93 filed log, Day One, Leg C.- *in:* Johnston, S. T., Hart, C. J. R., Mihalynuk, M. G., Brew, D. A. & Ford, A. B. (ed.): The Northern Intermontane Superterrane.- fieldguide to 1993 NUNA conference, Lakeview Marina, Marsh Lake, Yukon, August 22-28, 1993, pp. 31-41.

Heaman, L. & Parrish, R. (1991): U-Pb geochronology of accessory minerals.- *in:* Heaman L. & Ludden, J. N. (ed.): Short course handbook on applications of radiogenic isotope systems to problems in geology.- *Min.Assoc.Can* **19**, pp. 103-166.

Himmelberg, G. R., Ford, A. B. & Brew, D. A. (1984): Progressive metamorphism of pelite rocks in the Juneau area, southeastern Alaska.- *in:* Conrad, W. L. & Elliott, R. L. (ed.): The United States Geological Survey in Alaska. Accomplishments during 1981.- *U.S.Geol.Surv.Circular* **886**, pp. 131-134.

Himmelberg, G. R., Brew, D. A. & Ford, A. B. (1985): Ultramafic bodies in the Coast plutonic-metamorphic complex near Skagway, southeastern Alaska.- *in:* Accomplishment in Alaska 1984, *US Geol.Surv. Circular* **967**, pp. 92-93.

Hoeppener, R. (1955): Tektonik im Rheinischen Schiefergebirge: Eine Einführung.- *Geol.Rdsch.* **44**, pp. 26-58.

Hoffman, S. E., Wilson, M. & Stakes, D.S. (1986): Inferred oxygen isotope profile of Archaean oceanic crust, Onverdacht Group, South Africa.- *Nature* **321**, pp. 55-58.

Holdaway, M. J. & Lee, S. M. (1977): Fe-Mg Cordierite Stability in High Grade Pelitic Rocks Based on Experimental, Theoretical, and Natural Observations.- *Contrib.Mineral.Petrol.* **63**, pp. 175-198.

Holdaway, M. J. & Mukhopadhyay, B. (1993): A reevaluation of the stability relations of

andalusite: thermochemical data and phase diagram for the aluminium silicates.- *Am.Mineral.* **78**, pp. 298-315.

Hollister, L. S., Andronicos, C., Crawford, M., L., Davidson, C. M., Klepeis, K. A. & Rusmore, M. E. (1997): Geological data cannot rule out large scale (>1000 km) transcurrent motion across the Coast orogen.- *in:* Cook, F. & Erdmer, P. (comp.): 1997, Slave-Northern Cordillera Lithospheric Evolution (SNORCLE) Transect and Cordilleran Tectonics Workshop Meeting (March 7-9), University of Calgary, *Lithoprobe Report* No. **56**, pp. 155-159.

Hooper, P. R., Johnson, D. M. & Conrey, R. M. (1993): Major and trace element analyses of rocks and minerals by automated X-ray spectrometry.- Washington State University, Open File Report, 36 p.

Horner, R. B. (1983): Seismicity in the St. Elias region of northwestern Canada and southeastern Alaska.- *Bulletin of the Seismological Society of America* **73**, pp. 1117-1137.

Hudson, T., Plafker, G. & Dixon, K. (1982): Horizontal offset history of the Chatham Strait fault.- *US Geol.Surv.Circular* **844**, pp. 128 - 132.

Irving, E., Wynne, P. J., Thorkelsen, D. J. & Schiarizza, P. (1996): Large (1000 to 4000 km) northward movements of tectonic domains in the northern Cordillera, 83-45 Ma.- *J.Geoph.Res.* **101**, pp. 17901-17916.

Jackson, J. L., Gehrels, G. E, Patchett, P. J. & Mihalynuk, M. G. (1991): Stratigraphic and isotopic link between the northern Stikine terrane and an ancient continental margin assemblage, Canadian Cordillera.- *Geology* **19**, p. 1177-1180.

Jones, D.L., Silberling, N. J., Csejtey, Jr., B., Nelson, W. H. & Blome, C.D. (1980): Age and Structural Significance of Ophiolite and Adjoining Rocks in The Upper Chulitna District, South-central Alaska.- *US Geol.Surv.Prof.Pap.* **1121-A**, 21 p.

Johnston, S. T. (1993): The geologic evolution of Nisling assemblage and Stikine terrane in the Aishihik Lake area, southwest Yukon.- Ph.D. dissertation, Univ. of Alberta, Edmonton, 270 p.

Johnston, S. T. & Erdmer, P. (1995a): Hot-side-up aureole in southwest Yukon and limits on

terrane assembly of the northern Canadian Cordillera.- *Geology* **23**, pp. 419-422.

Johnston, S. T. & Erdmer, P. (1995b): Magmatic Flow and Emplacement Foliations in the Early Jurassic Aishihik Batholith, Southwest Yukon.- *in:* Miller, D. M. & Busby, C.: Jurassic Magmatism and Tectonics of the North American Cordillera.- *Geol.Soc.Amer.Spec.Pap.* **299**, pp. 65-82.

Johnston, S. T., Mortensen, J. K. & Erdmer, P. (1996): Igneous and metaigneous age constraints for the Aishihik metamorphic suite, southwest Yukon.- *Can.J.EarthSci.* **33**, pp. 1543-1555.

Johnston, S. T. & Timmerman, J. R. (1993a): Geology of the Aishihik Lake and Hopkins Lake Map areas (115 H6/7), southwestern Yukon.- *Yukon Exploration & Geology* **1993**, pp. 93-110.

Johnston, S. T. & Timmerman, J. R. (1993b): Geological Map of the Aishihik Lake area (115 H6).- *Exploration and Geological Services Division, Yukon, Indian and Northern Affairs Canada, Open File* **1994-1 (G)**.

Kindle, E.D. (1952): Dezadeash map-area, Yukon Territory.- *Geological Survey of Canada Memoir* **268**, 68 p.

Karig, D. E. (1974): Evolution of arc systems in the western Pacific. - *Ann.Rev. Earth Planet.Sci.* **2**, pp. 51-76.

Karig, D. E. (1982): Deformation in the forearc: implications for mountain belts.- *in:* Hsü, K. J. (ed.): Mountain Building Processes.- pp. 59-71. Academic Press, London.

Karig, D. E. & Sharman, G. F. (1975): Subduction and accretion in trenches.- *Bull.Geol.Soc. Am.* **86**, pp. 377-389.

Kohn, J. M. & Spear, F. S. (1991a): Error propagation for barometers: 1. Accuracy and precision of experimentally located end-member reactions.- *American Mineralogist* **76**, pp. 128-137.

Kohn, J. M. & Spear, F. S. (1991b): Error propagation for barometers: 2. Application to rocks.-

American Mineralogist **76**, pp. 138-147.

Le Couteur, P. C. & Tempelman-Kluit, D. J. (1976): Rb/Sr Ages and a profile of initial Sr $^{87}/Sr^{86}$ ratios for plutonic rocks across the Yukon Crystalline Terrane.- *Can.J.EarthSci.* **13**, pp. 319-330.

Loney, R. A. (1964): Stratigraphy and petrography of the Pybus-Gambier area, Admirality Island, Alaska.- *US Geol.Surv.Bull.* **1779**, 17 p.

Lowdon, J. A. (ed.) (1960): Age determinations by the Geological Survey of Canada, report 1- Isotopic Ages.- *Geological Survey of Canada*, Paper **60-17**, 51 p.

Lowe, C., Horner, R. B., Mortensen, J. K., Johnston, S. T. & Roots, C. F. (1994): New geophysical data from the northern Cordillera: preliminary interpretations and implications for the tectonics and deep geology.- *Can.J.EarthSci.* **31**, pp. 891-904.

Lowey, G. W. (1992): Variation in bed thickness in a turbidite succession, Dezadeash Formation (Jurassic-Cretaceous), Yukon, Canada: evidence of thinning-upward and thickening-upward cycles.- *Sedimentary Geology* **78**, pp. 217-232.

Makashima, A. & Nakamura, E. (1991): Calibration of Farady cup efficiency in a multicollector mass spectrometer.- *Chem.Geol.* **94**, pp. 105-110.

Marcantonio, F., Reisberg, L., Zindler, A., Wyman, D. & Hulbert, L. J. (1993): An isotopic study of the Ni-Cu-PGE-rich Wellgreen intrusion of the Wrangellia terrane: evidence for hydrothermal mobilization of Re and Os.- *Geochim.Cosmochim. Acta* **55**, pp. 1007-1017.

McConnell, R. G. (1905): The Kluane Mining District.- *Geol.Surv.Can. Annual Report* **16**, pp. 1A-18A.

McClelland, W. C., Anowitz, L. M. & Gehrels, G. E. (1991): Thermobarometric constraints on the structural evolution of the Coast Mountains batholith, central southeastern Alaska.- *Can.J.EarthSci.* **28**, pp. 912-928.

McClelland, Gehrels, G. E., Samson, S. D. & Patchett, P. J. (1992): Structural and geochronologic relations along the western flank of the Coast Mountains batholith: Stikine

River to Cape Fanshaw, central southeastern Alaska.- *J.Struct.Geol.* **14**, pp. 475-489.

McCulloch, M. T. & Wasserburg, G. J. (1978): Sm-Nd and Rb-Sr chronology of continental crust formation.- *Science* **200**, pp. 1003-1011.

McLennan, S. M. & Hemming, S. (1992): Samarium/neodymium elemental and isotopic systematics in sedimentary rocks.- *Geochim.Cosmochim. Acta* **56**, pp. 887-898.

Mezger, J. E. (1995): The Kluane Metamorphic Assemblage, SW Yukon - first steps towards developing a tectonic model.- *Cordilleran Tectonics Workshop Meeting 1995, Ottawa-Carleton Geoscience Centre, February 10-12, 1995*, p 11.

Mezger, J. E. & Creaser, R. A. (1996): Backarc basin setting of the Kluane Metamorphic Assemblage and sinistral strike-slip along a proto-Denali fault: Evidence from isotope and microtectonic studies in the SW Yukon.- *Geol.Soc.Amer.Abstr.Programs.* **28 (7)**. p. A 312.

Monger, J. W. H., Price, R. A. & Templeman-Kluit, D. J. (1982): Tectonic accretion and the origin of the two major metamorphic and plutonic welts in the Canadian Cordillera.- *Geology* **10**, pp. 70-75.

Monger, J. W. H., Wheeler, J. O., Tipper, H. W., Gabrielse, H., Harms, T., Struik, L. C., Campbell, R. B., Dodds, C. J., Gehrels, G. E. & O'Brien, J. (1991): Part B. Cordilleran terranes.- *in:* Upper Devonian to Middle Jurassic assemblages, Chapter 8 *in:* Gabrielse, H., Yorath, C. J. (eds.): Geology of the Cordilleran Orogen in Canada, The Geology of Canada, no.4.- *Geol.Sur.Can.*, pp. 281-327.

Monger, J. W. H., van der Heyden, P., Journeay, J. M., Evenchick, C. A. & Mahoney, J. B. (1994): Jurassic-Cretaceous basins along the Canadian Coast Belt: Their bearing on pre-mid-Cretaceous sinistral displacements.- *Geology* **22**, pp. 175-178.

Moore, J. C. (1989): Tectonics and hydrogeology of accretionary prisms: role of décollement zone.- *J.Struct.Geol.* **11**, pp. 95-106.

Mortensen, J. K. (1992): Pre-mid-mesozoic tectonic evolution of the Yukon-Tanana terrane, Yukon and Alaska. *Tectonics* **11**, No.4, pp. 836-853.

Mortensen, J. K. & Erdmer, P. (1992): U-Pb, Ar-Ar and K-Ar Ages for Metamorphism of the Kluane and Aishihik Assemblages in Southwestern Yukon.- *Radiogenic Age and Isotopic Studies; Report 6; Geological Survey of Canada*, Paper **92-2**, pp. 135-139.

Muehlenbachs, K. (1986): Alteration of the Oceanic Crust and the ^{18}O History of Seawater.- *in:* Valley et al. (ed.): Stable Isotopes in High Temperature Geological Processes.- *Min.Soc.Am. Reviews in Mineralogy* **16**, pp. 425-444.

Muller, J. E. (1953a): Preliminary map Kluane Lake (West Half), Yukon Territory (Descriptive Notes).- *Geological Survey of Canada*, Paper **53-20**, pp. 1-9.

Muller, J. E. (1953b): Kluane Lake map-area, Yukon Territory.- *Geological Survey of Canada*, Paper **58-9**, pp. 1-9, with accompanying map 19-1958.

Muller, J. E. (1958): Tectonics of the Shakwak lineament, southwest Yukon and eastern Alaska.- *Bull.Geol.Soc.Am.* **69**, pp. 1619-1620.

Muller, J. E. (1967): Kluane lake map-area, Yukon Territory (115G, 115F E1/2). *Geological Survey of Canada Memoir* **340**, 137 p.

Nokleberg, W.J., Foster, H. L. & Aleinikoff, J.N. (1989): Geology Of The Northern Copper River Basin, Eastern Alaska Range, and Southern Yukon-Tanana Upland.- *in:* Sedimentation and Tectonics of Western North America, Vol.1. Proceedings from the 28th International Geological Congress.

Nokleberg, W. J., Jones, D. L. & Silberling, N. J. (1985): Origin and tectonic evolution of the Maclaren and Wrangellia terranes, eastern Alaska, Alaska.- *Bull.geol.Soc.Am.* **96**, pp. 1251-1270.

Norrell, G. T., Teixell, A. & Harper, G. D. (1989): Microstructure of serpentine mylonites from the Josephine ophiolite and serpentinization in retrogressive shear zones, California.- *Geol.Soc. Am.Bull.* **101**, pp. 673-682.

Page, R. A. & Plafker, G. & Puplan, H. (1995): Block rotation in east-central Alaska: A framework for evaluating earthquake potential? - *Geology* **23**, pp. 629-632.

Pangaea Scientific (1995): SpheriStat 2.0 for Windows 3.1 manual.- 198 p.

Passchier, C. W & Trouw, R. A. J. (1996): Microtectonics- Springer, Berlin, 289 p.

Patton, W. W., Box, S.E. & Grybeck, D. J. (1994): Ophiolites and other mafic-ultramafic complexes in Alaska.- *in:* Plafker, G. & Berg, H. C. (ed.): The Geology of Alaska.- *Geol.Soc.Amer. The Geology of North America* **G-1**, pp. 671-686.

Pettijohn, F. J., Potter, P. E. & Siever, R. (1987): Sand and sandstone, 2nd edition.- Springer Verlag, 553 p.

Plafker, G., Nokleberg, W.J. & Lull, J.S. (1989): Bedrock geology and tectonic evolution of Wrangellia, Peninsular, and Chugach terranes along the Trans-Alaska Crustal Transect in the Chugach Mountains and Southern Copper River Basin, Alaska..-*J.Geophys.Res.* **94**, pp. 4255 - 4295.

Platt, J. P. (1986): Dynamics of orogenic wedges and uplift of high-pressure metamorphic rocks.- *Geol.Soc.Amer.Bull.* **97**, pp. 1037-1053.

Powell, R. & Holland, T. (1990): Calculated mineral equilibria in the pelite system, KFMASH (K_2O - FeO - MgO - Al_2O_3 SiO_2 - H_2O).- *Am.Mineral.* **72**, pp. 255-272.

Ramsey, J. G. (1967): Folding and fracturing of rocks.- McGraw-Hill, New York, 568 p.

Reed, B. L. & Lanphere, M. A. (1974): Offset Plutons and History of Movement along the McKinley Segment of the Denali Fault System, Alaska.- *Bull.Geol.Soc.Am.* **85**, pp. 1883-1892.

Richardson, S.W., Gilbert, M. C. & Bell, P.M. (1969): Experimental determination of kyanite-andalusite and andalusite and sillimanite equilibria: the aluminium silicate triple point.- *Amer.J.Sci.* **266**, pp. 259-272.

Richter, D.H. & Matson, N.A. (1971): Quarternary Faulting in the Eastern Alaska Range.- *Bull.Geol.Soc.Am.* **82**, pp. 1529 - 1540.

Ridgway, K. D., DeCelles, P. G., Cameron, A. R. & Sweet, A. R. (1992): Cenozoic syntectonic

sedimentation and strike-slip basin development along the Denali fault system, Yukon Territory.- *Yukon Geology* **3**, *Exploration and Geological Services Division, Yukon, Indian and Northern Affairs Canada*, pp. 1-26.

Rosenbusch, H. (1877): Die Steiger Schiefer und ihre Contactzone an den Graniten von Barr-Andlau und Hohwald.- *Abh.Geol. Specialkarte Elsass-Lothr.* **1**, pp. 79 - 393.

Ross, G. M., Boghossian, N. D., Patchett, P. J. & Gehrels, G. E. (1995): Where did all that mud come from? Provenance evolution of the Cordilleran miogeocline from neodymium isotope system studies.- *Cordilleran Workshop, Carleton University, Program with Abstracts*, p. 12.

Rubie, D. C. (1984): A thermal-tectonic model for high-pressure metamorphism and deformation in the Sesia Zone, Western Alps.- *J.Geol.* **92**, pp. 21-36.

Rubin, C.M., Saaleby, J.B., Cowan, D.S, Brandon, M.T. & McGroder, M.F. (1990): Regionally extensive mid-Cretaceous west-vergent thrust system in the northwestern Cordillera: Implications for continent-margin tectonism.- *Geology* **18**, pp. 276 - 280.

Samson, S. D., McClelland, W.C., Patchett, P. J., Gehrels, G. E. & Anderson, R. G. (1989): Evidence from neodymuim isotopes for mantle contributions to Phanerozoic crustal genesis in the Canadian Cordillera.- *Nature* **337**, pp. 705-709.

Samson, S. D., McClelland, W.C., Patchett, P. J., Gehrels, G. E. & Anderson, R. G. (1990a): A detailed isotope investigation of the Taku and Yukon Crystalline terranes SE Alaska: Ancient continental material between juvenile crust of the Canadian Cordillera.- *Geol.Assoc.Can.Min.Assoc.Can.Abstr. Programs* **15**, p. 117.

Samson, S. D., Patchett, P. J., Gehrels, G. E. & Anderson, R. G. (1990b): Nd and Sr isotopic characterization of the Wrangellia Terrane and implications for crustal growth of the Canadian Cordillera.- *J.Geol.* **98**, pp. 749-762.

Samson, S. D., Patchett, P. J., McClelland, W.C. & Gehrels, G. E. (1991a): Nd and Sr isotopic constraints on the petrogenesis of the west side of the northern Coast Mountains batholith, Alaskan and Canadian Cordillera.- *Can.J.EarthSci.* **28**, pp. 939-946.

Samson, S. D., McClelland, W.C., Patchett, P. J. & Gehrels, G. E. (1991b): Nd isotopic

characterization of metamorphic rocks in the Coast Mountains, Alaskan and Canadian Cordillera: ancient crust bounded by juvenile terranes.- *Tectonics* **10**, pp. 770-780.

Schmidt, W. (1925): Gefügestatistik.- *Tschermaks miner.petrogr.Mitt.* **30**, pp. 392-423.

Souther, J. G. (1991): Volcanic Regimes.- Chapter 14 *in:* Gabrielse, H., Yorath, C. J. (eds.): Geology of the Cordilleran Orogen in Canada, The Geology of Canada, no.4.- *Geol.Sur.Can.*, pp. 475-490.

Spear, F. S. (1993): Metamorphic Phase Equilibria and Pressure-Temperature-Time Paths.- *Mineral.Soc.Amer.Monograph*, 799 p.

Spear, F. S. & Cheney, J. T. (1989): A petrogenitic grid for pelitic schists in the system SiO_2 - Al_2O_3 - FeO - MgO - K_2O - H_2O.- *Contrib.Mineral.Petrol.* **101**, pp. 149-164.

Spry, A. (1969): Metamorphic Textures.- Pergamon (Oxford), 350 p.

Stanley, W.D., Labson, V.F., Nokleberg, W.J., Csejtey, B. & Fisher, M.A. (1990): The Denali fault system and Alaska Range of Alaska: Evidence for underplated Mesozoic flysch from magnetotelluric surveys.- *Bull.Geol.Soc.Am.* **102**, pp. 160-173.

Stevens, R. A. (1994): Structural and tectonic evolution of the Teslin tectonic zone, Yukon: a doubly-vergent transpressive shear zone.- Ph.D. dissertation, Univ. of Alberta, Edmonton, 252 p.

Stevens, R. A., Delabio, R. N. & Lachance, G. R. (1982): Age determinations and geological studies - K-Ar Isotopic Ages, Report 16.- *Geological Survey of Canada*, Paper **82-2**, pp. 15-26.

Stout, J.H. & Chase, C.G. (1980): Plate Kinematics of the Denali fault system.- *Can.J.EarthSci.* **17**, pp. 1527 - 1537.

Sturrock, D. L., Armstrong, R. L. & Maxwell, R. B. (1980): Age and Sr isotopic composition of the Pyroxenite Creek Ultramafic Complex, southwestern Yukon Territory: An Alaskan-type ultramafic intrusion.- *Geol.Surv.Can.*, Paper **80-1B**, pp. 185-188.

Taylor, H.P. (1967): The zoned ultramafic complexes of southeastern Alaska.- *in:* Wyllie, P. J. (ed.): Ultramafic and related rocks.- John Wiley and sons, New York, p. 96-116.

Taylor, S. R. & McLennan, S. M. (1985): The Continental Crust: its Composition and Evolution.- Blackwell Scientific Publications, Oxford, 312 p.

Tempelman-Kluit, D. J. (1974): Reconaissance geology of Aishihik Lake, Snag and part of Stewart River map-areas, west-central Yukon (115A, 115F, 115G and 115K).- *Geological Survey of Canada*, Paper **73-41**, 97 p.

Tempelman-Kluit, D. J. (1980): Evolution of physiography and drainage in southern Yukon.- *CanJ.EarthSci.* **17**, pp. 1189-1203.

Tempelman-Kluit, D. J. & Currie, R. (1978): Reconnaissance rock geochemistry of Aishihik Lake, Snag and Stewart River map-areas in the Yukon crystalline terrane.- *Geol.Surv.Can. Paper* **77-8**, 72 p.

Tempelman-Kluit, D.J. & Wanless, .K. (1975): Potassium-Argen Age Determinations of Metamorphic and Plutonic Rocks in the Yukon Crystalline Terrane.- *CanJ.EarthSci.* **12**, pp. 1895-1909.

Thériault, R. J. & Ross, G. M. (1991): Nd -isotopic evidence for crustal recycling in the 2.0 Ga subsurface of western Canada.- *Can.J.EarthSci.* **28**, pp. 1140-1147.

Thirlwall, M. F. (1982): A triple-filament method for rapid and precise analyses of rare-earth elements by isotope dilution.- *Chem.Geol.* **35**, pp. 155-166.

Thirlwall, M. F. (1991): Long-term reproducibility of multicollector Sr and Nd isotope ratio analyses.- *Chem.Geol.* **94**, pp. 85-104.

Thompson, A. B. (1976): Mineral reactions in pelitic rocks II: Calculations of some P-T-X (Fe-Mg) phase relations.- Am.J.Sci. 276, pp. 425-454.

Tilley, C. E. (1924): The facies classification of metamorphic rocks.- *Geol.Mag.* **61**, pp. 167-171.

Turner, D. L., Smith, T. E. & Forbes, R. B. (1974): Geochronology of offset along the Denali fault system in Alaska.- *GSA abstracts with program* **6**, pp. 268-269.

Twiss, R. J. & Moores, E. M. (1992): Structural Geology.- 532 p., W.H. Freeman and Company, New York.

van Heyden, P. (1992): A middle Jurassic to Eary Tertiary Andean-sierran arc model for the Coast belt of British Columbia.- *Tectonics* **11**, pp. 82 - 97.

Wahrhaftig, C., Turner, D.L., Weber, F.R. & Smith, T.E. (1975): Nature and timing of movements on Hines Creek strand of Denali fault system, Alaska.- *Geology* **3**, pp. 463 - 466.

Wasserburg, G. J., Jacobsen, S. B., DePaolo, D. J., McCulloch, M. T. & Wen, T. (1981): Precise determination of Sm/Nd ratios, Sm and Nd isotopic abundances in standard solutions.- *Geochim.Cosmochim. Acta* **45**, pp. 2311-2323.

Watson, G. S. (1966): The statistics of orientation data.- *Jour.Geol.* **74**, 786-797.

Wheeler, J. O. & McFeely, P. (comp.) (1991): Tectonic Assemblage Map of the Canadian Cordillera, *Geological Survey of Canada*, Map **1712A**, scale 1:2,000,000.

Wheeler, J. O., Brookfield, A. J., Gabrielse, H., Monger, J. H. W., Tipper, H. W. & Woodsworth, G. J. (comp.) (1991): Terrane Map of the Canadian Cordillera, *Geological Survey of Canada*, Map **1713A**, scale 1:2,000,000.

White, J. C. (1997): Deformation Processes Along the Denali Fault System.- *in:* Cook, F. & Erdmer, P. (comp.): 1997, Slave-Northern Cordillera Lithospheric Evolution (SNORCLE) Transect and Cordilleran Tectonics Workshop Meeting (March 7-9), University of Calgary, *Lithoprobe Report* No. **56**, pp. 143-145.

Woodcock, N. H. (1977): Specification of fabric shapes using an eigenvalue method.- *Geol.Soc.Amer.Bull.* **88**, pp. 1231-1236.

Woodsworth, G. J., Anderson, R. G. & Armstrong, R. L. (1991): Plutonic Regimes. Chapter 8 *in:*

Gabrielse, H. & Yorath, C. J. (ed.): Geology of the Cordilleran Orogen in Canada.- *Geological Survey of Canada, Geology of Canada*, **No.4**, pp. 491-531.

Wynne, P. J., Irving, E., , Maxson, J. A. & Kleinsphen, K. L. (1995): Paleomagnetism of the Upper Cretaceous strata of Mount Tatlow: Evidence for 3000 km of northward displacement of the eastern Coast Belt, British Columbia.- *J.Geoph.Res.* **100**, pp. 6703-6091.

Yardley, B. W. D. MacKenzie, W. S. & Guilford, C. (1990): Atlas of metamorphic rocks and their textures.- Longman Scientific & Technical, Harlow, 120 p.

APPENDICES

Appendix 1-1: NTS map index of study area

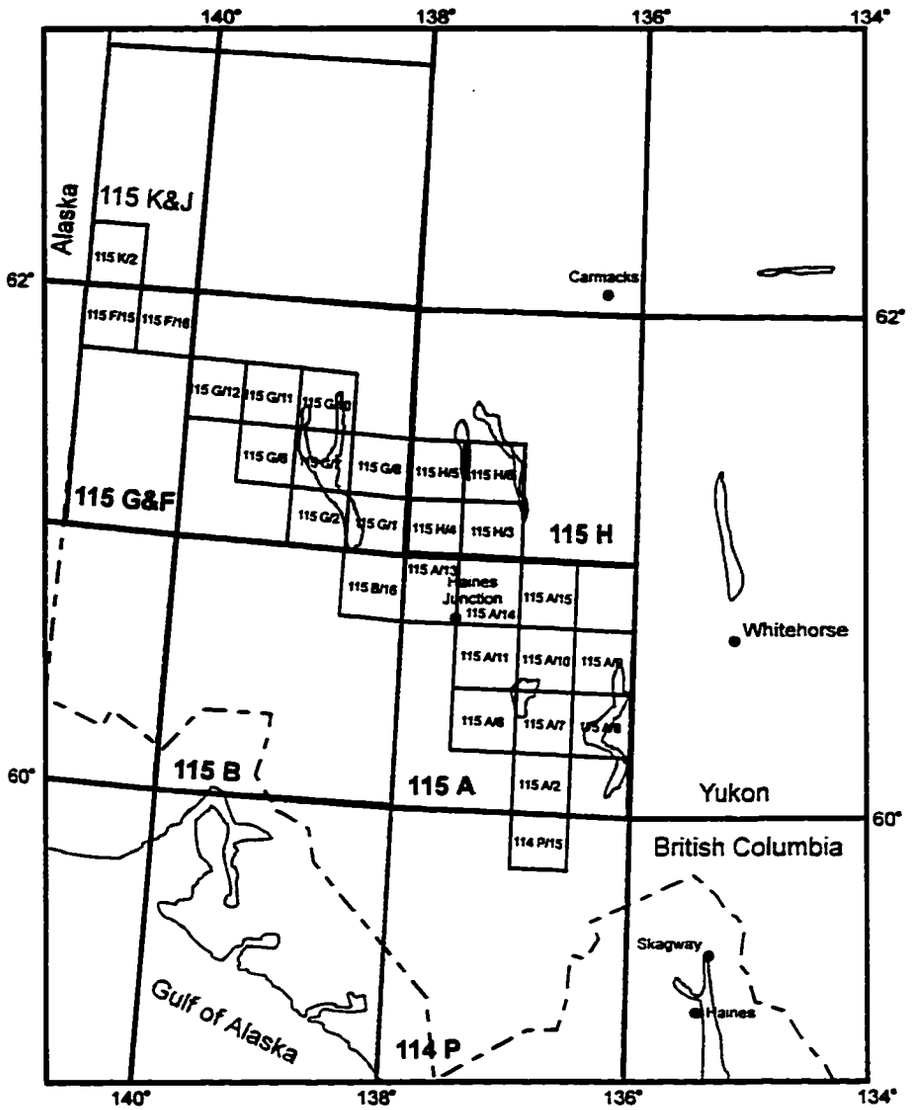

1:250,000

115 A/7	Kluhini River	115 G/2	Congdon Creek	115 G/6	Duke River
114 P	Tatshenshini River	115 A/8	Sandpiper Creek	115 G/7	Burwash Landing
115 A	Dezadeash	115 A/9	Jojo Lake	115 G/8	Gladstone Creek
115 B	Kaskawulsh	115 A/10	Mount Bratnober	115 G/10	Serpenthead Lake
115 G&F	Kluane Lake	115 A/11	Kathleen Lakes	115 G/11	Nuntaea Creek
115 H	Aishihik Lake	115 A/13	Kloo Lake	115 G/12	Lynx Creek
115 K&J	Snag	115 A/14	Canyon	115 H/3	Ittlemit Lake
		115 A/15	Cracker Creek	115 H/4	McKinley Creek
1:50,000		115 B/16	Jarvis River	115 H/5	Sekulmun Lake
114 P/15	Parton River	115 F/15	Canyon Mountain	115 H/6	Aishihik Lake
115 A/2	Takhanne River	115 F/16	Koidern	115 K/2	Dry Creek
115 A/6	Mush Lake	115 G/1	Cultus Creek		

Appendix 2-1: Thin section sample localities and observed mineral phases

Sample	rock type	Long (W) / Lat (N)	major phases (>5 vol%)	minor phases (<5 vol%)
89-32a	1	138°07'10", 61°13'20"	qtz, pl, bt, st	ms, grt, chl, tur, sil, grp
89-33	1	138°06'40", 61°13'50"	qtz, pl, bt, grt	st, sil, ms, tur, and, grp, o
89-34a	1	138°06'15", 61°14'10"	qtz, pl, bt, and, sil	st, grt, grp, tur, ms
89-34d	9	138°06'15", 61°14'10"	pl, hbl, qtz	-
89-36	2	138°07'50", 61°13'00"	qtz, pl, ms	chl, bt, grt, grp, o, tur
89-37	2	138°08'35", 61°12'40"	qtz, pl, chl, ms	bt, tur, grp, grt, czo, o
89-38	2	138°09'30", 61°12'10"	qtz, pl, ms, chl	bt, tur, ap, grp, o
89-39	2	138°09'40", 61°11'50"	qtz, pl, ms, chl	grp, bt, tur, ap, spn
89-40	2	138°10'10", 61°11'35"	qtz, pl, chl, ms	bt, grp, tur, o, czo, ep
89-41a	2	138°10'35", 61°11'20"	qtz, pl, ms, chl	bt, ap, o, czo, ep
89-42	2	138°09'40", 61°10'55"	qtz, pl, ms, chl	bt, grp, tur, o, spn
89-43	2	138°08'20", 61°10'57"	qtz, pl, ms, chl	bt, ap, tur, grp, czo, o, ep
89-44aa	1	138°07'20", 61°13'05"	qtz, pl, bt	ms, st, chl, grt, grp, o, ap
89-45b	1	138°06'30", 61°14'40"	qtz, pl, bt, sil	st, grt, and, crd, ap, tur, grp
89-45c	1	138°06'30", 61°14'40"	qtz, pl, bt	ap, grt, o
89-46a	1	138°06'00", 61°15'10"	qtz, pl, sil	-
89-46b	1	138°06'00", 61°15'10"	qtz, pl, bt	sil, grt, grp, crd, ms, o
89-47	1	138°06'00", 61°15'40"	qtz, pl, bt	ms, grp, crd, tur, st, sil, grt
89-48	1	138°06'00", 61°15'55"	qtz, bt, pl	sil, ms, chl, grt, grp, o
89-49a	1	138°06'15", 61°16'30"	qtz, pl, bt	chl, crd, grt, ms, ap, grp, o
89-49b	5	138°06'15", 61°16'30"	hbl, qtz, pl	chl, o
89-51a	1	138°07'10", 61°17'25"	qtz, pl, bt	ms/ser, sil, grp, o, crd
89-52a	3	138°03'45", 61°11'50"	qtz, act, pl	o
89-52b	2	138°03'45", 61°11'50"	qtz, pl, chl	bt, ms, grt, czo, tur, grp
89-53	1	138°03'00", 61°12'20"	qtz, pl, ms, bt, chl, st	grt, ap
89-55a	9	138°03'00", 61°12'40"	tlc, srp, ol	cal
89-55A	1	138°03'00", 61°12'40"	qtz, pl, bt, st	chl, grt, ap, tur, ms
89-56	1	138°02'35", 61°12'55"	qtz, pl, bt, ms/ser, chl	grt, grp, st, tur
89-57	1	138°01'40", 61°13'15"	qtz, pl, bt	sil, grt, st, grp, o, ms, ap
89-58a	3	138°02'10", 61°13'15"	hbl, pl, qtz	ep, ap
89-59	1	138°02'00", 61°13'40"	qtz, pl, bt, sil	ms, st, grp, grt, o, tur, ap
89-60a	1	138°04'00", 61°15'15"	qtz, pl, bt, sil	ms, st, crd, chl
89-61	1	138°02'45", 61°13'40"	qtz, bt, pl	crd, sil, grp, ms, ap, tur
89-62a	1	138°02'30", 61°15'15"	qtz, pl, bt, sil	grt, ms, chl
89-62b	1	138°02'30", 61°15'45"	qtz, pl, bt	hc, tur, ms, chl, crd, grt
89-63	1	138°02'00", 61°14'55"	qtz, pl, bt	ms, chl, grp, grt, ap, crd, tur
89-64	1	138°02'00", 61°14'30"	qtz, bt, pl, sil	crd, grt, o, grp
89-65	1	138°02'00", 61°14'10"	qtz, pl, bt, sil	crd, grt, st, grp, ap, tur
89-66a	2	138°45'20", 61°15'05"	pl, qtz, ms, chl	grp, tur, aln
89-67a	2	138°44'50", 61°19'50"	qtz, pl, ms, chl	grp, tur, ap, czo
89-68	2	138°45'15", 61°20'25"	qtz, pl, chl, ms	grp, tur, cal
89-69	2	138°46'00", 61°20'20"	qtz, pl, ms, chl, grp	ep, tur, cal
89-72	2	138°47'20", 61°19'00"	qtz, pl, ms, chl	grp, czo, tur, cal
89-73a	2	138°47'40", 61°18'48"	qtz, pl, ms, chl, grp, cal	-
89-74a	2	138°43'03", 61°16'35"	qtz, pl, ms, chl	grp,o, cal
89-75	2	138°42'50", 61°16'05"	qtz, pl, ms, chl	ep, grp, o, tur
89-76a	2	138°42'25", 61°15'55"	qtz, cal, pl, ms, chl	grp, o, tur
89-78a	3	138°38'10", 61°14'30"	act, chl, pl	ep, czo, ap
89-78d	3	138°38'10", 61°14'30"	act, Cr-mica	cal
89-80	3	138°36'30", 61°14'10"	chl, fsp, cal	qtz, ep, czo

Appendix 2-1 (continued):

Sample	rock type	Long (W) / Lat (N)	major phases (>5 vol%)	minor phases (<5 vol%)
89-81	2	138°34'25", 61°13'25"	qtz, pl, ms, chl	ep, czo, grp, tur
89-82	2	138°32'15", 61°13'55"	qtz, pl, ms, chl	ep, grp, tur
89-83	2	138°28'45", 61°10'55"	qtz, pl, ms, chl	ep
89-85a	1	138°25'45", 61°07'50"	qtz, pl, bt	chl, grp, grt, ap, tur
89-95a	1	137°26'30", 60°49'35"	pl, qtz, bt, ms	and, grp, o, ap ,tur, zrn
89-96	1	137°25'00", 60°50'00"	qtz, pl, bt, ms	chl, grp, and, ap
89-111a	1	136°46'40", 60°40'20"	qtz, bt, pl, crd	hc, chl, ms, zrn, o, ap
89-112a	1	137°03'10", 60°42'55"	qtz, pl, bt	and, ms, chl, tur, st, grt, grp
89-113a	1	137°04'10", 60°51'35"	qtz, pl, bt	sil, ms, and, o
89-114a	1	136°49'00", 60°49'00"	qtz, bt, pl	crd, ser, sil, o
89-117a	1	137°01'30", 60°54'25"	qtz, bt, pl	ser, crd, sil, zrn, o
89-118	5a	137°01'50", 60°58'10"	qtz, hbl, pl	bt, px, czo
90-20	1	136°51'30", 60°42'05"	qtz, bt, ms, pl	ser, chl, o, grp, sil, crd
90-21	1	136°50'45", 60°40'55"	qtz, pl, crd, bt	ms/ser, o, grp, sil
90-22	1	136°49'35", 60°41'00"	qtz, bt, pl	chl, ep, ms/ser, o, grp
90-23	1	136°48'40", 60°41'30"	qtz, pl, bt	crd, sil, grp, o
90-24	1	136°47'10", 60°41'40"	qtz, bt, pl	ms, sil, grt, crd, zrn, grp, o
90-25-1	1	136°46'50", 60°41'45"	qtz, pl, bt	ms, chl, crd, o
90-25-3	1	136°46'50", 60°41'45"	qtz, bt, pl	ms, chl, crd, hc, sil
90-26	1	136°46'15", 60°41'30"	qtz, pl, bt, crd	sil
90-27	1	136°52'00", 60°41'10"	qtz, pl, bt	crd, chl, ms, sil, o
90-28	1	136°53'30", 60°41'25"	qtz, pl, bt	crd, chl, sil, grp, o, tur
90-29-1	1	136°53'30", 60°41'25"	qtz, bt, pl	sil, ep, czo, ap, grt, tur
90-29-2	1	136°53'30", 60°41'25"	sil, bt, pl, qtz	ms, grt
90-30	1	136°54'50", 60°41'35"	qtz, pl, bt	sil, grt, grp, o, ap
90-31	1	136°55'00", 60°42'10"	qtz, pl, bt	sil, grt, grp, o, ap
90-32-1	1	136°54'00", 60°42'35"	qtz, pl, sil	bt, ms
90-33	1	136°43'50", 60°42'00"	qtz, pl, bt, crd	ms, sil, hc, ep, grp, o, zrn
90-34	1	136°40'15", 60°44'20"	qtz, pl, bt, crd	chl, hc, sil, zrn, grp, o
90-35	1	136°33'20", 60°43'10"	qtz, pl, bt, crd, kfs	ser, sil, hc, grt, chl, ap, grp, o
90-36	2	138°15'00", 61°08'00"	qtz, pl, ms, cal	chl, grp, tur, czo
90-37	2	138°15'50", 61°07'30"	qtz, pl, ms	bt, grp, o, ep, czo
90-38	1, 2	138°17'20", 61°07'05"	qtz, pl, bt, chl	ms, tur, grp, o
90-39	1	138°17'20", 61°06'45"	qtz, pl, bt, ms/ser	ep, tur, grp, o
90-40	1	138°16'20", 61°06'10"	qtz, pl, bt	chl, ms, grt
90-41	1	138°11'10", 61°05'40"	qtz, pl, bt	ms, chl, ep, grt, o, grp
90-42	1, 2	138°10'00", 61°05'35"	qtz, pl, bt, ms	chl, ep, tur, czo, grp, o
93-1	4	138°41'40", 61°22'45"	ol, tlc, srp, chr	mag
93-4	5a	138°39'45", 61°23'40"	hbl, pl	bt, qtz, chl, ap, cal, o
93-7b	8	138°43'00", 61°16'20"	chl, qtz, cal	ap, pl, rt
93-23	2	138°23'30", 61°11'50"	qtz, pl, czo, chl, cal	ms, grp, aln
93-32b	5	138°33'50", 61°22'05"	hbl, pl, qtz	bt, kfs, ap, ep, o
93-36	1	138°35'50", 61°21'40"	qtz, pl, bt, chl, and	ms, grt, sil, crd, st, ap, grp, cal
93-38b	9	138°38'10", 61°22'20"	alt, hbl, chl	qtz, ep, cal, ap
93-39	5	138°38'00", 61°22'40"	qtz, pl, bt, hbl	chl, ap, ms, o, spn, zrn
93-41a	5	138°44'00", 61°23'40"	hbl, pl, qtz, bt	o, cal, ap
93-43	5	138°44'28", 61°23'25"	hbl, pl, bt	qtz, o, cal, ap
93-44	4	138°44'40", 61°23'20"	ol, act, srp	o
93-55	1	137°39'30", 61°08'30"	qtz, bt, pl, grp	grt, ms, cal, and, st, tur
93-60b	1	137°41'15", 61°06'40"	qtz, bt, pl	ms, grp, ap, chl

Appendix 2-1 (continued):

Sample	rock type	Long (W) / Lat (N)	major phases (>5 vol%)	minor phases (<5 vol%)
93-64	1	137°39'30", 61°05'55"	qtz, chl, pl, bt, grp	ap, grt, ms, tur, czo, zrn
93-77	1	137°03'45", 60°43'00"	qtz, pl, bt	grt, st, grp, ap, ms, tur, zrn
93-80	1	137°05'55", 60°44'15"	qtz, pl, bt, st	grt, ms, grp, ap, chl
93-83	1	137°05'55", 60°46'45"	qtz, pl, bt, st, grp	ms, chl, ap, grt, ilm, tur
93-87	1	137°08'15", 60°45'30"	qtz, bt, pl, ms, chl	grt, st, grp, ilm, tur, ap, o
93-95	8	136°59'30", 61°41'30"	qtz, pl, chl	cal
93-96	1	136°57'36", 60°42'15"	qtz, bt, pl, sil	grt, grp, ms, tur
93-99	1	136°58'20", 60°40'25"	qtz, bt, pl	hc, crd, ap, grp, ms, zrn, sil
93-102/1	1	137°11'00", 60°54'55"	qtz, pl, bt, sil, ms, gr, crd	ilm, spn, zrn
93-104	1	137°12'30", 60°54'00"	qtz, bt, pl, and	sil, ap, grp, grt, ms, st, tur
93-115	1	137°17'45", 60°56'30"	qtz, bt, pl	crd, sil, grp, ap, ms, tur
93-123	1	137°21'10", 60°57'00"	qtz, bt, pl, sil, grp	crd, ap, ms, zrn
93-126/1	1	137°35'17", 60°05'55"	qtz, pl, bt, ms	st, chl,grp,and,ap,cal,grt,ilm,tur
93-128b	1	137°35'35", 60°04'20"	qtz, pl, chl, bt	ap, ms, grp, ap, tur
93-136	1	137°33'20", 61°03'30"	qtz, pl, bt, chl	st, ms, grp, ap, tur
93-139	1	137°30'50", 61°04'20"	qtz, pl, bt, ms	chl, gr, grt, and, st, ap, tur
93-140	1	137°31'00", 61°03'42"	qtz, pl, bt, ms, st	grt, grp, sil, and, tur, jar
93-142	1	138°26'50", 61°18'00"	qtz, bt, pl, chl, ms	and, crd, grp, cal, ap, st
93-143	2	138°27'00", 61°17'35"	qtz, pl, chl, ms	grp, bt, rt, tur, spn
93-148	2	138°27'15", 61°16'05"	chl, pl, qtz, grp, ms	ap, bt, tur
93-150	2	138°22'55", 61°14'00"	qtz, ms, pl, chl	grp, tur, bt, ap
93-154a	2	138°17'55", 61°11'35"	qtz, pl, chl, ms	grp, ep, ap, tur, spn
93-156	2	138°16'00", 61°12'20"	qtz, pl, chl, ms	ap, spn, tur
93-158	2	138°14'30", 61°13'00"	qtz, pl, chl, ms	bt, grp, tur, ap
93-159a	3	138°14'00", 61°12'35"	qtz, chl, ms, czo, pl, pl	hbl, spn, o
93-164/1	3	138°12'30", 61°11'15"	qtz, bt, chl, czo	ms, o
93-167	2	138°18'00", 61°12'50"	pl, qtz, chl, ms	grp, bt, ap, czo
93-172	2	138°18'05", 61°10'55"	pl, qtz, chl, ms	grp, czo
93-177	1	138°11'00", 61°14'25"	qtz, pl, bt, st, chl, grt	and, grp, ap, ms, tur
93-181	9	138°14'45", 61°14'35"	pl, hbl, cal	chl, o
93-182	1	138°15'00", 61°14'45"	qtz, pl, bt, st	ms, grp, ap, chl, tur
93-183	1	138°15'30", 61°15'10"	qtz, pl, bt, st, grp	grt, and, ms, ap, tur
93-185/1	4	138°25'50", 61°15'20"	srp, ol	chr, mag, cal
93-186	1	139°03'35", 61°26'00"	qtz, pl, bt, ms, grp	grt, st, ap, chl, tur
93-190b	4	138°49'35", 61°23'05"	srp, tlc, ol, mag	idd, chl
93-195a	7	138°09'00", 60°56'00"	chl, qtz, o, hbl, ep, pl	aln, ser
93-200	5	138°43'40", 61°38'45"	qtz, pl, bt, hbl	ap, o, ep
93-200b	10	138°43'40", 61°38'45"	qtz, bt, ms, sil, pl	o, chl
93-207b	10	138°41'15", 61°40'40"	qtz, ms, chl	pl, grt, grp, o
93-223	7	139°14'00", 61°24'25"	alt, qtz, chl, grp	cal, o
93-231	10	140°08'20", 61°52'25"	qtz, ms, bt	grt, o
93-235	11	140°08'20", 61°53'15"	qtz, pl, ms, bt, crd	o
93-236	11	140°15'00", 61°54'25"	act, pl, ep	cal, o, qtz
93-253	6	136°59'10", 60°17'40"	cal, qtz, chl, bt, grp, pl	ep
93-262/1	6	136°57'15", 60°10'00"	qtz, ms, grp	o, spn
93-275	1	136°58'30", 60°54'15"	qtz, bt, pl, crd	sil
94-3	2	138°48'00", 61°19'00"	qtz, ms, chl, cal	aln, grp, pl
94-4a	8	138°47'45", 61°19'05"	cal, qtz, pl	o, chl, ap, zrn
94-4b	8	138°47'45", 61°19'05"	qtz, cal, pl	rt
94-12	2	138°45'15", 61°20'30"	qtz, ms, chl, pl	grp, cal, bt, ap

Appendix 2-1 (continued):

Sample	rock type	Long (W) / Lat (N)	major phases (>5 vol%)	minor phases (<5 vol%)
94-17a	2	138°49'30", 61°23'30"	pl, qtz, ms, chl	bt, ep, czo, aln, ab, grp, ilm, tur
94-20a	4g	138°49'15", 61°23'20"	Cam, cal, tlc	ms, pl
94-20b	4	138°49'15", 61°23'20"	srp, tlc, ol	chr, mag
94-26b	5	138°43'50", 61°23'50"	pl, cpx, bt	qtz, ap, zrn
94-36	2	138°36'30", 61°14'10"	pl, qtz, chl, ms	ab, grp, cal
94-39	2	138°43'03", 61°16'35"	qtz, ms, chl, pl	cal, grp, czo
94-41b	8	138°43'00", 61°16'20"	cal, chl, qtz, pl	o
94-45	2	138°39'10", 61°20'00"	qtz, pl, chl, ms	grp, czo
94-47	1	138°37'20", 61°20'55"	qtz, pl, bt, st	ms, grp, ap, grt
94-51	2	138°33'20", 61°19'50"	qtz, pl, chl, ms	czo, grp, bt, ap, tur
94-58	1	138°23'20", 61°16'50"	qtz, bt, pl, ms	st, and, grp, grt, tur, chl
94-60a	2	138°24'25", 61°16'10"	pl, qtz, chl, ms	ep, aln, ab, ap
94-60b	3	138°24'25", 61°16'10"	pl, qtz, chl, bt, hbl	ep
94-60c	9	138°24'25", 61°16'10"	tlc, srp	o
94-60e	1	138°24'20", 61°16'20"	qtz, pl, bt	ab, grt, chl, ap, ms, tur, grp
94-62	1	138°21'00", 61°15'50"	qtz, pl, ms	bt, chl, grt, grp
94-63	2	138°20'30", 61°15'40"	qtz, pl, chl, ms	bt, tur, grp
94-72	2	138°30'25", 61°16'40"	qtz, pl, chl, ser	grp, tur, czo, aln
94-76	2	138°27'50", 61°15'50"	qtz, chl, pl, ms	ilm, grp, ap, tur
94-81	1	137°04'10", 60°51'35"	qtz, pl, bt	o, grt, sil, grp, crd, ap
94-84	7	137°56'15", 60°51'50"	qtz, chl, pl	grp, ep
94-87	7	137°59'30", 60°51'45"	chl, ep, qtz, hbl	pl, cal
94-89b	6	137°57'20", 61°51'10"	qtz, ms/ser	cal, o
94-94	1	137°20'20", 60°58'40"	qtz, pl, bt, crd	grt, grp, o, sil
94-98	1	137°18'30", 61°00'10"	qtz, pl, bt	grt, o, ap, sil
94-105	1	137°25'45", 61°04'50"	qtz, pl, bt	crd, sil, ms, grp, ilm, tur, kfs
94-108	1	137°28'20", 61°03'10"	qtz, pl, bt	st, and, grt, sil, grp, ms
94-115	1	137°22'30", 61°03'05"	qtz, pl, bt	crd, ms, sil, tur
94-118	1	137°20'00", 61°04'40"	qtz, pl, bt	crd, sil, zrn, ms, grp
94-120	1	137°17'30", 61°03'20"	qtz, pl, bt	crd, grt, sil, ms, o, kfs
94-123	2	137°43'00", 61°03'55"	qtz, pl, bt	chl, ep, czo, grp
94-130	1	137°34'40", 61°01'05"	qtz, pl, bt, chl, grp	st, grt, ms
94-133	1	137°31'30", 60°58'05"	qtz, bt, pl, sil	grt, grp, ms, tur
94-145	5d	137°34'00", 60°57'30"	pl, px, bt	hbl, ap
94-146	1	137°34'00", 60°57'00"	qtz, pl, bt, crd, sil	grt, st, ms, ap, tur, grp
94-147a	1	137°34'00", 60°56'45"	bt, sil, qtz, pl, ilm	grt, zrn
94-147c	1	137°34'00", 60°56'45"	qtz, pl, bt	crd, grt, sil, grp
94-147d	5	137°34'00", 60°56'45"	qtz, pl, bt	grt, ser, chl
94-153	1	137°37'30", 60°57'30"	qtz, pl, chl, bt, ms	grp, grt
94-172	1	137°55'10", 61°10'40"	qtz, pl, bt, ms, st	chl, grt, grp
94-173	1	137°54'40", 61°09'55"	qtz, pl, bt	and, ilm, chl, ms, grp, tur
94-174	1	137°53'10", 61°12'50"	qtz, bt, pl, crd	ilm, ms/ser, grt, hc, sil, ap
94-185a	4	137°50'42", 61°10'40"	tlc, ol, srp	chr, chl, mag
94-191a	7	136°58'20", 60°17'35"	Chl, cal, hbl	qtz, ep
94-192	6	136°58'20", 60°17'20"	qtz, bt, ms	chl, o
94-195	5g	136°58'00", 60°12'35"	chl, pl, cpx, hbl	o, ap
94-197a	6	136°58'00", 60°11'45"	qtz, o, grp	ser
94-204a	6	137°56'30", 60°06'30"	qtz, bt, chl, grp, cal	pl
94-204b	6	137°56'30", 60°06'30"	qtz, grp, o, bt	grt
94-214	12	136°42'00", 59°56'57"	qtz, bt, st, and	pl, o, chl

Appendix 2-1 (continued):

Sample	rock type	Long (W) / Lat (N)	major phases (>5 vol%)	minor phases (<5 vol%)
94-235a	5	136°53'30", 60°04'55"	pl, qtz, bt, hbl	chl, ap, cal, zrn
94-237a	6	136°55'40", 60°04'40"	qtz, ms	grt,pl
94-237b	5	136°55'40", 60°04'40"	pl, qtz, bt, hbl	ap, zrn, cal
94-241a	7	138°07'00", 60°55'35"	chl, qtz, ep	-
94-242	6	138°06'20", 60°53'54"	qtz, bt	grt, ser
94-243	6	138°05'35", 60°53'40"	qtz, bt, o, grp	-
94-252	1	136°56'10", 60°34'05"	qtz, pl, bt, ms/ser, crd	kfs, hc, chl, ilm
94-259b	8	136°59'30", 60°34'35"	pl, qtz, bt, hbl	-
94-259c	1	136°59'30", 60°34'35"	qtz, bt, pl, crd, ms/ser	hc, chl
94-266	1	137°05'00", 60°36'10"	qtz, pl, bt	grp, ms/ser, chl, tur
94-276	1	136°46'50", 60°41'45"	qtz, pl, bt	ill, chl, ms, ap
94-277b	5	136°47'30", 60°41'55"	pl, qtz, bt	hbl, ap, zrn
94-277c	1	136°47'30", 60°41'55"	qtz, pl, ms, bt	chl, o, grt, zrn
94-277d	1	136°47'30", 60°41'55"	qtz, pl, bt	grt, ms, ser, grp, zrn, o
94-281	1	136°50'00", 60°41'10"	qtz, pl, bt	crd, grp, ms, zrn
94-283a	1	136°48'20", 60°42'20"	qtz, pl, bt, crd	ser, o, grt, sil, chl, kfs
94-290	5	136°47'30", 60°42'15"	qtz, pl, bt	chl, zrn
94-292/1	1	136°43'00", 60°42'30"	pl, qtz, bt, crd	ms, sil, chl, hc, ap, zrn
94-297/1	1	136°42'20", 60°43'55"	qtz, pl, bt	o, ap
94-293/2	6	137°41'25", 60°46'35"	qtz, bt/ms, grp, ep	-
94-299	5	138°06'45", 61°02'10"	qtz, pl, bt, chl	ms, grp, grt, ap
94-301	1	138°07'50", 61°04'00"	pl, qtz, bt	chl, tur, grp
94-303	2	138°08'20", 61°04'55"	qtz, pl	bt, ms, chl, grp, grt, czo, tur
94-337	11	139°02'40", 61°35'05"	qtz, bt	o, pl, ms
94-341	11	139°03'00", 61°34'15"	qtz, pl, bt, and	ms/ser, chl, crd, sil
94-344	11	139°02'40", 61°34'42"	qtz, pl, bt	ms, crd, and, o
94-345	11	139°01'20", 61°34'42"	hbl, qtz, pl, ep	-
94-346	1	139°04'00", 61°26'12"	qtz, pl, bt, grp	st, grt, tur, ms
94-358a	12	136°48'50", 60°30'10"	qtz, bt, ky, st	pl, crd, grt, hc, ser, o
94-366	12	136°44'40", 60°28'55"	qtz, bt, pl	grt, ky, ap
94-368	12	136°45'45", 60°29'40"	qtz, bt, pl	grt, tur, chl
94-372	6	136°55'25", 60°04'30"	alt, qtz, cal, pl ?	-
94-376	7	137°00'45", 60°18'30"	qtz, grp, chl, pl	o, cal
94-377	6	137°01'00", 60°18'55"	qtz, pl, grp	ap
94-387	1	137°25'25", 60°50'10"	qtz, pl, bt	and, ms, grp, chl, tur, ap
95-6	11	140°11'50", 61°53'35"	qtz, ms, o, grp	bt
95-13a	7	137°18'15", 60°43'50"	srp, hbl	cal, o
95-16a	7	137°17'55", 60°44'40"	chl, qtz, ep	bt, hbl, o
95-16b	7	137°17'55", 60°44'40"	hbl, ep, czo	qtz
95-22	2	137°40'00", 60°52'05"	qtz, pl, ms, chl	grp, o
95-26	6	136°57'00", 60°06'22"	qtz, bt, chl, ms	o, grp
95-29b	12	136°55'00", 60°13'52"	qtz, bt	hbl, czo, grt, pl
95-29c	12m	136°55'00", 60°13'52"	cal, qtz	ms
95-31	12	136°53'35", 60°22'58"	qtz, bt	grt, ky, pl
95-33	12	136°51'10", 60°23'00"	qtz, pl, bt	grt, st, ky, chl
95-37	12	136°54'56", 60°21'15"	qtz, czo, bt, tur	grt, o, hbl, pl
95-39	1	137°05'40", 60°33'47"	qtz, pl, bt	crd, grp, o, kfs, ms
95-42	3	138°49'30", 61°23'03"	qtz, hbl, ep	pl, bt
95-53b	10	138°41'15", 61°40'40"	qtz, grt, ms, bt	chl, czo
95-55	10q	138°41'53", 61°41'17"	qtz, ms	bt, o, chl

Appendix 2-1 (continued):

Sample	rock type	Long (W) / Lat (N)	major phases (>5 vol%)	minor phases (<5 vol%)
95-58	2	138°24'47", 61°11'35"	qtz, pl, chl, ms	grp, czo
95-64	2	138°17'55", 61°11'35"	qtz, pl, chl, ms	grp, ep, tur
95-65	2a	138°18'10", 61°11'10"	cal, act	spn, rt, ep
95-67	2	138°17'03", 61°10'10"	qtz, chl, pl, ms	grp, ep, aln
95-68a	3	138°17'58", 61°09'35"	qtz, ep, czo, pl, chl	-
95-68c	3	138°17'58", 61°09'35"	qtz, czo, ms, chl	ep, cal
95-71	1	138°23'00", 61°07'18"	qtz, pl, bt	ms, chl, grp, grt, tur
95-74	12	136°50'35", 60°33'44"	qtz, bt, pl, ms/ser, crd	-
95-76b	6	136°59'50", 60°19'48"	qtz, cal, o, ms, chl	-
95-77b	7	137°35'55", 60°47'35"	chl, pl	ep, czo, cal, o, hbl
JRT 93-16	13	137°27'30", 61°23'00"	qtz, ms, bt, grt	sil, tur, o
STJ 93-42	13	137°10'40", 61°10'40"	qtz, ms, grt, pl, bt	tur, st, o

Samples collected by P. Erdmer (89-, 90-), J. Mezger (93-, 94-, 95-) J.R. Timmerman (JRT), S.T. Johnston (STJ); first number denotes year of collection.

rock types listed above:

1: bt-qtz schist (aluminous) of KMA
2: ms-chl-qtz schist (calcic) of KMA
3: Ca-Mg-Fe-rich layers of KMA
4: olivine serpentinite of KMA
5: Ruby Range Batholith granodiorite,
    5a: amphibolite, 5d: diorite
6: Dezadeash Formation slate, phyllite
7: epidote-chlorite schist
8: felsic dykes
9: mafic dykes
10: Nasina Assemblage mica schist
    10q: quartzite
11: White River Assemblage mica schist
12: Nisling assemblage schist
    12m: marble
13: Aishihik Metamorphic Suite mica schist

Appendix 2-2: Electron microprobe analyses of Cr-muscovite in ultramafic layers of the KMA

	89-78A		89-78D	
	average of 7 points	average of 10 points on 5 grains	average of 6 points on one grain	dark bands in previous grain (2 pts)
SiO_2	56.50	53.26	53.71	53.71
TiO_2	0.11	0.10	0.10	0.12
Al_2O_3	19.60	25.26	24.49	26.76
Cr_2O_3	1.89	1.48	2.11	0.04
FeO	3.60	1.86	1.84	1.83
MnO	0.05	0.02	0.02	0.03
MgO	4.53	3.55	3.59	3.51
CaO	0.01	0.03	0.02	0.01
Na_2O	0.01	0.14	0.17	0.13
K_2O	11.13	11.27	11.12	11.41
Total	97.43	96.97	97.17	97.21
Number of ions based on 11 oxygen:				
Si	3.722	3.502	3.526	3.675
Ti	0.005	0.005	0.005	0.006
Al	1.957	1.522	1.895	2.187
Cr	0.077	0.098	0.110	0.002
Fe	0.199	0.103	0.101	0.100
Mn	0.003	0.001	0.001	0.001
Mg	0.445	0.348	0.352	0.341
Ca	0.001	0.002	0.001	0.001
Na	0.001	0.018	0.021	0.017
K	0.935	0.945	0.932	0.939
Total	6.931	6.958	6.944	6.951

Appendix 2-3: Ca-Fe-Mg-rich layers in the Kluane metamorphic assemblage

Sample	location	rock type	field relation
89-52a	138°03'35" 61°11'50"	epidote-bearing hornblende-plagioclase schist	foliated layer in garnetiferous biotite-muscovite schist
89-58a	138°02'10" 61°13'15"	epidote-bearing hbl-pl-qtz schist epidote is being replaced by opaque mineral	within biotite-muscovite schist
89-80	138°36'30" 61°14'10"	plagioclase-epidote-actinolite-Cr-biotite schist	
93-12	138°38'00" 61°14'30"	fuchsite-actinolite schist and plagioclase-epidote-actinolite-Cr-biotite schist	boudinaged layers within muscovite-chlorite schist
93-120	137°20'10" 61°56'15"	plagioclase-hornblende schist	float sample in biotite schist
93-152	138°20'45" 61°13'25"	Cr-biotite-actinolite schist	5x10 cm lense within muscovite-chlorite schist
93-159	138°13'50" 61°12'50"	Cr-biotite-actinolite schist and plagioclase-epidote-actinolite-Cr-biotite schist	large layer (>1m thickness, 150m width)
93-168	138°18'00" 61°12'50"	Cr-biotite-actinolite schist	layer within (thickness ?) muscovite-chlorite schist
93-173	138°18'40" 61°11'15"	Cr-biotite-actinolite schist	boudinaged 10 cm thick layers in muscovite-chlorite schist
94-60b	138°24'25" 61°13'15"	altered epidote-bearing hbl-bt-pl-qtz schist	near lower contact of Swanson Creek olivine serpentinite lense
95-42	138°49'30" 61°23'03"	biotite bearing epidote-hornblende schist contains no Cr-biotite	foliated layer within zoisite-bearing biotite-muscovite schist
95-65	138°18'10" 61°11'10"	altered zoisite-bearing actinolite schist (?)	50 cm thick, 15 m wide boudinaged layer within muscovite-chlorite schist
95-68	138°17'58" 61°09'35"	epidote-chlorite-plagioclase schist epidote-bearing muscovite-chlorite schist	10-15 m thick layer quartz rich white layer (no plagioclase)

Appendix 2-4: Age determinations of the Ruby Range Batholith

	Sample	Rock type	Coordinates (W, N)	Age (Ma)	Method	Reference
(1)	GSC 59-12	qtz monzonite	138°03', 61°21'	176	K-Ar (biotite)	Lowdon (1960)
(2)	GSC 59-13	gneissic bt-granodiorite	138°45', 61°25'	58 ±4	K-Ar (biotite)	Lowdon (1960)
(3)	GSC 60-31	bt-qtz monzonite	136°59', 61°05'	65	K-Ar (biotite)	Lowdon (1961)
(4)	GSC 60-32	foliated bt-granodiorite	138°08', 61°01'	58 ±4	K-Ar (biotite)	Lowdon (1961)
(5)	B 48.9	bt-hbl granodiorite	137°01'00", 61°06'30"	48.9 ±2.3	K-Ar (biotite)	Tempelman-Kluit & Wanless (1976)
				55.4 ±3.3	K-Ar (hornblende)	
(6)	B 51.6	hbl granodiorite	137°00'00", 61°06'15"	51.6 ±2.4	K-Ar (biotite)	Tempelman-Kluit & Wanless (1976)
				53.8 ±3.2	K-Ar (hornblende)	
(7)	B 67.6	hbl-bt granodiorite	137°00'50", 61°14'30"	67.6 ±2.7	K-Ar (biotite)	Tempelman-Kluit & Wanless (1976)
				68.3 ±3.4	K-Ar (hornblende)	
(8)	TO72-393aIII	hbl-bt-qtz monzonite	137°40'30", 61°13'30"	53 ±1	Rb/Sr (bt, pl, wr)	LeCouteur & Tempelman-Kluit (1975)
(9)	81 Cac 74-1	bt-hbl granodiorite	136°51'00", 60°02'30"	67 ±1	Rb/Sr (bt, pl, wr)	LeCouteur & Tempelman-Kluit (1975)
(10)	GSC 81-90	granite	138°31'12", 61°23'20"	54.1 ±2.4	K-Ar (biotite)	Stevens et al. (1982)
(11)	W 7	granodiorite	139°58', 61°46'	56.0 ±1.6	K-Ar (biotite)	Farrar et al. (1988)
(12)	W 13	monzogranite	139°21', 61°37'	55.5 ±1.6	K-Ar (biotite)	Farrar et al. (1988)
(13)	W 18	monzogranite	138°56', 61°41'	55.8 ±1.6	K-Ar (biotite)	Farrar et al. (1988)
(14)	W 32	granodiorite	138°25', 61°36'	63.0 ±1.8	K-Ar (biotite)	Farrar et al. (1988)
(15)	W 48	qtz diorite	138°39', 61°31'	55.7 ±1.6	K-Ar (biotite)	Farrar et al. (1988)
(16)	W 54	qtz diorite	138°44', 61°23'	55.5 ±1.6	K-Ar (biotite)	Farrar et al. (1988)
(17)	W 61	granodiorite	137°29', 60°49'	50.6 ±1.6	K-Ar (biotite)	Farrar et al. (1988)
(18)	W 77	monzonite	136°07', 60°35'	56.9 ±1.8	K-Ar (biotite)	Farrar et al. (1988)
(19)	W 90	qtz diorite	136°21', 60°21'	56.4 ±1.8	K-Ar (biotite)	Farrar et al. (1988)
(20)	W 103	granodiorite	136°07', 60°08'	55.9 ±1.6	K-Ar (biotite)	Farrar et al. (1988)
(21)	W 104	qtz diorite	136°53', 60°03'	66.7 ±2.0	K-Ar (biotite)	Farrar et al. (1988)
(22)	86-79	hbl-qtz diorite	136°59'41", 61°11'50"	69.6, 78.6	U-Pb (zircon)	Johnston (1993)
(23)	87-40	hbl-bt granodiorite	137°03'58", 61°00'25"	69.7-87.0	U-Pb (zircon)	Johnston (1993)
(24)	87-42	biotite granite	136°59'39", 61°04'55"	55.8 ±0.7	U-Pb (zircon)	Johnston (1993)
(25)	87-70	hbl granodiorite	137°03'25", 61°19'23"	78.6 ±0.6	U-Pb (zircon)	Johnston (1993)
(26)	JK-PE 1	ms-grt granite dyke	136°03'40", 60°51'35"	54.7 ±0.9	U-Pb (monazite)	Mortensen (unpublished data)
(27)	?	bt granite dyke	136°03'40", 60°51'35"	70	U-Pb (zircon)	Mortensen (unpublished data)

Numbers in brackets refer to locations on map in Appendix 2-6.

Appendix 2-5: Age determinations of mica schists of the KMA and phyllites of the DF

	Sample	Rock type	Coordinates (W, N)	Age (Ma)	Method	Reference
(28)	GSC 59-11	bt-qtz schist	138°07', 61°17'	140 ±11	K-Ar (biotite)	Lowdon (1960)
(29)	GSC 81-88	ms-chl schist	138°35'30", 61°15'00"	54.7 ±2.3	K-Ar (muscovite)	Stevens et al. (1982)
(30)	GSC 81-89	bt-qtz schist	138°36'30", 61°21'12"	52.8 ±2.2	K-Ar (biotite)	Stevens et al. (1982)
(31)	KLL 1-1	bt-qtz schist	138°40', 61°22'	61.7 ±2.0	K-Ar (biotite)	Farrar et al. (1988)
(32)	KLL 2-1	ms-chl schist	138°27', 61°10'	42.5 ±1.4	K-Ar (whole rock)	Farrar et al. (1988)
(33)	KLL 2-5	ms-chl schist	138°43', 61°21'	50.9 ±1.6	K-Ar (whole rock)	Farrar et al. (1988)
(34)	PE 89-65	bt-qtz schist	138°03'55", 61°18'05"	54.7 ±1.8	K-Ar (biotite)	Mortensen & Erdmer (1992)
				57.0 ±0.2	U-Pb (monazite)	
				56.3 ±0.3	U-Pb (xenotime)	
(35)	PE 89-83	ms-chl schist	138°27'45", 61°10'40"	43.4 ±1.9	Ar-Ar (muscovite)	Mortensen & Erdmer (1992)
(36)	PE 89-85	bt-qtz schist	138°25'50", 61°07'50"	39.4 ±0.9	Ar-Ar (biotite)	Mortensen & Erdmer (1992)
(37)	PE 89-111	bt-qtz schist	136°46'20", 60°40'10"	45.3 ±0.9	K-Ar (biotite)	Mortensen & Erdmer (1992)
				57.1 ±0.2	U-Pb (monazite)	
(38)	PE 89-113	bt-qtz schist	138°27'45", 60°51'35"	52.0 ±0.8	K-Ar (biotite)	Mortensen & Erdmer (1992)
				56.3 ±0.5	U-Pb (monazite)	
				55.9 ±0.3	U-Pb (monazite)	
(39)	PE 89-114	ms-chl schist	136°48'05", 60°49'35"	50.2 ±0.8	K-Ar (biotite)	Mortensen & Erdmer (1992)
				56.9 ±0.2	U-Pb (monazite)	
(40)	PE 89-117	bt-qtz schist	137°01'30", 60°54'20"	52.0 ±2.8	K-Ar (biotite)	Mortensen & Erdmer (1992)
				57.4 ±0.2	U-Pb (monazite)	
				58.0 ±0.2	U-Pb (monazite)	
(41)	PE 89-101	bt-qtz schist	136°36'10", 60°29'10"	55.3 ±0.7	Ar-Ar (biotite)	Mortensen & Erdmer (1992)
(42)	30-1	DF phyllite	136°57'00", 60°06'00"	68.2 ±1.8	K-Ar (whole rock)	Lowey (pers. comm., 1995)
(43)	49-1	DF phyllite	136°58'00", 60°11'00"	60.2 ±1.9	K-Ar (whole rock)	Lowey (pers. comm., 1995)
(44)	JM 94-3	ms-chl schist	138°48'00", 61°19'00"	51.14 ±0.56	Ar-Ar (muscovite)	this study

Numbers in brackets refer to locations on map in Appendix 2-6.

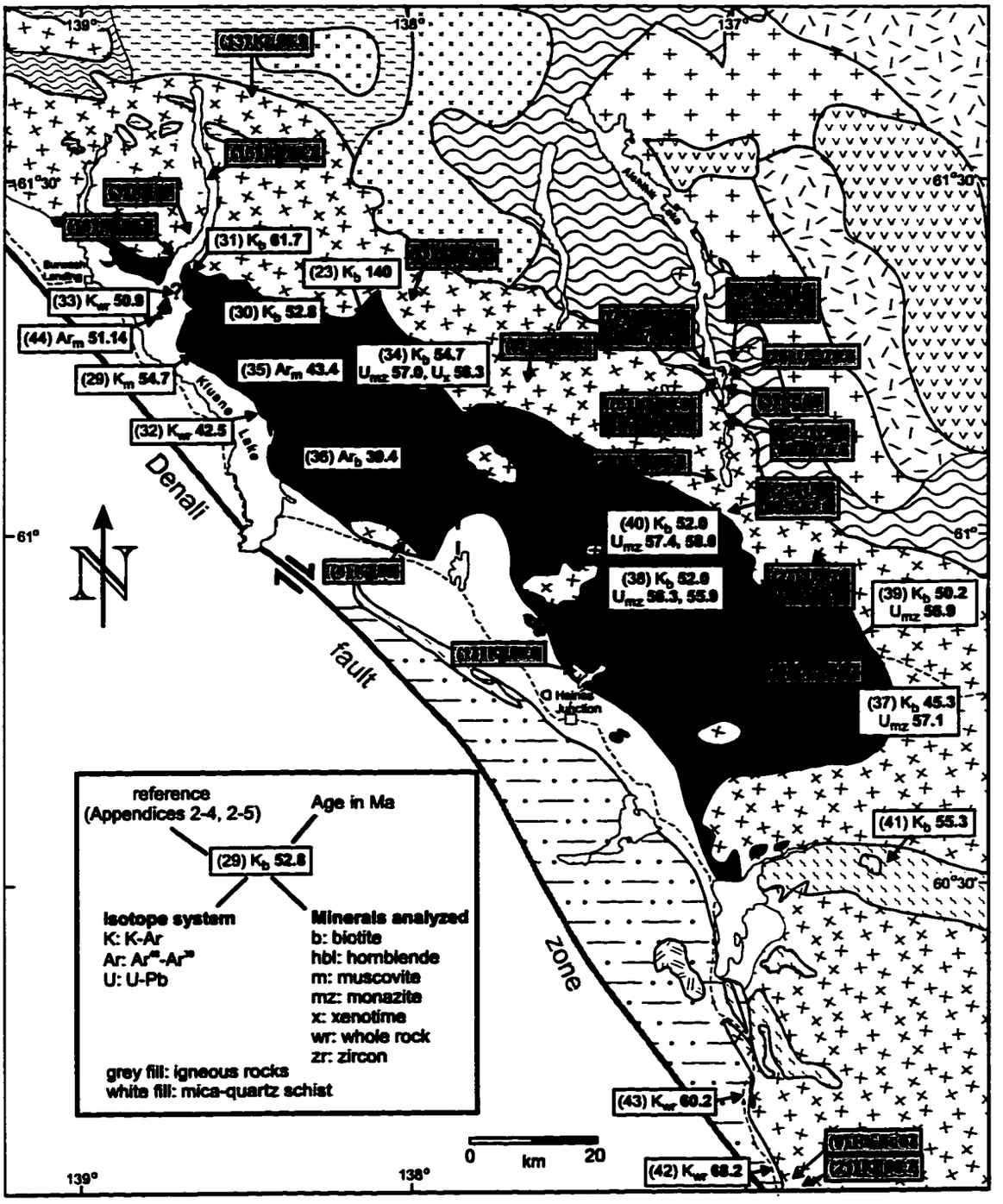

Appendix 2-6: Localities of radiometric age determinations of mica-quartz schist of the KMA and phyllites of the Dezadeash Formation (white fill) and igneous rocks of the Ruby Range Batholith and the Coast Plutonic Complex (grey fill). The numbers in parentheses refer to references listed in Appendices 2-4 and 2-5. Note that the localities of samples 37, 38 and 41 are shown incorrectly in the original papers by Mortensen & Erdmer (1992) and Erdmer & Mortensen (1993). The geology is the same as in Figure 2-1.

Appendix 2-7: ^{40}Ar-^{39}Ar geochronology of calcic schist of the KMA

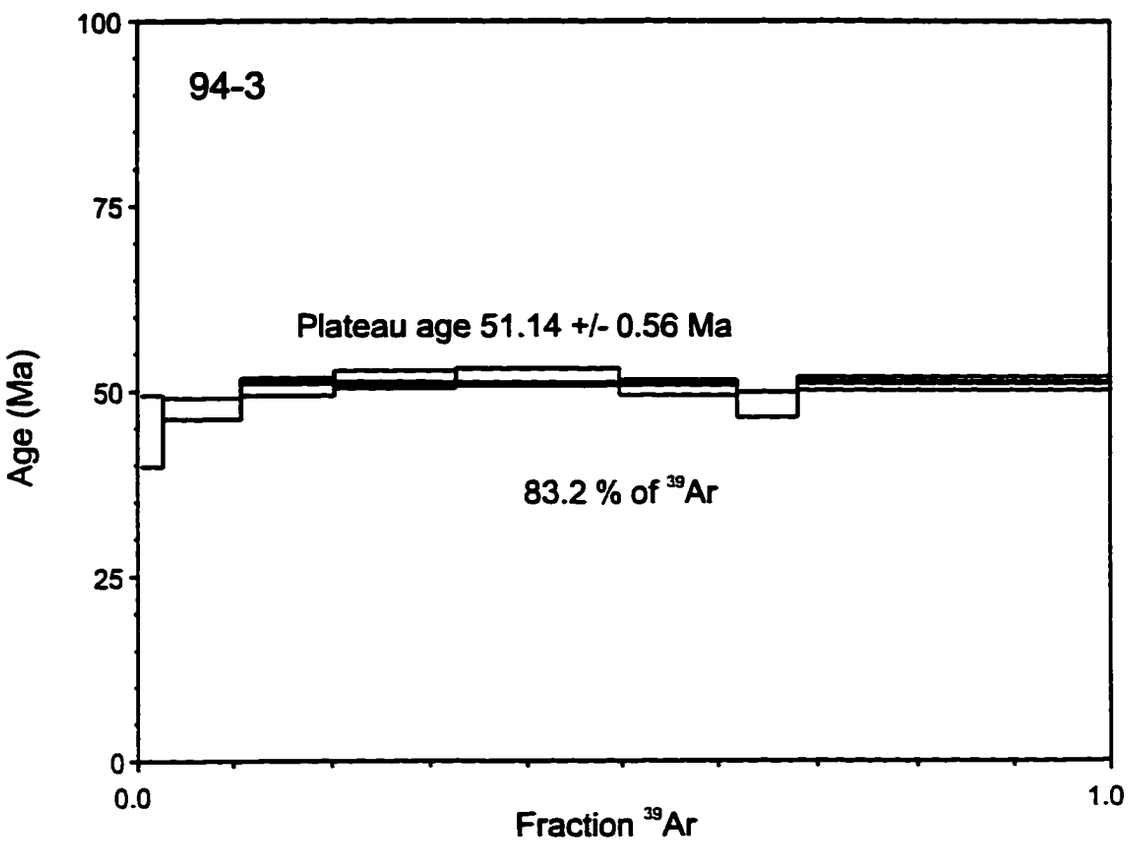

Appendix 2-8: Muscovite and whole rock Rb-Sr isochrons of calcic schists of the Kluane metamorphic assemblage

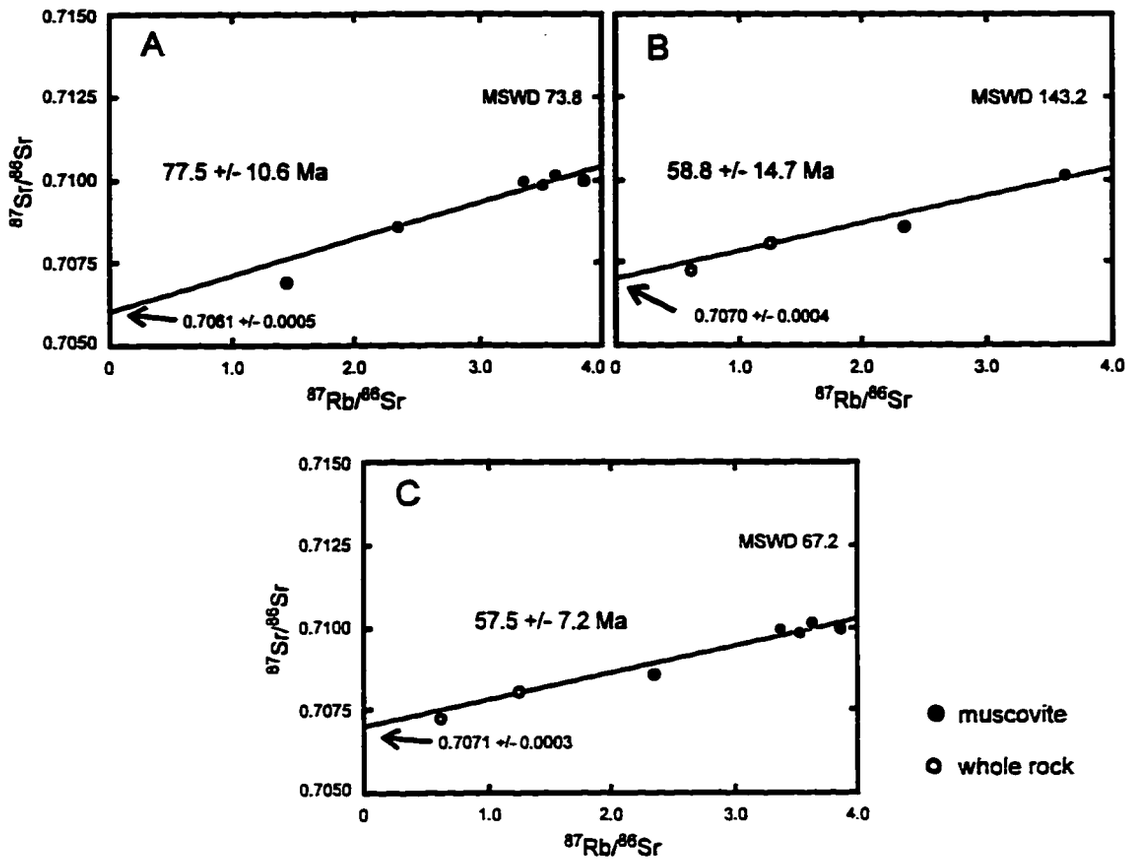

Sample	Rb (ppm)	Sr (ppm)	Rb/Sr	$\frac{^{87}Rb}{^{86}Sr}$	error*	$\frac{^{87}Sr}{^{86}Sr}$	error in 6.place*
Muscovite:							
JM 93-156	301	242	1.24	3.5863	± 0.035	0.710185	27
JM 94-17	234	177	1.32	3.8300	± 0.038	0.710039	23
JM 94-33	194	399	0.49	1.1405	± 0.011	0.707061	38
JM 94-36	257	322	0.80	2.3060	± 0.023	0.708657	23
JM 94-51	255	224	1.14	3.2994	± 0.033	0.710051	44
JM 94-173	242	205	1.18	3.4139	± 0.034	0.709839	39
Whole rock:							
JM 93-156	93	216	0.43	1.2423	± 0.012	0.708336	22
JM 94-36	42	185	0.23	0.6609	± 0.007	0.707231	49

* errors are given as 2σ

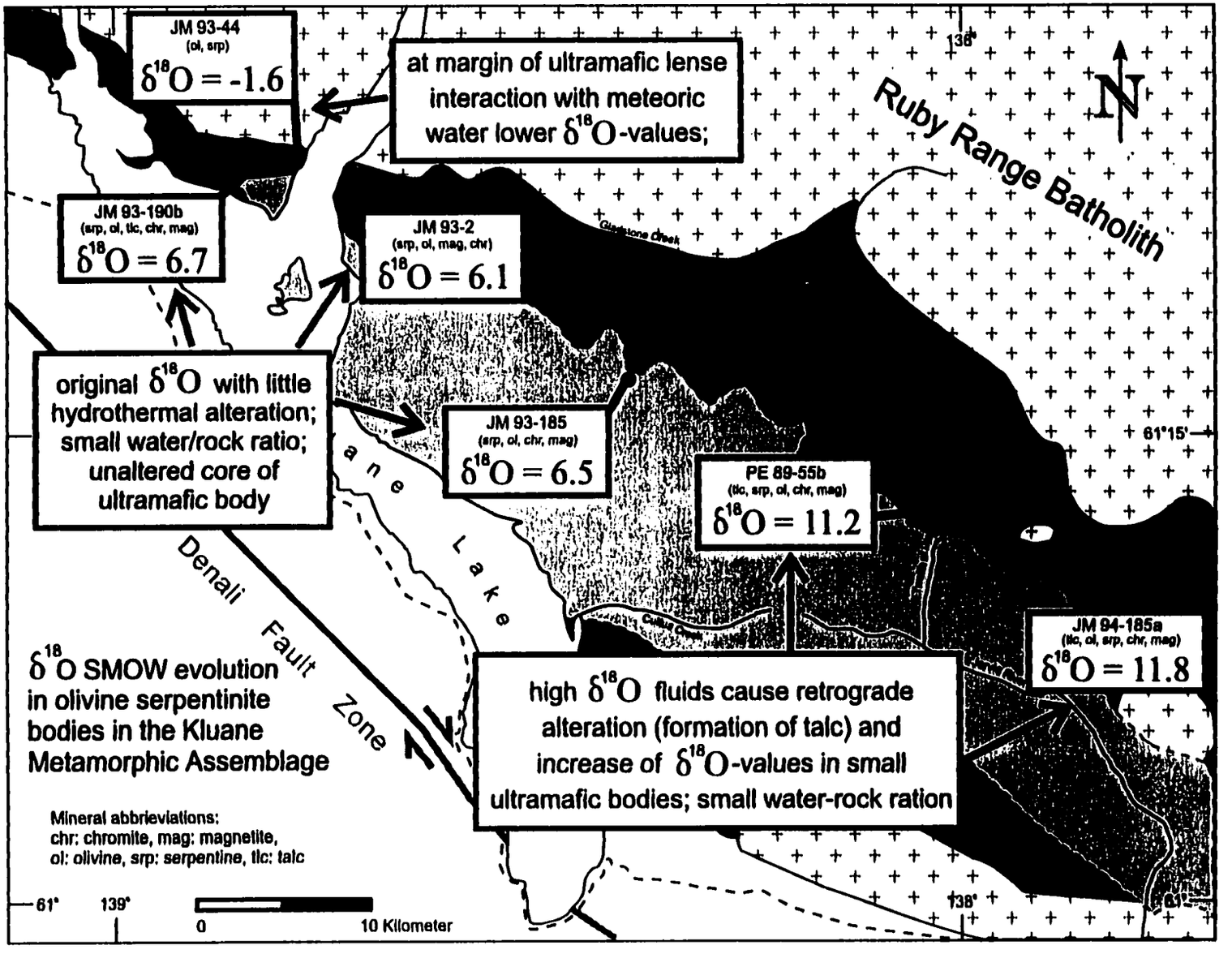
JM 93-44
(ol, srp)
δ18O = -1.6
at margin of ultramafic lense interaction with meteoric water lower δ18O-values;
Ruby Range Batholith
N
138°
JM 93-190b
(srp, ol, tlc, chr, mag)
δ18O = 6.7
JM 93-2
(srp, ol, mag, chr)
δ18O = 6.1
original δ18O with little hydrothermal alteration; small water/rock ratio; unaltered core of ultramafic body
JM 93-185
(srp, ol, chr, mag)
δ18O = 6.5
61°15'
PE 89-55b
(tlc, srp, ol, chr, mag)
δ18O = 11.2
Denali Fault Zone
Kluane Lake
JM 94-185a
(tlc, ol, srp, chr, mag)
δ18O = 11.8
δ18O SMOW evolution in olivine serpentinite bodies in the Kluane Metamorphic Assemblage
high δ18O fluids cause retrograde alteration (formation of talc) and increase of δ18O-values in small ultramafic bodies; small water-rock ration
Mineral abbrieviations:
chr: chromite, mag: magnetite,
ol: olivine, srp: serpentine, tlc: talc
61°
139°
138°
0
10 Kilometer

Appendix 2-9: Location and $\delta^{18}O$ SMOW values[1] of olivine serpentinites of the Kluane Metamorphic Assemblage

Sample	Location	Long./Lat.	field relationship	Modal mineral composition[2]	yield (µmoles/mg)	$\delta^{18}O$ SMOW
93-2*	Doghead Pt. east shore Talbot Arm, Kluane Lake	138°41'40" 61°22'45"	eastern margin of large lense (>1 km stratigraphic thickness); distance to contact with Ruby Range Batholith not precisely known (few 100 m)	olivine, serpentine, magnetite, chromite (estimate from polished section)	8.46	6.1 ‰
93-44*	Doghead Pt. Kluane Lake	138°44'40" 61°23'10"	northern margin of large lense; close to intrusive contact	olivine (80%) serpentine (20%) magnetite, chromite (5%),	10.09 9.88	-1.1 ‰ -2.2 ‰ (repeat)
93-185	Swanson Creek, Ruby Range	138°25'50" 61°15'20"	150 - 200 m thick lense within mica-quartz schist of KMA; location within lense not known	olivine (30%) serpentine (65%) magnetite, chromite (5%), calcite	11.74	6.5 ‰
93-190b*	Doghead Pt. Kluane Lake	138°49'40" 61°23'05"	central part of large lense at Doghead Point; farther away from intrusive contact of Ruby Range Batholith than JM 93-44	olivine (10-15%) serpentine (60-70%) talc (10%) iddingsite (2-3%), pentlandtite, chromite, magnetite (5%)	13.65	6.7 ‰
94-185a	Ruby Creek, Ruby Range	137°50'42" 61°10'42"	resistive rocks on flat plateau; contact with biotite-quartz schist of KMA exposed; size of lense unknown, but apparently small (few tens of meters)	olivine (20-30%) serpentine (10-20%) talc (50%) chromite, magnetite Cr-enstatite (~5%)	11.40	11.8 ‰
89-55b	Snyder Creek, Ruby Range	138°03'00" 61°12'42"	small ultramafic body (<100 m) within biotite-quartz schist of KMA	olivine (15%) serpentine (30-40%) talc (50%) calcite (tr) magnetite, chromite	12.08	11.2 ‰

* samples are from the same ultramafic body

1: Oxygen isotope analyses done by F. Longstaffe at the University of Western Ontario. Reproducability of quartz standards ± 0.03 ‰.

2: modal mineral composition detemined by thin section estimates, except for sample JM 93-2, where no thin section is available.

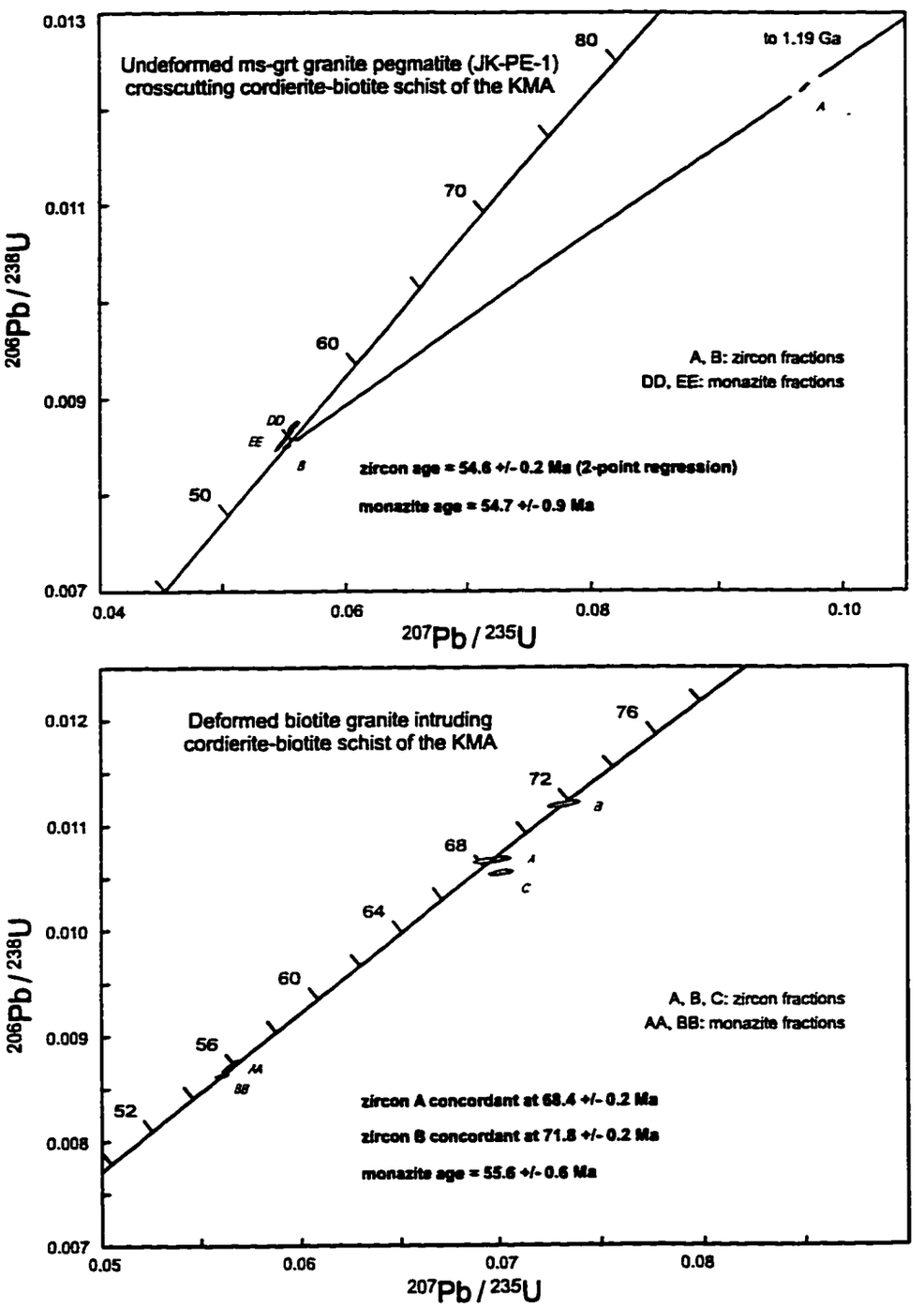

Appendix 2-10: Concordia plots of dykes intruding the KMA. Analyses by J. Mortensen, University of British Columbia, (unpublished data, 1996, 1997)

Appendix 2-11: Dykes intrusive in the KMA

Sample	coordinates	rock type	thickness	strike	field relationship
93-7b	138°43'00"	fine grained greenish	5-6 m	100°	crosscutting ms-chl schist
94-41b	61°16'20"	porphyry			
93-10	138°41'10"	fine grained greenish	5-7 m	150°	crosscutting ms-chl schist
	61°15'35"	porphyry			
94-43	138°41'30"	fine grained greenish	float sample, continuation of dyke as 93-10		
	61°15'50"	porphyry			
93-30	138°34'50"	fine grained greenish	?	70°	crosscuts Ruby Range
	61°23'40"	porphyry, less altered			Batholith
93-95	136°59'30"	fine grained blueish-gray	3-5 m	10°	crosscuts ms-chl schist
	61°41'30"	porphyry			
94-4a	138°47'45"	fine grained greenish	3 m	40/45	parallel ms-chl schist foliation
	61°19'05"	porphyry			
94-4b	138°47'45"	fine grained greenish	3 m	45°	deflects ms-chl schist foliation
94-4c	61°19'05"	porphyry and aphanite			two parallel dykes 50 m apart
94-6	138°47'25"	greenish aphanite	4 m	45°	deflects ms-chl schist foliation
	61°19'05"				
94-8	138°47'10"	greenish aphanite	?	float sample, continuation of 94-6	
	61°19'10"				
94-9	138°47'10"	greenish aphanite	?	float sample, continuation of 94-4c	
	61°19'20"				
94-14	138°45'00"	fine grained greenish	1-2 m	90°	crosscuts ms-shl schist
	61°20'00"	porphyry			continuation of 94-4 or 94-6
94-31a	138°41'35"	fine grained blueish-gray	1 m	160°	crosscuts ultramafic
	61°22'50"	porphyry			
94-34	138°33'15"	greenish aphanite	20 cm	40/35	parallels ms-chl
	61°13'00"				schist foliation
94-37	138°38'05"	fine grained greenish	4 m	60°	crosscuts ms-chl schist
	61°14'30"	porphyry			
94-38b	138°38'45"	greenish aphanite	4 m	50°	crosscuts ms-chl schist
	61°14'35"				
94-64	138°40'20"	fine grained greenish	1-2 m	160°	crosscuts ms-chl schist
	61°15'30"	porphyry			
94-65	138°39'50"	fine grained greenish	1 m	80/30	parallels ms-chl schist foliation
	61°15'35"	porphyry			
94-68	138°38'40"	fine grained greenish	4 m	150/20	parallels ms-chl schist foliation
	61°15'10"	porphyry			
94-259b	136°59'30"	fine grained grey	?	?	crosscuts ms-chl schist
	60°34'35"	porphyry			
94-349	139°04'35"	fine grained greenish	2-3 m	90°	crosscuts ms-chl schist
	61°29'20"	porphyry			
89-67	138°44'50"	fine grained greenish	?	?	float sample, continuation
	61°19'50"	porphyry			of 94-6 ?

Appendix 2-11 (continued):

Sample	coordinates	rock type	thickness	strike	field relationship
93-38	138°38'10" 61°22'20"	fine grained diorite	5 m	55° vertical	crosscuts biotite schist
93-112	137°14'50" 61°55'30"	fine grained dark green diorite	?	?	float sample in biotite schist
93-115	137°17'45" 60°56'30"	diorite	3 m	80°	crosscuts biotite schist
93-133	137°31'30" 61°02'52"	fine grained diorite	3-4 m	20°	crosscuts biotite schist
93-134	137°32'15" 61°03'15"	porphyritic andesite (hbl)	?	?	float sample in biotite schist
93-145	137°27'15" 61°16'35"	fine grained diorite	5 m	?	crosscuts biotite schist
93-148	137°27'15" 61°16'05"	fine grained diorite	5 m	?	crosscuts biotite schist
93-179	138°13'35" 61°14'00"	fine grained diorite	5 m	20°	three parallel dykes 200m spaced in biotite schist
93-181	138°14'45" 61°14'35"	fine grained diorite	1 m	20°	crosscuts biotite schist
94-53	138°23'50" 61°19'10"	diorite	?	?	float sample in biotite schist
94-108	137°28'20" 61°03'10"	fine grained hbl granodiorite	5 m	20°	crosscuts biotite schist
94-109	137°29'20" 61°02'15"	fine grained hbl granodiorite	5 m	20°	crosscuts biotite schist continuation of 94-108
94-113	137°22'15" 61°04'00"	fine grained diorite	?	?	float in biotite schist
94-116 117	137°20'40" 61°03'30"	diorite	?	?	float sample in biotite schist
94-127	137°38'10" 61°03'05"	fine grained mafic	?	?	float sample in muscovite-biotite schist
94-128	137°36'20" 61°02'30"	fine grained mafic	?	?	float sample in muscovite-biotite schist
94-158	137°32'15" 61°01'00"	fine grained mafic	5 m	30°	crosscuts biotite schist
94-170	137°55'00" 61°11'40"	fine grained mafic	5-10 m	90°	crosscuts RRB
94-177	137°54'30" 61°14'30"	fine grained mafic	5-10 m	0°	crosscuts RRB
94-277	136°47'30" 60°41'55"	fine grained dark grey mafic	?	330/25	parallel to strike of KMA
94-285	136°45'15" 60°41'30"	two greyish black fine grained mafic	15 cm 30 cm	0° 130/50	crosscuts biotite schist parallel to strike of KMA
89-34	138°06'15" 61°14'10"	porphyritic andesite	?	?	biotite schist
STJ 94-2	137°08'40" 61°00'30"	dark mafic	?	20°	crosscuts cordierite-biotite schist and granitic dyke

Appendix 3-1: Shear-sense indicators deducted from field observations, oriented samples and oriented thinsections

Station	Location (longitude/latitude)		Orientation (foliation/lineation)		Indicators	hangingwall motion
Kluane metamorphic assemblage						
Field observation:						
94-3	138°48'00"	61°19'00"	45/40	102/24	σ-qtz boudin	up
94-15	138°44'40"	61°19'45"	15/45	95/10	δ-qtz porph.	up
94-36	138°36'30"	61°14'10"	40/55	119/16	sheared qtz boudin	up
94-281	136°50'00"	60°41'10"	300/35	265/30	folded qtz vein	down
94-348	139°04'30"	61°27'00"	300/20	290/18	δ	down
95-66	138°17'36"	61°10'45"	20/30	92/19	c'-shear bands	down
Thin section:						
94-3	138°48'00"	61°19'00"	45/40	102/24	δ	up
94-12	138°45'15"	61°20'15"	340/20	269/07	δ	down
94-20c	138°49'15"	61°23'20"	30/55	108/16	C/S	up
94-36	138°36'30"	61°14'10"	40/55	119/16	δ	up
94-39	138°43'04"	61°16'35"	70/22	102/19	δ	up
94-45	138°39'10"	61°20'00"	45/50	335/16	δ	down
94-47	138°37'20"	61°20'55"	10/45	89/10	c'-shear bands	up
94-51	138°33'20"	61°19'00"	15/40	72/24	c'-shear bands	up
94-58	138°23'20"	61°16'50"	85/40	44/32	δ	up
94-60e	138°24'20"	61°16'20"	350/30	280/12	δ, C/S	down
94-62	138°21'00"	61°15'50"	70/25	108/20	δ	up
94-63	138°20'30"	61°15'40"	40/30	89/27	δ	up
94-72	138°30'25"	61°16'40"	310/30	266/22	δ	down
94-76	138°27'45"	61°15'50"	10/15	81/08	δ, C/S	up
94-123	137°43'00"	61°03'55"	90/20	74/19	δ, C/S	up
94-130	137°34'40"	61°01'05"	130/15	45/02	δ	up
94-133	137°31'30"	60°58'05"	140/35	65/10	δ, C/S	up
94-146	137°34'00"	61°57'00"	115/20	73/15	δ, C/S	up
94-153	137°37'30"	60°57'30"	200/25	249/17	δ	down
94-172	137°55'10"	61°10'40"	350/45	58/21	δ	up
94-173	137°54'40"	61°09'55"	350/20	66/05	δ, C/S	up
94-266	137°05'00"	60°36'10"	180/15	231/10	δ	down
95-22	137°40'00"	60°52'05"	198/54	276/16	δ, C'-shear bands	down
95-58	138°24'47"	61°11'35"	40/40	114/15	δ	up
95-64	138°17'55"	61°11'35"	45/50	122/15	δ	up
95-67	138°47'25"	61°10'10"	330/32	52/05	δ	up
Hand sample:						
94-68	138°35'40"	61°15'10"	150/20	103/14	δ	up
94-74	138°28'55"	61°16'10"	0/20	52/17	δ	up
94-108	137°28'20"	61°03'10"	20/15	20/15	C/S	up
94-125	137°40'10"	61°03'25"	115/40	73/32	δ	up
94-173	137°54'20"	61°09'50"	350/20	66/05	δ	up
94-263	137°03'12"	60°36'20"	125/55	69/39	δ	up
94-305	138°07'45"	61°05'20"	15/40	52/34	δ	up

Appendix 3-1 (continued):

Station	Location (longitude/latitude)		Orientation (foliation/lineation)		Indicators	hangingwall motion
94-173	137°54'20"	61°09'50"	350/20	66/05	δ	up
94-263	137°03'12"	60°36'20"	125/55	69/39	δ	up
94-305	138°07'45"	61°05'20"	15/40	52/34	δ	up
94-307	138°09'50"	61°05'30"	20/40	62/32	δ	up
94-347	139°04'10"	61°26'45"	240/30	308/12	σ	down
95-20	137°39'00"	60°51'08"	195/54	270/27	c'-shear bands	down
95-41	138°49'40"	61°22'35"	05/75	276/03	δ	down
95-62	138°21'00"	61°12'15"	18/30	99/05	δ	up
Ruby Range Batholith						
Field observation:						
94-26	138°43'30"	61°23'55"	350/40	70/10	rotated qtz boudin	down
Hand sample:						
94-26c	138°43'25"	61°23'40"	25/70	111/09	C/S	down
Chlorite schist						
Thin section:						
94-84	137°56'15"	60°51'45"	210/45	165/35	δ domino str. in epidote	up
94-191	136°58'30"	60°17'30"	110/85	196/40	δ-px porph.	down
Dezadeash Formation						
Thin section:						
94-237	136°55'40"	60°04'38"	75/35	155/07	rotated grt	up
94-242	138°06'20"	60°53'54"	220/88	220/88	rotated grt	up
94-293/2	137°41'20"	60°06'55"	220/75	293/48	C/S	up
95-26	136°56'30"	60°06'55"	95/27	73/25	rotated porph	up
95-37	136°54'56"	60°21'15"	85/32	114/29	rotated grt, bt	up

Appendix 3-2: Mesoscopic folds in the Kluane metamorphic assemblage

Station	fold type[1]	inclination[2]	vergence	fold axis	wavelength	amplitude
Western Ruby Range:						
93-22	open, symmetrical	-	-	110/10	-	-
93-23	open, asymmetrical	steep	SW	350/25	3 m	1 m
93-146	tight, disharmonic with parasitic folds	recumbent	SE	90/15	15 cm	15 cm
93-149	open, symmetrical	upright	-	10/12	1 m	10 cm
93-150	open, symmetrical	upright	-	165/06	50 cm	10 cm
93-151	open, symmetrical	upright	-	110/20	-	-
93-154	close, disharmonic	gentle	W	20/65	40 cm	30 cm
	kink fold	moderate	NW	55/35	10 cm	5 cm
	close, asymmetrical	moderate	E	160/50	20 cm	20 cm
93-155	open	upright	-	335/18	30 cm	3 cm
93-156	open	upright	-	330/40	20 cm	10 cm
93-158	open	upright	-	292/16	1.5 m	25 cm
93-160	open, symmetrical	upright	-	80/12	-	-
93-161	open	-	-	345/30	-	-
93-162	open	-	-	90/35	-	-
93-167	asymmetrical isoclinal anticline with parasitic folds	steep	S	110/20	5-10 m 75 cm	3-4 m 15 cm
93-168	open, symmetrical	upright	-	340/08	1 m	10 cm
93-169	asymmetrical, tight-open	various	-	345/20	-	-
93-172	asymmetrical open S-ward thrust	moderate	W	300/07	40 cm	10 cm
93-173	ptygmatic actinolite	-	-	320/20	cm	mm-cm
93-174	open	gentle	SW	330/20	2 m	10 cm
94-2	asymmetrical tight	steep	NE	320/20	15 cm	5 cm
	open		NE	350/25	50 cm	10 cm
94-4	asymmetrical, open contact with altered dyke	-	N	100/35	-	-
94-9	asymmetrical open-tight	steep	NW	150/10	50 cm	5-10 cm
94-16	asymmetrical, open	steep	S	330/10	1.5 m	10-20 cm
	parasitic folds				10 cm	2-3 cm
	crenulation folds				mm	mm
94-32	close, asymmetrical	steep	N	120/05	10-20 cm	10 cm
94-33	asymmetrical, tight	moderate	S	300/10	2 cm	1.5 cm
94-35	asymmetrical, close with parasitic folds	steep	SW	300/05	few cm mm	cm mm
94-36	asymmetrical, open with parasitic folds	steep	SW	130/10	0.3-1 m	10-30 cm
94-39	symmetrical, open	upright	-	-	-	-
94-42	asymmetrical open-close	-	SW	135/15	0.1-1 m	cm
94-44	crenulation	-	-	135/02	1 cm	5 mm
94-54	open	moderate	-	10/10	10-15 cm	3-5 cm
94-64	open with crenulation folds	upright	SE	130/20	20-30 cm	5-10 cm
94-66	open	upright	-	150/40	-	-
	with crenulation folds			130/15	cm	mm-cm
94-68	open	upright	-	100/20	10-20 cm	10 cm

Appendix 3-2 (continued):

Station	fold type[1]	inclination[2]	vergence	fold axis	wavelength	amplitude
94-68	crenulation folds open to close	moderate	E	160/25	50 cm	10 cm
94-69	isoclinal	-	-	90/30	cm	cm
94-70	asymmetrical, tight SW thrusting	moderate	SW	300/05	-	-
	symmetrical, open	upright	-	110/10	20 cm	5 cm
94-72	asymmetrical, tight	moderate	SW	330/25	30 cm	20 cm
94-79	symmetrical, open	steep	SE	140/25	0.5-1 m	5 cm
94-173	symmetrical, open	steep	SW	300/25	-	-
94-300	isoclinal	-	NE	300/25	-	-
94-301	asymmetrical, close-tight	steep	S	120/50 290/15, 110/10	0.3-1 m	5-30 cm
94-302	asymmetrical, tight	steep	S	110/20	20 cm	30 cm
94-303	open	-	NE	310/15	20 cm	5 cm
94-304	open	steep	SW	310/30	-	-
94-305	symmetrical, open	upright	-	320/25	50 cm	5 cm
94-306	symmetrical, open	upright	-	310/10	0.5-1 m	5 cm
	crenulation folds	-	-	110/10	0.5-1 cm	5 mm
94-307	asymmetrical, open	-	-	315/20	-	-
95-58	asymmetrical, open	moderate	SW	320/24	10-30 cm	5-20 cm
	crenulation	-	-	310/20	-	-
95-59	asymmetrical, open	moderate	SW	325/20	10-30 cm	5-10 cm
95-60	asymmetrical, open	moderate	SW	310/05	up to 1 m	5-10 cm
	crenulation	-	-	310/05	1 mm	1 mm
95-62	crenulation	-	-	315/11	-	-
95-66	asymmetrical, open	steep	W	345/35	20-30 cm	10 cm
95-67	asymmetrical, close	gentle	SW	310/30	-	-
95-72	isoclinal	recumbent	-	315/15	0.5 -1 m	20 cm
Olivine serpentinite near Doghead Point:						
93-190	crenulation folds	-	-	50/40	5 mm	3 mm
93-191	crenulation folds	-	-	130/18	5 mm	3 mm
93-192	asymmetrical open	moderate	NW	105/30	1 m	20 cm
94-20	crenulation fold	gentle	S	50/30	5 mm	2-3 mm
	tight	-	W	-	cm	cm
94-21	symmetrical, open	moderate	W	150/25	50cm	25 cm
94-23	crenulation	-	-	190/25	1 cm	5 mm
95-43	crenulation	-	-	115/16	5 mm	3 mm
95-47	asymmetrical, close with crenulation	steep	N	265/40	10 cm	3 cm
95-49	crenulation	-	-	255/35	-	-
Eastern and southern Ruby Range:						
93-63	asymmetrical, close	moderate	SW	330/12	10 cm	5 cm
	open	-	-	330/12	10 cm	5 cm
93-65	kink fold	moderate	-	350/18	10 cm	5 cm
93-122	symmetrical, open	upright	-	290/06	-	-
93-123	crenulation	-	-	300/11	5 mm	2-3 mm
94-92	asymmetrical, open	moderate	SW	125/20	50 cm	20 cm
94-93	symmetrical, open	steep	NE	300/18	0.5-1 m	5 cm
94-98	symmetrical, open	upright	-	70/25	30 cm	15 cm
94-91	asymmetrical, open	moderate	SW	135/30	0.5-1 m	5-10 cm
94-101	symmetrical, open	upright	-	110/45	50 cm	5 cm

Appendix 3-2 (continued):

Station	fold type[1]	inclination[2]	vergence	fold axis	wavelength	amplitude
94-102	symmetrical, open	upright	-	80/25	50 cm	5 cm
94-117	symmetrical, open	upright	-	0/15	20 cm	3 cm
94-118	open	moderate	W	350/15	few m	0.5-1 m
	kink folds, close	moderate	W	350/10	10-15 cm	2-5 cm
	with shear zones (40/30) indicating hw down					
94-119	symmetrical, open	upright	-	350/10	10-50 cm	2-10 cm
	with parasitic crenulation					
94-120	symmetrical, open	upright	-	130/15	10 cm	2-3 cm
94-125	asymmetrical kink	steep	NW	175/15	20-30 cm	5 cm
94-128	asymmetrical, open	steep	SW	140/25	50 cm	10 cm
94-135	asymmetrical,	moderate	NW	50/20	10-20 cm	5 cm
	open-close					
94-141	open	recumbent	-	60/50	20-50 cm	10-20 cm
94-146	symmetrical, open	upright	-	80/05	10-30 cm	2-5 cm
94-151	asymmetrical, open	moderate	E	10/10	10 cm	5 cm
	with parasitic folds					
	asymmetrical, close	gentle	NE	150/25	1 m	50 cm
	crenulation in hinges					
94-153	symmetrical, open	steep	SW	150/25	0.5-1 m	5 cm
94-156	symmetrical, open	upright	-	120/25	0.5-1 m	5 cm
94-386	symmetrical, open	upright	-	130/25	1-2 m	10 cm
95-20	open	moderate	SW	135/34	1 m	10 cm
95-21	crenulation	-		123/28	0.5-1 cm	0.5-1 cm
95-22	open	moderate	SW	135/24	0.75 m	10-20 cm
Dezadeash Range:						
93-81	symmetrical, open	recumbent	-	140/12	50 cm	20 cm
93-82	asymmetrical, kink	moderate	NE	140/15	-	-
93-84	asymmetrical, open	gentle	N	130/25	1 m	20 cm
93-86	asymmetrical, open	gentle	SW	135/15	2 m	50 cm
93-87	asymmetrical, open	gentle	-	135/15	-	-
	with parasitic crenulation					
93-88	asymmetrical, open	gentle	-	125/16	-	-
93-90	asymmetrical, open	gentle	-	135/25	1-1.5 m	10 cm
93-99	asymmetrical, close	recumbent	-	90/12	1.5 m	1 m
	symmetrical, open	upright	-	90/12	20 cm	5 cm
94-252	symmetrical, open	gentle	W	0/10	20 cm	5 cm
94-263	symmetrical, open	steep	E	170/60	10 cm	1-2 cm
94-265	symmetrical, open	steep	W	110/10	10-15 cm	2-5 cm
	with crenulation	-	-	95/00	mm	mm
94-270	crenulation	-	-	110/10	mm	mm
94-274	crenulation	-	-	100/03	mm	mm
94-275	open	steep	S	290/20	few cm	cm
94-276	asymmetrical, open	steep	NW	220/20	20-30 cm	5-10 cm
94-279	asymmetrical	recumbent	-	315/25	cm	cm
94-280	asymmetrical, open	steep	NE	300/15	20-30 cm	5 cm
94-283	asymmetrical,isoclinal	gentle	NE	130/20	-	-
94-297-1	open	steep	W	0/10	-	-

1: interlimb angle: open:120°-71° ; close:70°-31° ; tight:30°-1° ; isoclinal: 0°;
2: recumbent: 0°-10°; gentle: 11°-30°; moderate: 31°-60°; steep: 61° -80°; upright: 81°-90°;
(after Twiss & Moores 1992).

Appendix 3-3

Application of SpheriStat (version 2.0)

SpheriStat 2.0 (Pangaea Scientific, 1995) is a Windows-based program able to produce stereoplots, circular rose diagrams and maps, calculate principle directions and provide a number of structural analyses. SpheriStat graphics can be imported into any graphics software for further enhancement.

The SpheriStat data base consists of station identification, group identification, azimuth and inclination. Optional are station coordinates, weighing of points and additional text information.

Stereoplots of structural data presented in this thesis are equal area (Schmidt) lower hemisphere projections, unless noted otherwise. Point density distribution was calculated using the Gaussian counting method. Compared to the fixed-circle counting methods (Schmidt, Starkey, Kamb), which have sharp cut-off points, the Gaussian method includes all data points weighted by the function of the cosine of the angular distance from the counting station. As a result the contours calculated with the Gaussian method are smoother than fixed-circle contours. The counting function used by the Gaussian method is a Fisher function: $w=\exp[k(\cos(\theta)-1]$, where θ is the angular distance and k is the kurtosis. SpheriStat calculates the expected count $E=N/k$, representing an uniform distribution of N points, and the standard deviation σ as the square root of the variance (integral of $(w-E)^2$ over the half sphere). A value of k=100, as applied in this study, represents a counting area of 1%. Contour intervals are shown as multitudes of σ.

Principle directions or eigenvectors, which measure the clustering of the whole data set, are calculated independently from the counting method. The eigenvectors are three orthogonal vectors with a certain magnitude, the so-called eigenvalues. The smallest eigenvector represents the normal to the best fit plane through the data points. The largest eigenvector is the direction of the statistically largest clustering. Eigenvectors are calculated by summing the

matrix of the products and cross-products of the direction cosines of each data point. The eigenvector of the resulting matrix is calculated by the Jacobi method. The diagonal components of the matrix are the eigenvalues. The sum of the eigenvalues is N, the total number of data points (Watson, 1966).

A method to analyse the fabric shape of stereographic projections was developed Woodcock (1977). Two ratios of the natural logarithms of normalized eigenvalues S_1, S_2, S_3 of the eigenvectors E_1, E_2, E_3, respectively, are plotted on a 'modified Flinn diagram', named after Ramsay's (1967) modification of the Flinn strain diagram, which describes strain shapes (Flinn, 1962). SpheriStat uses the modified Flinn diagram and calculates the Woodcock ratios K and C. The K-ratio, $K=[\ln(S_1/S_2)/\ln(S_2/S_3)]$, describes the pattern (girdle or cluster), while the C-ratio, $C=\ln(S_1/S_2)$, describes the pattern strength (weakly to strong developed).

Appendix 3-4: Station localities and structural data [1]

Sample	rock	Long (W) / Lat (N)	foliation	lineation	fold axes [2]	NTS map [3]
89-39	2	138°09'40", 61°11'50"	0/35			115 G/1
89-40	2	138°10'10", 61°11'35"	340/45		330/10, 65/10	115 G/1
89-41	2	138°10'35", 61°11'20"	340/35		0/16	115 G/1
89-42	2	138°09'40", 61°10'55"	5/35			115 G/1
89-43	2	138°08'20", 61°10'57"	357/43			115 G/1
89-45	1	138°06'30", 61°14'40"	350/15			115 G/1
89-47	1	138°06'00", 61°15'40"	350/15			115 G/8
89-48	1	138°06'00", 61°15'55"	350/15			115 G/8
89-49	1	138°06'15", 61°16'30"	200/20			115 G/8
89-50	1	138°06'50", 61°17'10"	350/25		250/05	115 G/8
89-52	2,3	138°03'45", 61°11'50"	20/35			115 G/1
89-53	1	138°03'00", 61°12'20"	40/35			115 G/1
89-54	1	138°03'00", 61°12'30"	20/35		15/15	115 G/1
89-55	1	138°03'00", 61°12'40"	0/25			115 G/1
89-56	1	138°02'35", 61°12'55"	0/35			115 G/1
89-57	1	138°01'40", 61°13'15"	0/30			115 G/1
89-58	3	138°02'10", 61°13'15"	0/35			115 G/1
89-59	1	138°02'00", 61°13'40"	0/45			115 G/1
89-60	1	138°04'00", 61°15'15"	0/25			115 G/1
89-61	1	138°02'45", 61°13'40"	240/35			115 G/8
89-62	1	138°02'30", 61°15'15"	250/15			115 G/8
89-62	1	138°02'30", 61°15'45"	250/20			115 G/8
89-63	1	138°02'00", 61°14'55"	330/25			115 G/1
89-64	1	138°02'00", 61°14'30"	350/25			115 G/1
89-65	1	138°02'00", 61°14'10"	350/25			115 G/1
89-66	2	138°45'20", 61°15'05"	60/35			115 G/7
89-67	2	138°44'50", 61°19'50"	60/35			115 G/7
89-68	2	138°45'15", 61°20'25"	50/40			115 G/7
89-69	2	138°46'00", 61°20'20"	60/30			115 G/7
89-70	2	138°46'30", 61°20'00"	60/40			115 G/7
89-71	2	138°46'50", 61°19'20"	70/25			115 G/7
89-72	2	138°47'20", 61°19'00"	90/25		350/15 (SW)	115 G/7
89-73	2	138°47'40", 61°18'48"	60/20			115 G/7
89-74	2	138°43'03", 61°16'35"	70/50			115 G/7
89-75	2	138°42'50", 61°16'05"	70/50		135/30 (Cr)	115 G/7
89-76	2	138°42'25", 61°15'55"	100/30		320/25	115 G/7
89-77	2	138°48'15", 61°15'30"	100/30		350/10	115 G/7
89-78	3	138°38'10", 61°14'30"	60/30		140/10	115 G/2
89-79	2	138°37'12", 61°14'22"	60/25			115 G/2
89-80	3	138°36'30", 61°14'10"	30/50			115 G/2
89-81	2	138°34'25", 61°13'25"	40/40		310/05 (SW)	115 G/2
89-82	2	138°32'15", 61°13'55"	300/40		340/20	115 G/2
89-83	2	138°28'45", 61°10'55"	0/40		320/10 (SW)	115 G/1
89-85	1	138°25'45", 61°07'50"	20/55		75/15	115 G/1
89-95	1	137°26'30", 60°49'35"	180/70			115 A/14
89-96	1	137°25'00", 60°50'00"	180/60			115 A/14
89-97	12m	136°33'00", 60°30'15"	50/70			115 A/10
89-98	12	136°33'25", 60°30'07"	50/60		110/50	115 A/10
89-99	12	136°34'00", 60°30'01"	130/35		110/40 (cr)	115 A/10
89-100	12	136°35'10", 60°29'55"	130/40			115 A/7
89-101	12	136°36'17", 60°29'55"	140/50			115 A/7

Appendix 3-4 (continued):

Sample	rock	Long (W) / Lat (N)	foliation	lineation	fold axes [2]	NTS map [3]
89-102	12	136°37'05", 60°29'45"	130/50			115 A/7
89-103	12	136°32'10", 60°29'59"	150/45			115 A/7
89-105	12	136°32'10", 60°29'40"	140/50			115 A/7
89-106	12	136°30'30", 60°31'05"	205/85		110/30	115 A/10
89-107	12m	136°31'30", 60°31'10"	205/85		150/50	115 A/10
89-108	12	136°33'10", 60°31'20"	190/80			115 A/10
89-109	12	136°35'13", 60°31'15"	20/65			115 A/10
89-110	12m	136°33'50", 60°30'38"	50/60			115 A/10
89-112	1	137°03'10", 60°42'55"	190/30			115 A/11
89-114	1	136°49'00", 60°49'00"	135/45		20/10	115 A/15
89-117	1	137°01'30", 60°54'25"	190/64			115 A/14
89-118	5a	137°01'50", 60°58'10"	15/77			115 A/14
90-20	1	136°51'30", 60°42'05"	250/20			115 A/10
90-21	1	136°50'45", 60°40'55"	320/35			115 A/10
90-22	1	136°49'35", 60°41'00"	320/35			115 A/10
90-23	1	136°48'40", 60°41'30"	260/40			115 A/10
90-24	1	136°47'10", 60°41'40"	300/15			115 A/10
90-25	1	136°46'50", 60°41'45"	310/35			115 A/10
90-27	1	136°52'00", 60°41'10"	285/40			115 A/10
90-28	1	136°53'30", 60°41'25"	230/30			115 A/10
90-29	1	136°53'30", 60°41'25"	235/15			115 A/10
90-30	1	136°54'50", 60°41'35"	230/20			115 A/10
90-32	1	136°54'00", 60°42'35"	230/20			115 A/10
90-36	2	138°15'00", 61°08'00"	0/40		90/30	115 G/1
90-38	1, 2	138°17'20", 61°07'05"	40/50			115 G/1
90-39	1	138°17'20", 61°06'45"	35/35			115 G/1
90-40	1	138°16'20", 61°06'10"	35/45			115 G/1
90-41	1	138°11'10", 61°05'40"	35/45			115 G/1
90-42	1, 2	138°10'00", 61°05'35"	25/55			115 G/1
89-32	1	138°07'10", 61°13'20"	0/40			115 G/1
89-34	1	138°06'15", 61°14'10"	0/40			115 G/1
89-35	1	138°06'15", 61°14'20"	10/35			115 G/1
89-36	2	138°07'50", 61°13'00"	10/35			115 G/1
89-37	2	138°08'35", 61°12'40"	20/45			115 G/1
89-38	2	138°09'30", 61°12'10"	350/40			115 G/1
93-8	2	138°42'55", 61°16'35"	80/34			115 G/7
93-11	2	138°38'10", 61°14'30"	53/46			115 G/2
93-13	2	138°29'45", 61°14'45"	90/27			115 G/1
93-14	2	138°28'50", 61°15'25"	50/28			115 G/8
93-15	2	138°27'48", 61°15'50"	25/15			115 G/8
93-16	2	138°27'00", 61°15'15"	33/25			115 G/8
93-17	2	138°26'10", 61°15'00"	33/15			115 G/8
93-18	2	138°24'50", 61°15'16"	50/15			115 G/8
93-19	2	138°23'30", 61°14'30"	70/20			115 G/1
93-20	2	138°22'00", 61°13'50"	45/13			115 G/1
93-21	2	138°21'00", 61°12'15"	40/25			115 G/1
93-22	2	138°22'00", 61°11'58"	40/35		110/10	115 G/1
93-23	2	138°23'30", 61°11'50"			350/25	115 G/1
93-24	2	138°24'15", 61°11'50"	40/34			115 G/1
93-25	2	138°25'00", 61°11'45"	30/39			115 G/1
93-27	5	138°37'25", 61°24'20"	27/57			115 G/7

Appendix 3-4 (continued):

Sample	rock	Long (W) / Lat (N)	foliation	lineation	fold axes [2]	NTS map [3]
93-32	5	138°33'50", 61°22'05"	280/55, 340/50			115 G/7
93-33	1	138°33'40", 61°21'45"	10/36			115 G/7
93-34	1	138°33'50", 61°21'28"	0/27			115 G/7
93-35	1	138°34'50", 61°21'28"	350/25			115 G/7
93-36	1	138°35'50", 61°21'40"	10/22			115 G/7
93-37	1	138°36'10", 61°22'00"	0/29			115 G/7
93-38	9	138°38'10", 61°22'20"	6/29			115 G/7
93-39	5	138°38'00", 61°22'40"	327/60			115 G/7
93-41	5	138°44'00", 61°23'40"	355/55			115 G/7
93-43	5	138°44'28", 61°23'25"	50/45			115 G/7
93-44	4	138°44'40", 61°23'20"	0/50			115 G/7
93-45	1	137°05'05", 60°52'02"	178/56			115 A/14
93-46	1	137°05'20", 60°52'20"	162/43			115 A/14
93-47	1	137°06'15", 60°52'20"	175/55			115 A/14
93-48	1	137°07'35", 60°52'18"	175/55			115 A/14
93-49	1	137°08'20", 60°52'19"	170/42			115 A/14
93-50	1	136°47'00", 60°49'35"	195/41			115 A/15
93-51	1	136°47'20", 60°49'45"	172/70			115 A/15
93-52	1	136°45'30", 60°49'40"	184/58			115 A/15
93-54	1	136°37'30", 61°09'00"	85/56			115 H/4
93-55	1	137°39'30", 61°08'30"	70/22			115 H/4
93-56	1	137°39'30", 61°08'10"	50/21			115 H/4
93-57	1	137°38'50", 61°07'27"	72/24			115 H/4
93-58	1	137°38'55", 61°07'00"	85/30			115 H/4
93-59	1	137°40'50", 61°06'55"	56/24			115 H/4
93-61	1	137°40'50", 61°06'17"	45/32			115 H/4
93-62	1, 2	137°40'00", 61°05'56"	34/21			115 H/4
93-63	1, 2	137°39'50", 61°05'57"			330/12	115 H/4
93-64	2	137°39'30", 61°05'55"	57/36			115 H/4
93-65	1	137°39'30", 61°06'20"	69/31		350/18	115 H/4
93-66	1	137°38'20", 61°06'35"	68/20			115 H/4
93-67	1	137°41'53", 61°07'45"	55/39			115 H/4
93-68	1	137°41'55", 61°08'00"	65/29			115 H/4
93-70	1	137°40'55", 61°07'18"	50/27			115 H/4
93-71	1	137°43'00", 61°09'45"	60/24			115 H/4
93-72	1	137°02'25", 60°44'50"	175/20			115 A/11
93-73	1	137°01'50", 60°44'25"	185/20			115 A/11
93-74	1	137°01'35", 60°44'20"	188/23			115 A/11
93-76	1, 5	137°03'10", 60°42'55"	170/34			115 A/11
93-77	1	137°03'45", 60°43'00"	195/31			115 A/11
93-78	1	137°04'25", 60°43'00"	193/33			115 A/11
93-79	1	137°05'25", 60°44'20"	185/40			115 A/11
93-80	1	137°05'55", 60°44'15"	210/55			115 A/11
93-81	1	137°07'05", 60°43'35"			140/12	115 A/11
93-82	1	137°06'40", 60°43'15"	225/39		140/15	115 A/11
93-83	1	137°05'55", 60°46'45"	205/75			115 A/14
93-84	1	137°06'15", 60°46'20"			130/25	115 A/14
93-85	1	137°07'10", 60°45'50"	70/45			115 A/14
93-86	1	137°08'20", 60°46'00"	35/50		135/15	115 A/14
93-87	1	137°08'15", 60°45'30"	45/65		135/15	115 A/14
93-88	1	137°08'35", 60°45'10"			125/16	115 A/14

Appendix 3-4 (continued):

Sample	rock	Long (W) / Lat (N)	foliation	lineation	fold axes [2]	NTS map [3]
93-89	1	137°07'35", 60°45'25"	215/75			115 A/14
93-90	1	137°03'48", 60°45'15"	215/83		135/25	115 A/14
93-91	1	137°03'20", 60°41'20"	210/34			115 A/11
93-92	1	137°02'45", 60°41'17"	200/30			115 A/11
93-93	1	137°01'25", 60°41'15"	205/26			115 A/11
93-94	1	136°59'45", 60°41'05"	205/20			115 A/10
93-95	8	136°59'30", 61°41'30"	205/20			115 A/10
93-96	1	136°57'36", 60°42'15"	220/19			115 A/10
93-97	1	136°57'45", 60°41'30"	210/16			115 A/10
93-98	1	136°58'00", 60°40'50"	215/14			115 A/10
93-99	1	136°58'20", 60°40'25"			90/12	115 A/10
93-101	1	137°10'55", 60°55'30"	180/15			115 A/14
93-102	1	137°11'00", 60°54'55"	210/08			115 A/14
93-103	1	137°11'40", 60°54'30"	66/34			115 A/14
93-104	1	137°12'30", 60°54'00"	110/19			115 A/14
93-105	1	137°12'50", 60°53'45"	120/20			115 A/14
93-106	1	137°14'45", 60°53'55"	115/17			115 A/14
93-107	1	137°15'00", 60°54'10"	180/36			115 A/14
93-108	1	137°14'45", 60°57'00"	150/20			115 A/14
93-110	1	137°14'40", 60°56'10"	65/17			115 A/14
93-111	1	137°14'00", 60°55'52"	80/15			115 A/14
93-113	1	137°14'50", 60°55'15"	110/12			115 A/14
93-114	1	137°16'10", 60°54'30"	130/18			115 A/14
93-115	1	137°17'45", 60°56'30"	95/20			115 A/14
93-116	1	137°18'35", 60°56'00"	135/20			115 A/14
93-117	1	137°19'00", 60°55'53"	70/20			115 A/14
93-118	1	137°19'30", 60°56'00"	130/15			115 A/14
93-119	1	137°19'40", 60°56'08"	110/12			115 A/14
93-121	1	137°20'50", 60°56'07"	40/35			115 A/14
93-122	1	137°20'40", 60°56'50"	358/34		290/06	115 A/14
93-123	1	137°21'10", 60°57'00"			300/11	115 A/14
93-124	1	137°21'00", 60°57'10"	325/30			115 A/14
93-125	1	137°18'50", 60°56'40"	100/20			115 A/14
93-126	1	137°35'17", 60°05'55"	40/29			115 H/4
93-127	1	137°35'25", 61°05'00"	50/24			115 H/4
93-128	1	137°35'35", 60°04'20"	70/17			115 H/4
93-129	1	137°35'10", 61°04'18"	70/23			115 H/4
93-130	1	137°34'15", 61°04'15"	55/22			115 H/4
93-131	1	137°32'00", 61°03'40"	40/14	55/09		115 H/4
93-132	1	137°31'10", 61°03'15"	75/20			115 H/4
93-133	1	137°31'30", 61°02'55"	45/20			115 H/4
93-135	1	137°32'50", 61°03'15"	70/18			115 H/4
93-136	1	137°33'20", 61°03'30"	65/20			115 H/4
93-139	1	137°30'50", 61°04'20"	45/25			115 H/4
93-142	1	138°26'50", 61°18'00"	15/34			115 G/8
93-144	2	138°27'00", 61°17'05"	45/20			115 G/8
93-145	2	138°26'20", 61°16'38"	10/21			115 G/8
93-146	2	138°26'10", 61°16'28"	15/24		90/15	115 G/8
93-147	2	138°26'10", 61°16'20"	300/19			115 G/8
93-148	2	138°27'15", 61°16'05"	19/24			115 G/8
93-149	2	138°27'40", 61°15'07"			10/12	115 G/8

Appendix 3-4 (continued):

Sample	rock	Long (W) / Lat (N)	foliation	lineation	fold axes [2]	NTS map [3]
93-150	2	138°22'55", 61°14'00"		100/02	165/06	115 G/1
93-151	2	138°21'45", 61°13'45"			110/20	115 G/1
93-154	2	138°17'55", 61°11'35"			20/65, 325/20	115 G/1
93-155	2	138°16'15", 61°12'05"	15/55		335/18	115 G/1
93-156	2	138°16'00", 61°12'20"			330/24	115 G/1
93-157	2	138°15'15", 61°12'48"	14/17		170/15	115 G/1
93-158	2	138°14'30", 61°13'00"			292/16	115 G/1
93-160	2	138°13'40", 61°12'20"	335/70		80/12	115 G/1
93-161	2	138°13'15", 61°12'10"			345/30	115 G/1
93-162	2	138°13'00", 61°12'00"			90/35	115 G/1
93-163	2	138°12'40", 61°11'50"	340/40			115 G/1
93-164	3	138°12'30", 61°11'15"	355/40			115 G/1
93-165	2	138°12'50", 61°12'35"	355/50			115 G/1
93-166	2	138°15'35", 61°13'20"	85/06			115 G/1
93-167	2	138°18'00", 61°12'50"			110/20	115 G/1
93-168	2, 3	138°18'00", 61°12'30"	20/50		340/08	115 G/1
93-169	2	138°18'10", 61°12'10"			345/20	115 G/1
93-170	2	138°18'00", 61°11'55"	40/50			115 G/1
93-171	2	138°18'00", 61°11'15"	40/50			115 G/1
93-172	2	138°18'05", 61°10'55"			300/07	115 G/1
93-173	2	138°18'40", 61°11'20"			320/20	115 G/1
93-174	2	138°19'10", 61°11'22"	25/38		330/35	115 G/1
93-175	2	138°13'30", 61°13'40"	340/20			115 G/1
93-176	2	138°13'20", 61°13'48"	25/20			115 G/1
93-177	1	138°11'00", 61°14'25"	55/25			115 G/1
93-178	1	138°13'55", 61°12'30"	0/25			115 G/1
93-180	1	138°14'15", 61°14'25"	10/43			115 G/1
93-182	1	138°15'00", 61°14'45"	50/30			115 G/1
93-184	1	138°15'20", 61°16'00"	0/35			115 G/8
93-186	1	139°03'35", 61°26'00"	200/50			115 G/6
93-188	1	138°51'20", 61°22'35"	0/80			115 G/7
93-189	1	138°50'25", 61°22'40"	355/60			115 G/7
93-190	4	138°49'35", 61°23'05"	30/50		50/40	115 G/7
93-191	4	138°49'30", 61°23'10"	240/65		130/18	115 G/7
93-192	4	138°49'15", 61°23'20"	145/50		100/30	115 G/7
93-193	4	138°49'45", 61°23'25"	355/70			115 G/7
93-194	7	138°08'25", 60°55'48"	240/50			115 B/16
93-195	7	138°09'00", 60°56'00"	160/90			115 B/16
93-196	7	138°07'45", 60°55'18"	195/75			115 B/16
93-199	10	138°42'55", 61°25'15"			340/40	115 G/7
93-200	5	138°43'40", 61°38'45"	150/70			115 G/10
93-201	10m	138°43'55", 61°37'55"	165/20		100/25, 180/20	115 G/10
93-204	10	138°42'50", 61°36'55"	140/55			115 G/10
93-205	10	138°41'53", 61°40'15"	40/30		340/15, 60/35	115 G/10
93-206	10	138°41'40", 61°40'27"	45/45		310/04	115 G/10
93-207	10	138°41'15", 61°40'40"	30/25		10/25, 130/02	115 G/10
93-208	10	138°40'48", 61°39'10"	40/30			115 G/10
93-218	14	139°14'20", 61°23'05"	190/85 (b)			115 G/6
93-219	14	139°14'20", 61°23'20"	190/70 (b)			115 G/6
93-223	15	139°14'00", 61°24'25"		240/70	140/40	115 G/6
93-224	14	139°27'10", 61°28'10"	180/35 (b)			115 G/6

Appendix 3-4 (continued):

Sample	rock	Long (W) / Lat (N)	foliation	lineation	fold axes [2]	NTS map [3]
93-225	15	139°25'55", 61°29'05"			130/40	115 G/15
93-226	11	140°11'50", 61°53'35"	210/85		300/30	115 F/16
93-227	11m	140°11'15", 61°53'20"	150/75			115 F/16
93-229	11	140°08'20", 61°52'05"	60/30			115 F/16
93-230	11	140°08'20", 61°52'20"	60/30			115 F/16
93-231	11	140°08'20", 61°52'25"			310/20	115 F/16
93-232	11	140°08'30", 61°52'37"	280/30			115 F/16
93-233	11	138°08'20", 61°52'40"	250/55		335/08	115 F/16
93-234	11	138°08'22", 61°52'50"	230/70			115 F/16
93-235	11	140°08'20", 61°53'15"		330/25	320/20	115 F/16
93-236	11	140°15'00", 61°54'25"	65/80			115 F/16
93-237	11	140°17'15", 61°55'10"	40/80			115 F/16
93-239	14	140°31'00", 61°57'40"	345/80			115 F/15
93-244	11	140°34'48", 62°02'48"	80/50		65/45	115 K/2
93-245	11	140°35'15", 62°03'00"	95/50			115 K/2
93-246	11	140°35'00", 61°03'15"	150/65		95/50	115 K/2
93-247	12	137°07'50", 60°37'05"	180/35			115 A/9
93-249	12	137°08'15", 60°36'50"	180/55			115 A/9
93-250	12	137°08'15", 60°36'18"	180/40			115 A/9
93-252	6	137°43'40", 60°24'55"	260/80 (b)			115 A/11
93-253	7	136°59'10", 60°17'40"			320/50	115 A/7
93-254	7	136°58'58", 60°18'03"	340/60		50/50	115 A/6
93-255	6, 12	136°58'22", 60°18'10"	70/60			115 A/7
93-256	12	136°58'00", 60°18'12"			70/35	115 A/7
93-257	12	136°57'12", 60°17'40"			85/40	115 A/7
93-259	6	136°58'15", 60°11'07"	220/85 (b)			115 A/2
93-260	6	136°57'50", 60°10'40"	0/85 (b)		250/85, 310/60	115 A/2
93-261	6	136°57'20", 60°10'12"	270/70 (b)			115 A/2
93-262	6	136°57'15", 60°10'00"	280/75 (b)			115 A/2
93-267	6	136°41'20", 59°52'55"	250/60 (b)			114 P/15
93-269	6	136°41'40", 60°46'35"	180/50 (b)			115 A/13
93-270	7	136°44'10", 60°45'05"	245/50		165/05	115 A/13
93-272	6	136°45'30", 60°45'20"	320/40 (b)			115 A/13
93-273	1	137°01'15", 60°54'10"	200/85			115 A/14
93-274	1	137°00'35", 60°54'20"	0/65			115 A/14
93-275	1	136°58'30", 60°54'15"	30/45			115 A/15
93-276	1	137°58'45", 60°54'00"	0/60			115 A/15
94-1	2	138°45'30", 61°19'12"	30/40	100/15		115 G/7
94-2	2	138°47'20", 61°18'42"	40/35		350/25 (NE)	115 G/7
94-3	2	138°48'00", 61°19'00"	60/40	105/15		115 G/7
94-4	8	138°47'45", 61°19'05"	50/40	100/35		115 G/7
94-6	2, 8	138°47'30", 61°19'05"	0/60			115 G/7
94-7	2	138°47'10", 61°19'05"	55/10	115/05		115 G/7
94-8	2	138°47'05", 61°19'08"	54/50	120/25		115 G/7
94-9	2, 8	138°47'00", 61°19'20"			150/10	115 G/7
94-10	2, 8	138°46'50", 61°19'30"	60/20	120/10		115 G/7
94-11	2	138°46'00", 61°20'10"	75/30			115 G/7
94-12	2	138°45'15", 61°20'30"	340/20	269/07		115 G/7
94-13	2	138°46'00", 61°20'15"	30/60	100/15		115 G/7
94-15	2	138°44'10", 61°19'45"	15/45			115 G/7
94-16	2	138°45'00", 61°19'20"	60/27	100/20	330/10	115 G/7

Appendix 3-4 (continued):

Sample	rock	Long (W) / Lat (N)	foliation	lineation	fold axes [2]	NTS map [3]
94-17	2	138°49'30", 61°23'30"	0/70	90/15		115 G/7
			30/45	112/07		
94-18	2	138°49'05", 61°22'40"	15/52			115 G/7
94-19	4	138°49'03", 61°23'00"	0/40			115 G/7
94-20	4, 4g	138°49'15", 61°23'20"	30/35, 160/58	108/16	50/30 (cr)	115 G/7
94-21	4	138°48'30", 61°23'22"			150/30 (SW)	115 G/7
94-22	4	138°48'00", 61°23'22"	210/80			115 G/7
94-23	4	138°47'15", 61°23'22"	210/55		190/25 (cr)	115 G/7
94-24	4	138°47'00", 61°23'25"	40/70			115 G/7
94-25	4	138°44'40", 61°23'20"	20/30			115 G/7
94-26	5	138°43'50", 61°23'50"	350/40	70/10	300/70 (cr)	115 G/7
94-28	5	138°40'45", 61°24'45"	15/70			115 G/2
94-32	1	138°25'45", 61°07'50"	30/30		300/05	115 G/1
94-33	2	138°27'45", 61°10'40"	15/45, 10/65 (ccl)	310/20	300/10	115 G/1
94-34	2	138°33'15", 61°13'00"	40/35			115 G/2
94-35	2	138°34'25", 61°13'25"	65/30, 40/45	130/05 (cr),	300/05 (SW)	115 G/2
94-36	2	138°36'30", 61°14'10"	40/55	119/16	330/20 (cr)	115 G/2
94-37	2	138°38'05", 60°14'30"	60/35		140/10 (cr)	115 G/2
94-38	2	138°38'45", 60°14'35"	65/22			115 G/2
94-39	2	138°43'03", 61°16'35"	65/25	102/10	135/15	115 G/2
94-40	2	138°42'50", 61°16'05"	55/25	105/10		115 G/7
94-42	2	138°41'15", 61°15'30"			135/15 (SW)	115 G/7
94-44	2	138°42'25", 61°16'35"	60/20	110/10	135/00 (cr)	115 G/7
94-45	2	138°39'10", 61°20'00"	45/40	335/16		115 G/7
94-46	1	138°38'10", 61°20'40"	25/40	110/20		115 G/7
94-47	1	138°37'20", 61°20'55"	10/45	90/10		115 G/7
94-48	1	138°36'45", 61°20'40"	0/40			115 G/7
94-49	1	138°39'35", 61°21'40"	350/33			115 G/7
94-50	1	138°40'00", 61°21'10"	10/25			115 G/7
94-51	2	138°33'20", 61°19'50"	0/34	75/10		115 G/7
94-52	1	138°24'30", 61°19'30"	10/40			115 G/8
94-54	1	138°23'50", 61°19'00"	20/33			115 G/8
94-55	1	138°22'45", 61°18'00"	340/15	265/05		115 G/8
94-56	1	138°22'40", 61°17'50"	355/15			115 G/8
94-57	1	138°22'45", 61°17'20"	135/25	90/20		115 G/8
94-58	1	138°23'20", 61°16'50"	80/40	90/40		115 G/8
94-59	1	138°24'00", 61°16'38"	80/35	85/30		115 G/8
94-60	1	138°24'20", 61°16'20"	25/50	90/05		115 G/8
94-61	1	138°20'40", 61°16'20"	40/40	71/36		115 G/8
94-62	1	138°21'00", 61°15'50"	70/25	108/20		115 G/8
94-63	2	138°20'30", 61°15'40"	40/30	89/21		115 G/8
94-64	2	138°40'20", 61°15'30"	80/35	88/15		115 G/7
94-65	2	138°39'50", 61°15'35"	80/30			115 G/7
94-68	2	138°35'40", 61°15'10"	150/20	110/15	160/25 (E)	115 G/7
94-69	2	138°33'15", 61°15'30"	60/35		90/30	115 G/7
94-70	2	138°32'35", 61°15'27"	35/50		110/10	115 G/7
94-71	2	138°31'00", 61°16'30"	50/20			115 G/7
94-72	2	138°30'25", 61°16'40"	310/30	270/10	330/25	115 G/7
94-73	2	138°29'35", 61°16'35"	0/25			115 G/8
94-74	2	138°28'55", 61°16'10"	0/20	52/17		115 G/8
94-75	2	138°28'30", 61°16'03"	10/10			115 G/8

Appendix 3-4 (continued):

Sample	rock	Long (W) / Lat (N)	foliation	lineation	fold axes [2]	NTS map [3]
94-76	2	138°27'50", 61°15'50"	10/15	70/05		115 G/8
94-77	2	138°29'55", 61°15'10"	65/30	110/25		115 G/8
94-78	2	138°31'20", 61°15'42"	50/35	100/15		115 G/2
94-79	2	138°33'30", 61°14'55"	45/40			115 G/2
94-80	2	138°35'25", 61°14'05"	40/55			115 G/2
94-81	1	137°04'10", 60°51'35"	180/60	110/25		115 A/14
94-82	1	137°01'10", 60°54'15"	30/85			115 A/14
94-83	1	137°01'50", 60°58'10"	15/75			115 A/14
94-84	7	137°56'15", 60°51'50"	210/45	165/35		115 A/13
94-85	7	137°57'50", 60°51'40"	210/35		145/20 (cr)	115 A/13
94-86	7	137°38'10", 60°51'30"	195/60			115 A/13
94-87	7	137°59'30", 60°51'45"	210/85	285/15		115 A/13
94-88	6, 7	138°00'03", 60°51'50"	25/75			115 B/16
94-89	6	137°57'20", 61°51'10"	180/55	124/39	110/20	115 A/13
94-90	1	137°29'40", 60°08'30"	200/80			115 A/14
94-91	1	137°29'30", 60°08'30"			135/30 (SW)	115 A/14
94-92	1	137°27'40", 60°08'30"	220/85		125/20 (SW)	115 A/14
94-93	1	137°21'00", 60°08'30"	0/20		300/18 (NE)	115 A/14
94-94	1	137°20'20", 60°58'40"	35/30			115 A/14
94-95	1	137°19'30", 60°58'38"	0/40			115 A/14
94-96	1	137°18'40", 60°59'30"	10/60			115 A/14
94-98	1	137°18'30", 61°00'10"	115/30		70/25	115 H/3
94-99	1	137°18'45", 61°00'45"	90/30			115 H/3
94-100	1	137°18'15", 61°01'37"	45/60			115 H/3
94-101	1	137°17'10", 61°00'05"	110/45		110/45	115 H/3
94-102	1	137°16'00", 61°00'35"	50/30		80/25	115 H/3
94-103	1	137°25'50", 61°06'10"	300/45			115 H/3
94-105	1	137°25'45", 61°04'50"	35/30	356/24		115 H/3
94-106	1	137°26'40", 61°04'30"	50/30			115 H/3
94-107	1	137°27'15", 61°04'02"	60/30			115 H/3
94-108	1	137°28'20", 61°03'10"	20/15	20/15		115 H/3
94-109	1	137°29'20", 61°02'15"	40/15			115 H/3
94-110	1	137°28'35", 61°02'00"	45/15	355/10		115 H/3
94-111	1	137°26'45", 61°02'10"	55/20			115 H/3
94-112	1	137°24'30", 61°03'00"	35/35			115 H/3
94-113	1	137°22'15", 61°04'06"	30/15			115 H/3
94-114	1	137°22'30", 61°03'30"	30/25			115 H/3
94-115	1	137°22'30", 61°03'05"	30/22			115 H/3
94-116	1	137°20'37", 61°03'25"	310/10			115 H/3
94-117	1	137°20'25", 61°03'40"	290/22		0/15	115 H/3
94-118	1	137°20'00", 61°04'40"	325/20		350/10 (N)	115 H/3
94-120	1	137°17'30", 61°03'20"	150/20	79/07	130/15	115 H/3
94-121	1	137°22'50", 61°02'45"	30/25			115 H/3
94-122	2	137°44'10", 61°04'15"	100/15			115 H/4
94-123	2	137°43'00", 61°03'55"	90/20			115 H/4
94-124	2	137°40'55", 61°03'40"	100/40			115 H/4
94-125	1	137°40'10", 61°03'25"	130/35	73/32	175/15	115 H/4
94-126	1	137°39'00", 61°03'15"	100/30	60/18		115 H/4
94-127	1	137°38'10", 61°03'05"	120/20			115 H/4
94-128	1	137°36'30", 61°02'25"	125/30	60/10	140/25 (SW)	115 H/4
94-129	1	137°35'10", 61°01'40"	125/20			115 H/4

Appendix 3-4 (continued):

Sample	rock	Long (W) / Lat (N)	foliation	lineation	fold axes [2]	NTS map [3]
94-130	1	137°34'40", 61°01'05"	140/15	50/05		115 H/4
94-131	1	137°34'25", 61°00'30"	150/15			115 H/4
94-132	1	137°33'10", 61°00'05"	100/15	50/10		115 H/4
94-133	1	137°31'30", 60°58'05"	140/20	55/05		115 A/13
94-134	1	137°34'00", 60°57'45"	100/35			115 A/13
94-135	1	137°30'00", 60°57'30"			50/20 (SW)	115 A/13
94-136	1	137°30'20", 60°56'55"	145/45			115 A/13
94-137	1	137°29'45", 60°56'30"	140/35			115 A/14
94-139	1	137°28'25", 60°55'50"	145/70	192/62		115 A/14
94-140	1	137°27'12", 60°55'40"	15/80			115 A/14
94-143	1	136°32'40", 60°58'00"	100/40	80/35		115 A/13
94-144	1	136°34'00", 60°57'50"	140/35			115 A/13
94-145	5d	137°34'00", 60°57'30"	200/80			115 A/13
94-146	1	137°34'00", 60°57'00"	115/20	75/10	80/05	115 A/13
94-147	1	137°34'00", 60°56'45"	150/60	106/26		115 A/13
94-148	5	137°34'18", 60°56'22"	150/45			115 A/13
94-149	1, 5	137°35'15", 60°55'50"	130/40			115 A/13
94-150	1, 5	137°36'35", 60°55'30"	110/30	80/25		115 A/13
94-151	1	137°38'40", 60°55'45"	180/25	50/20	10/35 (E)	115 A/13
94-152	1	137°37'50", 60°56'40"	150/15	65/01		115 A/13
94-153	1	137°37'30", 60°57'30"	220/30	45/20	150/25	115 A/13
94-154	1	137°33'55", 60°58'13"	150/25			115 A/13
94-155	1	137°30'20", 60°59'20"	55/35	96/27		115 A/13
94-156	1	137°31'30", 60°59'50"	130/40	65/15	120/25	115 A/13
94-157	1	137°31'45", 61°00'18"	90/30	50/15		115 H/4
94-159	1	137°32'20", 61°01'10"	115/25	54/10		115 H/4
94-160	1	137°31'10", 61°01'00"	110/25	45/12		115 H/4
94-161	1	137°29'00", 61°00'05"	110/25	40/15		115 H/3
94-162	1	137°28'10", 61°00'18"	170/50			115 H/3
94-163	1	137°28'20", 60°59'55"	180/88			115 A/14
94-165	5	137°52'45", 61°12'55"	60/75	106/69		115 H/4
94-168	1	137°39'30", 61°08'30"	60/35	65/35		115 H/4
94-171	1	137°39'30", 61°08'30"	320/45			115 H/4
94-172	1	137°55'10", 61°10'40"	350/45	70/15		115 H/4
94-173	1	137°54'40", 61°09'55"	0/25	60/15	340/20	115 H/4
94-174	1	137°53'10", 61°12'50"	30/60	66/45		115 H/4
94-175	1	137°53'30", 61°13'18"	120/30	90/15		115 H/4
94-176	1	137°54'50", 61°12'55"	0/25			115 H/4
94-178	5	137°55'10", 61°14'45"	0/55			115 H/4
94-179	1	137°56'25", 61°14'45"	90/20			115 H/4
94-180	1	137°57'40", 61°15'03"	130/10			115 H/5
94-181	1	137°57'40", 61°16'05"	180/20			115 H/5
94-182	1	137°59'40", 61°15'10"	180/50			115 H/5
94-183	1	137°59'40", 61°16'50"	170/50			115 H/5
94-184	1	137°54'10", 61°14'48"	30/35			115 H/4
94-185	4	137°50'42", 61°10'40"	0/25	37/16		115 H/4
94-186	6	137°04'30", 60°19'19"	150/35 (b)			115 A/6
94-187	6	137°04'57", 60°19'20"	140/45 (b)			115 A/6
94-188	6	137°03'00", 60°21'10"	270/85 (b)	180/40		115 A/6
94-189	6	137°03'00", 60°22'52"	60/88 (b)			115 A/6
94-190	6	137°02'40", 60°23'20"	55/75			115 A/6

Appendix 3-4 (continued):

Sample	rock	Long (W) / Lat (N)	foliation	lineation	fold axes [2]	NTS map [3]
94-191	7	136°58'20", 60°17'35"		190/45	30/45	115 A/7
94-192	6	136°58'20", 60°17'20"	110/70	60/50	30/40	115 A/7
94-193	12	136°57'40", 60°38'45"	80/75		70/70	115 A/7
94-194	12	136°57'45", 60°16'35"			50/60 (SW)	115 A/7
94-196	6	136°58'15", 60°11'07"	40/80			115 A/2
94-197	6	136°58'00", 60°11'45"	260/80	120/63		115 A/2
94-198	6	136°57'20", 60°10'12"	270/60		350/35	115 A/2
94-199	6	136°58'20", 60°11'37"	240/45			115 A/2
94-200	6	136°59'10", 60°09'50"	70/85 (b)			115 A/2
94-201	6	136°58'45", 60°09'15"	70/85 (b)			115 A/2
94-202	6	136°57'40", 60°07'38"	250/80			115 A/2
94-203	6	136°56'30", 60°06'22"	100/30	55/20		115 A/2
94-204	6	137°56'30", 60°06'30"	120/45	80/30	160/20 (cr)	115 A/2
94-206	7	136°39'50", 59°53'30"	30/40	309/16	80/30 (cr)	114 P/15
94-207	6	136°39'30", 59°53'45"	45/45			114 P/15
94-209	6	136°40'20", 59°54'07"	40/35			114 P/15
94-210	6, 7	136°40'40", 59°54'10"	30/60			114 P/15
94-211	6	136°41'15", 59°54'27"	40/65			114 P/15
94-212	6	136°41'30", 59°54'45"	20/35		320/30	114 P/15
94-213	6	136°41'20", 59°55'15"	100/65			114 P/15
94-214	12	136°42'00", 59°56'57"	120/50	100/45		114 P/15
94-216	12	136°39'40", 59°43'05"	140/40	171/36		114 P/15
94-218	6	136°39'15", 59°43'05"	20/35			114 P/15
94-220	6, 7	136°41'10", 59°43'05"	20/55			114 P/15
94-221	6, 7	136°41'12", 59°43'05"	230/70			114 P/15
94-222	6	136°41'12", 59°43'05"	70/70		30/15 (E)	114 P/15
94-223	6	136°41'15", 59°43'05"	30/65			114 P/15
94-224	6, 7	136°41'12", 59°43'05"	55/60		150/30 (cr)	114 P/15
94-229	6	136°39'10", 59°43'05"	45/50		90/15 (S)	114 P/15
94-230	6	136°38'45", 59°43'05"	50/65			114 P/15
94-234	5	136°53'00", 60°03'00"	350/30			115 A/2
94-237	5, 6	136°55'40", 60°04'40"	70/35	150/05		115 A/2
94-238	7	138°07'25", 60°55'48"	230/60		240/55 (cr)	115 B/16
94-239	7	138°07'45", 60°55'20"	200/80	120/75		115 B/16
94-240	7	138°07'40", 60°54'15"	200/55	240/50		115 B/16
94-241	7	138°07'00", 60°55'35"	230/55		175/50 (W)	115 B/16
94-242	6	138°06'20", 60°53'54"	220/88	220/88		115 B/16
94-243	6	138°05'35", 60°53'40"	35/88		110/10	115 B/16
94-244	6	138°05'15", 60°53'30"	10/85			115 B/16
94-245	6	138°04'30", 60°53'25"	20/85			115 B/16
94-246	6	138°03'55", 60°53'20"	10/75		120/65 (cr)	115 B/16
94-248	7	138°04'25", 60°54'00"	180/75			115 B/16
94-249	7	138°05'00", 60°54'10"	200/75			115 B/16
94-250	7	138°06'35", 60°54'45"	20/85			115 B/16
94-252	1	136°56'10", 60°34'05"	260/45			115 A/10
94-253	1	136°55'25", 60°34'10"	230/55			115 A/10
94-259	1	136°59'30", 60°34'35"	145/35	130/32		115 A/10
94-263	1	137°03'12", 60°36'20"	125/70	80/60	170/60	115 A/11
94-264	1	137°03'35", 60°36'35"	125/50			115 A/11
94-265	1	137°03'50", 60°36'40"	180/25		110/10 (W)	115 A/11
94-266	1	137°05'00", 60°36'10"	180/15			115 A/11

Appendix 3-4 (continued):

Sample	rock	Long (W) / Lat (N)	foliation	lineation	fold axes [2]	NTS map [3]
94-267	1	137°05'05", 60°35'50"	225/25	231/10		115 A/11
94-268	1	137°05'10", 60°35'38"	180/40			115 A/11
94-269	1	137°04'45", 60°35'20"	170/55			115 A/11
94-270	1	137°05'45", 60°36'20"	190/25		110/13 (cr)	115 A/11
94-271	1	137°04'25", 60°37'00"	230/25			115 A/11
94-272	1	136°46'20", 60°42'40"	210/35	288/09		115 A/10
94-273	1	136°45'50", 60°42'50"	200/25	290/05	100/03	115 A/10
94-274	1	136°46'55", 60°43'20"	190/75		100/03 (cr)	115 A/10
94-275	1	136°47'50", 60°41'25"	200/60		290/20 (S)	115 A/10
94-276	1	136°46'50", 60°41'45"	340/30		220/20	115 A/10
94-277	1, 5	136°47'30", 60°41'55"	320/35	330/33		115 A/10
94-278	1	136°48'00", 60°42'10"	350/10			115 A/10
94-279	1	136°48'30", 60°41'40"	250/35	142/15	315/25	115 A/10
94-280	1	136°49'40", 60°41'25"	35/40	298/06	300/15	115 A/10
94-281	1	136°50'00", 60°41'10"	320/40	265/30		115 A/10
94-282	5	136°59'30", 60°34'35"	210/35	137/11		115 A/10
94-283	1	136°48'20", 60°42'20"	60/55	138/16	130/20 (NE)	115 A/10
94-284	1	136°45'40", 60°42'15"	110/70			115 A/10
94-285	1	136°45'15", 60°41'30"	270/55			115 A/10
94-286	1	136°45'20", 60°46'08"	280/75			115 A/10
94-287	1	136°46'10", 60°40'30"	295/75			115 A/10
94-288	1	136°48'00", 60°40'00"	25/40			115 A/10
94-289	1	136°49'00", 60°39'45"	25/20			115 A/10
94-290	5	136°47'30", 60°42'15"	50/15	110/07		115 A/10
94-291	1	136°43'55", 60°43'00"	315/25			115 A/10
94-292/1	1	136°43'00", 60°42'30"	320/40			115 A/10
94-293/1	1	136°42'40", 60°43'05"	250/25	270/20		115 A/10
94-294/1	1	136°42'15", 60°43'05"	330/30			115 A/10
94-295/1	1	136°41'40", 60°43'12"	280/40			115 A/10
94-296/1	1	136°41'20", 60°43'40"	270/50			115 A/10
94-2971	1	136°42'20", 60°43'55"	270/50			115 A/10
94-293/1	6	137°41'25", 60°46'35"	220/75	293/48	130/20	115 A/13
94-294/2	7	137°44'10", 60°46'12"	90/00	167/33	180/35	115 A/13
94-295/2	6	137°45'30", 69°45'20"	315/45			115 A/13
94-297/2	5	138°06'25", 61°04'45"	20/80			115 G/1
94-298	5	138°06'45", 61°02'10"	20/75			115 G/1
94-299	1	138°06'45", 61°02'10"	0/65	70/45		115 G/1
94-300	1	138°07'10", 61°02'50"	10/55		300/25 (SW)	115 G/1
94-301	1	138°07'50", 61°04'00"	10/35		110/10 (S)	115 G/1
94-302	1	138°08'00", 61°04'12"			110/20 (S)	115 G/1
94-303	1, 2	138°08'20", 61°04'55"	0/35		310/15	115 G/1
94-304	2	138°08'10", 61°04'55"	10/40	70/20	310/30	115 G/1
94-305	2	138°07'45", 61°05'15"	10/40	52/34	320/25	115 G/1
94-306	2	138°08'50", 61°05'17"	20/40	90/10	310/10	115 G/1
94-307	2	138°09'50", 61°05'30"	20/40	62/32	315/20	115 G/1
94-308	1, 2	138°10'20", 61°05'00"	20/45	355/30	300/20 (SW)	115 G/1
94-309	15	138°37'50", 61°08'10"	350/50		170/30	115 G/2
94-315	14	138°48'11", 61°13'11"	70/50			115 G/2
94-316	16	138°54'50", 61°15'30"	210/45		130/15	115 G/7
94-317	15	136°14'10", 61°23'37"	190/35			115 G/7
94-318	14	139°14'10", 61°23'40"	180/45			115 G/8

Appendix 3-4 (continued):

Sample	rock	Long (W) / Lat (N)	foliation	lineation	fold axes [2]	NTS map [3]
94-321	14m	139°14'20", 61°23'10"	200/85			115 G/8
94-322	14	139°14'20", 61°23'05"	190/85	110/15		115 G/8
94-329/1	15	139°14'05", 61°24'20"	225/65			115 G/8
94-330	11	138°59'40", 61°33'30"	190/85	110/10		115 G/10
94-331	11	138°59'58", 61°35'10"	190/80			115 G/10
94-333	11	139°01'30", 61°35'20"	280/75			115 G/11
94-334	11	139°02'30", 61°35'20"	315/30			115 G/11
94-335	11	139°02'35", 61°35'22"	340/20			115 G/11
94-336	11	139°02'40", 61°34'15"	300/40	250/35	300/50 (S)	115 G/11
94-337	11	139°02'40", 61°35'05"	300/50		300/45 (SW)	115 G/11
94-338	11	139°01'35", 61°34'50"	210/80			115 G/11
94-339	11	139°02'40", 61°34'45"	190/80			115 G/11
94-341	11	139°03'00", 61°34'15"	10/75	292/38		115 G/11
94-342	11	139°02'00", 61°34'50"	340/55			115 G/11
94-343	11	139°02'40", 61°34'45"	210/70			115 G/11
94-344	11	139°01'25", 61°34'42"	210/75	278/44		115 G/11
94-345	11	139°01'15", 61°34'42"	170/80	260/15		115 G/11
94-346	1	139°04'00", 61°26'12"	220/70	290/15		115 G/8
94-347	1	139°04'10", 61°26'45"	240/30	310/25		115 G/8
94-348	1	139°04'25", 61°27'02"	300/20	290/18		115 G/8
94-350	1	139°05'35", 61°27'38"	350/20	290/08		115 G/8
94-351	1	139°06'10", 61°27'38"	30/15			115 G/8
94-352	1	139°06'15", 61°27'12"	0/15			115 G/8
94-353	15	139°25'55", 61°29'05"	170/55			115 G/6
94-354	14	139°26'30", 61°29'25"	210/55	100/25	130/20 (N)	115 G/6
94-355	12	136°52'35", 60°30'40"	130/70			115 A/10
94-356	12	136°51'50", 60°30'02"	160/30			115 A/10
94-357	5	136°50'55", 60°29'48"	100/40			115 A/7
94-358	12	136°48'50", 60°30'10"	150/50	145/42	110/40 (cr)	115 A/10
94-359	12	136°59'30", 60°34'35"	180/35	120/15		115 A/10
94-360	12	136°48'22", 60°29'48"			150/35	115 A/7
94-361	12	136°48'22", 60°29'32"	160/55	104/39		115 A/7
94-364	12	136°45'20", 60°28'40"	180/55			115 A/7
94-366	12	136°44'40", 60°28'55"	70/55	150/05		115 A/7
94-367	12	136°45'00", 60°29'00"	250/88	330/30		115 A/7
94-368	12	136°45'45", 60°29'40"	200/60	150/50	125/15	115 A/7
94-369	12	136°50'00", 60°30'25"	320/75			115 A/7
94-370	12	136°51'00", 60°30'55"	160/50		120/45 (cr)	115 A/10
94-371	5, 6	136°54'50", 60°04'09"	50/35	70/40		115 A/2
94-372	6	136°55'25", 60°04'30"	60/40			115 A/2
94-373	6	136°57'25", 60°05'30"	30/40			115 A/2
94-374	6	136°59'40", 60°11'00"	50/45			115 A/2
94-375	6	136°59'50", 60°11'15"	50/35			115 A/2
94-376	7	137°00'45", 60°18'30"	75/75	175/10		115 A/6
94-377	6	137°01'00", 60°18'55"	70/85			115 A/6
94-378	6	137°01'20", 60°19'08"	70/80			115 A/6
94-379	7	137°01'05", 60°19'22"	70/80			115 A/6
94-380	7	137°00'50", 60°19'25"	55/65			115 A/6
94-381	7	137°01'00", 60°19'40"	90/80			115 A/6
94-382	7	137°00'47", 60°19'52"	180/55		160/55 (cr)	115 A/6
94-383	7	137°00'40", 60°19'57"	110/40			115 A/6

Appendix 3-4 (continued):

Sample	rock	Long (W) / Lat (N)	foliation	lineation	fold axes [2]	NTS map [3]
94-384	7	137°00'30", 60°20'02"	90/70		0/05 (cr)	115 A/6
94-386	1	137°26'30", 60°49'35"	200/70	285/05	130/25	115 A/14
94-387	1	137°25'25", 60°50'10"	60/60	125/39		115 A/14
94-388	1	136°46'15", 60°49'25"	150/40	125/37		115 A/15
95-1	11	140°08'20", 61°52'05"	95/33			115 F/16
95-2	11	140°08'30", 61°52'25"	255/34		315/15 (SW)	115 F/16
95-3	11	140°08'30", 61°52'37"			315/22 (NE)	115 F/16
95-4	10	140°08'32", 61°52'45"	285/33	280/31		115 F/16
95-5	11m	140°11'15", 61°53'20"	150/75			115 F/16
95-6	11	140°11'50", 61°53'35"	34/87			115 F/16
95-7	11	140°15'05", 61°54'25"	235/89, 60/80	150/20		115 F/16
95-8	11	140°16'30", 61°54'55"	228/78			115 F/16
95-9	11	140°17'15", 61°55'10"	47/80	59/75		115 F/16
95-10	5d	140°19'35", 61°55'55"	90/80			115 F/16
95-11	11m	139°47'52", 61°43'45"	180/50			115 G/12
95-12	11m	139°48'05", 61°43'40"	190/46			115 G/12
95-16	7	137°17'55", 60°44'40"	240/70	150/24		115 A/11
95-17	7	137°17'35", 60°44'20"	240/85			115 A/11
95-19	2	137°39'05", 60°51'00"	195/68	282/16		115 A/11
95-20	2	137°39'00", 60°51'08"	200/58	270/27	135/34 (SW)	115 A/13
95-21	2	137°39'00", 60°51'40"	207/57	268/21	123/28 (cr)	115 A/13
95-22	2	137°40'00", 60°52'05"	200/60	278/20	135/24 (SW)	115 A/13
95-23	17	137°02'50", 61°01'20"	150/54	80/21		115 H/3
95-24	1	136°03'40", 60°51'35"	163/48	95/34		115 A/14
95-25	6	136°55'40", 60°04'40"	60/42	86/39		115 A/2
95-26	6	136°57'00", 60°06'22"	95/27	73/25		115 A/2
95-29b	12	136°55'00", 60°13'52"	175/60		270/65	115 A/2
95-29c	12m	136°55'00", 60°13'52"	185/63			115 A/2
95-31	12	136°53'35", 60°22'58"	35/27	107/09	0/15	115 A/7
95-33	12	136°51'10", 60°23'00"	45/61	318/06		115 A/7
95-34	12	136°51'35", 60°22'40"	35/40			115 A/7
95-35	12	136°51'48", 60°22'30"	15/21, 42/71			115 A/7
95-36	12	136°52'48", 60°22'35"	15/49, 35/35			115 A/7
95-37	12 ?	136°54'56", 60°21'15"	85/32	105/22		115 A/7
95-38	1	137°05'45", 60°33'37"	198/37			115 A/11
95-39	1	137°05'40", 60°33'47"	218/43			115 A/11
95-41	1	138°49'40", 61°22'35"	05/75	87/16		115 G/7
95-42	3	138°49'30", 61°23'03"	28/55			115 G/7
95-43	4	138°49'35", 61°23'05"	180/60		115/16 (cr)	115 G/7
95-44	4	138°49'55", 61°23'10"	260/58			115 G/7
95-45	4	138°49'57", 61°23'20"	180/65			115 G/7
95-46	4	138°50'10", 61°23'13"	170/88, 305/80			115 G/7
95-47	4	138°51'00", 61°23'08"	324/61		265/40 (N)	115 G/7
95-48	4	138°50'50", 61°23'00"	175/77			115 G/7
95-49	1, 4	138°51'20", 61°22'53"	10/41, 334/85	300/21	255/25 (cr)	115 G/7
95-51	10	138°41'53", 61°40'15"	66/40		125/08 (cr)	115 G/10
95-52	10	138°41'40", 61°40'27"	32/55			115 G/10
95-53	10	138°41'15", 61°40'40"	25/22	110/06	160/10 (E)	115 G/10
95-54	10q	138°41'10", 61°41'15"	65/12	25/05		115 G/10
95-55	10q	138°41'53", 61°41'17"	65/20	39/18		115 G/10
95-56	10q	138°39'53", 61°40'25"	45/45			115 G/10

Appendix 3-4 (continued):

Sample	rock	Long (W) / Lat (N)	foliation	lineation	fold axes [2]	NTS map [3]
95-57	2	138°26'00", 61°11'00"		30/35	90/14	115 G/1
95-58	2	138°24'47", 61°11'35"	45/55	97/21	310/20 (cr)	115 G/1
95-59	2	138°23'30", 61°11'50"	50/45, 65/50 (ccl)		325/20 (SW)	115 G/1
95-60	2	138°22'25", 61°11'53"	25/20		310/05 (SW)	115 G/1
95-61	2	138°21'45", 61°12'05"	50/29	95/21		115 G/1
95-62	2	138°21'00", 61°12'15"	25/25	90/08	315/11 (cr)	115 G/1
95-63	2	138°19'30", 61°11'45"	40/55	104/22		115 G/1
95-64	2	138°17'55", 61°11'35"	20/50	95/10		115 G/1
95-65	3	138°18'10", 61°11'10"	35/35			115 G/1
95-66	2	138°17'30", 61°10'45"	20/30, 55/60 (ccl)	92/19	345/35 (W)	115 G/1
95-67	2	138°17'03", 61°10'10"	330/32	52/05	310/30 (SW)	115 G/1
95-68	3	138°17'58", 61°09'35"	30/40	72/32	310/30	115 G/1
95-69	2	138°18'40", 61°09'25"	10/60			115 G/1
95-70	1	138°24'20", 61°07'23"	30/30			115 G/1
95-71	1	138°23'00", 61°07'18"	18/27, 345/68(ccl)	105/03		115 G/1
95-72	1	138°22'23", 61°07'18"	55/46	98/23	315/15	115 G/1
95-73	1	136°50'57", 60°33'40"	245/68			115 A/10
95-74	1	136°50'35", 60°33'44"	235/50			115 A/10
95-76	6	136°59'50", 60°19'48"	105/25			115 A/13
STJ 94-1	1	137°07'50", 61°00'15"	28/81, 24/74			115 H/3
STJ 94-1b	1	137°07'50", 61°00'15"	54/72	10/45		115 H/3
STJ 94-2	1	137°08'40", 61°00'30"	37/81, 30/74			115 H/3
STJ 94-3	1	137°08'45", 61°00'35"	63/79			115 H/3
STJ 94-4	1	137°09'30", 61°00'37"	68/44, 34/56	120/33		115 H/3
STJ 94-5	1	137°10'15", 61°00'30"	70/64			115 H/3
STJ 94-5b	1	137°10'15", 61°00'30"	56/44			115 H/3
STJ 94-6	1	137°10'45", 61°00'50"	50/68			115 H/3
STJ 94-7	1	137°11'10", 61°01'00"	47/58			115 H/3
STJ 94-8	1	137°11'55", 61°00'00"	35/41, 29/47			115 H/3
STJ 94-9	1	137°12'40", 61°00'35"	58/57, 49/45			115 H/3
STJ 94-10	1	137°14'12", 61°00'30"	73/46, 53/37			115 H/3
STJ 94-11	1	137°14'45", 61°00'20"	61/47			115 H/3

Structural data collected by P. Erdmer (89-, 90-), J. E. Mezger (93-, 94-, 95-), S. Johnston (STJ); first number denotes year of collection.

1: Foliation data are listed as dip direction/dip of schistosity, unless noted (b) or (ccl), indicating bedding and crenulation cleavage, respectively. Lineation, fold axes and crenulation fold axes (cr) data are noted as trend/plunge.

2: The quadrant in parenthesis denotes direction of vergence of axial plane, if known.

3: NTS map number of 1:50,000 scale topographical maps; see map index in Appendix 1-1 for location.

Rock types:

1: KMA: bt-qtz schist
2: KMA: ms-chl-qtz schist
3: KMA: Ca-Mg-Fe layers
4: KMA: olivine serpentinite
5: RRB: granodiorite,
  5a: amphibolite,
  5d: quartz diorite
6: DF: shale, slate, phyllite
7: PMvs
8: felsic dykes
9: mafic dykes
10: Nasina Assemblage:
  mica schist
  10q: quartzite,
  10m: marble
11: White River Assemblage:
  mica schist
  11m: marble, calc-silicate
12: Nisling assemblage:
  bt-qtz schist
  12m: marble
14: Hasen Creek Formation:
  mud-, silt-, sandstone
15: Station Creek Formation:
  metavolcanics
16: Nicolai Greenstone
17: Hydrotunnel orthogneiss

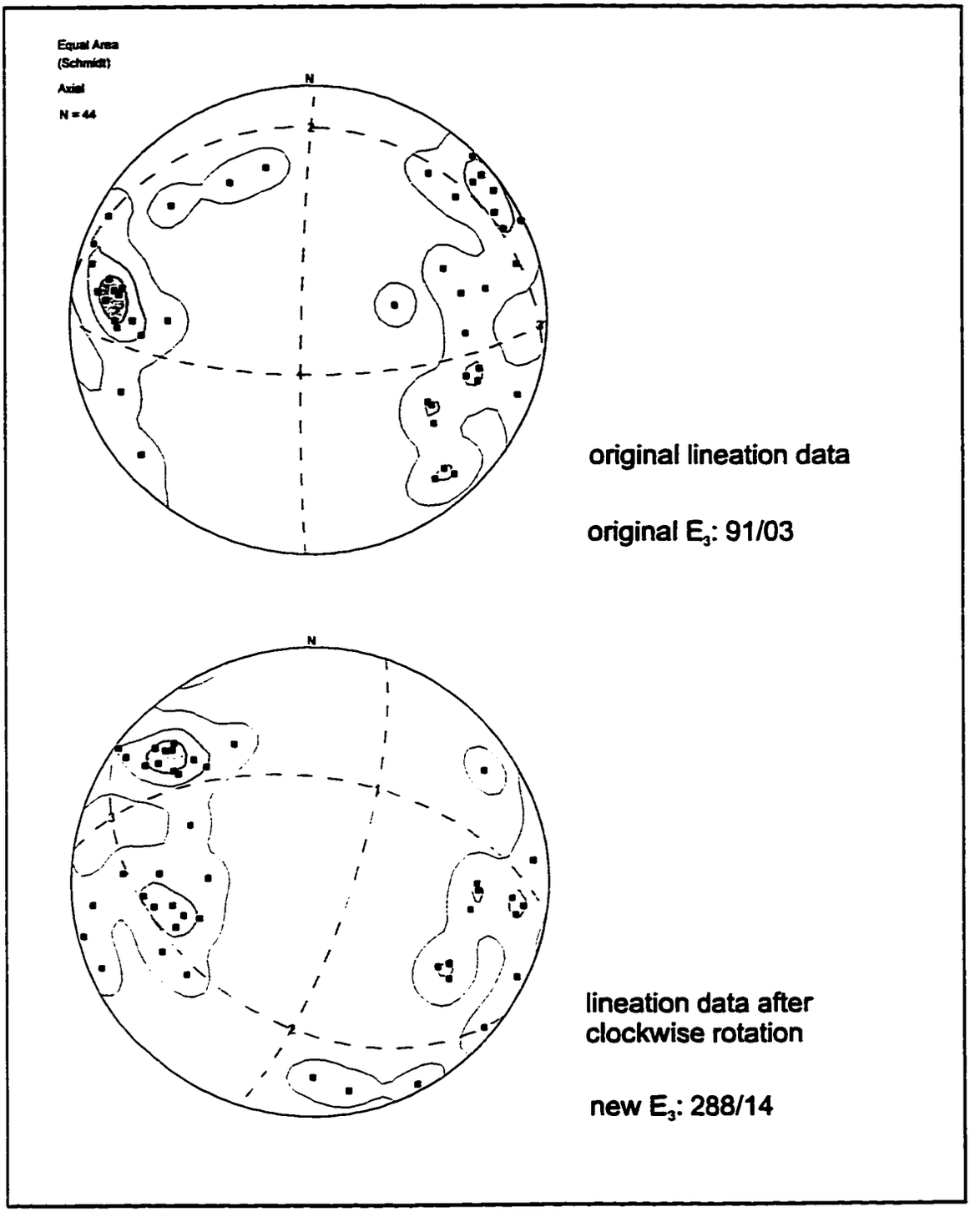

Appendix 3-5: 60° clockwise rotation of lineation from the southwestern limb of the eastern structural domain of the KMA around an axis of 115/10, the approximate trend and plunge of the regional F_{n+3}-fold axis.

Appendix 3-6: Restoration of lineation and shear-sense indicators of southwestern limb in the eastern domain of the KMA to pre-F_{n+3}-folding and northward tilting[1].

Location	measured lineation	shear-sense	lineation after rotation	new shear-sense
94-123	74/19	up	84/24	up
94-125	73/32	up	90/40	up
94-130	45/02	up	45/30	up
94-133	65/10	up	72/32	up
94-146	73/15	up	83/26	up
94-153	249/17	down	65/20	up
94-263	69/39	up	114/50	up
94-266	231/10	up	50/24	up
94-387	125/39	up	115/30	up
95-20	270/27	down	71/15	up
95-22	276/16	down	88/16	up

1: Lineation and sense of shear of south-dipping planes on southwestern limb are rotated around a fold axis of 115/10, until plane containing the lineation dips approximately 20-40° to north-northeast.

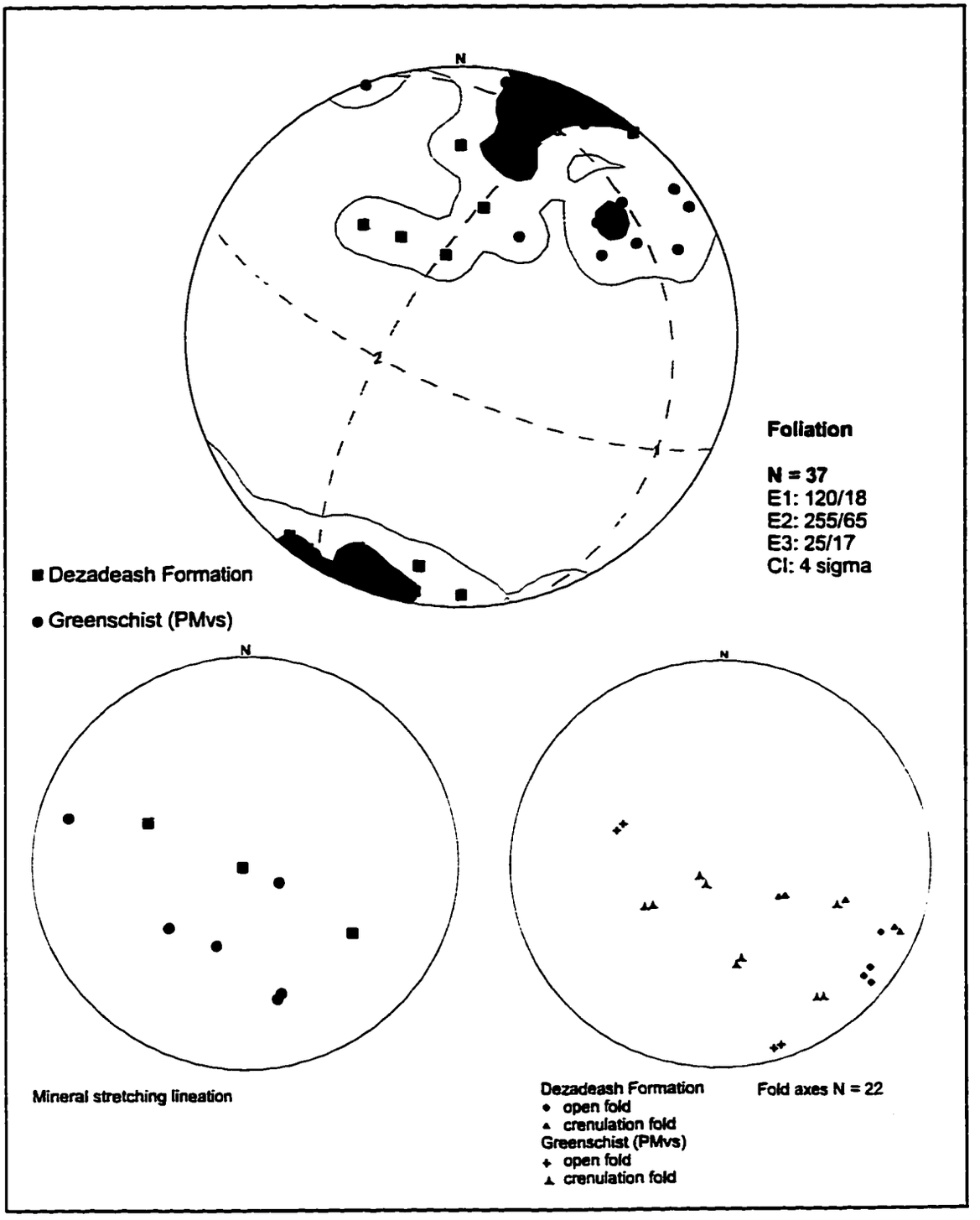

Appendix 3-7: Foliation, mineral stretching lineation and fold axes orientation of phyllites if the Dezadeash Formation and the greenschist (PMvs) between Telluride Creek and Kathleen River. Equal area (Schmidt) projection of lower hemisphere.

Appendix 4-1

Electron microprobe conditions and mineral standards

All geothermobarometric studies were undertaken at the University of Alberta microprobe lab using two microprobe models, an ARL-SEMQ and a JEOL JXA-8900R. Operation conditions for both microprobes included an acceleration voltage of 15 kV, a beam current of 15 nA, measured at a Farraday Cup, a peak count of 20 sec, with 10 sec high background and 10 sec low background. The precision of oxides with several weight percent is approximately σ=1% of measurement, while oxides with less than one weight percent σ=10-20% (P. Wagner, pers. comm., 1997). For data reduction the programs phi-rho-3 by Tracor Northern (ARL-SEMQ) and Z-A-F by JEOL (JEOL JXA-8900R) were used.

The composition of the probed minerals was determined by using the following standards:

Biotite:	Al	Biotite
	Ca	Rhodonite
	Cl	Scapolite
	F	Biotite
	Fe	Kakanui Kaersuitite and high Fe Biotite
	K	Biotite
	Mg	Kakanui Kaersuitite
	Mn	Willemite
	Na	Kakanui Kaersuitite
	Si	Biotite
	Ti	Kakanui Kaersuitite
Cordierite:	Al	Anorthite
	Fe	Kakanui Kaersuitite
	Na	Anorthoclase
	K	Anorthoclase
	Mg	Osumilite
	Mn	Willemite
	Si	Plagioclase
	Ti	Kakanui Kaersuitite
Garnet:	Al	Roberts Victor Garnets
	Ca	Roberts Victor Garnets
	Fe	Fayalite
	Mg	Roberts Victor Garnets
	Mn	Willemite
	Si	Roberts Victor Garnets
	Ti	Kakanui Kaersuitite
Muscovite:	Al	Muscovite
	Ca	Rhodonite
	Cl	Scapolite
	F	Bioitite
	Fe	Kakanui Kaersuitite
	K	Muscovite
	Mn	Willemite
	Na	Kakanui Kaersuitite
	Si	Muscovite
	Ti	Kakanui Kaersuitite
Plagioclase:	Al	Plagioclase
	Ca	Plagioclase/Anorthite
	Fe	Osumilite
	K	Anorthoclase/Sanidine
	Mn	Willemite
	Na	Anorthoclase
	Si	Plagioclase
Spinel:	Al	Chromite
	Cr	Chromite
	Fe	Ilmenite
	Mg	Chromite
	Mn	Ilmenite
	Si	Fayalite
	Ti	Ilmenite
	Zn	Gahnite

Reference number of standards:

Anorthite	USNM 137041
Anorthoclase	USNM 13868
Biotite	not available
Chromite	USNM 117175
Fayalite	USNM 143965
Gahnite	USNM 145883
Ilmenite	USNM 96189
Kakanui Kaersutite	USNM 110752
Muscovite	not available
Osumilite	USNM 143967
Plagioclase	USNM 115900
Rhodonite	not available
Roberts Victor Garnets	USNM 87375
Scapolite	USNM R-6600-1
Willemite	not available

Appendix 4-2: Mineral assemblage and analyzed minerals of geothermobarometry samples

Sample #	Mineral assemblage 1. major (>5 vol.%) 2. minor (<5 vol.%) 3. access. (< 1 vol.%)	Garnets: size in µm grains/points analyzed number of profiles	other mineral phases grains/points analyzed	garnet grains
Kluane metamorphic assemblage				
89-33	1. qtz, pl, bt 2. grt, sil, and, ms 2. grp, tur, o	500 - 1000 2 / 25 2	bt: 4 / 17 ms: 4 / 14 pl: 5 / 13	graphitic inclusions in garnet, grains are embayed, rims altered.
89-49a	1. qtz, pl, bt 2. crd, chl, grt, ms, grp 3. o	1000 3 / 35 3	bt: 6 / 24 pl: 4 / 16 crd: 4 / 12	anhedral to subhedral, graphite inclusion-free.
89-85a	1. qtz, pl, bt 2. grt, grp 3. ms, chl, ap, tur	500 - 1000 2 / 24 2	bt: 3 / 16 pl: 3 /12	graphitic inclusions in garnet, grains are embayed.
90-35	1. qtz, pl, bt, crd, kfs 2. grp, sil, grt 3. ms, ser, chl, hc, ap, o	150 - 500 2 / 22 1	bt: 4 / 22 spl: 12 / 12 crd: 3 / 15 pl: 3 / 10	subhedral, clear, inclusion-free.
93-55	1. qtz, bt, pl, grp 2. grt, ms, cc 3. st, and, tur, o	400 - 700 4 / 37 4	bt: 7 / 12 ms: 4 / 10 pl: 3 / 14	inclusions of graphite and plagioclase in garnet.
93-64	1. qtz, pl, chl, bt, grp 3. ms, grt, tur, czo, ap, zrn, o	200 - 450 4 / 31 4	bt: 8 / 11 ms: 5 / 7 pl: 2 / 8	inclusion-free, clear garnet.
93-77	1. qtz, pl, bt, 2. grt, grp, st 3. ms, ap, tur, zrn, o	700 - 1000 3 / 25 3	bt: 7 / 10 ms: 3 / 6 pl: 3 / 21	anhedral, embayed garnet.
93-80	1. qtz, bt, pl 2. st, grp, grt, ms 3. ap, chl, o	1000 - 2000 2 / 12 2	bt: 6 / 11 ms: 5 / 7 pl: 2 / 10	graphitic inclusions in garnet, grains are embayed, rims altered
93-87	1. qtz, bt, pl 2. ms, chl 3. grt, st, sil, ilm,ap,tur,o	600 - 750 3 / 13 3	bt: 13 / 7 ms: 5 / 7 pl: 2 / 10	garnets are subhedral, minor inclusions.
93-126	1. qtz, pl, bt 2. ms, st, chl, grp 3. grt, and, ap, ilm,	250 1 / 10 1	bt : 7 / 13 ms: 5 / 8 pl: 2 / 10	inclusion-free subhedral garnet.
93-140	1. qtz, pl, bt, st, ms 2. grt, grp 3. sil, and, tur, ap, jar	200 - 700 2 / 18 2	bt: 7 / 12 ms: 7 12 pl: 3 / 15	graphitic inclusions in garnet, grains are embayed, rims altered
93-177	1. qtz, pl, bt, st 2. grt, ms, grp, chl 3. ap, tur	500 - 1100 2 / 10 2	bt: 9 / 14 ms: 6 / 8 pl: 3 / 17	graphitic inclusions in garnet, grains are embayed, rims altered
93-183	1. qtz, bt, pl 2. st, grp 3. grt, and, ap, ms, tur	250 - 750 3 / 15 -	bt: 11 / 16 ms: 4 / 4 pl: 4 / 12	graphitic inclusions in garnet, grains are embayed, rims altered
94-47	1. qtz, pl, bt, st 2. ms, grp 3. grt, ap	750 2 / 13 2	bt: 5 / 21 ms: 5 / 18 pl: 8 / 31	subhedral, partly poikilitic, clear garnet grains.
94-81	1. qtz, pl, bt 2. grt, crd, grp 3. sil, ms, ap, o	500 - 2000 2 / 20 2	bt: 6 / 24 crd: 6 / 12 ms: 2 / 8 pl: 4 / 8	graphitic inclusions in garnet, grains are embayed, rims altered

Appendix 4-2 (continued):

Sample #	Mineral assemblage 1. major (>5 vol.%) 2. minor (<5 vol.%) 3. access. (< 1 vol.%)	Garnets: size in µm grains/points analyzed number of profiles	other mineral phases grains/points analyzed	garnet grains
94-120	1. qtz, bt, pl 2. crd, kfs, grt, chl 3. grp, sil, ms, o	250 - 1000 2 / 20 2	bt: 5 / 31 crd: 4 / 12 pl: 6 /23	clear, poikilitic garnets
94-147c	1. qtz, bt, pl 2. crd, grt, sil, grp	600 - 2800 3 / 29 2	bt: 10 / 40 pl: 8 / 32 crd: 6 / 12	clear, completely inclusion-free, poikilitic garnets
94-172	1. qtz, bt, pl 2. st, grp, ms, grt 3. chl, o	500 - 2000 3 / 27 3	bt: 8 / 32 ms: 6 / 21 pl: 8 / 48	anhedral, embayed, core replaced by biotite
94-277d	1. qtz, pl, bt 2. grt 3. grp, zrn, ms, o	700 - 800 2 / 21 2	bt: 16 / 59 pl: 3 / 15	clear, anhedral elongated poikilitic grains
94-283a	1. qtz, pl, bt, crd 2. ms, grp 3. grt, sil, ser, chl, o	500 - 1500 4 / 20 2	bt: 13 / 59 crd: 4 / 12 pl: 3 / 15	relatively inclusion-free, clear garnets
94-346	1. qtz, pl, bt 2. ms, chl, grp, grt 3. tur, o	700 - 1600 2 / 20 2	bt: 5 / 30 ms: 8 / 24 pl: 3 / 15	clear, inclusion-free, subhedral
95-71	1. qtz, pl, bt 2. ms, chl, grp, grt 3. tur, o	150 1 / 16 1	bt: 4 / 28 ms: 5 / 23 pl: 3 / 15	inclusion-free, subhedral garnet.
Ruby Range Batholith (granodiorite)				
94-147d	1. qtz, bt, pl 2. grt 3. ms, chl	650 - 1000 2 /17 2	bt: 10 / 40 ms: 4 / 16 pl: 10 / 48	clear, inclusion-free.
Aishihik Metamorphic Suite (schist)				
93-42	1. qtz, ms, grt, pl, bt 2. st 3. sil, tur, o	1500 - 3000 2 / 30 2	bt: 9 / 26 ms: 2 / 20 pl: 5 / 20	quartz inclusions
Nasina Assemblage (N of Talbot Arm, Kluane Lake)				
95-53b	1. qtz, bt, grt, ms 2. chl, czo	1000 - 5000 2 / 58 3	bt: 10 / 40	quartz inclusions indicate rotation during growth, snowball garnet.
Nisling assemblage east of Dezadeash Lake				
94-368	1. qtz, bt, pl 2. grt 3. tur, chl	2000 2 / 21 2	bt: 5 / 22	anhedral, relative inclusion-free, altered rims
Dezadeash Formation				
94-204b	1. grp, qtz, bt 3. grt	30 - 80 3 / 11 3	bt: 5 / 30	euhedral, unaltered
94-242	1. qtz, bt, grp 2. grt 3. ms	1300 - 1500 2 / 19 1	bt: 4 / 18	subhedral to euhedral

Appendix 4-3: Electron microprobe analyses and calculated endmembers of garnets

	89-33			89-49a			89-65a			90-35		
	2 grains			3 grains			2 grains			2 grains		
Oxides	Rim	Core	Average	Rim	Core	Average	Rim	Core	Average	Rim	Core	Average
(wt.%)	(2 pts)	(6 pts)	(25 pts)	(10 pts)	(6 pts)	(35 pts)	(8 pts)	(2 pts)	(24 pts)	(7 pts)	(2 pts)	(22 pts)
SiO2	37.61	37.70	37.63	37.68	38.02	37.92	37.37	37.71	37.56	37.42	37.33	37.31
TiO2	0.15	0.04	0.07	0.01	0.01	0.01	0.02	0.11	0.07	0.02	0.00	0.01
Al2O3	21.53	21.48	21.45	21.58	21.71	21.69	21.59	21.40	21.52	21.35	21.62	21.44
FeO	31.04	27.26	31.20	32.57	33.71	33.26	28.26	23.51	26.29	32.38	32.66	32.19
MnO	6.40	6.78	4.54	5.25	3.27	3.93	7.11	7.58	7.25	4.69	4.10	4.86
MgO	2.17	1.81	2.68	2.96	3.84	3.58	1.72	1.20	1.52	2.58	2.50	2.21
CaO	1.81	5.73	2.88	0.88	0.86	0.88	3.10	7.94	5.18	0.98	0.93	0.96
Total:	100.71	100.80	100.45	100.93	101.41	101.27	99.17	99.41	99.40	99.41	99.14	98.99
Cations per 12 oxygen												
Si	3.008	3.000	3.004	3.003	3.001	3.001	3.020	3.022	3.021	3.023	3.019	3.027
Ti	0.009	0.002	0.004	0.000	0.000	0.000	0.001	0.006	0.004	0.001	0.000	0.001
Al	2.029	2.015	2.018	2.027	2.019	2.023	2.057	2.021	2.040	2.032	2.060	2.050
Fe2+	2.076	1.814	2.083	2.171	2.225	2.201	1.910	1.575	1.769	2.187	2.208	2.184
Mn	0.433	0.457	0.307	0.355	0.218	0.264	0.487	0.513	0.494	0.321	0.281	0.334
Mg	0.259	0.215	0.319	0.351	0.452	0.423	0.207	0.143	0.183	0.310	0.302	0.267
Ca	0.155	0.487	0.247	0.075	0.073	0.074	0.268	0.682	0.445	0.085	0.080	0.083
Total:	7.969	7.991	7.982	7.983	7.989	7.987	7.950	7.962	7.955	7.959	7.951	7.947
End member (mol %)												
Grossular	5.30	16.36	8.34	2.54	2.45	2.51	9.34	23.41	15.38	2.92	2.79	2.90
Pyrope	8.85	7.24	10.79	11.90	15.23	14.26	7.21	4.90	6.32	10.67	10.51	9.31
Almandine	71.02	61.03	70.47	73.54	74.97	74.31	66.51	54.08	61.21	75.36	76.91	76.13
Spessartine	14.84	15.37	10.40	12.02	7.35	8.92	16.95	17.61	17.09	11.05	9.79	11.67
Fe/(Fe+Mg)	0.8892	0.8939	0.8672	0.8607	0.8312	0.8390	0.9022	0.9169	0.9064	0.8760	0.8797	0.8911

	93-55			93-64			93-77			93-80		
	4 grains			4 grains			3 grains			2 grains		
Oxides	Rim	Core	Average	Rim	Core	Average	Rim	Core	Average	Rim	Core	Average
(wt.%)	(4 pts)	(4 pts)	(37 pts)	(5 pts)	(4 pts)	(31 pts)	(1 pt)	(3 pts)	(25 pts)	(1 pt)	(2 pts)	(12 pts)
SiO2	36.90	37.16	37.09	36.91	37.00	36.94	37.46	36.60	37.02	37.07	36.58	36.84
TiO2	0.07	0.12	0.09	0.06	0.06	0.06	0.01	0.14	0.13	0.02	0.09	0.09
Al2O3	21.78	21.67	21.70	21.65	21.79	21.75	21.72	21.17	21.27	21.62	21.16	21.39
FeO	29.39	26.17	27.76	25.89	25.55	25.57	29.47	17.06	21.44	32.93	28.50	29.57
MnO	8.03	7.35	7.31	13.02	12.95	13.01	4.25	15.04	10.01	3.27	4.68	3.93
MgO	2.03	1.13	1.59	1.42	1.41	1.44	2.00	0.43	0.80	2.54	1.46	1.54
CaO	2.05	7.17	5.00	1.59	2.03	1.86	4.70	8.77	8.71	3.02	6.79	6.53
Na2O	0.04	0.03	0.03	0.05	0.03	0.04	0.17	0.06	0.12	0.04	0.02	0.03
Cr2O3	n/a	n/a	n/a	n/a	n/a	n/a	0.02	0.02	0.02	0.02	0.05	0.03
Total:	100.28	100.79	100.57	100.59	100.81	100.68	99.80	99.30	99.52	100.53	99.31	99.94
Cations per 12 oxygen												
Si	2.965	2.958	2.964	2.973	2.971	2.970	3.001	2.968	2.983	2.970	2.966	2.966
Ti	0.016	0.026	0.020	0.013	0.013	0.013	0.001	0.009	0.008	0.001	0.005	0.005
Al	2.063	2.033	2.043	2.055	2.061	2.061	2.051	2.023	2.020	2.041	2.022	2.030
Fe2+	1.975	1.741	1.855	1.744	1.715	1.719	1.974	1.157	1.445	2.206	1.933	1.991
Mn	0.546	0.495	0.495	0.889	0.880	0.886	0.288	1.033	0.684	0.222	0.321	0.268
Mg	0.244	0.133	0.189	0.171	0.168	0.173	0.239	0.052	0.097	0.303	0.177	0.185
Ca	0.176	0.611	0.428	0.137	0.175	0.161	0.403	0.762	0.752	0.259	0.590	0.564
Na	0.006	0.005	0.005	0.007	0.005	0.006	0.026	0.009	0.019	0.006	0.003	0.004
Cr	0.000	0.000	0.000	n/a	n/a	n/a	0.001	0.001	0.001	0.001	0.003	0.002
Total:	7.991	8.003	7.996	7.990	7.988	7.989	7.985	8.016	8.008	8.011	8.019	8.015
End member (mol %)												
Grossular	6.00	20.49	14.41	4.65	5.94	5.46	13.89	25.37	25.25	8.67	19.54	18.74
Pyrope	8.28	4.48	6.38	5.82	5.72	5.89	8.22	1.74	3.26	10.14	5.84	6.16
Almandine	67.15	58.41	62.54	59.31	58.38	58.50	67.96	38.51	48.59	73.77	63.96	66.18
Spessartine	18.57	16.62	16.68	30.22	29.95	30.15	9.93	34.38	22.90	7.42	10.66	8.92
Fe/(Fe+Mg)	0.8902	0.9288	0.9074	0.9107	0.9107	0.9085	0.8921	0.9567	0.9372	0.8791	0.9164	0.9149

Appendix 4-3 (continued):

	93-87			93-128			93-140			93-177		
	3 grains			1 grain			2 grains			2 grains		
Oxides	Rim	Core	Average	Rim	Core	Average	Rim	Core	Average	Rim	Core	Average
(wt.%)	(3 pts)	(3 pts)	(13 pts)	(1 pt)	(1 pt)	(10 pts)	(1 pt)	(2 pts)	(18 pts)	(2 pts)	(2 pts)	(10 pts)
SiO2	36.94	37.23	37.08	37.47	37.04	37.10	37.15	37.39	37.33	36.68	36.46	36.88
TiO2	0.06	0.11	0.10	0.04	0.09	0.05	0.04	0.09	0.09	0.04	0.12	0.12
Al2O3	21.35	21.38	21.41	21.77	21.79	21.77	21.64	21.97	21.88	21.33	21.16	21.28
FeO	32.22	27.98	29.04	28.59	28.27	28.09	30.47	29.28	29.37	32.68	26.31	27.83
MnO	5.55	4.74	5.00	10.10	10.20	10.04	6.65	6.12	5.75	4.88	8.16	6.81
MgO	2.25	1.38	1.61	2.14	1.96	2.03	1.84	1.77	2.02	2.34	1.26	1.53
CaO	1.89	7.77	6.06	1.07	1.59	1.46	2.37	4.45	4.34	1.91	6.27	5.53
Na2O	0.06	0.03	0.05	0.06	0.03	0.03	0.01	0.01	0.03	0.03	0.04	0.03
Cr2O3	0.03	0.06	0.06	n/a	n/a	n/a	n/a	n/a	n/a	0.03	0.02	0.02
Total:	100.34	100.71	100.40	101.24	100.97	100.59	100.17	101.07	100.81	99.90	99.79	100.03
Cations per 12 oxygen												
Si	2.972	2.978	2.973	2.988	2.983	2.976	2.988	2.988	2.97	2.970	2.955	2.973
Ti	0.007	0.003	0.006	0.009	0.020	0.012	0.008	0.019	0.02	0.002	0.007	0.008
Al	2.011	2.029	2.023	2.046	2.054	2.058	2.051	2.055	2.05	2.036	2.021	2.021
Fe2+	1.868	2.173	1.947	1.906	1.891	1.884	2.050	1.944	1.95	2.213	1.783	1.876
Mn	0.321	0.379	0.339	0.682	0.691	0.682	0.453	0.411	0.39	0.335	0.560	0.465
Mg	0.164	0.270	0.193	0.254	0.234	0.242	0.221	0.209	0.24	0.283	0.152	0.183
Ca	0.664	0.163	0.520	0.091	0.136	0.127	0.204	0.378	0.37	0.165	0.544	0.477
Na	0.005	0.009	0.007	0.009	0.005	0.004	0.002	0.002	0.01	0.005	0.008	0.005
Cr	0.005	0.002	0.004	n/a	n/a	n/a	n/a	n/a	n/a	0.002	0.001	0.002
Total:	8.016	8.008	8.012	7.985	7.993	7.986	7.978	7.987	7.99	8.011	8.030	8.010
End member (mol %)												
Grossular	5.47	22.03	17.29	3.12	4.62	4.32	6.98	12.82	12.52	5.52	17.90	15.90
Pyrope	9.06	5.43	6.44	6.67	7.92	8.26	7.54	7.13	8.12	9.43	5.01	6.11
Almandine	72.77	61.91	64.94	64.97	64.06	64.18	70.01	66.06	66.21	73.88	58.66	62.52
Spessartine	12.70	10.63	11.32	23.25	23.41	23.24	15.48	13.98	13.14	11.17	18.43	15.47
Fe/(Fe+Mg)	0.8893	0.9193	0.9097	0.8823	0.8900	0.8860	0.9028	0.9026	0.8908	0.8868	0.9213	0.9109

	93-183			94-47			94-81			94-129		
	4 grains			2 grains			2 grains			2 grains		
Oxides	Rim	Core	Average	Rim	Core	Average	Rim	Core	Average	Rim	Core	Average
(wt.%)	(3 pts)	(3 pts)	(15 pts)	(4 pts)	(3 pts)	(13 pts)	(4 pts)	(2 pts)	(20 pts)	(2 pts)	(2 pts)	(10 pts)
SiO2	37.21	37.29	37.20	37.11	37.21	37.18	37.02	37.6	37.49	36.89	37.09	37.03
TiO2	0.04	0.06	0.05	0.03	0.11	0.07	0.01	0.02	0.02	0.02	0.00	0.01
Al2O3	21.45	21.38	21.37	21.46	21.51	21.43	21.55	21.54	21.54	21.70	21.97	21.74
FeO	29.49	28.78	29.03	30.69	29.36	29.94	32.43	32.90	32.79	32.62	33.19	32.86
MnO	7.13	7.46	7.40	8.26	8.97	8.76	6.89	6.36	6.26	5.30	4.16	4.64
MgO	2.39	2.18	2.20	2.24	2.14	2.20	2.42	2.60	2.56	2.37	2.80	2.62
CaO	1.72	2.13	2.07	1.36	2.62	2.06	1.21	1.53	1.34	1.16	1.29	1.22
Na2O	0.03	0.03	0.05	n/a	n/a	n/a	n/a	n/a	n/a	n/a	n/a	n/a
Total:	99.46	99.31	99.37	101.14	101.92	101.64	101.52	102.53	101.99	100.05	100.5	100.13
Cations per 12 oxygen												
Si	3.003	3.011	3.005	2.976	2.982	2.989	2.982	2.974	2.978	2.977	2.970	2.980
Ti	0.009	0.013	0.011	0.002	0.006	0.004	0.000	0.001	0.001	0.001	0.000	0.001
Al	2.040	2.034	2.035	2.028	2.018	2.017	2.032	2.008	2.017	2.063	2.073	2.061
Fe2+	1.990	1.943	1.961	2.058	1.954	1.999	2.169	2.178	2.178	2.201	2.223	2.211
Mn	0.487	0.510	0.506	0.581	0.605	0.593	0.467	0.426	0.421	0.363	0.282	0.316
Mg	0.288	0.262	0.265	0.267	0.254	0.262	0.288	0.306	0.303	0.285	0.335	0.314
Ca	0.149	0.184	0.179	0.117	0.223	0.176	0.103	0.129	0.114	0.100	0.110	0.105
Na	0.005	0.005	0.008	n/a	n/a	n/a	n/a	n/a	n/a	n/a	n/a	n/a
Total:	7.970	7.962	7.970	8.008	8.023	8.019	8.022	8.021	8.012	7.990	7.993	7.989
End member (mol %)												
Grossular	5.10	6.35	6.15	3.88	7.35	5.79	3.41	4.25	3.78	3.40	3.74	3.58
Pyrope	9.87	9.05	9.10	8.90	8.37	8.64	9.51	10.08	10.05	9.65	11.34	10.66
Almandine	68.30	67.01	67.36	68.54	64.35	66.00	71.65	71.66	72.21	74.65	75.35	75.03
Spessartine	16.72	17.59	17.39	18.67	19.92	19.56	15.42	14.01	13.96	12.30	9.57	10.74
Fe/(Fe+Mg)	0.8737	0.8810	0.8810	0.8851	0.8849	0.8842	0.8808	0.8795	0.8783	0.8855	0.8692	0.8756

Appendix 4-3 (continued):

	93-147c			94-147d			94-172			94-277d		
	4 grains			3 grains			3 grains			2 grains		
Oxides	Rim	Core	Average	Rim	Core	Average	Rim	Core	Average	Rim	Core	Average
(wt.%)	(7 pts)	(4 pts)	(29 pts)	(4 pts)	(3 pts)	(13 pts)	(1 pt)	(3 pts)	(27 pts)	(4 pts)	(3 pts)	(21 pts)
SiO2	37.12	36.88	37.14	36.7	37.55	37.17	37.47	37.80	37.72	37.12	37.39	37.16
TiO2	0.01	0.08	0.04	0.01	0.05	0.03	0.01	0.12	0.09	0.01	0.03	0.01
Al2O3	22.06	21.95	22.00	22.26	22.17	22.3	21.41	21.54	21.76	21.71	21.98	21.87
FeO	33.82	33.09	33.29	32.36	31.01	31.83	33.48	31.23	32.38	31.23	31.16	31.34
MnO	1.77	1.86	1.84	1.77	1.67	1.63	5.06	3.31	2.53	4.50	3.07	3.73
MgO	3.87	4.19	4.13	4.63	5.29	5.11	2.34	1.60	1.75	3.39	3.98	3.78
CaO	1.26	1.12	1.17	1.42	1.49	1.43	1.84	6.19	5.77	1.34	1.86	1.52
Total:	99.91	99.16	99.60	99.16	99.23	99.5	101.61	101.78	102.01	99.30	99.45	99.42
Cations per 12 oxygen												
Si	2.986	2.963	2.970	2.941	2.980	2.955	2.99	2.989	2.977	2.989	2.986	2.980
Ti	0.001	0.005	0.003	0.001	0.003	0.002	0.00	0.007	0.005	0.001	0.002	0.001
Al	2.078	2.078	2.073	2.103	2.074	2.090	2.01	2.007	2.024	2.060	2.069	2.067
Fe2+	2.260	2.223	2.227	2.168	2.058	2.116	2.23	2.065	2.137	2.103	2.081	2.102
Mn	0.120	0.126	0.125	0.120	0.112	0.110	0.34	0.222	0.169	0.307	0.208	0.254
Mg	0.461	0.501	0.492	0.553	0.626	0.605	0.28	0.188	0.206	0.407	0.473	0.452
Ca	0.108	0.096	0.100	0.122	0.126	0.122	0.16	0.524	0.487	0.115	0.158	0.130
Total:	7.994	7.993	7.990	8.007	7.980	7.999	8.01	8.001	8.006	7.981	7.978	7.986
End member (mol %)												
Grossular	3.66	3.26	3.40	4.11	4.32	4.13	5.22	17.47	16.24	3.94	5.42	4.43
Pyrope	15.63	17.01	16.72	18.66	21.43	20.49	9.24	6.28	6.88	13.88	16.20	15.40
Almandine	76.65	75.44	75.63	73.17	70.41	71.67	74.18	68.85	71.23	71.72	71.27	71.54
Spessartine	4.06	4.29	4.24	4.06	3.83	3.72	11.35	7.40	5.65	10.46	7.12	8.63
Fe/(Fe+Mg)	0.8306	0.8160	0.8189	0.7968	0.7666	0.7777	0.8892	0.9164	0.9120	0.8379	0.8148	0.8229

	94-283a			94-346			95-71		
	4 grains			2 grain			1 grain		
Oxides	Rim	Core	Average	Rim	Core	Average	Rim	Core	Average
(wt.%)	(5 pts)	(3 pts)	(20 pts)	(7 pts)	(3 pts)	(20 pts)	(6 pts)	(4 pts)	(15 pts)
SiO2	35.91	36.00	36.19	37.76	37.72	37.79	37.01	36.80	36.83
TiO2	0.00	0.03	0.01	0.02	0.06	0.04	0.06	0.04	0.06
Al2O3	21.76	21.86	21.84	21.41	21.49	21.42	21.41	21.44	21.44
FeO	34.90	34.17	34.29	32.34	30.83	31.63	26.32	25.82	25.95
MnO	2.31	1.94	2.13	5.36	6.67	5.90	10.98	11.11	11.00
MgO	2.97	3.44	3.25	2.39	1.97	2.24	1.25	1.17	1.21
CaO	1.05	1.14	1.08	1.69	2.57	2.09	2.51	3.22	3.00
Total:	98.91	98.57	98.79	100.97	101.30	101.12	99.54	99.60	99.50
Cations per 12 oxygen									
Si	2.932	2.933	2.944	3.014	3.005	3.012	3.005	2.988	2.992
Ti	0.000	0.002	0.001	0.001	0.004	0.002	0.003	0.003	0.004
Al	2.094	2.100	2.095	2.014	2.017	2.012	2.049	2.052	2.053
Fe2+	2.383	2.329	2.333	2.158	2.053	2.108	1.787	1.753	1.763
Mn	0.160	0.134	0.147	0.362	0.450	0.398	0.755	0.764	0.757
Mg	0.362	0.417	0.394	0.284	0.234	0.267	0.151	0.142	0.147
Ca	0.091	0.099	0.094	0.145	0.220	0.178	0.218	0.280	0.261
Total:	8.021	8.015	8.008	7.978	7.983	7.979	7.968	7.983	7.978
End member (mol %)									
Grossular	3.05	3.33	3.18	4.90	7.43	6.04	7.50	9.53	8.92
Pyrope	12.08	14.02	13.28	9.63	7.92	9.03	5.18	4.84	5.02
Almandine	79.53	78.14	78.59	73.18	69.44	71.43	61.39	59.63	60.21
Spessartine	5.34	4.50	4.94	12.28	15.21	13.50	25.93	26.00	25.86
Fe/(Fe+Mg)	0.8681	0.8478	0.8555	0.8837	0.8976	0.8877	0.9222	0.9250	0.9231

Appendix 4-3 (continued):

	Nasina			Nasina			Nisling			Aishihik		
	93-287			96-53b			94-368			93-42		
	4 grains			2 grains			2 grains			2 grains		
	Rim	Core	Average	Rim	Core	Average	Rim	Core	Average	Rim	Core	Average
Oxides	(2 pts)	(3 pts)	(19 pts)	(6 pts)	(4 pts)	(51 pts)	(3 pts)	(2 pts)	(21 pts)	(6 pts)	(3 pts)	(30 pts)
SiO2	38.12	37.86	37.88	37.28	38.03	37.22	38.81	38.60	38.88	37.81	37.96	37.81
TiO2	0.08	0.17	0.10	0.12	0.10	0.11	0.04	0.11	0.05	0.04	0.10	0.06
Al2O3	21.68	21.41	21.40	20.31	20.96	20.36	21.92	22.11	22.15	21.56	21.46	21.54
FeO	36.44	29.18	32.26	31.32	27.14	30.32	30.36	30.73	30.74	34.47	28.95	32.91
MnO	0.29	4.35	2.10	0.21	5.09	2.22	1.83	2.28	1.81	1.37	4.70	1.65
MgO	2.09	0.87	1.23	0.87	0.39	0.54	6.03	6.06	6.30	2.41	1.18	1.88
CaO	2.94	7.28	6.11	7.57	7.96	7.49	1.80	1.86	1.74	3.34	6.55	5.06
Total:	101.61	101.11	101.09	97.68	99.67	98.27	100.79	101.73	101.74	101.00	100.90	100.91
Cations per 12 oxygen												
Si	3.020	3.009	3.013	3.055	3.054	3.045	3.018	2.987	3.001	3.006	3.017	3.006
Ti	0.000	0.010	0.006	0.007	0.006	0.007	0.002	0.006	0.003	0.002	0.006	0.004
Al	2.020	2.005	2.006	1.962	1.984	1.963	2.009	2.016	2.014	2.020	2.011	2.018
Fe2+	2.410	1.939	2.145	2.147	1.824	2.075	1.974	1.989	1.984	2.291	1.923	2.187
Mn	0.020	0.293	0.142	0.014	0.346	0.154	0.121	0.149	0.119	0.092	0.317	0.111
Mg	0.250	0.103	0.146	0.107	0.047	0.066	0.699	0.699	0.725	0.286	0.139	0.223
Ca	0.250	0.620	0.521	0.665	0.687	0.657	0.150	0.154	0.144	0.285	0.558	0.432
Total:	7.970	7.979	7.978	7.957	7.948	7.966	7.974	7.999	7.989	7.982	7.972	7.981
End member:												
Grossular	8.50	20.97	17.63	22.67	23.62	22.25	5.09	5.16	4.84	9.62	19.01	14.63
Pyrope	8.41	3.49	4.95	3.64	1.62	2.25	23.76	23.37	24.41	9.68	4.74	7.54
Almandine	82.44	65.63	72.64	73.21	62.83	70.29	67.05	66.49	66.76	77.58	65.44	74.07
Spessartine	0.66	9.91	4.79	0.48	11.94	5.21	4.10	4.99	3.99	3.12	10.81	3.76
Fe/(Fe+Mg)	0.9075	0.9495	0.9362	0.9527	0.9748	0.9690	0.7383	0.7400	0.7323	0.8891	0.9325	0.9076

Dezadeash Formation slates and phyllites

	94-204b			94-237a			94-242		
	4 grains			2 grain			2 grain		
	Rim	Core	Average	Rim	Core	Average	Rim	Core	Average
Oxides	(4 pts)	(2 pts)	(11 pts)	(6 pts)	(5 pts)	(31 pts)	(4 pts)	(1 pts)	(19 pts)
SiO2	37.42	37.36	37.36	37.44	37.28	37.36	37.43	37.32	37.19
TiO2	0.02	0.02	0.02	0.11	0.13	0.13	0.24	0.41	0.31
Al2O3	21.74	21.62	21.68	21.74	21.67	21.68	21.87	21.88	21.79
FeO	27.74	27.58	27.72	20.45	18.46	19.54	19.81	11.07	15.70
MnO	12.13	12.19	12.14	19.12	21.63	20.40	11.92	19.50	15.19
MgO	1.51	1.62	1.61	1.21	1.10	1.16	2.16	0.56	1.30
CaO	1.50	1.45	1.49	1.88	1.72	1.87	5.96	9.08	7.96
Total:	102.05	101.83	102.02	101.94	101.98	102.15	99.38	99.82	99.44
Cations per 12 oxygen									
Si	2.981	2.982	2.978	2.984	2.977	2.977	2.992	2.980	2.979
Ti	0.001	0.001	0.001	0.006	0.008	0.008	0.014	0.025	0.018
Al	2.041	2.034	2.037	2.042	2.039	2.036	2.060	2.059	2.057
Fe2+	1.848	1.841	1.848	1.363	1.233	1.302	1.324	0.739	1.051
Mn	0.818	0.824	0.820	1.291	1.463	1.377	0.807	1.319	1.031
Mg	0.180	0.192	0.191	0.143	0.130	0.138	0.258	0.067	0.155
Ca	0.128	0.124	0.127	0.160	0.147	0.160	0.510	0.777	0.683
Total:	7.997	7.999	8.002	7.989	7.996	7.997	7.964	7.966	7.974
End member:									
Grossular	4.31	4.17	4.26	5.41	4.94	5.37	17.55	26.77	23.38
Pyrope	6.05	6.45	6.40	4.85	4.39	4.64	8.91	2.30	5.32
Almandine	62.13	61.74	61.88	46.08	41.46	43.74	45.73	25.48	36.02
Spessartine	27.51	27.64	27.46	43.65	49.20	46.25	27.82	45.45	35.29
Fe/(Fe+Mg)	0.9113	0.9054	0.9063	0.9047	0.9043	0.9041	0.837	0.9173	0.8713

Appendix 4-4: Electron microprobe analyses of biotite

	89-33	89-49a		89-85a	90-35		93-55	93-64	93-77	93-80
	4 grains	6 grains		3 grains	8 grains		7 grains	8 grains	8 grains	6 grains
Oxides	Average	Contact	Matrix	Average	Contact	Matrix	Average	Average	Average	Average
(wt.%)	(17 pts)	(16 pts)	(8 pts)	(16 pts)	(10 pts)	(12 pts)	(12 pts)	(11 pts)	(13 pts)	(11 pts)
SiO2	35.02	34.65	34.76	36.23	35.37	35.21	34.47	34.54	35.60	35.73
TiO2	1.72	2.58	2.70	1.66	3.93	4.14	1.82	1.65	1.92	1.87
Al2O3	19.19	18.34	18.05	18.30	17.98	17.82	19.18	18.54	19.18	19.1
FeO	19.43	21.36	22.02	19.05	23.34	23.54	20.51	20.78	19.90	19.17
MnO	0.11	0.19	0.18	0.19	0.20	0.16	0.20	0.28	0.10	0.09
MgO	9.74	8.71	8.58	10.67	7.63	7.56	8.46	8.06	9.10	9.58
CaO	0.00	0.01	0.00	0.01	0.01	0.00	0.03	0.03	0.02	0.02
Na2O	0.18	0.17	0.23	0.14	0.12	0.16	0.09	0.08	0.15	0.13
K2O	8.91	9.57	9.07	9.16	9.32	9.29	9.23	8.98	8.99	8.84
F	0.00	0.00	0.00	0.00	0.00	0.00	0.00	0.00	0.00	0.00
Cl	0.01	0.02	0.01	0.01	0.09	0.06	0.01	0.01	0.01	0.01
Total	94.32	95.60	95.61	95.41	97.97	97.94	94.00	92.95	94.99	94.54
Cations per 22 oxygen										
Si	5.377	5.335	5.353	5.486	5.345	5.331	5.359	5.435	5.430	5.45
Ti	0.198	0.299	0.312	0.189	0.447	0.471	0.213	0.196	0.221	0.214
Al	3.472	3.327	3.275	3.265	3.203	3.180	3.514	3.438	3.450	3.435
Fe2+	2.495	2.750	2.836	2.412	2.950	2.980	2.667	2.734	2.539	2.445
Mn	0.015	0.025	0.023	0.024	0.025	0.021	0.026	0.037	0.012	0.012
Mg	2.230	2.000	1.971	2.409	1.720	1.706	1.960	1.892	2.071	2.179
Ca	0.001	0.001	0.000	0.002	0.002	0.000	0.004	0.006	0.004	0.004
Na	0.055	0.051	0.070	0.040	0.034	0.047	0.028	0.023	0.044	0.038
K	1.745	1.879	1.782	1.769	1.796	1.794	1.830	1.802	1.750	1.720
Total	15.588	15.668	15.623	15.597	15.521	15.528	15.601	15.562	15.522	15.497

	93-87	93-126	93-140	93-177	93-183	94-47	94-61		94-120	94-147c
	7 grains	7 grains	6 grains	9 grains	11 grains	5 grains	8 grains		5 grains	10 grains
Oxides	Average	Average	Average	Average	Average	Average	Contact	Matrix	Average	Contact
(wt.%)	(13 pts)	(13 pts)	(12 pts)	(14 pts)	(16 pts)	(21 pts)	(24 pts)	(8 pts)	(31 pts)	(32 pts)
SiO2	34.77	33.49	33.92	34.17	35.22	34.84	34.40	34.17	35.48	34.86
TiO2	1.37	1.52	1.63	1.45	1.63	1.71	1.55	3.08	3.70	2.72
Al2O3	19.13	18.73	18.62	18.52	19.43	19.09	18.92	20.01	18.73	19.32
FeO	19.68	20.09	19.62	19.51	18.47	18.72	19.35	19.82	20.98	17.67
MnO	0.10	0.24	0.13	0.10	0.15	0.14	0.14	0.18	0.17	0.04
MgO	9.22	8.73	9.02	9.35	9.80	9.25	9.23	7.28	7.64	9.63
CaO	0.03	0.02	0.03	0.03	n/a	0.01	0.02	0.02	0.01	0.01
Na2O	0.14	0.13	0.19	0.20	0.29	0.25	0.20	0.14	0.18	0.24
K2O	8.53	8.94	8.96	8.39	8.42	8.82	8.68	9.04	9.18	8.47
F	0.00	0.01	0.00	0.00	n/a	0.00	0.00	0.00	0.00	0.00
Cl	0.01	0.01	0.01	0.01	n/a	0.00	0.01	0.00	0.03	0.01
Total	92.99	91.89	92.12	91.73	93.41	92.86	92.50	93.74	96.09	92.97
Cations per 22 oxygen										
Si	5.413	5.330	5.365	5.401	5.416	5.419	5.391	5.300	5.392	5.372
Ti	0.161	0.182	0.194	0.172	0.189	0.200	0.183	0.359	0.423	0.316
Al	3.510	3.514	3.471	3.451	3.521	3.500	3.494	3.658	3.354	3.508
Fe2+	2.564	2.674	2.595	2.578	2.375	2.434	2.537	2.570	2.667	2.276
Mn	0.014	0.032	0.017	0.014	0.020	0.019	0.019	0.024	0.021	0.006
Mg	2.139	2.071	2.126	2.204	2.247	2.145	2.155	1.684	1.732	2.212
Ca	0.005	0.003	0.004	0.005	0.000	0.002	0.003	0.002	0.001	0.001
Na	0.042	0.040	0.057	0.061	0.086	0.074	0.060	0.041	0.054	0.073
K	1.694	1.814	1.808	1.691	1.652	1.751	1.735	1.789	1.780	1.665
Total	15.540	15.659	15.638	15.577	15.504	15.544	15.577	15.427	15.424	15.428

Appendix 4-4 (continued):

	94-147c	94-147d		94-172	94-277d		94-283a		94-346	95-71
		10 grains		8 grains	16 grains		13 grains		5 grains	4 grains
Oxides	Matrix	Contact	Matrix	Average	Contact	Matrix	Contact	Matrix	Average	Average
(wt.%)	(5 pts)	(32 pts)	(8 pts)	(32 points)	(27 pts)	(32 pts)	(18 pts)	(41 pts)	(30 pts)	(24 pts)
SiO2	34.76	35.37	35.55	34.50	35.60	35.14	34.90	34.51	36.16	36.31
TiO2	3.12	2.66	3.11	1.71	2.30	3.38	3.35	3.77	1.55	1.64
Al2O3	19.25	18.69	18.26	20.04	18.24	17.75	17.90	17.61	19.59	18.73
FeO	17.82	16.83	17.16	19.03	19.57	19.34	20.58	21.00	19.90	20.47
MnO	0.05	0.05	0.04	0.11	0.36	0.36	0.26	0.27	0.09	0.23
MgO	9.27	10.77	10.66	8.77	9.90	9.34	8.71	8.10	8.98	9.32
CaO	0.03	0.01	0.02	0.03	0.15	0.15	0.16	0.16	0.01	0.01
Na2O	0.25	0.18	0.18	0.11	0.21	0.22	0.36	0.33	0.17	0.12
K2O	8.65	8.72	8.85	8.79	9.12	9.16	8.84	8.65	8.63	8.94
F	0.00	0.00	0.00	0.00	1.11	1.10	1.08	1.04	0.00	0.00
Cl	0.00	0.02	0.02	0.01	0.13	0.13	0.10	0.10	0.00	0.01
Total	93.20	93.32	93.84	93.09	96.71	96.06	96.25	95.54	95.09	95.77
Cations per 22 oxygen										
Si	5.355	5.414	5.425	5.35	5.419	5.393	5.367	5.357	5.484	5.501
Ti	0.361	0.307	0.356	0.20	0.264	0.390	0.388	0.440	0.177	0.187
Al	3.496	3.372	3.284	3.66	3.272	3.210	3.244	3.222	3.501	3.343
Fe2+	2.296	2.155	2.189	2.47	2.491	2.482	2.647	2.727	2.523	2.593
Mn	0.006	0.006	0.005	0.01	0.047	0.047	0.034	0.036	0.012	0.029
Mg	2.130	2.457	2.425	2.03	2.247	2.138	1.997	1.875	2.031	2.105
Ca	0.005	0.002	0.003	0.00	0.025	0.024	0.027	0.027	0.002	0.002
Na	0.075	0.054	0.054	0.03	0.063	0.064	0.109	0.098	0.051	0.035
K	1.700	1.703	1.723	1.74	1.772	1.793	1.733	1.713	1.669	1.727
Total	15.423	15.471	15.465	15.50	15.599	15.541	15.544	15.497	15.449	15.522

	Nisling assemblage		Nasina Assemblage		Aishihik Metamorphic Suite		Dezadeash Fm.	
	94-368		95-53b		93-42		94-204b	94-242
	5 grains		10 grains		6 grains		5 grains	6 grains
Oxides	Contact	Matrix	Contact	Matrix	Contact	Matrix	Average	Average
(wt.%)	(10 pts)	(12 pts)	(16 pts)	(24 pts)	(20 pts)	(6 pts)	(30 pts)	(18 pts)
SiO2	36.33	37.17	34.87	35.53	34.75	35.04	35.79	36.66
TiO2	1.41	1.53	1.61	1.91	2.24	2.20	1.56	1.34
Al2O3	18.01	18.04	17.79	17.59	18.89	18.82	18.87	18.70
FeO	15.23	13.47	19.82	18.19	21.72	20.82	20.35	13.81
MnO	0.06	0.05	0.20	0.19	0.06	0.05	0.23	0.19
MgO	12.68	13.82	8.73	9.93	8.49	8.67	8.89	12.94
CaO	0.01	0.00	0.17	0.15	0.00	0.01	0.04	0.02
Na2O	0.22	0.22	0.19	0.20	0.18	0.24	0.07	0.16
K2O	8.43	8.44	8.29	8.61	9.23	9.25	8.86	8.87
F	0.00	0.00	1.20	1.26	0.00	0.00	0.00	0.00
Cl	0.00	0.00	0.10	0.08	0.00	0.01	0.02	0.01
Total	92.38	92.76	92.97	93.64	95.58	95.11	94.67	92.71
Cations per 22 oxygen								
Si	5.554	5.599	5.518	5.541	5.335	5.383	5.487	5.552
Ti	0.162	0.173	0.192	0.224	0.262	0.254	0.180	0.153
Al	3.244	3.203	3.318	3.234	3.421	3.408	3.409	3.339
Fe2+	1.948	1.696	2.623	2.374	2.794	2.675	2.609	1.749
Mn	0.008	0.007	0.027	0.026	0.008	0.006	0.029	0.025
Mg	2.890	3.104	2.058	2.309	1.944	1.987	2.031	2.923
Ca	0.002	0.001	0.029	0.025	0.013	0.039	0.006	0.003
Na	0.064	0.065	0.058	0.061	0.030	0.004	0.021	0.047
K	1.644	1.623	1.673	1.712	1.803	1.812	1.732	1.716
Total	15.515	15.470	15.496	15.505	15.609	15.567	15.505	15.507

Appendix 4-5: Electron microprobe analyses of muscovite

	89-33	93-55	93-64	93-77	93-80	93-87	93-126	93-140	93-177
Oxides	4 grains	4 grains	5 grains	3 grains	6 grains	5 grains	5 grains	7 grains	6 grains
(wt.%)	(14 pts)	(10 pts)	(7 pts)	(6 pts)	(9 pts)	(7 pts)	(8 pts)	(8 pts)	(8 pts)
SiO2	46.81	47.58	48.33	47.51	48.48	48.67	49.12	47.51	48.15
TiO2	0.29	0.36	0.33	0.27	0.32	0.31	0.29	0.51	0.29
Al2O3	34.85	36.21	34.90	35.71	35.81	35.48	35.27	36.13	35.94
FeO	0.91*	1.04	1.84	1.36	1.16	1.37	1.24	0.96	1.12
MnO	0.01	0.02	0.02	0.02	0.01	0.01	0.02	0.02	0.02
MgO	0.63	0.62	0.91	0.80	0.75	0.92	0.80	0.58	0.74
Na2O	1.17	0.81	0.68	0.59	0.96	0.70	0.92	0.86	1.05
K2O	9.27	9.55	9.24	9.37	9.19	9.18	9.24	9.37	8.96
F	n/a	0.00	0.00	0.00	0.00	0.00	0.00	0.00	0.00
Cl	0.01	0.02	0.01	0.01	0.01	0.01	0.00	0.01	0.01
Total	93.93	96.20	96.25	95.64	96.68	96.64	96.89	95.95	96.27
Cations per 22 oxygen									
Si	6.252	6.205	6.297	6.227	6.274	6.299	6.341	6.205	6.254
Ti	0.029	0.035	0.032	0.026	0.032	0.030	0.028	0.050	0.028
Al	5.488	5.566	5.359	5.516	5.464	5.413	5.367	5.562	5.502
Fe3+	0.091	0.102	0.180	0.135	0.113	0.133	0.120	0.094	0.109
Mn	0.001	0.002	0.002	0.002	0.001	0.001	0.002	0.002	0.002
Mg	0.125	0.121	0.176	0.156	0.144	0.176	0.153	0.113	0.144
Na	0.304	0.204	0.171	0.150	0.240	0.175	0.231	0.218	0.264
K	1.579	1.588	1.536	1.568	1.517	1.516	1.522	1.560	1.484
Total	13.871	13.822	13.755	13.781	13.785	13.744	13.764	13.805	13.787

	93-183	94-47	94-81	94-147d	94-172	94-346	95-71	AMS 93-42
Oxides	4 grains	5 grains	2 grains	4 grains	6 grains	8 grains	5 grains	2 grains
(wt.%)	(4 pts)	(18 pts)	(8 pts)	(16 pts)	(21 pts)	(24 pts)	(23 pts)	(20 pts)
SiO2	46.00	46.65	46.65	48.33	47.16	46.56	47.22	46.54
TiO2	0.39	0.44	0.78	0.14	0.36	0.19	0.18	0.67
Al2O3	34.97	34.07	35.23	34.84	35.95	34.45	33.85	34.79
FeO	0.92	0.88	1.02	1.19	0.88	0.91	1.75*	1.25*
MnO	0.01	0.00	0.01	0.00	0.00	0.01	0.01	0.00
MgO	0.69	0.66	0.41	0.75	0.48	0.61	1.33	0.55
Na2O	1.25	1.22	0.57	0.33	1.06	1.26	0.53	1.08
K2O	8.98	10.04	9.64	9.25	9.10	10.42	9.91	9.72
Cl	n/a	n/a	n/a	0.01	0.01	0.01	0.00	0.01
Total	93.21	93.95	94.31	94.85	95.00	94.40	94.780	94.61
Cations per 22 oxygen								
Si	6.193	6.277	6.223	6.374	6.223	6.251	6.283	6.202
Ti	0.039	0.045	0.078	0.014	0.035	0.019	0.018	0.068
Al	5.548	5.404	5.538	5.415	5.592	5.452	5.308	5.464
Fe3+	0.093	0.099	0.114	0.131	0.098	0.102	0.175	0.126
Mn	0.001	0.000	0.001	0.000	0.000	0.001	0.001	0.000
Mg	0.138	0.132	0.082	0.147	0.094	0.122	0.264	0.109
Na	0.326	0.318	0.147	0.085	0.271	0.329	0.137	0.280
K	1.542	1.724	1.640	1.559	1.534	1.785	1.682	1.652
Total	13.881	13.999	13.823	13.726	13.847	14.061	13.867	13.901

* Fe2O3

Appendix 4-6: Electron microprobe analyses of plagioclase

	89-33	89-49a	89-85a	90-35	93-55	93-64	93-77	93-80
	5 grains	4 grains	3 grains	3 grains	3 grains	2 grains	3 grains	3 grains
Oxides	Average	Average	Average	Average	Average	Average	Average	Average
(wt.%)	(13 pts)	(16 pts)	(12 pts)	(10 pts)	(14 pts)	(8 pts)	(21 pts)	(18 pts)
SiO2	59.97	62.04	58.55	60.75	60.63	57.35	60.07	61.69
Al2O3	25.54	24.39	26.32	24.74	24.18	25.96	25.22	24.21
FeO	0.11	0.06	0.03	0.05	0.06	0.28	0.14	0.04
MnO	0.01	0.01	0.01	0.02	0.01	0.01	0.00	0.00
CaO	5.83	4.88	7.68	5.76	5.50	7.51	6.66	5.61
Na2O	8.10	8.65	7.38	8.20	8.36	7.08	7.62	8.17
K2O	0.06	0.14	0.08	0.29	0.00	0.00	0.10	0.07
Total	99.63	100.17	100.05	99.80	98.73	98.19	99.80	99.79
Cations per 8 oxygen								
Si	2.675	2.743	2.615	2.706	2.724	2.611	2.678	2.739
Al	1.342	1.271	1.386	1.299	1.280	1.393	1.325	1.267
Fe	0.004	0.002	0.001	0.002	0.002	0.011	0.005	0.001
Mn	0.000	0.000	0.000	0.001	0.000	0.000	0.000	0.000
Ca	0.279	0.231	0.368	0.275	0.265	0.366	0.318	0.267
Na	0.701	0.741	0.639	0.708	0.729	0.625	0.659	0.703
K	0.005	0.008	0.005	0.016	0.000	0.000	0.006	0.004
Total	5.006	4.996	5.014	5.007	5.000	5.005	4.991	4.981
End member (mol %)								
Albite	71.24	75.63	63.16	70.85	73.34	63.03	67.04	72.20
Anorthite	28.30	23.58	36.37	27.53	26.66	36.97	32.40	27.40
Orthoclase	0.46	0.79	0.48	1.63	0.00	0.00	0.56	0.40

	93-87	93-126	93-140	93-177	93-183	94-47	94-81	94-81
	2 grains	2 grains	3 grains	3 grains	4 grains	7 grains	8 grains	8 grains
Oxides	Average	Average	Average	Average	Average	Average	Rim	Core
(wt.%)	(10 pts)	(10 pts)	(15 pts)	(16 pts)	(16 pts)	(27 pts)	(24 pts)	(24 pts)
SiO2	62.61	59.54	60.29	61.96	60.66	61.95	60.12	60.32
Al2O3	24.58	24.46	24.31	24.71	25.94	24.73	25.59	25.48
FeO	0.12	0.05	0.07	0.06	0.06	0.04	0.11	0.03
MnO	0.00	0.01	0.01	0.00	0.01	0.00	0.01	0.01
CaO	5.87	6.13	5.75	5.40	6.61	5.31	6.45	6.35
Na2O	8.08	7.82	8.15	8.70	8.03	9.61	7.56	7.63
K2O	0.07	0.00	0.00	0.07	0.08	0.09	0.15	0.19
Total	101.33	98.01	98.59	100.90	101.40	101.73	99.97	99.99
Cations per 8 oxygen								
Si	2.738	2.698	2.714	2.725	2.664	2.712	2.673	2.680
Al	1.267	1.307	1.290	1.281	1.342	1.276	1.341	1.334
Fe	0.004	0.002	0.003	0.002	0.002	0.001	0.004	0.001
Mn	0.000	0.000	0.000	0.000	0.000	0.000	0.000	0.000
Ca	0.275	0.298	0.277	0.254	0.311	0.249	0.307	0.302
Na	0.685	0.687	0.712	0.742	0.684	0.816	0.652	0.657
K	0.004	0.000	0.000	0.004	0.005	0.005	0.008	0.011
Total	4.973	4.992	4.996	5.008	5.008	5.060	4.985	4.985
End member (mol %)								
Albite	71.07	69.80	71.96	74.13	68.44	76.23	67.41	67.76
Anorthite	28.51	30.20	28.04	25.46	31.11	23.30	31.74	31.14
Orthoclase	0.42	0.00	0.00	0.41	0.46	0.47	0.85	1.10

Appendix 4-6 (continued):

	94-81	94-120	94-147c		94-147c	94-147d		
		6 grains	8 grains			8 grains		
Oxides	Average	Average	Rim	Core	Average	Rim	Core	Average
(wt.%)	(48 pts)	(23 pts)	(16 pts)	(16 pts)	(32 pts)	(24 pts)	(24 pts)	(48 pts)
SiO2	60.22	60.40	59.42	59.75	59.59	59.38	59.07	59.23
Al2O3	25.54	25.64	25.87	25.66	25.77	26.00	26.05	26.02
FeO	0.07	0.04	0.12	0.04	0.08	0.13	0.04	0.08
MnO	0.01	0.01	0.01	0.01	0.01	0.00	0.00	0.00
CaO	6.40	6.40	6.54	6.39	6.47	6.90	6.94	6.92
Na2O	7.60	8.79	7.86	7.99	7.92	7.36	7.31	7.33
K2O	0.17	0.25	0.08	0.09	0.08	0.09	0.13	0.11
Total	99.98		99.90	99.93	99.91	99.86	99.61	99.73
Cations per 8 oxygen								
Si	2.677	2.659	2.650	2.662	2.656	2.648	2.641	2.644
Al	1.338	1.331	1.360	1.347	1.354	1.366	1.374	1.370
Fe	0.003	0.001	0.004	0.001	0.003	0.005	0.002	0.003
Mn	0.000	0.000	0.000	0.000	0.000	0.000	0.000	0.000
Ca	0.305	0.302	0.313	0.305	0.309	0.330	0.335	0.332
Na	0.655	0.750	0.679	0.690	0.685	0.636	0.632	0.634
K	0.009	0.014	0.004	0.005	0.005	0.005	0.007	0.006
Total	4.987	5.057	5.010	5.010	5.012	4.990	4.991	4.989
End member (mol %)								
Albite	67.59	70.37	68.18	68.98	68.58	65.52	64.90	65.21
Anorthite	31.44	28.31	31.39	30.50	30.94	33.97	34.38	34.17
Orthoclase	0.98	1.32	0.44	0.52	0.48	0.51	0.72	0.61

	94-147d		94-172					94-277d
	2 zoned grains		7 grains			zoned grain		3 grains
Oxides	Rim	Core	Rim	Core	Average	Rim	Core	Average
(wt.%)	(6 pts)	(6 pts)	(21 pts)	(21 pts)	(42 pts)	(3 pts)	(3 pts)	(15 pts)
SiO2	59.25	54.64	61.52	61.90	61.71	63.74	62.17	60.19
Al2O3	26.10	28.96	24.79	24.51	24.65	22.80	23.21	25.43
FeO	0.12	0.02	0.07	0.04	0.05	0.01	0.00	0.03
MnO	0.01	0.00	0.01	0.01	0.01	0.01	0.00	0.01
CaO	7.13	10.62	5.51	5.24	5.38	3.63	4.75	6.43
Na2O	7.26	5.23	8.25	8.37	8.31	9.36	8.67	7.71
K2O	0.08	0.11	0.10	0.10	0.10	0.11	0.15	0.30
Total	99.94	99.58	100.23	100.17	100.20	99.64	98.95	100.08
Cations per 8 oxygen								
Si	2.641	2.469	2.721	2.736	2.729	2.820	2.779	2.677
Al	1.371	1.543	1.292	1.277	1.284	1.189	1.223	1.332
Fe	0.005	0.001	0.002	0.001	0.002	0.000	0.000	0.001
Mn	0.000	0.000	0.000	0.000	0.000	0.000	0.000	0.000
Ca	0.340	0.514	0.261	0.248	0.255	0.172	0.228	0.306
Na	0.627	0.458	0.707	0.718	0.712	0.803	0.751	0.665
K	0.005	0.006	0.006	0.006	0.006	0.006	0.009	0.017
Total	4.989	4.991	4.990	4.987	4.988	4.990	4.989	4.998
End member (mol %)								
Albite	64.51	46.84	72.61	73.81	73.21	81.83	76.08	67.29
Anorthite	35.02	52.52	26.82	25.58	26.20	17.56	23.05	31.00
Orthoclase	0.47	0.64	0.57	0.61	0.59	0.61	0.87	1.71

Appendix 4-6 (continued):

	KMA			AMS	feldspar porphyry dyke
	94-283a	94-346	95-71	93-42	94-4b
	3 grains	4 grains	3 grains	5 grains	2 grains
Oxides	Average	Average	Average	Average	Average
(wt.%)	(15 pts)	(20 pts)	(15 pts)	(20 pts)	(17 pts)
SiO2	60.76	61.266	60.38	61.34	67.26
Al2O3	24.90	25.039	25.16	24.79	20.97
FeO	0.03	0.016	0.02	0.06	0.08
MnO	0.00	0.004	0.00	0.00	0.00
CaO	5.78	5.686	6.43	5.45	1.41
Na2O	8.19	9.424	7.83	8.33	9.62
K2O	0.23	0.106	0.12	0.13	0.22
Total	99.90	101.542	99.92	100.11	99.54
Cations per 8 oxygen					
Si	2.703	2.691	2.687	2.718	2.946
Al	1.305	1.296	1.319	1.295	1.083
Fe	0.001	0.001	0.001	0.002	0.003
Mn	0.000	0.000	0.000	0.000	0.000
Ca	0.276	0.268	0.306	0.259	0.066
Na	0.706	0.803	0.675	0.715	0.817
K	0.013	0.006	0.007	0.007	0.012
Total	5.004	5.065	4.995	4.996	4.927
End member (mol %)					
Albite	70.97	74.58	68.32	72.85	91.22
Anorthite	27.71	24.87	31.02	26.41	7.39
Orthoclase	1.33	0.55	0.66	0.75	1.39

Appendix 4-7: Electron microprobe analyses of cordierite

	89-49	90-35			93-99	94-81	94-120	94-147c	94-283a
		with spl	no spl	Total					
Oxides	4 grains	2 grains	1 grain	3 grains	1 grain	6 grains	2 grains	6 grains	4 grains
(wt.%)	12 pts	12 pts	3 pts	15 pts	11 pts	12 pts	12 pts	12 pts	12 pts
SiO2	48.07	47.99	48.24	48.04	48.56	48.11	48.19	48.21	47.99
TiO2	0.02	0.01	0.01	0.01	-	0.01	0.00	0.00	0.00
Al2O3	33.98	34.04	34.01	34.03	33.50	34.12	33.23	33.75	33.80
FeO	9.20	10.33	10.45	10.36	10.99	9.68	9.96	7.63	9.99
MnO	0.42	0.44	0.44	0.44	0.31	0.54	0.36	0.11	0.21
MgO	7.81	7.42	7.47	7.43	6.29	7.66	7.70	9.05	7.60
Na2O	0.51	0.19	0.18	0.18	0.17	0.19	0.17	0.24	0.21
K2O	0.02	0.03	0.03	0.03	0.00	0.02	0.02	0.02	0.03
Total:	100.01	100.43	100.83	100.51	99.82	100.34	99.63	99.01	99.83
Cations per 18 oxygen									
Si	4.904	4.896	4.904	4.897	4.985	4.900	4.945	4.922	4.913
Ti	0.001	0.001	0.001	0.001	-	0.001	0.000	0.000	0.000
Al	4.086	4.093	4.075	4.089	4.053	4.096	4.019	4.062	4.079
Fe2+	0.785	0.882	0.889	0.883	0.944	0.825	0.855	0.652	0.855
Mn	0.036	0.038	0.038	0.038	0.027	0.047	0.031	0.009	0.018
Mg	1.187	1.128	1.131	1.129	0.963	1.163	1.178	1.377	1.160
Na	0.100	0.037	0.036	0.037	0.034	0.038	0.033	0.048	0.041
K	0.003	0.003	0.004	0.004	0.000	0.002	0.002	0.003	0.004
Total:	11.103	11.077	11.077	11.077	11.006	11.072	11.063	11.072	11.070
Mg/(Mg+Fe)	0.60	0.56	0.56	0.56	0.50	0.59	0.58	0.68	0.58

Appendix 4-8: Electron microprobe analyses of spinel

	90-35						93-99	
	nucleating in							
	cordierite 1		cordierite 2		Total			
	(6 pts)	Recalc	(6 pts)	Recalc	(12 pts)	Recalc	(14 pts)	Recalc
SiO2	0.01	0.01	0.01	0.01	0.01	0.01	0.16	0.16
TiO2	0.01	0.01	0.00	0.00	0.00	0.00	0.05	0.05
Al2O3	56.37	56.37	56.21	56.21	56.29	56.29	55.32	55.32
Cr2O3	0.08	0.08	0.09	0.09	0.08	0.08	0.15	0.15
FeO	34.16	32.17	34.32	32.42	34.24	32.29	37.89	35.21
Fe2O3		2.22		2.12		2.17		2.97
MnO	0.40	0.40	0.42	0.42	0.41	0.41	0.36	0.36
MgO	2.85	2.85	2.77	2.77	2.81	2.81	2.35	2.35
NiO	0.00	0.00	0.01	0.01	0.01	0.01	0.09	0.09
ZnO	3.53	3.53	3.22	3.22	3.38	3.38	1.17	1.17
Total	97.41	97.64	97.05	97.26	97.23	97.45	97.54	97.84
Cations per 4 oxygen								
Si	0.000	0.000	0.000	0.000	0.000	0.000	0.005	0.005
Ti	0.000	0.000	0.000	0.000	0.000	0.000	0.001	0.001
Al	1.961	1.949	1.962	1.950	1.961	1.950	1.935	1.919
Cr	0.002	0.002	0.002	0.002	0.002	0.002	0.004	0.004
Fe2+	0.843	0.789	0.850	0.798	0.847	0.794	0.940	0.866
Fe3+		0.049		0.047		0.048		0.066
Mn	0.010	0.010	0.011	0.010	0.010	0.010	0.009	0.009
Mg	0.126	0.125	0.122	0.121	0.124	0.123	0.104	0.103
Ni	0.000	0.000	0.000	0.000	0.000	0.000	0.002	0.002
Zn	0.077	0.076	0.071	0.070	0.074	0.073	0.026	0.025
Total	3.018	3.000	3.018	3.000	3.018	3.000	3.025	3.000

Recalculation after Droop (1987): Fe3+ = 8 x (1 - 3 / total cation);
Fe2O3 = 1.1113 x wt.% FeO x Fe3+ / (fe2+ + Fe3+)

Appendix 4-9

Application of the computer program TWQ 2.02

TWQ 2.02 (Thermobarometry With estimation of EQuilibrium state) is a DOS-based computer program (Berman, 1996). To calculate a P-T intersection, the user selects end-member components of all mineral phases involved in the various equilibria (e.g., almandine, pyrope, grossular, annite, phlogopite, muscovite, anorthite, Fe-cordierite, andalusite and/or sillimanite). Thermodynamic data (molar enthalpy, entropy, volume and heat capacity) for end member phases are taken from Aranovich & Berman (1996) and Berman & Aranovich (1996). Compositional files must then be created for phases showing significant solid solution. In the case of the present study, these files contain data on garnet, plagioclase, muscovite, biotite and cordierite, obtained through electron microprobe analyses (Appendices 4-3 through 4-8). The mineral compositions are converted to activities using the activity-composition models of Berman & Aranovich (1996) for garnet and cordierite, Berman (in prep.) for biotite, Chatterjee & Froese (1975) for muscovite and Fuhrman & Lindsley (1988) for feldspar. Using these thermodynamic and compositional data, the TWQ program then calculates the location of all possible equilibria within a selected P-T window (Appendix 4-10).

Some or all the following equilibria were considered for each sample:

(12) phl + alm = ann + py

(13) py + ms + grs = 3 an + phl

(14) 2 sil/and + qtz + grs = 3 an

(15) py + ms = phl + qtz + 2 sil/and

(16) ms + grs + alm = ann + 3 an

(17) alm + ms = 2 sil/and + qtz + ann

(18) and = sil

(19) 4 sil + 5 qtz + 2 alm = 3 Fe-crd

(20) 4 sil + 5 qtz + 2 py + 2 ann = 3 Fe-crd + 2 phl

(21) 6 sil + 5 grs + 3 Fe-crd = 2 alm + 15 an

(22) 3 Fe-crd + 5 grs + 2 phl + 6 sil = 2 py + 15 an + 2 ann

(23) 3 qtz + 2 py + 6 an + 2 ann = 3 Fe-crd + 2 grs + 2 phl

(24) 2 alm + 6 an + 3 qtz = 2 grs + 3 Fe-crd

Reaction (12) is the biotite-garnet thermometer (Ferry & Spear, 1978), reaction (14) is the GASP reaction. Reaction (19) is a version of reaction (8). Reactions (12) - (18) can be calculated for staurolite zone samples, while for cordierite zone samples lacking primary muscovite reactions (12), (14) and (19) to (24) are calculated. If no aluminosilicates are chosen only reactions (12), (13) and (16) are computed and all three intersect at one point. This occurs because only two of these reactions are independent, the third being a linear combination of the other two. As such, the intersection does not provide any information on how well constrained the P-T estimate is. With the choice of an aluminosilicate the six equilibria define three independent reactions, which allow for the qualitative evaluation of the state of equilibrium of the sample. The tightness of the intersections is displayed on the diagram by a triangle, defined by the intersections of reactions (12), (14) and (15) for staurolite zone samples (Berman, 1991) and reactions (12), (21) and (23) for cordierite zone samples.

In the case where andalusite and sillimanite are both present in the rock, ten equilibria can be calculated, four of which are linearly independent. The resulting intersections do not differ much from the ones calculated with only one aluminosilicate, since the equilibria using andalusite are in the same position as those for sillimanite, but have a slightly shallower slope.

It should be noted calculations for all samples assume the presence of andalusite or sillimanite even if no aluminosilicate mineral is actually present in the sample. In effect, this procedure calculates the position equilibria (14), (15) and (17) assuming $a_{Al2SiO5}=1$ even though the absence of any aluminosilicate mineral in the rock necessarily indicates $a_{Al2SiO5}<1$. The validity of the resulting P-T estimates can be evaluated by considering the tightness of intersections obtained in the aluminosilicate-free samples and the agreement between these

intersections and independent P-T estimates. Relatively tight intersections of ± 1 kbar and ± 30°C are in fact obtained for several aluminosilicate-free samples (93-64, 93-87, 93-177 and 94-47, see Appendix 4-10). In all these cases, nearby rocks contain either andalusite (samples 93-64, 87, 177) or both andalusite and sillimanite (94-47). Thus, with the exception of sample 93-177, the P-T estimates obtained for the aluminosilicate-free samples are in, or within error of, the appropriate aluminosilicate stability field. Sample 94-47 is a particularly interesting case. Although no aluminosilicates are found in this rock, a sample from an outcrop 1 km away contains coexisting fibrolite and andalusite. The pressure and temperature calculation for 94-47 correctly places it close to the sillimanite-andalusite reaction curve. These results suggest that $a_{Al2SiO5}$~1 for all samples considered in this study and in turn that even the aluminosilicate-free samples provide valid P-T estimates.

Appendix 4-10

Equilibria reactions calculated by TWQ 2.02 for garnet-biotite-muscovite-plagioclase and garnet-biotite-plagioclase-cordierite assemblages of the KMA. For each sample the reactions using garnet core and garnet rim values along with average biotite values, and if available, contact biotite values are plotted. Garnet rim reaction equilibria curves were used for P-T estimation and are summarized in Figure 4-10. Note that the scale varies between samples. IR denotes number of independent reactions.

89-33

left: garnet rim, average biotite
right: garnet core, average biotite

4 independent reactions

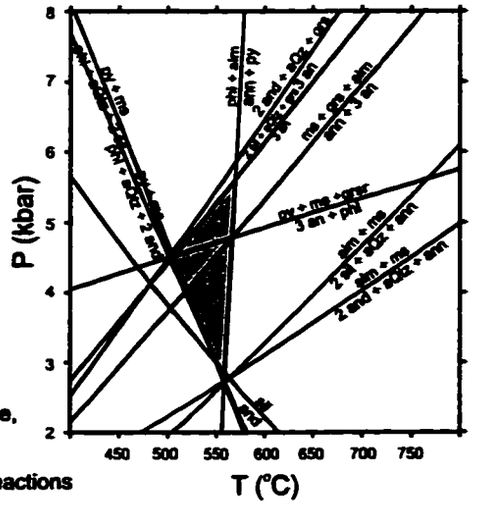

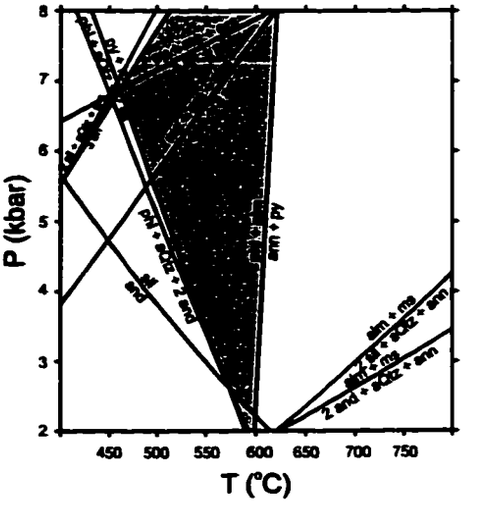

93-55

left: garnet rim, average biotite
right: garnet core, average biotite

3 independent reactions

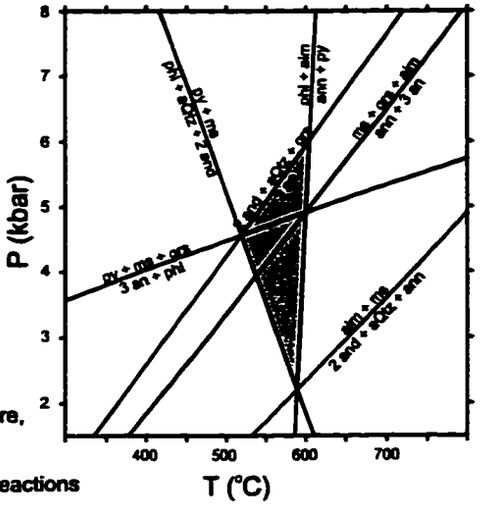

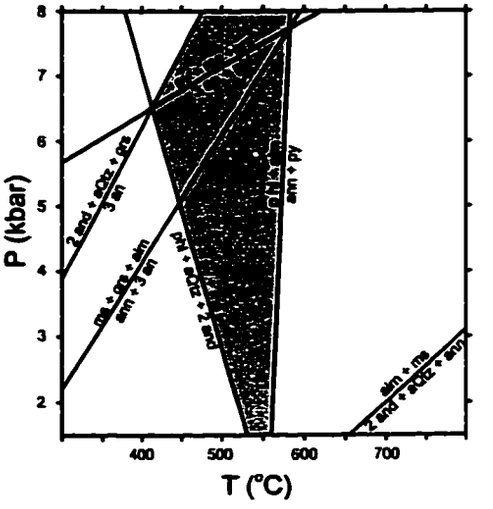

93-77

left: garnet rim, average biotite
right: garnet core, average biotite

3 independent reactions

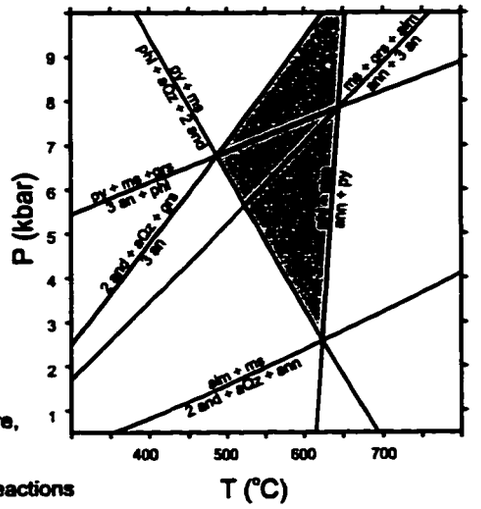

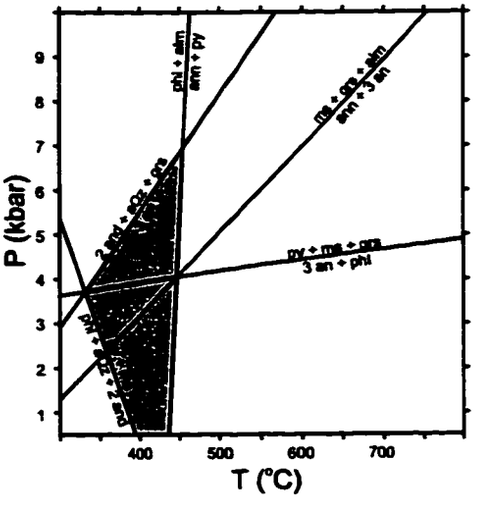

Appendix 4.10: Equilibria reactions calculated by TWQ 2.02 for KMA biotite-quartz schist of the staurolite zone.

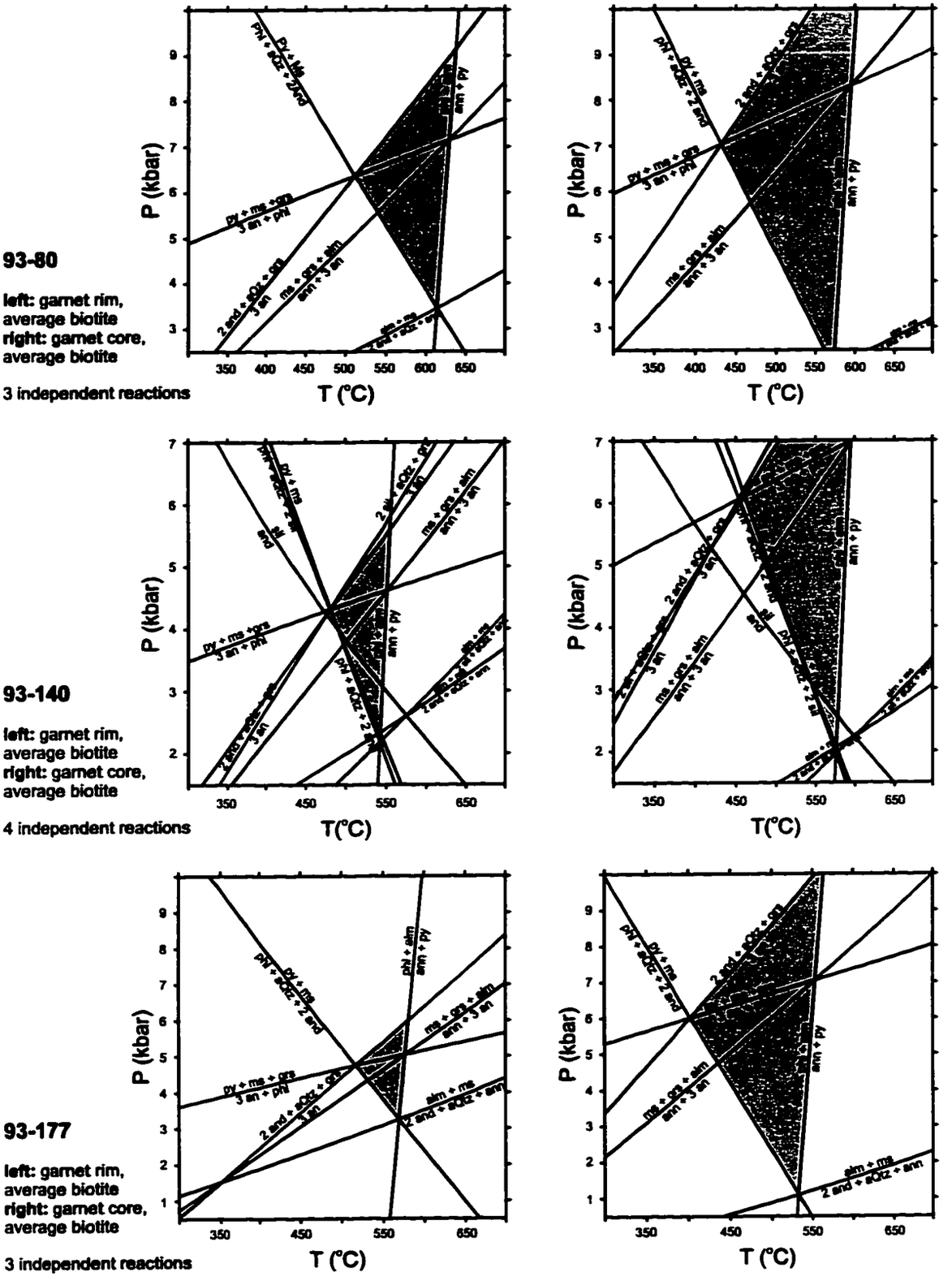

Appendix 4.10 (continued): Equilibria reactions calculated by TWQ 2.02 for KMA biotite-quartz schist of the staurolite zone.

93-183

left: garnet rim, average biotite
right: garnet core, average biotite

3 independent reactions

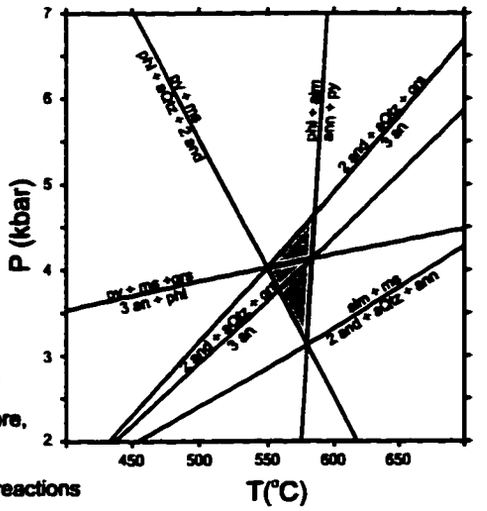

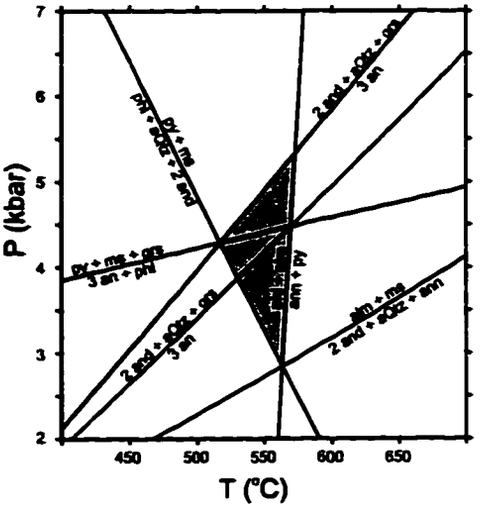

94-172

left: garnet rim, average biotite
right: garnet core, average biotite

3 independent reactions

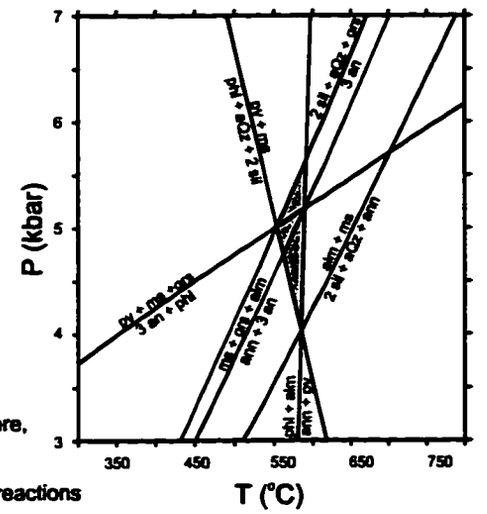

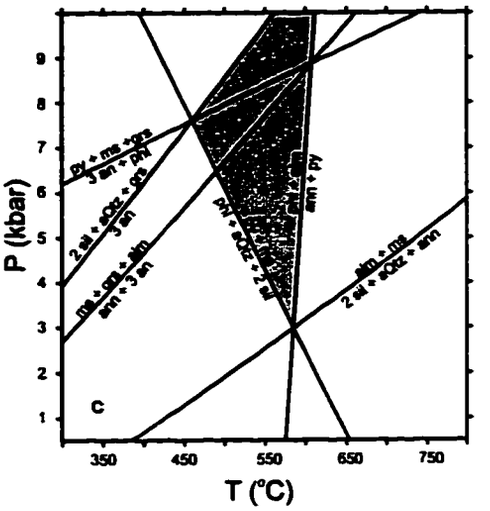

94-346

left: garnet rim, average biotite
right: garnet core, average biotite

3 independent reactions

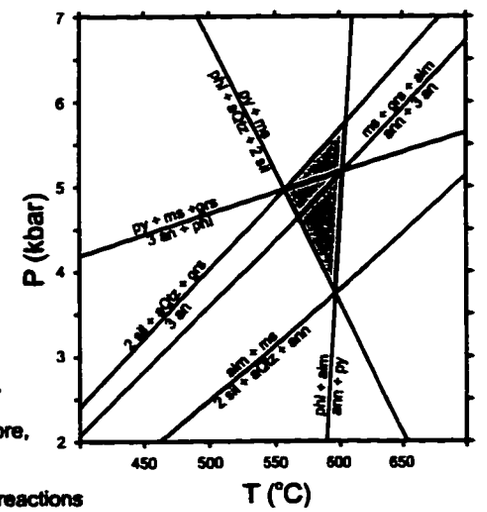

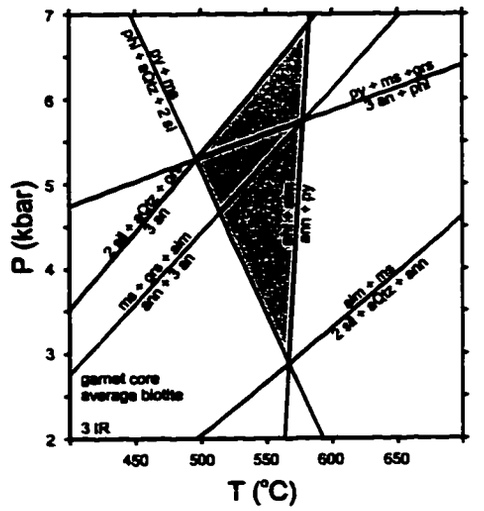

Appendix 4.10 (continued): Equilibria reactions calculated by TWQ 2.02 for KMA biotite-quartz schist of the staurolite zone.

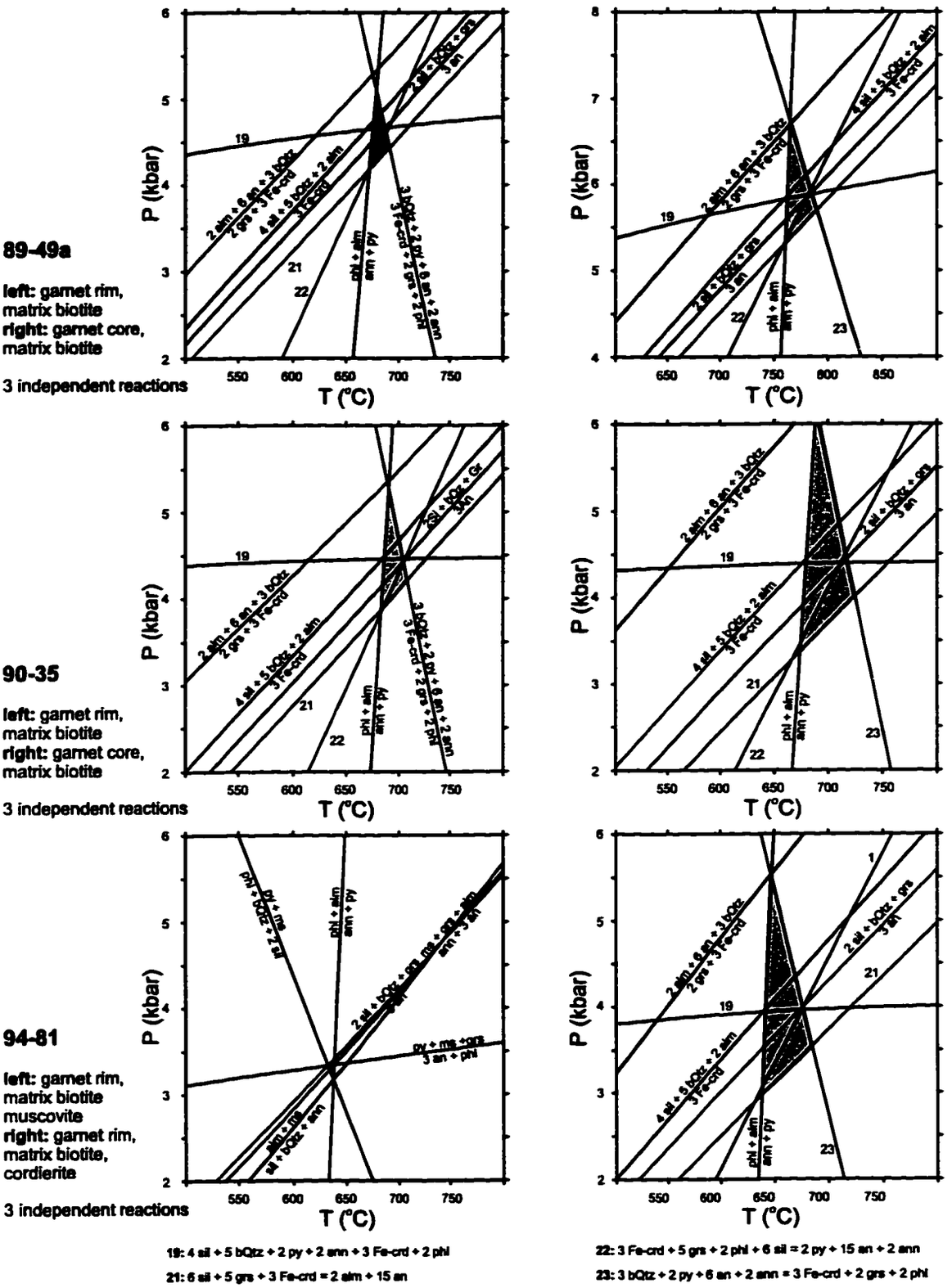

Appendix 4.10 (continued): Equilibria reactions calculated by TWQ 2.02 for cordierite-bearing biotite-quartz schist of the KMA.

94-120

left: garnet rim, average biotite
right: garnet core, average biotite

3 independent reactions

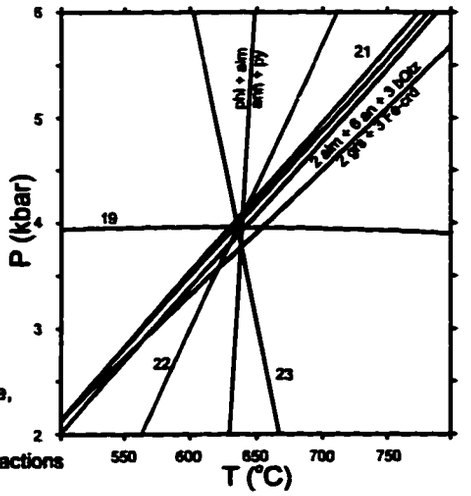

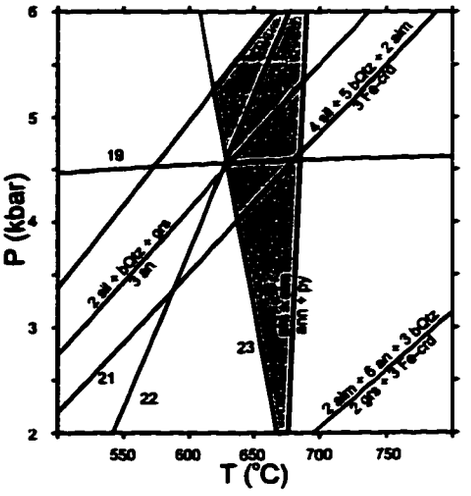

94-147c

left: garnet rim, matrix biotite
right: garnet core, matrix biotite

3 independent reactions

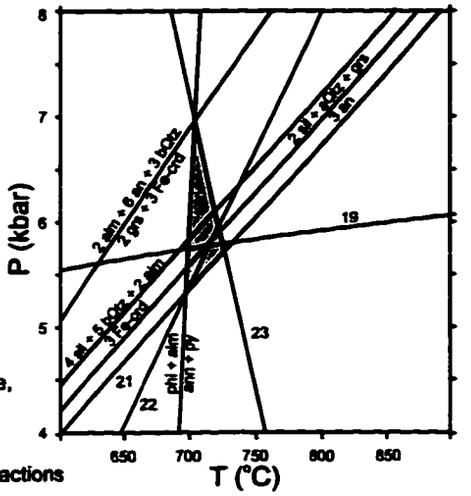

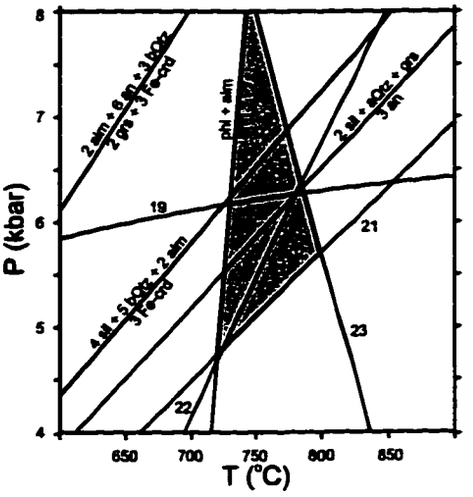

94-147d

left: garnet rim, contact biotite
right: garnet core, matrix biotite

3 independent reactions

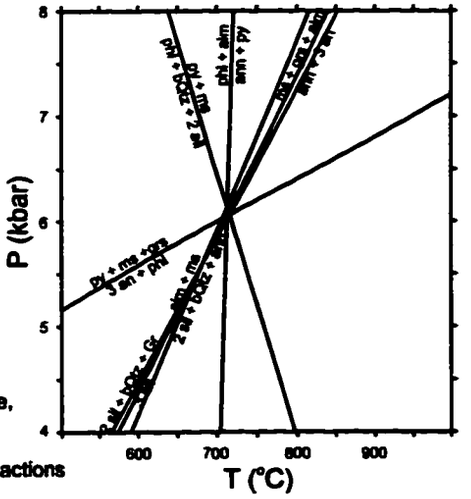

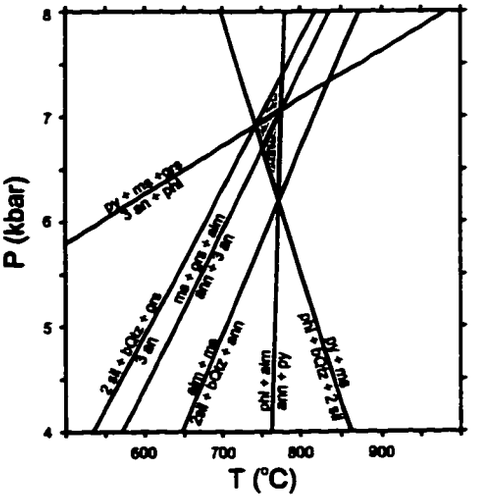

19: 4 sil + 5 bQtz + 2 py + 2 ann + 3 Fe-crd + 2 phl

21: 6 sil + 5 grs + 3 Fe-crd = 2 alm + 15 an

22: 3 Fe-crd + 5 grs + 2 phl + 6 sil = 2 py + 15 an + 2 ann

23: 3 bQtz + 2 py + 6 an + 2 ann = 3 Fe-crd + 2 grs + 2 phl

Appendix 4.10 (continued): Equilibria reactions calculated by TWQ 2.02 for cordierite-bearing biotite-quartz schist of the KMA.

19: 4 sil + 5 bQtz + 2 py + 2 ann + 3 Fe-crd + 2 phl

21: 6 sil + 5 grs + 3 Fe-crd = 2 alm + 15 an

22: 3 Fe-crd + 5 grs + 2 phl + 6 sil = 2 py + 15 an + 2 ann

23: 3 bQtz + 2 py + 6 an + 2 ann = 3 Fe-crd + 2 grs + 2 phl

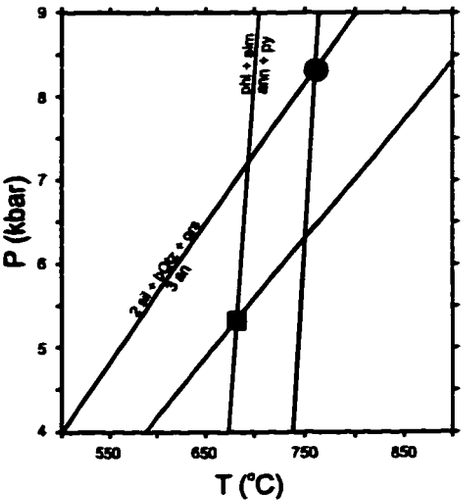

94-277d

square: garnet rim, contact biotite
circle: garnet core, matrix biotite

2 independent reactions

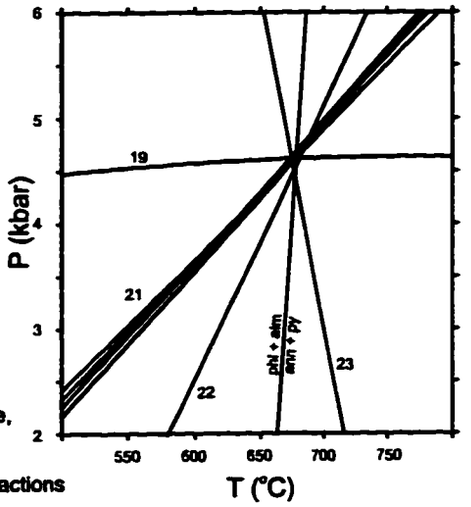

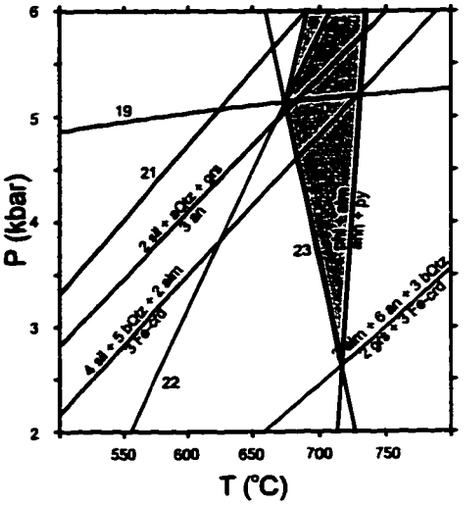

94-283a

left: garnet rim, matrix biotite
right: garnet core, matrix biotite

3 independent reactions

Appendix 4.10 (continued): Equilibria reactions calculated by TWQ 2.02 for cordierite-bearing biotite-quartz schist of the KMA.

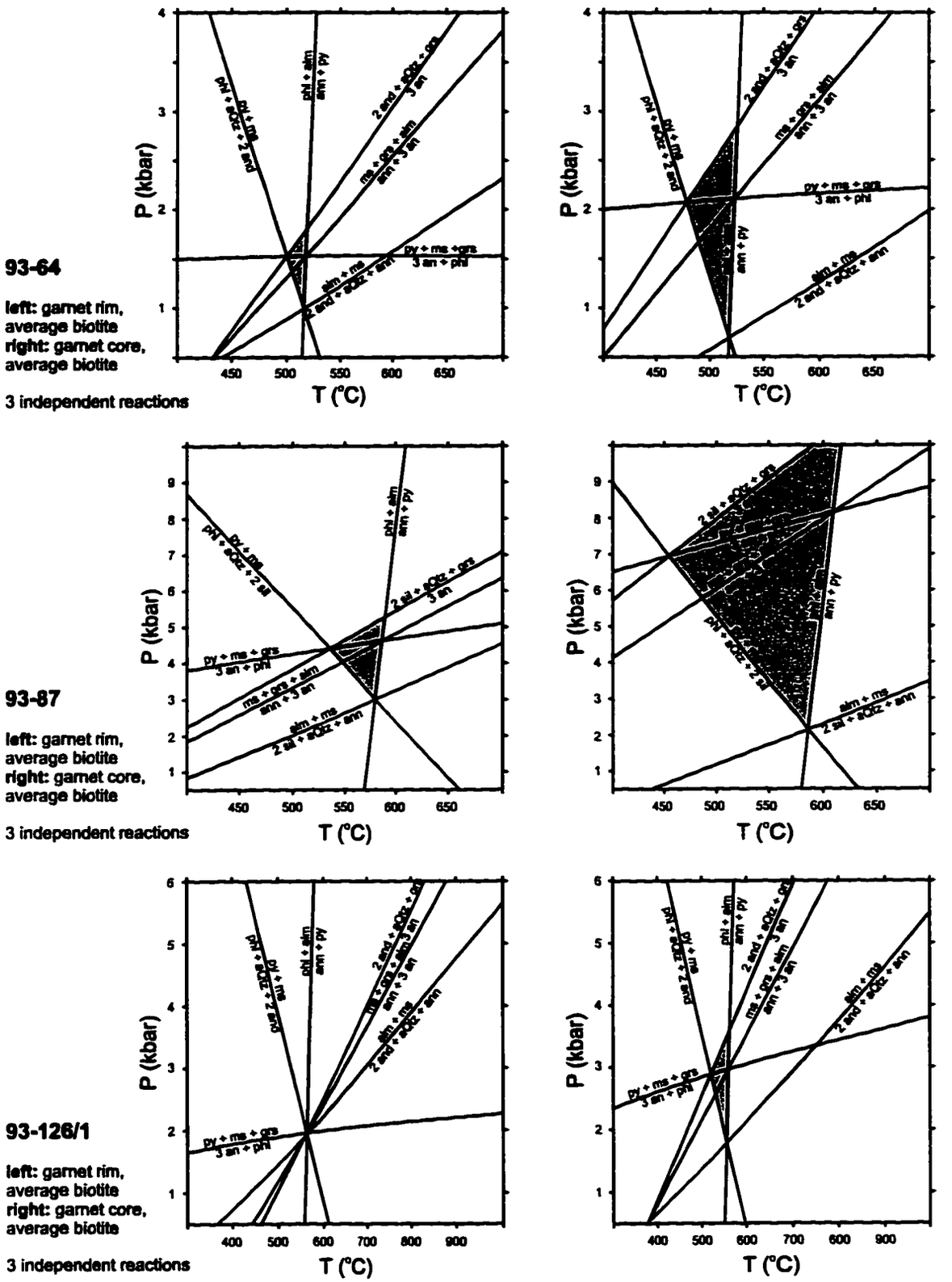

Appendix 4.10 (continued): Equilibria reactions calculated by TWQ 2.02 for staurolite bearing KMA biotite-quartz schist of the western Dezadeash Range (93-87) and the Killermun Lake area (93-64 and 93-126).

94-47

left: garnet rim, contact biotite
right: garnet core, average biotite

4 independent reactions

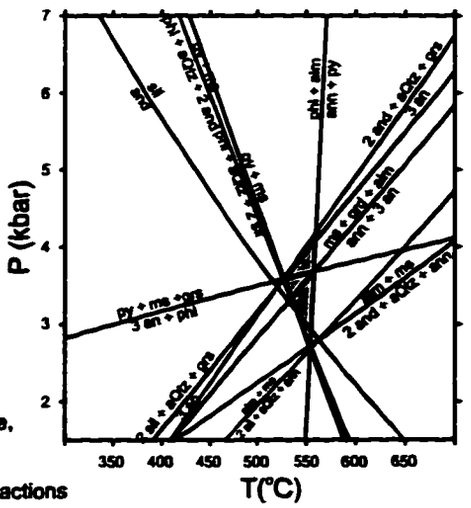

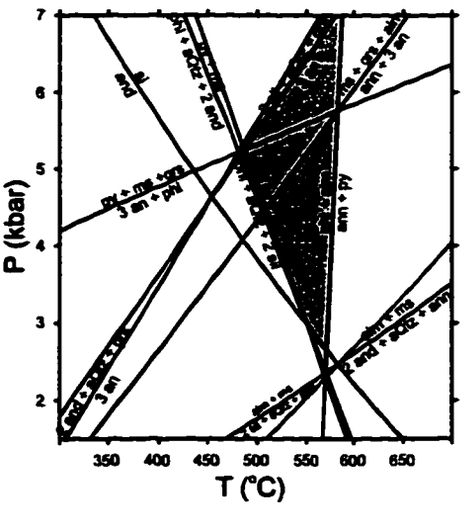

95-71

left: garnet rim, contact biotite
right: garnet core, average biotite

3 independent reactions

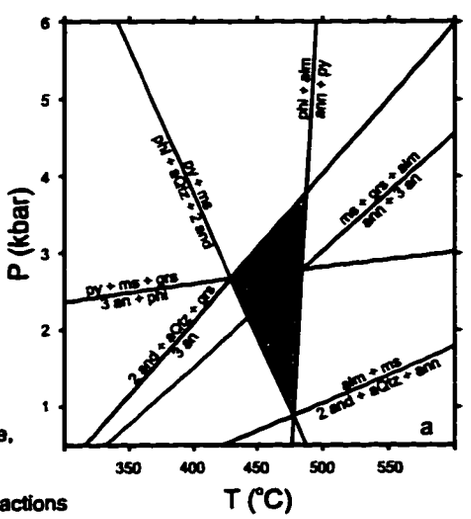

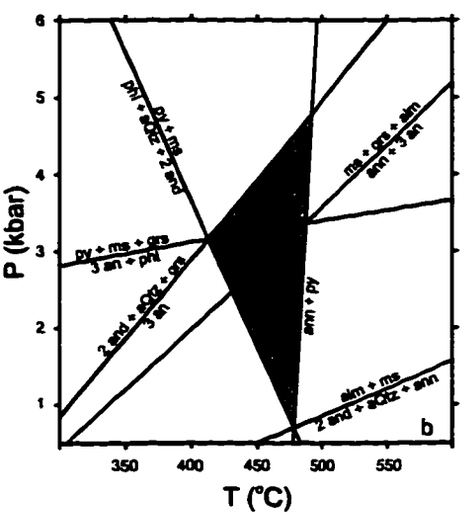

89-85a

square: garnet rim, average biotite
circle: average garnet, average biotite
upper right corner: garnet core, average biotite

2 independent reactions

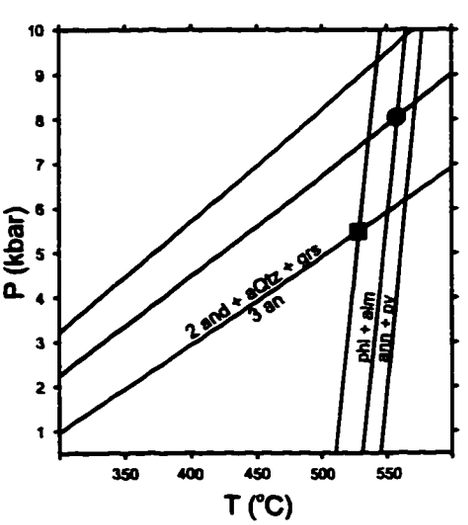

Appendix 4.10 (continued): Equilibria reactions calculated by TWQ 2.02 KMA biotite-quartz schist (staurolite-bearing, 94-47) of Gladstone Creek area and the western Kluane Hills (95-71, 89-85a).

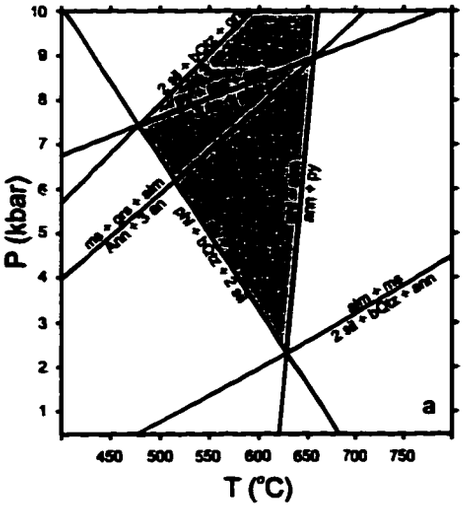

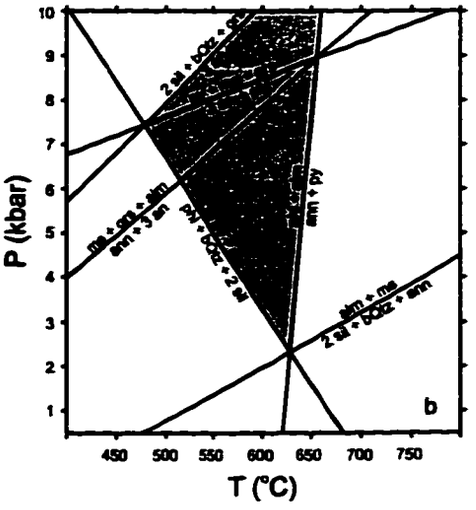

93-42

a) garnet core and average biotite, muscovite and plagioclase;
b) garnet rim, contact biotite and average muscovite and plagioclase;
c) garnet values from grossular poor zone close to rim, contact biotite, average muscovite and plagioclase.

3 independent reactions

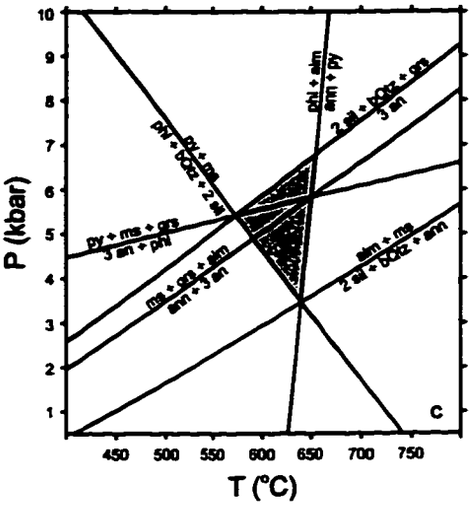

95-53b (lower left)

ma: matrix biotite values, average garnet
mc: matrix biotite values, core garnet
r1, r2, r3: specific garnet rim and contact biotite values
rr: garnet rim and contact biotite rim values

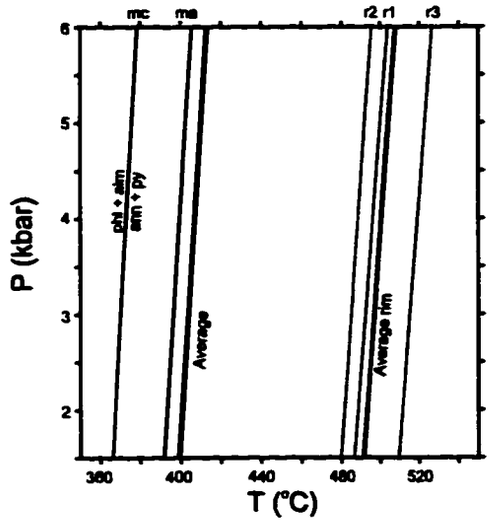

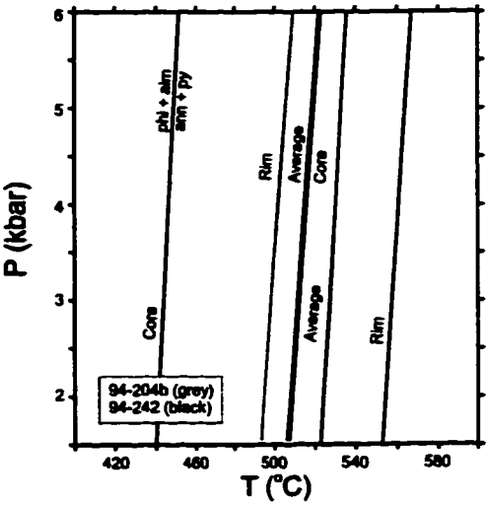

Appendix 4.10 (continued): Equilibria reactions calculated by TWQ 2.02 for mica-quartz schist of the AMS (93-42) and the Nasina Assemblage (95-53b) and phyllites of the DF (94-204b, 94-242).

Appendix 4-11: Compositional zoning profiles of garnets staurolite-free KMA biotite-quartz schist

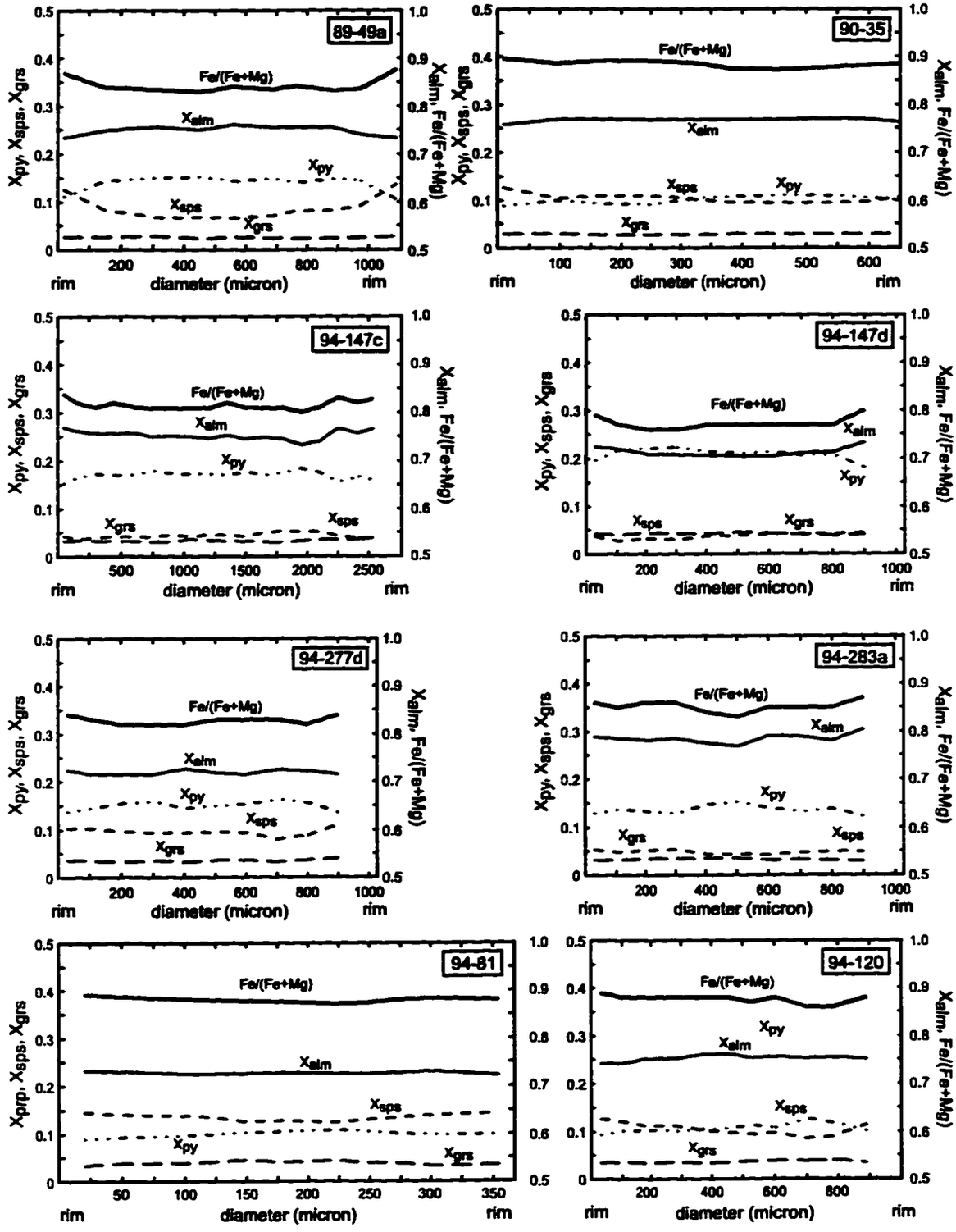

Appendix 4-11 (continued):

staurolite-bearing KMA biotite-quartz schist

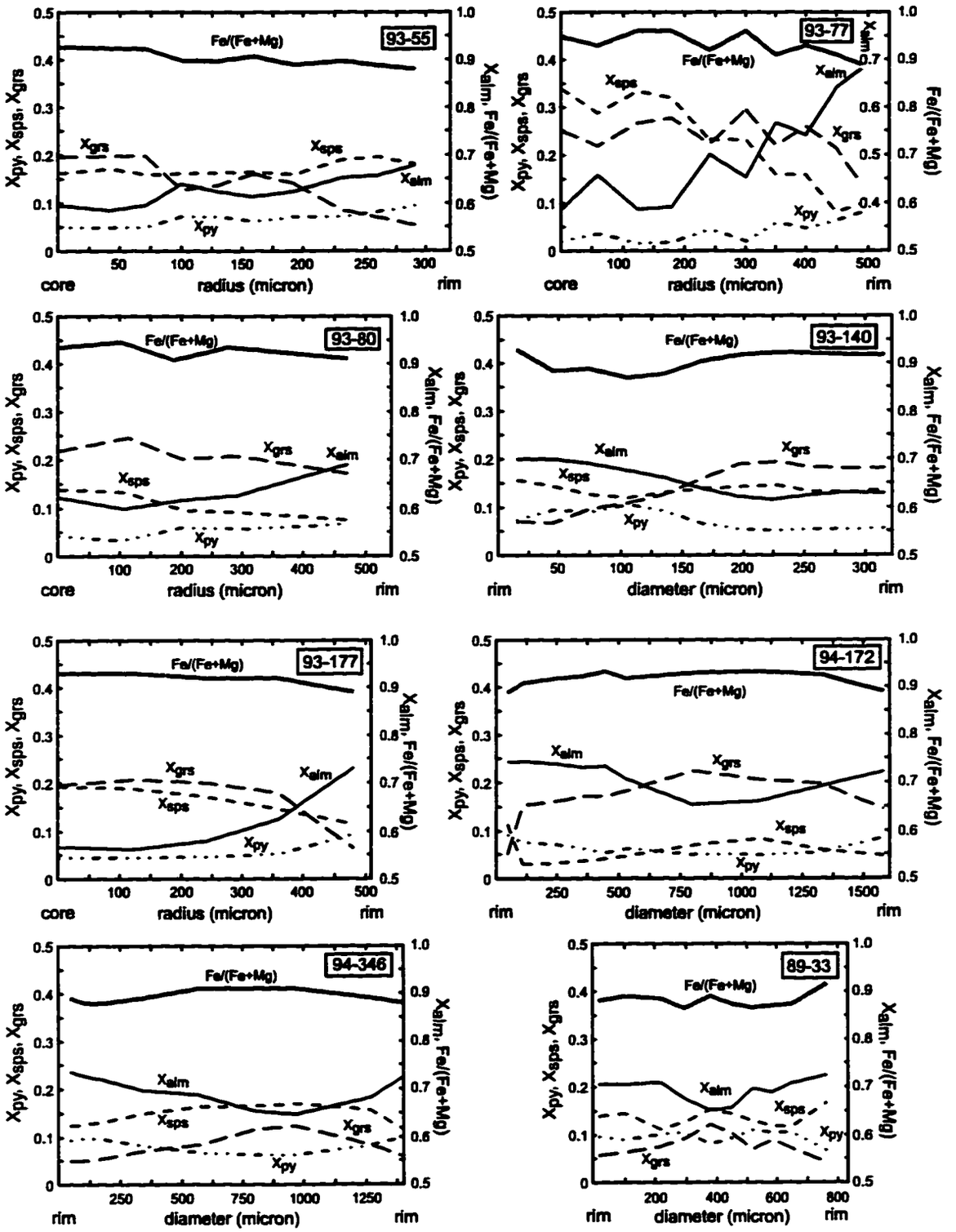

Appendix 4-11 (continued):

KMA biotite-quartz schist

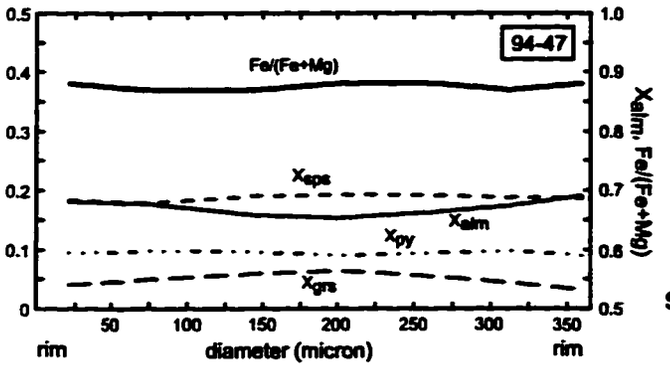

staurolite-bearing

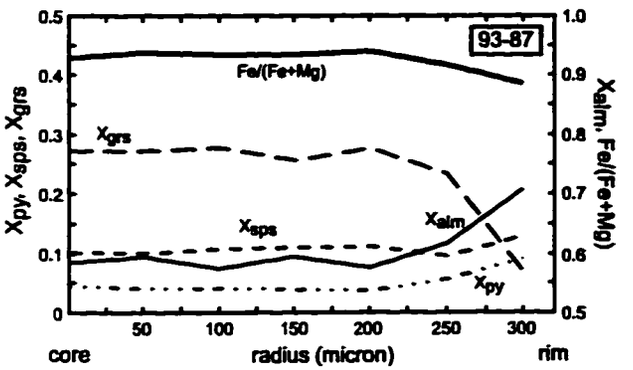

low P schist from
Killermun Lake intrusion

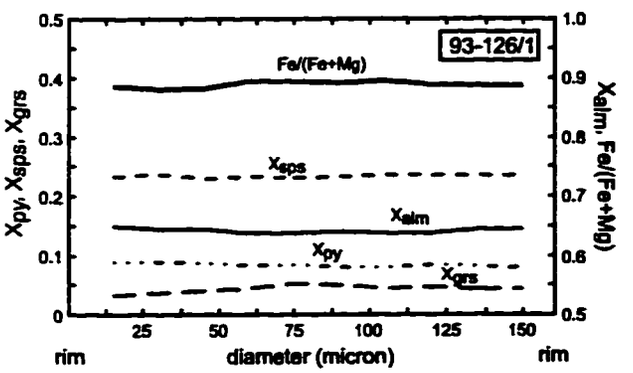

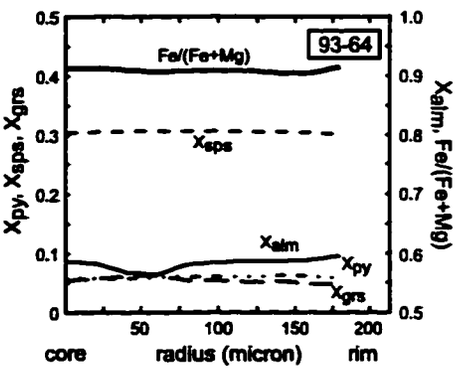

western
Kluane Hills

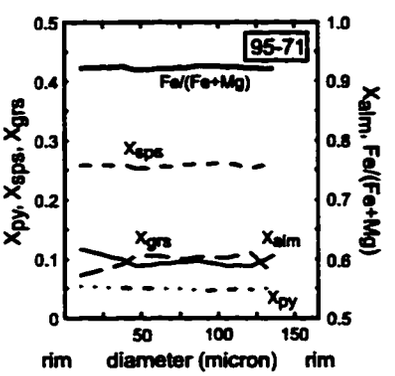

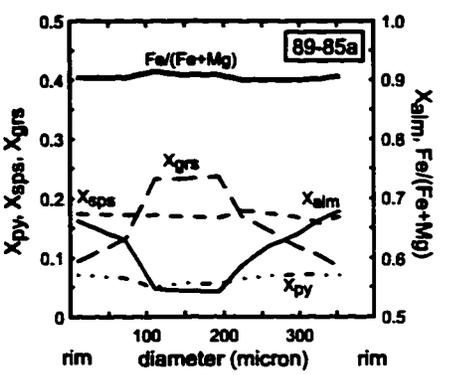

Appendix 4.11 (continued):

Pericratonic assemblages

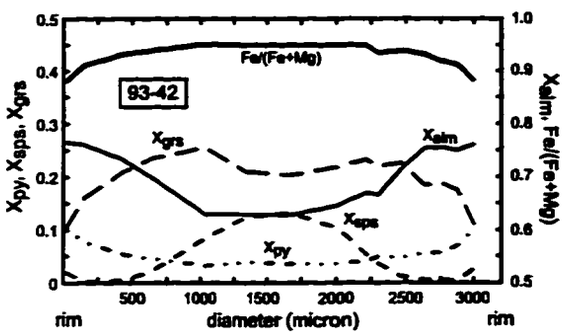

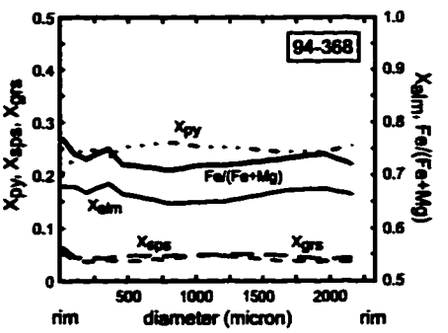

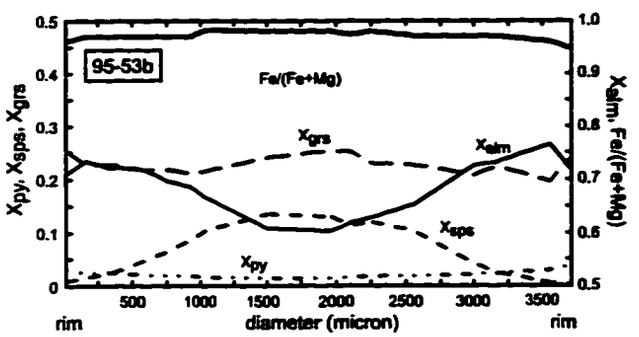

93-42: mica-quartz schist, Aishihik Metamorphic Suite, Aishihik Lake

94-368: micaceous quartzite, Nisling assemblage, east of Dezadesh Lake

95-53b: micaceous quartzite,Nasina Assemblage, north end of Talbot Arm, Kluane Lake

Island arc overlap assemblage: Dezadeash Formation

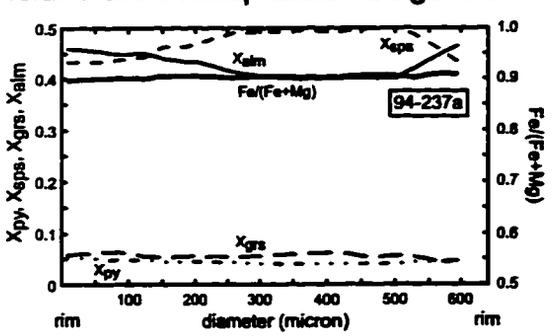

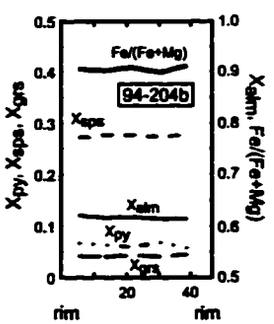

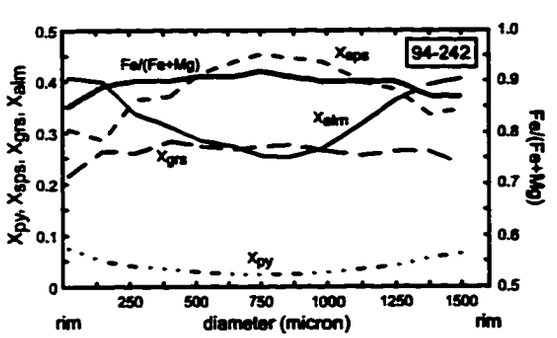

94-237a: slate, Tatshenshini River

94-204b: slate, Million Dollar Falls provincial campground

94-242: phyllite, Telluride Creek

Appendix 5-1: Descriptions and locations of samples analyzed for geochemistry and Nd, Sr, ^{40}Ar-^{39}Ar isotopes

sample	sample description[1]	longitude (W)	latitude (N)
major element geochemistry:			
Kluane metamorphic assemblage:			
90-39	graphitic ms-bt-qtz schist (al)	138°17'30"	60°06'15"
94-115	sil-bearing crd-bt-qtz schist (al)	137°22'30"	61°03'05"
94-387	graphitic and-bt-ms-qtz schist (al)	137°25'25"	60°50'10"
Nisling assemblage:			
94-358	crd-bearing ky-grt-bt-qtz schist	136°48'50"	60°30'10"
Sm/Nd:			
Kluane metamorphic assemblage:			
93-96	graphitic sil-grt-qtz schist (al)	136°56'36"	60°42'15"
93-136	graphitic grt-st-chl-ms-bt-qtz schist (al)	137°33'20"	61°03'35"
93-156*	graphitic ms-chl-qtz schist (ca)	138°16'00"	61°12'20"
94-36*	graphitic ms-chl-qtz schist (ca)	138°36'30"	61°14'10"
94-82	sil-bearing crd-bt-qtz schist (al)	137°01'10"	60°54'10"
94-272	bt-qtz schist (al)	136°46'20"	60°42'40"
94-297/1	orthoamphibole-bt-pl-qtz schist	136°42'00"	60°43'55"
94-346	grt-st-bt-qtz schist (al)	139°04'00"	61°26'12"
Dezadeash Formation:			
94-190	graphitic slate	137°02'40"	60°23'05"
94-204b	graphitic slate	136°56'30"	60°06'30"
Aishihik Metamorphic Suite:			
93-14	bt-ms-qtz schist (PAMqb)	137°29'00"	61°23'20"
93-16	sil-grt-bt-ms-qtz schist (PAMqb)	137°27'30"	61°23'00"
93-42	st-bt-grt-ms-qtz schist (PAMfs)	137°10'40"	61°23'45"
93-67	bt-ms-qtz schist (PAMqb)	137°28'20"	61°26'30"
Rb/Sr muscovite:			
94-17a	graphitic ep-bt-ms-chl-qtz schist (ca)	138°49'45"	61°23'30"
94-33	graphitic ms-chl-qtz schist (ca)	138°27'45"	61°10'40"
94-51	czo-ms-chl-qtz schist (ca)	138°33'15"	61°19'00"
94-173	and-ms-chl-bt-qtz schist (al)	137°53'50"	61°09'50"
Ar^{40}-Ar^{39}:			
94-3	cc-ms-chl-qtz schist (ca)	138°48'00"	61°19'00"

* denotes samples that were also analyzed for whole rock and muscovite Rb/Sr.

1: 'al' and 'ca' denotes aluminous and calcic schist of the KMA, 'PAMfs' and 'PAMqb' are units of the AMS after Johnston & Timmerman (1993a, b).

Appendix 5-2

Analytical procedures for geochemistry and Nd and Sr isotope studies

---

A suite of 11 samples of graphitic mica-quartz schist of the KMA, 2 slate samples of the DF, 4 mica-quartz schist samples of the AMS and one mica-quartz schist of the Nisling assemblage were selected for whole rock geochemical analyses. The DF and AMS samples along with 8 of the KMA samples were also analyzed for their Nd isotopic signature. Two KMA samples were analyzed for their Sr whole rock and muscovite signatures. Sr isotopes were also analyzed on two additional KMA samples. The samples are described in Appendix 5-1 and are shown on map on Figure 5-5.

Whole rock geochemistry:

The samples were crushed to gravel size avoiding contact with metal and subsequently grinded to ~35 micron using a tungsten carbide swing mill and an agate grinder. Major and trace elements were determined at the Washington State University by x-ray fluorescence (XRF) and inductively coupled plasma mass spectrometry (ICPMS), respectively, as described by Hooper et al. (1993).

Neodymium isotopic analyses:

Neodymium isotopic analyses were performed by the author at the University of Alberta. The following analytical procedure description is modified after Creaser et al. (1997). Sample powders were weighed, totally spiked with a ^{150}Nd-^{149}Sm tracer solution, and dissolved in 12 ml of a 5:1 mix of 24N HF and 16N HNO_3 in sealed teflon vessels at 160°C for ~120 hours. The solution was evaporated to dryness, 10 ml of 6N HCl was added to the residue heated at 160°C for 24 hours to dissolve fluorides. This solution was evaporated to dryness and dissolved in 6 ml of 0.75N HCl. After filtering to remove graphite the solution was centrifuged at 5000 rpm for 5 minutes. The REE were

separated as a group using standard cation chromatography. Borosilicate glass and polypropylene Bio-Rad Econo-Columns, containing 4.4 ml of a wet Bio-Rad AG50W-X8 cation resin with a mesh size of 200-400, were used. Subsequent separation of Nd from Sm was done by Di(2-ethylhexyl phosphate) chromatography (HDEHP), using heat-shrink TFE 4:1 (Zeus #164553, 7/8") columns with Bio-Rad BioBeads SX-8 (200-400 mesh) resin.

The purified Nd and Sm fractions were analyzed for isotopic composition using VG354 and Micromass MM30 mass spectrometers, respectively. Total procedural blanks for Nd and Sm are 0.5 ng. The ^{150}Nd-^{149}Sm tracer solution consists of highly purified ^{150}Nd (97.62 at.%) and ^{149}Sm (97.22 at.%), as determined by direct calibration in triplicate against a mixed Sm/Nd normal solution (Wasserburg et al., 1981) with a reproducibility of better than ±0.01% for ^{150}Nd and ±0.03% for ^{149}Sm concentrations. Isotopic analyses of Nd used a dynamic multicollector routine, correcting raw ratios both for variable mass-discrimination to ^{146}Nd/^{144}Nd = 0.7219 using an exponential law after Wasserburg et al. (1981) and for the effects of low abundance, non-^{150}Nd, tracer Nd isotopes. Sm was analyzed in static multicollector mode and corrections made both for variable mass-discrimination to ^{152}Sm/^{154}Sm = 1.17537 using the exponential law of Wasserburg et al. (1981), and for the effects of low abundance, non-^{149}Sm, tracer Sm isotopes on ^{152}Sm/^{154}Sm. During the course of this study a dissolution of the spiked standard rock BCR-1 yielded ^{143}Nd/^{144}Nd = 0.512634 ± 9 (ϵ_{Nd} = -0.1) and ^{147}Sm/^{144}Nd = 0.1378 and a spiked aliquot of the La Jolla Nd isotopic standard had a ^{143}Nd/^{144}Nd value of 0.511848 ± 8 after separation of Nd from spike Sm by HDEHP chromatography. These values are in good agreement with previous determinations of BCR-1 and La Jolla (Thirlwall, 1982, 1991; Makashima & Nakamura, 1991). Multiple analyses of an unspiked in-house Nd isotopic standard yielded an external reproducibility of ± 0.000016 (2σ), which is taken as the minimum uncertainty estimate of ^{143}Nd/^{144}Nd for the analyzed samples of this study. As an additional check of accuracy for Nd isotopic analyses, all totally spiked samples were monitored for recovered ^{145}Nd/^{144}Nd, which was

determined to be 0.348407 for the average of analyzed samples here. This value is also in good agreement with previous unspiked determinations of $^{145}Nd/^{144}Nd$, as reported in Thirlwall (1991).

Strontium isotopic analyses:

The samples that were also analyzed for Sr were spiked with a high-quality SRM988 spike with a $^{84}Sr/^{86}Sr$ value >1700. Rb and Sr were extracted separately from the sample during REE separation using the cation chromatography, as described in Nd analyses above, and evaporated to dryness. The residues containing Rb and Sr were taken up in an oxalic acid/HCl mix solutions, loaded on heat-shrink TFE 4:1 (Zeus #164553, 7/8") columns with wet Bio-Rad AG50W-X8 cation resin (mesh size: 200-400) and cleaned from oxalic acid by using HCl. The purified Rb and Sr fractions were analyzed for isotopic composition using Micromass MS30 and VG354 mass spectrometers, respectively.

Muscovite separation was done separately from the above described procedures for whole rock samples. The sample material was crushed to grain size (0.5-1 mm) in a manual metal crusher and agate mill. Mineral separation was done by shaking sample material over filter paper, followed by using a Frantz magnetic separator and subsequently by heavy liquid fractionation with Sodiumpolytungstate (STP). The resulting fraction was highly enriched in muscovite (>98 vol.%). X-ray diffractionation (XRD) recorded minute amounts of chlorite, quartz and graphite. Rb and Sr were separated from muscovite by using the same analytical procedures as described above, except that the spike used was a ORNL spike with a $^{84}Sr/^{86}Sr$ value of ~460.

Appendix 5-3: Neodymium studies in the North American Cordillera

Reference	Terrane affinity	Location	Rock type[a]	Age (T)	$\varepsilon_{Nd}(0)$	$\varepsilon_{Nd}(T)$	T_{DM}	Conclusion
McCulloch & Wasserburg (1978)	YTT	Alaska Range	Birch Creek schist (qtz-serizite schist) (1) greenschist f.	late Precambrian	-27		2.33 Ga	Precambrian source from the Canadian shield
Aleinikoff et al. (1981)	YTT	Yukon Tanana Upland	augengneiss (1)	345 Ma		-20	1875 Ma	Crustal contamination of Proterozoic age
Farmer et al. (1987)	YTT	central-southcentral Alaska (TACT route)	monzogranites (7) tonalite (1)	Cretaceous	-2.7	-14.1 to -8.9	1.8 Ga	partly derived from felsic continental crust
Arth et al. (1988)	Taku, CMB	Ketchikan, SE Alaska	Taku tonalites (3) granites (2) CMB granodiorites (4)	89 - 135 Ma 20 Ma 53 - 55 Ma	-1.3 to -0.7 -2.1 to +0.3 -5.8 to -3.7		Taku and CMB have different intrusion history prior to Mid Tertiary	
Bennett & Hansen (1988)	YTT	eastern Alaska southern Yukon	orthogneiss (10)	Devonian-Mississippian	-16 to -14		2-2.3 Ga	Precambrian crustal source; YTT has remained same position relative to ancestral NA.
Samson et al. (1989)	ST, AX	SE Alaska	AX (28) igneous rocks sediments	90-560 Ma 140-560 Ma	-1.3 to +10.3 -3.8 to +3.0	+3.3 to +9.7 0.0 to +5.0	ST and AX crust are completely juvenile, mantle derived material.	
			ST (22) igneous rocks sediments	65-400 Ma 155-270 Ma	-1.7 to +7.2 -0.2 to +5.7	-0.4 to +7.7 +1.3 to +6.3		
Samson et al. (1990a)	YCT Taku (TT)	Taku Inlet - Prince Rupert (SE Alaska)	YCT (48) TT	Permian-Triassic	as low as -26 -4.6 to +4		1.1-2.45 Ga	YCT more evolved than ST, WR and AX (modern arc)
Samson et al. (1990b)	WR	Vancouver and Queen Charlotte Islands Chilkat Penninsular	igneous rocks clastic sediments (31)	90-420 Ma	-1.1 to +7.5 -1.7 to + 5.7	+2.9 to +7.3 +1.0 to +7.0	340-860 Ma	WR completely juvenile, mantle derived material.

Appendix 5-3 (continued):

Reference	Terrane affinity	Location	Rock type*	Age (T)	$\epsilon_{Nd}(0)$	$\epsilon_{Nd}(T)$	T_{DM}	Conclusion
Jackson et al. (1990)	Northern CC	W of Teslin Lake (southern Yukon)	sandstone (NST) (5) argillites (NCC) (2)	Triassic	0 to +5 -9		NST derived from modern arc NCC of continental origin deposited on oceanic environment, no volcanic detritus	
Andrew et al. (1991)	WR	Vancouver Island	intrusive and volcanic rocks (27)	50 -370 Ma	-1 to +9.4	+2.6 to +9.4	Variety of magma sources from strongly to moderately depleted through time underlying WR	
Samson et al. (1991a)	CMB	SE Alaska	CMB foliated granodiorite (13) Tonalite (3)	55 - 83 Ma 220-336 Ma	-3.5 to -0.7 -6.8 to -2.6	-0.2 to -3.0 - 4.7 to +1.5	620-1070 Ma 760-1260 Ma	no correlation with age, lithology and geographic location; mixture of Early Proterozoic crust and younger juvenile crust YTT is probable source of CMB
Samson et al. (1991b)	Gravina Belt Taku, YTT	Taku Inlet - LeConte Bay (SE Alaska)	Gravina Belt (7) (seds / volcanics)	Jurassic - Cretaceous	-2.1 to +7.6	-1.1 to +8.3	100-900 Ma	juvenile belt formed in arc basins within AX
			Pluton intruding Gravina Belt (3)	mid-Cretaceous	+3.6 to +4.9	+4.4 to +3.3	320-350 Ma	mantle derived melts incorporating AX crust
			Taku (8) metased,sediment Intrusive (1)	Permian - Triassic	-5.5 to +3.3 +4.1	+5.1	440-1430 Ma 330 Ma	less juvenile than AX, WR, ST
			Metamorphic assemblages (amphibolite grade) east of Taku Terrane (36) a) Tracy Arm (quartzite, bt-gneiss) b) Endicott Arm (metased./metavolc.) c) Port Houghton (quartzite, bt-schist) d) Ruth (sandstone, bt-schist, bt-gneiss)		? ? Permian ?	-26 to +0.5 -10 to +1.2 -9.4 to -2.4 -9.4 tp +2.0	800-2450 Ma 910 Ma 390-660 Ma 1.4-1.6 Ga	substancial Precambrian crustal componen

Appendix 5-3 (continued):

Reference	Terrane affinity	Location	Rock type[a]	Age (T)	$\epsilon_{Nd}(0)$	$\epsilon_{Nd}(T)$	T_{DM}	Conclusion
Jackson et al. (1991)	Nisling ST	Wilson Bay, Atlin Lake (N British Columbia)	Nisling Terrane (3) a) Boundary Range b) Florence Range	Palaeozoic ?	 -2.4 -20 to -15.6		 910 Ma 1.77-2.45 Ga	older crustal material in basal unit indicates upper Triassic link between ST and Nisling terranes
			Northern Stikine (7) Laberge Group Stuhini Group basal clastic unit	 Jurassic Triassic	 -2.2 -1.0 to +4.7 -12.7 to -10	 -0.5 +1.3 to +6.1	 920 Ma 390-660 Ma 1.4-1.6 Ga	
			Intrusives: gabbro, granodiorite (5)	Triassic Cretaceous	+1.5 to +7.4 -2.1 to -2.6	+4.0 to +6.9 -1.8 to -1.3	490 Ma 710-770 Ma	
Marcantonio et al. (1993)	WR	Quill Creek Intrusive Complex (Kluane Lake SW Yukon)	ultramafic (3) gabbro (5)	232 Ma	+2 to +2.75 +0.5 to +2.2	+2.9 to +4.5 +2 to +3.5		mafic/ultramfic intrusions partly contaminated by Permian shales and sandstones
Creaser et al. (1996)	YTT	Teslin Tectonic Zone, south central Yukon	Nisutlin assemblage (metasediments) (14)	pre-Early Missippian (350 Ma)	-7.2 to +0.5 -6.9 to -17.9 -24 to -28.4	-3.9 to +3.4 -3.7 to -14.3 -20 to -24.3	0.93-1.33 Ga 1.47-2.25 Ga 2.45-2.78 Ga	detrital input from proximal arcs and distal NA craton, TTZ rocks located on outermost margin of ancient NA

a: numbers in parenthesis indicate numbers of analysed samples
AX: Alexander terrane; CC: Cache Creek terrane; CMB: Coast Mountain Batholith; ST: Stikine terrane; WR: Wrangellia terrane; YCT: Yukon Crystalline Terrane; YTT: Yukon Tanana Terrane

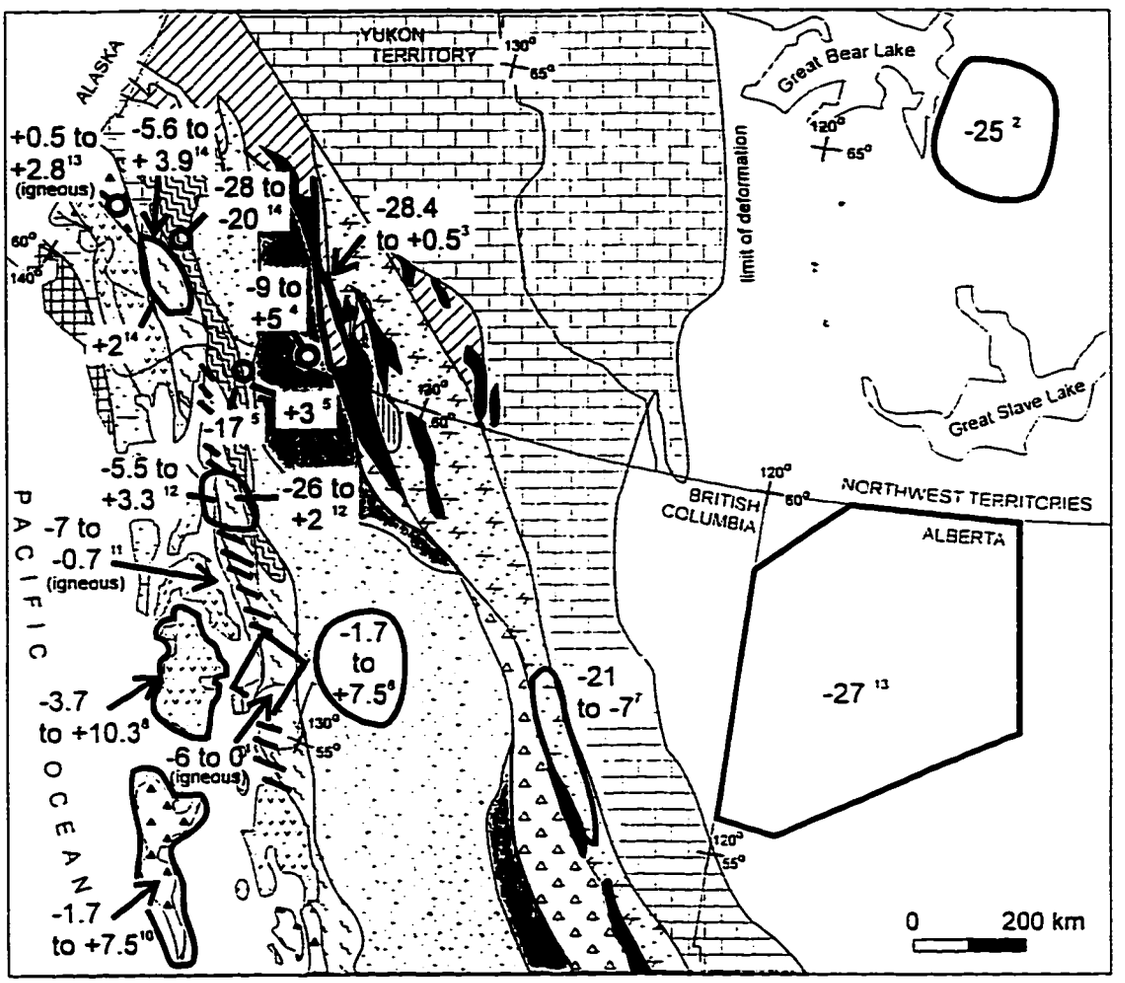

Appendix 5-4: Generalized terrane map (modified after Wheeler et al., 1991) with the location of all published neodymium data including this study. The numbers refer to $\epsilon_{Nd}(0)$-values. Smaller numbers indicate references. 1: Arth et al. (1988), 2: Bowring & Podosek (1989), 3: Creaser et al. (1997), 4: Jackson et al. (1990), 5: Jackson et al. (1991), 6: Marcantonio et al. (1993), 7: Ross et al. (1995), 8: Samson et al. (1989), 9:Samson et al. (1990a), 10: Samson et al. (1990b), 11: Samson et al. (1991a), 12: Samson et al. (1991b), 13: Thériault & Ross (1991), 14: this study.